Novel thienyl dyes

And

Related metal carbonyl complexes

This thesis is presented for the degree of

Doctor of Philosophy

By

Nicola Boyle B.Sc.

Under the supervision of

Dr. Mary Pryce

At

Dublin City University

School of Chemical Sciences

January 2011

<u>Declaration</u>

I hereby certify that this material, which I now submit for assessment on the programme of study leading to the award of Doctor of Philosophy is entirely my own work, that I have exercised reasonable care to ensure that the work is original, and does not to the best of my knowledge breach any law of copyright, and has not been taken from the work of others save and to the extent that such work has been cited and acknowledged within the text of my work.

Signed: _____   Student number: _____

Date: _____

Dedication

To the memory of my parents

<u>Acknowledgements</u>

smiley face). And Zoe – Master of the analogy – never stop the comparisons. Thank you to you all for listening to the Friday speech ("Next week, I'm going to start……") so often over the past few years and for bearing with me while I was writing up. I feel some days I may have made Lynda Blair look normal! I have very fond memories of our extended lunches and slagging matches and not so many memories of our Ivy house days and nights out. Thank god for the photo keyrings in McGowans!

Outside the lab, I owe my gratitude to many people as well. To all my friends, (who shall remain nameless!) you know who you are. Thanks for reminding me that chemistry isn't the be all and end all when social occasions called – and there were quite a few over the years! Also, thank you for encouraging me to work hard in the final stages of my research, when chemistry was the be all and end all. A special word of thanks to Bernie for the constant reminders to have a "PMA all the way" and for the fun times – Friday club in Holland? And to Melissa, you know too much for us not to be friends!!! Its 12 years since the Hallmark days and I wouldn't be surprised if you recount every adventure we've taken in those years. I was told once that we are lucky in life if we have two or three people that we can call true friends – you girls fulfill that role for me. There is a whole other world outside of college and I am delighted to have shared it with all you guys. Now that I am nearing the finishing post - and I hope I'm not being too presumptuous when I say this – stick the champers on ice!!!

To my family, Finola, Jason and Mark, you each played a very important role in my life over the last 6 years. I never would have got through it without you and appreciate everything you have done for me. Finola, my godmother, thanks for the support you gave me over the years and for all the Saturdays spent mooching in the Marshes. Jason, thanks for being an unwavering support to me – you are my rock (thanks for keeping me fed too!). Mark, thanks for so many things but most of all, the advice - "the world is a tough place, you need to toughen up little girl" – and I really am now. We shall celebrate in style when the time comes.

It feels strange writing these acknowledgements; at many times I felt I would never make it. However, you all in your own way have made this happen for me and I will never forget it. Thank you.

<u>Quotation</u>

However, until a chemist has separated a gram of porphyrin by column chromatography and seen the purple lustrous crystals made by his or her own hands (and split all over their bench and lab coat, or over the inside of their rotary evaporator), then they really cannot say they've worked with porphyrins.

The Colours of Life

Lionel R. Milgrom

Table of Contents

Publications

- M. Klok, **N.M. Boyle**, M.T. Pryce, A. Meetsma, W.R. Browne, B.L. Feringa, "MHz unidirectional rotation of molecular motors", *J. Am. Chem. Soc.*, **2008**, 130, 10484.

- M.A.H. Alamiry, **N.M. Boyle**, C.M. Brookes, M.W. George, C. Long, P. Portius, M.T. Pryce, K.L. Ronayne, X.Z. Sun, M. Towrie, K.Q. Vuong, "Unusually slow photodissociation of CO from $(\eta^6\text{-}C_6H_6)M(CO)_3$ (M = Cr or Mo): A time-resolved infrared, matrix isolation and DFT investigation", *Organometallics*, **2009**, 28, 1461.

- **N.M. Boyle**, J. Rochford, M.T. Pryce, "Thienyl porphyrins – synthesis, photophysics and applications", *Coord. Chem. Rev.*, **2010**, 254, 77.

- A.C. Coleman, **N.M. Boyle**, C. Long, R. Augulis, A. Pugzlys, P.H.M. van Loosdrecht, W.R. Browne, B.L. Feringa, K.L. Royayne, M.T. Pryce, "Optically induced *cis-trans* isomerisation of $(\eta^6\text{-}cis\text{-stilbene})Cr(CO)_3$", *Dalton Trans.*, **2010**, 39, 2201.

- **N.M. Boyle**, A.C. Coleman, C. Long, K.L. Ronayne, W.R. Browne, B.L. Feringa, M.T. Pryce, "Evidence of cobalt-cobalt bond homolysis and wavelength dependent CO loss in $(\mu_2\text{-alkyne})Co_2(CO)_6$", *Inorg. Chem.*, **2010**, 49. 10214.

Abstract

Chapter one serves as an introduction to the principles and methods used throughout this thesis. The principles of photophysics are discussed generally and also in relation to porphyrins and dipyrromethenes. Potential applications for the novel thienyl dyes and related metal carbonyl complexes synthesised are then presented. This is followed by an outline of the techniques of laser flash photolysis, time-resolved infrared (TRIR) spectroscopy and time correlated single photon counting.

Chapter two involves the study of thienyl porphyrins. This chapter begins with a literature survey on the synthesis, photophysics and electrochemistry of thienyl porphyrin systems. The synthesis of the porphyrins studied is given, followed by their photophysical and electrochemical properties. The effect of the thienyl moiety on the ground state and excited state properties of the porphyrin macrocycle is examined

Chapter three commences with a general introduction to Sonogashira-Hagihara type cross coupling reactions and is followed by a literature survey on the synthesis and photochemistry of thienyl based organometallic systems. The synthesis of the novel systems produced for this study is then described and the photophysical properties are examined. Electrochemical data are also presented. The photochemistry of the $Co_2(CO)_6$ complexes are examined by steady state photolysis in the presence of a trapping ligand. Three of the complexes were studied by TRIR on a picosecond timescale and the quantum yields of CO loss were determined at a range of excitation wavelengths.

Chapter four commences with a literature survey focusing on the photophysics of pyridyl porphyrins and related organometallic systems. The synthesis of the monopyridyltriphenyl porphyrin and metal carbonyl derivatives produced for this study is described. The photochemistry of the complexes was examined by pump and probe TRIR spectroscopy on a picosecond timescale.

Chapter five contains with a short literature review on the synthesis and photophysics of dipyrromethanes and dipyrrin compounds. The synthesis of a series of substituted thienyl dipyrromethanes, related dipyrrin complexes and corresponding dicobalt complexes is presented. Preliminary photophysical measurements are discussed.

Finally chapter six discusses future work for chapters 3, 4 and 5.

Abbreviations

PS_I / P_{700}	Photosystem I
PS_{II} / P_{680}	Photosystem II
Chl	Chlorophyll
OEC	Oxygen evolving complex
Pheo	Pheophytin
$NADP^+$ / NADPH	Nicotinamide adenine dinucleotide phosphate
ATP	Adenosine triphosphate
LF	Ligand Field
IL	Intra Ligand
CT	Charge Transfer
MLCT	Metal to Ligand Charge Transfer
LMCT	Ligand to Metal Charge Transfer
CTTS	Charge Transfer to Solvent
HOMO	Highest Occupied Molecular Orbital
LUMO	Lowest Unoccupied Molecular Orbital
BODIPY	Borondifluoride dipyrromethene
$^3O_2$	Ground state oxygen
$^1O_2$	Singlet excited state oxygen
PDT	Photodynamic therapy
ALA	δ-Aminolevulinic acid
TDPH	Tetrapyrrole-dependant photodynamic herbicides
CO-RM	Carbon Monoxide Releasing Molecule
TRIR	Time resolved infrared
TRrR	Time resolved resonance Raman
TC-SPC	Time correlated single photon counting
TAC	Time to amplitude convertor
PM1/2	Photomultiplier ½
MCA	Multichannel pulse analyser
ZnTPP	Zinc tetra phenyl porphyrin

ZnTThP	Zinc tetra thienyl porphyrin
FWHM	Full width half maximum
IRF	Instrument response function
SCE	Saturated calomel electrode
STM	Scanning Tunneling Microscopy
ITO	Indium tin oxide
TEM	Transmission emission spectroscopy
AFM	Atomic force microscopy
DM-β-CD	Dimethoxy-β-cyclodextrin
TM-β-CD	Trimethoxy-β-cyclodextrin
$O_2^{\cdot-}$	Superoxide anion radical
IPCE	Incident photon-to-current efficiency
η_{max}	Maximum power conversion efficiency
TM-SFM	Tapping-mode scanning force microscopy
fs-HRS	Femtosecond – hyper Rayleigh scattering
β	Molecular first hyperpolarisability
NMR	Nuclear magnetic resonance
FT-IR	Fourier transform – infrared
ppm	Parts per million
J	Coupling constant
NLO	Non linear optics
OTE	Oligo(2,5-thienylethynylene)
ICT	Intramolecular charge transfer
H_{ECC}	Effective conjugation length
R_g	Radius of gyration
PL	Photoluminescence
ETB	1,4-bis(2-ethynyl-3-thienyl)benzene
CAS	Complete active space
DFT	Density functional theory
QTAIM	Quantum theory of atoms in molecules
BCP	Bond critical point

f$_4$fos	1,2-Bis(diphenylphosphino)tetrafluorocyclobutene
f$_6$fos	1,2-Bis(diphenylphosphino)hexafluorocyclopentene
f$_8$fos	1,2-Bis(diphenylphosphino)octafluorocyclohexene
f$_4$AsP	1,1-Diphenylphosphino-2-dimethylarsino-tetrafluorocyclobutene-1
dab	*N,N'*-Di-*tert*butylethylenediimine
dppm	Bis(diphenylphosphino)methane
dppe	1,2-Bis(diphenylphosphino)ethane
dppf	1,1-Bis(diphenylphosphino)ferrocene
DCE	1,2-Dichloroethane
D-π-A	Donor – π – Acceptor
PKR	Pauson Khand reaction
PhCCPh	Diphenylacetylene
PhCCPh-Co$_2$(CO)$_6$	Diphenylacetylene dicobalt hexacarbonyl
FcCCH	Ethynylferrocene
FcCCH-Co$_2$(CO)$_6$	Ethynylferrocene dicobalt hexacarbonyl
MPyTPP	Monopyridyltriphenyl porphyrin
c-DPyDPP	*cis*-Dipyridyldiphenyl porphyrin
t-DPyDPP	*trans*-Dipyridyldiphenyl porphyrin
TrPyMPP	Tripyridylmonophenyl porphyrin
TPyP	Tetrapyridyl porphyrin
EnT	Energy transfer
bpy	Bipyridine
EPR	Electron paramagnetic resonance
TRVIS	Time Resolved visible absorbance spectroscopy
GC-MS	Gas chromatography – mass spectrometry
BODIPY	Borondifluoride dipyrrin

Chapter 1

Introduction

Chapter one serves as an introduction to the principles and methods used throughout this thesis. The principles of photophysics are discussed generally and also in relation to porphyrins and dipyrromethenes. Potential applications for the novel thienyl dyes and related metal carbonyl complexes synthesised are then presented. This is followed by an outline of the techniques of laser flash photolysis, time-resolved infrared (TRIR) spectroscopy and time correlated single photon counting.

1.1 Principles of photophysics

The absorbance of a photon of light, with energy $h\nu$, by a molecule generally causes a valence electron in the absorbing species to be promoted to an orbital of higher energy and results in the formation of an electronically and vibrationally excited state of that particular species (Rxn. 1). This excited state species can then decay back to the ground state through spontaneous emission (Rxn. 2) or through stimulated emission (Rxn. 3). The spontaneous downward transition of an excited state electron can occur by emission of light (radiative decay) or by conversion of the excess energy into heat (non-radiative decay).

Rxn. 1 $\qquad\qquad\qquad$ $M + h\nu \rightarrow M^*$

Rxn. 2 $\qquad\qquad\qquad$ $M^* \rightarrow M + h\nu$

Rxn. 3 $\qquad\qquad\qquad$ $M^* + h\nu \rightarrow M + 2h\nu$

These ground and excited "states" are defined by the distribution of all nuclei and all electrons within the molecule, the wave function of the molecule. Electrons have much less inertia than nuclei; consequently they can adjust their position and motion almost instantaneously. Since the motions of electrons in orbitals are much more rapid than nuclear motion, electronic and nuclear motions can be treated separately in terms of an approximate wave function. This separation of nuclei and electrons is known as the Born-Oppenheimer approximation and assumes that the heavy nuclei remain motionless while the light electrons move around them.

Electronic motions occur at a faster timescale ($< 10^{-13}$ s) than nuclear motion ($10^{-11} - 10^{-13}$ s); as a result nuclei remain essentially stationary during an electronic transition (absorbance or emission). This is the Franck-Condon principle.[1] For this reason when a molecule in its ground state absorbs a photon it forms a metastable excited electronic configuration (Franck-Condon excited state) where the nuclear geometry is characteristic of the ground state. Following the production of this Franck-Condon excited state, rapid

vibrational relaxation to the lowest vibrational level of the electronic excited state occurs producing a thermally and vibrationally equilibrated excited state on a time scale of the order 10^{-12} s. This equilibrated excited state is known as a *"thexi"* state. *Thexi* states have a definite chemical structure, chemical reactivity and absorbance spectrum and hence can be considered as excited state isomers of the ground state.

There are several relaxation pathways by which such *thexi* states can return to their ground state and knowledge of these pathways is essential to understanding the photophysics and photochemistry of the molecule. On formation of the high energy singlet (S_n) or *thexi* state vibrational relaxation can occur to a lower excited state by internal conversion or intersystem crossing. Internal conversion is the non-radiative relaxation to a lower excited state and occurs between states of the same multiplicity ($S_n \rightarrow S_1$, $S_1 \rightarrow S_0$, and $T_n \rightarrow T_1$, where n > 1). Intersystem crossing is the non-radiative decay between two states of different multiplicity ($S_1 \rightarrow T_1$).

Radiative decay to the ground state (luminescence) can also take place when an excited state molecule loses its excitation energy as a photon of light. This emission of light occurs as either fluorescence or phosphorescence. Fluorescence is caused by the decay between states of the same multiplicity ($S_1 \rightarrow S_0$), whereas phosphorescence is a result of decay between states of different multiplicity ($T_1 \rightarrow S_0$). In accordance with Kasha's rule, emission occurs only from the lowest energy excited state of the molecule. Therefore, as with the initial Franck-Condon excited state, vibrational relaxation to the lowest energy excited state must occur by rapid internal conversion before emission can proceed.[2] It is the efficiency with which internal conversion or intersystem crossing takes place that controls the type of emission. Differentiation between the two luminescence processes is possible as each emission occurs on a different timescale.[1] These transitions are illustrated in figure 1.
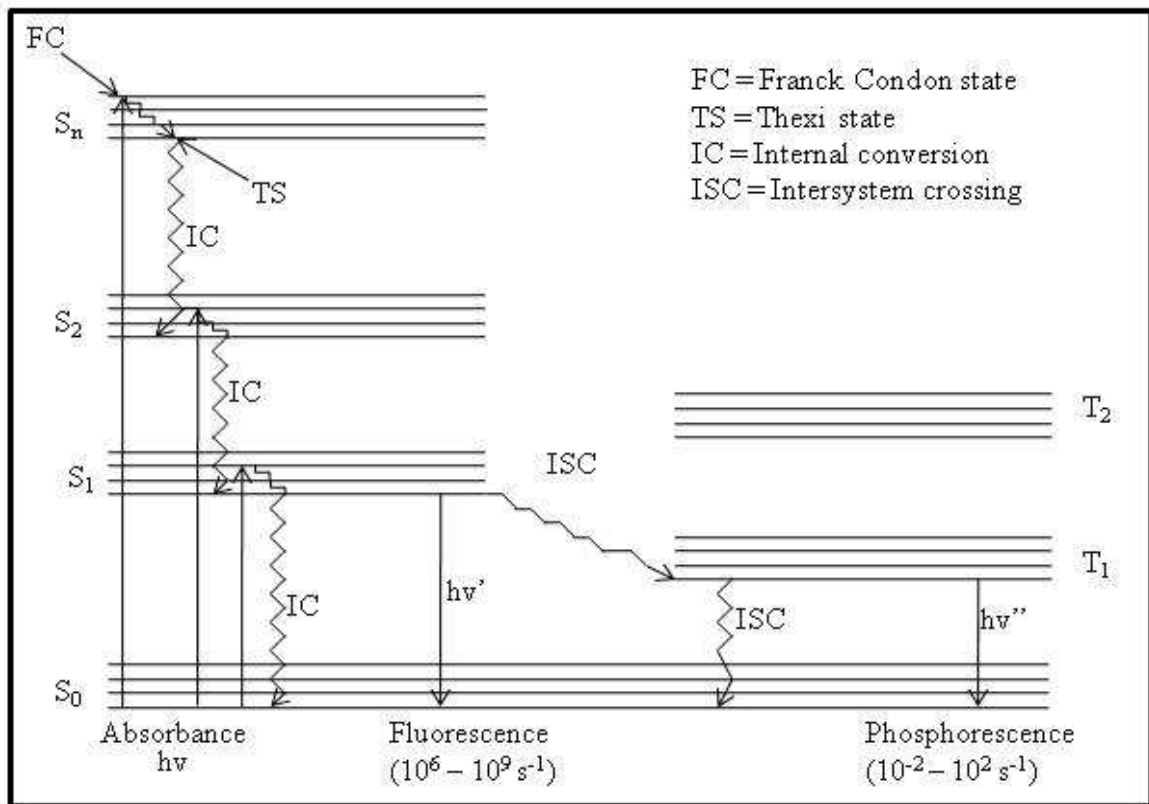
Figure 1   Jablonski Diagram

As emission from the $S_1 \rightarrow S_0$ level is spin allowed fluorescence is spontaneous and short lived with lifetimes generally in the range 1 ps – 1 μs. Vibrational relaxation to the first excited singlet state prior to emission consumes energy such that when radiative emission occurs it is at lower energy than the absorbed radiation. This re-emission of less energetic photons, which have longer wavelengths than the absorbed photons, is known as a Stokes shift (Fig. 2, a). Often the fluorescence spectrum is a mirror image of the absorbance spectrum. At room temperature it is typically the $v = 0$ vibrational level of the S_0 ground state that is populated, so excitation following absorbance is from the $v = 0$ of S_0 to any vibrational level of S_1. The return fluorescence begins in the $v = 0$ level of S_1 to the various vibrational levels of S_0 resulting in the mirror image (Fig. 2, b).
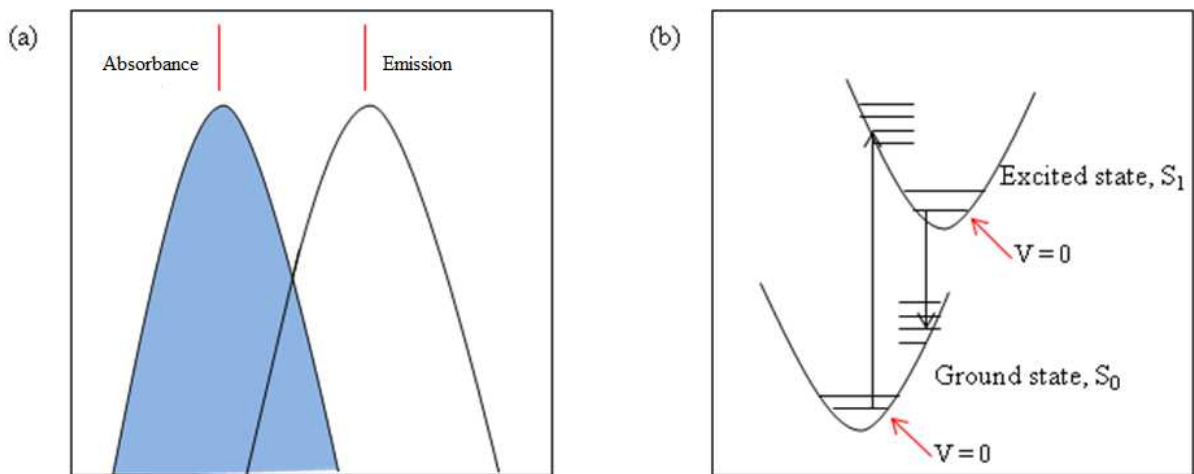
Figure 2   (a) The Stokes shift in the absorbance and emission spectra is defined as the difference between their maxima. (b) Diagrammatical representation of mirror image absorbance and fluorescence transitions.

Phosphorescence, emission from $T_1 \rightarrow S_0$, is considered "spin forbidden" and takes place on a much slower time scale ranging from 1 μs to many seconds. As the T_1 state is lower in energy than the S_1 state phosphorescence occurs at longer wavelengths than fluorescence. The processes of intersystem crossing and phosphorescence are both spin-forbidden but can occur where there is spin-orbit coupling. Intersystem crossing can proceed where vibrational coupling between the singlet excited state and triplet excited state occurs. Spin-orbit coupling increases with increasing atomic number thereby enhancing the rates of formally spin forbidden processes. This is known as the *heavy atom effect*. As a result of the heavy atom effect a decrease in fluorescence quantum yield and an increase in triplet quantum yield are observed, together with a decrease in triplet lifetime (phosphorescence).[1]

The electron distribution of a molecule is primarily what determines its reactivity. In the excited state, the electron distribution is changed with respect to the ground state thus the reactivity has also changed. Molecular orbital theory is used to describe electronic transitions in terms of localisation of electron density from origin to destination. Such transitions include:

1. *Ligand-Field (LF) d-d transitions*

   These excited states are usually called *d-d transitions* as the excited state arises from electron transitions between metal d orbitals. Such transitions result in an angular rearrangement of electron density, with no change in distribution between ligands and metal. The angular rearrangement of the metal electron has little effect on internal redox processes (i.e. towards the homolytic fission of metal–ligand bonds) but has important consequences in changing the reactivity of the metal towards ligand substitution or isomerisation reactions. The excitation of an electron from a metal orbital directed away from the ligand to an orbital directed towards a ligand can cause: an increase in metal to ligand repulsion with lengthening of the metal to ligand bond distance and subsequent detachment or nucleophilic attack of the metal.

2. *Intra-ligand transitions (IL)*

   Electron transitions between two molecular orbitals primarily centred on the ligand orbital give rise to intra-ligand transitions, also called *ligand centred transitions*. These transitions do not affect the charge distribution between the ligands and metal or the bonding structure of the complex directly. They may however change the donor-acceptor properties, dipole moment of the excited state species.

3. *Charge-transfer transitions (CT)*

   These are transitions between molecular orbitals centred on the metal and molecular orbitals centred on the ligands and are sometimes referred to as *electron transfer transitions*. The charge transfer transitions can be further subdivided into *metal to ligand* (MLCT; d-π^*) and *ligand to metal* (LMCT; σ or π-d) charge transfer depending on where the excited electron originates. These transitions cause the radial redistribution of the electron density between the central metal and ligands. Charge transfer excited states increase the reactivity towards substitution reactions as the oxidation state of the metal is changed. MLCT transitions increase the positive charge on the metal facilitating nucleophilic attack by other ligands. In LMCT transitions the electron is generally transferred into an antibonding metal orbital. Transitions to the solvent medium can occur. Charge transfer from a metal centred orbital to a solvent orbital is called *charge transfer to solvent* (CTTS).

1.2.1 Porphyrins

Porphyrins are a large class of pigments known for their intense purple colour. The basic structure, first proposed by Kuster in 1912, consists of a large macrocycle containing 20 carbon atoms and four nitrogen atoms.[3] The atoms are arranged as four pyrrole units linked through α and α' positions by four methine bridges. The first synthetic porphyrin to be reported was the "heme" porphyrin, containing an iron at its core.

The most basic, unsubstituted porphyrin is called *porphine* (Fig. 3, a) and its structure is the basic skeleton that all other porphyrins possess. There are two types of substituted porphyrin: β substituted porphyrins (Fig. 3, b), which have one or more substituents on the pyrrole rings (all naturally occurring porphyrins are of this type) and *meso* substituted porphyrins (Fig. 3, c), which have substituents attached to the methine bridge (the *meso* position). The majority of synthetically produced porphyrins are the latter type. Highly substituted or over crowded porphyrins have substituents at both the β and *meso* positions.[4]

(a)   (b)   (c)
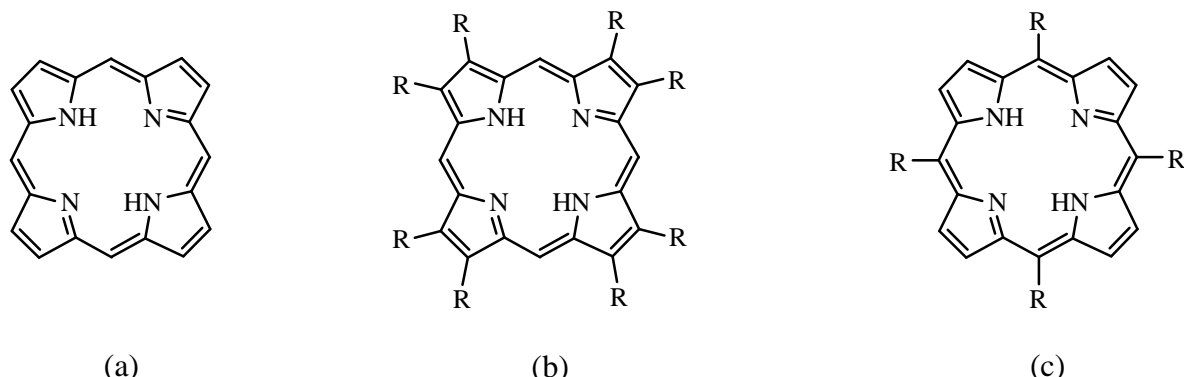
Figure 3   *Basic structure and substitution pattern of porphyrins (R = alkyl or aromatic substituents)*

Porphyrins that contain two internal protons (N-H protons) are referred to as freebase porphyrins. These protons on the central nitrogens are weakly acidic ($pK_a \approx 16$) and can be readily displaced by various metals (Zn, Mg, Cu, Ni, Pd) to yield the corresponding metalloporphyrin (Rxn. 4). Metalloporphyrins can be split into two classes: regular and irregular and are discussed below.

Rxn. 4 $H_2P + M^{2+} \leftrightarrow MP + 2H^+$
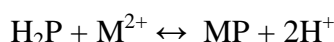
1.2.2 Properties of porphyrins

The porphyrin system consists of 22 π electrons, 18 of which are delocalised over the macrocycle. Hence, porphyrins are aromatic molecules as they obey Huckel's rule of aromaticity ($4n + 2$ π electrons, where n = 4). X-ray crystallography has shown that porphyrins are planar molecules (all atoms are in sp^2 configuration) while heat of combustion experiments also confirmed aromaticity.

The aromatic nature of porphyrins can also be observed in the ^1H NMR signals. The two endocyclic protons (N-H protons) are shielded by the aromatic ring current and their resonance is shifted to a high field position, beyond TMS, typically between -2 and -4 ppm. Upon displacement of the internal protons by a metal ion the high field signal is no longer observed. The diamagnetic ring current also affects the external protons at the β and *meso* positions. In this case, the deshielding effect causes a downfield shift in resonances for these protons.

Perhaps the most distinctive feature of a porphyrin is its UV-visible spectrum. The spectrum consists of two distinctive regions: the B or Soret band region and the Q band region, which occur in the near ultraviolet and visible parts of the electromagnetic spectrum respectively (Fig. 4). A strong transition to the second excited state ($S_0 \rightarrow S_2$) known as the "B" (strongly allowed) or "Soret" band usually occurs between 390 – 430 nm and is the most intense absorbance in the spectrum having molar extinction coefficients of the order 10^5 M^{-1} cm^{-1}. Two weak transitions to the lowest excited singlet state ($S_0 \rightarrow S_1$) are commonly referred to as the "Q" bands (Q – quasi allowed). They are in the lower energy region of the spectrum, generally observed between 500 – 700 nm. Metalloporphyrins give rise to two Q bands as they possess D_{4h} symmetry whereas the less symmetrical freebase porphyrins, with D_{2h} symmetry, display four Q bands. In metalloporphyrins, the lowest energy transition, sometimes referred to as α, is denoted Q(0,0) and arises from the lowest energy excited singlet state. The higher energy band, sometimes referred to as β, is a vibrational satellite of the Q(0,0) band and is denoted Q(1,0). When the central metal is replaced by two hydrogens, as in freebase porphyrins, the reduction in symmetry causes a splitting of the Q bands, where the Q(0,0) splits into $Q_x(0,0)$ and $Q_y(0,0)$ and its vibrational overtone Q(1,0) splits into $Q_x(1,0)$ and $Q_y(1,0)$ thus doubling the number of Q bands to four.[4]
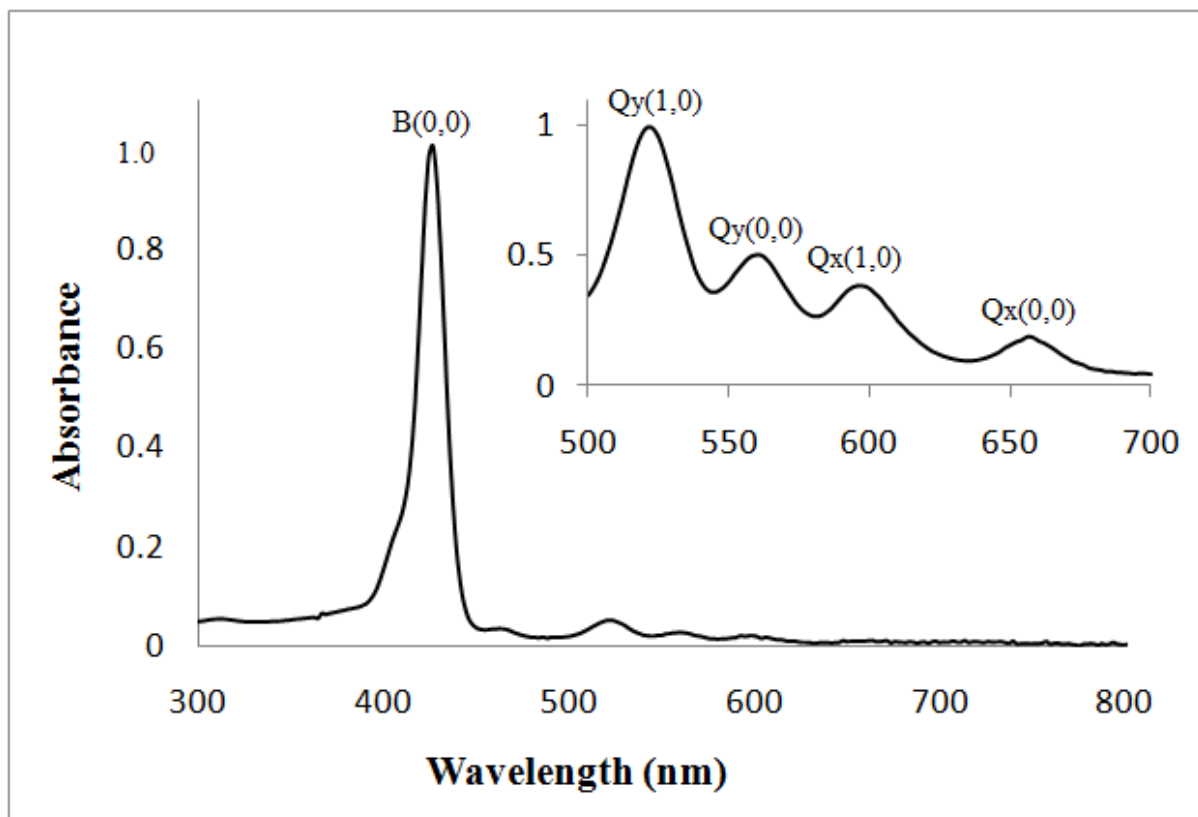
Figure 4   *Absorbance spectrum of a typical freebase porphyrin (**H₂TThP**) where the Soret band and Q bands (insert) are clearly evident.*

Metalloporphyrins can be categorised as either regular or irregular and display three types of absorbance spectra called *normal*, *hypso* and *hyper*, where the effects of the interaction of the metal and porphyrin orbitals is observed. Regular metalloporphyrins display *normal* absorbance and emission spectra which are largely determined by the porphyrin π electrons as the central metal has very little interaction with the porphyrin orbitals. However a decrease in the fluorescence of regular metalloporphyrins is observed in accordance with the *heavy atom effect*. In irregular metalloporphyrins there is extensive interaction between the porphyrin π electrons and the electrons of the central metal ion. Irregular porphyrins produce *hypso* and *hyper* absorbance spectra. *Hypso* absorbance spectra are hypsochromically shifted with respect to *normal* porphyrins and *hyper* absorbance spectra display prominent additional absorbance bands in the region λ > 320 nm. The position of the Q bands also relies on the central metal and whether it has any axial ligands.[4]

Gouterman et al. developed the four-orbital model to illustrate how the Soret and Q bands arise from porphyrin π-π* transitions (Fig. 5).[5] The absorbance bands of porphyrin systems arise from transitions between two HOMOs and two LUMOs. The π orbitals are two non degenerate orbitals labelled a_{2u} and a_{1u} for HOMO and HOMO-1 respectively, while the LUMO π* orbitals are two degenerate orbitals labelled e_g. For *porphine*, the electronic configuration of the ground state is $^1A_{1g}$ comprised of $(a_{1u}^2 \, a_{2u}^2)$. The lowest excited singlet state configurations are $^1(a_{2u}^1 \, e_g^1)$ and $^1(a_{1u}^1 \, e_g^1)$. The degenerate nature of these singlet states causes strong configurational interaction between them. Mixing of the transition dipoles of the two configurations in a constructive manner results in the intense Soret B(0,0) band, while mixing of transition dipoles in a deconstructive manner corresponds to the relatively weak Q(0,0) band. The closer the degeneracy of the $(a_{2u}^1 \, e_g^1)$ and $(a_{1u}^1 \, e_g^1)$ configurations, the weaker the Q(0,0) band becomes. In freebase porphyrins, the symmetrical axis along the internal protons lifts the degeneracy of the e_g (π*) orbital causing the Q(0,0) band of the metalloporphyrin to split into $Q_x(0,0)$ and $Q_y(0,0)$ each with a vibronic overtone.

e_g LUMO

a_{1u} HOMO-1 a_{2u} HOMO
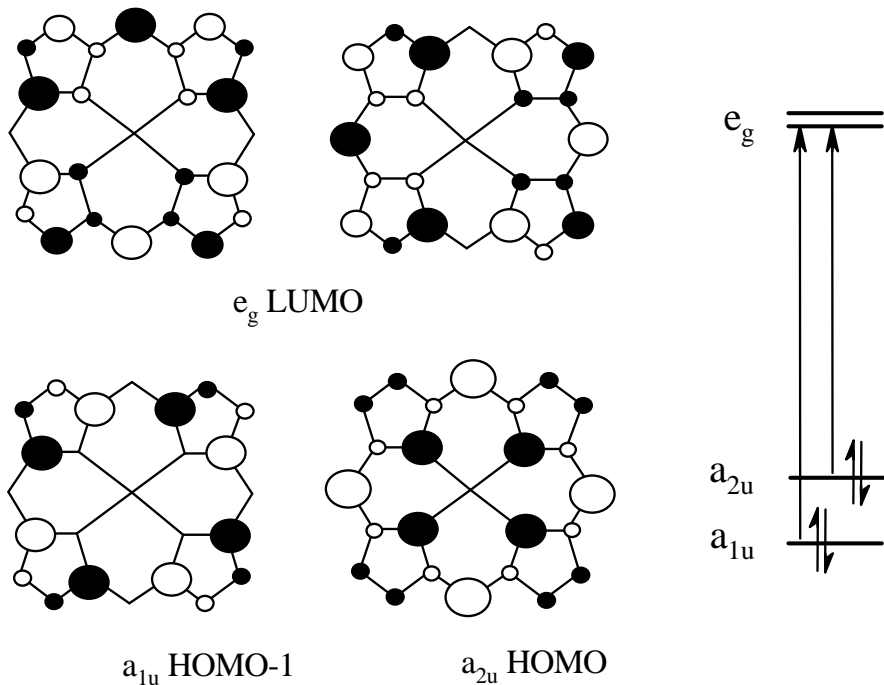
Figure 5   *Goutermans four orbital model.[6]*

1.3.1   Dipyrromethenes

Dipyrromethenes, also called dipyrrins, are formally composed of a pyrrole ring and an azafulvene attached through the α positions by a methine bridge (Fig. 6, a and b). A dipyrromethane has one less degree of unsaturation possessing a methylene bridge (Fig. 6, c). Similar to porphyrins, they can be substituted at the β pyrrolic position or the *meso* position on the bridge (Fig. 6).

(a)   (b)   (c)
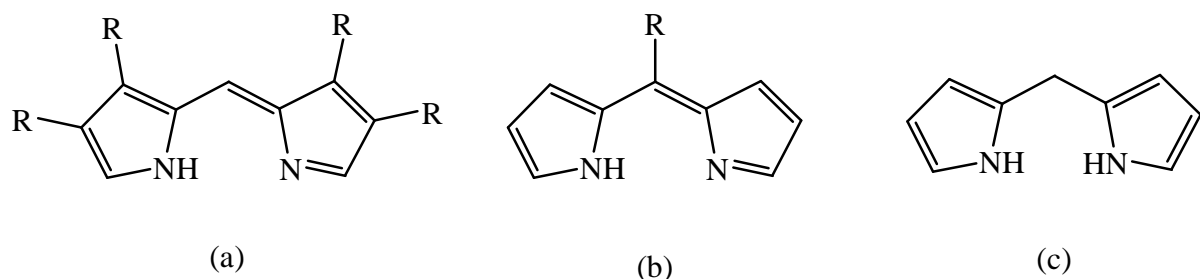
Figure 6   *(a) β substituted dipyrromethene (b)* meso *substituted dipyrromethene and (c) basic structure of dipyrromethane. (R = alkyl or aromatic substituent).*

Dipyrromethenes readily coordinate to divalent metals (M = Zn, Co, Cu, Ni and Pt) to give homoleptic bis(dipyrrinato)metal complexes similar to porphyrins (Fig. 7, a). Dipyrrins can also easily undergo fluoroboration to coordinate with a boron atom to form 4,4-difluoro-4-bora-3a,4a-diaza-s-indacene dyes (Fig. 7, b). They are commonly referred to as borondifluoride dipyrromethenes or BODIPY dyes since their commercialisation.

(a)   (b)
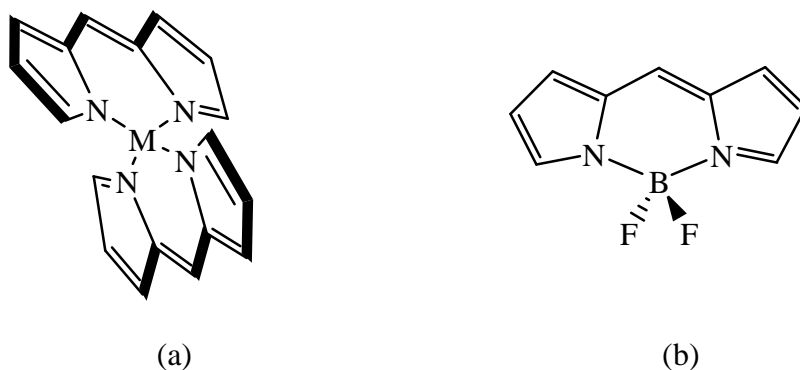
Figure 7   *(a) Bis(dipyrrinato)metal complex where M = Zn, Co, Cu, Ni, Fe and Pt (b) borondifluoride dipyrrin*

1.3.2 Properties of borondifluoride dipyrrins

Borondifluoride dipyrrins are flat bipyrrolic structures linked by a BF_2 group. Quantum mechanical calculations and X-ray crystallography have confirmed the planar structure of the molecule. In its most basic unsubstituted form, the dye possesses C_{2v} point symmetry. BODIPY dyes are neutral molecules, however, they have a zwitterionic structure where a positive charge is delocalised throughout the π-system. It was first proposed that the boron atom has a net positive charge due to the electronegative nature of both the fluorine and nitrogen atoms linked to it. However quantum mechanical calculations have shown the negative electronic density of the molecule localised mainly on the F atoms and to a lesser extent the N atoms. The resonance structures are shown in figure 8. The BF_2 group does not take part in the delocalised π-system but instead gives rigidity to the structure. Thus borondifluoride dipyrromethenes can be classified as quasi-aromatic molecules.
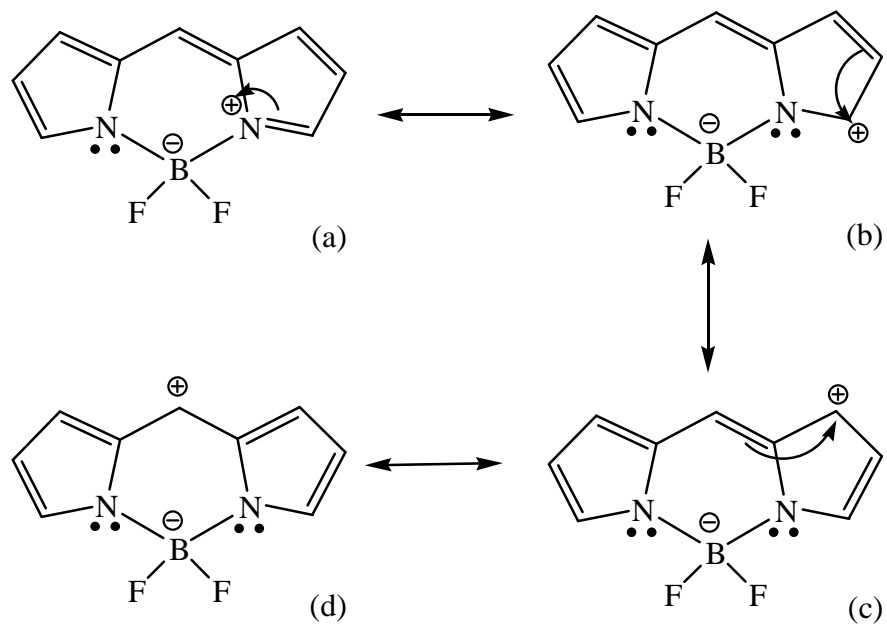
Figure 8   Zwitterionic structures of borondifluoride dipyrromethenes.

BODIPYs possess excellent photophysical properties such as high absorbance coefficients (molar extinction coefficients are of the order 10^5 M^{-1} cm^{-1}) and high fluorescence

quantum yields (typically $\Phi = 0.7$). Their optical properties are easily manipulated by modification of the pyrrole core, the *meso* position and the boron substituents. The absorbance and emission maxima occur at wavelengths in the range 480-700 nm but vary with substituents (Fig. 9). A strong absorbance in the green part of the visible spectrum, at approximately 500 nm, is attributed to the π-π* transition from the ground state to the first excited state ($S_0 \rightarrow S_1$) of the molecule. The shoulder observed at higher energy is assigned to an out-of-plane vibration of the aromatic C-H skeleton. Less intense absorbance bands located in the range 350-400 nm can be attributed to π-π* transitions from the ground state to higher excited states (S_2 or higher).

The intense fluorescence of these compounds has become their most recognised property. The fluorescence spectrum is generally the mirror image of the absorbance spectrum with a weak Stokes shift (~500 cm^{-1}). The shape and position of the fluorescence band is independent of excitation wavelength, in keeping with singlet emitting states and excitation spectra generally match absorbance spectra allowing for the conclusion that emitted light is from the singlet excited state. Substitution of the BODIPY framework can lead to large shifts of their spectral properties and increase the quantum yield close to unity. The fluorescence decay curve of the dyes can be analysed by mono-exponential decay with lifetimes typically in the nanosecond range.
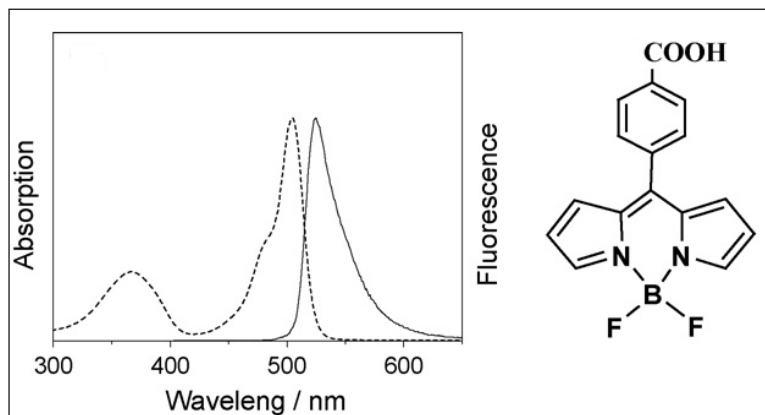
Figure 9   *Absorbance spectrum and corresponding emission spectrum of a substituted phenyl borondifluoride dipyrromethene in CH$_2$Cl$_2$.*[7]

1.4 Singlet oxygen

Molecular oxygen in its ground state has triplet multiplicity, $^3\Sigma_g^-$. Excitation causes rearrangements of the electron spins within the degenerate orbitals and results in two possible singlet states, $^1\Delta_g$ and $^1\Sigma_g^+$, above the triplet state. The electronic configurations of these excited states differ only by the electron configuration in the π antibonding orbitals (Fig. 10). The transition from the first excited state to the ground state $^1O_2$ ($^1\Delta_g$) $\rightarrow$ $^1O_2$ ($^3\Sigma_g^-$) is spin forbidden and as such $^1\Delta_g$ O_2 is a relatively long lived species. The decay of the second excited state, $^1O_2$ ($^1\Sigma_g^+$) $\rightarrow$ $^1O_2$ ($^1\Delta_g$) is short lived as it is a spin allowed transition and occurs with almost unit efficiency. Being spin and symmetry forbidden, the metastability of $^1\Delta_g$ state allows the direct observation of the $^1\Delta_g \leftrightarrow {}^3\Sigma_g^-$ transition in both the absorbance and emission spectra.[8]

State Orbital Assignment
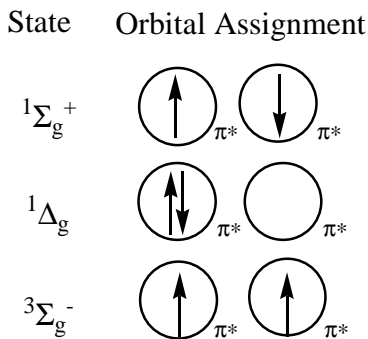
Figure 10   *Representation of molecular oxygen lowest triplet and singlet states.*

Deactivation of singlet excited state oxygen by other species to return to its ground state can occur in two ways: physical quenching where excited singlet state oxygen is deactivated without oxygen consumption or product formation (Rxn. 5) or chemical quenching where a "quencher" reacts with the singlet oxygen and new products are formed (Rxn. 6). Singlet excited state oxygen is more oxidising than ground state oxygen and therefore is more electrophilic. Owing to the high reactivity of $^1O_2$ with substrates, the chemistry of $^1O_2$ has been extensively studied. Typical reactions include oxidations of alkenes (ene-type reactions, [2+2] cycloadditions), 1,3-dienes ([4+2] cycloadditions), aromatic compounds and heterocycles.[8]

Rxn. 5 $$^1O_2 + A \rightarrow {}^3O_2 + A$$

Rxn. 6 $$^1O_2 + Q \rightarrow P$$
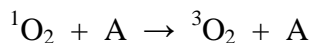
where A = atoms/ molecules that encounter singlet oxygen, Q = quencher and P = product.

The main method of production of $^1O_2$ is by photosensitisation reactions, the requirements for which are oxygen, light of appropriate wavelength and a photosensitiser capable of absorbing and using that energy to excite oxygen to its singlet state. Sensitiser excitation is typically achieved *via* a one photon transition from the ground state, S_0, to a singlet state, S_n, followed by relaxation to the lowest excited singlet state, S_1, with subsequent intersystem crossing to generate the sensitiser triplet excited state, T_1. As discussed previously, the triplet state lifetime is longer (µs) than that of the singlet state lifetime (ns), thus allowing the photosensitiser triplet excited state to react with molecular oxygen. This occurs in two ways, defined as Type I and Type II, according to the nature of the quencher (Fig. 11). Type I involves hydrogen-atom abstraction or electron transfer between the excited sensitiser and a substrate to give free radicals. These free radicals can then react with oxygen to form an active oxygen species, i.e. superoxide radical anion (Fig. 12, Rxn. 7). Type II involves energy transfer during a collision from the excited sensitiser to triplet oxygen to generate singlet oxygen (Fig. 12, Rxn. 8).
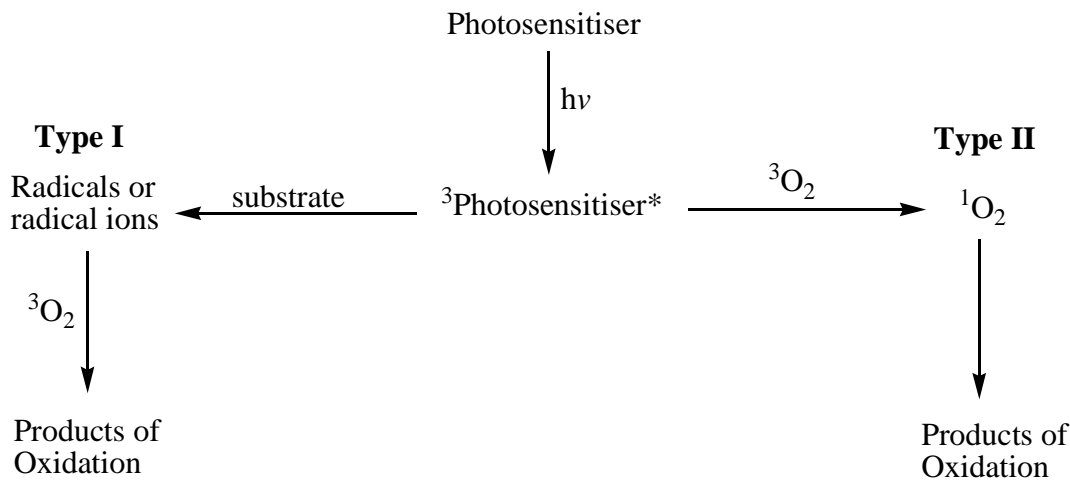
Figure 11   Two pathways (Type I and Type II) of molecular oxygen sensitisation.

Generally a photosensitiser molecule can produce 10^3 – 10^5 molecules of $^1O_2$ before being degraded through photobleaching or photodegradation by $^1O_2$. Photodegradation refers to the process in which singlet oxygen reacts with a material resulting in its degeneration, while photobleaching refers specifically to the degradation of dyes by singlet oxygen. The quantum yield of singlet oxygen formation, Φ_Δ, is dependent on the quantum yield of the triplet state of the sensitiser, Φ_T, though competing reactions must be considered (Fig. 12, Rxn. 9). These include monomolecular radiative and non-radiative processes (Fig. 12, Rxn. 10 and 11) and bimolecular reactions such as physical deactivation by molecular oxygen or electron transfer (Fig. 12, Rxn. 12 and 13). Quenching of the excited state sensitiser by molecular oxygen through electron transfer processes (Fig. 12, Rxn. 13) yields the superoxide radical anion (Type I quenching).[8]

Rxn. 7	$^3Sens^* \xrightarrow{Q} Radical\ Q^{\cdot} \xrightarrow{^3O_2}$ Oxygenated Products
Rxn. 8	$^3Sens^* + {}^3O_2 \xrightarrow{K_{en}} {}^1Sens + {}^1O_2$
Rxn. 9	$\Phi_\Delta = \Phi_T\ S_\Delta\ Sq$
Rxn. 10	$^3Sens^* \xrightarrow{K_r} {}^1Sens + hv''$
Rxn. 11	$^3Sens^* \xrightarrow{K_{nr}} {}^1Sens$
Rxn. 12	$^3Sens^* + O_2 \xrightarrow{K_d\,O_2} {}^1Sens + O_2$
Rxn. 13	$^3Sens^* + O_2 \xrightarrow{K_{et}} P^+ + O_2^{\cdot\,-}$
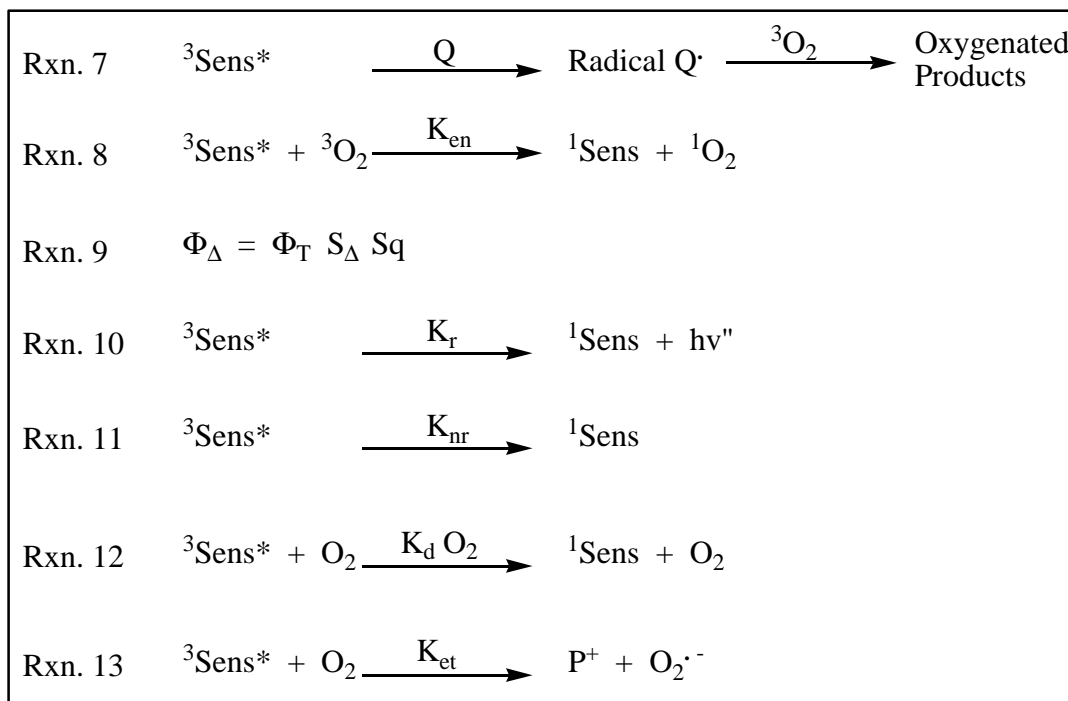
Figure 12   Singlet oxygen production and processes affecting yield and efficiency, where Sens = sensitiser, Q = quencher, K_{en} = rate of energy transfer, S_Δ = fraction of triplet molecules quenched by oxygen and yielding singlet oxygen, S_q = fraction of oxygen dependant triplet deactivations, K_r = rate of radiative decay, K_{nr} = rate of nonradiative decay, K_dO_2 = rate of deactivation by O_2 and K_{et} = rate of electron transfer.

Typically photosensitisers are divided into three categories: organic dyes and aromatic hydrocarbons, porphyrins and other porphyrinoid compounds, and transition metal complexes. Photosensitisers should exhibit the following properties (1) high extinction coefficients in the spectral region of excitation; (2) a triplet state with appropriate energy to allow efficient energy transfer to ground state oxygen; (3) long lived triplet state lifetimes ($\tau_T > 1$ μs) with high quantum yields ($\Phi_T > 0.4$); and (4) high photostability. Porphyrins and their derivatives have the ability to absorb several wavelengths in the UV-vis spectrum and they also possess long lived triplet states that allow for high quantum yields. Substitution around the macrocycle, coordination of metal ions at its centre and axial ligation of the central metal ion allow for the tuning of the photophysical properties of porphyrins. Aggregation of the photosensitiser is not desirable as photodynamic efficiency decreases due to the decreased sensitising ability of dimers and higher aggregates. Aggregation can be circumvented by bulky substituents on the periphery of the porphyrin macrocycle.

Singlet oxygen has found application in areas such as waste water treatment[9] and fine chemical synthesis[10] and in photodynamic processes. The photodynamic effect is the damage caused to living tissue by the combination of a photosensitiser, light and oxygen. Due to the rapid reaction of singlet oxygen with biomolecules, direct spectroscopic evidence of singlet oxygen in photodynamic therapy (PDT) is difficult to find. It is generally accepted the $^1O_2$ ($^1\Delta_g$) is the major participant.[11]

Blood sterilisation, but more specifically, decontamination of freshly frozen plasma units is carried out using PDT.[12] Methylene blue is known for its lack of toxicity to humans and is an effective photosensitiser in destroying extracellulary-enveloped viruses. Silicon-based phthalocyanines are also under investigation for sterilisation of blood components.[13]

Photodynamic therapy is a relatively new type of cancer treatment.[12] In PDT of cancer, a photosensitiser, visible light and oxygen are combined to produce lethal agents which destroy or inactivate tumour cells. In is widely agreed that singlet oxygen is the primary

cytotoxic agent responsible for the photobiological activity. The dual selectivity of PDT arises from the preferential accumulation of photosensitiser in diseased tissue and the ability to confine activation of the photosensitiser by illumination of the tumour region only. This allows for tumour destruction without effecting normal healthy tissue. The majority of sensitisers investigated to date are of porphyrinoid structure.[14] First generation photosensitisers included haematoporphyrin derivative (HpD) and its analogues, which were the first compounds to be authorised for clinical use. These PDT agents were a mixture of about ten components. Poor selectivity, long retention times and poor reproducibility of biological effects meant a second generation of photosensitisers was required. This second generation of PDT sensitisers were structurally distinct compounds with long wavelength absorbance. Third generation photosensitisers use second generation photosensitisers bound to carriers for a higher selective accumulation in the tumour.[8]

In a similar manner photodynamic herbicides and insecticides use the toxic effects of singlet oxygen to destroy unwanted plants or pests. Photodynamic herbicides cause the accumulation of chlorophyll and heme metabolic intermediates (tetrapyrroles) in green plants.[15] These accumulated tetrapyrroles, once exposed to light, act as photosensitisers for the production of singlet oxygen which kills the treated plants through oxidation of their tissues while leaving untreated plants unharmed. δ-Aminolevulinic acid, (ALA), is the main precursor of all tetrapyrroles in plant and animal cells and as such the main component in these tetrapyrrole-dependant photodynamic herbicides (TDPH). The insecticidal effects of photosensitisers have also been studied.[16] Organic dyes, such as xanthenes, were extensively examined for this purpose. They possess the high photosensitising capabilities required and their poor photostability is in fact advantageous. Persistence of conventional insecticides in the environment is a serious issue but is eliminated by the facile decomposition of xanthene dyes. More recently porphyrin-based insecticides have been investigated. These compounds can be activated by a range of wavelengths and have shown to be effective as insecticides.

1.5 Carbon monoxide – releasing molecules (CO-RMs)

Carbon monoxide (CO) is widely considered to be an environmental poison but CO, like nitric oxide (NO), elicits essential biological functions in humans when formed in discrete quantities.[17] Akin to the change in attitude towards NO, the reputation of CO as a noxious polluting gas is changing to that of a vital messenger molecule important for processes in all living organisms. In high concentrations the toxic effects of carbon monoxide are typified at biological levels by the high affinity of CO for haemoglobin and cytochromes, both of which carry out oxygen transport and mitochondrial respiration. However at low concentrations CO can be utilised for therapeutic purposes in the resolution of various pathological states.[18] CO has been shown to regulate vessel tone and blood pressure, exert anti-inflammatory actions, inhibit platelet aggregation and suppress rejection of transplanted hearts. Heme is oxidised at the α-position of the protoporphyrin ring by heme oxygenase to generate ferrous iron, carbon monoxide and biliverdin. Two isoforms of heme oxygenase exist (HO-2 and HO-1) suggesting that the cells have evolved to regulate heme consumption and ultimately the production of CO. Basal production of carbon monoxide in humans is estimated to be 6 μmol Kg^{-1} day^{-1} and this rate increases significantly in pathological states such as asthma, cystic fibrosis and diabetes as the body responds to counteract these conditions.[19] Therefore the development of Carbon Monoxide – Releasing Molecules (CO-RMs) should be emphasised as encouraging prospects for therapeutic agents.

While some main group elements have been shown to bind and release CO, the obvious choice for CO-releasing molecules are transition metal complexes with one or more carbon monoxide ligands. Mann and Motterlini have created the foundations in this area, by demonstrating that some homoleptic and non-homoleptic transition metal carbonyl complexes can act as CO-RMs in biological systems.[20] Metal carbonyl complexes should satisfy some essential prerequisites for later *in vivo* applications including reasonable water solubility, controlled release of CO ligands with known follow up products (simple CO exchange or further reaction) and non-toxicity prior to and after decomposition.

The bonding in metal carbonyls will be discussed in detail in chapter three. For the purposes of carbon monoxide release, dissociation of CO from metal complexes is a result of the cleavage of the metal carbonyl (M-CO) bond. Consequently a relatively weak M-CO bond is favourable. There are several different approaches for potential CO delivery. Photochemical cleavage using smooth light irradiation in order to promote CO release has been examined, though this technique has limited applications at sites which are not directly exposed to the body's surface.[21] The use of prodrugs (i.e. methylene chloride) that are catabolised by hepatic enzymes to generate CO have been examined. Also under investigation is the transport and delivery of CO by means of specific CO carriers. The chemistry of transition metals allows them to be effectively modified by coordination of biological ligands to the metal centre in order to render the molecule less toxic and more water soluble while modulating the liberation of CO. While this research is still in its infancy, complexes that have been characterised as potential CO-RMs include those that contain a heavy metal such as nickel, cobalt or iron surrounded by carbonyl (CO) groups as coordinated ligands.[22] Studies have shown that certain ligands in a metal complex can promote, either electronically or sterically, dissociation of CO.[23] The extent and rate of CO release from CO-RMs is assessed by measuring the conversion of deoxy myoglobin to myoglobin-CO.[20,21] Motterlini et al. also discovered that the rate of CO release from CO-RMs, which can be fine tuned to achieve fast or slow release, allows the modification of the ensuing biological effect. The complexes, $[Fe(CO)_5]$, dinuclear $[Mn(CO)_{10}]$ and $[\{Ru(CO)_3Cl_2\}_2]$ were among the first complexes reported to release carbon monoxide in biological models and also to promote relaxation of blood vessels *in vitro*.[20]

In organometallic chemistry, substitution by loss of CO is a common feature though it is rarely studied in aqueous media. Further studies are necessary to elucidate the full requirements for effective CO release and to understand the delicate balance between CO liberation and CO-RM stability. Limited numbers of CO-RMs have been examined. Thus the development of new molecules or complexes which release CO under physiological conditions at specific sites needs to be further investigated. It is also likely that many CO releasing molecules synthesised for other uses (i.e. as catalysts in organic synthesis) may possess the properties required of a CO-releasing molecule in biological systems.

1.6.1   Laser flash photolysis

The technique of laser flash photolysis was developed by Norrish and Porter during the 1950's.[24] They were awarded the Nobel Prize in 1967 for their studies of extremely fast chemical reactions.   Using very short pluses of energy to disturb the equilibrium, observation of short-lived intermediates present in photochemical processes was possible.

The fundamental technique of laser flash photolysis involves irradiation of a sample with a high intensity pulse of light (e.g. laser or discharge lamp) within a very short time, which produces a high concentration of excited state species (transient species, radical or photoproduct) in that time interval.   With its short pulse duration, high intensity and monochromatic nature, laser radiation is ideal for this purpose.   By monitoring the evolution of the system in time using UV-vis or IR detection, the reaction kinetics can be determined.

Using UV-vis detection, the changes in the absorbance of an excited state transient species as it undergoes thermal relaxation to the parent compound can be observed. However for UV-vis detection to be viable there are two factors that must be considered. Primarily, the thermal relaxation of the excited state must occur on a longer timescale than the lifetime of the laser pulse itself. Secondly, the excited state absorbance spectrum must be sufficiently different from the parent compound so that the changes can be observed. Well resolved characteristic absorbance spectra aid the identification of intermediates whereas transient species with low molar extinction coefficients may not be detected.

A significant disadvantage of UV-vis monitored laser flash photolysis is the lack of structural information available for a particular system. However when coupled with time-resolved infrared (TRIR) and time-resolved resonance Raman (TRrR) spectroscopy it becomes a much more comprehensive technique.   The infrared spectrum of metal carbonyls observed in the carbonyl stretching region (1700 – 2200 cm^{-1}) allows structural information to be obtained. The number and intensity of the infrared bands, which is dependent on the molecular symmetry, provide a direct signal as to the geometry of a molecule.

1.6.2   Laser flash photolysis with UV-vis detection

A schematic diagram of the laser flash photolysis instrumentation is given in figure 13. The excitation source is a neodymium yttrium aluminium garnet (Nd:YAG) laser, which operates at a frequency of 1064 nm. The host YAG crystals are implanted with Nd atoms of approximately one part per hundred. The main advantage of the YAG host material is its relatively high thermal conductivity which removes wasted heat, thus allowing these crystals to operate at high repetition rates of many pulses per second. Using non – linear optics, the fundamental frequency of 1064 nm can be doubled, tripled or quadrupled to generate a second, third or fourth harmonic frequency at 532, 355 or 266 nm respectively. This allows specific excitation pathways within a system to be selected. Amplification of the laser power can be carried out by varying the voltage across an amplifier flash tube. At a frequency of 355 nm, the energy generated is typically 45 mJ per pulse and the lifetime of the laser pulse approximately 10 ns.

The circular laser pulse is diverted *via* a Pellin Broca prism through an optical trigger (which prepares the transient digitiser) onto the sample cuvette. The transient digitiser (a Hewlett Packard HP 54510A oscilloscope) detects the transient species. Positioned at right angles to the laser beam is the monitoring light source, is an air – cooled 275 W Xenon arc lamp that monitors any changes induced in the sample. Throughout the experiment UV-vis filters are employed between the Xenon arc lamp and the sample to prevent excessive photodegradation. After passing through the sample the monitoring beam is directed to the entrance slit of an Applied Photophysics f/3.4 monochromator *via* a circular lens. A Hamatsu 5 stage photomultiplier operating at 850 V is situated at the exit slit of the monochromator. Following activation of the optical trigger the transient digitiser (oscilloscope) measures changes in the absorbance *via* a variable load transistor.
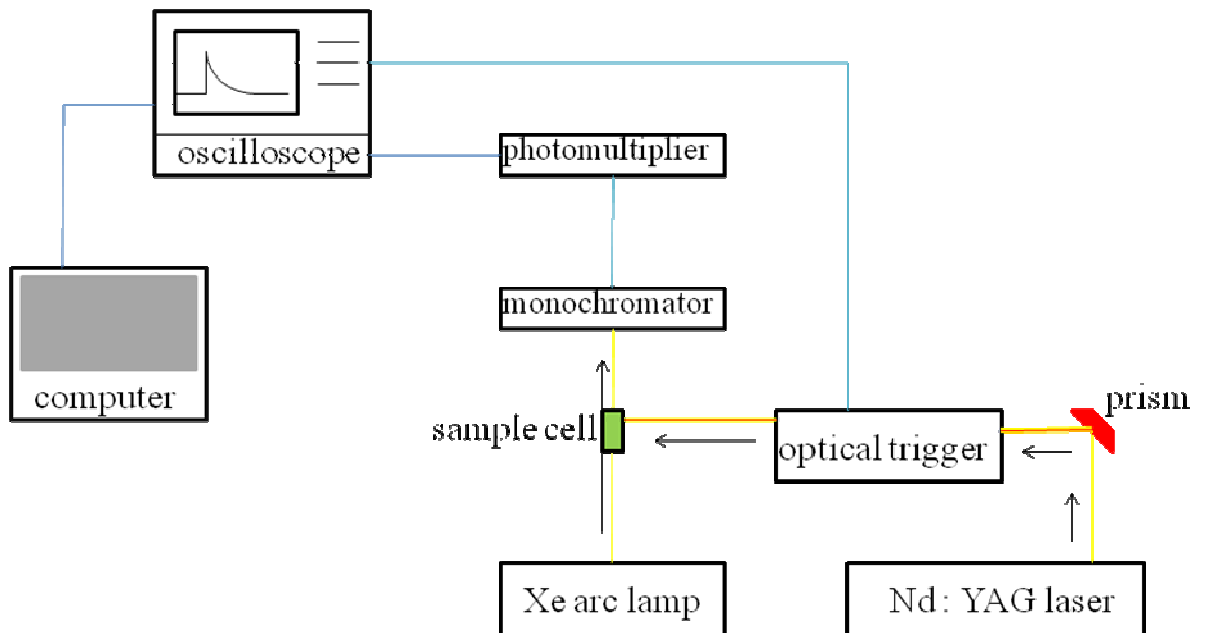
Figure 13   *Schematic diagram of laser flash photolysis instrumentation.*

A typical transient signal is obtained in the following manner: Initially the amount of monitoring light being transmitted through the sample solution prior to the laser flash, I_0, is recorded. I_0 (mV) is the voltage corresponding to the amount of light detected by the photomultiplier tube when the Xenon arc lamp shutter is open less the voltage generated by stray light when the shutter is closed. While firing the laser, the Xenon arc lamp shutter is simultaneously opened, allowing the laser pulse to pass through the sample cuvette and the amount of light transmitted to be recorded (I_t). According to the Beer – Lambert law absorbance = log (I_0/I_t). The change in intensity of the monitoring beam transmitted through the sample is measured as a function of time and/or wavelength. Therefore a typical trace depicts the change in absorbance/voltage with time. The time-resolved absorbance may then be analysed by first or second order kinetics. Transient absorbance difference spectra are obtained as a result of point by point build up by changing the wavelength of the monochromator (usually every 10 nm) with consistent time-base and voltage settings. Solvents of spectroscopic purity are required to limit impurities while sample solutions must also be optically transparent for the monitoring beam. A general procedure describing sample preparation for laser flash photolysis experiments is given in appendix A.

1.6.3 Time resolved infrared spectroscopy

While time resolved optical spectroscopy allows the elucidation of kinetic information from a transient species, the broad and often featureless absorbance bands observed in the UV-vis following excitation give little structural information. For this reason time resolved infrared (TRIR) spectroscopy is a very complementary technique. TRIR spectroscopy involves the direct observation of transient species evolving over time using IR detection. Laser flash photolysis is used to generate the intermediates in solution while ultra fast IR spectroscopy monitors the photophysical or photochemical processes over time. Infrared bands with distinct absorbance frequencies (e.g. C=O stretching vibrations) allow transient species in metal carbonyl systems to be examined.[25]

As organometallic compounds include functional groups with characteristic frequencies, sensitive to molecular structure, this is a particularly useful tool for spectroscopic characterisation and kinetic studies. TRIR involves a pump and probe configuration where a laser pulse excites ("pumps") a sample and IR spectroscopy operating in a very fast time range "probes" the generation of excited state transient species. Conventional ns TRIR systems use a XeCl excimer laser or Nd:YAG laser as the pump source, which operates at the 308 nm output of the XeCl excimer and the third harmonic (355 nm) of the Nd:YAG laser. A flow cell set up may be used during IR detection to avoid photodecomposition of the sample and allow for signal averaging. An IR probe source such as a globar (black body radiation) combined with a monochromator is frequently used, while for investigation of metal carbonyl photoreactions CO lasers have been utilized.[25]

Ultrafast TRIR systems such as the Picosecond Infrared Absorbance and Transient Excitation (PIRATE) facility at the Rutherford Appleton Laboratories (RAL) provide pump and probe spectroscopy with picosecond time resolution. This system allows the interrogation of the structural relaxation and reactivity of short lived (ps) intermediates formed in solution during a chemical reaction. A Ti:sapphire "pump" laser operating at 1KHz repetition rate with an average of 2 – 3 mJ per pulse is used while < 1 ps snap shots of the IR region of interest "probe" the progress of the reaction. TRIR studies discussed later were carried out at RAL and a full description of the TRIR spectroscopy instrumentation is available in a number of annual reports published by the Central Laser Facility at RAL.[26]

1.7   Time correlated – single photon counting

Time correlated single photon counting (TC-SPC) is used to calculate luminescence lifetimes (or luminescence decay) by measuring the time of emission of individual fluorescent photons. The technique relies on the theory that the probability distribution for emission of a single photon after excitation yields the actual intensity against time distribution of all photons emitted as a result of the excitation. A probability distribution is constructed by measuring the single photon emission following a large number of excitation flashes. The time to amplitude convertor (TAC) is the essential part of the system as it transforms the arrival time of the photon between start and stop voltages. Simply put, it is not possible to measure the arrival time of all the photons emitted by the fluorescent species as a result of the excitation flash. Consequently arrival time of the first photon is recorded by the TAC and then only if it arrives in a given time interval after the flash.

A schematic diagram of the single photon counting instrumentation is shown in figure 14. Initially a flash of light excites a fluorescent species causing it to emit a photon from the excited state. Light from the excitation source is monitored by a photomultiplier (PM1) and a signal from it (the "start" signal) initiates the time sweep of the TAC. A second photomultiplier (PM2) monitors the fluorescent photons and the first photon registered by PM2 during the sweep of the TAC acts as a "stop" signal. An output signal is generated by the TAC, whose voltage is proportional to the time difference between the start and stop signals. This process is repeated to build up the time correlation. The pulse output of the TAC is amplified and used to sample a section of the time-to-amplitude convertor range. It is then expanded to cover the full range of a multichannel pulse height analyser (MCA). The MCA converts the voltage signal from the TAC to a time channel. Each channel is a unit division on the time axis and can be varied from 0.2 ns to a few microseconds per channel. The number of counts in each channel is directly proportional to the fluorescent intensity and so a probability histogram (counts versus time) is generated. The contents of the MCA are displayed on an oscilloscope where the build up of the fluorescence decay curve can be visually followed. The data collected consists of the sum of counts due to photon emission from the excited species and counts due to random background. Deconvolution methods are required to extract the inherent decay information. The quality

of the lifetime data is judged by two criteria: the random nature of the residual plot and the chi^2 (χ^2) value which should be between 1 and 1.1.[27]
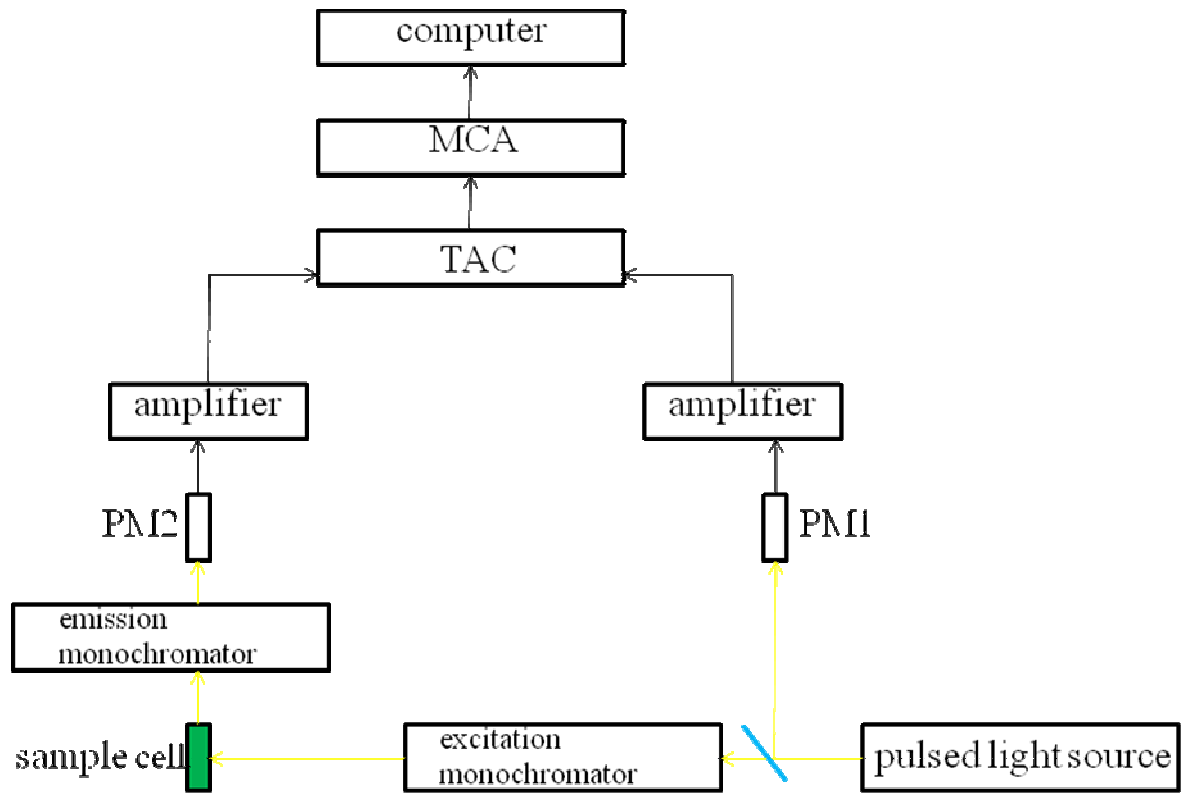
Figure 14   Schematic diagram of single photon counting instrumentation.

1.8   Conclusions

The techniques discussed in this introductory chapter were applied to the compounds synthesised throughout this research. Thienylethynyl substituted porphyrins had their ground state and excited state properties investigated. The photophysics of a series of thienyl acetylenic compounds and their corresponding cobalt carbonyl complexes were examined. Pyridyl porphyrin metal carbonyls (M = W or Cr) were examined by TRIR to elucidate the initial excited states populated following excitation. Finally the absorbance of a series of thienyl dipyrromethane dyes was obtained with a view to synthesising BODIPY complexes in the future. In all cases, assessment focused on the fundamental chemistry of the compounds in question in the hope that it shall enhance our ability to create and improve practical applications in photochemical processes.

1.9 Bibliography

1   *Principles in Fluorescence Spectroscopy, 3rd Edition,* J.R. Lakowicz, Springer Science + Business Media, **2006**.

2   *Chemistry and Light*, P. Suppan, The Royal Society of Chemistry, Cambridge, **1994**.

3   W.Z. Kuster, *Physiol. Chem.*, **1912**, 82, 463.

4   *The Colours of Life: an introduction to the chemistry of porphyrins*, L.R. Milgrom, Oxford University Press, 1997.

5   (a) M. Gouterman, *J. Mol. Spectrosc.*, **1961**, 6, 138. (b) *The Colours of Life: an introduction to the chemistry of porphyrins,* L.R. Milgrom, Oxford University Press, **1997**.

6   J. Rochford, Ph.D thesis, **2004**, Dublin City University, Dublin 9.

7   A. Cui, X. Peng, J. Fang, X. Chen, Y. Wu, B. Guo, *J. Photochem, Photobiol., A. Chem.*, **2007**, 186, 85.

8   M.C. DeRosa, R.J. Crutchley, *Coord. Chem. Rev.*, **2002**, 233, 351.

9   P. Esser, B. Pohlmann, H.D. Scharf, *Angew. Chem.*, **1994**, 106, 2093.

10   P. Wagler, B. Heller, O. Orther, K.H. Funkn, G. Oehme, *Chem. Ing. Technol.*, **1996**, 68, 823.

11   K. Lang, J. Mosinger, D.M. Wagnerovà, *Coord. Chem. Rev.*, **2004**, 248, 321.

12   W.M. Sharman, G.M. Allen, J.E. van Lier, *Drug Discov. Today*, **1999**, 4, 507.

13   N.L. Olenick, A.K. Antunez, M.E. Clay, B.D. Rihter, M.E. Kenny, *J. Photochem. Photobiol.*, **1993**, 57, 242.

14   P.G. Calzavara-Plinton, M. Venturini, R. Sala, *JEADV*, **2007**, 21, 439.

15   C.A. Rebeiz, K.N. Reddy, O.B. Nadihalli, J. Velu, *J. Photochem. Photobiol.,* **1990**, 52, 1099.

16   (a) T. Ben Amor, G. Jori, *Insect Biochem. Mol. Biol.,* **2000** 30, 915. (b) C.A. Rebiez, L.J. Gut, K. Lee, J.A. Juvik, C.C. Rebiez, C.E. Bouton, *Crit. Rev. Plant Sci.*, **1995**, 14, 329.

17   (a) M.A. Gillman, F.J. Lichtigfeld, *Nature*, **1994**, 367, 28. (b) A.R. Butler, D.L.H. Williams, *Chem. Soc. Rev.*, **1993**, 22, 233.

18   L.E. Otterbein, F.H. Bach, J. Alam, M. Soares, H. Tao Lu, M. Wysk, R.J. Davis, R.A. Flavell, A.M. Choi, *Nat. Med.,* **2001**, 166, 4185.

19   R. Alberto, R. Motterlini, *Dalton Trans.*, **2007**, 1651-1660.

20   R. Motterlini, B.E. Mann, T.R. Johnston, J.E. Clark, R. Foresti, C.J. Green, *Curr. Pharm. Des.*, **2003**, 9, 2525

21   R. Motterlini, J.E. Clark, R. Foresti, P. Sarathchandra, B.E. Mann, C.J. Green, *Circ. Res.*, **2002**, 90, E17-E24.

22   W.A. Herrmann, *J. Organomet. Chem.*, **1990**, 383, 21.

23   (a) D.J. Darensbourg, K.K. Klausmeyer, J.H Reibenspies, *Inorg. Chem.*, **1995**, 34, 4933. (b) D.J. Darensbourg, K.K. Klausmeyer, J.H Reibenspies, *Inorg. Chem.*, **1996**, 35, 1529. (c) J. Pearson, J. Cooke, J. Takats, R.B. Jordan, *J. Am. Chem. Soc.*, **1998**, 120, 1434.

24   R.G. Norrish, G. Porter, *Nature*, **1950**, 164, 685.

25   K. Mc Farlane, B. Lee, J. Bridgewater, P.C. Ford, *J. Organomet. Chem.,* **1998**, 554, 49.

26   M .Towrie, P.D. Bailey, R. Barton, P. Matousek, A.W. Parker, M.W. George, D.C. Grills, *Laser Science Development – Lasers for Science Facility, The PIRATE Development,* Central Laser Facility Annual Report, **2000/2001** 165.

27   J.F Rabek, *Single-Photon Correlation method* in *Experimental Methods in Photochemistry and Photophysics Part 2*, Wiley Interscience, **1982**.

Chapter 2

The synthesis, photophysics and electrochemical properties of a series of zinc(II) tetra thien-2-yl porphyrins and related zinc(II) tetra phenyl porphyrins.

Chapter two involves the study of thienyl porphyrins. This chapter begins with a literature survey on the synthesis, photophysics and electrochemistry of thienyl porphyrin systems. The synthesis of the porphyrins studied is given, followed by their photophysical and electrochemical properties. The effect of the thienyl moiety on the ground state and excited state properties of the porphyrin macrocycle is examined.

2.1   **Literature Survey**

2.1.1   *Meso* or β thienyl porphyrins (direct attachment to porphyrin macrocycle)

2.1.1.1   **Synthesis**

The first reported thienyl substituted porphyrin, *meso* tetra(thien-2-yl)porphyrin (**H₂P1**, Fig. 1) was synthesised by Triebs et al. in 1968.[1] The direct condensation of pyrrole and 2-thiophenecarboxaldehyde *via* an adapted Rothemund method[2] (route A, Fig. 1) resulted in the pure porphyrin in 9 % yield. The Adler-Longo method,[3] reacting equi-molar amounts of 2-thiophenecarboxaldehyde and pyrrole in refluxing propionic acid followed by recrystallisation, was later applied by Torréns et al. however the yield was never reported (route B, Fig. 1).[4] Both *meso* tetra(thien-2-yl)porphyrin and *meso* tetra(thien-3-yl)porphyrin, produced by the Adler-Longo method, using 2- and 3-thiophenecarboxaldehyde respectively to give the target compounds (**H₂P1** and **H₂P2**, Fig. 2), was later reported by Bhyrappa and Bhavana.[5]
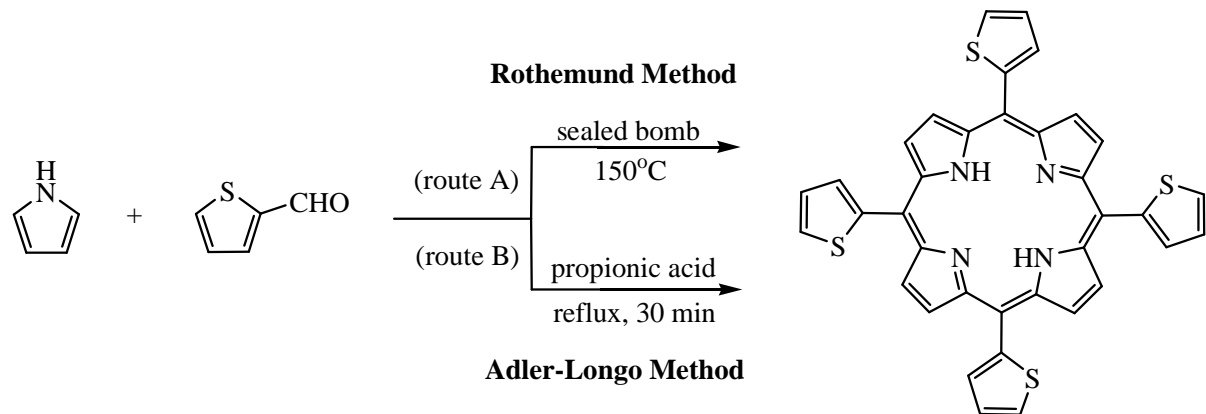
Figure 1   *Rothemund (route A) and Adler-Longo (route B) synthesis of* meso *tetra(thien-2-yl)porphyrin (**H₂P1**).*

Later the Lindsey method,[6] the acid catalysed condensation of an aldehyde and pyrrole to form porphyrinogen followed by oxidation to give porphyrin, was applied to the synthesis of thienyl porphyrins. This method is advantageous as it avoids the highly oxidising environments of both the Rothemund and Adler-Longo methods. Ono et al. synthesised a series of *meso*- and β- dodecasubstituted thienyl porphyrins (**H₂P1**, **H₂P3**, **H₂P4**, **H₂P5**, Fig. 2) including their zinc and copper metallated derivatives using an adapted version of Lindsey's method.[7] Thienyl carboxaldehydes and 3,4-diarylpyrroles were used to synthesise highly substituted dodecathienyl porphyrins in an attempt to alter the redox potentials of the macrocyclic structure by inducing ruffling of the planar geometry of the porphyrin.

	Ar	Ar'	M
P1		—H	2H, Zn(II), Cu(II), Mg(II)
P2		—H	2H, Zn(II), Cu(II), Fe(III)
P3			2H, Zn(II), Cu(II)
P4			2H, Zn(II), Cu(II)
P5			2H, Zn(II), Cu(II)
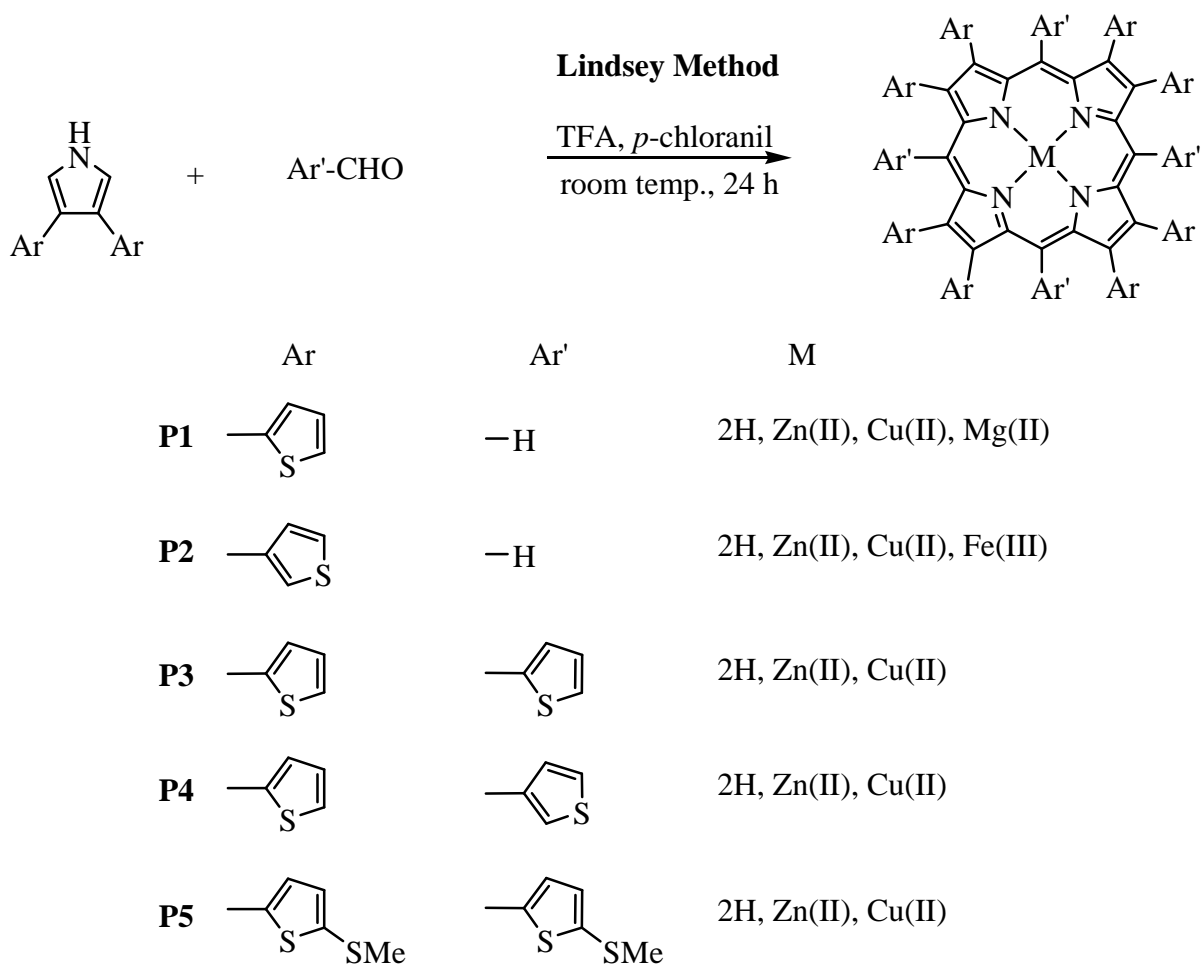
Figure 2   Synthesis and structures of highly substituted thienyl porphyrins reported by Ono et al.[7]

A series of uncrowded *meso* tetraarylporphyrins (e.g. **H₂TPP**) and β- octaarylporphyrins (e.g. 2,3,7,8,12,13,17,18-octaphenyl porphyrin) as well as a number of highly crowded systems including 5,10,15,20-tetrakis(thien-3-yl)-2,3,7,8,12,13,17,18-octaphenyl porphyrin (**H₂P6**, Fig. 3) and 5,10,15,20-tetraphenyl-2,3,7,8,12,13,17,18-octakis(thien-3-yl)-porphyrins (**H₂P7**, Fig. 3) were synthesised directly *via* the Lindsey method.[8] Some intermediately crowded systems, such as nickel(II) 5,10,15,20-tetraphenyl-2,3-bis(thien-3-yl)porphyrin (**NiP8**, Fig. 3), were produced. The intermediately crowded porphyrin, **NiP8**, was synthesised by a Suzuki coupling reaction with nickel(II)-2,3-dibromotetraphenyl porphyrin and thiophene-3-boronic acid.

P6: Ar₁ = Thien-3-yl, Ar₂ = Phenyl
P7: Ar₁ = Phenyl, Ar₂ = Thien-3-yl

P8: Ar = Thien-3-yl
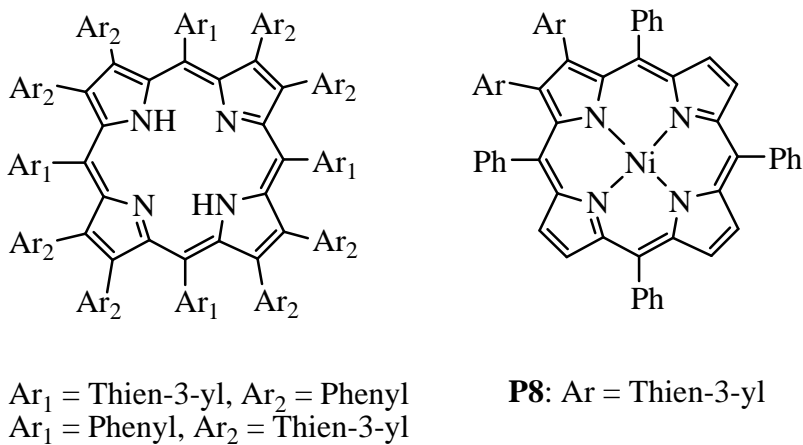
Figure 3   Highly substituted porphyrins synthesised by Medforth et al.[8]

The majority of studies to date use an adapted Lindsey procedure as the milder conditions are better suited to thienyl porphyrin synthesis although a number of alternative approaches have been reported. Bonar-Law reported an innovative process towards porphyrin synthesis by producing a range of porphyrins in surfactant solution.[9] This method involved multicomponent assembly in micelles. Micelles are dynamic clusters of surfactant molecules which have the ability to collect and concentrate species from aqueous solution and so promote porphyrinogen assembly by binding the product more tightly than the reactants. The initial steps of the reaction are: the concentration of the reactants in the micelle, their condensation into linear chains and their cyclisation into porphyrinogen.

Subsequently, the porphyrinogen is irreversibly oxidised to the porphyrin. Several aspects of this method were investigated including the time course of the reaction, reactant and surfactant concentration, as well as the reversibility of the reaction. In this way freebase *meso* tetra(thien-2-yl)porphyrin (**H₂P1**, Fig. 2) was produced, with an isolated yield of 24 %, which is comparable to reported yields *via* the Lindsey procedure.

Most recently, a novel high yielding synthesis of *meso* substituted porphyrins has been reported by Shi and Wheelhouse.[10] Using an adapted method of Lindsey and Woodfords,[11] commercially available porphine was initially converted to Mg(II)-porphine. Mg(II)-5,10,15,20-tetrakisbromoporphine was synthesised *via* bromination of the Mg(II)-porphine precursor in 81 % yield. Using standard Suzuki conditions, the authors coupled aryl boronic acid groups to the porphyrin macrocycle and afterwards removed the magnesium ion to yield the desired freebase porphyrins (Scheme 1). In this manner freebase tetra(thien-3-yl)porphyrin (**H₂P2**, Fig. 2) was produced in 41 % total yield, the highest yield reported to date. However as former methods involve the yield limiting porphyrinogen cyclisation step this method cannot be directly compared as the yield is based purely on the functionalisation of the commercially sourced porphine.
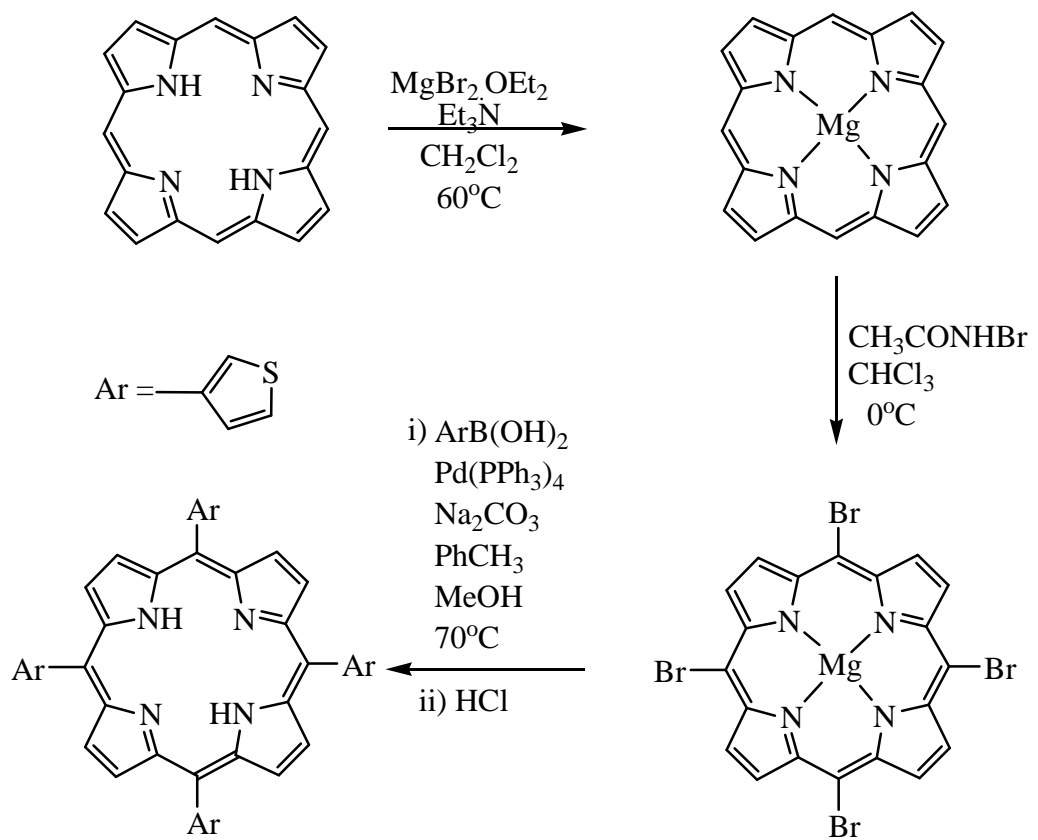
Scheme 1   *Shi and Wheelhouse procedure.*[10]

The Mac Donald 2+2 procedure,[12] involving the condensation of 3-formylthiophene with dipyrromethane to synthesise a *trans* porphyrin, 5,15-bis(thien-3-yl)porphyrin (**H₂P9**, Fig. 4), was reported by Arminger and Lash.[13]   The thien-2-yl isomer, 5,15-bis(thien-2-yl)porphyrin (**H₂P10**, Fig. 4), was later synthesised by a similar method.[14]
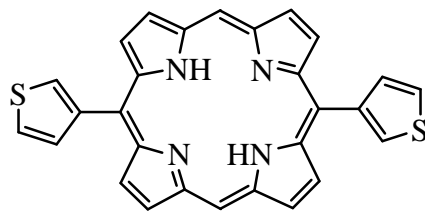
H₂P9
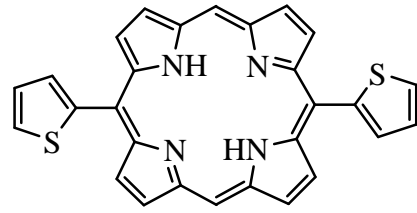
H₂P10

Figure 4   5,15-Bis(thienyl)porphyrin structural isomers prepared by the Mac Donald 2+2 procedure.[13, 14]

Similarly, the condensation of an alkylated dipyrromethane and 2-thiophenecarboxaldehyde in the presence of trichloroacetic acid with subsequent oxidation of the porphyrinogen resulted in the formation of **H₂P11** (Fig. 5).[15] The reaction of the dipyrromethane with 2',5-bithienylcarboxaldehyde gave **H₂P12** (Fig. 5). Their metal complexes (**ZnP11**, **ZnP12**, **CuP11** and **CuP12**) were readily produced using metal acetates.
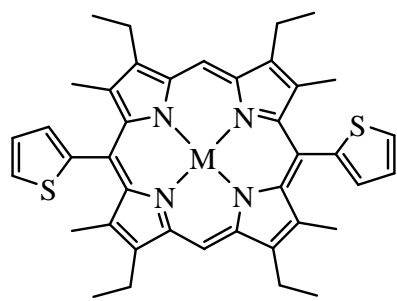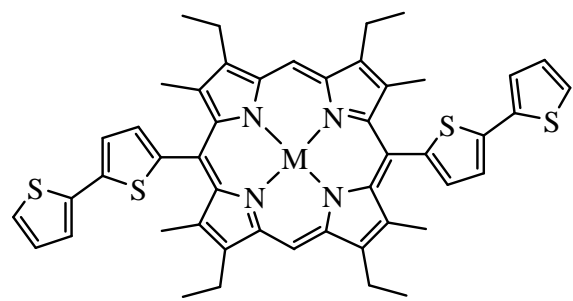
P11   M = 2H, Zn, Cu   **P12**

*Figure 5   Trans thienyl porphyrins **P11** and **P12**.*[15]

A series of *trans* porphyrins have been synthesised by Collis and co-workers using an adapted Lindsey method.[16] Alkylated dipyrromethanes were condensed with 2-/3-thiophenecarboxaldeyde to produce 5,15-bis(thienyl)porphyrins (**H₂P13**, **H₂P14**, **H₂P15**, **H₂P16** Fig. 6) with isolated yields of between 16 and 65 %. Further treatment of **H₂P14** with zinc acetate produced the metallated derivative (**ZnP14**).
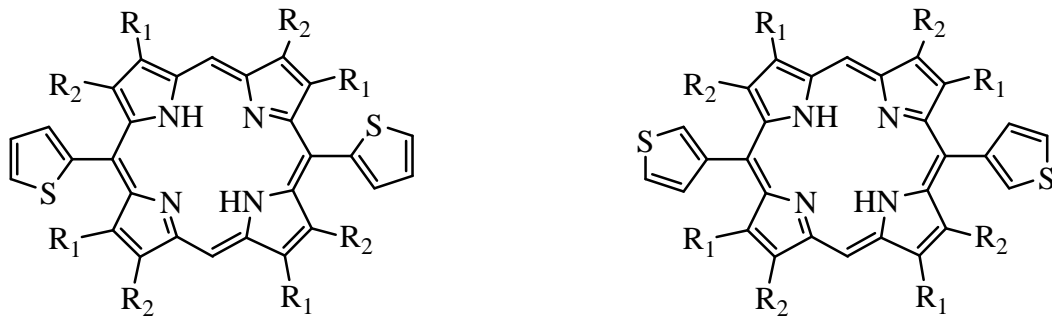
P13: R_1 = Me, R_2 = CH₂CH₂CO₂Me
P14: R_1 = Me, R_2 = CH₂CH₂CH₂CH₃

P15: R_1 = Me, R_2 = CH₂CH₂CO₂Me
P16: R_1 = Me, R_2 = CH₂CH₂CH₂CH₃

Figure 6   Examples of trans substituted porphyrins.[16]

The sterically hindered porphyrin *meso* tetrakis-5,10,15,20-([2',2":5",2'''-terthiophen]-3"-yl)porphyrin, (**H₂P17**, Fig. 7), and its *trans* substituted homologue, 5,15-bis([2',2":5",2'''-terthiophen]-3"-yl)-2,8,12,18-tetra-*n*-butyl-3,7,13,17-tetramethyl porphyrin (**H₂P18**, Fig. 7), were produced under Lindsey conditions from 3-formylthiophene. Initially **H₂P17** was synthesised using trifluoroacetic acid as catalyst with a resulting yield of 17 %. Repeating the procedure but using boron trifluoride diethyl etherate as the Lewis acid catalyst, resulted in a significantly higher yield (34 %) of the porphyrin. However ¹H NMR analysis revealed a complex array of signals. Due to the bulky nature of the terthiophene moiety, the product contained a mixture of four inseparable atropisomers. Molecular modelling indicated that the β-pyrrolic hydrogen clearly prevented the rotation of the bond joining the central thiophene ring, due to its interaction with the outer thiophene rings of the terthiophene moiety. Complete metallation of the porphyrin mixture proved difficult, due to the steric constraints imposed by some of the atropisomers. Condensation of 3'-

formylterthiophene with dipyrromethane gave the *trans* porphyrin **H₂P18** as a mixture of ββ- and αβ- atropisomers. ¹H NMR of the product indicated a statistical mixture of the ββ-*trans* and αβ-*trans* porphyrin.

P17: M = 2H or Zn

P18: ββ - and αβ - porphyrin
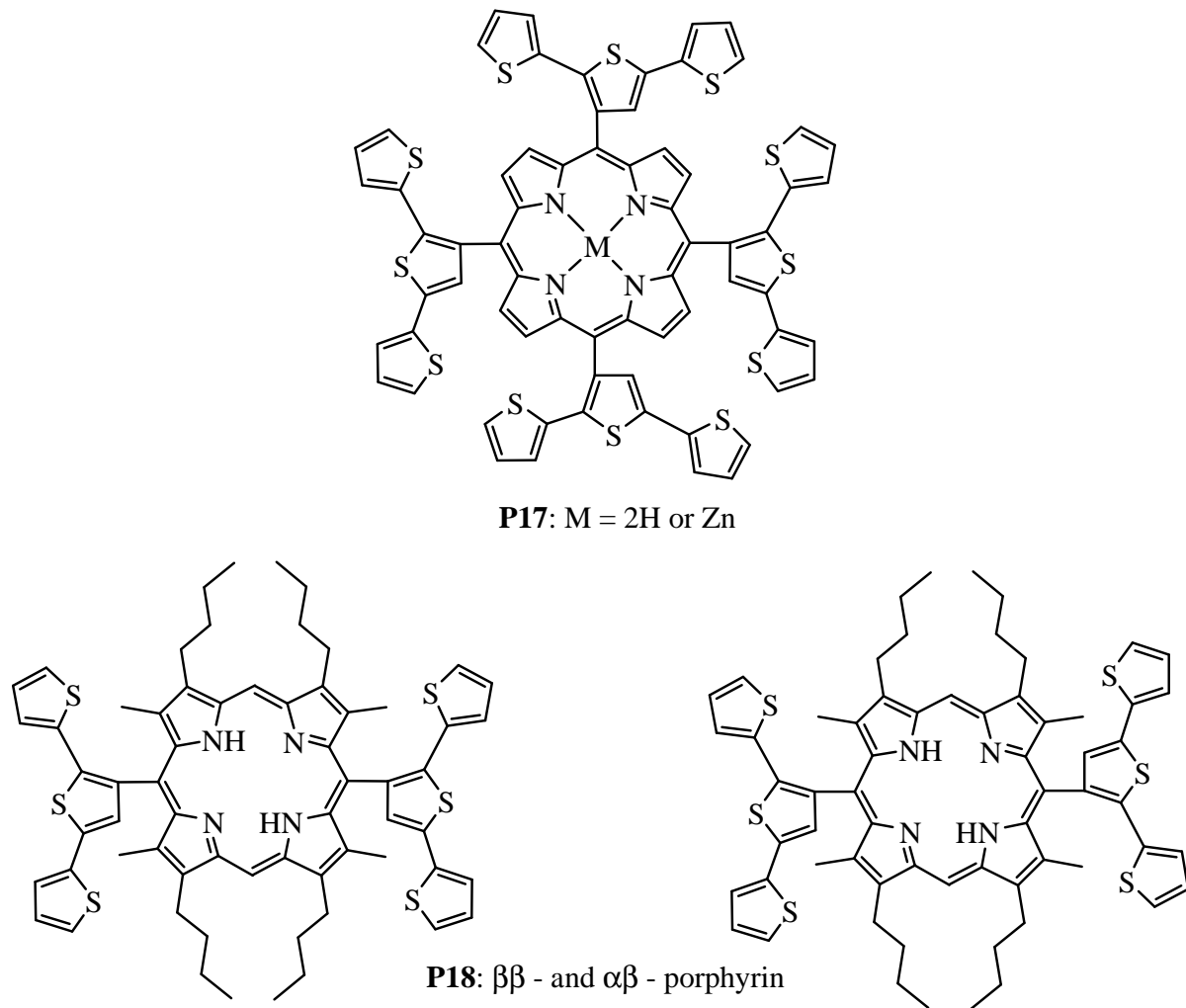
Figure 7   *P17 and P18 terthienyl porphyrins.*

Novel mono-substituted thienyl porphyrins zinc(II)-5-(5'-carboxythien-2'-yl)-10,15,20-trimesitylporphyrin (**ZnP19**, Fig. 8) and zinc(II)-5-(4'-carboxythien-2-yl)-10,15,20-trimesitylporphyrin (**ZnP20**, Fig. 8) have also been reported.[17] The precursor to **H₂P19**, 5-(5-methoxycarbonylthien-2-yl)-10,15,20-trimesitylporphyrin was synthesised *via* the Lindsey method and then hydrolysed to yield the target freebase porphyrin. Subsequent

metallation gave **ZnP19**. 5-(4'-cyanothien-2-yl)-10,15,20-trimesitylporphyrin, also produced by the Lindsey method, was converted to **H₂P20** and then to the zinc analogue **ZnP20**.
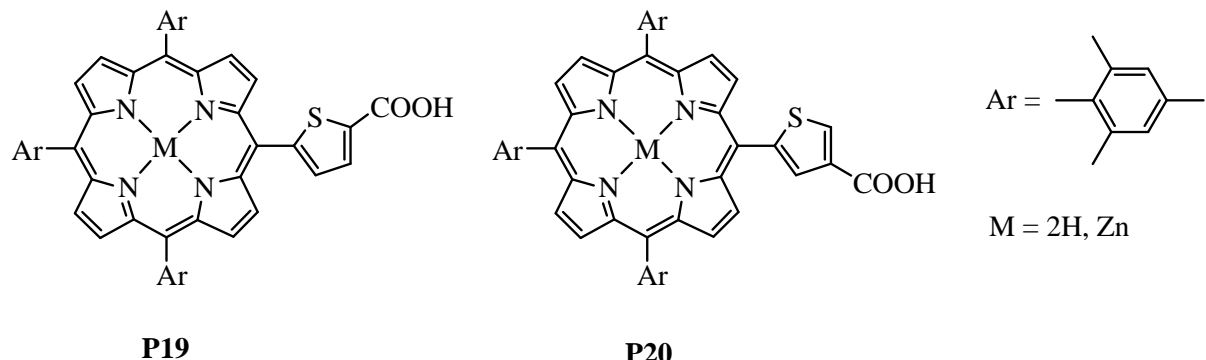
Figure 8   Mono-substituted carboxythienylporphyrins.

Utilising C-C coupling reactions thienylporphyrins can be further functionalised. Rochford et al. synthesised a complete series of mono-, di-, tri- and tetra- *meso* (thien-2-yl)porphyrins (**H₂P21** – **H₂P26**, Fig. 9) to fully investigate the influence of the thiophene ring on the ground and excited state properties of *meso* porphyrins.[18] The tetra substituted porphyrins were prepared according to Lindsey's standard procedure. The mono-, di- and tri- substituted porphyrins were prepared by a mixed aldehyde condensation of 5-bromo-2-thiophenecarboxaldehyde, benzaldehyde and pyrrole followed by metallation with zinc acetate and Sonogashira coupling with trimethylsilylacetylene. *Meso* trithienyl and triphenyl-porphyrin-ferrocene dyads (**H₂P27** and **H₂P28**, Fig. 37) were similarly synthesised *via* Lindsey's mixed aldehyde condensation and converted to their zinc(II) analogues.[19] The ground and excited state properties were then examined and compared to **ZnP1**.

ZnP1: R₁ = R₂ = R₃ = R₄

ZnP21: R₁ = R₂ = R₃ = R₄

ZnP22: R₁ = R₂ = R₃ = R₄

ZnP23: R₁ = R₂ = R₃ = R₄

ZnP24: R₁ ... R₂ = R₃ = R₄

ZnP25: R₁ = R₂ ... R₃ = R₄
R₁ = R₃ ... R₂ = R₄

ZnP26: R₁ = R₂ = R₃ ... R₄
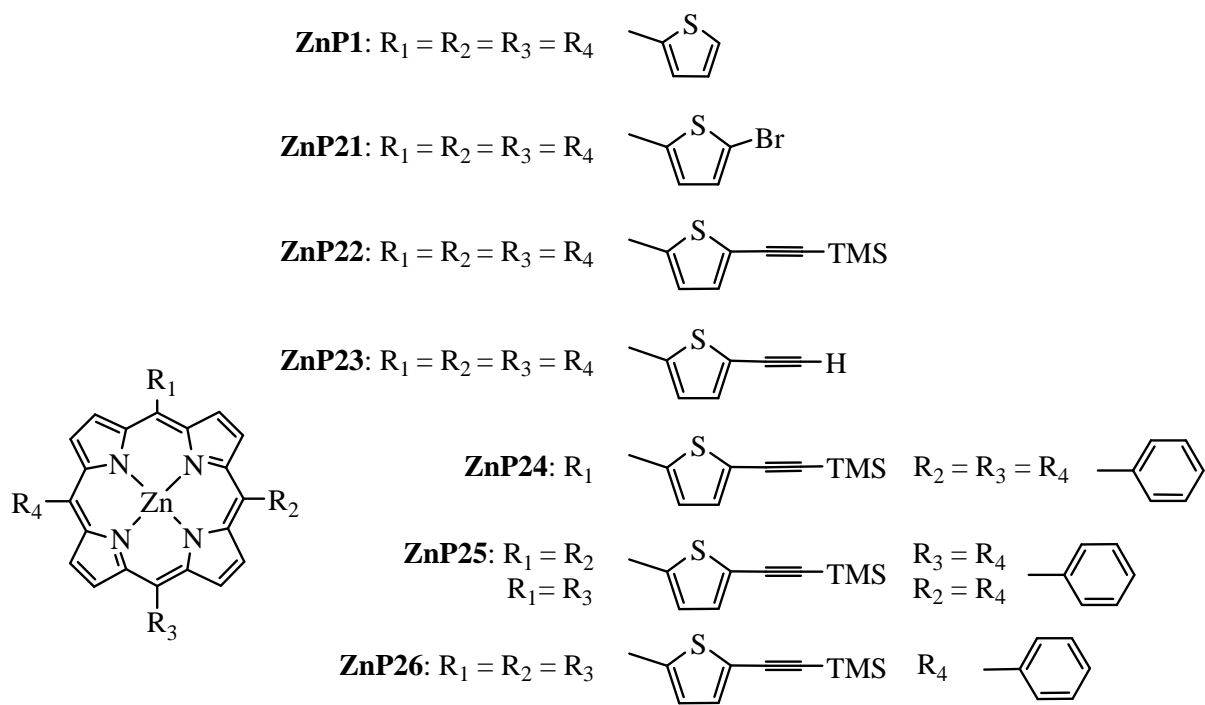
Figure 9   Various thienyl porphyrins with extended conjugation.

Modern metal-catalysed bond-forming reactions were employed and facilitated the construction of **ZnP29 – ZnP34** (Fig. 10).[20a] Combining electron-rich Suzuki-porphyrin synthon precursors, a variety of appropriately functionalised porphyrins were produced. These chromophores possess electron-poor thiophene and oligothiophene species linked by a direct carbon-carbon single bond or conjugated through an intervening ethynyl unit. Following this work, a series of conjugated zinc(II) porphyrin-based chromophores related to **ZnP32** were synthesised (**ZnP35 – ZnP38**, Fig. 11) *via* similar metal catalyzed cross-coupling reactions.[20b]

P29: n = 1
P30: n = 2
P31: n = 3

P32: n = 1
P33: n = 2
P34: n = 3

P35

P36

R =

P37

P38
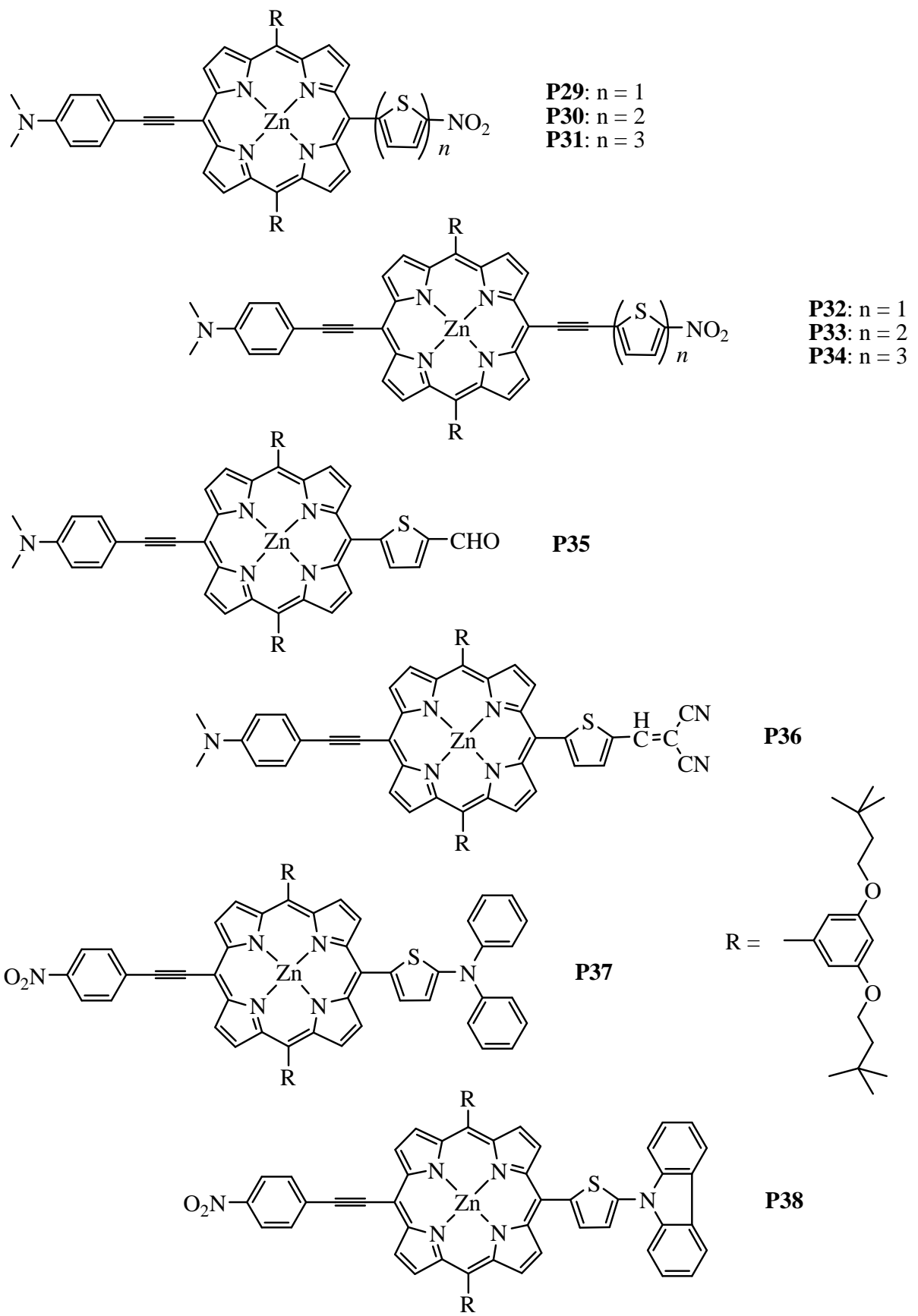
Figure 10   **ZnP29 – ZnP38**

Efficient intramolecular energy transfer from an anthryl donor moiety to a porphyrin acceptor *via* terminally substituted oligothiophene bridging units was reported for a large series of compounds (**H₂P39** – **H₂P59**, Fig. 11 and Table 1).[21] The porphyrins were synthesised *via* Lindsey's method with a mixed aldehyde reaction, where yields were consistent with a statistical incorporation of two aldehydes (6 – 10 %). *n*-Pentyl groups were incorporated into the oligothiophene chain to increase their solubility.
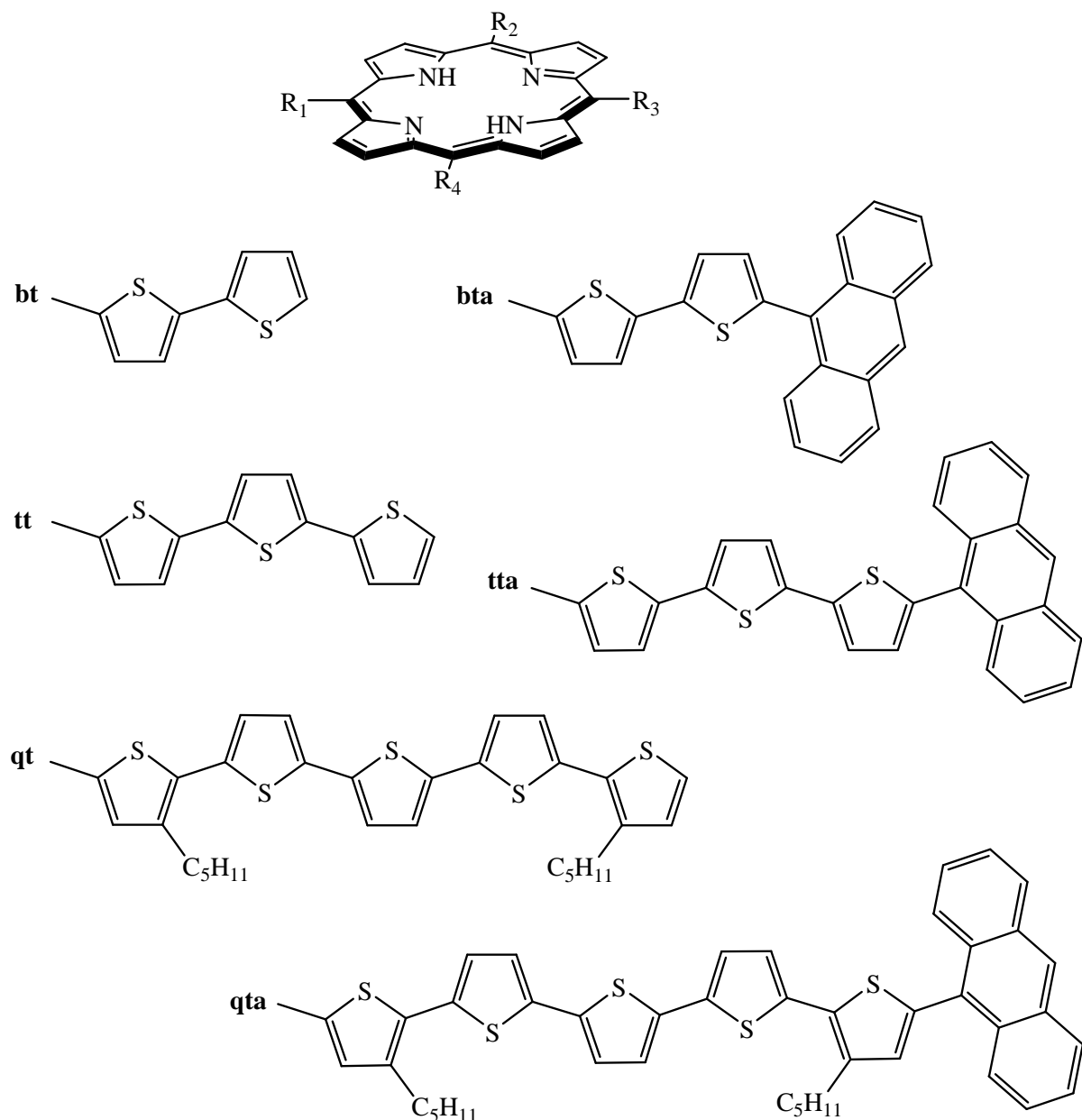
Figure 11   R groups used to make porphyrin-oligothiophene-anthracene triads.

Porphyrin	R_1	R_2	R_3	R_4
H₂P39	bt	bt	bt	bt
H₂P40	tt	tt	tt	tt
H₂P41	bta	n-pentyl	n-pentyl	n-pentyl
H₂P42	bta	n-pentyl	bta	n-pentyl
H₂P43	bta	bta	n-pentyl	n-pentyl
H₂P44	bta	bta	bta	n-pentyl
H₂P45	bta	bta	bta	bta
H₂P46	tta	n-pentyl	n-pentyl	n-pentyl
H₂P47	tta	n-pentyl	tta	n-pentyl
H₂P48	tta	tta	n-pentyl	n-pentyl
H₂P49	tta	tta	tta	n-pentyl
H₂P50	tta	tta	tta	tta
H₂P51	qt	n-pentyl	n-pentyl	n-pentyl
H₂P52	qt	n-pentyl	qt	n-pentyl
H₂P53	qt	qt	n-pentyl	n-pentyl
H₂P54	qt	qt	qt	n-pentyl
H₂P55	qta	n-pentyl	n-pentyl	n-pentyl
H₂P56	qta	n-pentyl	qta	n-pentyl
H₂P57	qta	qta	n-pentyl	n-pentyl
H₂P58	qta	qta	qta	n-pentyl
H₂P59	qta	qta	qta	qta

Table 1   R groups used to make porphyrin-oligothiophene-anthracene triads.

Post functionalisation of the porphyrin ring is often carried out in the preparation of polymeric thienyl systems. *Meso* tetrakis(2'5-bithienyl)porphyrin **H₂P60** (Fig. 12) and *meso* tetrakis([5',2":5",2'''-terthiophen]-2'-yl) porphyrin **H₂P61** (Fig. 12) were produced from the corresponding oligothienylcarboxaldehydes under standard Adler-Longo conditions, and their zinc(II) and palladium(II) metallated analogues were subsequently synthesised.[22] Two-dimensional porphyrin polymers containing oligothienyl bridges in the lateral direction were prepared by electrochemical oxidation of the *meso* tetrakis(oligothienyl)porphyrin metal complexes (Fig. 24).

M = 2H, Zn(II), Pd(II)
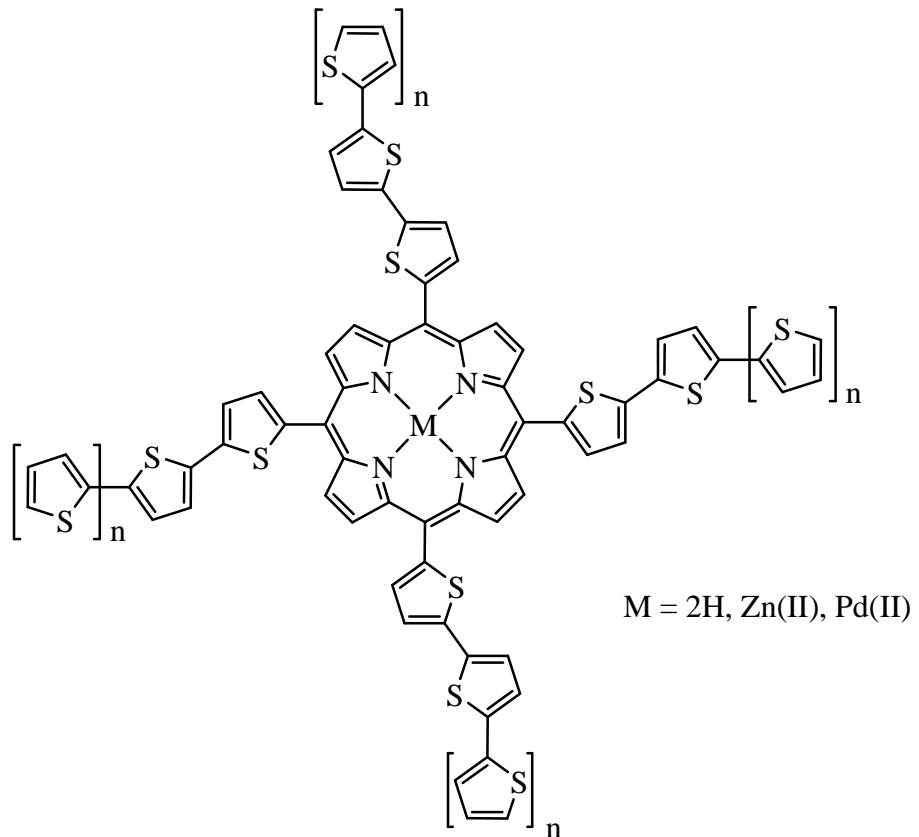
Figure 12   **P60**: *n = 0,* **P61**: *n = 1.*

The crystal structure of **ZnP1** (Fig. 2) indicates that the porphyrin possesses a wave like conformation with the central zinc ion residing in an inversion centre.[23] The macrocycle has a four coordinate geometry and a 24 atom core similar to zinc tetraphenylporphyrin (**ZnTPP**). **CuP1** (Fig. 2) was found to have a near planar porphyrin core with only slight puckering with a deviation of less than 0.01 Å observed for individual atoms in the mean plane. [24] In contrast **ZnP2** (Fig. 2) exhibits unusual planar and non-planar core features (Fig. 13).[25] In the case of the planar core, only minimal deviation from planarity is observed with the β-pyrrolic carbons showing marginal deviation from the mean plane (± 0.034 Å). In the case of the non-planar thienyl porphyrin, the β-pyrrolic carbons show significant deviation (± 0.422 Å) over the mean plane. This deviation suggests the conformation is a combination of saddle and marginal ruffle.
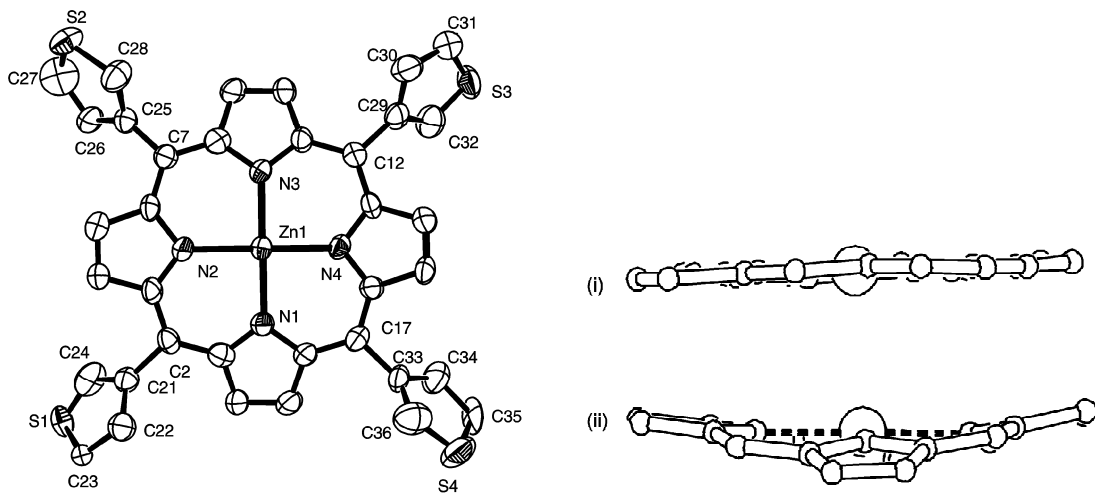
Figure 13   *Solid state crystal structure of the planar unit of **ZnP2**, (i) and (ii) indicate the side view of the planar and non-planar porphyrin units respectively.*[25]

The crystal structure of 5,10,15,20-tetrakis(5-methylthien-2-yl)porphyrin, **H₂P62**, possesses an essentially planar geometry with a slight waving conformation.[26] A direct correlation between the degree of porphyrin distortion and the bathochromic shift in the absorbance spectra was shown for a series of *meso-*, β- overcrowded porphyrins.[7] The macrocyclic core of the *trans* porphyrin (**H₂P10**, Fig. 4) adopts a saddle like conformation in the solid state with the two meso thienyl arms parallel to each other.[14] These arms are tilted with respect to the porphyrin mean plane at angles of ~ 50 ° (smaller than that of **ZnP2**). The porphyrins formed parallel layers aligned through the aromatic core with thienyl groups forming a staggered arrangement. The aromatic core of the porphyrins formed a supramolecular columnar structure (Fig. 14).
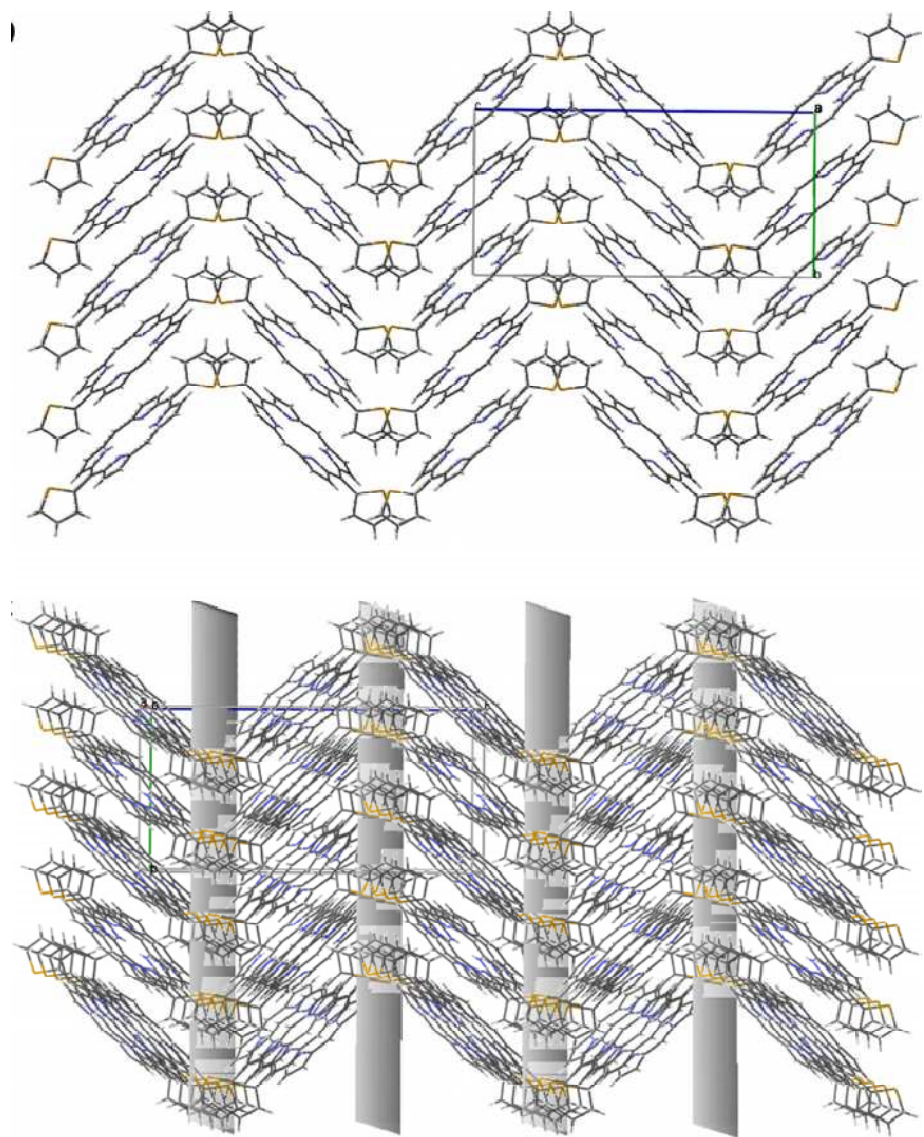
*Figure 14   Side view of stacking arrangement generated by **H₂P10** in the solid state.*[14]

2.1.1.2 Electronic and photophysical properties

The electronic and photophysical properties of thienyl porphyrins were investigated by several groups though there has been little consistency in describing the influence of the thienyl ring on the electronic properties of the porphyrin macrocycle. The absorbance spectrum of thienyl porphyrins has long been known to shift to longer wavelengths when compared to the tetraphenylporphyrin analogues. The spectral profile of the zinc(II) and copper(II) metallo derivatives (**ZnP1**, **ZnP2**, **CuP1**, **CuP2**, Fig. 2) reported by Bhyrappa and Bhavana are quite similar to those of the corresponding tetraphenylporphyrin (**ZnTPP** and **CuTPP**), each displaying an intense Soret and two Q bands.[5] Some minor bathochromic shifts were observed for **ZnP1** (**ZnTPP**: 422 nm, **ZnP1**: 427 nm, **ZnP2**: 422 nm), as shown in figure 15 with greater shifts observed for the copper analogues (**CuTPP**: 415 nm, **CuP1**: 421 nm, **CuP2**: 418 nm). The molar extinction coefficients were found to be comparable to other porphyrins.
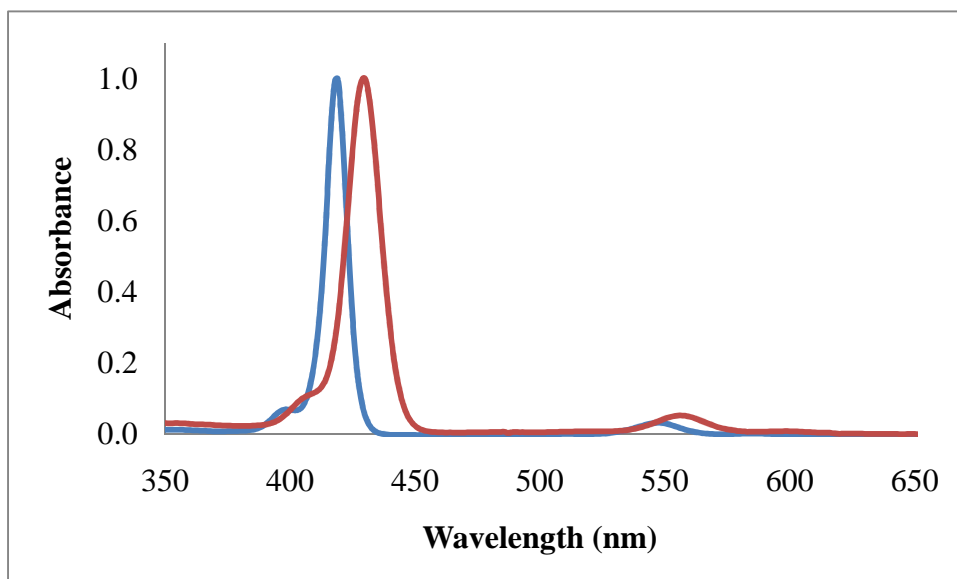
*Figure 15   Electronic absorbance spectra of **ZnTPP** (blue line) and **ZnP1**(red line) in CH$_2$Cl$_2$.*

Sun et al. reported the absorbance λ_{max} and extinction coefficients of **H₂P1**, **H₂P63**, **H₂P64**, **H₂P65** (Fig. 16) and observed red shifts of between 10 - 15 nm with respect to **H₂TPP**.[27] They postulated that the spectral shifts in the UV-vis spectra were due to an inductive effect by the thienyl group as opposed to the increased conjugation of the porphyrin π – system.
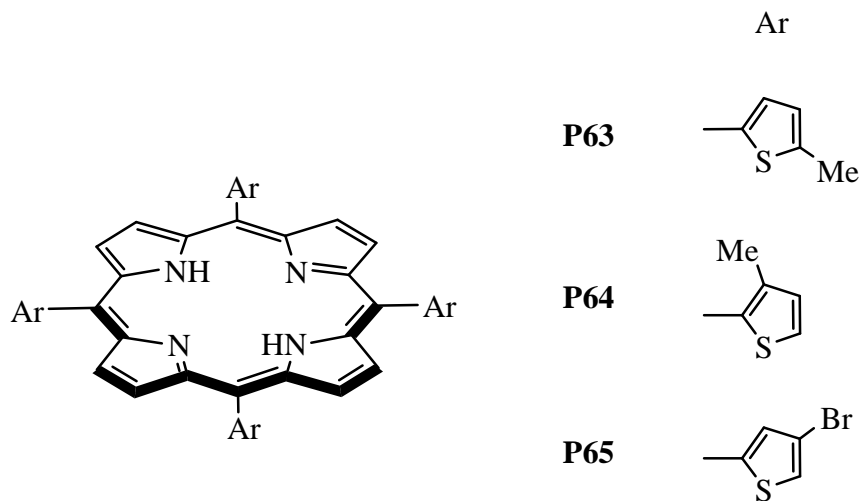
Figure 16   *Substituted meso thienyl porphyrins **H₂P63** – **H₂P65**.*

More recently Brückner et al. investigated the electronic absorbance properties of a series of thienyl porphyrins (**H₂P1** and **H₂P2**, Fig. 2, **H₂P63** and **H₂P64**, Fig. 17).[28] The Soret and Q bands of all the thienyl porphyrins were red shifted to some extent when compared to **H₂TPP** with its Soret band at 417 nm (Table 2). A bathochromic shift of 9 nm to 426 nm was reported for **H₂P1** with respect to **H₂TPP**. The Soret band of **H₂P2** was only slightly shifted to 421 nm (+ 4 nm). However the Soret band of methyl substituted thien-2-yl porphyrins was red shifted by some 8 – 13 nm depending on the position of the methyl group. Methyl substitution at the 5' position as in **H₂P63** resulted in a further 4 nm bathochromic shift to 430 nm, whereas substitution at the 3' position in **H₂P64** gave a slight hypsochromic shift (-1 nm to 425 nm). These observations although not conclusive do indicate the direct influence of the *meso* thienyl substituents on the electronic properties of the central porphine ring.

48

Porphyrin	λ_{max} Soret (nm)	λ_{max} Q bands (nm)	λ_{em} (nm)	Stokes shift (nm)
H$_2$TPP	417	514, 549, 588, 647	651, 715	4
H$_2$P1	426	523, 558, 594, 661	670, 720 (sh)	9
H$_2$P2	421	519, 556, 594, 653	661, 723	8
H$_2$P63	430	526, 569, 597, 665	674 (br)	9
H$_2$P64	425	520, 557, 597, 660	666, 725	6

Table 2   *Absorbance and emission data of* meso *tetrathienylporphyrins and **H$_2$TPP*** *in CH$_2$Cl$_2$.*[28]

As part of the investigation into the origin of these bathochromic shifts in the absorbance spectra of thienyl porphyrins, density functional theory was employed by Brückner et al. to compute the energy of the porphyrin system as a function of the rotation of a single meso aryl group.[28] There is less steric hindrance for the smaller 5 membered *meso* thienyl ring than for the larger 6 membered phenyl ring. In addition the thien-2-yl group lacks one *o*-phenyl H to β-pyrrole H interaction (Fig. 18). This should allow greater ease of rotation for the thien-2-yl porphyrins and also a somewhat more facile rotation for the thien-3-yl porphyrins. The computed rotational barriers of **H$_2$P1** and **H$_2$P2** confirm this greater ease of aryl rotation, being 50 and 75 % lower than that of **H$_2$TPP** respectively.

This suggests that, the previous proposal, of bathochromic shifts observed in thienyl porphyrins, due to the thienyl rings inductive effect, is over simplified. The molecular modelling results indicate that these shifts may be more dependent on the conformation which the thienyl groups adopt, allowing π-π orbital overlap of the thienyl and porphyrin ring systems, as opposed to solely the thienyl inductive effect.
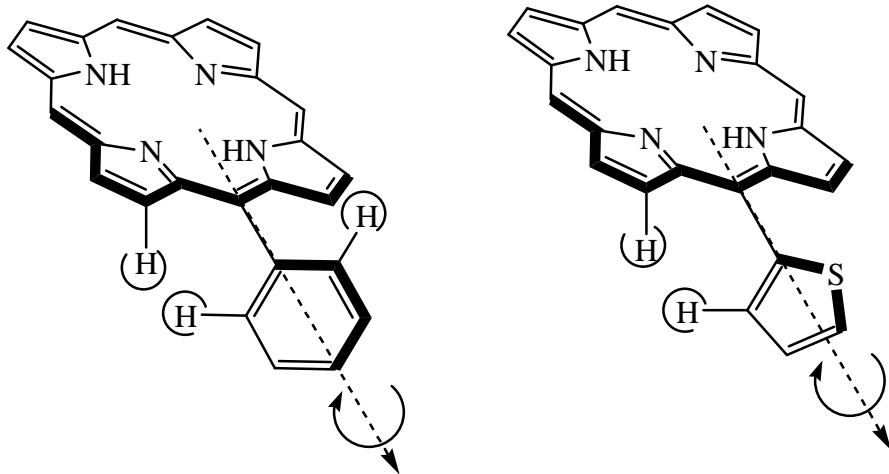
Figure 18   Barriers of rotation for phenyl and thienyl meso *substituents.*[28]

A direct correlation between the degree of porphyrin distortion and the bathochromic shift in absorbance spectra was shown for the overcrowded porphyrins (**H₂P3**, **H₂P4**, **H₂P5**, Fig. 2).[7] Remarkable bathochromic shifts of up to 100 nm of the Soret bands were observed. **H₂P3** and **H₂P5** have Soret bands with λ_{max} at 508 and 520 nm respectively. The Soret band of 2,3,5,7,8,10,12,13,15,17,18,20-dodecaphenylporphyrin was observed at 466 nm, indicating that along with the distortion of the macrocycle there is another factor influencing the bathochromic shifts in thienyl porphyrins.

A more recent study on porphyrins **ZnP21** – **ZnP26** (Fig. 9) suggests that the direct attachment of the aromatic thiophene ring at the *meso* position of the porphyrin ring does lead to electronic interaction of the two π-systems which can be enhanced by appropriate substitution.[18] By varying the substituent on the thiophene ring a bathochromic shift can be observed in the Soret band of the porphyrin. Again, when compared to **ZnTPP** the Soret band of **ZnP1** was red shifted by 8 nm to 430 nm, while the other tetra substituted porphyrins **ZnP21**, **ZnP22** and **ZnP23** are shifted by an additional 4 nm, 8 nm and 6 nm respectively. Such a strong shift would not be predicted on the basis of an inductive effect alone. More likely is the increased coupling of the overlapping π systems of the porphyrin and thiophene rings as is evidenced in the increasing FWHM of the porphyrin Soret.

Varying the number of 5-trimethylsilylethynylthien-2-yl groups around the porphyrin (**ZnP24**, **ZnP25** and **ZnP26**) also induces a 4 nm bathochromic shift for each thienyl moiety added (when compared to **ZnTPP** λ_{max} = 422 nm) such that the Soret band of **ZnP26** is observed at 438 nm.

The fluorescence spectrum of thienyl porphyrins exhibit characteristic singlet state emission consisting of two vibronic bands i.e. Q(0,0)* and Q(1,0)* in the range 550 - 800 nm (Fig. 19).[18] In the fluorescence spectrum of **H₂TPP** two λ_{max} are observed at 652 and 716 nm corresponding to Q(0,0)* and Q(1,0)*. **H₂P2** exhibits red shifted bands at 658 and 723 nm and even more bathochromically shifted is the spectrum of **H₂P1** with bands at 666 and 722 nm.[25] Fluorescence quantum yield (Φ_{fl}) of 0.006 was reported for **H₂P1**. This is lower than the values reported for **H₂P2** (0.010) and **H₂TPP** (0.120). A similar trend was observed for the zinc metallated derivatives with **ZnP1** and **ZnP2** exhibiting emission bands at 618, 658 and 605, 653 nm respectively. The fluorescence quantum yields of the metal complexes (**ZnP1**: 0.0013, **ZnP2**: 0.004) are also reduced compared to **ZnTPP** (0.033). The decrease in quantum yield of thien-2-yl porphyrins relative to thien-3-yl porphyrins has been attributed to the closer proximity of the sulphur to the porphyrin π-system.[25]
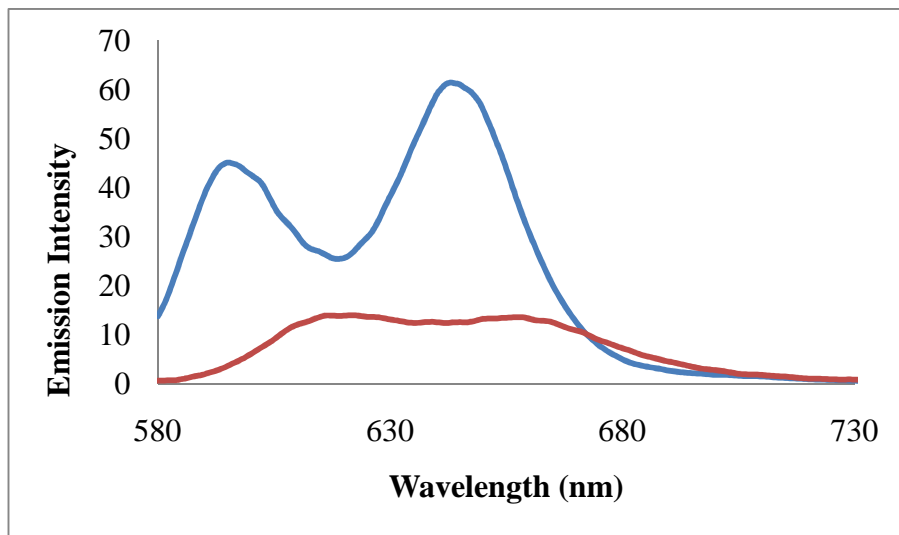
Figure 19   *Steady-state emission spectrum of **ZnTPP** (blue line) and **ZnP1** (red line) recorded in CH₂Cl₂ at room temperature.*

A reduction in singlet state lifetime was observed for the thienyl porphyrins (**H₂P1**, Fig. 2 and **H₂P63**, **H₂P64**, **H₂P65** Fig. 20) with respect to **H₂TPP** (Table 3).[27] This is attributed to the presence of the four "heavy" sulphur atoms on the periphery of the macrocycle. However suggestion of π-π overlap of the thienyl and porphyrin systems was also implied by the authors.

Porphyrin	τ_f (ns)	Φ_f	kf (1 / ns)
H₂TPP	9.8	0.11	0.102
H₂P1	1.11	0.013	0.09
H₂P63	1.31	0.014	0.76
H₂P64	1.47	0.014	0.68
H₂P65	1.20	0.017	0.83

Table 3   *Luminescence data of thien-2-yl porphyrins and **H₂TPP** in toluene at ambient temperature.*[27]
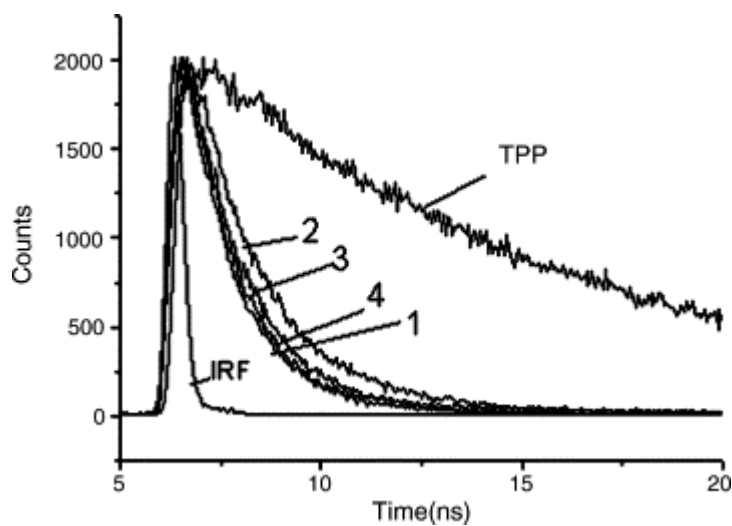
Figure 20   *Fluorescence decay signals of **H₂TPP, H₂P1** (1), **H₂P62** (3), **H₂P63** (2) and **H₂P64** (4) in toluene at ambient temperature. The detection wavelength is 660 nm. IRF indicates the instrument response function.*[27]

The fluorescence lifetimes of zinc(II) thienylporphyrins **ZnP21 – ZnP26** (Fig. 9) are in the range 1.36 – 0.52 ns. The shortest lifetime was that of **ZnP21**, bearing four heavy bromine atoms and it also possessed the lowest fluorescence quantum yield. The fluorescence emission spectra of **ZnP24 – ZnP26** show increased intensity with a concurrent red shift of their λ_{max} as the number of 5-trimethylsiylethynylthien-2-yl moieties were added, when compared to **ZnTPP**. The fluorescence quantum yield (Φ_{fl}) of the mono- and di-(5-trimethylsilylethynylthien-2-yl)porphyrins increase by 39 % and 27 % respectively compared to **ZnTPP**. Triplet excited state $^3(\pi\text{-}\pi^*)$ absorbance spectra and transient absorbance lifetimes were also obtained. Similar to **ZnTPP**, each porphyrin displayed a weak absorbance in the UV region with another more intense absorbance in the visible in the region. In the case of **ZnTPP** the λ_{max} is observed at 470 nm, however with the *meso* tetra(thien-2-yl)porphyrins the λ_{max} of each is observed in the region between 490 – 500 nm. A substantial increase in absorbance was also observed in the region 580 – 780 nm which the authors attribute to charge transfer to the peripheral thein-2-yl π system. **ZnP24**, **ZnP25**, **ZnP26** and **ZnP22** are all red shifted relative to **ZnTPP** with their λ_{max} occurring at 480, 480, 490 and 500 nm respectively. A decrease in triplet lifetime is observed for **ZnP1** (20 μs) **ZnP21** (7 μs) **ZnP22** (12 μs) and **ZnP23** (13 μs) relative to **ZnTPP** (24 μs). Increasing the number of 5-trimethylsilylethynylthien-2-yl moieties on the porphine also resulted in a decrease in the triplet lifetime: **ZnP24** (16 μs), **ZnP25** (11 μs) and **ZnP26** (10 μs). These excited state characteristics suggest relatively strong coupling of the porphyrin ring and the thien-2-yl π framework upon excitation. The combined studies of Brückner et al. and Rochford et al. show considerable electronic communication between the thienyl and porphyrin π-systems in both the ground and excited states. Thus earlier studies on thienyl porphyrins implying inductive effects alone were responsible for the change in photophysical properties relative to phenyl porphyrins need to be revised.

In *trans* thienyl porphyrins, the classic electronic spectra of the porphyrin is retained although it is hypsochromically shifted compared to both **H₂P1** (Fig. 1) and **H₂TPP**. The unsubstituted *trans* thienylporphyrin (**H₂P10**, Fig. 4) presents an intense Soret band with a maximum absorbance at 411 nm, with the Q bands showing a similar blue shift. The emission spectrum of **H₂P10** possesses a strong fluorescence, centred at 642 nm with a weak shoulder at 707 nm. The emission pattern is very similar to that of **H₂TPP** ($\lambda_{em} =$

653, 721 nm) only slightly blue shifted. The photophysical properties of the mono substituted porphyrins (Fig. 8) were also examined.[17] The Soret band at 425 nm for **ZnP19** and 424 nm for **ZnP20** are very similar to those of **ZnP1** (λ_{max} = 426 nm) but appear broader. The slightly increased broadening in **ZnP19** compared to **ZnP20** may be caused by the larger conjugation between the porphyrin core and the thiophene in **ZnP19**. The emission of **ZnP19** and **ZnP20** occurs at 608, 660 nm and 606, 661 nm respectively.

The on/off switching of porphyrin fluorescence through the use of a ferrocene/ferricenium (Fc/Fc$^+$) redox couple was reported for the zinc(II) tri(thien-2-yl)porphyrin-ferrocene dyad, **ZnP27** (Fig. 37).[19] The $^1(\pi\text{-}\pi^*)$ fluorescence of **ZnP27** is almost completely quenched in comparison to both **ZnP1** (Fig. 2) and **ZnTPP**, with no evidence of the $^3(\pi\text{-}\pi^*)$ excited state observed by transient absorbance spectroscopy (Fig. 21). Attachment of the ferrocene substituent at the *meso* position quenched both the $^1\pi\text{-}\pi^*$ and $^3\pi\text{-}\pi^*$ excited states of the porphyrin ring by a rapid electron transfer mechanism. The fluorescence of the dyad can be "switched on" by oxidation of the ferrocene to the ferricenium ion. The Fc/Fc$^+$ redox couple occurs 40 mV positive of the unsubstituted ferrocene and results in the appearance of a low-energy ferricenium ligand-to-metal charge transfer absorbance at 767 nm. Oxidation of Fe(II) to Fe(III) restores the porphyrin emission through preclusion of the electron-transfer process. The relative fluorescence quantum yield for **ZnP27**$^+$ is 71 % with respect to **ZnP1** the minor decrease in fluorescence is attributed to the quenching processes of intersystem crossing of the porphyrin $^1(\pi\text{-}\pi^*)$ excited state to the new LMCT state and energy transfer quenching by the ferricenium unit. Transient absorbance spectroscopy of the **ZnP27**$^+$ dyad produced transient signals indicative of the $^3(\pi\text{-}\pi^*)$ triplet excited state (Fig. 21). A triplet lifetime of 20 μs was obtained for **ZnP27**$^+$, a reduction of 50 % in comparison to **ZnP1** (40 μs). Similarly, the $^1(\pi\text{-}\pi^*)$ singlet excited state lifetime of 0.31 ns observed for **ZnP27**$^+$, is shorter than that of **ZnP1** (0.56 ns).
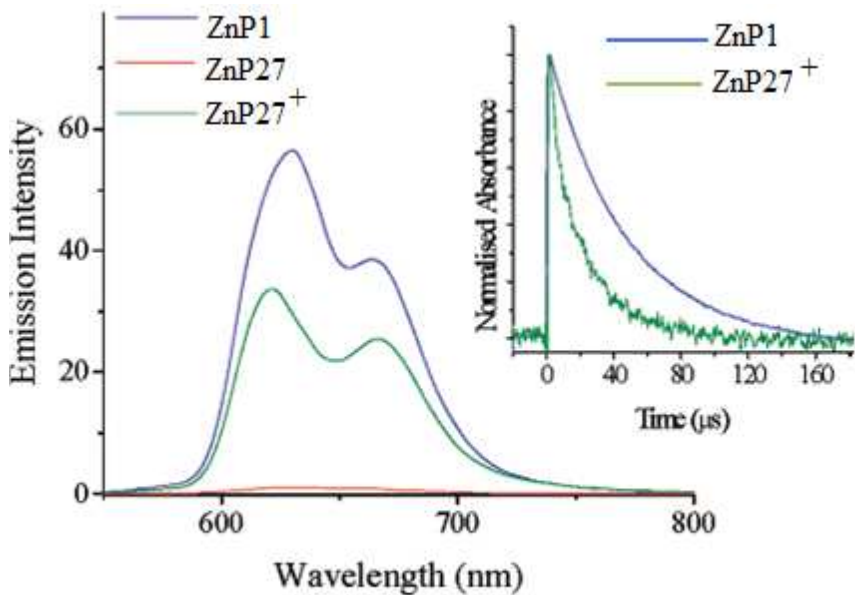
Figure 21 *Fluorescence spectra of **ZnTPP**, **ZnP27**, and **ZnP27**^{+} in ethanol. Inset: normalised transient absorbance decay traces of **ZnP1** and **ZnP27**^{+} at 490 nm (λ_{exc} 532 nm; 1 atm of argon, in ethanol).*[19]

The electronic absorbance properties of porphyrins, **ZnP29 – ZnP34** (Fig. 10), were examined (Table 4) and results indicated that both the λ_{max} of the Q bands and emission spectra are primarily dependent on whether the thiophene unit was linked to the macrocycle directly at the *meso*-carbon position (**ZnP29 – ZnP31**) or through an intervening ethynyl unit (**ZnP32 – ZnP34**) and was also affected by the number of thiophene units (n = 1, 2 or 3).[20] Modest Stokes shifts (350 to 1300 cm^{-1}) indicate that the derivatised zinc(II)porphyrins undergo modest to substantial excited state structural distributions. For each mode of connectivity the porphyrins that possess only a single thiophene unit (**ZnP29** and **ZnP32**) display the largest Stokes shift within their respective class. Consistent with this, **ZnP29** and **ZnP32** exhibit emission maxima at 698 nm and 714 nm the lowest energy within their respective structural class. The emission maxima of each class also follow a similar trend, in that; they shift hypsochromically with increasing number of thiophene units. The porphyrins with thiophene units bonded directly at the *meso* position (**ZnP29 – ZnP31**) displayed emission maxima values at 698, 669 and 662 nm respectively while porphyrins linked to the thiophene through the ethynyl moiety

(**ZnP32 - ZnP34**) displayed bathochromically shifted emission maxima which shift hypsochromically with increasing number of thiophene units at 714, 706 and 700 nm respectively. This is indicative of the increased excited-state electronic dipole moment due to extensive porphyrin-thiophene conjugation. **ZnP35**'s formyl group caused a blue shift in the Q band λ_{max} (676 nm), whereas the strong dicyanovinyl acceptor group in **ZnP36** caused a red shift (λ_{max} = 698 nm) relative to **ZnP32** (λ_{max} = 685 nm).

Porphyrin	Soret λ_{max} (nm)	λ_{em} (nm)	Stokes shift (cm^{-1})	β_{1300} (x 10^{-30}esu)
ZnP29	456	698	1298	2400
ZnP30	457	669	653	2200
ZnP31	458	662	495	4335
ZnP32	465	714	593	690
ZnP33	468	706	477	670
ZnP34	470	700	356	1170
ZnP35	461	696	425	1020
ZnP36	469	759	1151	785
ZnP37	458	713	812	810
ZnP38	459	682	375	1400

*Table 4   Electronic data of **ZnP29** – **ZnP38** recorded in THF.*[20]

In spite of the direct attachment of the π-systems of anthracene, oligothiophene and porphyrin in **H₂P39 – H₂P59** (Fig. 11), the individual molecular subunits were observed in the UV-vis spectra as in the spectra of supramolecular systems (Table 5).[21] For all anthracene-oligothiophene-porphyrin molecules, highly selective excitation of the terminal 9-anthryl unit at 258 nm is possible. The supramolecules all possess typical singlet emission from the porphyrin Q(0,0)* and Q(1,0)* emission bands. The emission bands are broadened and red shifted (~7 nm) compared to **H₂TPP**. Upon excitation at 258 nm, both

H₂P46 and **H₂P49** possess the typical porphyrin emission indicating energy transfer from the anthracene to the porphyrin chromophore. The authors estimate, on the basis of perfect matching of absorbance and excitation spectra, that energy transfer efficiency is 98 %. The bithiophene bridged systems, **H₂P42** and **H₂P44**, gave analogous results. Thus singlet-singlet energy transfer is the only quenching process involved. Similar results were found on increasing the length of the oligothiophene chain in **H₂P55** - **H₂P59**. Excitation of the intensive anthracene transition led to typical emission from the porphyrin end group. The mechanism of energy transfer, i.e. Förster or Dexter, could not be clearly defined for these systems. The authors did suggest however that due to vibronic coupling, energy is transferred from the anthryl donor to the porphyrin acceptor *via* an intramolecular vibrational relaxation process mediated by the oligothiophene chain. On comparing these results with similar polyene based systems Würthner et al. concluded that oligothiophenes were far superior with regard to mediating energy transfer and showed greater potential for application in molecular electronics.

Porphyrin	Anthracene λ_{max} (nm)	Soret band λ_{max} (nm)	Q bands (nm)
H₂P41	258	421	522, 559, 600, 657
H₂P42/P43	258	426	524, 564, 599, 657
H₂P46	258	422	522, 559, 599, 657
H₂P47/P48	258	428	525, 565, 600, 659
H₂P49	258	435	526, 573, 598, 663
H₂P55	254	419	519, 555, 601, 659

Table 5   Absorbance data for some of the supramolecular systems recorded in n-hexane.[21]

Okada et al. investigated substituent control of *J*-aggregate formation of insoluble porphyrins in protonated water.[29] Working primarily with phenyl substituted porphyrins it was found that substituents at the *meso* position affected aggregation to a higher extent.

Porphine and octaethylporphyrin did not form *J*-aggregates, indicating that aromatic rings at the *meso* position are necessary for aggregate formation. Furthermore aromatic rings with large steric bulk also did not aggregate. In protonated solution, however **H₂P2** (Fig. 2) did form *J*-aggregates. This was evidenced by changes in the absorbance spectra. The Soret band of the freebase monomer (420 nm) is first replaced by the protonated monomer absorbance (447 nm) which is in turn exchanged by a new absorbance at 481 nm. Simultaneously the observed Q band at 652 nm is bathochromically shifted to 678 nm and subsequently 756 nm. These bathochromic shifts in the absorbance spectra signify the assembly of "head-to-tail" aggregates. In most cases, AFM images of the *J*-aggregate films revealed square rod like microcrystals. The Soret band remained around 480 nm for the aggregates however the Q band absorbances were found to vary widely from 658 to 756 nm. It was also noted that the electron-donating character of the *meso* substituents affected the FWHM of the Q bands. These changes in the absorbance spectra suggest that the energy levels of the excited states of the porphyrin *J*-aggregates are substituent dependant.

2.1.1.3 Electrochemical properties and electropolymerisation

By monitoring shifts in the anodic and cathodic redox processes of the porphyrin the influence of the thienyl group on the HOMO and LUMO energies can be further examined. Each of the thienyl porphyrins, **H₂P1**, **H₂P2** and their zinc and copper analogues (Fig. 2), displayed two successive one-electron oxidations and two successive one-electron reductions (Fig. 22).[5] **H₂TPP** was also examined to delineate the effect of the thienyl groups. The observed potentials revealed striking differences in oxidation and reduction of **H₂P1** relative to **H₂P2** and **H₂TPP**. Both thienyl porphyrins showed a cathodic shift of the first oxidation (50 mV for **H₂P1$^{+/0}$** and 110 mV for **H₂P2$^{+/0}$**) with respect to **H₂TPP** (+1.0 V *vs.* Ag/AgCl). The first reduction of **H₂P2** was within experimental error when compared to **H₂TPP**, however **H₂P1$^{0/-}$** showed a substantial anodic shift of 140 mV which was primarily responsible for its reduced band gap and lower energy absorbance. A HOMO-LUMO energy gap of 1.98 eV was calculated for **H₂P1** compared to 2.18 eV for to **H₂P2** and 2.23 eV for **H₂TPP**. Similar trends were observed for the metallated analogues with the redox potentials of **ZnP2** and **CuP2** approaching those of **ZnTPP** and **CuTPP**. While the authors ascribed this band gap narrowing to thienyl substitution inductive effects the results can similarly be explained by the π-π overlap of the porphyrin and thienyl structures resulting in stabilisation of both the HOMO and LUMO orbitals, which corresponds well with the ground and excited state trends observed by Brückner et al. and Rochford et al. The electrochemical properties of **H₂P1** (Fig. 2), **H₂P62**, **H₂P63** and **H₂P64** (Fig. 12) were also investigated by cyclic voltammetry.[27] However in contrast to the previous results, the latter study showed two one-electron oxidations and only one, one-electron reduction process
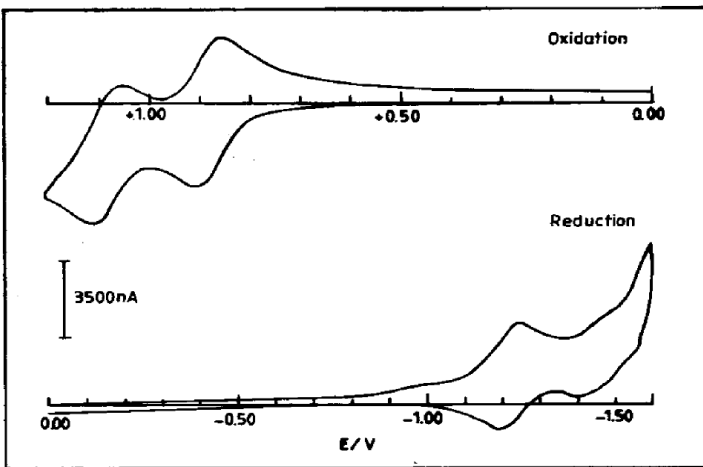
*Figure 22   Cyclic voltammogram of **ZnP1** in CH$_2$Cl$_2$ with 0.1M TBAHFP as supporting electrolyte.*[5]

Substitution of the thien-2-yl moiety caused significant changes in the redox potentials as observed in the cyclic voltammetry studies of **ZnP21** – **ZnP26** (Fig. 9). All porphyrins showed two one-electron oxidations and two one-electron reductions. The *meso* tetra(thien-2-yl)porphyrins showed an anodic shift in their first oxidation (**ZnP1**$^{+/0}$ 0.43, **ZnP21**$^{+/0}$ 0.61, **ZnP24**$^{+/0}$ 0.49, **ZnP23**$^{+/0}$ 0.49 V *vs.* Fc/Fc$^+$) when compared to **ZnTPP**$^{+/0}$ (0.34 V *vs.* Fc/Fc$^+$), indicating stabilisation of the HOMO orbital of the porphyrin ring system. Stabilisation of the LUMO orbitals also occurred with a decrease in the potential of the first reduction. Again **ZnP21** showed the largest effect with a decrease in its reduction potential of 240 mV compared to **ZnTPP**$^{0/-}$ -1.85 V *vs.* Fc/Fc$^+$. Increasing stabilisation of the HOMO and LUMO was observed on increasing thienyl substituents on the porphyrin ring as seen in **ZnP24**, **ZnP25**, **ZnP26** and **ZnP22**. A decrease in the reduction potential (i.e. LUMO energy) appeared to be the dominant factor in reducing the calculated HOMO-LUMO energy gap for these systems. The reduction in the band gap follows the order **ZnP22** (2.02 eV), **ZnP26** (2.02 eV), **ZnP25** (2.04 eV), **ZnP24** (2.06 eV) and **ZnTPP** (2.09 eV). Therefore by controlling the number of thienyl substituents on the porphyrin as well as the nature of the thienyl ring itself the band gap may be manipulated.

60

It is well established that the HOMO orbital of the porphyrin macrocycle is destabilised upon reduction of its planarity. Puckered porphyrins are easier to oxidise where as reduction is insensitive to the distortion, which lowers the HOMO-LUMO energy gap.[30] This was realised in the redox properties of the copper(II) metallated derivatives of the highly substituted porphyrins, **CuP3**, **CuP4** and **CuP5**, along with **CuP1** (Fig. 2).[7] Substitution of the porphyrin ring with thien-2-yl moieties in the *meso*- and β- positions increased the energy of the HOMO orbital as expected, however a stabilisation of the LUMO orbital also occurred resulting in an overall decreased energy gap of 1.89 eV for **CuP4**, 1.63 eV for **CuP3** and 1.48 eV for **CuP5**. HOMO-LUMO energy gaps of 2.34 eV and 2.20 eV were reported for **CuTPP** and **CuP1**.

Two reversible waves occur at -1.58 V and -2.04 V *vs.* SCE for *trans* dithienylporphyrin (**H_2P10**, Fig. 4).[14] Continual sweeps of **H_2P10** resulted in the deposition of a thin insoluble polymer on the electrode. Further investigation of this polymer layer showed that it belongs to the restricted family of "zero bandgap" polymers, that is, the oxidation potential is less than or equal to its reduction potential. Porphyrins with band gaps as low as +0.8 and +0.35 eV *vs.* SCE (**H_2TPP** and **ZnTPP** respectively) have been previously reported.[31] This is the first "zero bandgap polymer" in a poly (aryl-porphyrin) series. The authors are continuing their studies in order to explain such electrochemical behaviour.

Polymerisation by electrochemical oxidation was carried out on *trans* dithienylporphyrins **ZnP11** and **CuP11** (Fig. 5). Following electrochemical oxidation, the zinc(II) and copper(II) polymers, **poly-ZnP11** and **poly-CuP11**, were deposited on the surface of a gold-plate electrode. Peak currents at +1.1 V and +0.9 V *vs.* SCE, attributed to coupling of the thienyl groups at the *meso* position of the porphyrin, increased with increasing scan number, indicating, that the deposited porphyrin-thiophene copolymer formed a conductive film. Chemical oxidation of **H_2P12, ZnP12** and **CuP12** (Fig. 8), using $FeCl_3$ as oxidant, resulted in the corresponding co-polymers (**poly-H_2P12, poly-ZnP12** and **poly-CuP12**) in high yield (> 90 %). The conductivity of the co-polymer **poly-H_2P12**, doped with $FeCl_3$ was found to be over 10^{-6} S/cm. Increased conjugation between the bithienyl groups and

the porphyrin ring may have caused accelerated energy and electron transfer processes between the porphyrin and oligothiophene units.

The iron(III) porphyrin (**FeP2**, Fig. 2) also undergoes electropolymerisation. An anodic wave at ~1.3 V *vs.* Ag/AgCl was attributed to oxidation of the peripheral thien-3-yl groups in the monomer and a subsequent single broad anodic wave in the region +1.0 – 1.5 V *vs.* Ag/AgCl signified polymerisation of a porphyrin film (**poly-FeP2**, Fig. 23) onto the electrode.[32] The electrode modified with **poly-FeP2** demonstrated electroactivity due to the presence of the iron (II/III) couple and a mean redox potential of 0.0 V *vs.* Ag/AgCl suggested a low charge-transfer resistance within the semiconductive film. Bromoiron(III) *meso* tetrakis(thien-3-yl)porphyrin was coordinated with the axial ligand, 1-methylimidzole (im), to form the coordination complex **[Fe(im)P2]$^+$Br$^-$**. Electrodeposition of the complex resulted in a broad anodic wave in the range +0.8 – 0.15 V *vs.* Ag/AgCl and the polymerised complex was electroactive with a mean redox potential of +0.05 V *vs.* Ag/AgCl.

Fe(III)P2   **poly-FeP2**
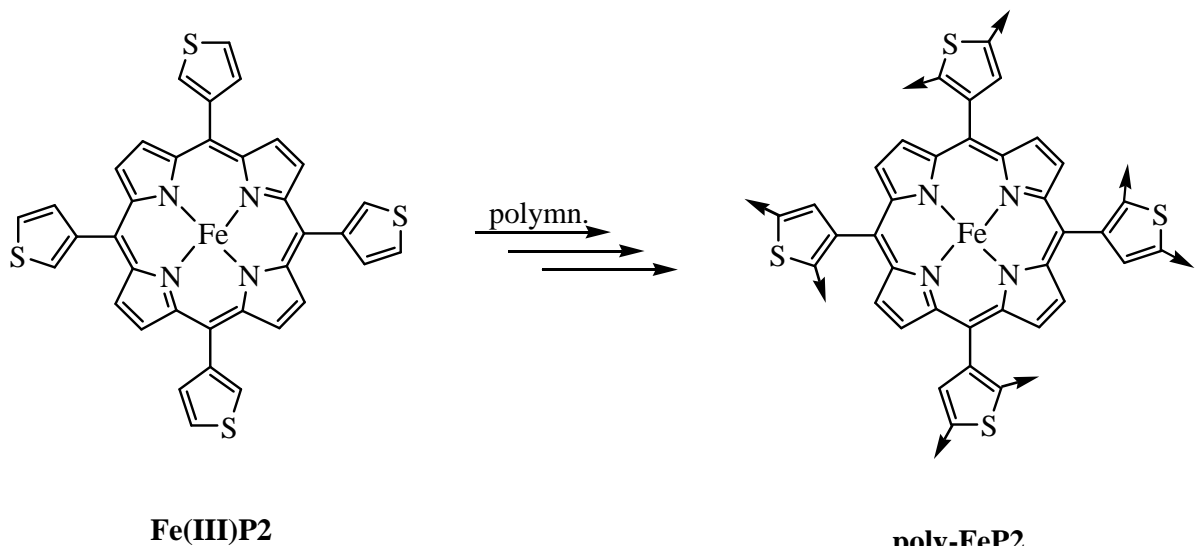
Figure 23   Polymerisation of **FeP2**.

The metalloporphyrins M**P60** and M**P61** (M = Zn, Pd, Fig. 12) were polymerised by electrochemical oxidative coupling of the *meso* oligothienyl groups.[22] The repeated oxidation of *meso* bithienyl groups of **ZnP60** was observed above +1.40 V *vs.* SCE, with the redox couple of the first oxidation of the porphyrin ring (observed at *ca.* +1.0 V *vs.* SCE) increased with increasing number of cycles. Deposition of a polymer (**poly-ZnP60**) onto the working electrode occurred during the course of the experiment. Electrochemical polymerisation of **ZnP61** (oxidation of the porphyrin ring: +0.60 V *vs.* SCE, oxidative coupling of terthienyl groups: +0.71 - 0.80 V *vs.* SCE) and the palladium complexes of bithienyl and terthienyl substituted porphyrin was achieved in a similar manner. Infrared analysis indicated that α-α coupling of the *meso*-oligothienyl groups occur to form a quasi-2D polymer (Fig. 24). Scanning tunnelling microscopy (STM) of an ultra thin film of **poly-ZnP61** prepared on a Au(III) substrate confirmed the quasi – 2D structure, although some disorder was included. Film thickness of 0.5 nm indicates a planar orientation of the porphyrin rings, with an alternating structure of porphyrin and oligothiophene moieties. The mean distance between the intersections was *ca.* 2.82 nm and the model distance between the monomer units was *ca.* 3 nm which supported the fact that **poly-ZnP61** formed a lattice. The d.c. conductivities of **poly-ZnP60** and **poly-PdP60** were 3 x 10^{-7} S/cm and 2 x 10^{-7} S/cm respectively. Layered polymers cells (ITO electrode/**poly-PdP60/poly-ZnP60/**Au electrode), constructed by the successive electrochemical polymerisation of **PdP60** and **ZnP60** showed electric rectifying properties. As the contacts between the individual polymers and the electrodes are ohmic, the rectifying properties are thought to arise from the molecular interface between **poly-ZnP30** and **poly-PdP60**.[33]
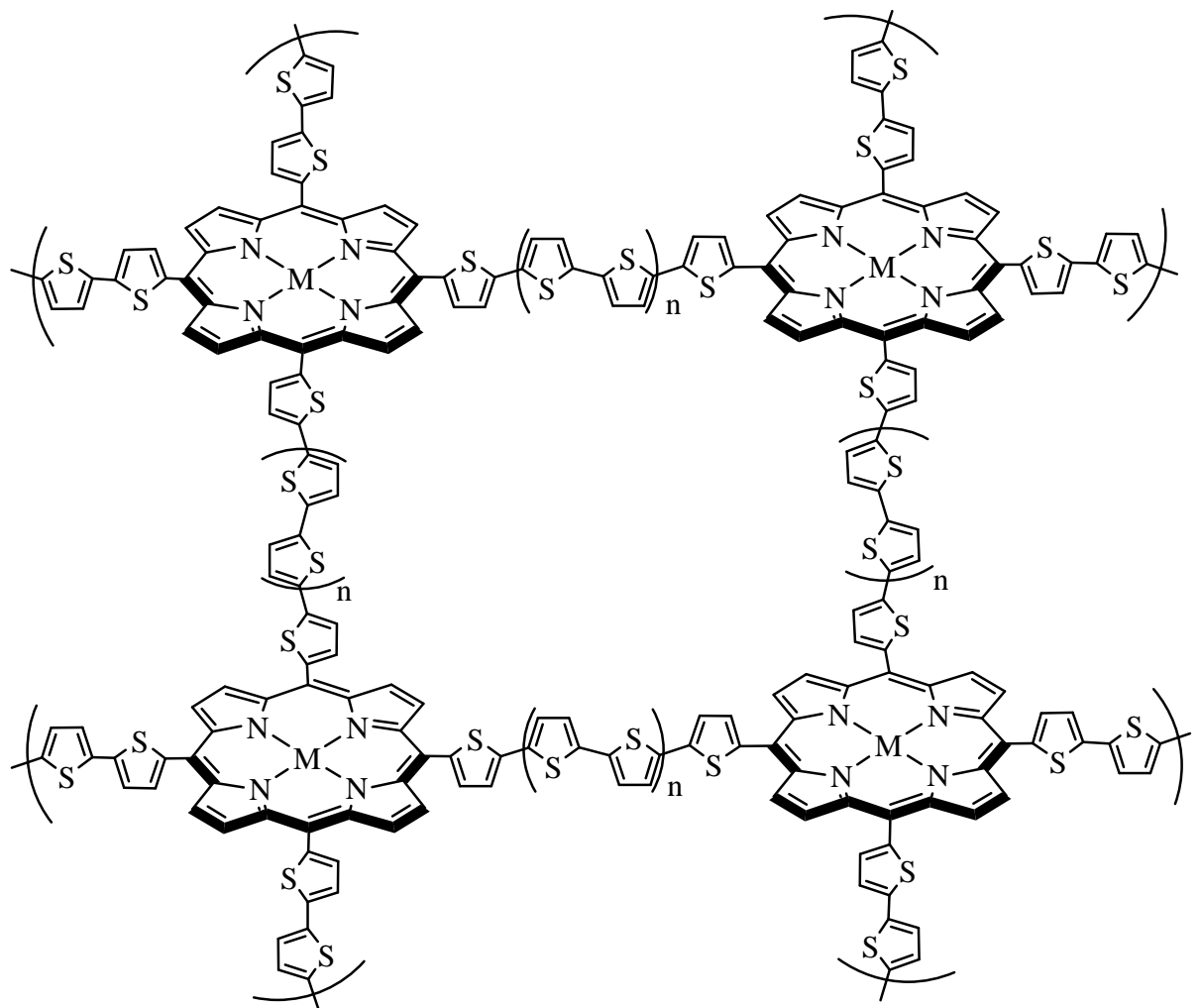
Figure 24   Proposed quasi 2D structures.

2.1.2 Thienyl porphyrins connected through a saturated or conjugated spacer

2.1.2.1 Synthesis

The design and synthesis of a series of thiophene appended porphyrin systems where the thiophene ring is fused to the periphery of the macrocycle *via* two aza linkages was reported by Crossley and Prashar.[34] The porphyrin precursors possessed a di-ketone functionality at the β position of the macrocycle which was reacted with 3,4-diaminothiophene to produce the laterally conjugated thienyl porphyrins (**H₂P66 – H₂P70**, Fig. 25). The aim was to attach the highly conjugated porphyrin systems to a gold surface through the sulphur atom of the fused thiophene ring in order to study the self assembly and molecular electronic properties of porphyrin based monolayers and thin films.
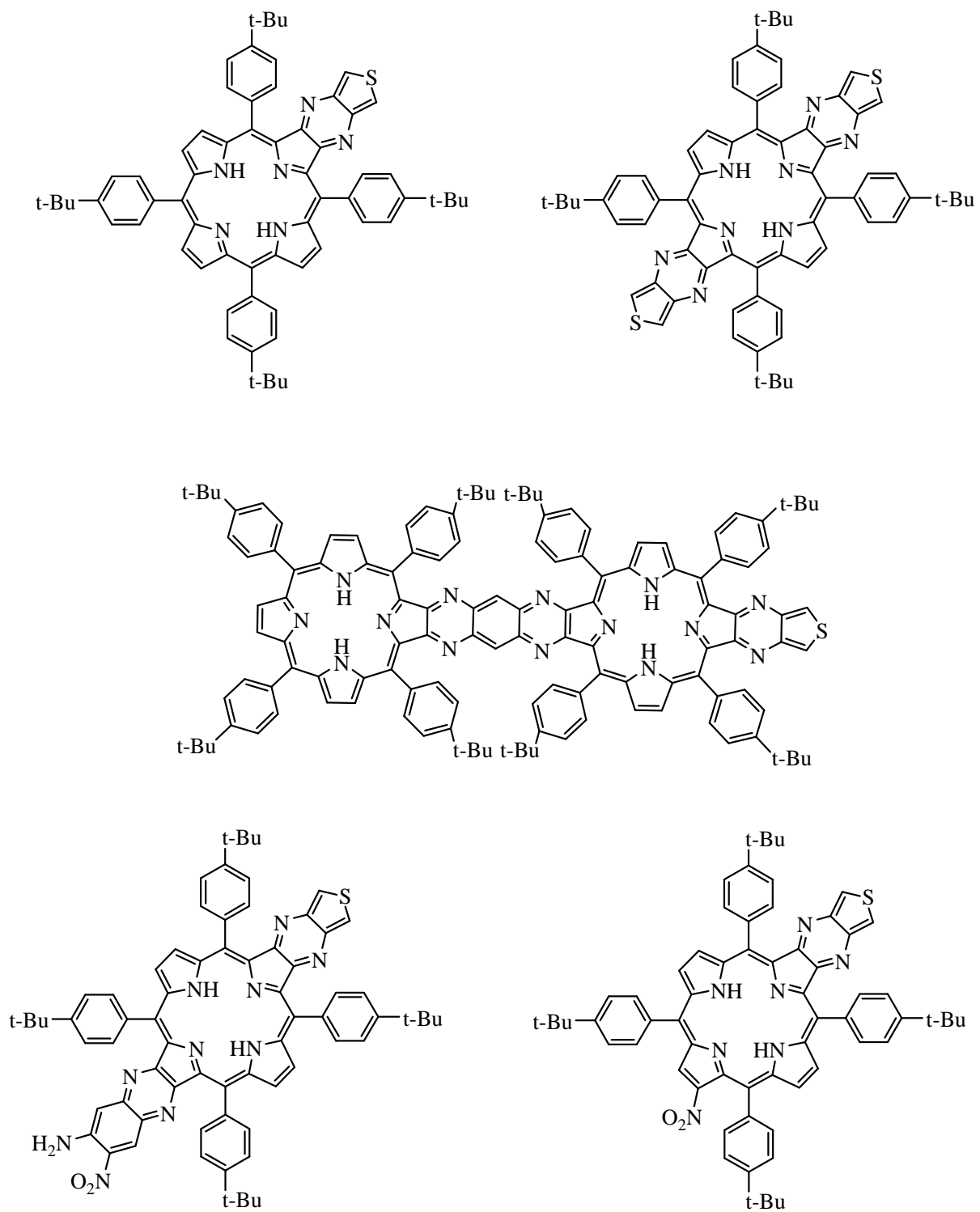
Figure 25   *Crossley and Prasher's fused thienyl porphyrins **H₂P66 – H₂P70**.*

Ono et al. synthesised a series of naphtoporphyrin systems using a series of pyrroles fused with aromatic rings (isoindole derivatives).[35] The aromatic nitro compound **1**, (Scheme 2) was reacted with ethylisocyanoacetate in the presence of DBU (1,8-diazabicyclo[5.4.0]undec-7-ene) to give fused pyrrole, **2**, in 60 % yield. Reduction of **2** to the hydroxymethyl pyrrole, **3**, is a crucial step in the reaction. Tetramerisation and oxidation of compound **3** generated the porphyrin **H₂P71**. However scrambling led to a mixture of four regioisomers. Only suitably controlled conditions for reduction and tetramerisation allowed the isolation of pure **H₂P71**. A similar fused porphyrin-thiophene system (**ZnP72**, Fig. 26) has also been reported by Callot et al.[36]
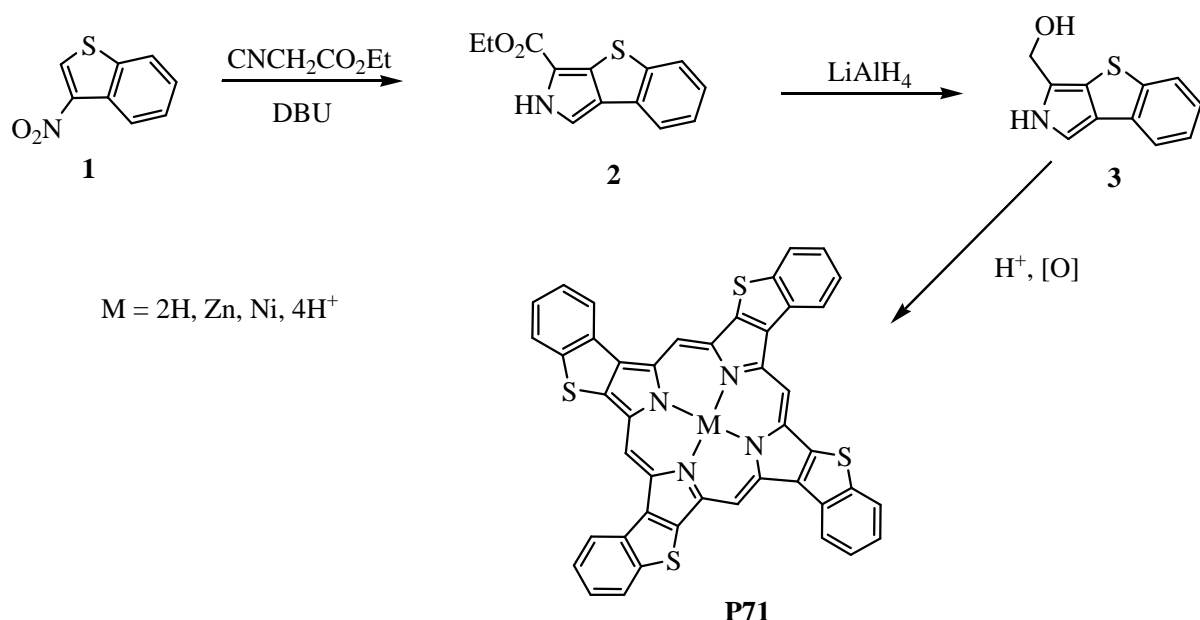
Scheme 2   *Synthesis of* **P71**.
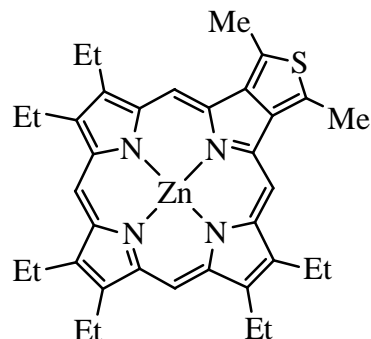
Figure 26   **ZnP72**.

3'-[5-(4-Phenoxy)-10,15,20-tritolylporphyrin]-2,2;-bithiophene (**H₂P73**, Fig. 27) and 3'-[5-(4-Phenoxy)-10,15,20-tritolylporphyrin]pentyl-2,2':5',2''-terthiophene (**H₂P74**, Fig. 27) were synthesised by coupling the porphyrin subunit [5-(4-phenoxy)-10,15,20-tritolylporphyrin)] to the relative oligothiophene by a Williamson ether synthesis to yield the tetraphenylporphyrin functionalised bithiophene in 88 % yield and the analogous terthiophene in 73 % yield.[37] The corresponding cobalt, nickel, zinc, iron and manganese complexes were also produced. In another study 5-(4-(1-hexylthien-3-yl)phenoxy)-10,15,20-tritolylporphyrin (**H₂P75**, Fig. 27) and the corresponding porphyrin without the thienyl group (5-(4-(1-hexyl)phenoxy)-10,15,20-tritolylporphyrin were synthesised by the Adler-Longo method.[38] The thienyl porphyrin **H₂P75** was also metallated with nickel in high yield.
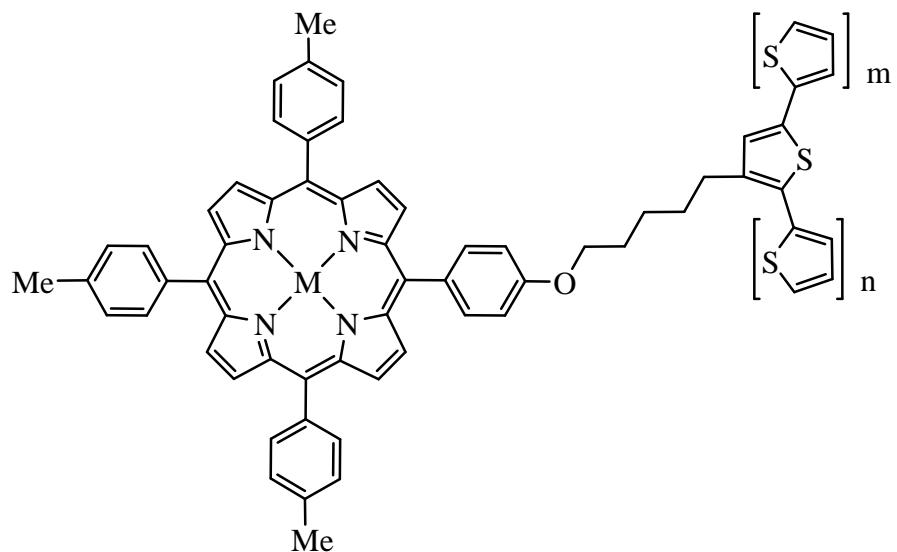
Figure 27   **P73**: *m = 1, n = 0, M = Zn(II), Ni(II), Co(II), Fe(III)Cl, Mn(III)Cl*

                      P74: *m = 1, n = 1, M = Ni(II), Co(II), Fe(III)Cl*

                      P75: *m = 0, n = 0, M = 2H, Ni(II)*

On reacting a thiophene substituted – benzaldehyde with 5-phenyldipyrromethane, 5,15-bis(4-(2-(3,4-ethylenedioxy)thienyl)phenyl)-10,20-diphenyl porphyrin (**H₂P76**, Fig. 28) and 5,15-bis(4-(2-thienyl)phenyl)-10,20-diphenyl porphyrin (**H₂P77**, Fig. 28) were produced along with their metal analogues in good yield.[39] The thiophene and 3,4-ethylenedioxythiophene moieties were chosen as polymerisation points on the porphyrin monomers as shown in figure 35.

P76

M = 2H, Zn   **P77**
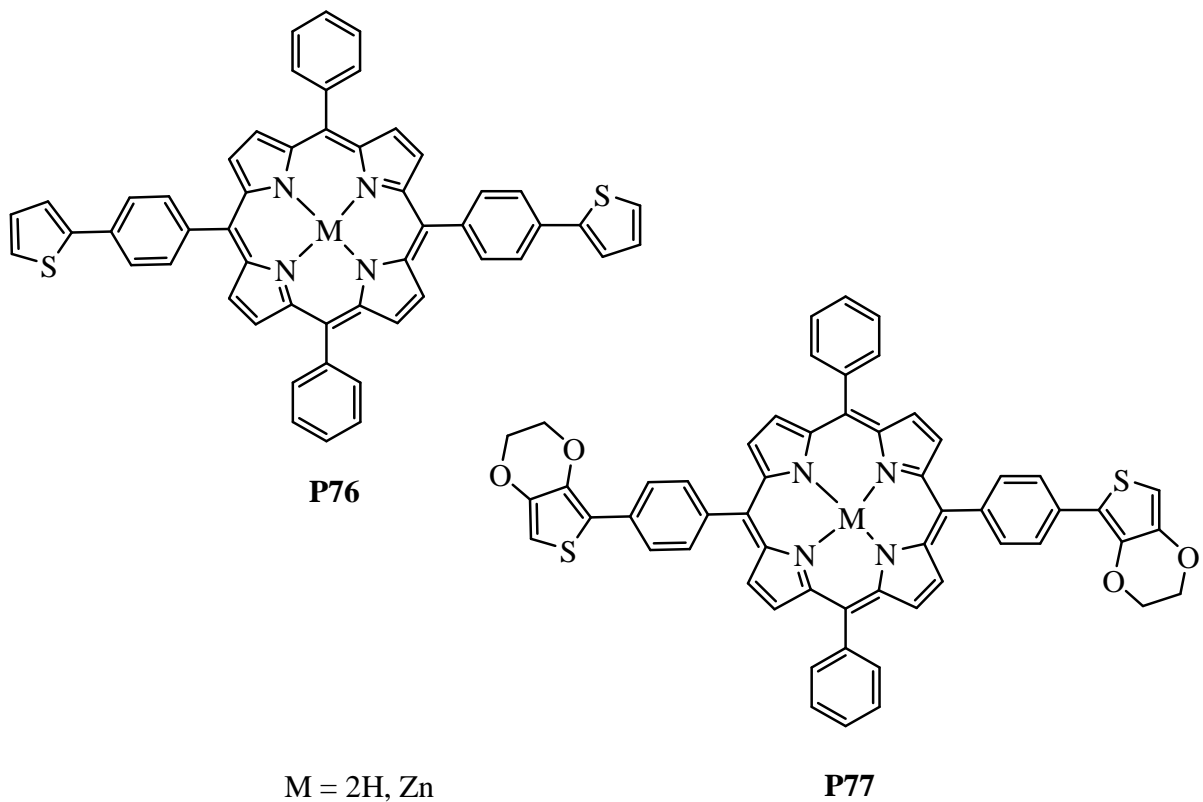
*Figure 28   Porphyrin monomers **P76** and **P77**.*

A number of phosphoric, P(V), porphyrin derivatives with two thienylalkoxy or oligothienylalkoxy groups at the axial position of the central metal atom have been synthesised.[40] The donor-photosensitiser-acceptor molecules were synthesised from dichlorophosphoric(V)-tetraphenylporphyrin and the corresponding thienyl or oligothienyl alcohol. Spectroscopic analysis confirmed that the two equivalent alkoxy groups were attached to the central phosphorus atom at the fifth and sixth coordination positions (Fig. 29).
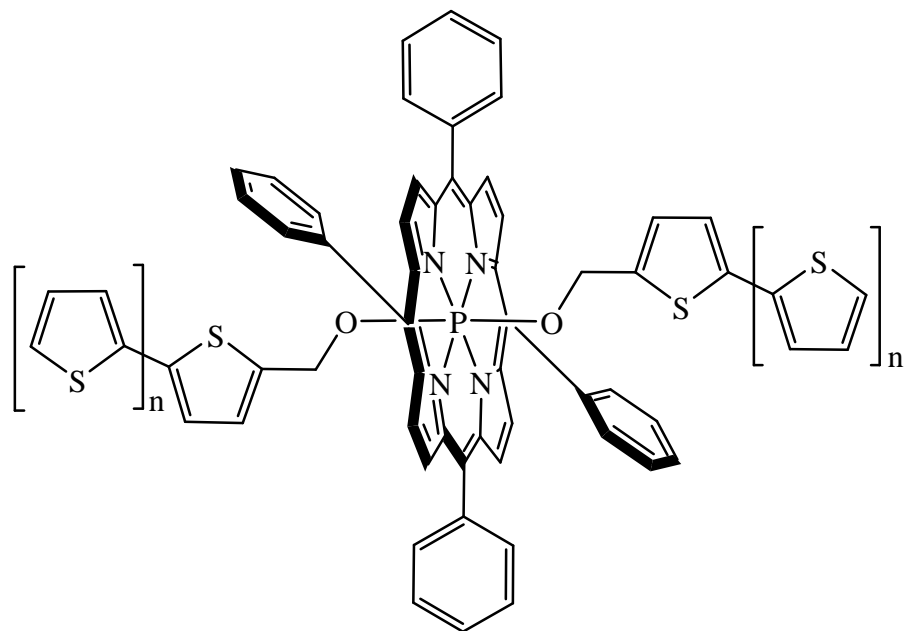
Figure 29 **P(V)P78:** *n = 0,* **P(V)P79:** *n = 1,* **P(V)P80:** *n = 2*

Zinc(II)-porphyrin polymers with *meso*-linked aryl and ethynyl spacers were synthesised using a combination of Stille and Sonogashira palladium coupling and Ni(cod)$_2$(bpy) coupling techniques.[41] The porphyrin monomers **H$_2$P81** – **H$_2$P85** were synthesised by the Mac Donald 2+2 reaction of bispyrrole and a range of aldehydes, followed by metallation with zinc yielding **ZnP81 – ZnP85** (Fig. 30). The porphyrin monomers were directly coupled to form homopolymers and also coupled to aryl units to form copolymers.
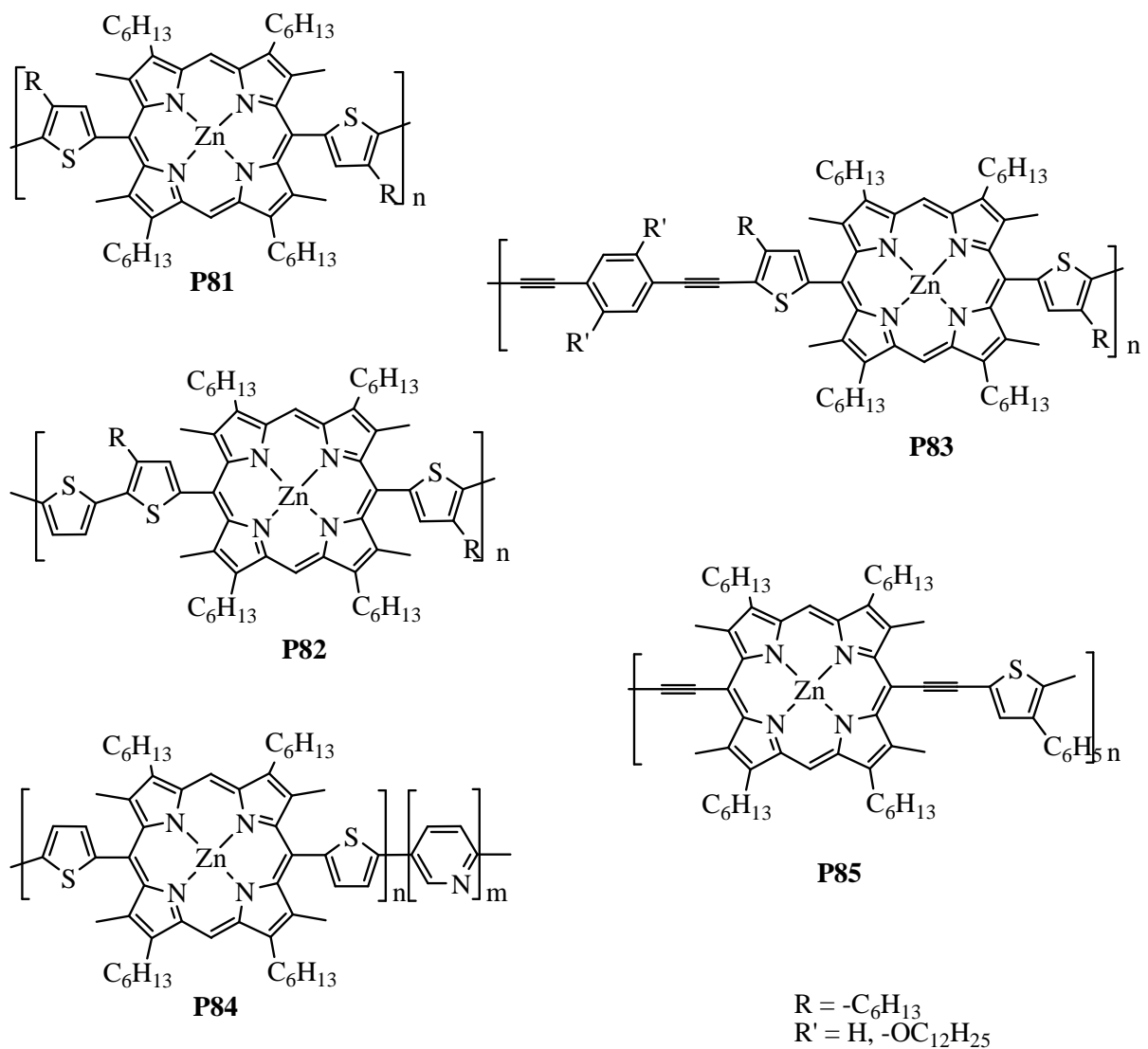
Figure 30   *Thienyl porphyrins with* meso-*linked aryl and ethynyl spacers.*

The oligothienyl linkage in multicomponent porphyrin systems is of great importance because it has two roles: it acts as a rigid spacer positioning two neighbouring centres at fixed distance with a well defined geometry, and the spacer can promote electronic communication, thus facilitating electron and/or energy transfer between two porphyrins. For this reason Odobel et al. synthesised a series of oligothiophene bridged bisporphyrins (**P86** – **P89**, Fig. 31).[42]   The novel bis-porphyrins are directly substituted at the *meso* position with an oligothiophene chain tethered by a single, double (*trans*) or triple bond. The porphyrins were produced by palladium catalysed cross coupling reactions (Stille,

71

Heck and Sonogashira) between 5-iodo-10,15,20-(3,5-di*tert*-butylphenyl)porphyrin and the oligothienyl chain. Subsequently either one or both of the linked porphyrins were metallated with zinc.

M = 2H, 2H; Zn(II), 2H; Zn(II), Zn(II)
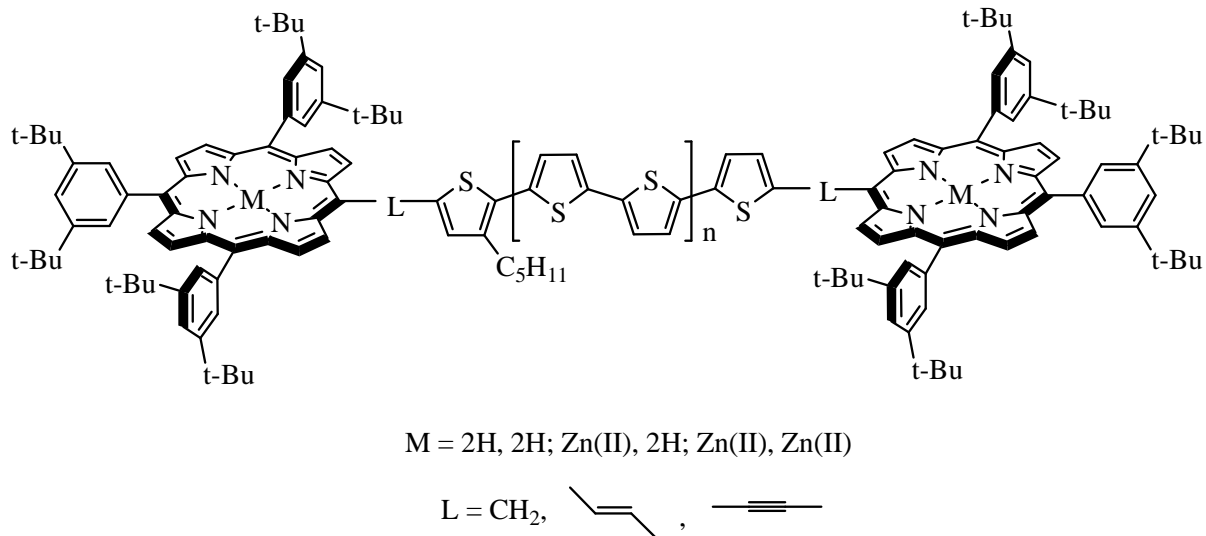
L = CH$_2$, \ , ═══

Figure 31   ***P86***: *n = 0, L = CH$_2$*

P87: *n = 1, L = CH$_2$*

P88: *n = 1, L = trans vinyl link*

P89: *n = 1, L = ethynyl link.*

The synthesis of freebase and Zn(II) 5,15-bis(acetylene-4-(ethylenedioxy)thiophene)-10,20-bis(4-methoxycarbonylphenyl)porphyrins (**H$_2$P90** and **ZnP90**, Fig. 32) and their hydrophilic disodium dicarboxylate derivatives (**H$_2$P91** and **ZnP91**, Fig.32) have also been reported.[43] The porphyrin monomer synthesis begins with Sonogashira coupling of 2-iodo-3,4-(ethylenedioxy)thiophene with 3,3-diehtoxypropyne, followed by cyclisation with 5-(4-methoxycarbonylphenyl)dipyrromethane to give the porphyrin product, **H$_2$P90**, in 3 % yield.

M = 2H, Zn
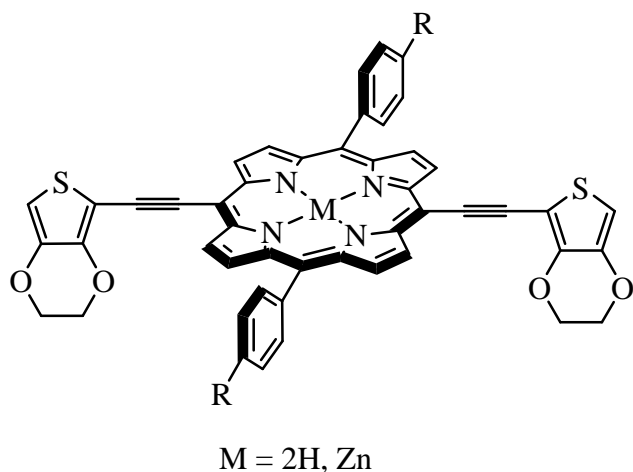
Figure 32   **P90**: *R = COOCH₃*

　　　　　　　P91: *R = COO⁻Na⁺.*

Kuo et al. presented a novel synthetic route to zinc tetrakis(ethynylaryl)porphyrins.[44] Using an adapted Sonogashira method, a range of electron donating substituents were coupled with 5,10,15,20-tetrakis(ethynyl)porphyrin and their redox properties examined. In this manner, zinc(II) 5,10,15,20-tetrakis(ethynylthien-2-yl) porphyrin, **ZnP92** was produced (Rxn. 1).
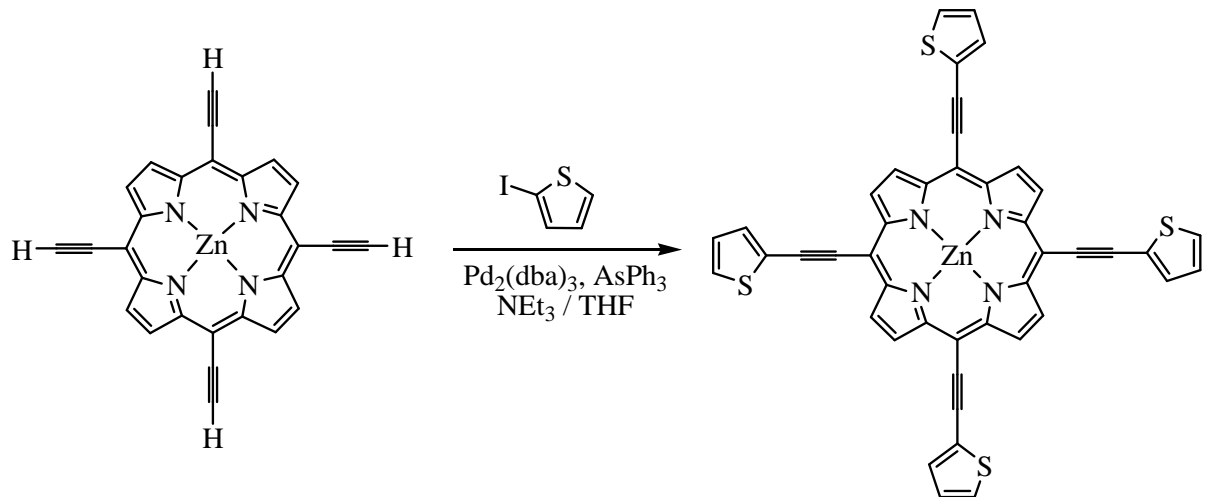
Rxn. 1   *Novel route to **ZnP92**.*

2.1.2.2 Electronic and photophysical properties

The extended π-system in the porphyrin with fused aromatic rings, **H₂P71** (Scheme 2), causes both the Soret and Q bands to red shift.[35] The Soret band of **H₂P71** was observed at 432 nm compared to 417 nm for **H₂TPP**. In order to compare the extent of π-conjugation between the porphyrin ring and the fused aromatics the absorbance spectrum of the diprotonated species was obtained. The Soret and Q bands were both red shifted the former more so than the latter. The diprotonated species displays a Soret band λ_{max} at 462 nm with Q bands at 604 and 659 nm. The metallated derivatives were also bathochromically shifted displaying Soret bands at 438 nm and 452 nm for **ZnP71** and **NiP71** respectively.

Decoupling of the two chromophores by the oxaalkyl spacer was observed in the electronic spectrum of **H₂P73** and **H₂P74** (structures in Fig. 27).[37] The spectral features consisted of an intense Soret band at 420 nm with Q bands between 510 and 650 nm due to porphyrin transitions and a π-π* transition between 290 – 350 nm due to the oligothiophene. The Soret band of **ZnP73** was bathochromically shifted by 2 nm compared to its freebase analogue (λ_{max} = 422 nm), whereas the **CoP73/74** and **NiP73/74** derivatives displayed hypsochromically shifted Soret bands at 412 and 416 nm respectively. Spectra of the Fe(III) and Mn(III) complexes showed highly red shifted Soret bands (**Fe(III)P73**: 511nm, **Fe(III)P74**: 512 nm, **Mn(III)P73**: 480 nm) with respect to the freebase porphyrins **H₂P73** and **H₂P74** (λ_{max} = 420 nm). An additional intense absorbance between 350 and 400 nm was assigned to charge transfer of occupied π-orbitals of the porphyrin to vacant d-orbitals of the central metal cation.

The metallated phosphoric(V) porphyrins with axial substituents also displayed a classic porphyrin spectrum with added spectral features due to the axial thienyl moiety at 232, 310 and 357 nm for **P(V)P78**, **P(V)P79** and **P(V)P80** (Fig. 29) respectively.[40] Soret bands were observed at wavelengths of 430, 428 and 431 nm for **P(V)P78**, **P(V)P79** and **P(V)P80** respectively with the two Q bands of each porphyrin in the range 558-604 nm. The fluorescence quantum yields and lifetimes in these systems were dependent on the number of thiophene units in the system (Table 6). A decrease of fluorescence lifetime and

quantum yield was observed with an increase in the number of thiophene units. Surprisingly the **P(V)P79** system showed a larger decrease in fluorescence lifetime and quantum yield than the **P(V)P80** analogue. Fluorescence quenching was observed for **P(V)P79** and **P(V)P80** compared to diethoxyP(V)tetraphenylporphyrin (τ = 4.4 ns) without thienyl moieties attached, which indicated that photoinduced electron transfer occurred from the oligothiophene moiety to the P(V) porphyrin unit of the 2,2'-bisthiophene and 2',2'':5'',2'''-terthiophene systems.

Porphyrin	λ_{em} (nm)	τ_f (ns)	Φ_f
P(V)P78	613, 668	4.10	2.7×10^{-2}
P(V)P79	615, 668	< 0.5	5.1×10^{-4}
P(V)P80	622, 673	0.80	3.9×10^{-3}

*Table 6   Luminescence data for phosphorus porphyrins **P78 – P80** in MeCN.*[40]

In the ethynyl-thienyl porphyrin, **ZnP92** (Rxn. 1), both the absorbance and emission maxima are bathochromically shifted compared to **H₂P1** (Fig. 2).[44]   The Soret band maximum was detected at 484 nm with emission bands observed at 703 and 774 nm.

The electronic spectra of the porphyrin systems connected with four types of oligothiophene bridges (structures in Fig. 31) showed many interesting characteristics.[42] UV-vis absorbance spectroscopy was used to determine the magnitude of the interporphyrin interactions. The absorbance spectra of **ZnZnP86** and **ZnZnP87** showed the least perturbation when compared to the reference porphyrin, zinc(II) 5,15-bis(3,5-di*tert*-butylphenyl)porphyrin. Their spectra were simply the sum of the porphyrin and the oligothiophene bridge indicating that direct attachment of oligothiophene unit to the porphyrin did not perturb the ground state properties. Inserting the vinyl or ethynyl linker between the quaterthiophene moiety and porphyrin core as in **ZnZnP88** and **ZnZnP89** imparted distinctive features to the absorbance spectra including broadening of the Soret bands.

ZnZnP89 underwent the largest red shift and highest intensification of Q bands within the series. The Soret region of **ZnZnP89** was split into two discernible transitions (Fig. 33), at 437 and 448 nm with a shoulder at 417 nm indicative of *J*-aggregate formation. **H₂H₂P89** and **ZnH₂P89** displayed single maxima at 442 and 444 nm respectively. Also a 20 % increase in the FWHM of the Soret band in **ZnZnP89** was observed compared to the other porphyrins in the **P89** series. However, the Q band region of **ZnH₂P89** is simply the sum of the spectra for **ZnZnP89** and **H₂H₂P89**. These spectra closely resembled those of structurally similar ethynyl-substituted zinc porphyrins, so the changes seen in the **P89** series were attributed to the effect of the ethynyl bridge, without any substantial influence from the quaterthiophene bridge. The changes observed were a result of a decrease in the HOMO-LUMO gap as a consequence of the increased π-conjugation in the system. The smaller vinyl moiety in the bridge of the dyads **ZnZnP88**, **H₂H₂P88** and **ZnH₂P88** resulted in Q bands that were also red shifted that can be similarily analysed. Thus, both vinyl or ethynyl substitution (**P88** and **P89**) at the *meso*-position gave rise to enhanced coupling between the two porphyrin units in comparison to the directly linked quaterthiophene bridge (**P86** and **P87**) which displayed weak interaction indicating only slight perturbation of the ground state properties of the porphyrin units. Similar to the absorbance spectra, the fluorescence spectra are altered by the nature of the bond linking the porphyrin units to the bis- or quaterthiophene bridge (Table 7). The fluorescence quantum yields for the zinc dyads increase in the order **ZnZnP87** < **ZnZnP86** < **ZnZnP88** ≈ **ZnZnP89**. The fluorescence quantum yields for the **H₂H₂** porphyrin series followed a similar trend. The largest Stokes shifts between were observed for the vinyl series, **P88**, indicating that the dyads undergo a significant reorganisation of nuclear coordinates in the excited state. The energy transfer in the asymmetrical dyads was also studied by fluorescence spectroscopy. Photoinduced energy transfer between asymmetrical **ZnH₂** porphyrins was investigated. The lowest excited singlet state of the zinc porphyrin was higher than that of the corresponding freebase porphyrin. Excitation of the asymmetrical dyad at 560 nm (the wavelength at which most light is absorbed by the zinc porphyrin) produced a fluorescence spectra with > 95 % emission from the freebase porphyrin. The fluorescence of the zinc porphyrin was almost completely turned off in each of the **ZnH₂** systems and fluorescence occurred from the freebase porphyrins. This indicated efficient energy transfer from the zinc porphyrin excited state to the nearby freebase porphyrin. The decrease in the zinc porphyrin fluorescence lifetime indicated a clear trend in energy

transfer from the slowest to the fastest of the order **ZnH$_2$P87 ≈ ZnH$_2$P88 > ZnH$_2$P86 > ZnH$_2$P89**.
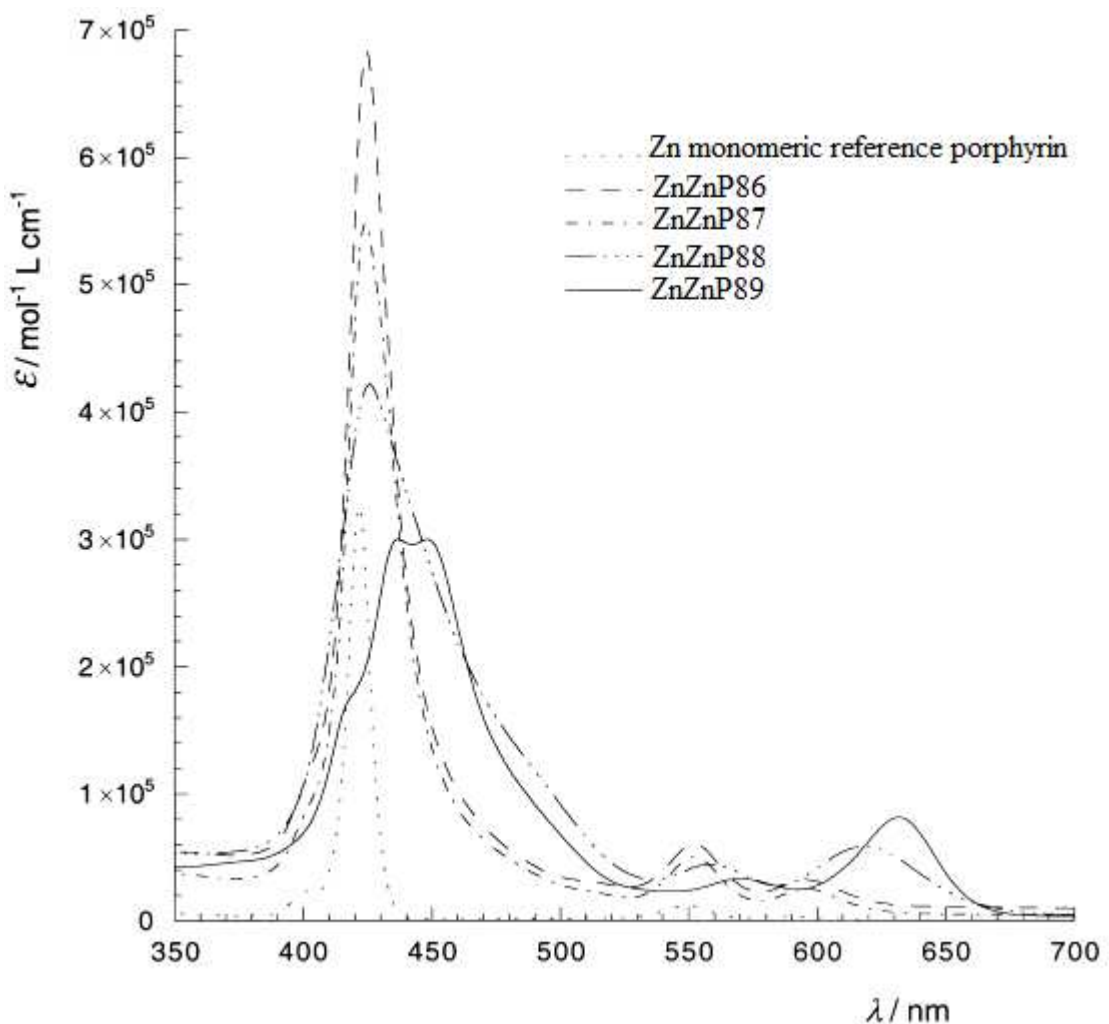
Figure 33   *Electronic absorbance spectra of **ZnZnP86**, **ZnZnP87**, **ZnZnP88** and **ZnZnP89** and zinc monomeric reference porphyrin in CH$_2$Cl$_2$.*[42b]

Porphyrin	λ_{em} (nm)	τ_f (ns)	Φ_f
ZnZnP86	624	1.60	0.10
ZnH$_2$P86	664	0.02	0.86
H$_2$H$_2$P86	662	3.90	0.86
ZnZnP87	626	1.30	0.09
ZnH$_2$P87	666	0.03	0.78
H$_2$H$_2$P87	667	3.50	0.78
ZnZnP88	676	1.30	0.17
ZnH$_2$P88	713	0.03	0.21
H$_2$H$_2$P88	717	3.40	0.22
ZnZnP89	657	1.40	0.18
ZnH$_2$P89	688	0.01	0.31
H$_2$H$_2$P89	690	6.20	0.34

*Table 7   Luminescence data for porphyrin dimers **P86** – **P89** in THF.*[42]

A Soret band λ_{max} at 460 nm was observed for **ZnP90** (Fig. 32) in dichloromethane, while **poly-ZnP91** displayed a hypsochromically shifted Soret band at 434 nm in dimethylsulfoxide.[43] An intense single fluorescence peak was observed at 720 nm for **ZnP90** whereas **poly-ZnP90** and **poly-ZnP91** produced two fluorescence bands at 650, 720 nm and 620, 660 nm respectively.

Electronic coupling between the adjacent porphyrin units in the polymer backbone of **poly-ZnP84** and **poly-ZnP85** (Fig. 30) resulted in splitting of the Soret band in the UV-vis spectra (Table 8).[41] The monomer **ZnP81** showed a sharp Soret peak at 417 nm with FWHM of *ca.* 20 nm. Polymers **poly-ZnP81**, **poly-ZnP83**, **poly-ZnP84** and **poly-ZnP85** gave peaks in the Soret and Q band region, the sharpness and intensity of which depended on the structure of the polymer. **Poly-ZnP85** with an ethynyl spacer directly bound to the *meso* position of the porphyrin ring displayed the largest shift for all Soret bands in the series. Polymers which have a spacing thiophene unit directly bonded to the zinc porphyrin units, such as **poly-ZnP81**, **poly-ZnP83** and **poly-ZnP84** (Fig. 30) display two emission peaks similar to those of the relative monomers. In accord with its UV-vis

spectrum, the photoluminescence of **poly-ZnP85** was at a longer wavelength than the other polymers.

Porphyrin	λ_{max} Soret (nm)	λ_{max} Q bands (nm)	λ_{ex} (nm)	λ_{em} (nm)
ZnP81	417	542, 583	417	592, 644
Poly-ZnP81	416	543, 582	416	590, 642
Poly-ZnP83	416	546, 584	416	590, 639
Poly-ZnP84	417, 431	547, 585	422	591, 646
Poly-ZnP85	454, 490	697	455	724

Table 8   *Electronic data for **P81** – **P85** in CHCl₃.*[41]

2.1.2.3 Electrochemical properties and electropolymerisation

HOMO-LUMO energy gaps of 2.06 and 2.01 eV *vs.* SCE were calculated for **ZnP71** and **NiP71** (Scheme 2) respectively.[35] These values correspond to a reduced HOMO-LUMO energy gap of almost 30 eV relative to **ZnTPP**. Cyclic voltammetry studies carried out on **H₂P73** and **H₂P74** (Fig. 27) reveal potentials comparable to the individual subunits which are in agreement with the UV-vis studies, confirming a lack of electronic communication.[37] Polymerisation of the freebase porphyrin monomer units, **H₂P73** and **H₂P74**, was not possible due to the interference of the porphyrins internal nitrogens with the oligothiophene radical cations. However electrochemical oxidation of the metallo-porphyrins lead to the corresponding porphyrin functionalised polythiophene. The metallo-bithiophene analogue M(II)/M(III)**P73**, showed a higher tendency to polymerise and gave thicker films. Only **Mn(III)P73** displayed low polymerisation trends. Electrochemical studies on the polymers displayed a combination of reversible redox waves for the conducting polythiophene backbone and the porphyrin redox centres (Table 9). Reduction of the metal centres of the porphyrin units at negative potentials was not observed due to the insulating character of the polythiophene backbone in the potential window monitored.

Porphyrin	Porphyrin Reduction (V)		Metal Cation (V)		Porphyrin Oxidation (V)		
	E(I)	E(II)	$E(M^{1+/2+})$	$E(M^{2+/3+})$	E(III)	E(IV)	E(V)
H₂P73	-2.03	-1.71	----	----	0.44	0.85	1.10
H₂P74	-2.05	-1.70	----	----	0.46	0.87	1.10
Co(II)P73	-1.95	----	-1.44	0.34	0.51	0.75	1.34
Co(II)P74	-1.95	----	-1.44	0.34	0.51	0.78	1.36
Ni(II)P73	----	-1.81	----	----	0.50	0.84	1.29
Ni(II)P74	----	-1.80	----	----	0.50	0.86	1.29
Fe(III)P73	----	-1.60	----	-0.86	0.55	0.98	1.24
Fe(III)P74	----	-1.57	----	-0.84	0.55	0.99	1.26
Mn(III)P73	-2.14	----	----	-0.81	0.63	1.06	1.28
Zn(II)P73	----	-1.92	----	----	0.23	0.50	0.76

*Table 9   Redox potentials of **P73** – **P74** in CH₂Cl₂ vs. Fc/Fc⁺.*[37]

In contrast, Ballarin et al. observed irreversible oxidation of the porphyrin moiety in a copolymer of **H₂P73** and the tetraphenylporphyrin-alkoxy-monothiophene unit, **H₂P75**.[38a] In a later study,[38b] the authors also investigated the nickel derivative, **NiP73**, and analysed the complexation ability of the porphyrin unit in the polymer chain. Both **H₂P73** and **NiP73** formed mechanically stable electrode surface films. For **H₂P73**, the oxidation process centred at +1.04 V *vs.* SCE, previously ascribed to the oxidation of the porphyrin-containing monomer, was observed along with an additional redox couple in the potential region +0.45 - 0.70 V *vs.* SCE attributed to oxidation of the co-polymer. Analysis of **NiP73** was quite different. The oxidation process recorded for **H₂P73** was no longer

present and a reversible system was evident with an oxidation potential of +0.94 V *vs.* SCE. This shift with respect to **H₂P73** was attributed to the nickel porphyrin core, however the highly distorted conformation of the porphyrin ring induced upon nickel(II) complexation should also be considered.

Electrochemical oxidation of **P(V)P79** and **P(V)P80** (Fig. 32) resulted in the formation of one dimensional polymers (Fig. 34).[40] **Poly-P(V)P79** and **poly-P(V)P80** were deposited onto the electrode as peak currents assigned to the redox reaction of the P(V) porphyrin increased. **Poly-P(V)P80** displayed a new anodic peak due to the oxidation of sexithiophene. The UV-vis absorbance of the bithiophene and terthiophene moieties (λ_{max} = 310, 357 nm respectively) disappeared upon polymerisation with strong quenching of the fluorescence in the polymers. In addition conductivities of **poly-P(V)P79** and **poly-P(V)P80** were strongly enhanced by photoirradiation.
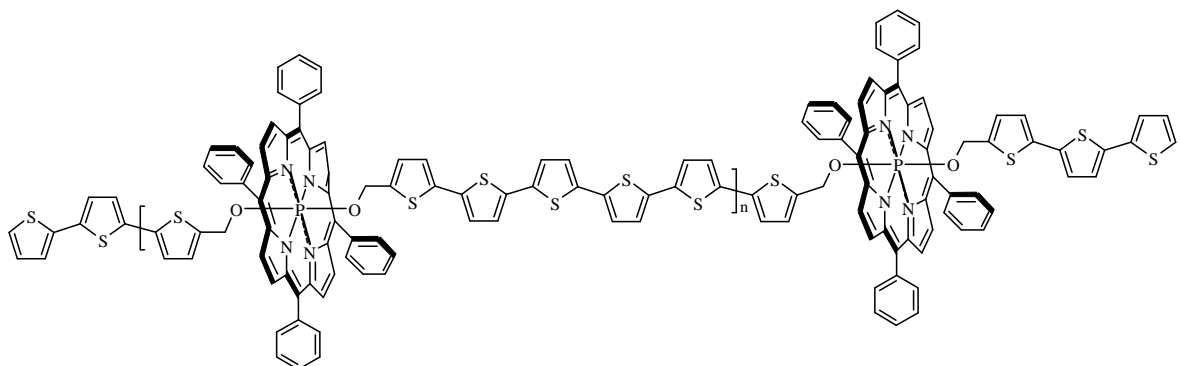
Figure 34   Polymeric oligothiophene chain of P(V)-tetraphenylporphyrins.

Zinc(II) 5,15-bis(4-(thien-2-yl)phenyl)-10,20,diphenylporphyrin (**ZnP76**) failed to form a polymer owing to its low solubility in a range of solvents.[39] Polymeric films of **ZnP77** (Fig. 35) were deposited on an array of electrodes in several solvents by electrochemical oxidation. During the polymerisation process, the polymer film remained electroactive indicating, that the film itself, has enough electrical conductivity to maintain the polymer growth process. An electrode modified with the **poly-ZnP77** exhibited two reversible one-electron porphyrin ring oxidations at +0.78 and +1.06 V *vs.* Ag/AgCl. With potential scan rates of 60-180 mV/s, the potential difference between oxidation and reduction peaks (ΔE_p)

was 50-100 mV, which indicated the high electroactivity of the porphyrin film. Deposited polymer layers ranging from 5×10^{-10} to 5×10^{-6} mol/cm^2 were reproducible. The synthesised polymer, **poly-ZnP77**, was considered to be two isolated redox systems: the porphyrin and the 5,5'bisphenyl-2,2'-bi(3,4-ethylene-dioxy-thiophene). Oxidation of the thienyl subunit occurred at +0.61 V *vs.* Ag/AgCl, cathodic of the porphyrin unit (+0.78 and +1.06 V *vs.* Ag/AgCl). Consequently the thienyl subunit in **poly-ZnP77** was only electroactive after oxidation of the porphyrin ring and as a result the oxidised state of the bithiophene subunit was trapped when the potential scan was reversed. The formation of two distinct redox units in the polymer chain, **poly-ZnP77**, was believed to be responsible for the observed charge trapping phenomenon, the mechanism for which was supported using model compounds.
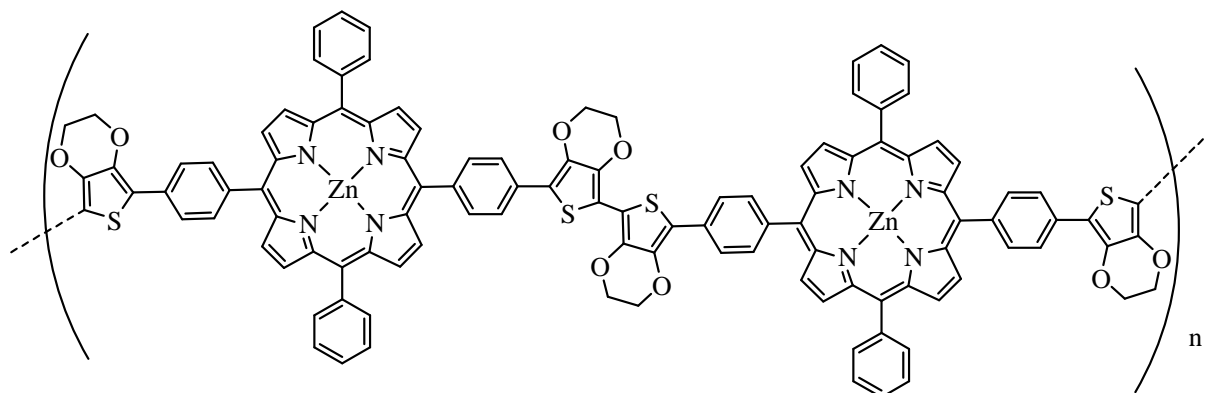
*Figure 35   **poly-ZnP77**.*

Polymerisation of the **ZnP90** and **ZnP91** complexes to their respective homopolymers was carried out by electrochemical oxidation.[43] The monomers were also successfully polymerised by chemical oxidation with iron(III)chloride. Cyclic voltammetry on **poly-ZnP90** reveals a zinc porphyrin oxidation in the range +0.6 – 0.9 V *vs.* Ag/AgCl while oxidation of the thiophene moiety was observed at higher potentials (>1.0 V *vs.* Ag/AgCl). Conductivity measurements of the hydrophobic zinc porphyrinate polymer **poly-ZnP90** on platinum electrodes gave upper values of 6×10^{-3} S/cm. Images of the sodium derivative of the zinc(II) polymer, **poly-ZnP91** (Fig. 36), were recorded by TEM and AFM. The

formation of uniform porphyrin wires of up to 2.5 μm in length (*ca.* 1200 monomer units) was confirmed, with a thickness of *ca.* 2 nm corresponding to the width of the porphyrin unit.
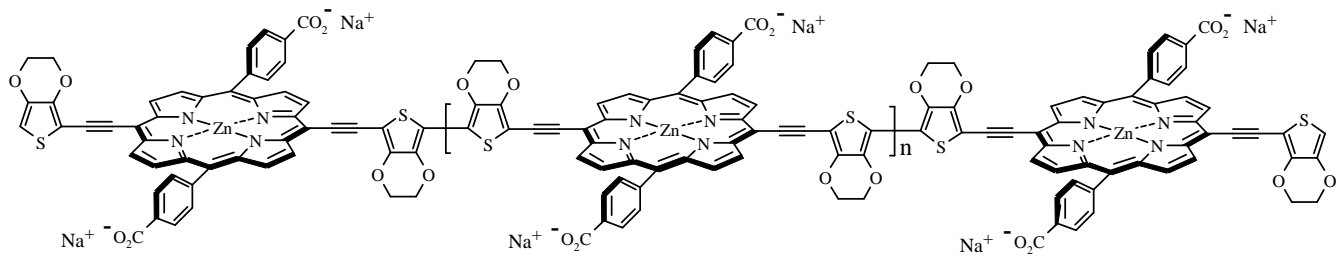
Figure 36   **poly-ZnP91**.

2.1.3 Applications

The various uses of porphyrins are widely studied and include such areas as catalytic,[45] therapeutic[46] and potential (opto-)electronic applications.[47] Extended π-conjugated porphyrin systems are increasingly investigated due to their applications towards advanced technologies, which include nonlinear optical materials.[20,48] By appending various chemical moieties onto the periphery of the porphyrin ring (e.g. functionalised thiophenes) the electronic and redox properties of the macrocycle in such systems can easily be modulated. Also varying the metal centre of the porphyrin allows these properties to be fine tuned. Desirable molecular and material properties, such as large hyperpolarisabilities, can therefore be imparted onto the porphyrin ring by appropriate substitution and metallation.

Their strong absorbance and fluorescence properties allow porphyrins wide used in (opto-) electronic systems. Redox control of *meso* zinc(II) trithienyl and triphenylporphyrin – ferrocene dyads (**ZnP27** and **ZnP28**, Fig. 37) allowed the on/off switching of porphyrin fluorescence through use of the ferrocene/ferricenium redox couple.[19] Quenching of the porphyrin fluorescence by excited-state electron transfer from the ferrocene to the porphyrin was easily reversed by oxidation to the ferricenium ion allowing the porphyrin fluorescence to be "switched on". The reversible "on" and "off" switching of the electron-transfer pathway allows for efficient control of the porphyrin luminescence.
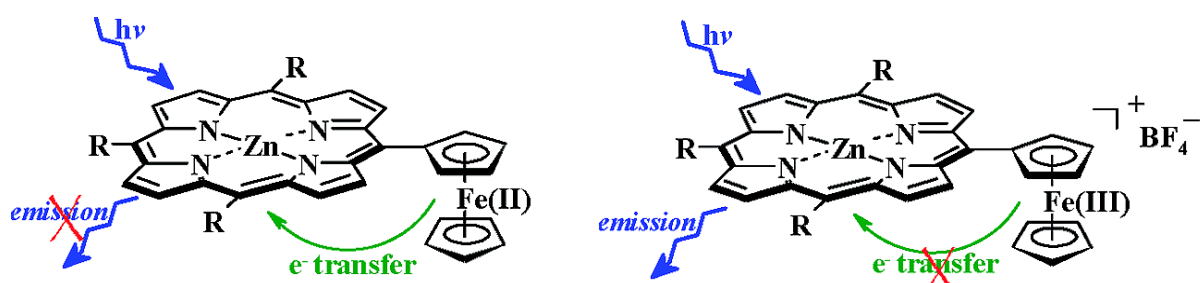
Figure 37   *On/off switching of porphyrin fluorescence in **ZnP27** and **ZnP27**$^+$.*[19]

Electrochemical studies of the thienyl porphyrins, **ZnP21 – ZnP26** (Fig. 10) have shown that the band gap can be controlled by varying the number of thienyl substituents on the porphyrin ring and by the nature of the thienyl moiety itself (e.g. thiophene *vs.* bromothiophene). As previously discussed the reduction in band gap followed the order **ZnP22** (2.02 eV), **ZnP26** (2.02 eV), **ZnP25** (2.04 eV), **ZnP24** (2.06 eV) and **ZnTPP** (2.09 eV). Thus, through molecular design, the application of thienyl porphyrins in (opto-)electronics such as dye sensitised solar cells and photovoltaic devices becomes a real possibility.

Supramolecular systems with magnesium *meso* tetrakis(thien-2-yl)porphyrin, (**MgP1**, Fig. 2) and β-cyclodextrins have been produced.[49] In a phosphate buffer solution of pH 5.4, **MgP1** was found to form 1:1 supramolecular systems with β-cyclodextrin and four other modified β-cyclodextrins. The cyclodextrin cavity offerred a hydrophobic environment for guest molecules with two of the modified cyclodextrins, dimethoxy-β-cyclodextrin (DM-β-CD) and trimethoxy-β-cyclodextrin (TM-β-CD), substantially increasing this hydrophobic environment. A bathochromic shift and decrease in extinction coefficient of the Soret band of **MgP1**, was observed upon formation of a supramolecular system of β-cyclodextrins with **MgP1**. When fluorescent substances move from a polar phase to a non-polar phase, the quantum efficiency of fluorescence increases. An enhancement in emission intensity and shift to shorter wavelength was noted for the DM-β-CD/**MgP1** and TM-β-CD/**MgP1** systems, indicative of the formation of supramolecular systems. These results showed that the modified β-cyclodextrins easily formed a supramolecular system with **MgP1**.

The **poly-FeP2** modified electrode is the first all-synthetic electrochemical sensor for the superoxide anion radical ($O_2^{\bullet-}$) due to its efficient electrocatalytic oxidation of $O_2^{\bullet-}$ to O_2. To mimic the iron centre of cytochrome-*c*, an iron(III) porphyrin modified electrode was developed by Yausa et al.[50] The **[Fe(im)P2]$^+$Br$^-$** electrode was applied to detect $O_2^{\bullet-}$ and results indicated that $O_2^{\bullet-}$ was catalytically oxidised at the modified electrode. The axial imidazole ligand enables the oxidation of $O_2^{\bullet-}$ by an outer-sphere process comparable to cytochrome-*c* mediated $O_2^{\bullet-}$ oxidation. The sensitivity of the system towards $O_2^{\bullet-}$ is 50

times higher than that obtained in a previous study using a modified cytochrome-*c*/Au electrode (typically ~6 nA μM^{-1} cm^{-2}).

Mono substituted porphyrins (**ZnP19** and **ZnP20**, Fig. 8) with *meso* 5-membered heteroaromatic groups were designed to evaluate the effects of the spacer on mesoporous TiO$_2$ nanoparticle films.[17] The carboxylic group ensured a single point of attachment to the surface. The three remaining mesityl *meso* substituents possess large steric bulk, reducing aggregation of the porphyrin molecules. Porphyrin – modified ITO/TiO$_2$ electrodes were produced by adsorbing the porphyrin onto the prepared ITO/TiO$_2$ electrode. **ZnP19** adsorbed quickly and formed a densely packed porphyrin monolayer whereas **ZnP20** adsorbed at a slower rate and formed a loosely packed monolayer. Total amounts of porphyrin adsorbed onto the TiO$_2$ film were calculated using surface area on the electrode and porphyrin densities. **ZnP19** was found to have a small density value of 2.0 x 10^{-11} mol cm^{-2} while **ZnP20** possessed a value of 1.2 x 10^{-10} mol cm^{-2}. The calculated porphyrin density value together with the tilt of the molecules is responsible for the packing on the surface. **ZnP20** was tilted almost parallel to the TiO$_2$ surface and so adsorbed in a tightly packed monolayer whereas **ZnP19's** horizontal orientation of the acid group resulted in a loosely packed monolayer. An ITO/TiO$_2$/porphyrin dye sensitised solar cell device sensitised with **ZnP19**, was found to possess high photovoltaic properties with maximum incident photon-to-current-efficiency (IPCE) of 65 % and maximum power conversion efficiency (η_{max}) of 3.1 %. Values of IPCE$_{max}$ = 34 % and η_{max} = 2.0 % were obtained for **ZnP20**. The higher effectiveness of **ZnP19** is attributed to the additional electron-transfer pathway through specific interaction between the sulphur atom in the bridge and the TiO$_2$ surface.

Friedlein et al. reported the self-assembly of supramolecular columns of large polycyclicaromatic hydrocarbons and thienyl porphyrins.[51] Ordered films of porphyrins with functional side arms (e.g. thiophene) are ideal for (opto-)electronic applications, where fast charge separation and transport are required. **ZnP21** (Fig. 6) was used for this "bottom-up" synthetic strategy of a highly ordered nanostructure at a molybdenum disulfide (MoS$_2$) surface. Bromination of the peripheral 5'-position of the thiophene

increased solubility and facilitated the self assembly of the columnar nanostructures in solution. Tapping-mode scanning force microscopy (TM-SFM) indicated the film was flat (10 nm thick, ±2 nm) and the surface was completely covered. Photoelectron spectroscopy was used to investigate the alignment of the nanostructures on the surface. Spectral changes observed upon annealing were attributed to increased structural order in the columnar arrangements. Cone-like photoelectron emission around the molecular axis (typical for π-electronic states of discotic molecules) indicated a flat orientation of the porphyrin rings, face to face with the surface substrate. The alignment of the columns is suited for solar cell applications.

The non-linear optical properties *viz.* the molecular first hyperpolarisability, β, was evaluated using femtosecond hyper-Rayleigh scattering (fs-HRS) pulsed laser measurements for a range of thienyl systems (**ZnP29 – ZnP38**, Fig. 11).[20] Exceptionally large dynamic hyperpolarisability values of 670 – 4350 x 10^{-30} esu were obtained at 1300 nm incident irradiation. The value of 4350 x 10^{-30} esu, obtained for **ZnP31**, was the largest β_{1300} value (measured at 1300 nm incident radiation) for an uncharged chromophore. Using the same technique the molecular first hyperpolarisability values of **ZnP35 – ZnP38** (Fig. 11) were determined. **ZnP35**'s formyl group drove a blue shift in the Q band (λ_{max} = 676 nm), whereas **ZnP36**'s strong dicyanovinyl acceptor caused a red shift in the Q band position (λ_{max} = 698 nm) relative to **ZnP32** (λ_{max} = 685 nm). Compounds **ZnP37** and **ZnP38** were analogues of **ZnP32** in which there was an inversion of charge-transfer direction. **ZnP38** showed diminished excited-state structural heterogeneity relative to **ZnP32** and **ZnP37**, caused by the planarity of the conjugated carbazolyl unit. As a result both **ZnP37** and **ZnP38** β_{1300} values (Table 4) exceeded that measured for **ZnP32**, but interestingly, **ZnP38** exceeded that of **ZnP32** and **ZnP35**, approximately 2-fold. These enhanced results indicated that further improvements in the already large magnitude for β_{1300} values within the porphyrin-oligothiophene based neutral dipolar chromophores should be possible.

A copolymer of **H₂P18** (Fig. 7) and terthiophene, **poly-H₂P18** (Fig. 38), was the basis for a novel photoelectrochemical cell.[52] The use of a porphyrin co-polymer enhanced the light

harvesting capabilities of a previously synthesised polythiophene-based photovoltaic device. Scanning electron microscopy of **poly-H₂P18** showed an open porous morphology (Fig. 39) which was beneficial for photovoltaics due to the larger surface area. A series of porphyrin to terthiophene monomer mole ratios were also investigated and equimolar amounts of each were found to give the best energy conversion results. This photovoltaic device had an energy conversion efficiency of 0.09 %. An additional increase (0.06 – 0.12 %) was also observed in the efficiency of the copolymer after soaking in a zinc(II) solution due to metallation of *ca.* 25 % of the porphyrin units on the polymer backbone.
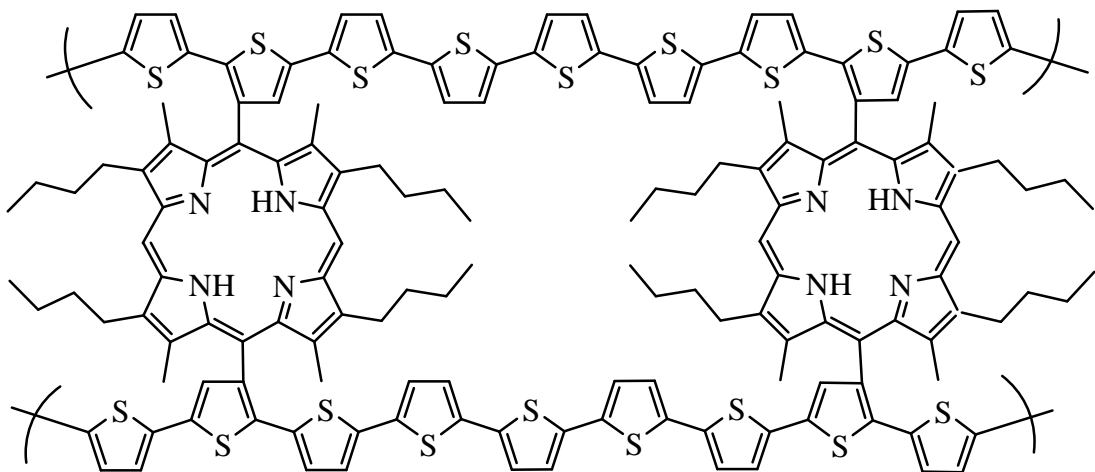
Figure 38 **Poly-H₂P18**.
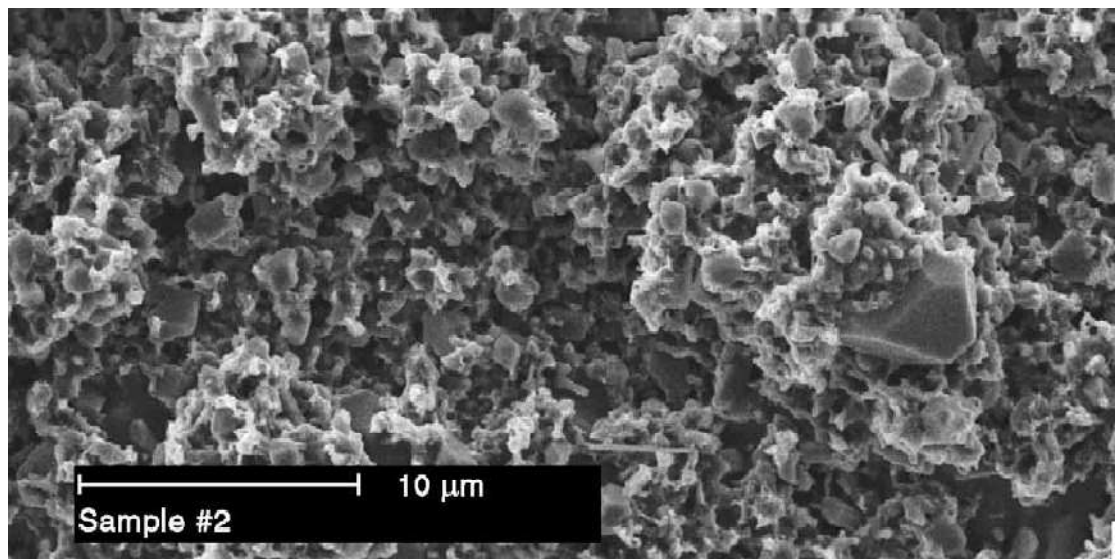
Figure 39   *Scanning electron micrograph of* **poly-H₂P18**.[52]

2.2   Abstract

The aim of this chapter is to gain information about the variability of the general types of spectra in connection with the variability of the structure in thienyl porphyrins. To date, there is still much discussion about the changes observed in the spectra of thienyl porphyrins. The question remains - are the changes observed in the spectra a result of the increased conjugation induced upon thienyl substitution of the porphyrin ring or a result of the conformation which the *meso* thienyl substituents adopt?

Historically, bathochromically shifted absorbance and emission spectra were attributed to the inductive effect of the *meso* thienyl moiety. However investigations carried out by Rochford et al. and Brückner et al. indicated that this explanation was over simplified. Rochford et al. synthesised a range of thienyl porphyrins (Fig. 9) which were compared to **ZnTPP**.[18] For the tetra substituted thienyl porphyrins both the absorbance and emission spectra were red shifted were compared to **ZnTPP**. By varying the number of thienyl rings and their substituents, the overall effect of the substitution pattern could be observed. Successive replacement of a phenyl ring with a thien-2-yl ring which had an ethynyltrimethylsilyl moiety at the thien-5-yl position resulted in sequential red shifts of 4 nm in the absorbance spectra for each ring replaced. The authors attributed the shifts to increased coupling of the overlapping π systems of the porphyrin and thiophene rings. Evidence for this included an increase in the FWHM of the porphyrin Soret band.

Brückner and co workers synthesised thienyl porphyrins with a methyl group attached at various position on the thienyl ring (Fig. 16).[28] Changes observed in the spectra indicated that the position of substituents on the *meso* thienyl groups had a direct influence on the electronic properties of the porphyrin ring. Subsequently, DFT was used to calculate the conformation which the thienyl rings adopted with respect to the porphyrin macrocycle. The results showed that the thienyl rings adopted a co-planar arrangement which may allow for greater π-π orbital overlap between the thienyl group and the porphyrin macrocycle.

Thus a series of *meso* tetra (thien-2-yl)porphyrins and *meso* tetra (phenyl)porphyrins were produced, each further substituted with ethynylbenzene, ethynylthien-2-yl or ethynylthien-3-yl moieties (Fig. 40).
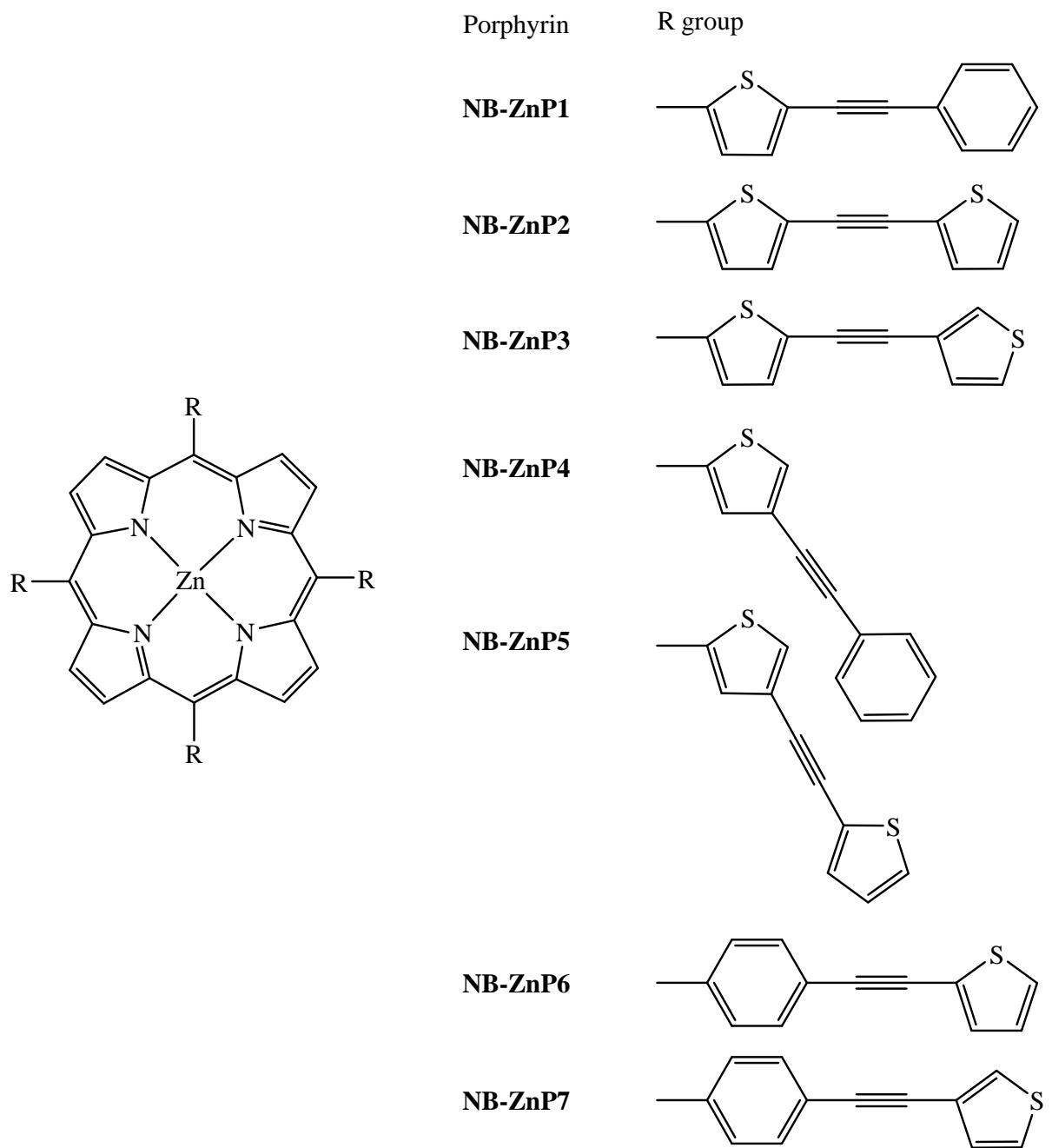
Figure 40   *Porphyrins produced for this study.*

Porphyrins **NB-ZnP1 – NB-ZnP3** were synthesised with substituents at the thien-5-yl position, in order to examine whether an additional aryl group would cause further coupling of the overlapping π systems and if so, the effect of the choice of aryl ring. Porphyrins **NB-ZnP4** and **NB-ZnP5** possess the same terminal substituents (ethynylbenzene and ethynylthien-2-yl) as **NB-ZnP1** and **NB-ZnP2**; however they are substituted at the thien-4-yl position. **NB-ZnP4** and **NB-ZnP5** can therefore be compared directly to **NB-ZnP1** and **NB-ZnP2** in order to examine how the conjugation pathway affects the spectra of porphyrin. Porphyrins **NB-ZnP6** and **NB-ZnP7** are phenyl substituted porphyrins which have been further substituted at the *para* position with ethynylthien-2-yl and ethynylthien-3-yl moieties respectively. These porphyrins can be compared **NB-ZnP2** and **NB-ZnP3** as they possess the same terminal substituents. However, the phenyl porphyrins, **NB-ZnP6** and **NB-ZnP7**, should adopt an idealised orthogonal arrangement with respect to the porphyrin plane. Thus, as the π systems of the porphyrin and *meso* substituents will no longer be overlapping any changes observed in the spectra can be attributed to the conformation rather than the coupling of the π systems.

Increased FWHM of the porphyrin Soret band is evidence of increased coupling of the overlapping π systems, thus UV-vis absorbance spectra shall be obtained to investigate the extent of this overlap. Emission spectra and lifetimes of the porphyrins may indicate how substitution pattern affects the singlet and triplet excited states that are formed following absorbance. Electrochemistry may provide information about the general excited states of the porphyrins under study relative to each other and **ZnTPP**.

For **NB-ZnP1 – NB-ZnP3**, substitution at the thien-5-yl position of the *meso* thienyl substituent would be expected to increase conjugation within the macrocycle. Therefore, bathochromic shifts in the absorbance and emission spectra are expected. The effective conjugation for **NB-ZnP4** and **NB-ZnP5** should be lower than in **NB-ZnP1 – NB-ZnP3** and therefore modest spectral shifts are expected with respect to **ZnTThP**. Porphyrins **NB-ZnP6** and **NB-ZnP7** have a phenyl ring attached to the porphyrin macrocycle so the properties of these porphyrins are expected to be more like **ZnTPP**. However the effect of terminal thienyl moiety can be examined by changes in the electronic properties.

2.3 Experimental

2.3.1 Materials

All operations were carried out under an atmosphere of argon or nitrogen using standard Schlenk techniques. All solvents were supplied by the Aldrich Chemical Company. Dichloromethane was dried over $MgSO_4$ prior to use. Methanol was distilled over magnesium turnings and iodine before use. All organic reagents were purchased from the Aldrich Chemical Company. Benzaldehyde, 5-bromo-2-thiophenecarboxaldehye and 4-bromo-2-thiophenecarboxaldehye were distilled using a Buchi Kügelrohr apparatus prior to use. Pyrrole was freshly distilled over potassium hydroxide before use. Anhydrous triethylamine, 1-phenylacetylene, 2-ethynylthiophene, 3-ethynylthiophene, 2-thiophenecarboxaldehyde, 4-bromobenzaldehyde, propionic acid, borontrifluoride diethyletherate and *p*-chloranil were all used without further purification. Bis(triphenylphosphine)palladium(II)chloride, triphenylphosphine and cuprous iodide were used as received in the coupling reactions. These reagents undergo in-situ formation of $Pd(PPh_3)_4$. Column chromatography was carried out using neutral silica gel (Merck, used as received). All mobile phases for column chromatography were dried over $MgSO_4$ prior to use. Solvents used in emission and lifetime measurements were of spectroscopic grade and used without further purification. All solvents were deoxygenated by purging with argon or nitrogen for ~10 minutes. The preface "**NB-**" is applied to compound codes indicating that these are novel compounds synthesised throughout this work.

2.3.2 Equipment

All syntheses involving air- and moisture-sensitive reagents were performed in oven or flame dried glassware. NMR spectra were recorded on a Bruker model AC 400 MHz spectrometer and Bruker model ANC 600 MHz spectrometer using $CDCl_3$ as solvent. All NMR spectra were calibrated according to the residual solvent peak, i.e. $CHCl_3$ at 7.26 ppm for all ^1H spectra and 77.16 ppm for all ^{13}C spectra. Chemical shifts (δ) are given in parts per million (ppm). Proton coupling constants (*J*) are given in Hertz (Hz). Melting points were measured on a Stuart Scientific SMP1 melting point apparatus. IR spectra were recorded on a Perkin-Elmer 2000 FT-IR spectrometer (2 cm^{-1} resolution) in a 0.1 mm sodium chloride liquid solution cell using spectroscopic grade dichloromethane. All UV-

vis spectra were measured on an Agilent Technologies 8453 photodiode array spectrometer using a 1 cm^3 quartz cell. Emission spectra (accuracy $\pm$ 5 nm) were recorded at 298 K using a LS50B luminescence spectrophotometer, equipped with a red sensitive Hammatsu R928 PMT detector, interfaced with Elonex PC466 employing Perkin-Elmer FL WinLab custom built software. Luminescence lifetime measurements were made using an Edinburgh Analytical Instruments (EAI) Time-Correlated Single Photon Counting apparatus (TCSPC) as described by Browne et al.[53] Cyclic voltammetry experiments were carried out using a CH instrument model 600a electrochemical workstation at a scan rate of 0.1 VS^{-1}. Electrochemical studies were conducted using a conventional three electrode system consisting of a 2 mm diameter Teflon shrouded glassy carbon working electrode, a platinum wire auxiliary electrode and a saturated calomel reference electrode. The solvent used in all experiments was spectrophotometric grade dichloromethane and the supporting electrolyte was 0.1 M TBAPF$_6$. Deoxygenation of the solutions was achieved by bubbling through nitrogen for approximately 10 minutes and a blanket of nitrogen was maintained over the solution during all experiments.

2.3.3 Synthesis

2.3.3.1 Procedure for the preparation of aldehydes *via* the Sonogashira reaction [54]

To a flame dried round bottom flask anhydrous triethylamine (~30 ml) was added and purged with nitrogen for 10 minutes. Following this, the appropriately substituted halogenated thiophenecarboxaldehyde was added and the solution was purged for a further 5 minutes. A catalytic quantity of bis(triphenylphosphine)palladium(II)chloride, triphenylphosphine and cuprous iodide were added to the flask followed by an excess of aryl alkyne in quick succession. The reaction mixture was refluxed overnight under an inert atmosphere and then allowed to cool. Excess aryl alkyne and solvent was removed under reduced pressure. The crude product was extracted from the brown oil by first adding *ca.* 5 ml of dichloromethane followed by the addition of *ca.* 25 ml of petroleum ether (or hexane). The solvent layer was then decanted off. This process was repeated several times until the washings remained colourless. The washings were combined and dried over magnesium sulphate. The solvent was then removed *via* rotary evaporation affording a dark viscous oil. The crude product was then purified using a Kügelrohr or by column chromatography as described for each compound.

2.3.3.1.1 5-(Phenylethynyl)thiophene-2-carboxaldehyde (A1)
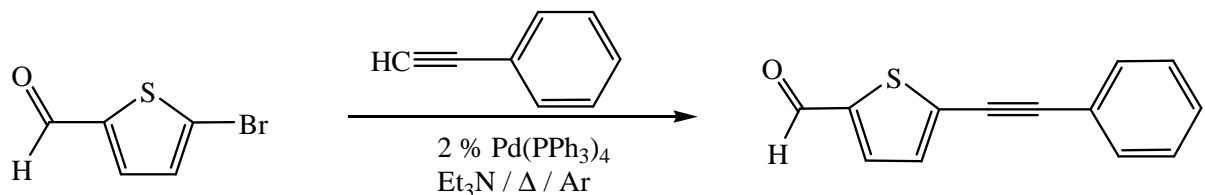
5-Bromothiophene-2-carboxaldehyde (6.0 mmol, 0.71 ml), bis(triphenylphosphine) palladium(II)chloride (0.12 mmol, 84 mg, 2 %), triphenylphosphine (0.24 mmol, 63 mg, 4%), cuprous iodide (0.12 mmol, 23 mg, 2 %) and 1-phenylacetylene (9.0 mmol, 0.99 ml) were used. The crude product was purified using a Kügelrohr (240 °C, 0.04 mmHg) which afforded a bright yellow solid. Yield: 102 mg, 4.8 mmol, 80 %. Spectroscopic data were in good agreement with reported data.[55]

¹H NMR (400 MHz, CDCl₃): 9.86 (1H, s), 7.67 (1H, d, J = 3.6 Hz), 7.55-7.52 (2H, m), 7.39-7.37 (3H, m), 7.31 (1H, d, J = 3.6 Hz) ppm. **m.p.** = 89 - 90 °C.

2.3.3.1.2   5-(Thien-2-ylethynyl)thiophene-2-carboxaldehyde (A2)
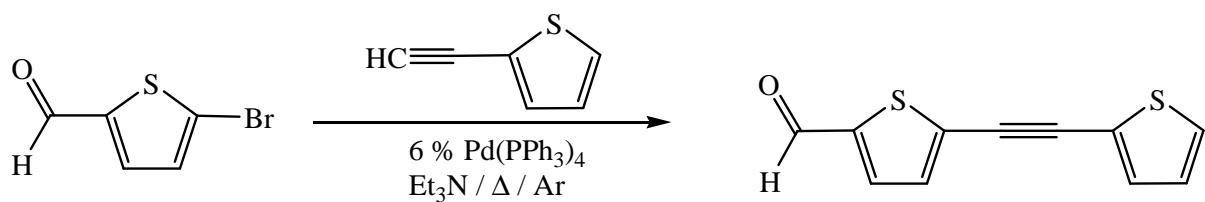
5-Bromothiophene-2-carboxaldehyde   (3.0   mmol,   0.36   ml),
bis(triphenylphosphine)palladium(II)chloride   (0.18   mmol,   126   mg,   6   %),
triphenylphosphine (0.36 mmol, 94 mg, 12%), cuprous iodide (0.18 mmol, 34 mg, 6 %)
and 2-ethynylthiophene (3.3 mmol, 0.35 ml) were used. The crude product was purified by
column chromatography on silica gel using CH_2Cl_2 : hexane (50:50) as mobile phase which
afforded an orange-yellow solid. Yield: 455 mg, 2.08 mmol, 69 %. Spectroscopic data
were in good agreement with reported data.[55b]

¹H NMR (400 MHz, CDCl₃): 9.87 (1H, s), 7.68 (1H, d, J = 4.0 Hz), 7.39-7.38 (1H, m),
7.36-7.35 (1H, m), 7.31 (1H, d, J = 4.0 Hz), 7.06-7.04 (1H, m) ppm. **m.p.** = 78 - 79 ℃.

2.3.3.1.3　5-(Thien-3-ylethynyl)thiophene-2-carboxaldehyde (NB-A3)
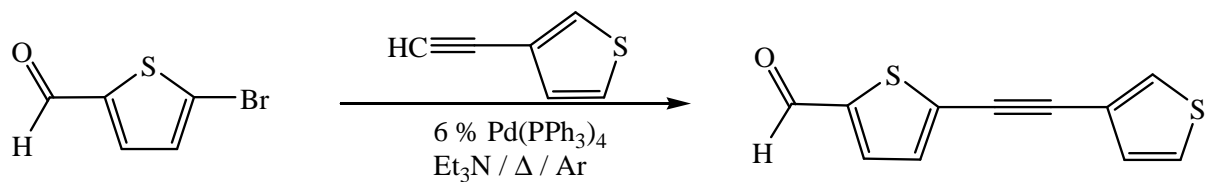
5-Bromothiophene-2-carboxaldehyde (1.5 mmol, 0.18 ml), bis(triphenylphosphine) palladium(II)chloride (0.6 mmol, 63 mg, 6 %), triphenylphosphine (0.18 mmol, 47 mg, 12 %), cuprous iodide (0.09 mmol, 17 mg, 6 %) and 3-ethynylthiophene (1.65 mmol, 0.16 ml) were used. The crude product was purified by column chromatography on silica gel using CH_2Cl_2 : hexane (50 : 50) as mobile phase which afforded a yellow solid. Yield: 245 mg, 1.12 mmol, 75 %.

^{1}H NMR (400 MHz, CDCl$_3$): 9.86 (1H, s), 7.66 (1H, d, J = 4 Hz), 7.61-7.60 (1H, m), 7.34-7.32 (1H, m), 7.29 (1H, d, J = 4 Hz), 7.21-7.20 (1H, m) ppm. **^{13}C NMR** (100 MHz, CDCl$_3$): 182.40, 143.78, 136.09, 132.91, 132.37, 130.25, 129.61, 125.92, 121.00, 93.19, 81.63 ppm. **IR** (CH$_2$Cl$_2$): (C=O) 1671 cm^{-1}, (C≡C) 2209 cm^{-1}. **m.p.**: 92 – 93 ºC.

2.3.3.1.4 4-(Phenylethynyl)thiophene-2-carboxaldehyde (NB-A4)
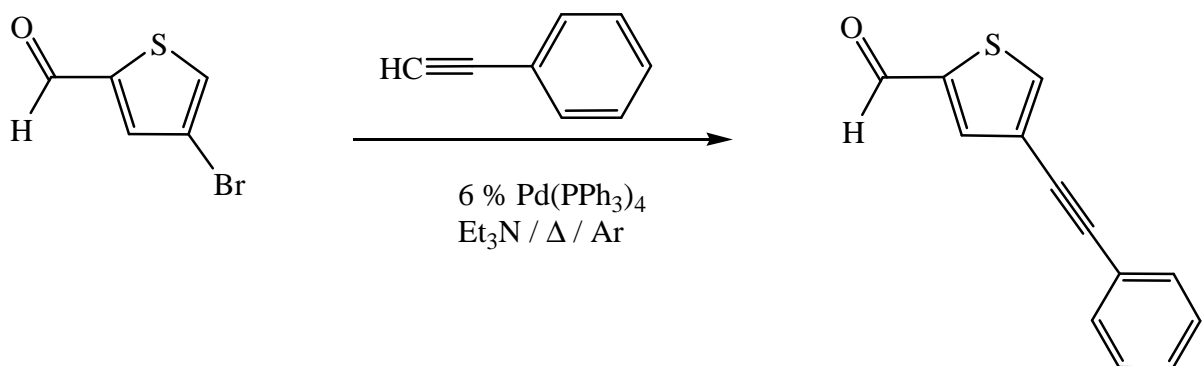
4-Bromo-2-thiophenecarboxaldehyde (2.6 mmol, 500 mg), bis(triphenylphosphine) palladium(II)chloride (0.16 mmol, 112 mg, 6 %), triphenylphosphine (0.31 mmol, 81 mg, 12 %), cuprous iodide (0.16 mmol, 30 mg, 6 %) and 1-phenylacetylene (3.27 mmol, 0.34 ml) were used. The crude product was purified by column chromatography using silica gel and CH_2Cl_2 : hexane (40:60) as mobile phase which afforded a bright yellow solid. Yield: 502 mg, 2.36 mmol, 91 %.

¹H NMR (400 MHz, CDCl₃): 9.92 (1H, d, J = 1.2 Hz), 7.87-7.86 (1H, m), 7.82 (1H, d, J = 4.0 Hz), 7.54-7.51 (2H, m), 7.38-7.35 (3H, m) ppm. **¹³C NMR** (100 MHz, CDCl₃): 182.59, 143.56, 138.44, 137.07, 131.63, 128.78, 128.48, 123.94, 122.43, 90.01, 82.77 ppm. **IR** (CH₂Cl₂): (C=O) 1675 cm⁻¹, (C≡C) 2214 cm⁻¹. **m.p.:** 128 – 129 °C.

2.3.3.1.5 4-(Thien-2-ylethynyl)thiophene-2-carboxaldehyde (NB-A5)
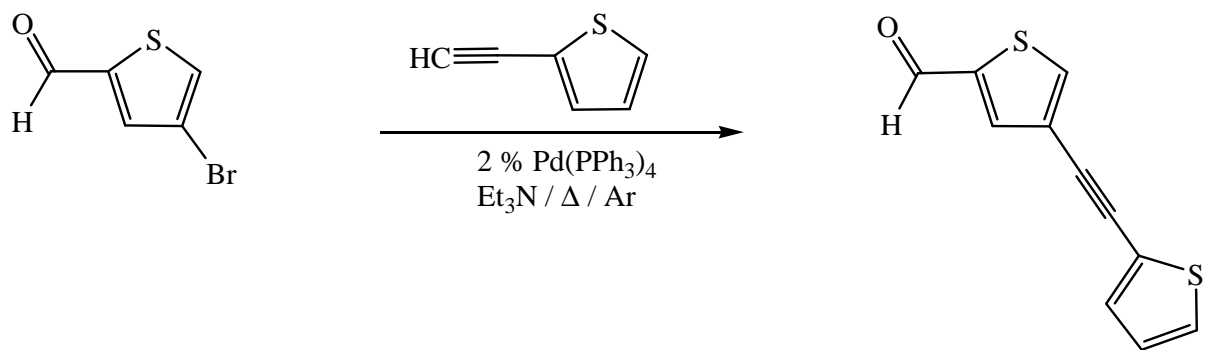
4-Bromothiophene-2-carboxaldehyde (2.6 mmol, 500 mg), bis(triphenylphosphine) palladium(II)chloride (0.16 mmol, 112 mg, 6 %), triphenylphosphine (0.31 mmol, 81 mg, 12 %), cuprous iodide (0.16 mmol, 30 mg, 6 %) and 2-ethynylthiophene (3.27 mmol, 0.35 ml) were used. The crude product was purified by column chromatography using silica gel and CH_2Cl_2 : hexane (50:50) as mobile phase which afforded a bright yellow solid. Yield: 471 mg, 2.16 mmol, 83 %.

^{1}H NMR (400 MHz, CDCl$_3$): 9.92 (1H, d, J = 1.2 Hz), 7.86-7.85 (1H, m), 7.83-7.82 (1H, m), 7.33-7.32 (1H, m), 7.30-7.29 (1H, m), 7.03-7.01(1H, m) ppm. **^{13}C NMR** (100 MHz, CDCl$_3$): 182.54, 143.64, 138.19, 137.09, 132.50, 127.91, 127.24, 123.59, 86.44, 83.32 ppm. **IR** (CH$_2$Cl$_2$): (C=O) 1677 cm^{-1}, (C≡C) 2213 cm^{-1}. **m.p.:** 114 – 115 ºC.

2.3.3.1.6 4-(Thien-2-ylethynyl)benzaldehyde (NB-A6)
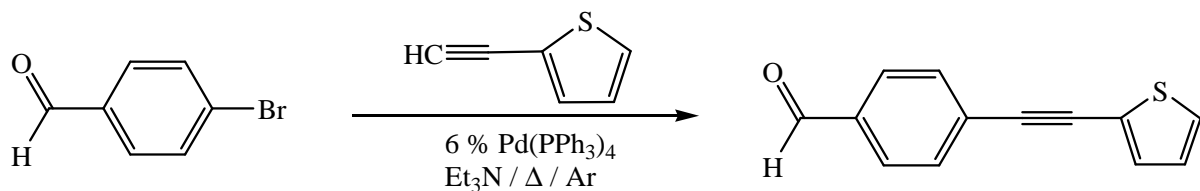
4-Bromo-benzaldehyde (3.0 mmol, 555 mg), bis(triphenylphosphine)palladium(II)chloride (0.18 mmol, 126 mg, 6 %), triphenylphosphine (0.36 mmol, 94 mg, 12%), cuprous iodide (0.18 mmol, 34 mg, 6 %) and 2-ethynylthiophene (3.0 mmol, 0.3 ml) were used. The crude product was purified by column chromatography on silica gel using CH_2Cl_2 : petroleum Ether 40:60 (75:25) as mobile phase which afforded an orange yellow solid. Yield: 597 mg, 2.81 mmol, 94 %.

^{1}H NMR (400 MHz, CDCl$_3$): 10.02 (1H, s), 7.86 (2H, d, J = 8.4 Hz), 7.66 (2H, d, J = 8.4 Hz), 7.36-7.33 (2H, m), 7.05-7.03 (1H, m) ppm. **^{13}C NMR** (100 MHz, CDCl$_3$): 191.42, 135.42, 132.89, 131.81, 129.62, 129.26, 128.38, 127.35, 122.45, 92.27, 86.80 ppm. **IR** (CH$_2$Cl$_2$): (C=O) 1701 cm^{-1}, (C≡C) 2206 cm^{-1}. **m.p.**: 101 – 103 ℃.

2.3.3.1.7 4-(Thien-3-ylethynyl)benzaldehyde (NB-A7)
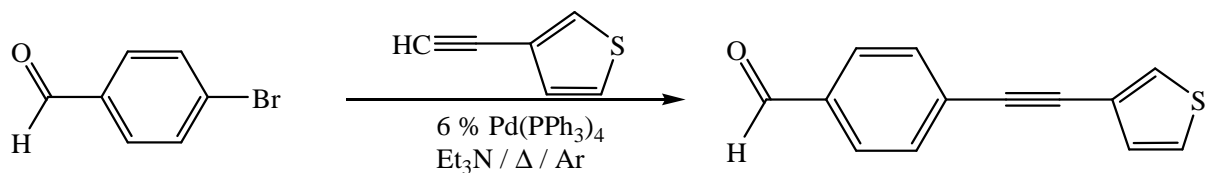
4-Bromobenzaldehyde (4.5 mmol, 833 mg), bis(triphenylphosphine)palladium(II)chloride (0.18 mmol, 126 mg, 6 %), triphenylphosphine (0.36 mmol, 94 mg, 12%), cuprous iodide (0.18 mmol, 34 mg, 6 %) and 3-ethynylthiophene (3.0 mmol, 0.29 ml) were used. The crude product was purified by column chromatography on silica gel using CH_2Cl_2 : petroleum ether 40:60 (75:25) as mobile phase which afforded an orange yellow solid. Yield: 522 mg, 2.46 mmol, 82 %.

¹H NMR (400 MHz, CDCl₃): 10.02 (1H, s), 7.86 (2H, d, *J* = 8.4 Hz), 7.66 (2H, d, *J* = 8.4 Hz), 7.60-7.59 (1H, m), 7.35-7.33 (1H, m), 7.23-7.22 (1H, m) ppm. **¹³C NMR** (100 MHz, CDCl₃): 191.46, 135.35, 132.00, 129.81, 129.74, 129.61, 125.74, 121.60, 88.65, 88.16 ppm. **IR** (CH₂Cl₂): (C=O) 1703 cm⁻¹, (C≡C) 2207 cm⁻¹. **m.p.:** 129 – 134 ºC.

2.3.3.2   Procedure for the preparation of porphyrins *via* the Adler method [3]

2.3.3.2.1   5,10,15,20-Tetraphenylporphyrin (H₂TPP)
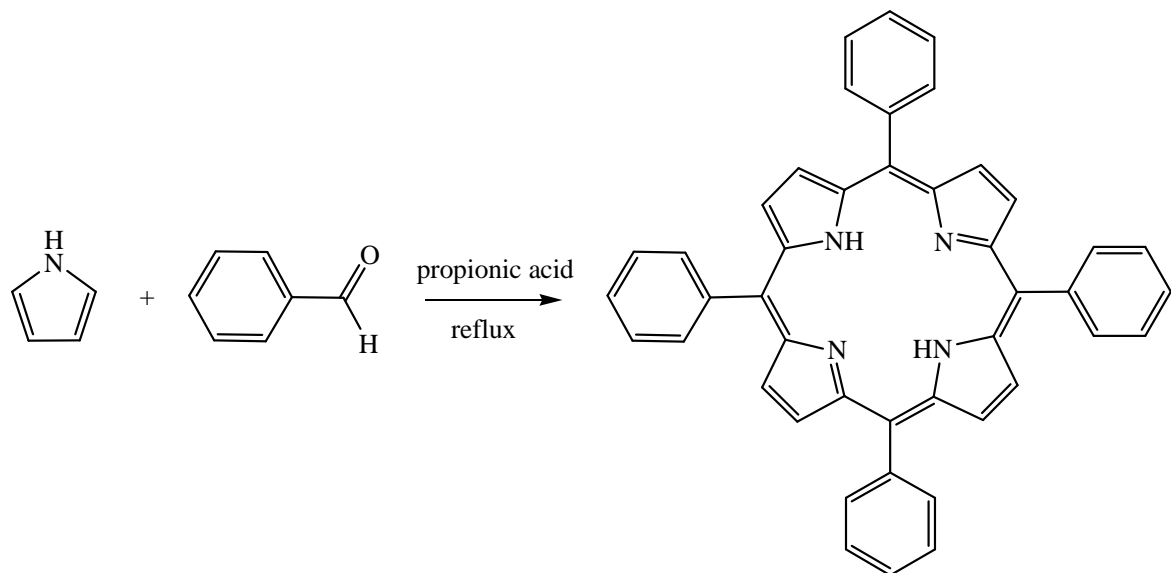
Benzaldehyde (30 mmol, 3.05 ml) and pyrrole (30 mmol, 2.08 ml) were added to 100 ml propionic acid. The reaction mixture was brought to reflux temperature for 90 minutes and then allowed to cool and left overnight. The porphyrin was filtered off and repeatedly washed with cold methanol affording a purple crystalline solid. Yield: 920 mg, 1.49 mmol, 20 %. Spectroscopic data were in good agreement with reported data.[56]

¹H NMR (400 MHz, CDCl₃): 8.85 (8H, s), 8.23-8.21 (8H, m), 7.77-7.75 (12H, m), -2.86 (2H,s) ppm. **¹³C NMR** (100 MHz, CDCl₃): 142.11, 134.52, 127.67, 126.65, 120.09 ppm.

2.3.3.3   Procedure for the preparation of porphyrins *via* the Lindsey method [6]

The freebase porphyrins were prepared *via* a modified version of Lindsey's two-step one-flask room temperature reaction for the synthesis of *meso*-substituted porphyrins. Molar equivalents of pyrrole and the appropriate aldehyde were dissolved in 200 ml of dichloromethane and the solution was purged with argon for 10 minutes. For the thienyl porphyrins the reaction mixture was then cooled to 0 ºC before the addition of the acid catalyst, $BF_3.OEt_2$ (0.1 equiv.). Cooling of the reaction mixture was not required for the tetraphenylporphyrins. The reaction mixture was allowed to stir overnight at room temperature. *p*-Chloranil (0.75 equiv.) was added to the solution and stirring continued for a further 6 hours [note: as *p*-chloranil is an oxidising agent the solution no longer needs to be kept under argon at this point.] The volume of solvent was then reduced to *ca*. 25 ml and the crude mixture was purified by column chromatography.

2.3.3.3.1   5,10,15,20-Tetra(thien-2-yl)porphyrin (H$_2$TThP)
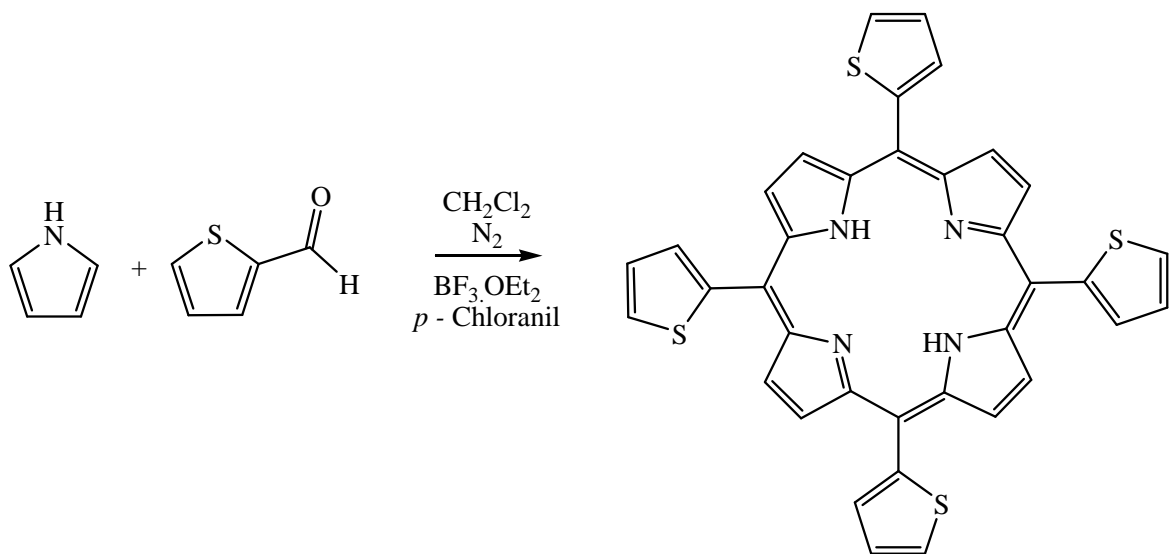
Pyrrole (5 mmol, 0.35 ml), 2-thiophenecarboxaldehyde (5 mmol, 0.47 ml), BF$_3$.OEt$_2$ (0.50 mmol, 63.36 µl) and *p*-chloranil (3.75 mmol, 922 mg) was used. The crude product was purified by column chromatography using silica gel and CH$_2$Cl$_2$ as mobile phase which afforded a greenish purple solid. Yield 145 mg, 0.23 mmol, 18 %. Spectroscopic data were in good agreement with the reported data.[56]

^{1}H NMR (400 MHz, CDCl$_3$): 8.97 (8H, s), 7.85 (4H, dd, ^3J = 3.2 Hz, ^4J = 1.2 Hz), 7.78 (4H, dd, ^3J = 5.2 Hz, ^4J = 1.2 Hz), 7.44 (4H, dd, ^3J = 5.2 Hz, ^4J = 3.2 Hz), -2.72 (2H, s) ppm. **^{13}C NMR** (100 MHz, CDCl$_3$): 146.90, 142.62, 133.89, 127.90, 126.08, 112.38 ppm.

2.3.3.3.2   5,10,15,20-Tetra(5-(phenylethynyl)thien-2-yl)porphyrin (NB-H₂P1)
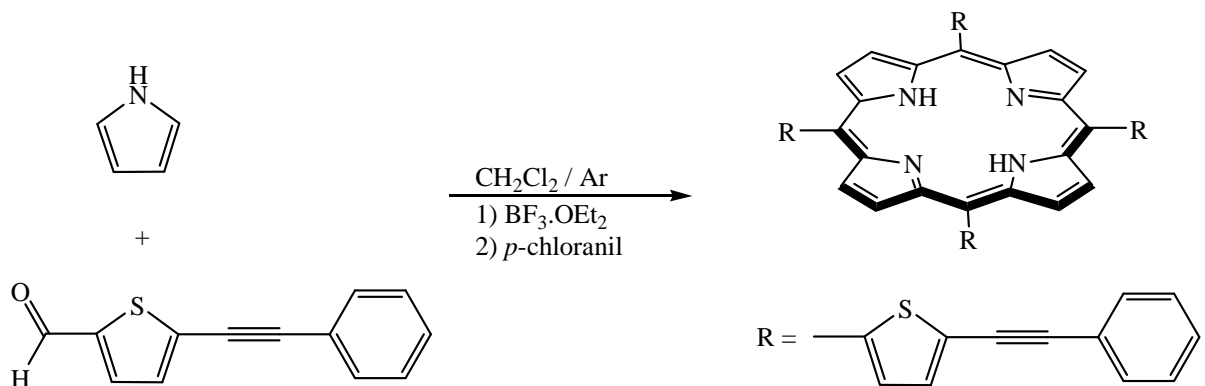
Pyrrole (3.53 mmol, 0.25 ml) and 5-(phenylethynyl)thiophene-2-carboxaldehyde (3.53 mmol, 750 mg), BF$_3$.OEt$_2$ (0.35 mmol, 45 μl) and *p*-chloranil (2.65 mmol, 645 mg) was used. The crude product was purified by column chromatography using silica gel and CH$_2$Cl$_2$: petroleum ether 40:60 (80:20) as mobile phase which afforded a greenish purple solid. Yield: 257 mg, 0.25 mmol, 28 %.

¹H NMR (600 MHz, CDCl$_3$): 9.15 (8H, s), 7.83 (4H, d, *J* = 3.6 Hz), 7.71 (4H, d, *J* = 3.6 Hz), 7.66-7.64 (8H, m), 7.43-7.39 (12H, m), -2.71 (2H, s) ppm. **¹³C NMR** (150 MHz, CDCl$_3$): 143.10, 133.03, 131.52, 130.60, 130.25, 127.70, 127.47, 125.27, 121.81, 110.81, 93.42, 81.53 ppm.

2.3.3.3.3   5,10,15,20-Tetra(5-(thien-2-ylethynyl)thien-2-yl)porphyrin (NB-H₂P2)
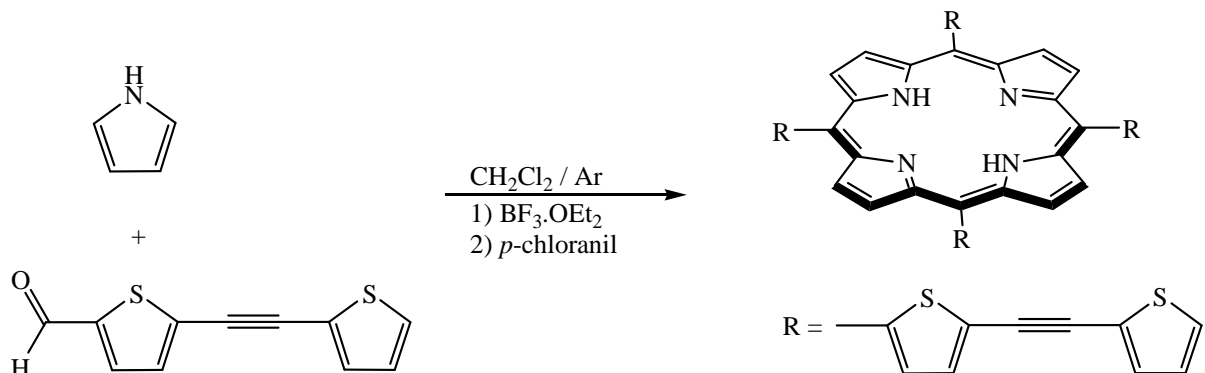
Pyrrole (1.37 mmol, 95 μl) and 5-(thien-2-ylethynyl)thiophene-2-carboxaldehyde (1.37 mmol, 300 mg), BF₃.OEt₂ (0.14 mmol, 18 μl) and *p*-chloranil (1.03 mmol, 253 mg) was used. The crude product was purified by column chromatography using silica gel and CH₂Cl₂ : petroleum ether 40:60 (80:20) as mobile phase which afforded a greenish purple solid. Yield: 83 mg, 0.08 mmol, 23 %.

¹H NMR (600 MHz, CDCl₃): 9.12 (8H, s), 7.82 (4H, d, *J* = 3.6 Hz), 7.79 (4H, d, *J* = 3.6 Hz), 7.70-7.69 (4H, m), 7.41-7.37 (4H, m), 7.10-7.06 (4H, m) -2.65 (2H, s) ppm. **¹³C NMR** (150 MHz, CDCl₃): 143.51, 133.09, 131.47, 130.43, 126.96, 126.32, 124.82, 121.86, 110.70, 86.68, 85.12. ppm.

2.3.3.3.4 5,10,15,20-Tetra(5-(thien-3-ylethynyl)thien-2-yl)porphyrin (NB-H₂P3)
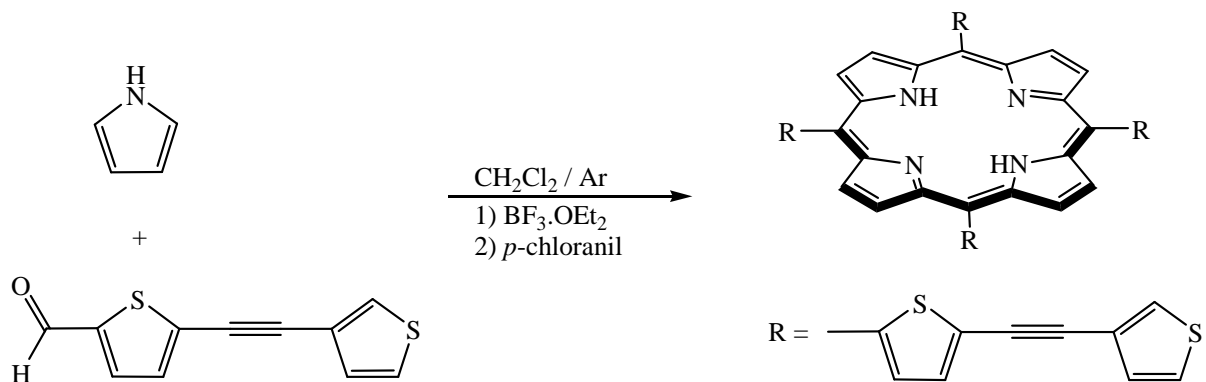
Pyrrole (1.37 mmol, 95 μl) and 5-(thien-3-ylethynyl)thiophene-2-carboxaldehyde (1.37 mmol, 300 mg), BF₃.OEt₂ (0.14 mmol, 18 μl) and *p*-chloranil (1.03 mmol, 253 mg) was used. The crude product was purified by column chromatography using silica gel and CH₂Cl₂ : petroleum ether 40:60 (80:20) as mobile phase which afforded a greenish purple solid. Yield: 61 mg, 0.06 mmol, 17 %.

¹H NMR (600 MHz, CDCl₃): 9.13 (8H, s), 7.82 (4H, d, *J* = 3.6 Hz), 7.70 (4H, d, *J* = 3.6 Hz), 7.67-7.66 (4H, m), 7.38-7.37 (4H, m), 7.36-7.31 (4H, m) -2.63 (2H, s) ppm. **¹³C NMR** (150 MHz, CDCl₃): 142.96, 132.96, 130.21, 128.83, 128.24, 125.17, 124.93, 124.70, 120.92, 117.81, 110.80, 88.68, 80.93 ppm.

2.3.3.3.5   5,10,15,20-Tetra(4-(phenylethynyl)thien-2-yl)porphyrin (NB-H₂P4)
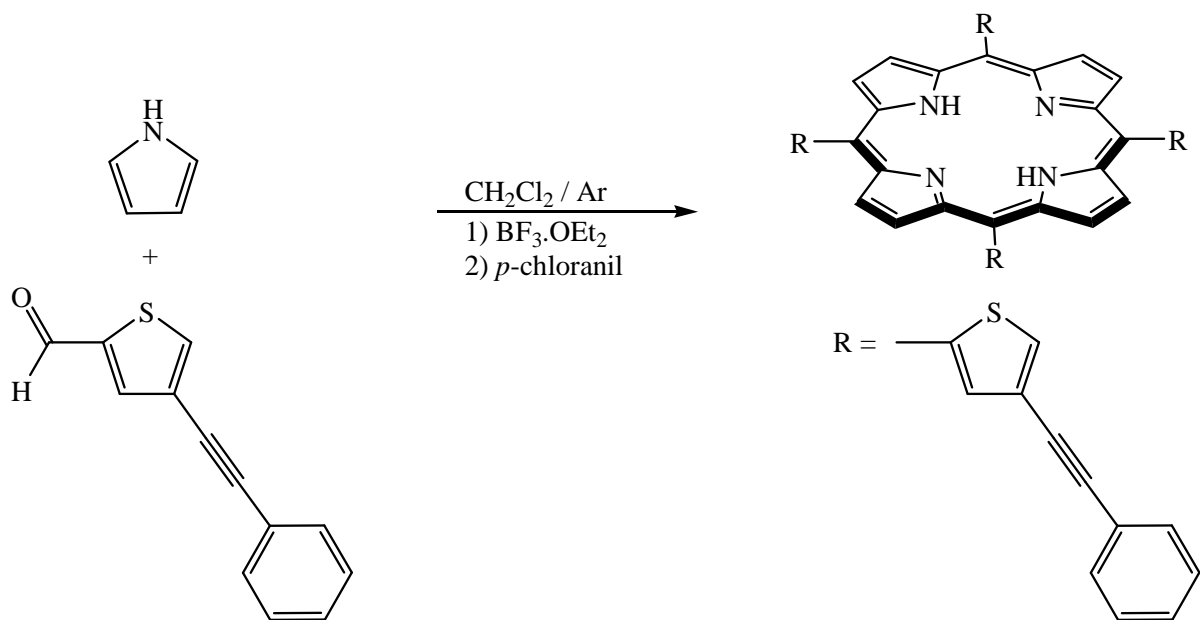
Pyrrole (2.0 mmol, 0.14 ml) and 4-(phenylethynyl)thiophene-2-carboxaldehyde (2.0 mmol, 424 mg), BF₃.OEt₂ (0.2 mmol, 25 μl) and *p*-chloranil (1.5 mmol, 369 mg) was used. The crude product was purified by column chromatography using silica gel and CH_2Cl_2 : Et_3N (99:1) as mobile phase which afforded a greenish purple solid. Yield 135 mg, 0.13 mmol, 26 %.

¹H NMR (600 MHz, CDCl₃): 9.12 (8H, s), 8.05 (4H, d, *J* = 1.2 Hz), 8.03 (4H, d, *J* = 1.2 Hz), 7.64-7.62 (8H, m), 7.41-7.38 (12H, m), -2.69 (2H, s) ppm. **¹³C NMR** (150 MHz, CDCl₃): 141.75, 134.98, 131.19, 130.63, 130.31, 127.49, 126.52, 126.20, 122.17, 120.10, 110.46, 87.35, 81.39 ppm.

2.3.3.3.6   5,10,15,20-Tetra(4-(thien-2-ylethynyl)thien-2-yl)porphyrin (NB-H₂P5)
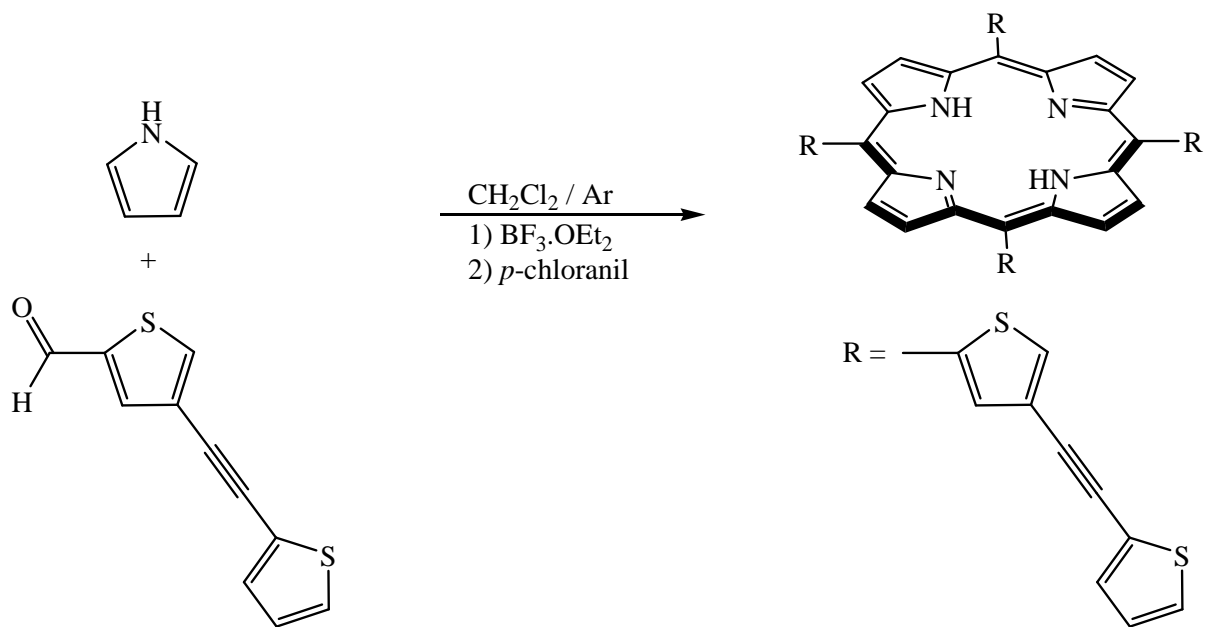
Pyrrole (1.65 mmol, 0.11 ml) and 4-(thien-2-ylethynyl)thiophene-2-carboxaldehyde (1.65 mmol, 360 mg), BF₃.OEt₂ (0.17 mmol, 21 µl) and *p*-chloranil (1.24 mmol, 304 mg) was used. The crude product was purified by column chromatography using silica gel and CH₂Cl₂ : Et₃N (99:1) as mobile phase which afforded a greenish purple solid. Yield: 61 mg, 0.06 mol, 14 %.

¹H NMR (600 MHz, CDCl₃): 9.12 (8H, s), 8.07 (4H, d, *J* = 1.2 Hz), 8.03 (4H, d, *J* = 1.2 Hz), 7.40 (4H, d, *J* = 3.6 Hz), 7.14 (4H, d, *J* = 3.6 Hz), 7.09 – 7.06 (4H, m), -2.64 (2H, s) ppm.   **¹³C NMR** (150 MHz, CDCl₃): 141.67, 134.85, 131.13, 130.33, 126.40, 126.12, 122.27, 120.11, 110.49, 105.45, 87.42, 81.41 ppm.

2.3.3.3.7 5,10,15,20-Tetra(4-(thien-2-ylethynyl)phenyl)porphyrin (NB-H₂P6)
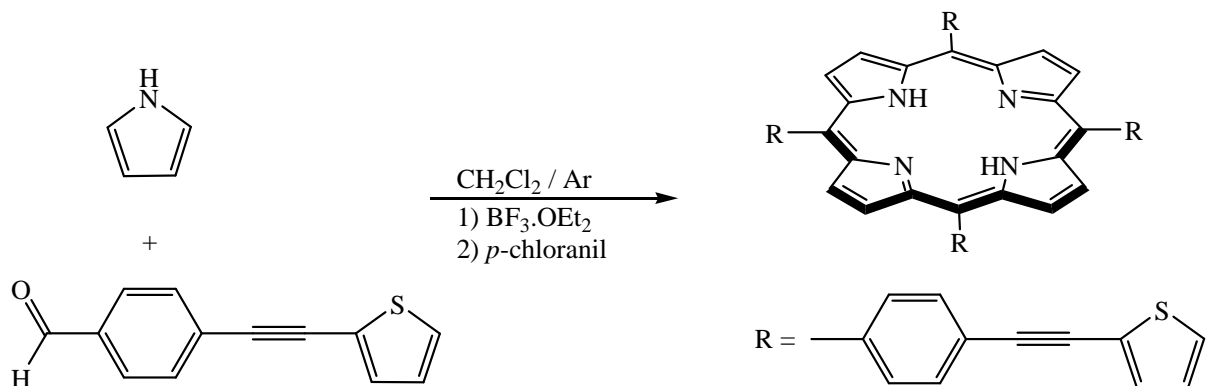
Pyrrole (1.44 mmol, 0.1 ml) and 4-(thien-2-ylethynyl)benzaldehyde (1.41 mmol, 300 mg), $BF_3.OEt_2$ (0.14 mmol, 18 μl) and *p*-chloranil (1.06 mmol, 260 mg) was used. The crude product was purified by column chromatography using silica gel and CH_2Cl_2 : Et_3N (99:1) as mobile phase which afforded a greenish purple solid. Yield 40 mg, 0.04 mol, 11 %.

¹H NMR (600 MHz, CDCl₃): 8.88 (8H, s), 8.21 (8H, d, *J* = 8.4 Hz), 7.92 (8H, d, *J* = 8.4 Hz), 7.44-7.42 (4H, m), 7.39-7.37 (4H, m), 7.11-7.09 (4H, m), -2.78 (2H, s) ppm. **¹³C NMR** (150 MHz, CDCl₃): 144.93, 133.58, 131.20, 128.85, 126.57, 126.25, 122.31, 121.59, 118.66, 82.89, 81.33 ppm

2.3.3.3.8   5,10,15,20-Tetra(4-(thien-3-ylethynyl)phenyl)porphyrin (NB-H$_2$P7)
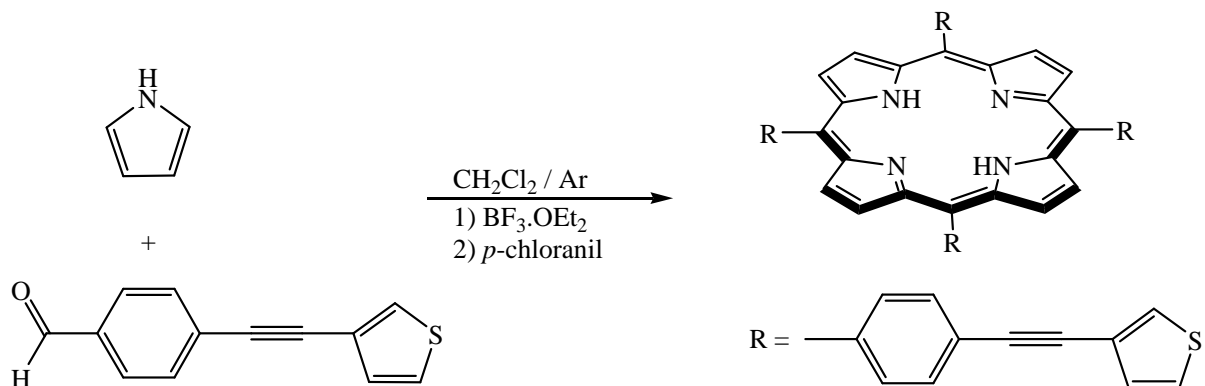
Pyrrole (1.44 mmol, 0.1 ml) and 4-(thien-3-ylethynyl)benzaldehyde (1.41 mmol, 300 mg), BF$_3$.OEt$_2$ (0.14 mmol, 18 μl) and *p*-chloranil (1.06 mmol, 260 mg) was used. The crude product was purified by column chromatography using silica gel and CH$_2$Cl$_2$: Et$_3$N (99:1) as mobile phase which afforded a greenish purple solid. Yield: 59 mg, 0.06 mmol, 16 %.

¹H NMR (600 MHz, CDCl$_3$): 8.88 (8H, s), 8.20 (8H, d, *J* = 8.4 Hz), 7.92 (8H, d, *J* = 8.4 Hz), 7.68-7.67 (4H, m), 7.40-7.38 (4H, m), 7.35-7.34 (4H, m), -2.78 (2H, s) ppm. **¹³C NMR** (150 MHz, CDCl$_3$): 141.73, 138.57, 134.35, 129.77, 129.71, 128.72, 127.65, 125.32, 115.81, 86.70, 81.53 ppm.

2.3.3.4   General procedure for metallation of porphyrins [57]

The appropriate porphyrin was dissolved in *ca.* 20 ml CH_2Cl_2 and the solution was purged with argon for 10 minutes. 1.5 equivalents of $Zn(OAc)_2$ was first dissolved in *ca.* 5 ml MeOH and then added to the porphyrin solution. The reaction mixture was allowed to stir for *ca.* 10 hours. All solvents were removed under reduced pressure leaving a purple solid. This solid was dissolved in CH_2Cl_2 and washed successively with 5 % aqueous $NaHCO_3$, followed by water. The organic layer was dried over $MgSO_4$ and the solvent removed under reduced pressure. The metalloporphyrins were purified by column chromatography using silica gel and CH_2Cl_2 (100 %) as mobile phase. All metalloporphyrins synthesised in this manner were typically obtained in > 95 % yield.

2.3.3.4.1   Zinc(II)-5,10,15,20-tetraphenylporphyrin (ZnTPP)
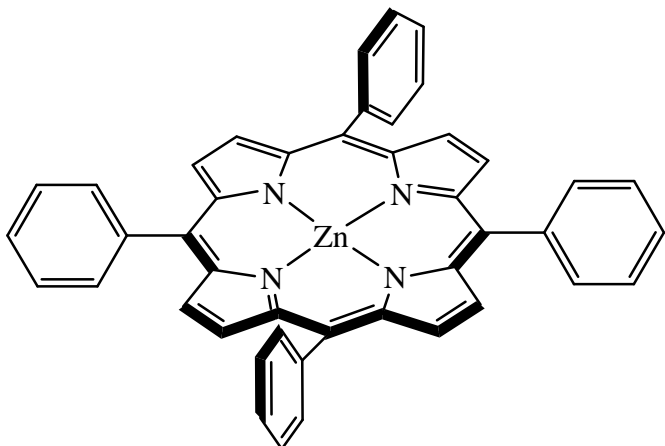
Spectroscopic data were in good agreement with reported data.[57]

¹H NMR (400 MHz, $CDCl_3$): 8.87 (8H, s) 8.18-8.15 (8H, m), 7.72-7.64 (12H, m) ppm.
¹³C NMR (100 MHz, $CDCl_3$): 150.16, 142.77, 134.39, 131.39, 127.45, 126.51, 121.09 ppm.

2.3.3.4.2   Zinc(II)-5,10,15,20-tetra(thien-2-yl)porphyrin (ZnTThP)
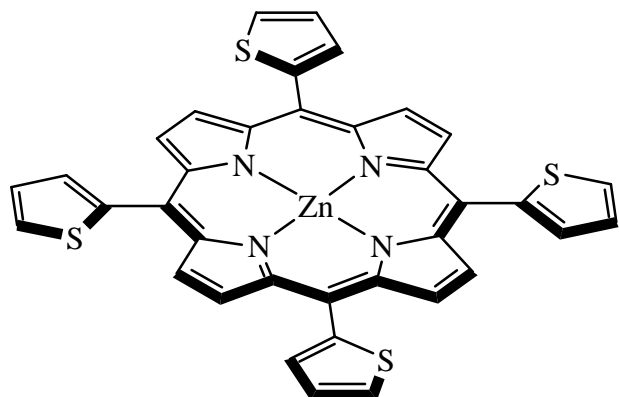
Spectroscopic data were in good agreement with reported data.[23]

¹H NMR (400 MHz, CDCl₃): 9.07 (8H, s) 7.84 (4H, dd, ^3J = 3.6 Hz, ^4J = 1.2 Hz), 7.77 (4H, dd, ^3J = 3.6 Hz, ^3J = 5.2 Hz), 7.44 (4H, dd, ^3J = 3.6 Hz, ^4J = 1.2 Hz) ppm. **¹³C NMR** (100 MHz, CDCl₃): 151.34, 143.00, 133.53, 132.15, 127.45, 125.94, 115.93, 113.17 ppm.

2.3.3.4.3   Zinc(II)-5,10,15,20-tetra(5-(phenylethynyl)thien-2-yl)porphyrin (NB-ZnP1)
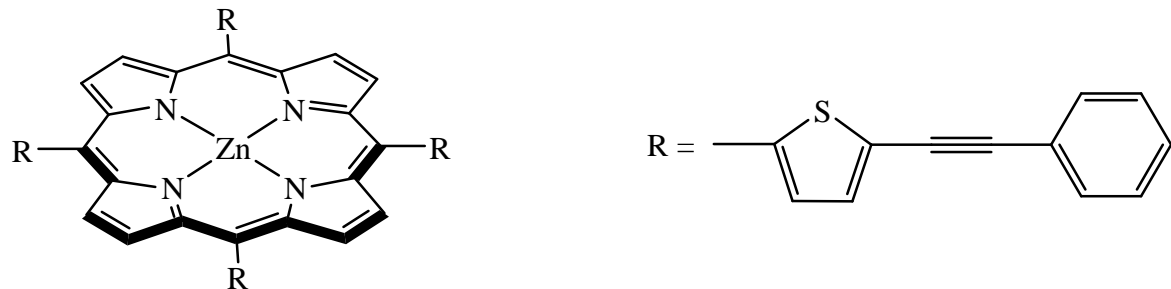
¹H NMR (400 MHz, CDCl₃): 9.21 (8H, s), 7.79 (4H, d, *J* = 3.6 Hz), 7.68 (4H, d, *J* = 3.6 Hz), 7.51-7.49 (8H, m), 7.34-7.32 (12H, m) ppm. **¹³C NMR** (100 MHz, CDCl₃): 150.12, 144.02, 132.59, 131.24, 130.52, 130.13, 127.55, 127.43, 124.59, 121.88, 111.37, 87.28, 84.49 ppm. **Mass. Spec.** (MALDI): calculated 1102.69, observed 1102.5.

2.3.3.4.4   Zinc(II)-5,10,15,20-tetra(5-(thien-2-ylethynyl)thien-2-yl)porphyrin (NB-ZnP2)
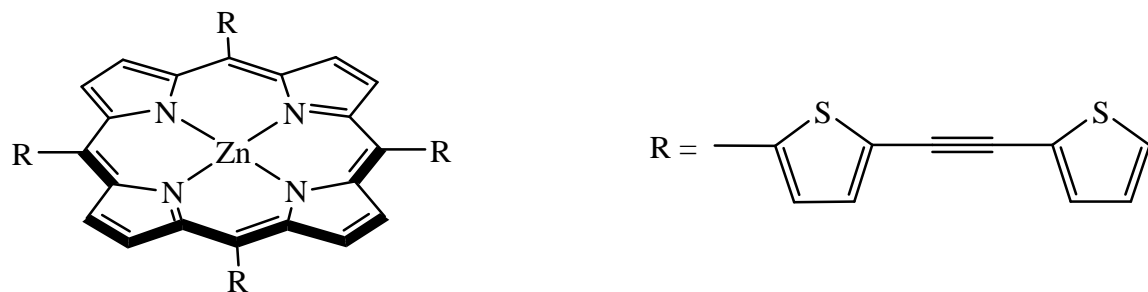
¹H NMR (600 MHz, CDCl₃): 9.21 (8H, s), 7.80 (4H, d, *J* = 3.0 Hz), 7.69 (4H, d, *J* = 3.0 Hz, 7.41-7.40 (4H, m), 7.37-7.36 (4H, m), 7.08-7.07 (4H, m) ppm. **¹³C NMR** (150 MHz, CDCl₃): 150.11, 144.37, 132.65, 131.39, 130.29, 126.83, 126.24, 124.14, 121.86, 111.32, 86.27, 85.26 ppm. **Mass. Spec.** (MALDI): calculated 1126.8, observed 1126.1.

2.3.3.4.5 Zinc(II)-5,10,15,20-tetra(5-(thien-3-ylethynyl)thien-2-yl)porphyrin (NB-ZnP3)
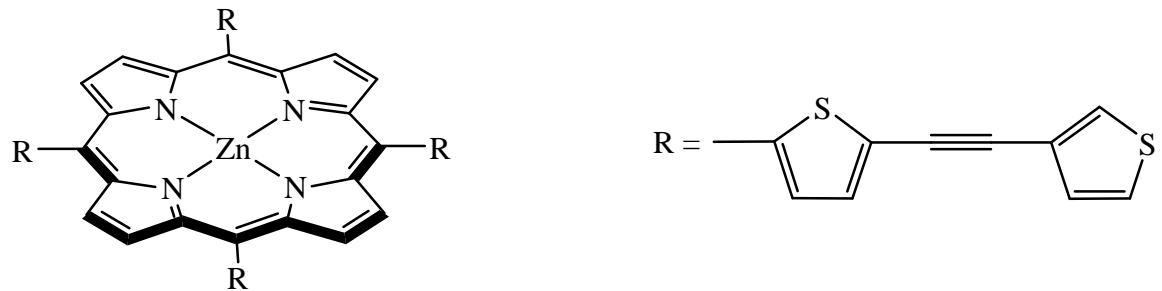
¹H NMR (600MHz, CDCl₃): 9.22 (8H, s), 7.79 (4H, d, *J* = 3 Hz), 7.68 (4H, d, *J* = 3Hz), 7.65-7.64 (4H, m), 7.37-7.36 (4H, m), 7.31-7.30 (4H, m) ppm. **¹³C NMR** (150 MHz, CDCl₃): 150.21, 144.02, 132.70, 131.40, 130.10, 128.80, 128.23, 124.73, 121.06, 111.54, 88.42, 81.17 ppm. **Mass. Spec.** (MALDI): calculated 1126.8, observed 1124.1.

2.3.3.4.6   Zinc(II)-5,10,15,20-tetra(4-(phenylethynyl)thien-2-yl)porphyrin (NB-ZnP4)
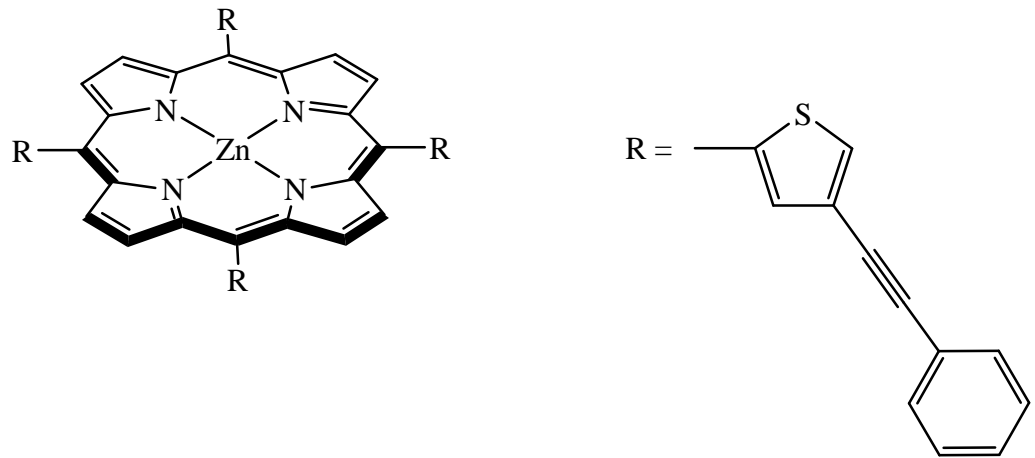
¹H NMR (600 MHz, CDCl₃): 9.13 (8H, s), 8.06 (4H, d, *J* = 1.3 Hz), 8.05 (4H, d, *J* = 1.3 Hz), 7.66-7.63 (8H, m), 7.42-7.38 (12H, m) ppm. **¹³C NMR** (150 MHz, CDCl₃): 150.22, 142.35, 139.57, 134.71, 131.35, 130.66, 129.73, 127.42, 122.10, 120.36, 111.33, 87.96, 84.02 ppm. **Mass. Spec.** (MALDI): calculated 1102.69, observed 1102.5

2.3.3.4.7 Zinc(II)-5,10,15,20-tetra(4-(thien-2-ylethynyl)thien-2-yl)porphyrin (NB-ZnP5)
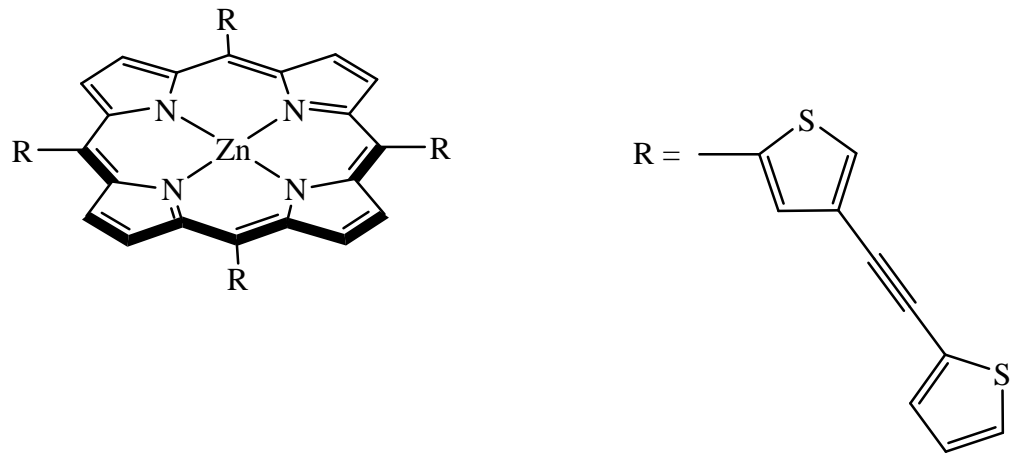
¹H NMR (400 MHz, CDCl₃): 9.21 (8H, s), 8.04 (4H, d, J = 1.2 Hz), 8.02 (4H, d, J = 1.2 Hz), 7.37-7.36 (4H, m), 7.32-7.31 (4H, m), 7.05-7.03 (4H, m) ppm. **¹³C NMR** (100 MHz, CDCl₃): 150.16, 142.27, 135.05, 133.20, 130.39, 126.45, 126.19, 122.38, 120.47, 111.26, 87.64, 83.99 ppm.

2.3.3.4.8 Zinc(II)-5,10,15,20-tetra(4-(thien-2-ylethynyl)phenyl)porphyrin (NB-ZnP6)
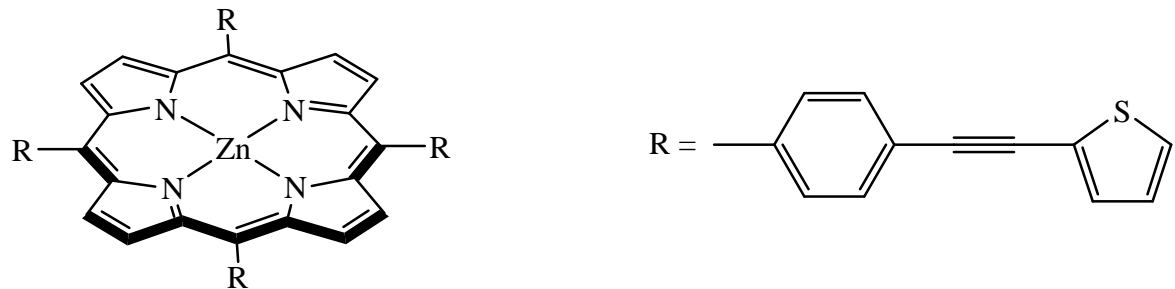
1H NMR (400 MHz, CDCl$_3$): 8.98 (8H, s), 8.23 (8H, d, *J* = 8.4 Hz), 7.93 (8H, d, *J* = 8.4 Hz), 7.47-7.44 (4H, m), 7.40-7.39 (4H, m), 7.19-7.15 (4H, m) ppm. **13C NMR** (100 MHz, CDCl$_3$): 150.07, 145.87, 133.28, 131.04, 129.05, 126.03, 121.63, 121.63, 121.51, 119.97, 82.79, 81.13 ppm. **Mass. Spec.** (MALDI): calculated 1102.69, observed 1101.7

2.3.3.4.9 Zinc(II)-5,10,15,20-tetra(4-(thien-3-ylethynyl)phenyl)porphyrin (NB-ZnP7)
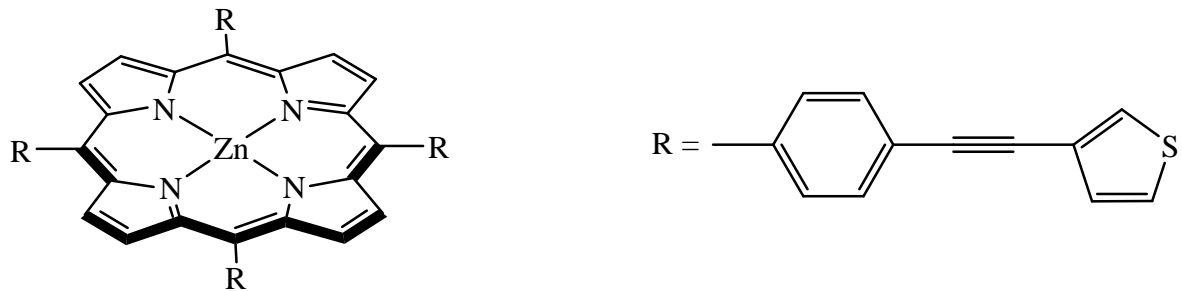
1H NMR (600 MHz, CDCl$_3$): 8.98 (8H, s), 8.23 (8H, d J = 8.4 Hz), 7.93 (8H, d, J = 8.4Hz), 7.69-7.68 (4H, m), 7.42-7.39 (4H, m), 7.35-7.34 (4H, m) ppm. **13C NMR** (150 MHz, CDCl$_3$): 150.49, 141.41, 139.28, 134.55, 129.62, 129.57, 128.79, 127.43, 125.15, 116.04, 85.88, 81.19 ppm. **Mass. Spec.** (MALDI): calculated 1102.69, observed 1102.6

2.4   Results

2.4.1   UV-vis absorbance studies

A UV-vis spectrum typical of the porphyrins discussed in this chapter is displayed in figure 41. The electronic absorbance spectral features (λ_{max} for Soret and Q bands) of porphyrins synthesised in this study in addition to the extinction coefficients are listed in table 10. The absorbance spectra of **ZnTPP** and **ZnTThP** have been previously reported in the literature.[5]   The solvatochromic effect for **NB-ZnP1** was studied in a range of solvents with the differences in absorbance λ_{max} of the Soret and Q bands listed in table 11.
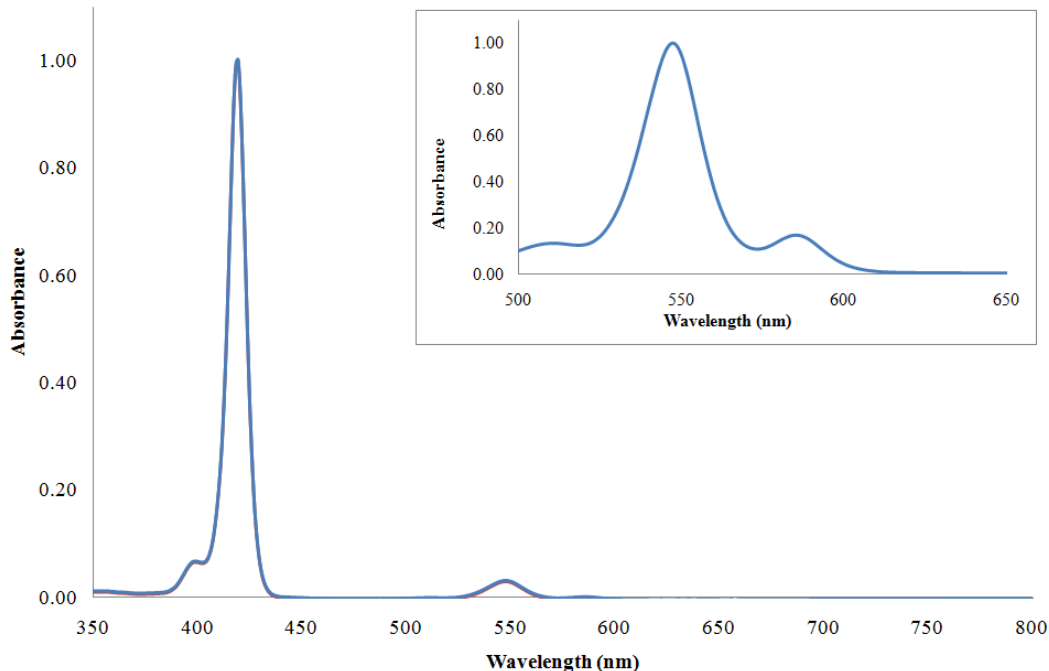
Figure 41   *Electronic absorbance spectrum of* **ZnTPP** *(insert Q bands region) recorded in CH₂Cl₂.*

Porphyrin	Soret (nm)	FWHM (cm^{-1})	Q bands (nm)
ZnTPP	419 (2.53)[a]	514	547 (9.72)[c]
			588 (1.90)[c]
ZnTThP	429 (2.84)[a]	813	556 (9.48)[c]
			600 (1.97)[c]
NB-ZnP1	439 (2.75)[a]	1197	559 (1.94)[b]
			603 (6.40)[c]
NB-ZnP2	439 (2.04)[a]	1350	559 (1.42)[b]
			603 (5.05)[c]
NB-ZnP3	439 (1.81)[a]	1252	559 (1.41)[b]
			603 (4.95)[c]
NB-ZnP4	429 (0.44)[a]	870	555 (0.26)[b]
			596 (0.45)[c]
NB-ZnP5	425 (0.47)[a]	828	550 (0.19)[b]
			590 (0.85)[c]
NB-ZnP6	426 (2.76)[a]	772	550 (9.97)[b]
			590 (2.30)[c]
NB-ZnP7	425 (2.69)[a]	775	550 (9.91)[b]
			590 (2.25)[c]

Table 10   *UV-vis absorbance data of porphyrins recorded in CH$_2$Cl$_2$. [a] Values in brackets refer to ε (x 10^5 M^{-1} cm^{-1}). [b] Values in brackets refer to ε (x 10^4 M^{-1} cm^{-1}). [c] Values in brackets refer to ε (x 10^3 M^{-1} cm^{-1}).*

Porphyrin	Soret (nm)	FWHM (cm^{-1})	Q bands (nm)
Toluene	439	1197	559, 602
Chloroform	442	1073	563, 607
DMSO	445	1059	570, 614

Table 11   *Solvatochromic behaviour of **NB-ZnP1** in different solvents.*

The Soret band of **ZnTPP** and **ZnTThP** were observed at 419 and 429 nm respectively. Tetra(thien-2-yl)porphyrins, **NB-ZnP1**, **NB-ZnP2** and **NB-ZnP3** were red shifted and displayed their Soret band at 439 nm (Fig. 42). This was a bathochromic shift of 20 nm when compared to **ZnTPP** and 10 nm with respect to **ZnTThP**. Porphyrins, **NB-ZnP4** and **NB-ZnP5**, with *meso* thien-2-yl units substituted at the thien-4-yl position were also shifted compared to **ZnTPP**, with both porphyrins displaying a λ_{max} at lower energy than **ZnTPP**. The Soret band of **NB-ZnP4** was observed at 429 nm, while for **NB-ZnP5** the Soret λ_{max} was at 425 nm. Both the porphyrins showed little or no change in their Soret band position with respect to **ZnTThP** (λ_{max} = 429 nm). They were however blue shifted when compared to the Soret bands of **NB-ZnP1** – **NB-ZnP3**. Brückner et al. observed that substitution of the *meso* thien-2-yl ring at the thien-5-yl position caused a red shift in the porphyrins Soret absorbance band while substitution at the thien-3-yl position caused a minor blue shift.[28] The tetra(phenyl)porphyrins, **NB-ZnP6** and **NB-ZnP7**, undergo modest shifts. Both their Soret band λ_{max}, observed at 426 nm, were red shifted (7 nm bathochromic shift) with respect to the related porphyrin, **ZnTPP**.

For porphyrins **NB-ZnP4** - **NB-ZnP7**, where small shifts were observed in the Soret band position, only minor changes were observed in the FWHM values (Table 10). However as the Soret band was shifted to lower energy for porphyrins **NB-ZnP1**, **NB-ZnP2** and **NB-ZnP3** the FWHM increases (FWHM: 1197, 1350 and 1252 cm^{-1} respectively). This suggested increased electronic and vibronic coupling between the π-systems of the porphyrin ring and the *meso* pendant arms.[58] Also an increase in the relative intensity of the Q(0,0) band can be observed as the electronic communication between the porphyrin and thienyl moieties increased. The ratio of the intensity of Q(0,0)/Q(1,0) bands (Fig. 43) increased significantly, with respect to **ZnTPP** and **ZnTThP**, for **NB-ZnP1**, **NB-ZnP2**, **NB-ZnP3**, **NB-ZnP5** and **NB-ZnP6**. Thus the relative energies ground state and first excited singlet state were altered by appropriate substitution.
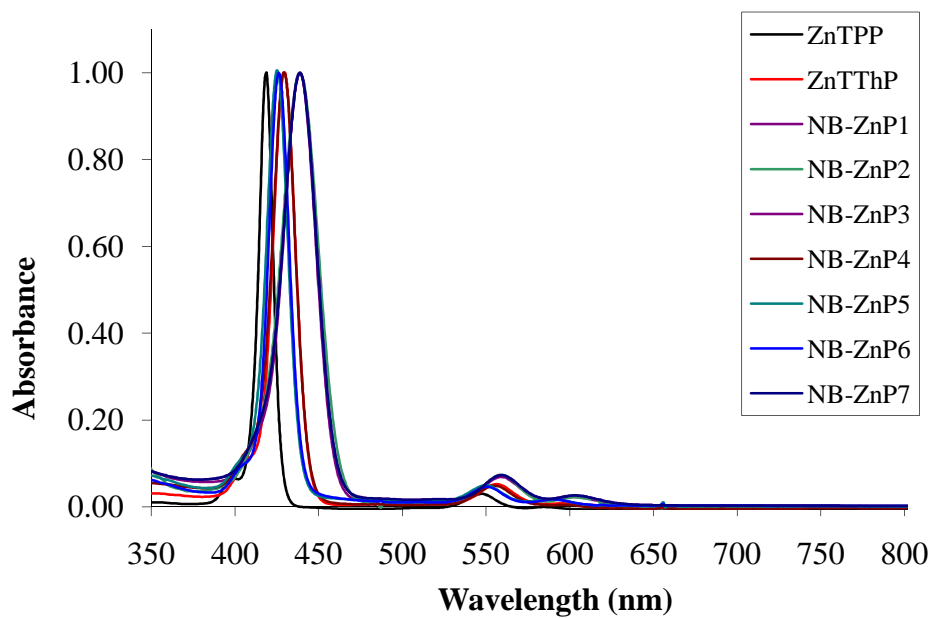
Figure 42   *UV-vis spectra of **ZnTPP**, **ZnTThP** and **NB-ZnP1** – **NB-ZnP7** in CH₂Cl₂ at room temperature. All spectra have been normalised at their λ_max.*
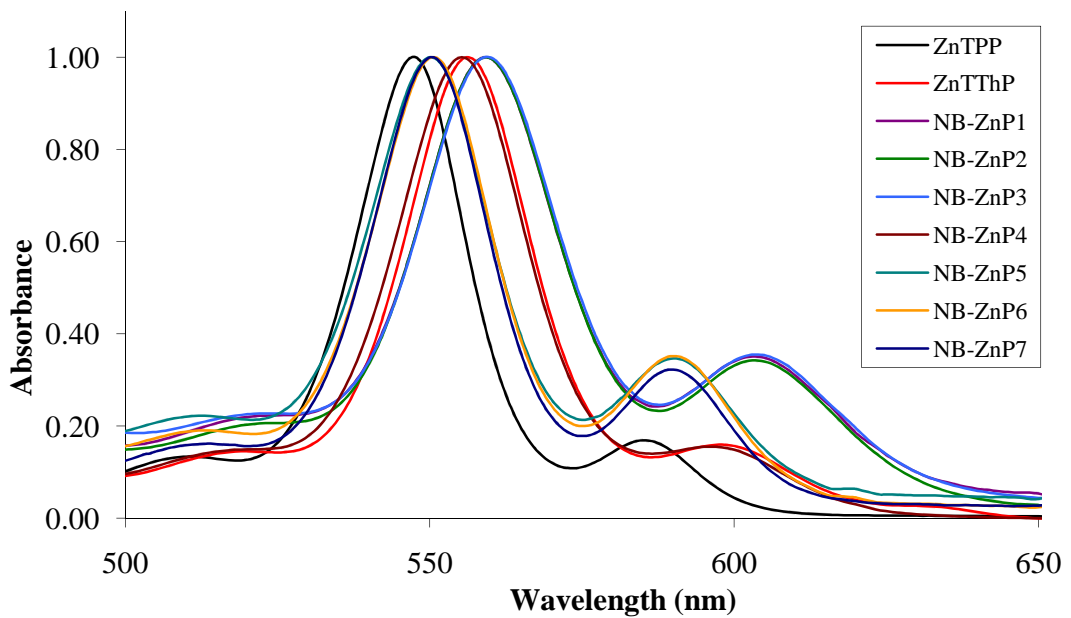
Figure 43   *UV-vis spectra of Q band region of **ZnTPP**, **ZnTThP** and **NB-ZnP1** – **NB-ZnP7** recorded in CH₂Cl₂ at room temperature. All spectra have been normalised at their λ_max.*

2.4.2   Steady – state fluorescence studies

Fluorescence spectra were obtained for the thienyl and phenyl substituted porphyrins produced and compared to **ZnTPP** and **ZnTThP**. Table 12 below presents the emission maxima of the Q bands of the porphyrins and their respective singlet lifetimes, while table 13 illustrates the solvatochromic effects induced in a range of solvents.

Porphyrin	λ_{max} (nm)	Stokes shift (cm^{-1})	$^1\tau$ (ns)
ZnTPP	595, 643	200	1.83
ZnTThP	617, 658	459	1.41
NB-ZnP1	634	811	0.80
NB-ZnP2	635	836	0.72
NB-ZnP3	635	836	0.72
NB-ZnP4	613, 652	465	0.83
NB-ZnP5	601, 647	310	1.39
NB-ZnP6	605, 646	420	1.77
NB-ZnP7	603, 650	365	1.47

Table 12   *Fluorescence maxima and singlet lifetimes ($^1\tau$) of **ZnTPP**, **ZnTThP** and tetra aryl porphyrins studied, all recorded in CH$_2$Cl$_2$ at room temperature. Singlet lifetimes (+/- 0.03 ns)*

Solvent	λ_{max} (nm)	Stokes shift (cm^{-1})^a	$^1\tau$ (ns)
Toluene	634	838	0.94
Chloroform	638	801	0.91
DMSO	640	662	0.82

Table 13   *Fluorescence maxima and singlet lifetimes ($^1\tau$) of **NB-ZnP1** recorded in chloroform, toluene and DMSO.*

The fluorescence spectra of **ZnTPP**, **ZnTThP** and the novel porphyrins studied are shown below (Fig. 44 and 45). The first striking difference in the fluorescence spectra of *meso* tetra(thien-2-yl)porphyrins **NB-ZnP1**, **NB-ZnP2** and **NB-ZnP3** was that the emission bands which arise from the Q(0,0)* and Q(1,0)* excited states were totally unresolved due to the large red shift of the higher energy of the Q(0,0)* state, with the Q(1,0)* emission band stretching out to longer wavelengths (Fig. 44). **NB-ZnP4** retained the emission profile similar to **ZnTThP**, *albeit* with a slight increase in the intensity of its bands, while the fluorescence emission profile of **NB-ZnP5** was significantly increased in intensity and was hypsochromically shifted (the Q(0,0)* band underwent a 12 nm blue shift, Q(1,0)* band underwent a 5 nm blue shift). The fluorescence spectra observed for **NB-ZnP6** and **NB-ZnP7** although similar to that of **ZnTPP**, were red shifted. The intensity of the bands was generally higher than that of **ZnTPP** and also the Q(0,0)* band was more intense than the Q(1,0)*.
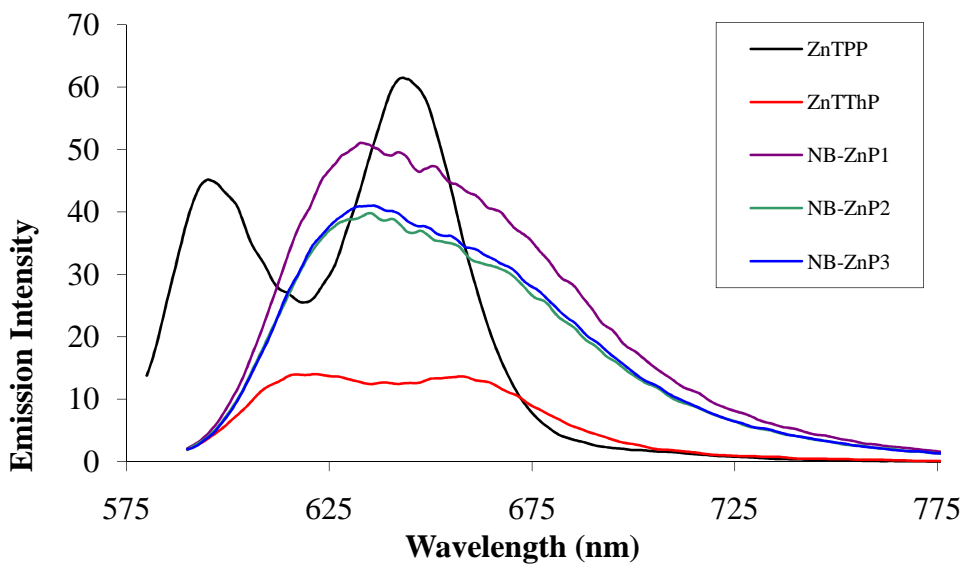
Figure 44   *Fluorescence spectra of **ZnTPP**, **ZnTThP** and **NB-ZnP1** – **NB-ZnP3**. All spectra were recorded in CH$_2$Cl$_2$ at room temperature (λ_{exc} = 555 nm, abs = 0.2 at 555 nm).*
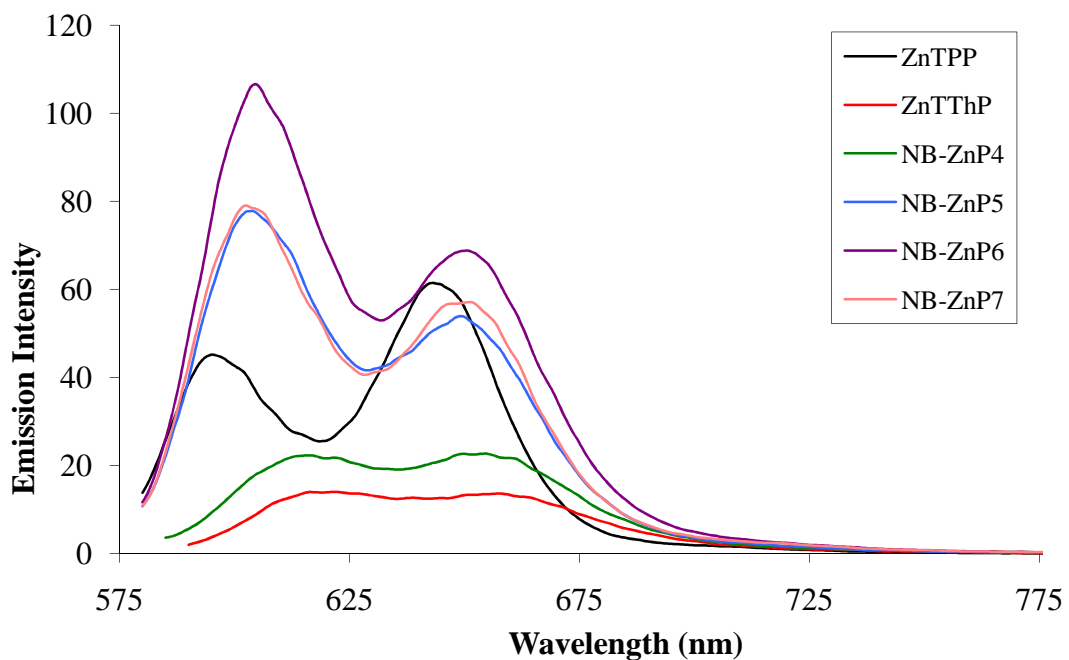
Figure 45   *Fluorescence spectra of **ZnTPP**, **ZnTThP** and **NB-ZnP4** – **NB-ZnP7**. All spectra were recorded in CH_2Cl_2 at room temperature (λ_{exc} = 555 nm, abs = 0.2 at 555 nm).*

The fluorescence lifetimes ($^1\tau$) were recorded in dichloromethane and are included in table 12. A lifetime of 1.83 ns was observed for **ZnTPP**, which is in good agreement with the literature reported value of 2.0 ns.[59] All porphyrins studied showed reduced fluorescence lifetimes relative to **ZnTPP**. The tetra(thein-2-yl)porphyrins studied showed a substantial decrease in lifetimes which ranged from 0.72 to 1.39 ns. The shortest lifetime observed in the series was that of **NB-ZnP2** and **NB-ZnP3** (0.72 ns). In keeping with its increased emission intensity **NB-ZnP5** possessed the longest lifetime in the thien-2-yl series (1.39 ns). The lifetime of both tetra(phenyl)porphyrins, **NB-ZnP6** and **NB-ZnP7**, was reduced to 1.56 and 1.47 ns respectively compared to **ZnTPP**. Typical fluorescence decays observed for **NB-ZnP1** and **NB-ZnP6** are shown in figure 46 and 47.
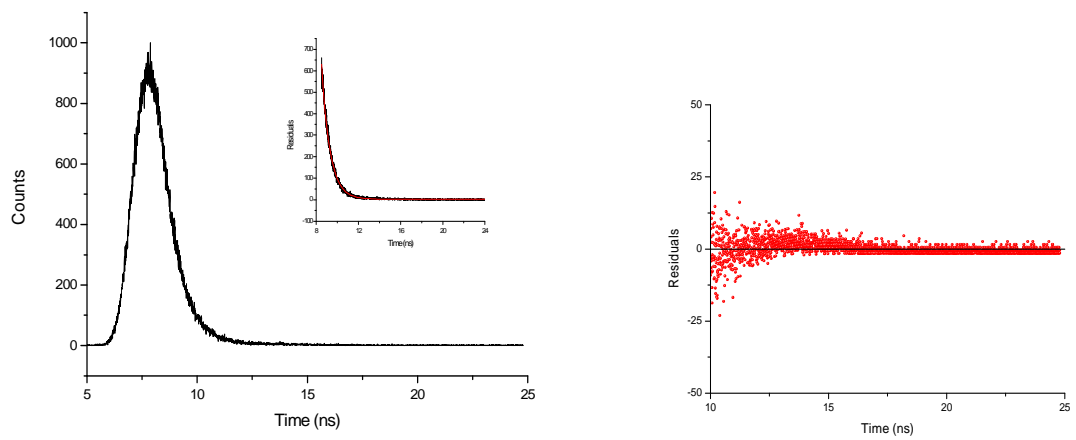
*Figure 46   Typical fluorescence decay observed for **NB-ZnP1** (τ = 0.80 ns) at 633 nm, following excitation at 630 nm. Singlet lifetime (+/- 0.03 ns).*
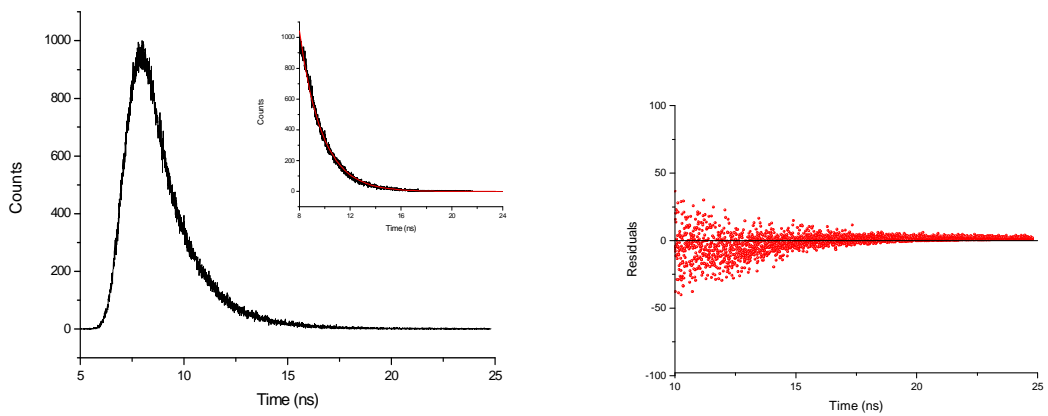
*Figure 47   Typical fluorescence decay observed for **NB-ZnP6** (τ = 1.77 ns) at 603 nm, following excitation at 630 nm. Singlet lifetimes (+/- 0.03 ns).*

2.4.3 Laser flash photolysis studies

Transient absorbance measurements following laser flash photolysis, at 355 and 532 nm, were carried out in toluene under one atmosphere of argon at room temperature with a typical sample absorbance of 0.08 ($\pm$ 0.02) AU. All transient species were formed within the lifetime of the laser pulse (*ca.* 10 ns) and were independent of excitation wavelength. The transient absorbance spectrum of each porphyrin was obtained between 350 and 600 nm. All porphyrins studied gave rise to a transient signal with a maximum in the region 440 – 500 nm. A typical transient decay observed following flash photolysis of **ZnTPP** at 532 nm excitation is shown in figure 48. The transient species is ascribed to the lowest energy $^3(\pi\text{-}\pi^*)$ triplet excited state of the porphyrin complex. A depletion was also observed in the Soret region of the spectrum attributed to the depletion of the porphyrin ground state. The lifetimes of the triplet excited state are given in table 14. Table 15 gives the results of a solvatochromic study of **NB-ZnP1**.

Porphyrin	$^3\tau$ (μs)
ZnTPP	24
ZnTThP	20
NB-ZnP1	9
NB-ZnP2	7
NB-ZnP3	11
NB-ZnP4	36
NB-ZnP5	51
NB-ZnP6	26
NB-ZnP7	54

Table 14   *Triplet lifetimes of porphyrins recorded in toluene at 1 atm argon. Triplet lifetimes (+/- 10 %) μs.*

Solvent	$^3\tau$ (μs)
Toluene	9
Dichloromethane	8
Ethyl Acetate	7
Acetonitrile	7
Dimethyl Sulfoxide	7

Table 15   *Triplet lifetimes of **NB-ZnP1** recorded in various solvents at 1 atm argon. Triplet lifetimes (+/- 10 %) µs.*
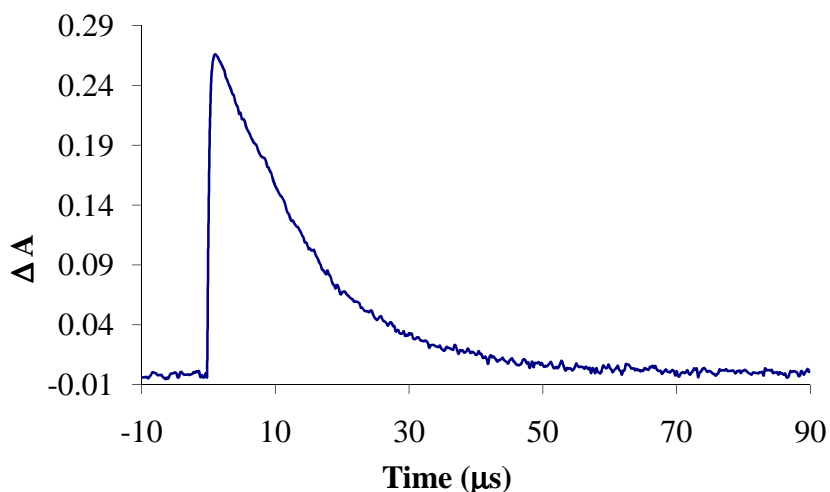
Figure 48   *Transient spectrum of **ZnTPP** in toluene following 532 nm excitation under 1 atm of argon.*

The excited state transient absorbance difference spectrum of **ZnTPP** was characterised by a weak absorbance from 300 to 390 nm in the ultraviolet region and a strong absorbance from 435 to 540 nm in the visible with a λ_{max} at 470 nm. A depletion observed between 400 and 435 nm which equated to the Soret band absorbance of the parent species. Isobestic points were present at 400, 435 and 538 nm indicating that the spectral changes were caused by a clean conversion between two states. At longer wavelengths only weak absorbances were observed.[18]

The excited state transient absorbance difference spectra of **ZnTThP** was red shifted relative to **ZnTPP** where the λ_{max} occurred at 490 nm. A depletion of the ground state was observed as a negative bleach centred at 430 nm. Weak absorbances were observed in the UV region from 300 – 390 nm with further weak absorbance detected in the region 550 – 600 nm.

The tetra(thien-2-yl)porphyrins, **NB-ZnP1** – **NB-ZnP5**, also showed bathochromically shifted transient absorbance difference spectra with respect to **ZnTPP**. Similar to **ZnTThP** the λ_{max} occurred between 450 and 520 nm. Lower energy absorbances that extended past 600 nm were also observed. The profile of the transient absorbance difference spectra and the lifetimes of the transient signals obtained were independent of excitation wavelength (Fig. 49 and 50). **NB-ZnP6** and **NB-ZnP7** possessed transient absorbance difference spectra very similar to that of **ZnTPP** with their λ_{max} at 450 nm, weak absorbances in the UV region and no additional absorbances obvious at longer wavelength.
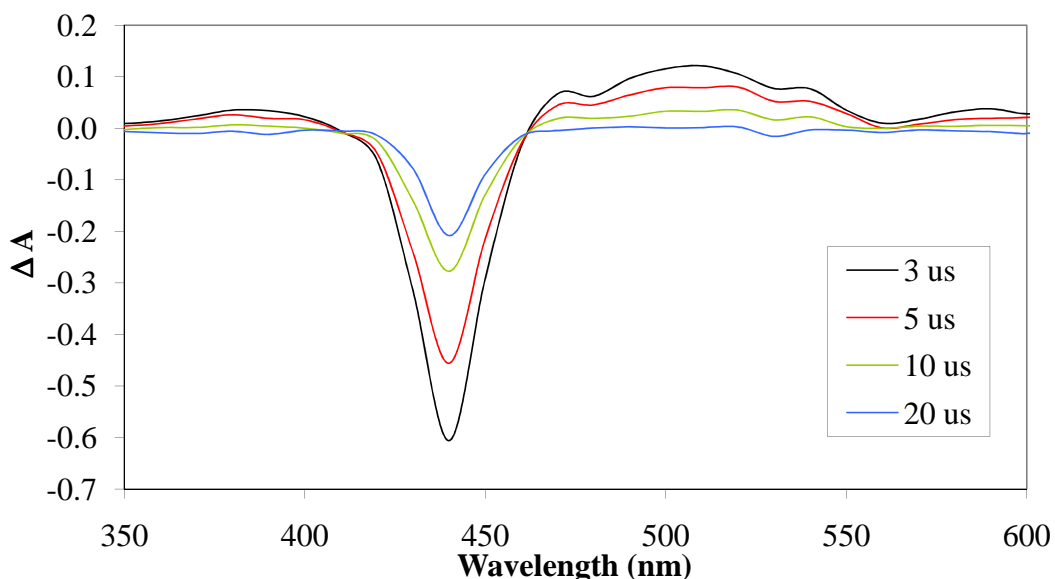
*Figure 49   Transient absorbance difference spectra of **NB-ZnP1** in toluene following 355 nm excitation under 1 atm argon.*
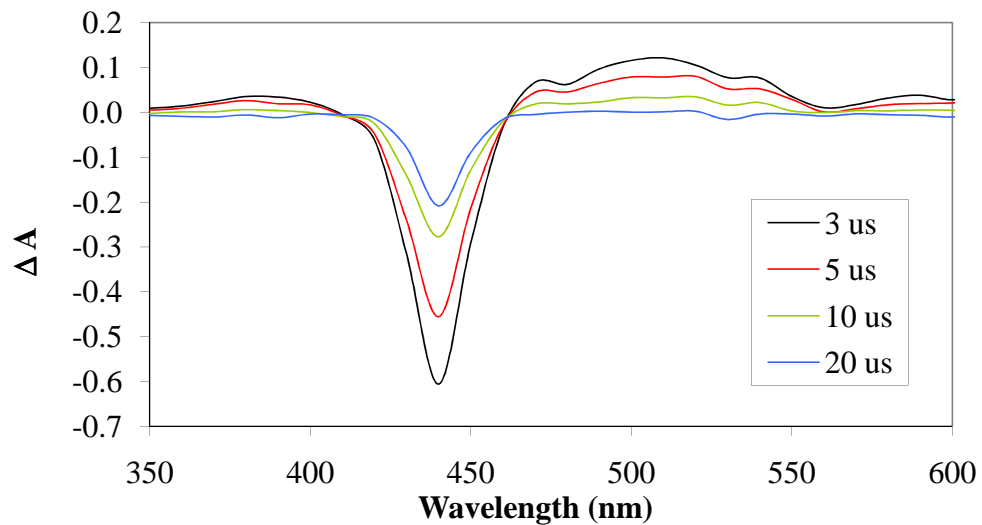
Figure 50   *Transient absorbance difference spectra of **NB-ZnP1** in toluene following 532 nm excitation under 1 atm argon.*
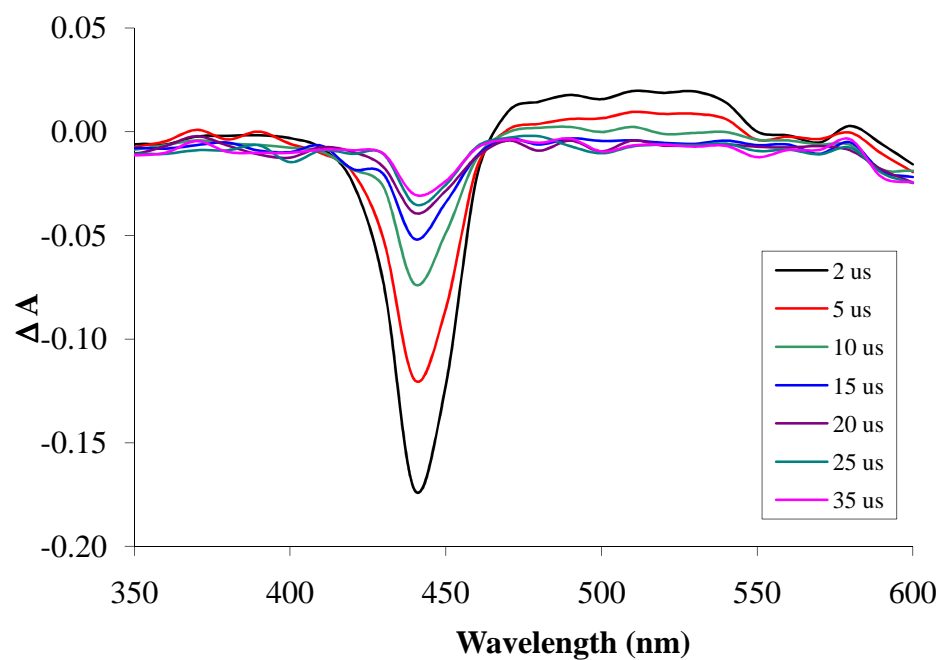
Figure 51   *Transient absorbance difference spectra of **NB-ZnP2** in toluene following 355 nm excitation under 1 atm argon.*
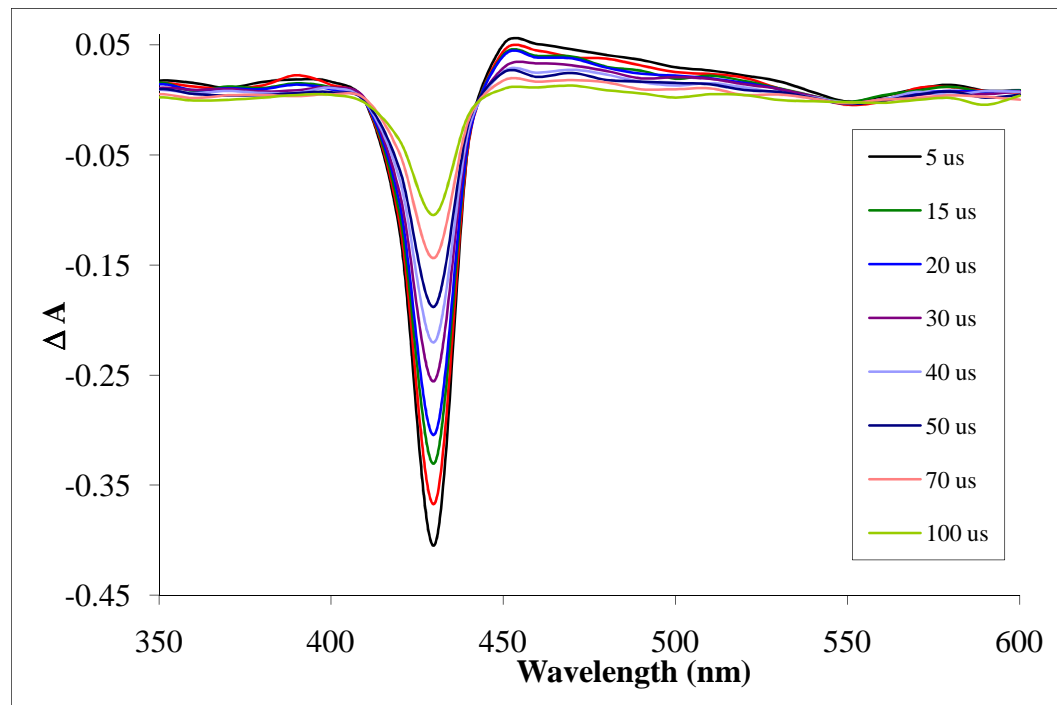
*Figure 52   Transient absorbance difference spectra of **NB-ZnP5** in toluene following 355 nm excitation under 1 atm argon.*
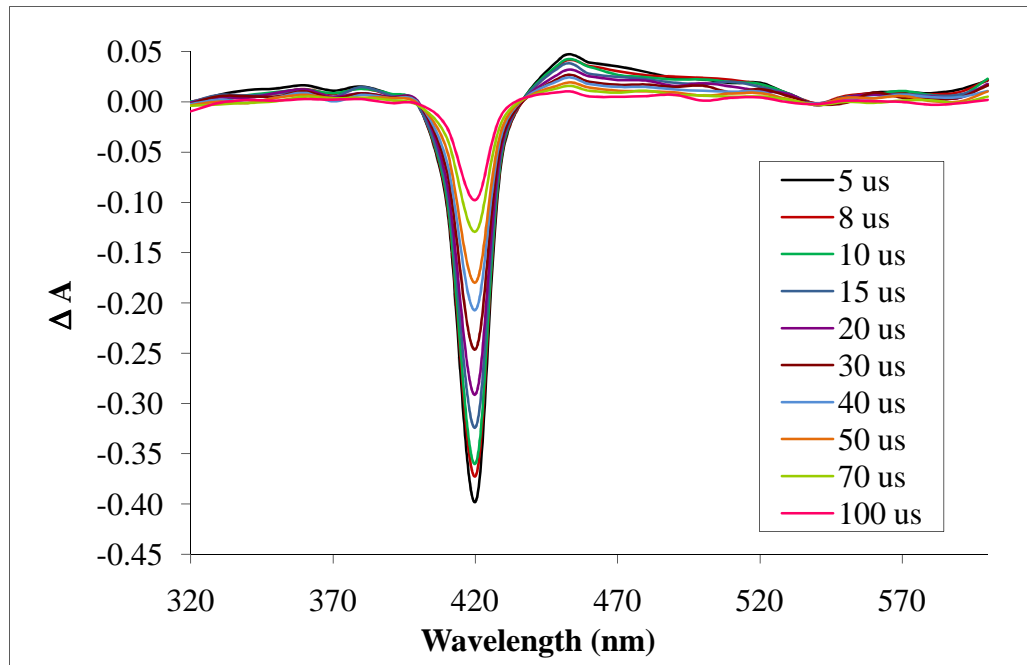
*Figure 53   Transient absorbance difference spectra of **NB-ZnP7** in toluene following 355 nm excitation under 1 atm argon.*

135

2.4.4 Electrochemistry

Porphyrins are electroactive systems and undergo multiple redox processes. The cyclic voltammogram of **ZnTThP** is shown in figure 54.[5] In general metalloporphyrins display one or two ring centred oxidations and one or two ring centred reductions. Substitution at the *meso* position of the porphyrin macrocycle had an effect on the electrochemistry of the porphyrin ring. The two $E_{1/2}$ values observed at positive potential (Table 16) correspond to the first and second reversible oxidations of the porphyrin π system which result in the formation of the porphyrin cation radical and porphyrin dication radical respectively. Generally there were two reduction processes observed at negative potential corresponding to the formation of the porphyrin anion radical and dianion species.
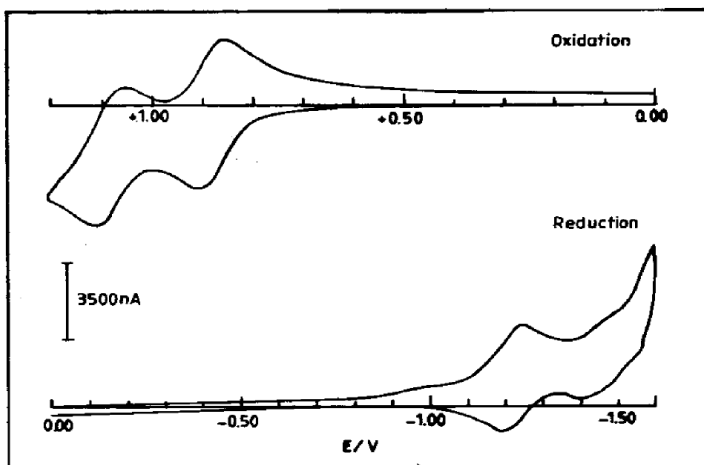
*Figure 54   Cyclic voltammogram showing oxidation and reduction waves of **ZnTThP** in CH$_2$Cl$_2$.[5]*

Porphyrin	Oxidation		Reduction			
	1st	2nd	1st			2nd
	$E_{1/2}$	$E_{1/2}$	E_{pc}	E_{pa}	$E_{1/2}$	E_{pc}
ZnTPP	0.78	1.08	-1.44	-1.38	-1.41	-1.83
NB-ZnP1	0.89	1.06	-1.19	-1.14	-1.16	-1.36
NB-ZnP2	0.90	1.06	-1.19	-1.16	-1.17	-1.49
NB-ZnP3	0.91	1.06	-1.19	-1.32	-1.26	-1.53
NB-ZnP4	0.85	1.15	-1.36	-1.26	-1.31	-1.70
NB-ZnP5	0.86	1.14	-1.36	-1.28	-1.32	-1.72
NB-ZnP6	0.86	1.13	-1.38	-1.44	-1.41	-1.69
NB-ZnP7	0.85	1.14	-1.38	-1.49	-1.43	-1.71

Table 16   Redox potentials of porphyrins recorded in CH$_2$Cl$_2$ reported vs. SCE.

Notably, all the *meso* tetrathein-2-yl porphyrins showed an anodic shift of their first oxidation relative to **ZnTPP**, which indicated a stabilisation of the HOMO orbital of the porphyrin. An anodic shift of 110, 120 and 130 mV was observed for **NB-ZnP1**, **NB-ZnP2** and **NB-ZnP3** respectively compared to **ZnTPP** ($E_{1/2}$ = +0.78 *vs*. SCE). Porphyrins **NB-ZnP4** and **NB-ZnP5** displayed a smaller shift in their first oxidation potential to +0.85 and +0.86 V *vs*. SCE (70 and 80 mV anodic shift), compared to the first oxidation of **ZnTPP**. Thus the stabilisation of the HOMO orbital was less pronounced when the *meso* thienyl ring is substituted in the thien-4-yl position. The tetraphenyl substituted porphyrins (**NB-ZnP6** and **NB-ZnP7**) underwent a similar shift of their first oxidation, observed 80 and 70 mV anodic of **ZnTPP**.

Destabilisation of the LUMO orbitals also occurs with a decrease in the potential of the first reduction. Again **NB-ZnP1 – NB-ZnP3** showed the largest effect with a decrease in their reduction potential compared to **ZnTPP**. The largest effect was observed for **NB-ZnP1** which displayed a reduction 250 mV anodic of **ZnTPP**. **NB-ZnP2** and **NB-ZnP3** showed their reduction at 240 and 150 mV anodic of **ZnTPP** respectively (**ZnTPP** $E_{1/2}$ = -1.41 *vs*. SCE). Destabilisation of the LUMO is less pronounced for the remainder of the porphyrins examined. Both thienyl porphyrins **NB-ZnP4** and **NB-ZnP5** were shifted by 100 and 90 mV respectively ($E_{1/2}$ = -1.31 V and -1.32 V *vs*. SCE). There was no evident shift in the first reduction of **NB-ZnP6** and only a slight cathodic shift for **NB-ZnP7** ($E_{1/2}$ = -1.43 V *vs*. SCE).
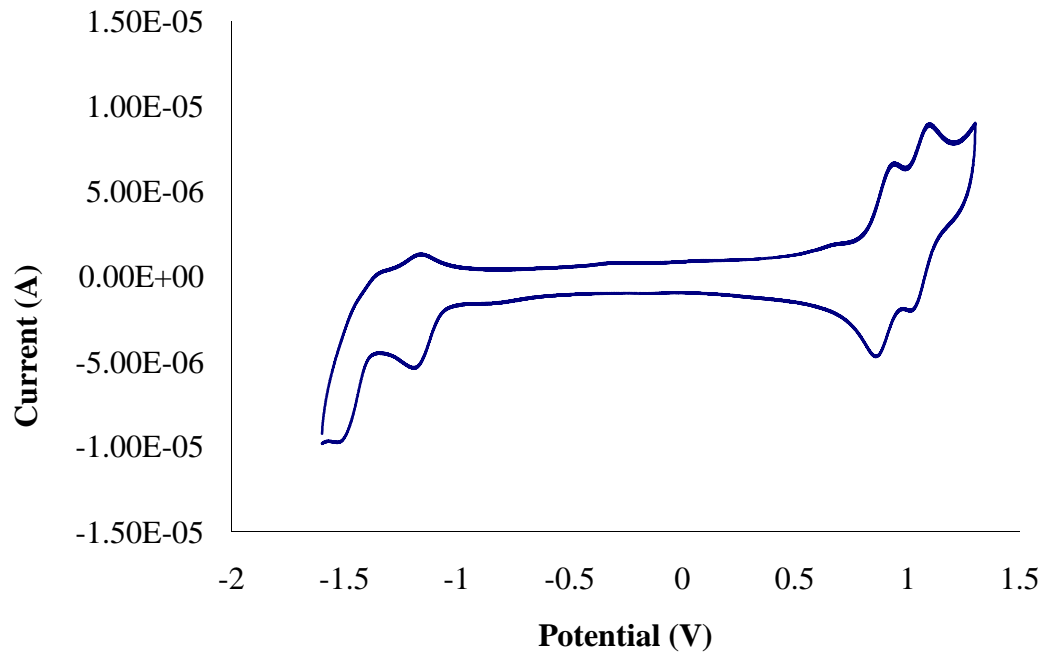
Figure 55   *Cyclic voltammogram of **NB-ZnP2** showing oxidation and reduction waves.*
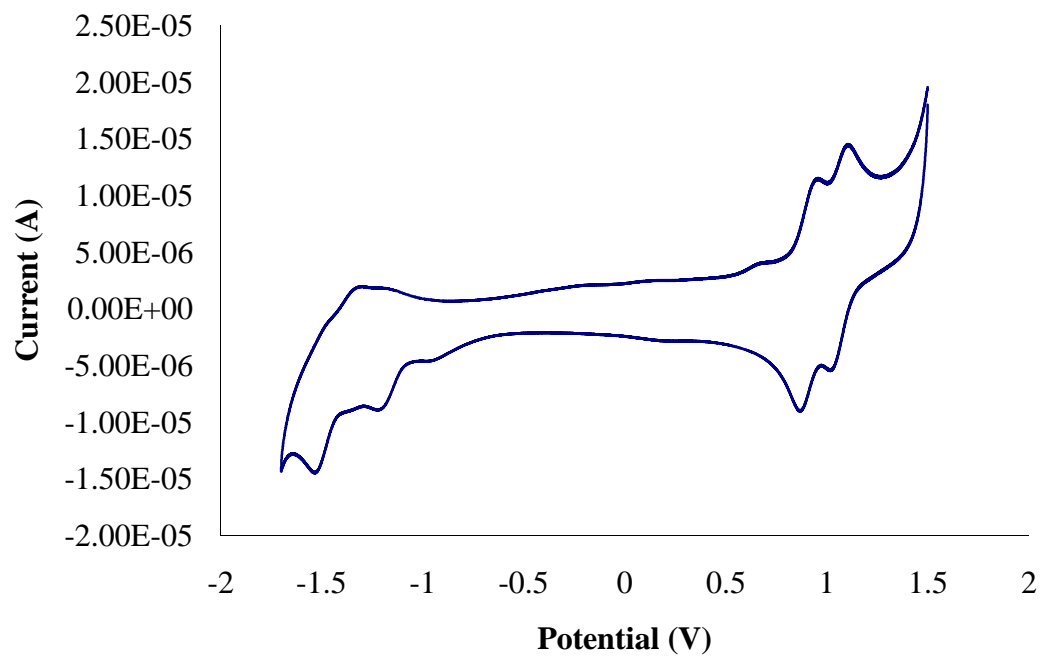
Figure 56   *Cyclic voltammogram of **NB-ZnP3** showing oxidation and reduction waves.*
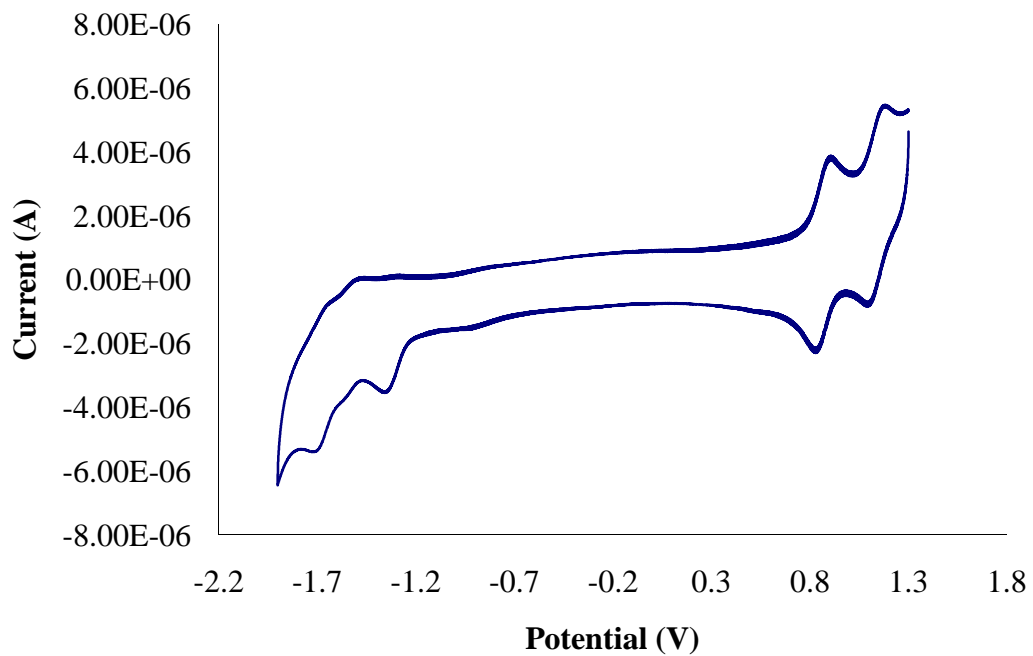
Figure 57   *Cyclic voltammogram of **NB-ZnP5** showing oxidation and reduction waves.*
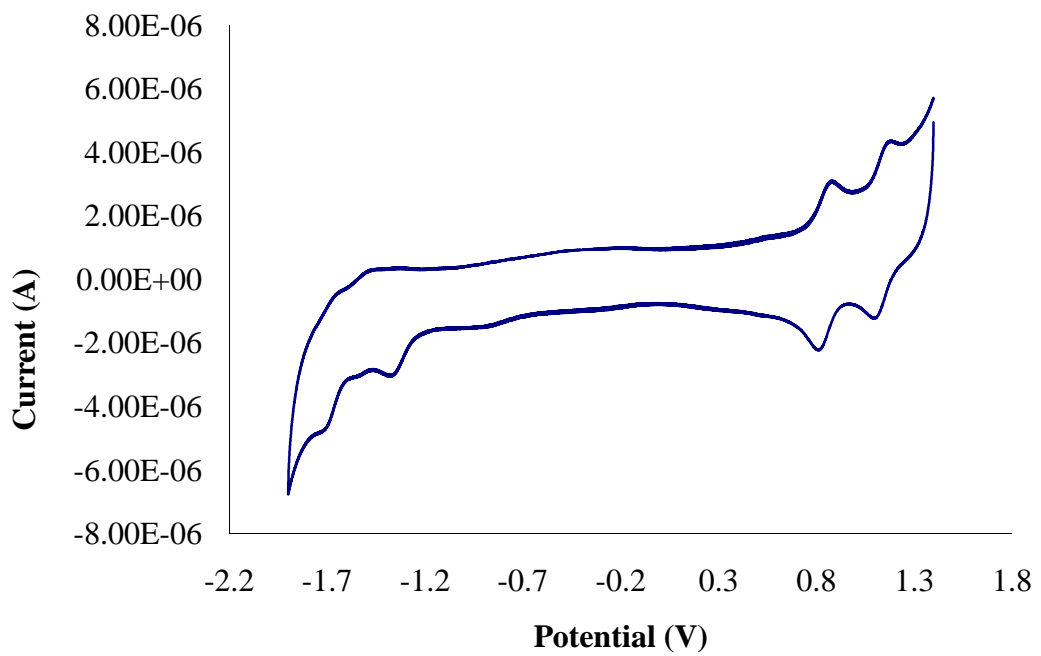
Figure 58   *Cyclic voltammogram of **NB-ZnP7** showing oxidation and reduction waves.*

2.5   Discussion

2.5.1   Synthesis and ^{1}H NMR spectra

The porphyrins produced in this study were synthesised using standard conditions involving the condensation of pyrrole with 4/5-substituted thien-2-ylcarboxaldehydes and 4-substituted benzaldehydes.   Initially **H$_2$TPP** was synthesised *via* the Adler method, although synthesis of **H$_2$TThP** by the same method proved problematic. This was ascribed to possible decomposition of the porphyrin under such harsh conditions, elevated temperature (141 ºC) and the acidic environment (propionic acid).   Using a modified Lindsey procedure, **H$_2$TThP** was produced in 18 % yield. It had previously been noted that addition of BF$_3$.OEt$_2$ to the reaction flask at 0 ºC improved the yields for thienyl porphyrins.[56] Thus this condition was employed for the synthesis of the *meso* tetra(thien-2-yl)porphyrins **NB-ZnP1** – **NB-ZnP5**. The reduction in temperature was not required for the phenyl substituted porphyrins, **NB-ZnP6** and **NB-ZnP7**. Metallation of all porphyrins using zinc acetate was carried out quantitatively. Melting points for all porphyrins were greater than 300 ºC.

Each of the porphyrins in this study are A$_4$-type *meso*-substituted porphyrins, which are of S$_4$ symmetry and possess a C$_4$ rotational axis through the metal centre perpendicular to the plane of the ring. As each of the β-pyrrolic protons is in an identical environment a sharp singlet is produced in the ^{1}H NMR spectra. This singlet occurs at 8.87 ppm for **ZnTPP** however it is shifted depending on the substituents. Porphyrins **NB-ZnP6** and **NB-ZnP7** which have the phenyl ring attached directly to the porphyrin macrocycle and are substituted at the *para* position with ethynylthien-2-yl and ethynylthien-3-yl groups respectively, display β-pyrrolic signals at 8.89 ppm in the ^{1}H NMR spectra. However the β-pyrrolic signal for *meso* tetra(thien-2-yl)porphyrin is shifted further downfield with **ZnTThP** displaying a signal at 9.07 ppm. For the (thien-2-yl)porphyrins in this study, **NB-ZnP1** - **NB-ZnP5**, the β-pyrrolic signal is observed in the range 9.20 – 9.22 ppm. This deshielding effect of the β-pyrrolic protons observed for the *meso* thien-2-ylporphyrins has previously been observed and was ascribed to an increase in the ring current of the porphyrin ring caused by delocalisation onto the peripheral thienyl units.[5,9,25,27,60] The presence of a singlet in the region -2.5 to -2.8 ppm arises from the endocyclic protons at the centre of the porphyrin which are exclusive to the freebase

porphyrins. The internal protons experience this high field shift because of the internal ring current of the porphyrin macrocycle.[61] The absence of this signal confirms the presence of a metal at the centre of the porphyrin ring. Figures 59 and 60 give an overlay of the aromatic region of the ^{1}H NMR spectra for the tetra substituted porphyrins **ZnTPP**, **ZnTThP**, and various porphyrins studied, all recorded in CDCl$_3$.
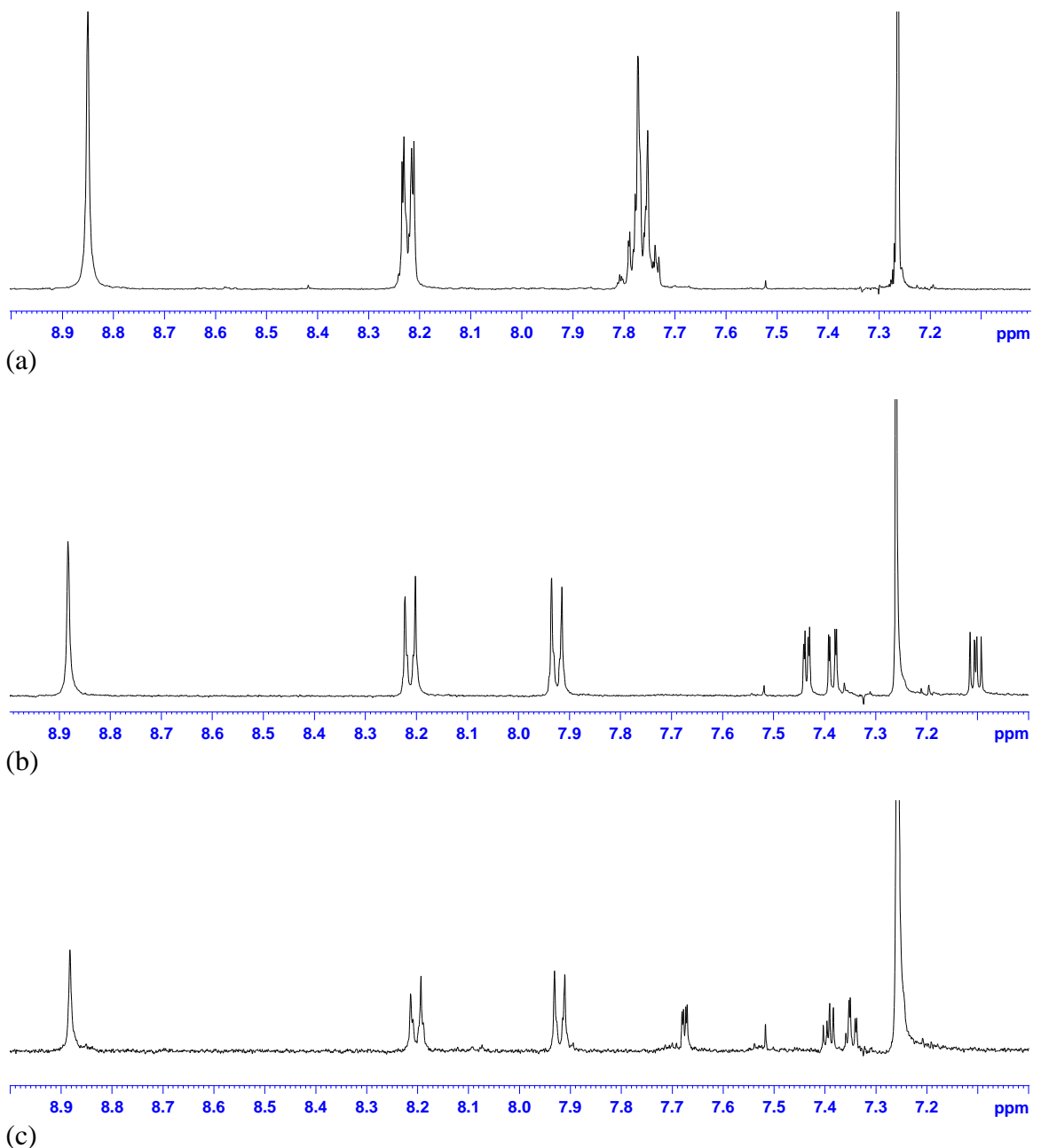
Figure 59   *An overlay of the aromatic region of the ^{1}H NMR spectra (δ) for **H₂TPP** (a),*
               ***NB- H₂P6** (b) and **NB- H₂P7** (c) in CDCl₃.*
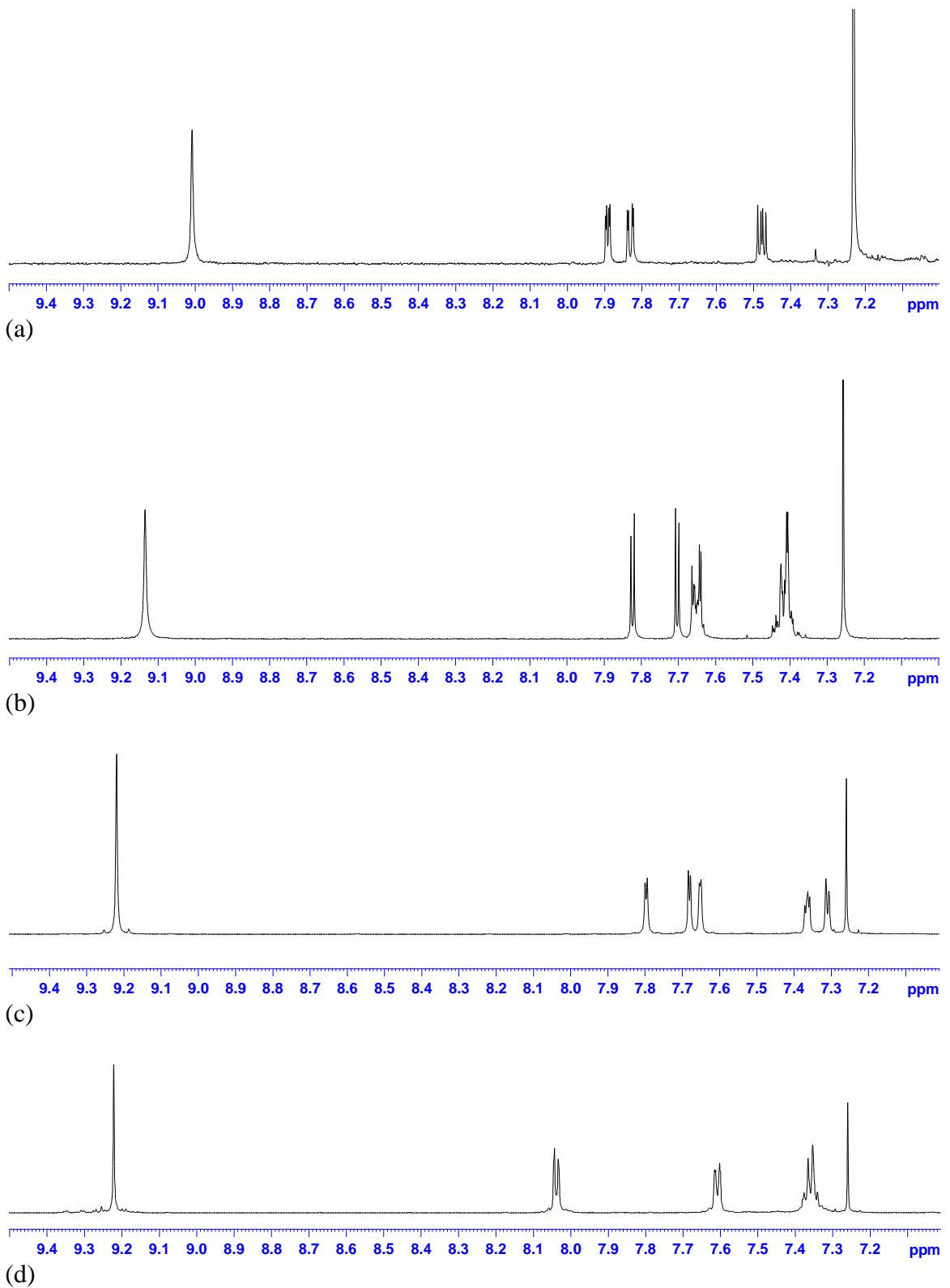
Figure 60   *An overlay of the aromatic region of the ^1H NMR spectra (δ) for **ZnTThP** (a), **NB-ZnP1** (b), **NB-ZnP3** (c) and **NB-ZnP4** (d) in CDCl₃.*

2.5.2   UV-vis absorbance studies

Historically there have been mixed reports as to whether there exists electronic communication between the porphyrin macrocycle and thienyl substituents when attached *via* the *meso*-position.[5,25,27,60]   However in more recent publications, the influence of thienyl substituents on ground and excited state electronics has been observed and the source of these changes were examined using both theoretical and experimental methods.[18,28]   Direct substitution of the porphine core with aromatic thiophene moieties does lead to electronic interaction between the two π-systems. This can also be enhanced through appropriate substitution of the thienyl groups. The UV-vis spectra of **NB-ZnP1** – **NB-ZnP7**, were shown in figure 42 and 43, are compared to **ZnTPP** and **ZnTThP**.

The UV-vis spectra of porphyrins, **NB-ZnP1** – **NB-ZnP3**, were bathochromically shifted with respect to both **ZnTPP** and **ZnTThP**. These porphyrins also possess the highest FWHM values for the porphyrin Soret band of all porphyrins studied. Bathochromic shifts in the UV-vis spectra and increasing FWHM of the Soret band are evidence of increased coupling of the overlapping π systems. Rochford et al. reported that appropriate substitution of the *meso* thienyl groups resulted in increased coupling of the π systems.[18] Therefore the changes observed for **NB-ZnP1** – **NB-ZnP3** may be due to enhanced delocalisation when substituents (ethynylbenzene, ethynyl-2-thiophene and ethynyl-3-thiophene respectively) were in the thien-5-yl position. Within this group changing the terminal aryl group attached to the *meso* thien-2-ylethynyl arms did not change the UV-vis spectra significantly. Although, the FWHM would suggest that the π systems of **NB-ZnP2**, which has two thien-2-yl moieties are coupled more strongly.

The UV-is spectra of porphyrins **NB-ZnP4** and **NB-ZnP5** were red shifted with respect to both **ZnTPP** but not **ZnTThP**. The Soret and Q bands were equal to and hypsochromically shifted respectively when compared to **ZnTThP**. Also the FWHM values were very similar to **ZnTThP**. The conjugation is not effective when the ethynylbenzene and ethynyl-2-thiophene are in the thien-4-yl position. This suggests that the conjugation pathway that allows for greatest $\pi – \pi$ overlap occurred when the ethynylaryl substituents are in the distal position of the *meso* thien-2-yl ring.

145

Changes in the absorbance spectra of thien-2-yl porphyrins substituted with a methyl group were reported.[28] When substituted at the thien-5-yl position, a red shift in the UV-vis spectrum was observed. While substitution with a methyl group in the thien-3-yl position caused a blue shift. The authors attributed this change in absorbance to the conformation the thienyl rings adopted. Thus substitution the thien-4-yl position may hinder the co-planar conformation of the thienyl rings with respect to the porphyrin macrocycle.

The UV-is spectra of porphyrins **NB-ZnP6** and **NB-ZnP7** were red shifted with respect to both **ZnTPP**. Substitution with ethynylthiophenes at the *para* position of the phenyl ring allowed for increased conjugation throughout the *meso* pendant arms. Studies on phenylacetylene building blocks have shown that *para* substituted phenylacetylene compounds possess greater conjugation of the π systems.[62] Although the phenyl rings are not co-planar to the porphyrin macrocycle, porphyrins **NB-ZnP6** and **NB-ZnP7** were red shifted and display higher FHWM values than **ZnTPP**. This indicates that there is increased coupling of the π systems even though the *meso* substituents lie in an idealised orthogonal manner with respect to the porphyrin macrocycle.

2.5.3   Steady – state fluorescence studies

The fluorescence spectra of porphyrins, **NB-ZnP1** – **NB-ZnP3**, were also shifted to higher energy with respect to both **ZnTPP** and **ZnTThP**. The Q(0,0)* band was red shifted to a greater extent than the Q(1,0)* band, such that the individual emission bands were totally unresolved. The changes in lifetime within the group were quite small, although all were reduced with respect to **ZnTThP**. This is in agreement with literature, where substitution of thienyl rings caused a reduction in singlet lifetimes.[27]

Porphyrins **NB-ZnP4** and **NB-ZnP5** displayed quite interesting fluorescence spectra. **NB-ZnP4** displayed a fluorescence spectrum typical of thienyl porphyrins with two Q* bands but with emission intensity higher than that of **ZnTThP**. However, **NB-ZnP5** possessed an emission profile that was significantly different from **NB-ZnP4** and **ZnTThP**. The Q(0,0)* band was bathochromically shifted with respect to both and the intensity of the emission was much higher. The lifetime of **NB-ZnP4** was reduced with respect to **ZnTThP** by approximately 40 %, whereas the lifetime of **NB-ZnP5** not reduced (within instrumental error).

For the phenyl substituted porphyrins, **NB-ZnP6** and **NB-ZnP7**, a minor red shift in the Q(0,0)* and Q(1,0)* emission bands was observed together with an increase in the intensity of the Q(0,0)* band relative to **ZnTPP**. The emission spectra are the mirror image of the UV-vis spectra where a similar increase in the Q bands was observed. A reduction of fluorescence lifetimes, approximately 15 - 20 %, was also observed for the phenyl porphyrin analogues. Previously, a small reduction in fluorescence lifetime was noted for tetraphenylporphyrins when an additional phenylethynyl linker was placed between the porphyrin ring and the *meso* phenyl ring.[63]

2.5.4 Laser flash photolysis studies

The transient absorbance difference spectra were ascribed to the lowest $^3(\pi - \pi^*)$ porphyrin excited state. All transient signals recorded in this study fitted well with mono-exponential kinetics indicating unimolecular decay. Triplet lifetimes for **ZnTPP** and **ZnTThP** were previously reported as 24 and 20 μs respectively.[18] Triplet lifetimes reported throughout this study were (+/-) 10 % μs.

The transient absorbance difference spectra of the thienyl porphyrins, **NB-ZnP1** – **NB-ZnP5** were bathochromically shifted with respect to **ZnTPP** but in a similar range to **ZnTThP**. Low energy absorbances that extended past 600 nm were observed. These excited state characteristics suggested an increase in the electronic coupling of the porphyrin ring and the thienyl π-network upon excitation and possibly charge transfer onto the peripheral thien-2-yl π-system. These lower energy absorbance bands were not observed for the phenyl substituted porphyrins **NB-ZnP6** and **NBZn-P7**.

The lifetimes of the porphyrins varied widely with substitution pattern. Thienyl porphyrins substituted in the distal position, **NB-ZnP1** – **NB-ZnP3**, were significantly reduced in comparison to both **ZnTPP** and **ZnTThP**. There was little change within the series as the terminal group was changed from benzene to 2-thiophene to 3-thiophene. Lifetimes were similar to those reported previously for substituted thien-2-ylethynyl porphyrins.[18]

Upon further substitution of the *meso* thien-2-yl moieties at the thien-4-yl position, **NB-ZnP4** and **NB-ZnP5**, significant changes in the triplet lifetimes were observed. The lifetime of the former was 36 μs and the latter, 51 μs. These are greatly increased compared to **ZnTThP** (20 μs). Also unexpected was the increase from **NB-ZnP4** to **NB-ZnP5** when only the terminal aryl group was changed.

The phenyl porphyrins **NB-ZnP6** and **NB-ZnP7** also showed some deviation from the norm. **NB-ZnP6** possessed a lifetime similar to that of **ZnTPP**. This is not surprising given that both have a phenyl ring attached to the porphyrin macrocycle which lie orthogonal to each other. The lifetime of **NB-ZnP7** is almost double that of the other phenyl porphyrins. As only the terminal aryl group has changed this is somewhat unusual.

2.5.5   NB-ZnP1 solvatochroism

Modest red shifts were observed in the UV-vis spectra for the Soret band λ_{max} of **NB-ZnP1** on going from toluene (λ_{max} = 439 nm) to chloroform (λ_{max} = 442 nm) to DMSO (λ_{max} = 445 nm) as can be seen in figure 61. Bathochromic shifts were also observed in the Q band region of the spectrum (Table 11).

The fluorescence spectra showed similar solvatochromic behaviour. As the Q(0,0)* emission band of **NB-ZnP1** was red shifted to a greater extent than the Q(1,0)* band, a convergence of the bands occurred and the porphyrin fluorescence appeared as a single broad emission, nonetheless this emission band was red shifted on increasing solvent polarity from 634 nm in toluene to 638 nm in chloroform to 640 nm in DMSO.
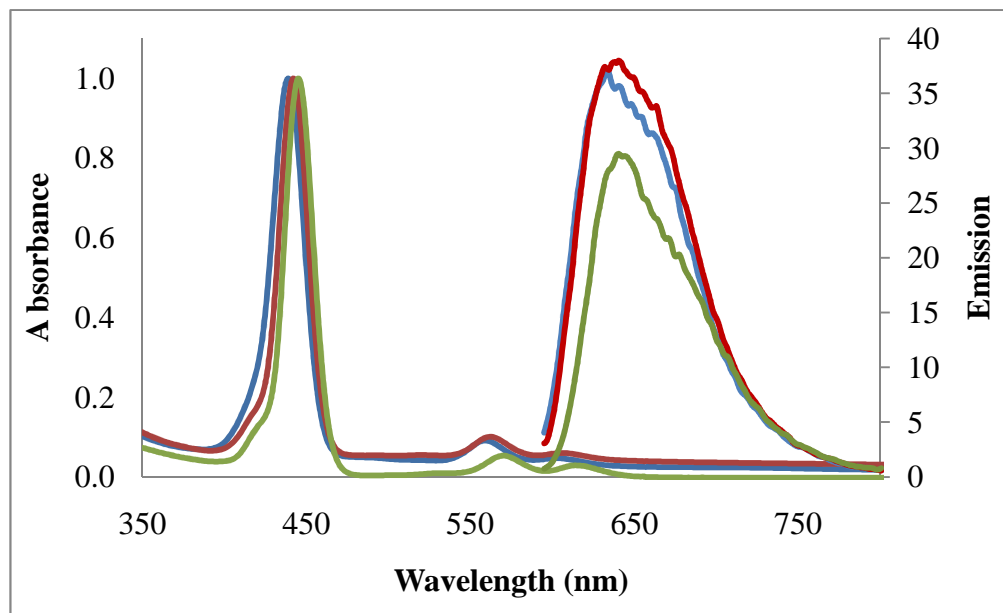
Figure 61   An overlay of the UV-vis absorbance and fluorescence emission spectra of **NB-ZnP1** *recorded in toluene (blue), chloroform (red) and DMSO (green). Absorbance spectra have been normalised at their λ_{max}. Emission spectra were recorded at room temperature (λ_{exc} = 555 nm, abs. = 0.2 at 555 nm).*

The transient absorbance difference spectra of **NB-ZnP1** were recorded in various solvents of increasing polarity (ethyl acetate, acetonitrile and DMSO) between 450 and 800 nm following 532 nm excitation under 1 atm argon. In all solvents the spectral characteristics observed were similar to those discussed previously. The lifetime of the transient species were all within instrumental error (8 ± 1 µs, Table 15). However, a substantial increase in the lower energy absorbances was observed ranging from 580 nm to 800 nm (Fig. 62). This was possibly due to an excited state charge transfer transition. The transition gains oscillator strength on increasing the solvent polarity. The appearance of this low-energy band and the enhancement of the absorbance in polar media suggest that there was enhanced electronic communication between the porphyrin π-system and the *meso* thien-2-yl substituents on going from the ground state to the excited state of **NB-ZnP1**.
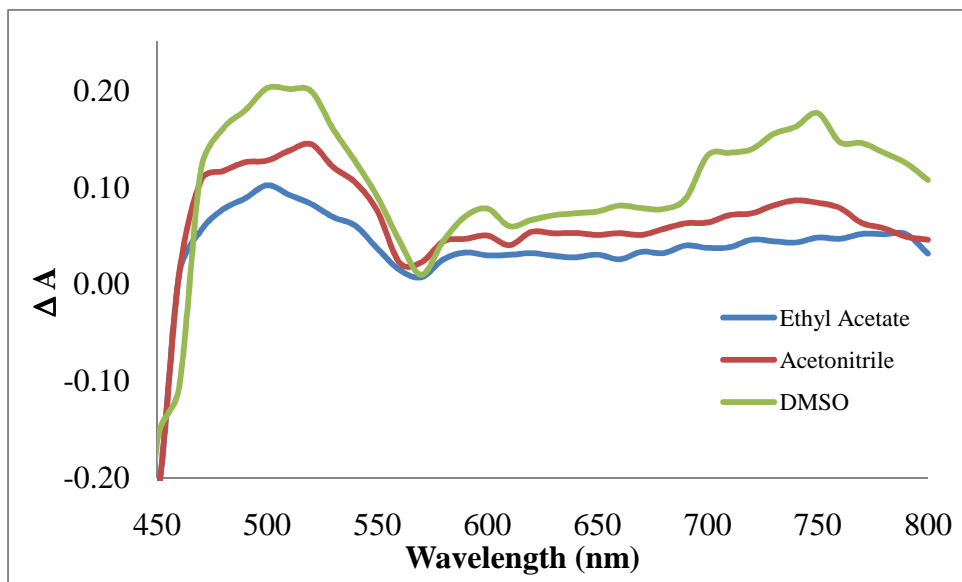
Figure 62 *An overlay of transient absorbance difference spectra of* **NB-ZnP1** *in various solvents following 532 nm excitation under 1 atm argon. Each plot is taken 2 µs after the laser pulse.*

2.5.6 Influence of arylethynyl spacers on the photophysical properties of porphyrins

A study of arylethynyl spacer units at the *meso* position of porphyrin macrocycle was previously reported.[63] The contribution of phenylethynyl spacers to the ground and excited singlet state was studied through changes in the absorbance and fluorescence spectra as well as fluorescence lifetime and fluorescence quantum yield. Figure 63 depicts a series 5,10,15,20-tetraarylporphyrins (**A**) and 5,10,15,20-(arylethynyl)phenyl porphyrins (**B**) reported in the literature

$$Ar = C_6H_5$$
$$4\text{-}CH_3C_6H_4$$
$$4\text{-}CF_3C_6H_4$$
$$4\text{-}O_2NC_6H_4$$
$$3,5\text{-}(CF_3)_2C_6H_3$$
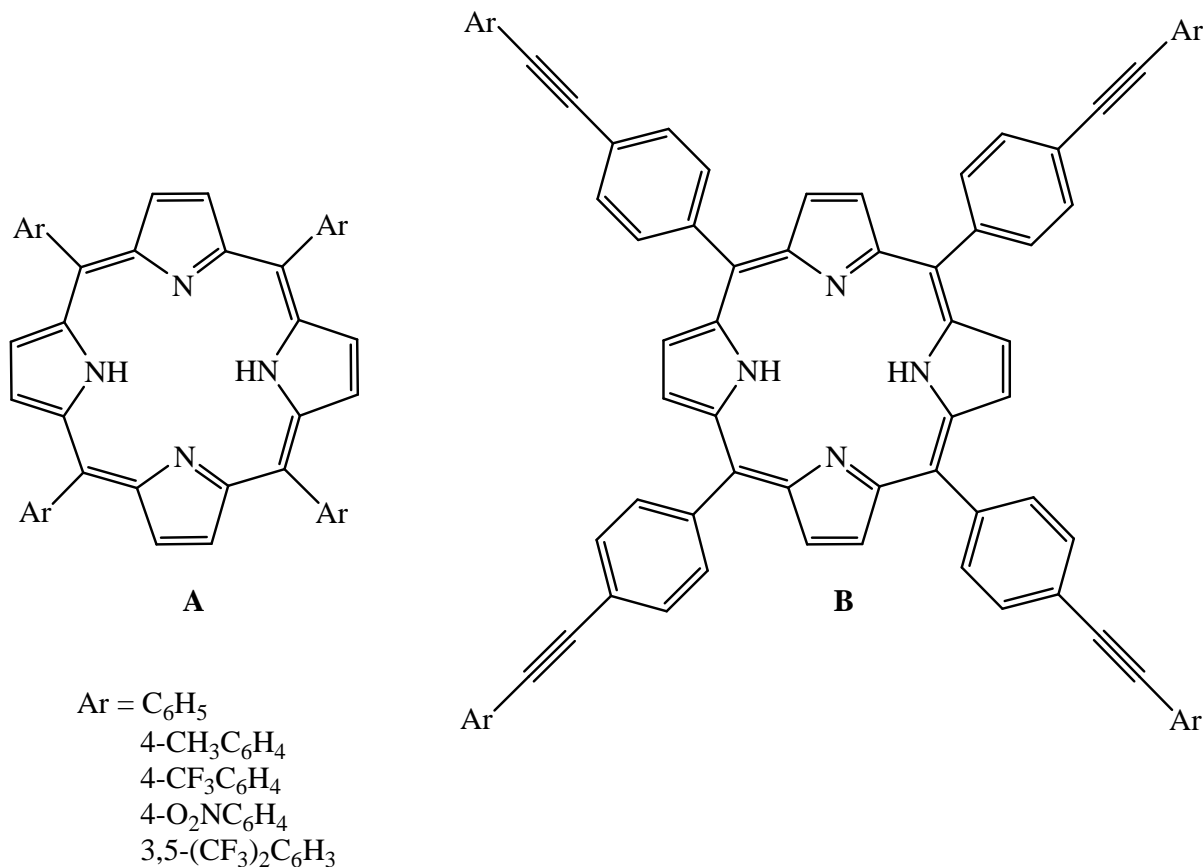
*Figure 63   Series **A**, phenyl substituted porphyrins and series **B**, phenyl substituted porphyrins with an additional phenylethynyl spacer unit.*

Comparison of the absorbance spectra of series **A** and series **B** showed only small differences in the λ_{max} ($\pm$ 5 nm). From the absorbance spectra the authors concluded that the aryl substituents of **A** and 4-(arylethynyl)phenyl substituents of **B** were not strongly coupled to the porphyrin core. More distinct changes in the fluorescence properties were

observed when **A** and **B** were compared. The emission maxima were almost identical but the excited state lifetimes for porphyrins in series **B** were consistently shorter (3 – 15 %) than those observed for series **A** and fluorescence quantum yields were consistently higher for series **B** compared to **A**.   The phenylethynyl spacer allowed minimal electronic communication between the porphyrin core and the aryl substituent in both the ground state and excited state (similarity of the absorbance and emission) which suggested the energy levels of the HOMO and LUMO were comparable for the series **A** and series **B**. However the contributions of a phenylethynyl spacer should be minimal as the electronic effects should were near identical when the aryl substituent itself was a phenyl ring.

When *meso* aryl groups are substituted with ethynyl units and further substituted with a second aryl moiety the influence on the ground sate and excited state electronics may be perturbed. The direct contribution from (aryl)ethynyl spacers to the photophysics of the excited state have not been extensively examined for porphyrin systems. Figure 64 represent three series of porphyrins each with three varying (aryl)ethynyl spacers.
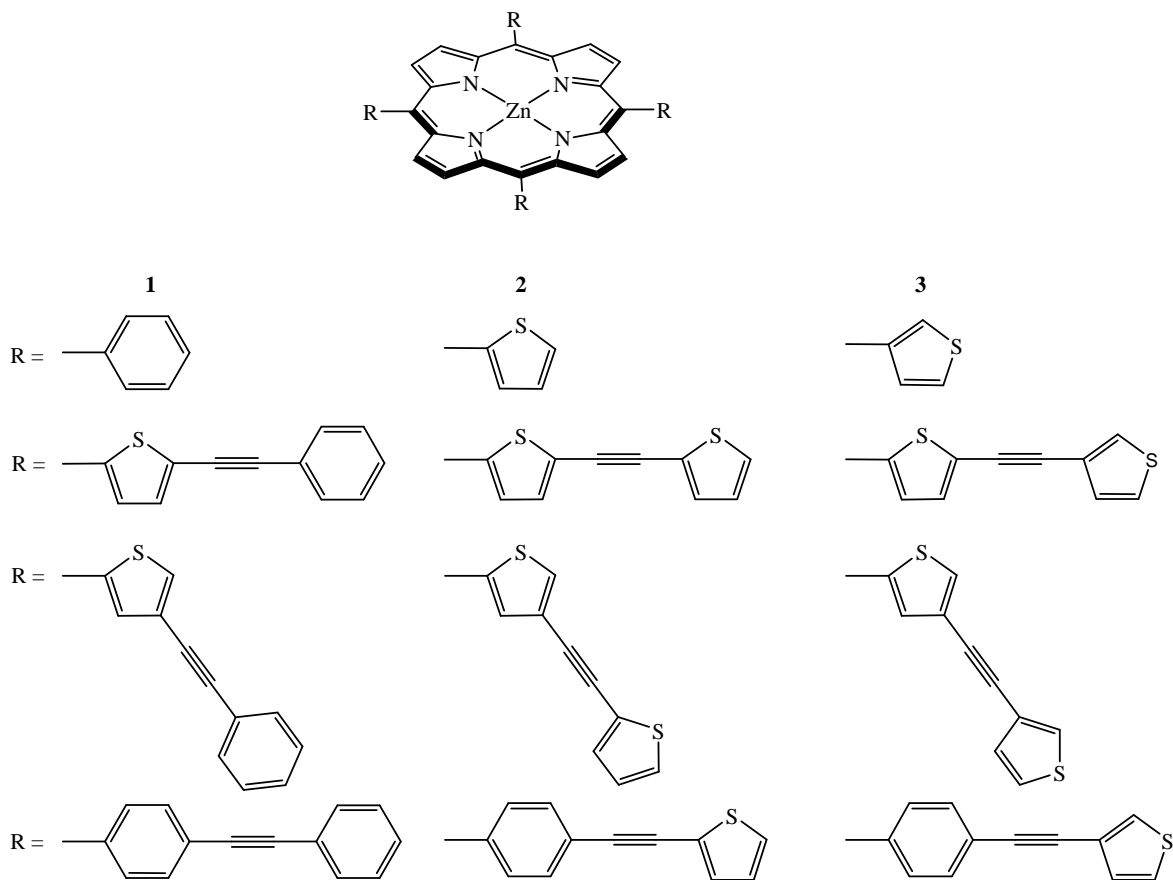
Figure 64　　　*Three series of porphyrins with various (aryl)ethynyl) spacers.*

In this study, series **2** is examined. **ZnTThP** is the parent porphyrin and **NB-ZnP2**, **NB-ZnP5** and **NB-ZnP6**, display three variations of arylethynyl spacer groups (Fig. 64). Substituents in the distal position of the thien-2-yl ring, as in **NB-ZnP2**, should possess the same steric requirements as **ZnTThP**, where the *meso* pendant arms lie in a co-planar arrangement with respect to the porphyrin macrocycle. It is possible that the substitution pattern on **NB-ZnP5** may hinder the co-planar arrangement favoured by thien-2-yl groups. As noted earlier, the steric requirements for a five membered *meso* thienyl ring are smaller than that of a six membered *meso* phenyl ring.[28] In the case of **NB-ZnP6**, the phenyl groups should lie in a low energy conformation, arranged in an idealised orthogonal fashion with respect to the mean plane of the porphyrin. Table 17 below presents the ground state and excited state data for the porphyrins.

	Soret λ_{max} (nm)	Q bands (nm)	Stokes shift (cm^{-1})	Emission λ_{max} (nm)	$^1\tau$ (ns)	$^3\tau$ (μs)
ZnTThP	429	556, 600	489	617, 657	1.36	20
NB-ZnP2	439	559, 603	836	635	0.72	7
NB-ZnP5	425	550, 590	310	601, 647	1.39	51
NB-ZnP6	426	550, 590	420	605, 646	1.56	26

*Table 17   Photophysical data of **ZnTThP** and (arylethynyl)thien-2-yl porphyrins, **NB-ZnP2**, **NB-ZnP5** and **NB-ZnP6**.*

Due to the contribution of conformations, in which the thienyl groups adopt idealised co-planar arrangements with the porphyrin ring, an efficient extension of the porphyrinic π-system through conjugation was observed. In the ground state this is signified as a red shift in the Soret band along with an increase in the FWHM value. This was the case for **NB-ZnP2** which possessed the same steric requirements as **ZnTThP** but also possessed an extended π-framework. The minor hypsochromic shift observed in the Soret λ_{max} of **NB-ZnP5** was attributed to a somewhat encumbered rotational barrier due to substitution pattern and the orthogonal orientation of the phenyl ring in **NB-ZnP6**. The fluorescence lifetime of **NB-ZnP5** (1.39 ns) was very close to that of **ZnTThP** (1.36 ns). However a reduction in singlet excited state lifetime was observed for **NB-ZnP2** (0.72 ns) and **NB-ZnP6** displayed an increase in fluorescence lifetime relative to **ZnTThP**.

A marked difference in triplet lifetime was also observed. The shortest triplet lifetime is that of **NB-ZnP2** (7 μs), significantly reduced compared to **ZnTThP** (20 μs). The triplet lifetime of **NB-ZnP6** (26 μs) is very similar to that of **ZnTPP** (24 μs) and **ZnTThP** (20 μs). Most interesting was **NB-ZnP5** that had a triplet excited state lifetime of 51 μs. This increase in $^3(\pi\text{-}\pi^*)$ triplet lifetime was indicative of increased communication of the thienyl groups with the porphyrin π-network.

2.5.7 Electrochemistry

Electrochemical studies were performed on the porphyrins to elucidate the effect of substitution on the porphyrin macrocycle. The results showed that substitution of the porphyrin ring system at the *meso* position had an effect on its electrochemistry. All the porphyrins showed two one-electron oxidations and one, one-electron reduction.

Examination of the redox data (Table 16) revealed that the first oxidation potentials were shifted to more positive potential when the six membered *meso* phenyl moiety of **ZnTPP** was replaced with five membered *meso* thienyl groups (**NB-ZnP1** – **NB-ZnP5**) indicating that the thienyl porphyrins are harder to oxidise than phenyl porphyrin. This stabilisation of the HOMO of the porphyrin macrocycle by the thienyl moiety was observed by Rochford et al.[18] and more recently by Ghosh et al.[64]

When the *meso* thien-2-yl moiety was substituted at the thien-5-yl position, the stabilisation was slightly higher. Higher oxidation potentials were observed for **NB-ZnP1** – **NB-ZnP3** compared to **NB-ZnP4** and **NB-ZnP5** which were substituted at the thien-4-yl position. Also the reduction potentials were shifted to less negative potentials for the thien-2-yl porphyrins **NB-ZnP1** – **NB-ZnP5**. On replacement of the *meso* phenyl group with a thienyl moiety the LUMO was destabilised.

An increase in oxidation potentials was also observed for the phenyl porphyrins **NB-ZnP6** and **NB-ZnP7** relative to **ZnTPP** indicating stabilisation of the HOMO occurred. The reduction potentials were observed more negative than that of **ZnTPP**. This indicated that the LUMO is also stabilised. This result is interesting. Stabilisation of both the HOMO and LUMO would not be expected as the *meso* substituents are not co-planar to the porphyrin macrocycle and the π systems do not overlap. However stabilisation is brought to the macrocycle by the *meso* phenyl(ethynylthienyl) moieties.

2.6   Conclusions

Porphyrins **NB-ZnP1 – NB-ZnP3** were synthesised with substituents at the thien-5-yl position, in order to examine whether an additional aryl group would cause further coupling of the overlapping π systems.   The results showed that it did in fact cause increased coupling with bathochromic shift in the absorbance spectra and an increase in the FWHM values of the Soret band.   No additional effect was observed in relation to the choice of terminal aryl ring. The singlet lifetime of the porphyrins were reduced relative to **ZnTThP** as were the triplet lifetimes.   Electrochemical analysis showed that extension of the conjugation on the *meso* thien-2-yl arms caused a stabilisation of the HOMO but destabilisation of the LUMO.

Porphyrins **NB-ZnP4** and **NB-ZnP5** possessed the same terminal substituents (ethynylbenzene and ethynylthien-2-yl) as **NB-ZnP1** and **NB-ZnP2**; however they are substituted at the thien-4-yl position. The conjugation of the *meso* substituents was not as effective in **NB-ZnP4** and **NB-ZnP5**.   The absorbance spectra were generally unchanged when compared to **ZnTThP**.   Both the singlet and triplet lifetimes were substantially changed.   The singlet lifetimes were reduced compared to **ZnTThP** but to a lesser extent than that observed for **NB-ZnP1 – NB-ZnP3**.   However the triplet lifetimes were significantly increased.   This would suggest that the conformation of the thien-2-yl substituents with respect to the porphyrin macrocycle is changed when the *meso* thienyl ring is substituted at the thien-4-yl position and that caused the increase in lifetime as opposed to conjugation within the *meso* substituents.

.

Porphyrins **NB-ZnP6** and **NB-ZnP7** are phenyl substituted porphyrins which have been further substituted at the *para* position with ethynylthien-2-yl and ethynylthien-3-yl moieties respectively.   These porphyrins possess the same terminal substituents as **NB-ZnP2** and **NB-ZnP3**. However, the phenyl porphyrins, **NB-ZnP6** and **NB-ZnP7**, should adopt an idealised orthogonal arrangement with respect to the porphyrin plane and in doing so the π systems of the porphyrin and *meso* substituents will no longer overlap.   The absorbance spectra of the phenyl porphyrins is bathochromically shifted with respect to **ZnTPP**.   There was a significant change in the fluorescence profile although the lifetimes

156

were only slightly altered. The most perceptible change was the triplet lifetime of **NB-ZnP7** which was double that of **ZnTPP**. Clearly there is a contribution from the *meso* substituents even though the conformation prevents coupling of the π systems. Electrochemical studies indicated the stabilisation of both the HOMO and LUMO orbitals for both phenyl porphyrins.

2.7 Bibliography

1   A. Treibs, N. Haeberie, *Justus Liebigs Ann. Chem.* **1968**, 718, 183.

2   P.J. Rothemund, *J. Am. Chem. Soc.*, **1936**, 58, 625.

3   A.D. Adler, F.R. Longo, J.D. Finerelli, J. Goldmacher, J. Assour, L. Korsakoff, *J. Org. Chem.*, **1967**, 32, 476.

4   M.A. Torréns, T.K. Straub, L.M. Epstein, *J. Am. Chem. Soc.*, **1972**, 94, 4160.

5   P. Bhyrappa, P. Bhavana, *Chem. Phys. Lett.*, **2001**, 349, 399.

6   J.S. Lindsey, I.C. Schreiman, H.C. Hsu, P. Kearney, A.M. Marguerettaz, *J. Org. Chem.*, **1987**, 52, 827.

7   N. Ono, H. Miyagawa, T. Ueta, T. Ogawa, H.Tani, *J. Chem. Soc., Perkin Trans. 1*, **1998**, 1595.

8   C. J. Medforth, R. E. Haddad, C. M. Muzzi, N. R. Dooley, L. Jaquinod, D. C. Shyr, D. J. Nurco, M. M. Olmstead, K. M. Smith, J.-G. Ma, J. A. Shelnutt, *Inorg. Chem.*, **2003**, 42, 2227.

9   R.P. Bonar-Law, *J. Org. Chem.*, **1996**, 61, 3623.

10   D.F. Shi, R.T. Wheelhouse, *Tet. Lett*., **2003**, 43, 9341.

11   J.S. Lindsey, J. N. Woodford, *Inorg. Chem.*, **1995**, 34, 1063.

12   G.P. Arsenault, E. Bullock, S.F. MacDonald, *J. Am. Chem. Soc.*, **1960**, 82, 4384.

13   Y.L.S.-T. Arminger, T.D. Lash, *J. Heterocycl. Chem.*, **1992**, 29, 523.

14   C.O. Paul-Roth, J. Letessier, S. Juillard, G. Simonneaux, T. Roisnel, J. Rault-Berthelot, *J. Mol. Struct.*, **2008**, 872, 105.

15   C.-S. Duanmu, Z.-P. Chen, X.-S. Yu, X. Zhou, *Chinese Journal of Chemistry*, **2004**, 22, 779.

16   G.E. Collis, W.M. Campbell, D.L. Officer, A.K. Burrell, *Org. Biomol. Chem.*, **2005**, 3, 2075.

17   S. Eu, S. Hayashi, T. Umeyama, A. Oguro, M. Kawasaki, N. Kadota, Y. Matano, H. Imahori, *J. Phys. Chem. C.,* **2007**, 111, 3528.

18   J. Rochford, S. Botchway, J.J. McGarvey, A.D. Rooney, M.T. Pryce, *J. Phys. Chem.*, **2008**, 112, 11611.

19   J. Rochford, A.D. Rooney, M.T. Pryce, *Inorg. Chem.*, **2007**, 46, 7247.

20   (a) T.-G. Zhang, Y. Zhao, I. Asselberghs, A. Persoons, K. Clays, M.J. Therin, *J. Am. Chem. Soc.*, **2005**, 127, 9710. (b) T.-G. Zhang, Y. Zhao, K. Song, I. Asselberghs, A. Persoons, K. Clays, M.J. Therin, *Inorg. Chem.*, **2006**, 45, 9703.

21   (a) F. Wurthner, M. S. Vollmer, F. Effenberger, P. Emele, D. U. Meyer, H. Port, H. C. Wolf, *J. Am. Chem. Soc.*, **1995**, 117, 8090. (b) M. S. Vollmer, F. Wurthner, F. Effenberger, P. Emele, D. U. Meyer, T. Stumpfig, H. Port, H. C. Wolf, *Chem. Eur. J.*, **1998**, 4, 260.

22   T. Shimidzu, H. Segawa, F. Wu, N. Nakayama, *J. Photochem. Photobiol. A: Chem.*, **1995**, 92, 121.

23   P. Bhavana, B. Verghese, P. Bhyrappa, *Acta. Crysta.*, C57, **2004**, 252.

24   Y. Diskin-Posner, S. Balasubramanian, G.K. Patra, I. Goldberg, *Acta. Cryst.*, E57 **2001**, m346.

25   P. Bhyrappa, M. Sankar, B. Varghese, P. Bhavana, *J. Chem. Sci.*, **2006**, 118, 393.

26   M. Bellizzi, P.C.D. Foss, R. Pelto, G. Crundwell, C. Bruckner, J.B. Updegraff III, M. Zeller, A.D. Hunter, *Z. Kristallogr.*, **2004**, 219, 129.

27   X. Sun, J. Zhang, B. He, *J. Photochem. Photobio. A: Chem.*, **2005**, 172, 283.

28   C. Bruckner, P.C.D. Foss, J.O. Sullivan, R. Pelto, M. Zeller, R.R. Birge, G. Crundwell, *Phys. Chem. Chem. Phys.*, **2006**, 8, 2402.

29   S. Okada, H. Segawa, *J. Am. Chem. Soc.*, **2003**, 125, 2792.

30   (a) K.M. Barkigia, L. Chantranupong, K.M. Smith, J. Fajer, *J. Am. Chem. Soc.*, **1988**, 110, 7566. (b) K. M. Kadish, E. Van Caemelbecke, G. Royal in The

Porphyrin Handbook, eds. K. M. Kadish, K. M. Smith, R. Guilard, Academic Press: Boston, **2000**; Vol. 8, ch. 55. (c) M. O. Senge in The Porphyrin Handbook eds. K. M. Kadish, K. M. Smith, R. Guilard, Academic Press: Boston, **2000**; Vol. 1; p 239.

31   C. Paul-Roth, J. Rault-Berthelot, G. Simonneaux, C. Poriel, M. Abdalilah, J. Ltessier, *J. Electroanal. Chem.*, **2006**, 597, 19.

32   M. Yuasa, K. Oyaizu, A. Yamaguchi, M. Ishikawa, K. Eguchi, T. Kobayashi, S. Tsutsui, *Polym. Adv. Technol.*, **2005**, 16, 616.

33   H. Maruyama, H. Sewaga, S. Sotoda, T. Sato, N. Kosai, S. Sagisaka, T. Shimidzu, K. Tanaka, *Synth. Metals*, **1998**, 96, 141.

34   M. J. Crossley, J. K. Prashar, *Tetrahedron. Lett.*, **1997**, 38, 6751.

35   N. Ono, H. Hironaga, K. Ono, S. Kaneko, T. Murashina, T. Ueda, C. Tsukamura, T. Ogawa, *J. Chem. Soc., Perkin Trans. 1*, **1996**, 417.

36   A. Rohrer, R. Ocampo, H. J. Callot, *Bull. Soc. Chim. Fr.*, **1997**, 134, 689.

37   M. Schaferling, P. Bauerle, *J. Mater. Chem.*, **2004**, 14 1132.

38   (a)B. Ballarin, S. Masiero, R. Seeber, D. Tonelli, *J. Electroanal. Chem.*, **1998**, 449, 173. (b) B. Ballarin, R. Seeber, L. Tassi, D. Tonelli, *Synth. Met.*, **2000**, 114, 279.

39   G. Li, S. Bhosale, S. Tao, R. Guo, S. Bhosale, F. Li, Y. Zhang, T. Wang, J.-H. Fuhrhop, *Polymer*, **2005**, 46, 5299.

40   (a) H. Segawa, N. Nakayama, T. Shimidzu, *J. Chem. Soc., Chem. Commun.*, **1992**, 784. (b) H. Segawa, N. Nakayama, F. Wu, T. Shimidzu, *Synth. Metals*, **1993**, 966, 55.

41   T. Yamamoto, N. Fukushima, H. Nakajima, T. Maruyama, I. Yamaguchi, *Macromol.*, **2000**, 33, 5988.

42   (a) P. Janvier, J.-Y. Lequestel, B. Illien, S. Suresh, E. Blart, J.-P. Quintard, F. Odobel, *Int. J. Quantum. Chem.*, **2001**, 84, 259. (b) F. Odobel, S. Suresh, E. Blart, Y. Nicolas, J.-P. Quintard, P. Janvier, J.-Y. Le Questel, B. Illien, D. Rondeau, P. Richomme, T. Häupl, S. Wallin, L. Hammarström, *Chem. Eur. J.*, **2002**, 8, 3027.

43   G. Li, T. Wang, A. Schulz, S. Bhosale, M. Lauer, P. Espindola, J. Heinze. J.-H. Fuhrhop, *Chem. Commun.*, **2004**, 552.

44   M.-C. Kuo, L.-A. Li, W.-N. Yen, S.-S. Lo, C.-W. Lee, C.-Y. Yeh, *Dalton Trans.*, **2007**, 1433.

45   G. Simonneaux, P. Le Maux, *Coord. Chem. Rev.* **2002**, 228, 43.

46   K. Lang, J. Mosinger, D. M. Wagnerová, *Coord. Chem. Rev.* **2004**, 248, 321.

47   M. Calvete, G. Ying Yang, M. Hanack, *Synth. Metals* **2003**, 141, 231.

48   K. McEwan, K. Lewis, G.-Y. Yang, L.-L. Chng, Y.-W. Lee, W.-P. Lau, K.-S. Lai, *Adv. Funct. Mater.*, **2003**, 13, 863.

49   X.X. Li, Y.-J. Guo, J.-W. Wang, L.-H. Kong, J.-H. Pan, *Supramol. Chem.*, **2008**, 20, 243.

50   M. Yuasa, K. Oyaizu, A. Yamaguchi, M. Ishikawa, K. Eguchi, T. Kobayashi, Y. Toyoda, S. Tsutsui, *Polym. Adv. Technol.*, **2005**, 16, 287.

51   (a) R. Friedlein, F. Von Kieseritzky, S. Braun, C. Linde, W. Osikowicz, J. Hellberg, R. Salaneck, *Chem. Comm.*, **2005**, 1974. (b) R. Friedlein, X. Crispin, W. Osikowicz, S. Braun, M.P. de Jong, C.D. Simpson, M.D. Watson, F. Von Kieseritzky, P. Samori, S.K.M. Jonsson, M. Fahlman, F. Jackel, J.P. Rabe, J. Hellberg, K. Mullen, W.R. Salaneck, *Synth. Metals*, **2004**, 147, 79.

52   J. Chen, A.K. Burrell, W. M. Cambell, D.L. Officer, C. O. Too, G. G. Wallace, *Electrochim. Acta.*, **2004**, 49, 329.

53   W.R. Browne, C.M. O'Connor, C. Villani, J.G. Vos, *Inorg. Chem.*, **2001**, 40, 5461.

54   (a) K. Sonogashira, Y. Tohda, N. Hagihara, *Tet. Lett.*, **1975**, 4467. (b) E.-I. Negishi, L. Anasticia, *Chem. Rev.*, **2003**, 103, 1979.

55   (a) A.S. Karpov, F. Rominger, T.J.J. Mueller, *J. Org. Chem.*, **2003**, 68, 1503. (b) F. Bohlmann, P. Herbst, *Chem. Ber.*, **1962**, 95, 2945.

56   Jonathon Rochford, Ph.D. thesis, Dublin City University, Dublin 9, **2004**.

57   A.D. Adler, F.R. Longo, F. Kampas, J. Kim, *J. Inorg. Nucl. Chem.*, **1970**, 32, 2443.

58   (a) A. Harriman, J. Davila, *Tetrahedron*, **1989**, 45, 4737. (b) H.N. Fonda, J.V. Gilbert, R.A. Cormier, J.R. Sprague, K. Kamioka, J.S. Connolly, *J. Phys. Chem.*, **1993**, 97, 7024.

59   E.G. Azenha, A.C. Serra, M. Pineiro, M.M. Pereira, J. Seixas de Melo, L.G. Arnaut, S.J. Formosinho, A.M.d'A. Rocha Gonsalves, *Chem. Phys.*, **2002**, 280, 177.

60   (a) I. Gupta, C.-H. Hung, M. Ravikanth, *Eur. J. Org. Chem.*, **2003**, 4392. (b) I. Gupta, M. Ravikanth, *J. Photochem. Photobiol. A: Chem.*, **2006**, 8, 2402.

61   E.B. Fleitcher, A.M. Shachter, *Inorg. Chem.*, **1991**, 30, 3763.

62   S.R. Halper, S.M. Cohen, *Chem. Eur. J.*, **2003**, 9, 4661.

63   G.A. Baker, F.V. Bright, M.R. Detty, S. Pandey, C.E. Stilts, H. Yao, *J. Porphyrins Phthalocynines*, **2000**, 4, 669.

64   A. Ghosh, S.M. Mobin, R. Fronhlich, R.J. Butcher, D.K. Maity, M. Ravikanth, *Inorg. Chem.*, **2010**, 49, 8287.

Chapter 3

The synthesis, photochemistry and electrochemical properties of a series of thiophene based dyads and the corresponding metal carbonyl complexes.

Chapter three commences with a general introduction to Sonogashira-Hagihara type cross coupling reactions. This is followed by a literature survey on the synthesis and photochemistry of thienyl based organometallic systems. The synthesis of the novel systems produced for this study is then described and the photophysical properties are discussed. Electrochemical data are also presented. The photochemistry of the $Co_2(CO)_6$ complexes are examined by steady state photolysis in the presence of a trapping ligand. Three of the complexes were studied by TRIR on a picosecond timescale and the quantum yields for the CO loss process was determined at a range of excitation wavelengths.

3.1 Literature Survey

3.1.1 Cross coupling reactions

Organometallic chemistry has provided several new methods to carry out carbon-carbon (or carbon-heteroatom) bond formation. Such processes, generally termed cross coupling reactions, have found a central place in organic synthesis with their scope increasing year on year. The Sonogashira-Hagihara reaction involves the coupling of terminal alkynes with aryl or vinyl halides under palladium catalysis (Rxn. 1), a procedure which has not changed much since originally reported in 1975.[1]
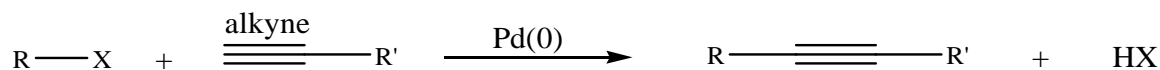
Rxn. 1   Sonogashira – Hagihara reaction.

Other important cross-coupling reactions include the Negishi,[2] Suzuki-Miyaura,[3] Heck[4] and Stille[5] reactions. A very detailed general overview of palladium catalysed alkynlation reactions has been compiled[6] and a review of palladium catalysed cross coupling reactions in organoboron compounds has also been published.[7] Further still, the use of Negishi cross coupling reactions in the generation of a new binding site in a Ru(bpy)$_2$ complex was reported,[8] while a detailed review of regioselective cross coupling reactions of multiple halogenated nitrogen-, oxygen-, and sulphur-containing compounds can also be found in press.[9]

The Sonogashira coupling is a catalytic process performed in the presence of an amine base, using a palladium(0) complex and generally requires copper iodide as a co-catalyst (Scheme 1). Initially the palladium catalyst is oxidised (to Pd(II)) and a cyclic reaction follows. Oxidative addition of the organic halide to the palladium takes place giving a Pd(II) intermediate. In parallel, Cu(I) coordinates to the alkyne terminal end and transmetallation occurs, so called because the nucleophile is transferred from the metal in the organometallic reagent to the palladium and the counterion moves in the opposite direction. Reductive elimination yields the final coupled product, with the Pd(0) catalyst ready for another cycle.
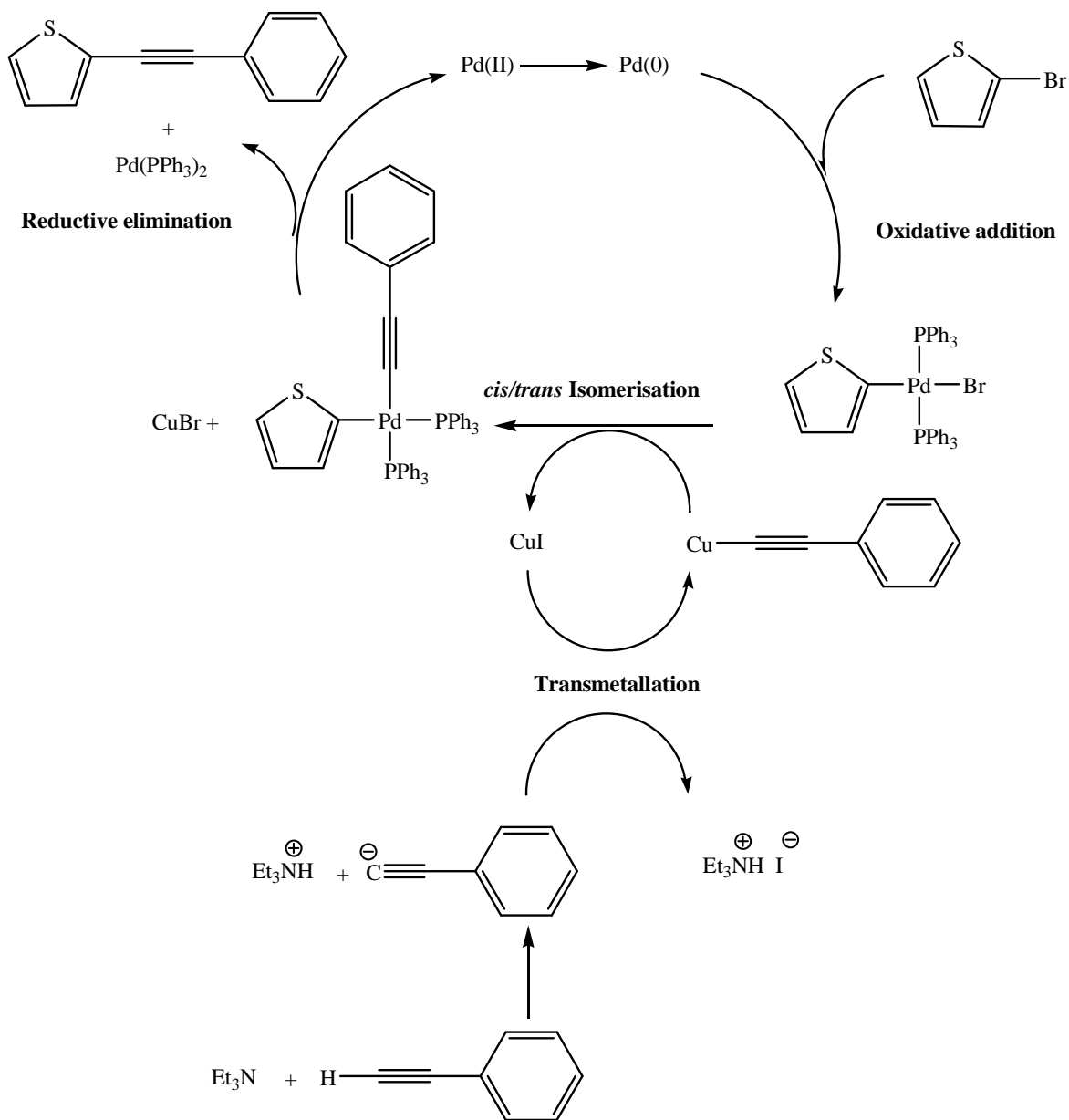
*Scheme 1   Sonogashira cross coupling reaction mechanism, using the formation of 2-
(phenylethynyl)thiophene (**NB-L1**) as an example.*

It is often convenient to use a stable and soluble Pd(II) source such as $Pd(PPh_3)_2Cl_2$ instead of Pd(0).   This precursor is reduced *in situ* to give the coordinately unsaturated catalytically active Pd(0) species. The reduction of Pd(II) to Pd(0) can be achieved with an amine. A stoichiometric excess of an amine, usually Et_3N, serves two purposes: it acts as a base to trap the halide and as a reducing agent for palladium.

3.1.2 Functionalised thiophenes

A series of functionalised thiophenes and bithiophenes were synthesised and their non-linear optical properties were studied by both computational and experimental methods.[10] The thiophenes contained combinations of dimethylamino and dimethylhydrazono π-donors along with nitro and dicyanovinyl π-acceptor groups. The first hyperpolarisability, β, is an important aspect for second-order NLO materials as the magnitude of β determines how efficient a given molecule will be in causing quadratic (second-order) NLO effects. The main molecular features for high β is a polarisable framework, such as an aromatic ring substituted with donor (D) and acceptor (A) moieties in a non-centrosymmetric fashion (**1**-**7**, Fig. 1). The calculated β(0) values for the lowest energy conformations were found to be in good agreement with experimental β(0) values. Comparison of **1** with **2** revealed that thiophene provides a more efficient delocalisation pathway than benzene. Addition of the imine (-N=CH-) unit to the π-electron conjugating pathway in hydrazone **3** caused a doubling of β with respect to **2**. Computational studies also revealed increased conjugation pathlength in **4**, with its dicyanovinyl acceptor as opposed to the nitro group in **2**, which led to an increase in β. Including both the hydrazone and dicyanovinyl in thiophene **5** resulted in a fivefold increase with respect to the **2**. Similarly the bithienyl with the hydrozone-dicyanovinyl combination, **6**, gave a β value about twice as high as the dimethylamino-nitro derivative, **7**. This suggests that thiophenes of this type could be used in NLO materials.

166
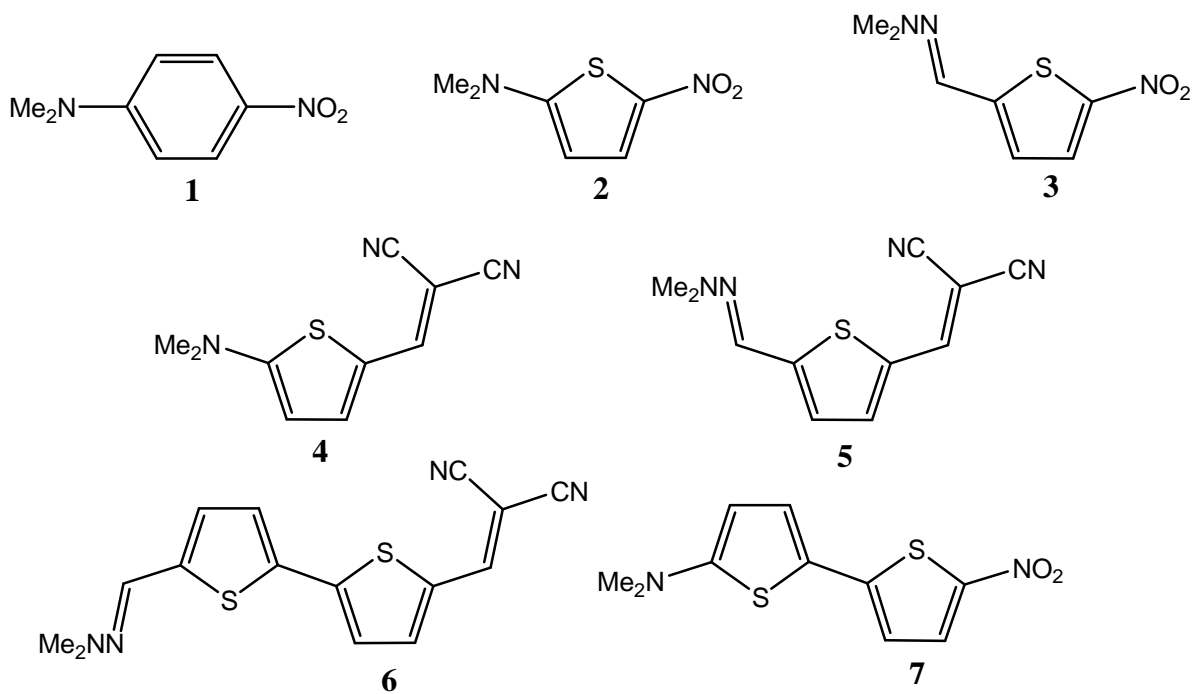
Figure 1   *Functionalised thiophenes and bithiophenes of the form (D-π-A).*

Donor-acceptor conjugated compounds are of considerable interest because they find potential applications in (opto)electronic devices such as field effect transistors and light emitting diodes. Studies have demonstrated that replacing the benzene core with another heterocycle such as thiophene, pyrrole or thiazole resulted in enhanced molecular hyperpolarisabilities.[11] Conjugated thiophene – pyrrole derivatives as donors with appropriate acceptor substitutes have been synthesised as candidates for push – pull systems (**8 - 13**, Fig. 2). The potential of these conjugated molecules as strong π-electron donor units functionalised with dicyanovinyl were examined. Larger bathochromic shifts of the absorbance maxima in the UV-vis spectra are observed as the acceptor strength of the dicyanovinyl group increases. The position of the dicyanovinyl group on the thiophene ring or on the pyrrole ring can be seen in the absorbance spectra, **8** λ_{max} = 454 nm whereas with **9** λ_{max} = 415 nm. The bathochromic shift observed for **8** is due to more extensive electron delocalisation. The position of the absorbance bands is largely affected by the substitution position of the dicyanovinyl group along with the group that was substituted onto the nitrogen atom of the pyrrole ring. Donor-acceptor substituted thienylpyrroles

167

have previously been shown to demonstrate strong solvatochromic behaviour and compounds **8 - 13** are no exception. Compounds **8** and **12** were examined in a range of 15 solvents. Respective energy shifts of $\Delta v = + 1130$ cm^{-1} and $+ 1263$ cm^{-1} were observed for their CT absorbance bands indicating positive solvatochroism. All compounds displayed two oxidative processes ascribed to the formation of the radical cation of the pyrrole but extraction of subsequent electrons gives rise to an irreversible process. As a consequence of the destabilising effect of the electron withdrawing dicyanovinyl group compounds **8** and **10-13** displayed their first oxidation between +0.46 – 0.68 V *vs.* Fc/Fc^{+}. The reduction of the thienylpyrroles was reversible one-electron process. A clear cathodic shift in the reduction peak was observed as the donor strength in the substituent group on the nitrogen of the pyrrole increases. Hyper-Rayleigh scattering was used to measure the first hyperpolarisability, β, of the compounds. For compounds **8** and **9** values of 526 x 10^{-30} and 85 x 10^{-30} esu respectively were obtained, which indicates that the positioning the dicyanovinyl group on the 5' position of the thiophene ring leads to larger nonlinearity than the same group on the 5-position of the pyrrole. The β value for **10 - 13** increased with the donor strength of the substituent on the nitrogen atom of the pyrrole ring along the series with **10** (364 x 10^{-30} esu) < **11** (439 x 10^{-30} esu) < **12** (651 x 10^{-30} esu).

8: R$_1$ = -CH=C(CN)$_2$, R$_2$ = H
9: R$_1$ = H, R$_2$ = -CH=C(CN)$_2$

10: R$_3$ = H
11: R$_3$ = 4-MeO
12: R$_3$ = 2,4-diMeO
13: R$_3$ = 4-F
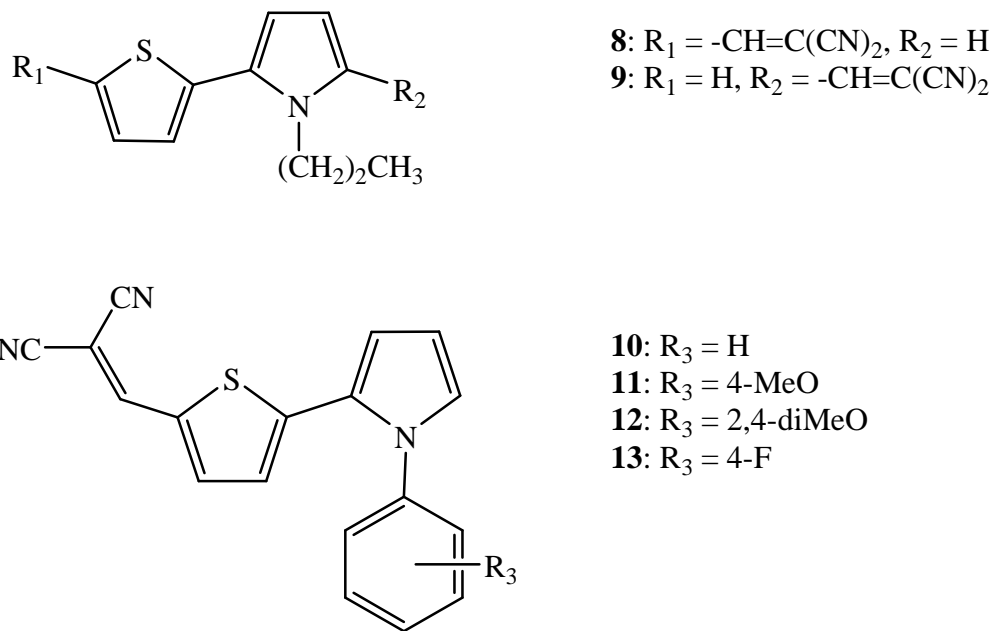
Figure 2   *Conjugated thiophene-pyrrole push – pull systems.*

3.1.3 Thiophene acetylene systems

A series of push-pull substituted oligo(2,5-thienyleneethynylene)s (OTE's) with alkylthio groups (R_1) and nitro groups (R_2) were synthesised (**14 - 18**, Fig. 3) and their electronic properties examined.[12] The donor-acceptor substitution caused polarisation within the molecule which was evident from the $\Delta \delta$ (^{13}C) values of the acetylenic carbon atoms. The $\Delta \delta$ (^{13}C) values were found to decrease with increasing chain length ($n = 2, 3, 4$) as extension of the conjugation led to increased distance between D and A, which therefore decreased the partial dipole moment at the chain ends. Further evidence for the D-π-A interaction can be observed in the absorbance spectra where intramolecular charge transfer (ICT) bands were observed. The parent compound **14**, displays a λ_{max} value of 317 nm whereas the substituted OTE **15** displays a λ_{max} value at 413 nm. The effect is strong for the small distance between the donor and acceptor sides in compound **15**. As the number of repeating units increases the extent of the bathochromic shift decreases (λ_{max} **15** = 413 nm, **16** = 426 nm, **17** = 427 nm, **18** = 428 nm).
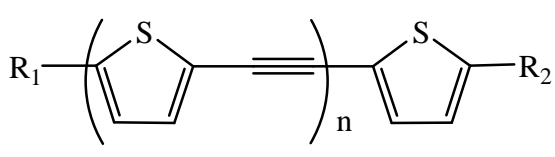
14: R_1 = H, R_2 = H, $n = 1$
15: R_1 = $SC_{12}H_{25}$, R_2 = NO_2, $n = 1$
16: R_1 = $SC_{12}H_{25}$, R_2 = NO_2, $n = 2$
17: R_1 = $SC_{12}H_{25}$, R_2 = NO_2, $n = 3$
18: R_1 = $SC_{12}H_{25}$, R_2 = NO_2, $n = 4$

Figure 3   Donor-acceptor substituted conjugated thienyl oligomers (D-π-A type).

Rodríguez et al. synthesised a large body of conjugated 2-arylethenyl and 2-arylethynyl thiophene structures (**19 - 34**, Fig. 4) in order to improve the nonlinear optical properties of these types of molecules.[13] All compounds in the series were synthesised *via* a sequence of heterocoupling (Sonogashira) or oxidative homocoupling reactions. Compounds **19** and **20** (Fig. 4) were initial conjugated 2-thienyl end-capped structures. The conjugation effect through the double or triple bond to the thiophene ring and the conjugated chains were considered. Extension of the 2-thienyl end-capped structures (to produce **23**, **24** and **25**) was carried out by coupling **21** and **22**. The *para* connection of the two acetylenic units (in

26 and **27**) guaranteed conjugated electronic communication in the follow-on compounds **28** – **34**, where **3**, **4**, **8** and **9** were coupled to 2,5'-thienyl positions. The conjugated molecules which integrate the thiophene rings and the end-capped N,N-dimethyaminophenyl unit (**28** and **29**) were constructed as this type of compound showed intrinsic electronic properties including luminescence and charge transport characteristics. Compound **19** exhibited a low quantum yield of fluorescence while for **20** no emission fluorescence was observed. The ethenyl conjugate, **23**, displayed two emission bands at λ_{max} = 427, 454 nm whereas the ethynyl conjugate molecule, **24**, possessed a unique emission band at λ_{max} 421 nm, with higher quantum yield. Compound **25** showed two fluorescence bands at λ_{max} = 390, 410 nm with a lower quantum yield than that of **24**. The reported quantum yields were 0.29, 0.36 and 0.30 for **23**, **24** and **25** respectively. All the 2,5 disubstituted thiophene conjugates (**28 - 34**) showed fluorescence emission bands with some noteworthy points. Each of the compounds **32 - 34** displayed two emission bands while compounds **28 - 31** showed just a single emission band. Increasing the number of ethynylphenyl units as in **28**, **29** and **32 - 34** caused a significant increase in the emission quantum yield (0.20, 0.42 and 0.54 for **32 - 34** respectively). In compounds **30** and **31**, where the double bond was replaced by a triple bond, an increase in quantum yields was observed (in order: 0.10 and 0.34). The authors have shown that by controlling the structure and dimensions of a compound the fluorescence properties can be fine tuned.
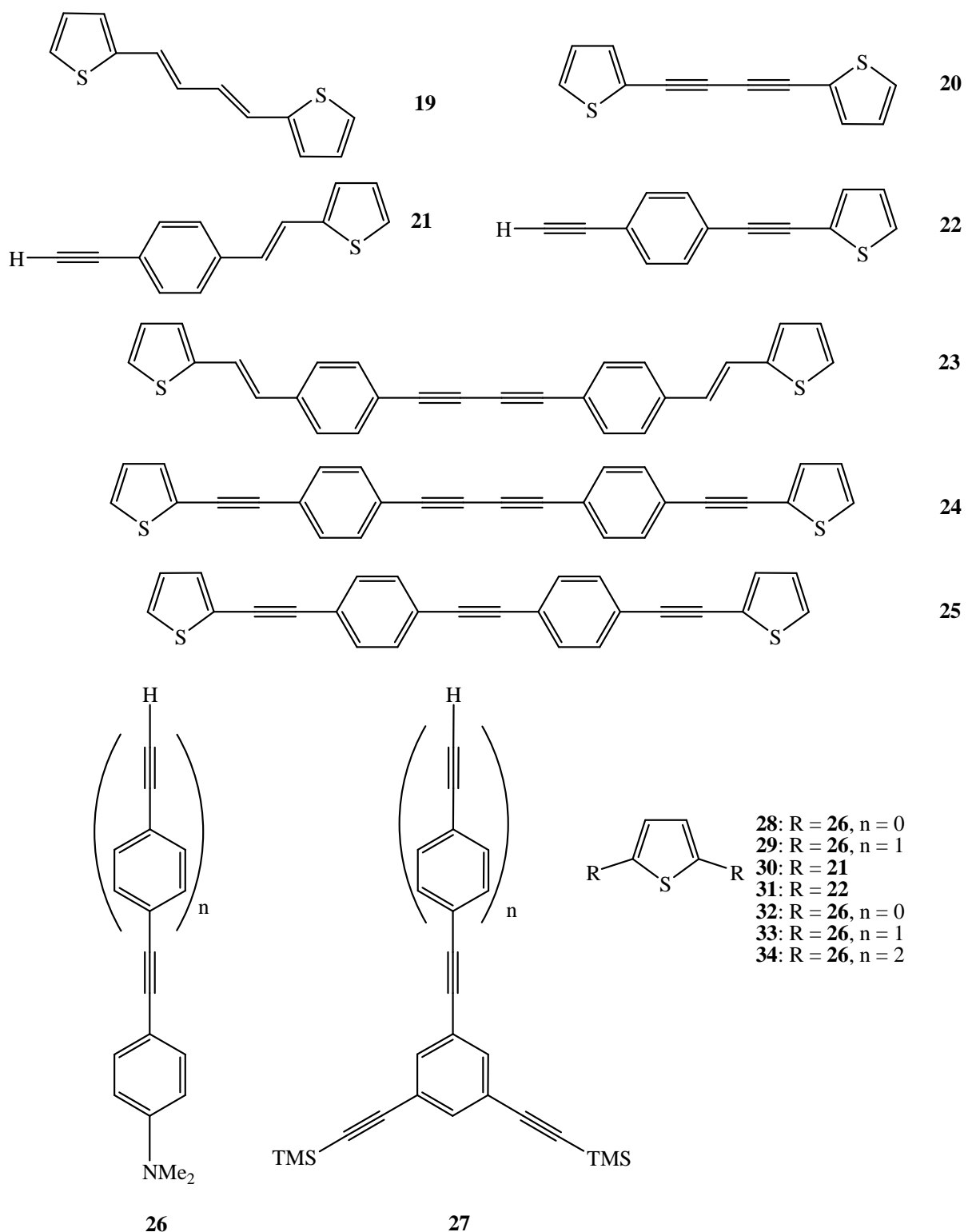
Figure 4   *Conjugated 2-arylethenyl and 2-arylethynyl thiophene structures.*

171

Several structures of π-conjugated polymers were examined to measure the impact that regioregularity had on the photoluminescence.[14] Compounds **35** and **36** (Fig. 5) were synthesised from monomers through selective formation of carbon – carbon bonds at specific locations. Three chain sequences of the polymers were made: 1: the head-to-tail sequence **35**, 2: the head-to-head and tail-to tail sequence **36**, and 3: a regiorandom sample which contained head-to-head and head-to-tail sequences in a ratio of about 50:50. The absorbance spectra of **35** and **36**, which were almost identical, suggested essentially the same conjugation length along the π-conjugated backbone in both polymers. The rigidity of the molecules as a result of the extended π-π conjugation was calculated. Using the Mark-Houwink equation values of 1.06 and 0.91 were obtained for **35** and **36** respectively. This indicated that the head-to-tail chain sequence of **35** had a slightly more rigid conformation in dilute solution. The radius of gyration, R_g, used to measure the stiffness of a polymer (R_g/M_w) also confirmed that **35** was more rigid. The chain stiffness of the regiorandom sample fell between that of **35** and **36** for both the Mark-Houwink and R_g/M_w values. Both **35** and **36** showed nearly identical absorbance spectra with the λ_{max} observed at 414 and 415 nm. They also displayed almost identical photoluminescence (PL) profiles with the emission λ_{max} at 453 and 478 respectively. However the quantum efficiency of **35** was higher than that of **36** (**35** $\Phi_n = 0.59$, **36** $\Phi_n = 0.53$), which the authors attributed to the relative molecular stiffness of the molecule. Both regioregular compounds had higher quantum efficiencies than that of the regiorandom compound ($\Phi_n = 0.42$). This indicated that the PL efficiency was affected not only by the relative content of head-to-tail sequences that determine the chain rigidity, but also by the detailed linkages between the chain sequences. The absorbance and fluorescence spectra of a solid state film of **36** are both red shifted in comparison to the film of **35**. It appeared that the more symmetrical chain sequence (head-to-head and tail-to-tail) of **36** allowed for better packing in the solid state. In the solid state the fluorescence of **36** was ~2.5 times stronger than that of film **35** and both have significantly stronger emission than the regiorandom sample. Thus, photoluminescence enhancement is dependent on structural regioregularity, especially in the solid state.

35

36
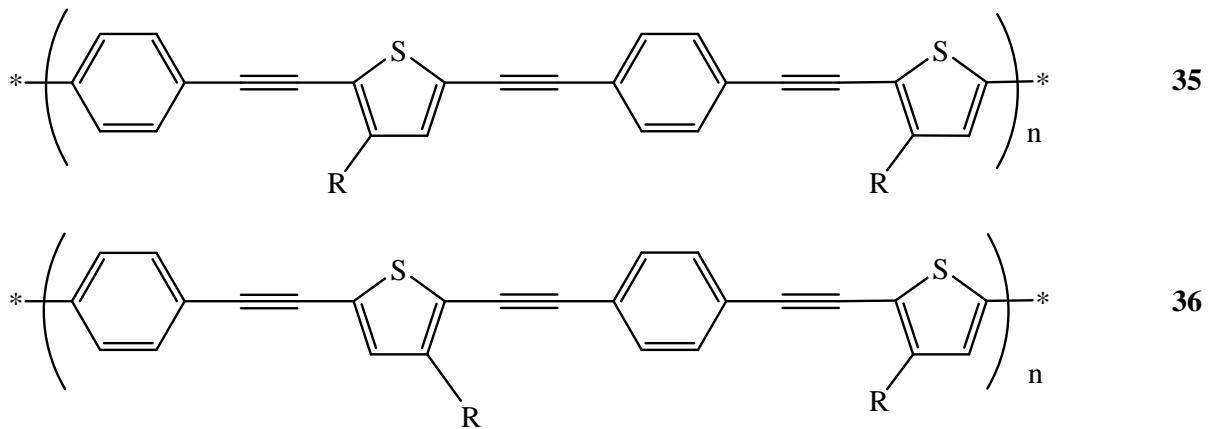
Figure 5   *Regioregular π-conjugated polymers where R = C₆H₁₃.*

The homologous series **37 - 40** (Fig. 6) are well defined oligomers, where tetramer **40** is the longest of the series and lacks the terminal silyl-protected triple bond, were synthesised by palladium-catalysed cross-coupling reactions (Sonogashira).[15]   Their optical and electrochemical properties were compared to that of a structurally related series of oligo(3-hexylthiophene)s as it gives insight into common and deviating physical properties between the two series. Increasing chain length of the conjugation system resulted in a progressive bathochromic shift of the absorbance maxima with enhancement of the extinction coefficient in steps of about 20,000 M^{-1} cm^{-1}. This is almost equal to the extinction coefficient of ethynylated bithiophene (ε = 18,800 M^{-1} cm^{-1}).   While **37** displayed an absorbance λ_{max} at 333 nm (ε = 18,800 M^{-1} cm^{-1}), the other homologues increased in order **38** (λ_{max} = 392 nm, ε = 40,800 M^{-1} cm^{-1}), **39** (λ_{max} = 471 nm, ε = 54,400 M^{-1} cm^{-1}) and **40** (λ_{max} = 427 nm, ε = 78,700 M^{-1} cm^{-1}). The emission maxima were red-shifted with increasing chain length. The bithiophene, **37**, displayed a λ_{em} at 410 nm and this was shifted steadily to longer wavelength for the higher homologues. The λ_{em} for the dimeric compound, **38**, shifted by 59 nm to 469 nm, with trimeric **39** bathochromically shifted to λ_{em} = 510 nm ($\Delta\lambda_{em}$ = 41 nm with respect to **38**). For the tetrameric compound, **40**, the change in emission maxima becomes less pronounced with the difference between the highest analogues, **39** and **40**, only 11 nm (λ_{em} of **40** = 521 nm). No overall trend was observed for the fluorescence quantum yields (**37**, **38**, **39**, **40**: Φ = 0.08, 0.46, 0.36, 0.43 respectively). The stepwise increase of the conjugation chain length led to an increased number of redox potentials which lay closer together. Monomer **37** displayed only one

oxidation wave (E^o = 0.75 V *vs.* Fc/Fc$^+$), **38** and **39** had two and three waves respectively (**38**: E^o = 0.56, 0.77 V *vs.* Fc/Fc$^+$, **39**: E^o = 0.50, 0.62, 1.00 V *vs.* Fc/Fc$^+$) and the tetramer **40** had four oxidation waves (E^o = 0.45, 0.50, 0.77, 0.94 V *vs.* Fc/Fc$^+$). No reduction waves were observed down to potentials of -2.1 V *vs.* Fc/Fc$^+$. A correlation of the maximum absorbance and emission energies versus the inverse number of atoms in the conjugation backbone presents clear linear relationships. There is a systematic change in the spectral features but particularly in the emission and oxidation behaviours. The influence of the triple bonds becomes more pronounced with increasing chain length.
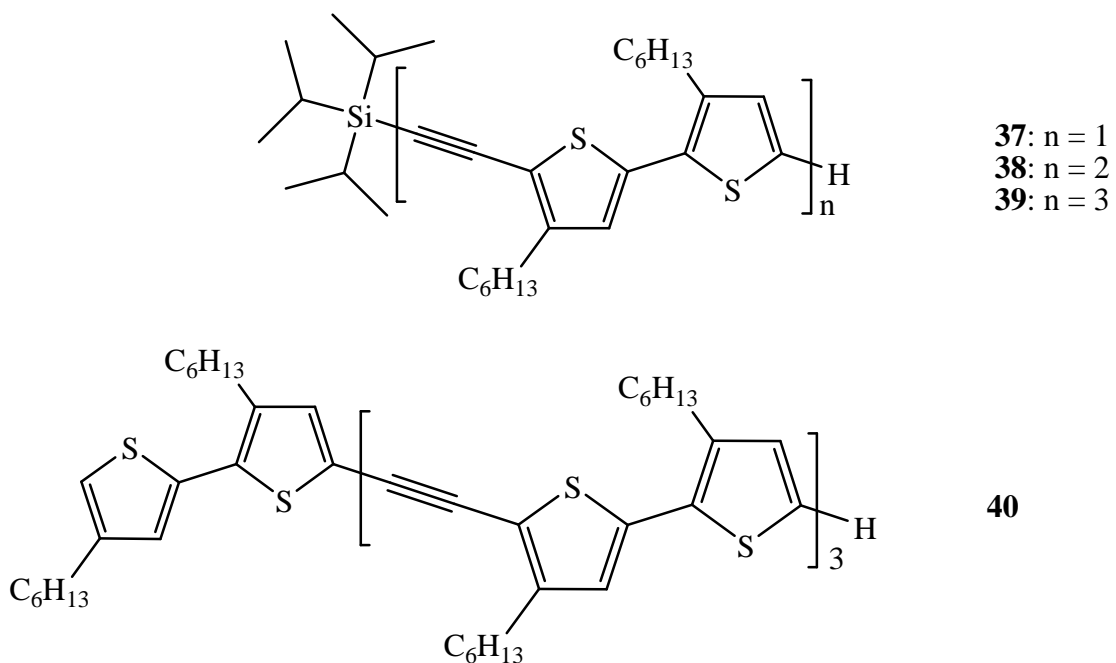
Figure 6   *Oligomeric series (monomer to tetramer) of ethynyl bithiophenes.*

Inspired by structures of metalloproteins, Toyota and co-workers used Sonogashira and Suzuki coupling techniques to synthesise a spacer, 1,4-bis(2-ethynyl-3-thienyl)benzene (ETB) (**41**, Fig. 7), which has a phenylene axis and a pair of thien-3-yl units at both ends of the axis.[16] Selective introduction of substituents at the terminal sp-carbon and/or 5-position of the thiophene rings (**42- - 55**, Fig. 7) made an easily tuneable spacer. UV-vis spectra of compounds were compared to the parent **41** (where R = H). Compounds **42, 49**

174

and **53**, the trimethylsilyl series, showed a bathochromic shift in the order **49** > **42** > **53**. Compared to **49** a significant red shift was observed in compound **42** with a concomitant increase in extinction coefficient which indicated the existence of increased π-conjugation through the central phenylene unit. Compound **53** with the biphenyl moiety showed the largest bathochromic shift among the three trimethylsilyl substituted derivatives however the difference in λ_{max} between **53** and **41** is relatively small suggesting that the extension of the π-system is hindered by the lack of co-planarity in the biphenyl species. The phenylethynyl derivatives **46**, **47**, **51**, **52** and **55** again showed a similar absorbance profile with the λ_{max} shifting to lower energy in the order **47** > **46** > **51** > **52**. Similar to the previous series, the spectrum of **46** exhibited the larger molar absorbances and **55** showed very little change compared to **46**. The pyridyl derivatives, **43-45**, **50** and **54**, gave comparable results. Compound **43** displayed the largest extinction coefficient, with the others following the order **43** > **45** > **44**. As expected, **54** did not show a significant red-shift compared to those of compounds **41** or **51** whereas the spectra of **43-45** did show large bathochromic shifts. This indicates that significant π-conjugation through the central phenylene moiety is possible.

41: R = H
42: R = TMS
43: R = 2-pyridyl
44: R = 3-pyridyl
45: R = 4-pyridyl
46: R = phenyl
47: R = 4-butylphenyl
48: R = 4-hexylphenyl

49: R = TMS, R' = phenyl
50: R = 2-pyridyl, R' = phenyl
51: R = R' = phenyl
52: R = phenyl, R' = H

53: R = TMS
54: R = 2-pyridyl
55: R = phenyl
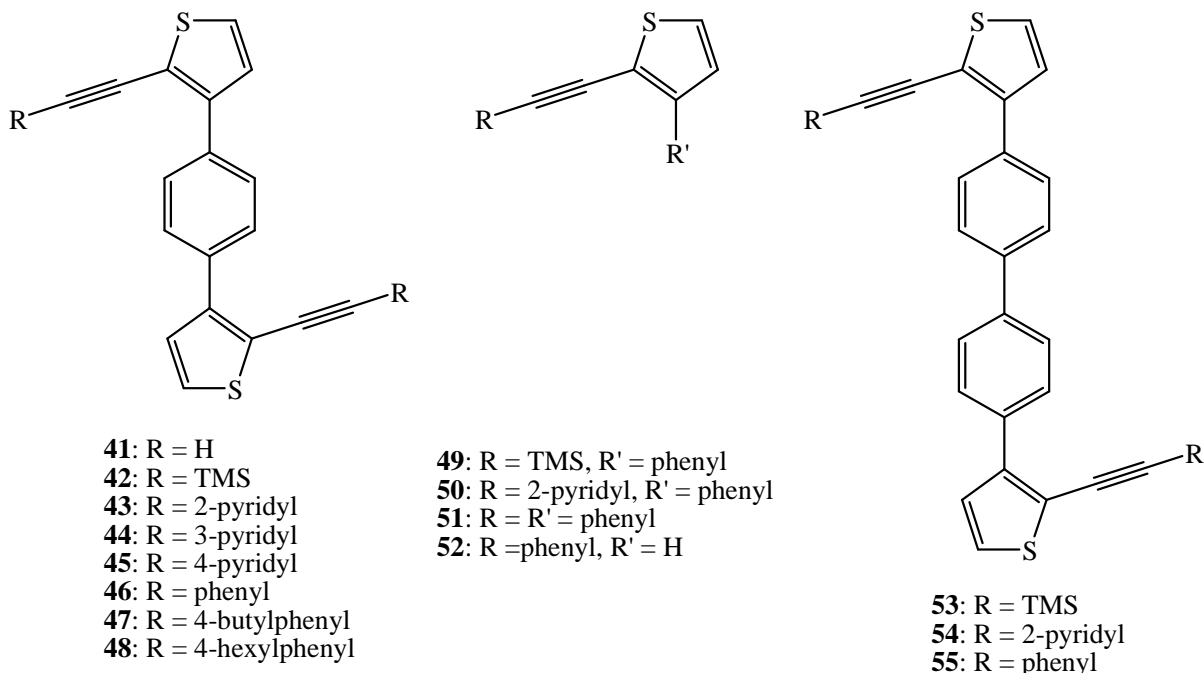
Figure 7   *ETB (1,4-bis(2-ethynyl-3-thienyl)benzene) spacers with various groups attached at both ends of the axis.*

A new class of radial oligothiophenes (**57 - 60**, Fig. 8) with oilgophene "arms" (**56**, Fig. 8) around a central aromatic core attached with alkynyl linkages were reported.[17] These radial "starlike" molecules included ethynyl units bound directly to the core and were expected to support extended π-conjugation of the molecule as well as adding coplanarity to the molecule. Both the absorbance and emission spectra were examined. Increasing the number of oligothiophene arms around the arene (benzene or thiophene) core caused the λ_{max} of the lowest π-π* transition to be red shifted (**57**: λ_{max} = 400 nm, **59**: λ_{max} = 458 nm). The λ_{max} of the unappended thiophene arm, **56**, was observed at 374 nm suggesting that the overall coordination of the oligothiophene arms to the arene core induced delocalisation of the π system. Solid state spectra of the homologues were also bathochromically shifted with respect to solution phase which is attributed to enhanced planarity of the molecule in the solid state. A similar trend was observed for the emission spectra, each displaying a red shifted emission λ_{max} as the number of thiophene rings increased (λ_{max} **57** = 520 nm, λ_{max} **59** = 615 nm) which were further bathochromically shifted in the solid state
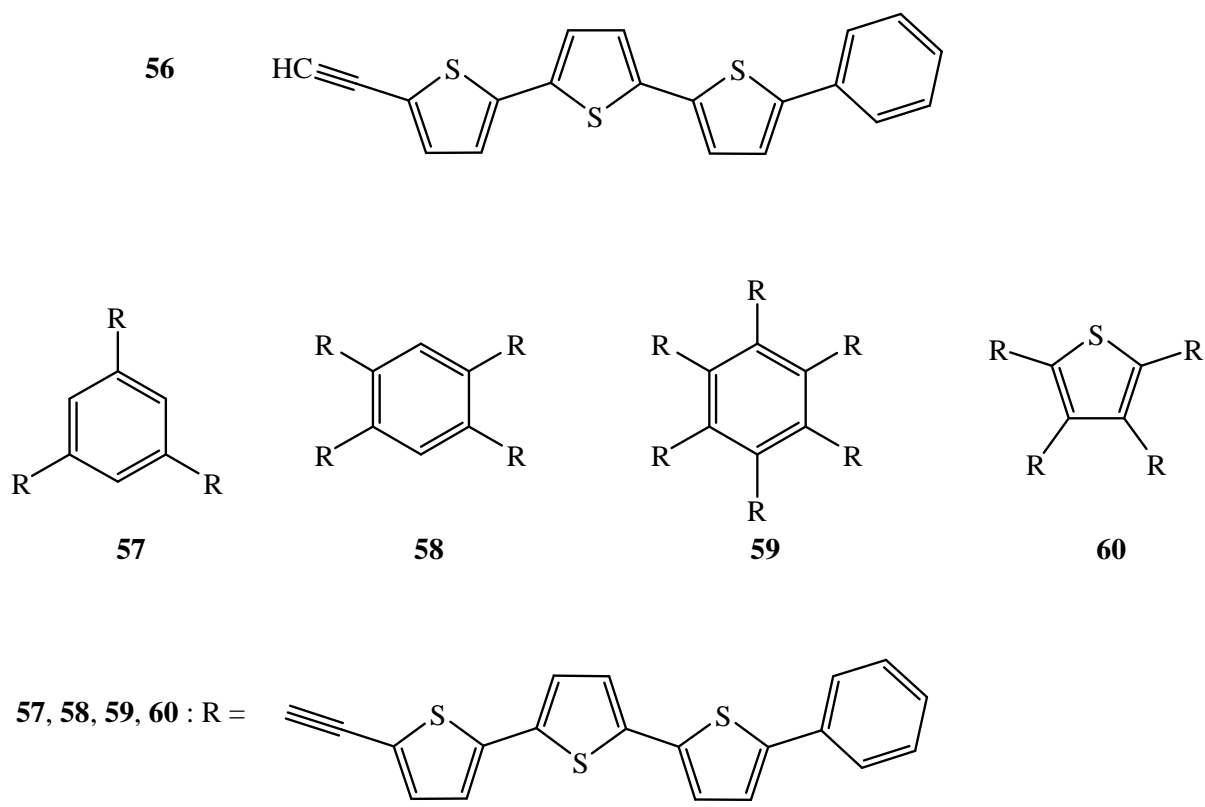
Figure 8   *Radial oligothiophenes with arene core.*

3.1.4　Bonding in metal carbonyl compounds

In order to discuss the bonding in metal carbonyl complexes, the carbon oxygen bond must first be examined. In carbon monoxide there is a σ-bond between the carbon and oxygen atoms and a lone pairs of electrons on each of the two atoms. There is also a doubly degenerate π-bonding orbital. The result of which is a triple bond $(\sigma)^2(\pi_x)^2(\pi_y)^2$ (Fig. 9 (a)). However this is a polar bond, and in the π-orbitals the electrons are almost four times as likely to be near the oxygen as near the carbon. The low dipole moment observed for carbon monoxide can be explained by the bonds polarity compensating for the strongly directional lone pair on the carbon atom. CO is an example of a good π acceptor. Such ligands are of great significance in organometallic chemistry as they form strong metal-ligand bonds.

In forming a metal-carbon σ-bond the metal employs its nd, $(n + 1)$p and $(n +1)$s vacant metal orbitals. The metal must possess vacant d-orbitals that can overlap with the lone pair on the carbon and this may be regarded as the formation of a metal-carbon σ-bond of the donor acceptor type. In the metal carbonyl there are filled non-bonding d-orbitals on the metal which have the correct symmetry to overlap with the empty orbitals of the CO, this orbital is the CO π*, a low-lying π-antibonding orbital of the carbon monoxide and it accepts electron pairs from the occupied metal d-orbitals (Fig. 9 (b)). As a result of this additional π-bond the d_π electrons that were metal centred now sometimes reside on the ligand. The metal has now donated electron density back to the ligands. This is referred to as *back bonding* and is a feature of M – L bonds where L is an unsaturated molecule. Back bonding allows electron density on the metal shift back to the ligands. As well as an additional π-bond, the transference of charge from the metal can be seen as a means of strengthening the original σ-bond (it contributes principally to the total bond energy) by removal of unfavourable charge separation induced by the donor σ-bond. This produces a "synergic" interaction between the two types of bonds and it is this interaction that accounts for the most part of the metal-carbon bond strength.
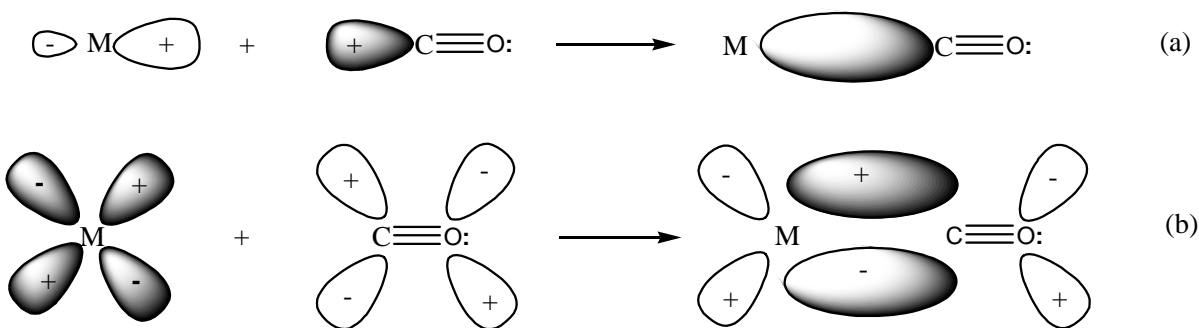
Figure 9   *(a) Formation of carbon-metal σ-bond. (b) Formation of metal-carbon π-bond.*

In addition to the previously discussed linear M–C–O bond, many metal carbonyl compounds possess a carbon monoxide group bonded to two or more metal atoms. This bridging effect in carbonyl compounds is generally confined to derivatives of the first row transition metals. Simplistically it can be assumed that bridging carbonyl groups contribute only one electron to each of the metal atoms forming σ-bonds with the metal electrons. The nature of the π-bonding is a little more complicated. The carbon-oxygen bond order is reduced as evidenced by a shift in CO stretching frequencies to ~1850 cm^{-1}. Another important type of bond found in metal carbonyls is the metal-metal bond. It is sometimes the only bond between two halves of a metal carbonyl but often found in conjunction with bridging carbonyl groups. With the exception of vanadium hexacarbonyl, all binary carbonyls obey the inert gas rule with (a) terminal carbonyl groups each contributing a pair of electrons to the outer of the metal atoms, (b) bridging carbonyls each contributing one electron to each of the metal atoms and (c) covalent metal-metal bonds formed by one electron from each metal atom bringing the total number of electrons to that of the next inert-gas shell.

3.1.5   Dicobalt hexacarbonyl complexes

The pioneering work of Reppe[18] and Hübel[19] in the field of alkyne – metal chemistry in the 1940's and 1960's respectively revealed the structural diversity of alkyne oligomerisation at metal centres.   Complexes of the (μ_2-alkyne)$Co_2(CO)_6$ series are among the earliest known organometallic compounds.[20]   The dicobaltatetrahedrane, $(RC\equiv CR')Co_2(CO)_6$, is the main product of alkynes reacting with $Co_2(CO)_8$ at room temperature.   One of the most widely reported and studied of these dicobalt hexacarbonyl complexes being diphenylacetylene dicobalt hexacarbonyl, **(μ_2-PhC$\equiv$CPh)Co$_2$(CO)$_6$.**

Dicobalt octacarbonyl is the simplest closed shell cobalt carbonyl, containing two types of carbonyl groups, i.e. bridge and terminal carbonyl groups as shown in figure 10 (a). Alkynes possess a pair of perpendicular mutually degenerate p-π orbitals.   The reaction of an alkyne with dicobalt octacarbonyl replaces two bridge carbonyl groups to form the organometallic complex (Rxn. 2, Fig. 10 (b)).   Bridge bonding observed in (μ_2-alkyne)$Co_2(CO)_6$ complexes are thought to arise from a combination of forward donation from the two bonding π molecular orbitals of the alkyne into the unfilled metal d orbitals and back donation from the filled metal orbitals into the vacant antibonding π molecular orbitals of the alkyne.[21]

Rxn. 2   RC≡CR' + Co₂(CO)₈ →(µ₂-RC≡CR')Co₂(CO)₆ + 2CO↑
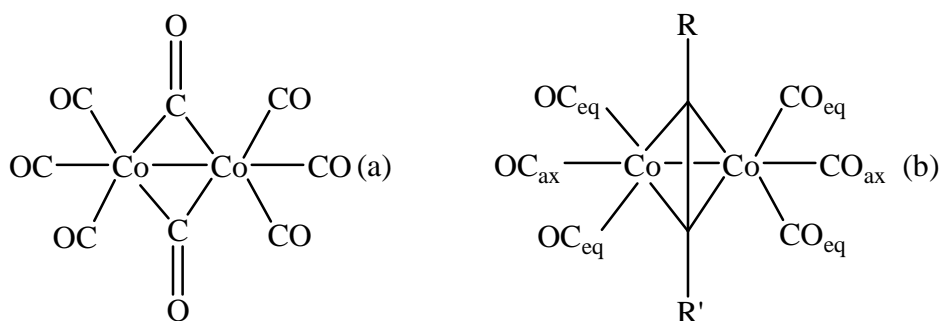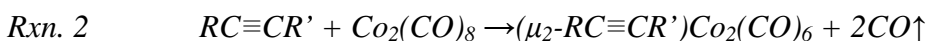
Figure. 10   (a) Structure of dicobalt octacarbonyl with bridging and terminal carbonyl groups, (b) structure of alkynyl dicobalt hexacarbonyl, (µ₂-R₂C₂)₂Co₂(CO)₆ showing the axial (ax) and equatorial (eq) carbonyl groups.

Sly reported the molecular configuration of diphenylacetylene dicobalt hexacarbonyl, one of the first molecules to exhibit a multi-point attachment of a single organic molecule to more than one metal.[22] The molecule was found to have six-fold coordination about each cobalt atom in a distorted octahedral with the C-C bond of the acetylene approximately normal to the Co-Co bond axis. The coordination about the acetylene carbon atoms is four-fold in a distorted tetrahedral configuration. This gives approximate C_{2v} symmetry to the molecule, except for the benzene rings. With most symmetric alkynes the molecules possess C_{2v} symmetry with distorted octahedral symmetry about the individual cobalt atoms.

A more recent theoretical study of the alkyne-bridged complex, $(\mu_2\text{-}C_2H_2)Co_2(CO)_6$, **61**, identified significant population of a Co-Co antibonding orbital along with Co-π* back bonding.[23] The authors used complete active space (CAS) methods along with Hartree-Fock and hybrid density functional theory (DFT) calculations for this study, as standard DFT and quantum theory of atoms in molecules (QTAIM) methods, although useful, were insufficient to reveal the fine detail in the region between bridged metal atoms. The occupation of bonding and antibonding orbitals in the CAS molecular calculations suggested a rather more complex picture of metal-metal and metal-ligand bonding than might be initially inferred. Using CAS in conjunction with QTAIM, a deeper insight into the bonding was gained. Surprisingly, there was no bond critical point (bcp) observed in the region between cobalt nuclei, although four Co-C_{alkyne} bonds were observed in the analysis, along with all other expected bond critical points (Co-C_{CO}, C-C, C-O and C-H). This indicated the presence of two three - membered metallocycles in the Co_2C core, sometimes referred to as a "butterfly arrangement". Hartree-Fock calculations explore metal-metal bonding where a value of 1.0 indicates a single bond. The authors, who calculated a value of 0.26 for $\delta(Co,Co)$, using an adjusted theoretical method, state that the atomic overlap data suggested a weak but non-zero overlap between the cobalt atoms. Another diagnostic tool which calculates the ratio of potential to kinetic energy density at bond critical points was employed. A value of less than one indicates closed shell interaction while a value of greater than two indicates a shared or covalent interaction. A value of 1.34 at the mid-point of the Co-Co vector and other values across the vector were observed. Consistent with other results, it points to some covalent character in the metal-metal region. The authors suggested that the complex was best described as a singlet

diradical with partial occupation of both bonding and antibonding orbitals between cobalt atoms.

The structure of (μ_2-alkyne)$Co_2(CO)_6$ derivatives are based on a central Co_2C_2 tetrahedrane with an external "R" group on each carbon and three terminal carbonyl groups on each cobalt (Fig. 10 (b)). The Co_2C_2 tetrahedrane in an (μ_2-R_2C_2)$Co_2(CO)_6$ complex had 12 skeletal electrons localised along its six bonds that include four Co-C bonds, one C-C bond and one Co-Co bond. As discussed above the Co-Co bond is considered to be a formal single bond however some singlet diradical character of the Co-Co interaction has been observed. Using DFT calculations, model complexes of the form (μ_2-R_2C_2)$Co_2(CO)_n$ ($n <$ 6) were used for a theoretical study investigating the preferred structure for alkynyl dicobalt hexacarbonyl complexes.[24] Structures of (μ_2-C_2H_2)$Co_2(CO)_6$ (**61**), (μ_2-C_2H_2)$Co_2(CO)_5$, (μ_2-C_2H_2)$Co_2(CO)_4$ were investigated (formal Co=Co double and Co≡Co triple bonds were required to give both cobalt atoms the favoured 18-electron configurations in the pentacarbonyl and tetracarbonyl respectively). An eclipsed C_{2v} structure was the preferred structure for (μ_2-C_2H_2)$Co_2(CO)_6$ (**61**, Fig. 11) with two axial carbonyls approximately *trans* to the Co-Co bond and the remaining four carbonyls are equatorial in approximate *trans* positions relative to the Co-C bonds attached to the acetylene carbon. The Co-CO bond lengths were predicted to be longer for those in equatorial positions (Co-CO_{eq} ~ 0.04 Å longer than Co-CO_{ax}) suggesting that the acetylene ligand has a stronger *trans* effect than the Co-Co bond. Three structures were found for the pentacarbonyl derivative, (μ_2-C_2H_2)$Co_2(CO)_5$. The lowest energy structure is derived by removal of an equatorial carbonyl group (a carbonyl group *trans* to the acetylene) and can be referred to as *eq*-(μ_2-C_2H_2)$Co_2(CO)_5$. The second is a C_{2v} singly bridged (μ_2-C_2H_2)$Co_2(CO)_4$(μ-CO) structure. The bridging carbonyl group exhibits a relatively low v(CO) stretch at 1878 cm^{-1} typical for bridging carbonyl groups compared to terminal carbonyl groups. The third pentacarbonyl structure is the result of loss of an axial carbonyl group, *ax*-(μ_2-C_2H_2)$Co_2(CO)_5$ and lies a predicted ~ 10 kcal above the equatorial structure. In both the axial and equatorial pentacarbonyl species one cobalt atom is assigned the favoured 18-electron configuration while the other cobalt atom bearing only two terminal carbonyls has only a 16-electron configuration. Removal of two carbonyl groups from the parent hexacarbonyl species resulted in (μ_2-C_2H_2)$Co_2(CO)_4$ to give six different structures.

The three lowest energy structures are derived by removal of two carbonyl groups from different cobalt atoms so that each have two $Co(CO)_2$ units in their structure.
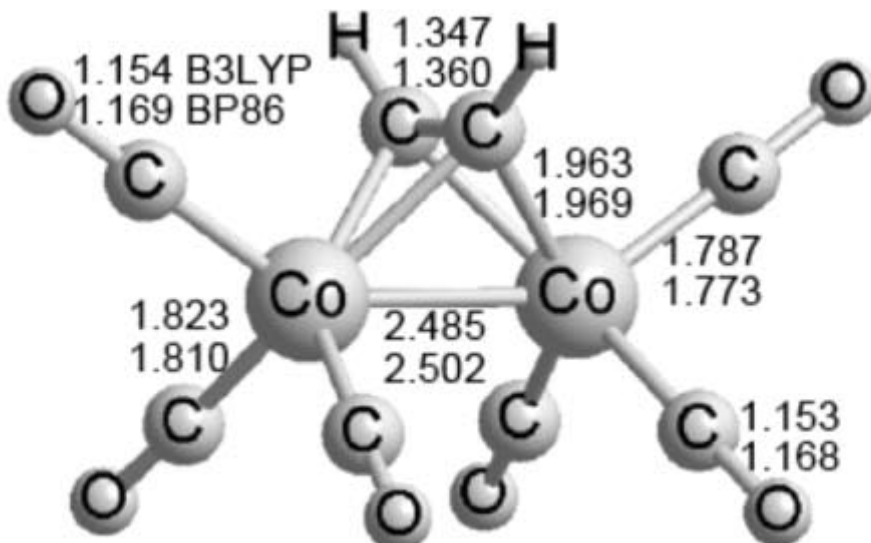
Figure 11   *(μ_2-C_2H_2)Co_2(CO)$_6$ (**61**) with proposed C_{2v} symmetry.*[24]

A series of oligothiophene derivatives were synthesised in which two dicobalt hexacarbonyl acetylides were π-conjugated onto both terminals of the oligothiophene.[25] A variety of substituents were grafted onto the oligothiophenes to tune their physical properties. Heck coupling techniques were used to produce the organic compounds (**62a –66a**, Scheme 2) and reaction with dicobalt octacarbonyl gave the alkyne dicobalt hexacarbonyl derivatives (**62b – 66b**, Scheme 2). The absorbance spectra of the oligothiophene moieties displayed moderately intense high energy transitions and a very intense lower energy transition which the authors attributed to π – π* localised excitation of the heteronucleus and π – π* transitions of the conjugated π – system, respectively. The λ_{max} values of the higher energy bands were blue-shifted on increasing the number of thienyl units (λ_{max} **62a** = 305 nm, **64a** = 257 nm, **66a** = 254 nm) with similar trends observed for the phenyl substituted oligomers. The complexes (**62b – 66b**) exhibited three characteristic bands: a moderately intense high-energy band, a strong medium-energy band and a weak low-energy band. The high energy bands were ascribed to the π – π* localised excitation within the organic component while the medium and low energy bands were

182

attributed to metal to ligand (d_{Co}-π^*_{ligand}) charge transfer transitions. Electrochemical studies of **62a – 66a** exhibited one highly irreversible oxidation process (two for **65a**), the potential of which decreases gradually on going from **62a** to **64a** to **65a** in the hexynyl substituted oligothiophene series and from **63a** to **65a** in the phenylethynyl substituted series, indicating the decrease of the π-conjugation length in serial order. The complexes (**62b – 66b**) exhibited two oligothiophene based oxidation processes (one for **63b**) between -0.2 and +1.5 V *vs.* Ag/AgCl, and one reduction process of the metal moiety between 0.0 and -1.6 V *vs.* Ag/AgCl, which was not observed for the oligothiophenes. The complexes only possess one irreversible reduction process compared to the two reductions commonly observed in these bimetallic systems the authors suggested that the redox centres were independent of each other. The lack of electronic communication between the metal centres is attributed to the reduction process followed by fast chemical reactions *via* an EC mechanism.

62: X = 1, R = *n*-butyl
63: X = 1, R = phenyl
64: X = 2, R = *n*-butyl
65: X = 2, R = phenyl
66: X = 3, R = *n*-butyl
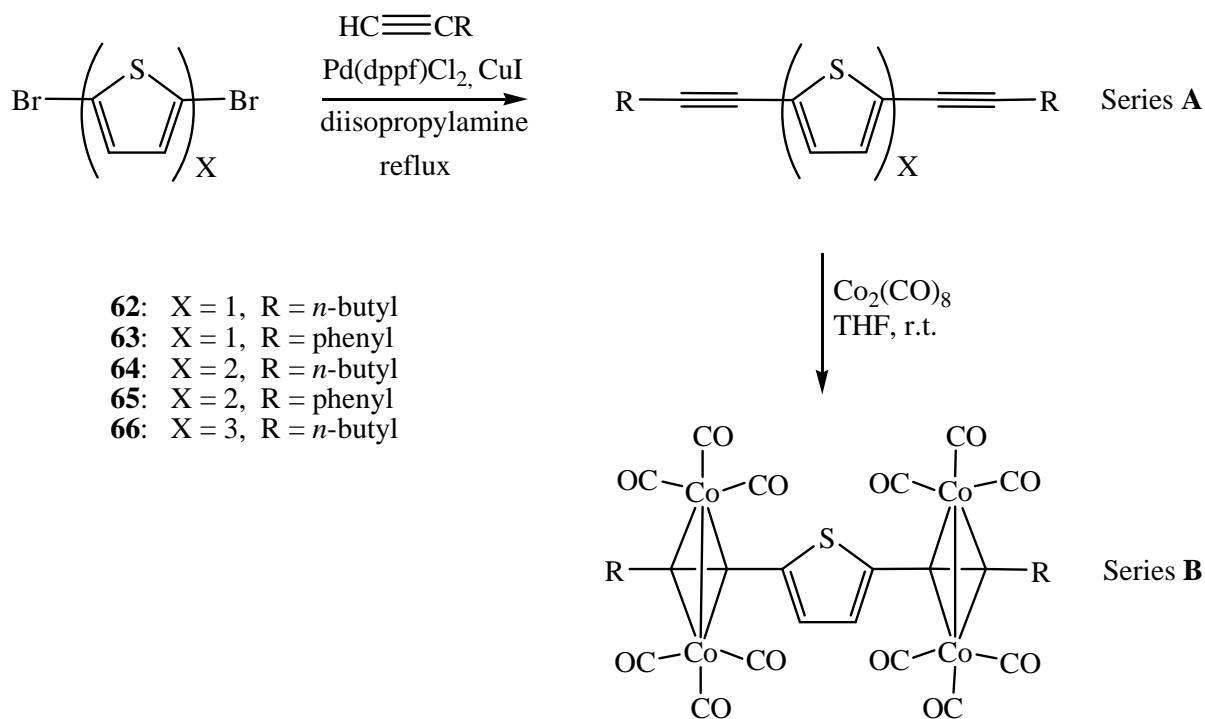
Scheme 3   *Synthesis of thienylethynyl ligands and corresponding bimetallic complexes.*

Ferrocene is an electron donating group where the ferrocenyl donor group can be linked *via* an electron-rich backbone to a polyaromatic acceptor moiety.[26] The attachment of adjacent organometallic moieties *via* alkyne linkages results in electronic interactions between metal atoms. These complexes are of interest because of the possibility of charge transfer along a conjugated backbone and the potential for tuneable redox behaviour. The modification of ferrocene substituted (μ_2-alkyne)$Co_2(CO)_6$ complexes enabled the assessment of the effect of structural changes imposed by changing the position and substituents on ferrocenylalkynes. The ferrocenylalkynyl ligands were synthesised by standard coupling methods followed by treatment with cobalt octacarbonyl to produce the complexes **67 - 72** in figure 12. The incorporation of one or two dicobalt carbonyl moieties into the alkynyl chain caused a reduction in triple bond character observed as a downfield shift in the proton and carbon NMR spectra of the products. Crystal structures of **68**, **69** and **72** were obtained and observed Co-Co bond lengths were in the range 2.46 – 2.47 Å, in agreement with previously reported dicobalt systems bridged by perpendicular alkynes. The interaction of the alkyne with $Co_2(CO)_6$ units resulted in delocalisation of the electron density onto the Co_2 unit which caused a lengthening of the alkyne bond, consistent with loss of triple bond character as observed in the NMR. In complex **68** the free alkyne unit retains its linearity as expected and the relevant bond length was consistent with the retention of its triple bond character (1.20 Å). Phosphine substitution of carbonyl ligands in the dicobalt hexacarbonyl complexes occurred. Complex **67** was treated with 1 equivalent of 1,1-bis(diphenylphosphino)methane (dppm) and 1.5 equivalents of 1,1-bis(diphenylphosphino)ferrocene (dppf) to produce the phosphine substituted ethynylferrocene : dppm in 1:1 ratio and ethynylferrocene : dppf in 2:3 ratio respectively. In this manner the electronic environment of the metal atoms can be modified *via* replacement of some carbonyl groups by suitable chiral phosphine ligands.

Fc — H   **67**

Co — Co

Fc — C_{60} — H   **70**

Co — Co

Fc ——— Fc   **68**

Co — Co

Fc — Fc ——— Ph   **71**

Co — Co

Fc — Fc   **69**

Co — Co   Co — Co

Fc — Fc — Ph   **72**

Co — Co   Co — Co

where Fc = Ferrocenyl and

= $Co_2(CO)_6$

Co — Co
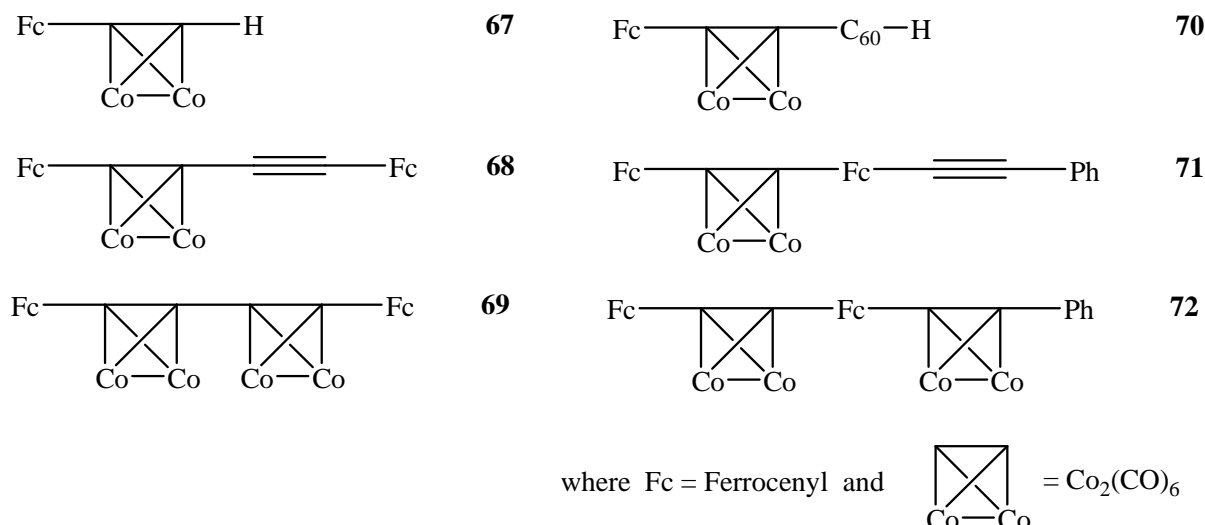
Figure 12   *Ferrocenyl alkynyl dicobalt hexacarbonyl complexes.*

Coleman et al. synthesised a series of pyrene-thiophene dyads and their corresponding dicobalt hexacarbonyl complexes (**73a\b – 76a\b**, Fig. 13).[27] In the UV-vis absorbance spectra a high energy transition was observed between 320 – 400 nm and ascribed to the π – π^* transitions within the pyrenylacetylene chromophore. Coordination of dicobalt carbonyl resulted in broader, less well-defined spectra with additional weak d-d bands in the range 580-600 nm that extended to approximately 700 nm. Visible excitation led to luminescence for all compounds in the series. No shift was observed in the emission bands following complexation which suggested the origin of the emission band is ligand based. At room temperature all compounds were found to be strongly luminescent. Compounds **73a** and **74a** displayed two emission bands at 404, 425 nm and 410, 430 nm respectively. For **75a** and **76a** a single intense emission band, at 503 and 612 nm respectively, was observed with significantly larger Stokes shifts (~3800 and ~4600 cm^{-1} respectively) indicating that the aldehyde and dicyanovinyl terminal units had a destabilising effect. The bathochromic shift in emission maxima, on altering the terminal moiety, was attributed to the electron accepting ability of the dicyanovinyl unit. Emission lifetimes were measured as 0.16, 0.64, 0.88 and 1.16 ns of **73a**, **74a**, **75a** and **76a**. Following coordination with $Co_2(CO)_6$ a large reduction in the emission intensity (> 95 %) was observed. Emission quenching had been previously reported for metal carbonyl complexed fluorescent organic compounds. Low temperature (77 K) emission studies showed no change in the emission bands of **73b** and **74b**. However the emission band of **75b** was blue shifted by 2650 cm^{-1} to

444 nm while the emission band of **76b** was blue shifted by ~2890 cm^{-1} to 520 nm. The authors attributed quenching to energy transfer to the cobalt carbonyl system. All compounds (**73a\b – 76a\b**) exhibited an oxidation in the range +1.0 – 1.1 V *vs.* Ag/Ag$^+$, which was assigned to the irreversible oxidation of the pyrene unit. Oxidation at high positive potentials led to the deposition of a film onto the working and counter electrode surfaces. This suggested that electropolymerisation occurred at high positive potentials, a process observed in other thiophene systems. An irreversible oxidation process is observed in the range +0.55 – 0.70 V *vs.* Ag/Ag$^+$ in all cases following complexation (**73b – 76b**). This was assigned to the oxidation of the cobalt metal centre. Steady state photolysis was carried out on **73b – 76b** with IR monitoring. Irradiation at $\lambda_{exc.} > 520$ nm in the presence of PPh$_3$, resulted in bleaching of the parent absorbance bands together with generation of product bands assigned to the pentacarbonyl species. Subsequent irradiation at $\lambda_{exc.} > 400$ nm caused further bleaching of the parent bands and an increase in intensity of the photoproduct. Also observed under these conditions were new bands assigned to the tetracarbonyl species.
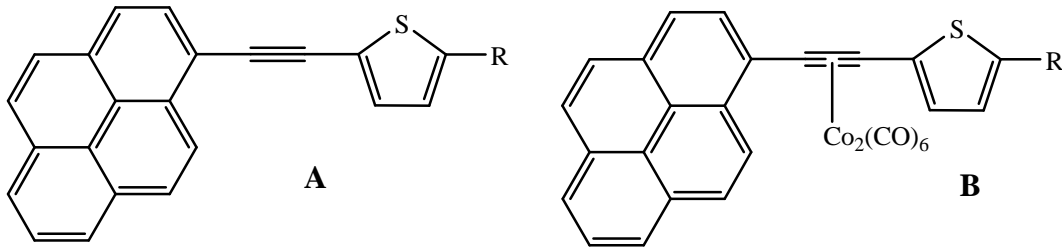
73 : R = H
74 : R = Br
75 : R = CHO
76 : R = CH(CN)$_2$

Figure 13   *Pyrenylethynylthienyl compounds and complexes with various end groups.*

(μ_2-Alkyne)Co$_2$(CO)$_6$ derivatives have been shown to undergo replacement of one or both axial CO groups upon heating with monodentate tertiary phosphines, phosphites and arsines.[28] Bidentate ligands, such as fluorocarbon- and hydrocarbon-bridged compounds, reacted similarly but they displaced two or four CO groups. The bidentate ligands tended to occupy equatorial coordination points about the metal atoms either by bridging two

cobalt atoms of the same molecule (Fig. 14, b) or by chelating to one of them (Fig. 14, c). An investigation into carbonyl substitution reactions of $(\mu_2\text{-}RC\equiv CR')Co_2(CO)_6$ (where R/R' = H, phenyl or CH_2OH) was under taken for a range of monodentate ligands (L). In each case, heating the $(\mu_2\text{-alkyne})Co_2(CO)_6$ complexes with the monodentate ligand resulted in the formation the pentacarbonyl product of the form $(\mu_2\text{-}RC\equiv CR')Co_2(CO)_5L$ (Rxn. 3). It was found that further reaction of the alkynyl dicobalt pentacarbonyl product with a monodentate ligand resulted in a greater substitution pattern for the complex i.e. disubstituted, trisubstituted and tetrasubstituted complexes of the form $(\mu_2\text{-}RC\equiv CR')Co_2(CO)_4L_2$, $(\mu_2\text{-}RC\equiv CR')Co_2(CO)_3L_3$ and $(\mu_2\text{-}RC\equiv CR')Co_2(CO)_2L_4$ respectively. Reaction of the ligand substituted carbonyl products $(\mu_2\text{-}RC\equiv CR')Co_2(CO)_{6\text{-}n}L_n$ with CO replaced the monodentate ligand to regenerate the parent compound (Rxn. 4). Fluorocarbon bridged ditertary phosphines and arsines (denoted as L-L) reacted with $(\mu_2\text{-alkyne})Co_2(CO)_6$ and produced complexes of form $(\mu_2\text{-alkyne})Co_2(CO)_4(L\text{-}L)$ which were ligand bridged. The bidentate ligands f_4fos and f_4fars (abbreviations pg. xv) produced the bridged disubstituted complexes (Rxn. 5) while further reaction of the disubstituted complex with f_4fars/f_4fos produced the tetrasubstituted complexes. The reaction of the tetrasubstituted alkynyl dicobalt carbonyl with CO resulted in the regeneration of the disubstituted complex (60 %) by displacement of one bidentate ligand with two CO molecules (Rxn. 6). Complexes of the formula $(\mu_2\text{-alkyne})Co_2(CO)_4(L\text{-}L)$ fall into two classes. The first class of $(\mu_2\text{-}RC\equiv CR')Co_2(CO)_4(L\text{-}L)$ complexes (where L-L = f_4fos, f_4fars, f_6fars, f_4AsP and dppm, (abbreviations pg. xv) all had terminal carbonyl stretching bands in their IR spectrum (in the region 1959 – 2038 cm^{-1}) similar to those of $(f_4fos)Co_2(CO)_6$, and hence the authors assigned a bridged structure to these complexes (Fig. 14, b). The second class of $(\mu_2\text{-}RC\equiv CR')Co_2(CO)_4(L\text{-}L)$ complexes (where L-L = f_6fos and f_8fos) had carbonyl stretching bands at higher frequencies (1963 – 2056 cm^{-1}), indicating that complexes of this type produced chelates (Fig. 14, b).

$(\mu_2\text{-}RC\equiv CR')Co_2(CO)_6 + P(CH_3O)_3 \rightarrow (\mu_2\text{-}RC\equiv CR')Co_2(CO)_5(P(CH_3O)_3) + CO$
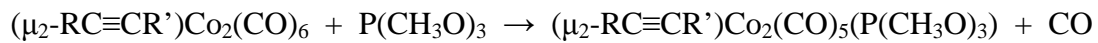
Rxn 3 Substitution with monodentate ligand P(CH$_3$O)$_3$ producing pentacarbonyl complex.

$(\mu_2\text{-}RC\equiv CR')Co_2(CO)_2(P(CH_3O)_3)_4 + CO \rightarrow (\mu_2\text{-}RC\equiv CR')Co_2(CO)_3(P(CH_3O)_3)_3$

Rxn. 4 Replacement monodentate ligands following reaction with CO.

$(\mu_2\text{-RC}\equiv\text{CR'})\text{Co}_2(\text{CO})_6 + \text{f}_4\text{fos} \rightarrow (\mu_2\text{-RC}\equiv\text{CR'})\text{Co}_2(\text{CO})_4(\text{f}_4\text{fos}) + 2\text{CO}$
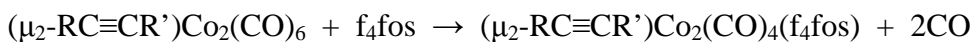
Rxn. 5 Substitution with bidentate ligand producing tetracarbonyl complex

$(\mu_2\text{-RC}\equiv\text{CR'})\text{Co}_2(\text{CO})_2(\text{f}_4\text{fos})_2 + 2\text{CO} \rightarrow (\mu_2\text{-RC}\equiv\text{CR'})\text{Co}_2(\text{CO})_4(\text{f}_4\text{fos})$

Rxn. 6 Replacement bidentate ligand following reaction with 2 equivalents of CO.
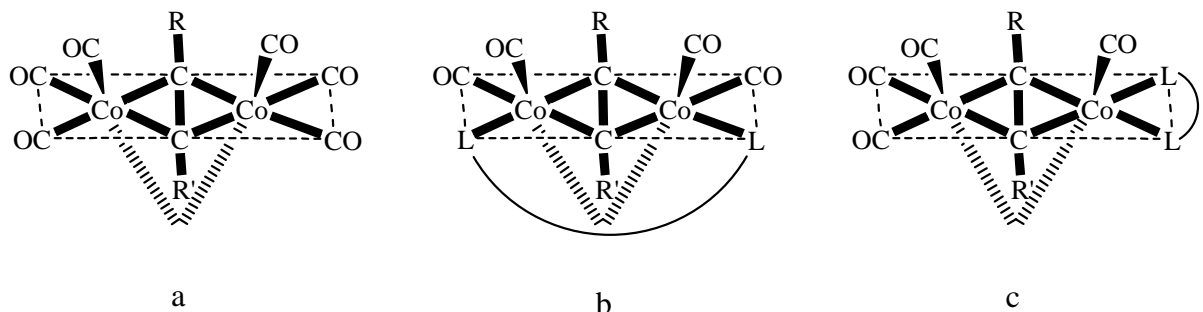
Figure 14   Representative structures of $(\mu_2\text{-RC}\equiv\text{CR'})\text{Co}_2(\text{CO})_6$ complex and the two classes of carbonyl bonded complexes.

Ford et al. used time resolved spectroscopy (TRIR) to extensively examine the reactive photoproducts produced on irradiation (continuous and flash photolysis) of the hyrdoformylation catalyst precursor $\text{Co}_2(\text{CO})_6(\text{PMePh}_2)_2$.[29]   The UV-vis absorbance spectrum of $\text{Co}_2(\text{CO})_6(\text{PMePh}_2)_2$ possessed a characteristic $\sigma\text{-}\sigma^*$ transition with a λ_{max} at 386 nm, assigned to a metal-metal bonded dimer by analogy to the spectra of similar compounds such as $\text{Co}_2(\text{CO})_8$. The infrared spectrum shows a carbonyl stretching band centred at 1953 cm^{-1} with shoulders at ~1928 and ~1975 cm^{-1}.

Continuous photolysis ($\lambda_{exc} = 365$ nm) of $\text{Co}_2(\text{CO})_6(\text{PMePh}_2)_2$ in benzene was carried out under different conditions: (1) under an atmosphere of argon, (2) under an atmosphere of CO and (3) under argon with added PMePh$_2$. (1) Photolysis under argon resulted in small decreases in the 386 nm absorbance band with no new bands appearing in the UV-vis spectrum. In the IR spectrum, similar irradiation caused slow bleaching of the parent band with new broad $\nu(\text{CO})$ stretches between 1980 and 2040 cm^{-1}, which were tentatively

188

assigned to the formation of a cobalt cluster complex. (2) Under an atmosphere of CO, photolysis at 365 nm resulted in significant changes on a much faster timescale. The $Co_2(CO)_6(PMePh_2)_2$ absorbance at 386 nm decreased in intensity and shifted hypsochromically with concomitant generation of a new absorbance at 340 nm and an isobestic point at 362 nm. This rapidly occurring spectral change ceased after ~90 s irradiation indicating that the system had reached a photostationary state (Rxn. 7). The changes observed were attributed to formation of a dinuclear complex such as $Co_2(CO)_7(PMePh_2)$ as the characteristic σ-σ* transition of a Co-Co bond remained. The IR difference spectrum produced positive peaks at 1987, 2022 and 2078 cm^{-1}, which suggested the formation of the $PMePh_2$ loss product as the bands matched well with literature results for the spectrum of $Co_2(CO)_7(PPh_3)$. (3) Photolysis of $Co_2(CO)_6(PMePh_2)_2$ in benzene under argon with added $PMePh_3$ led to very different spectral changes in the infrared. A decrease in parent bands was observed while new bands formed at 1749, 1770 and 1998 cm^{-1}, consistent with the formation of $Co_2(CO)_5(PMePh_2)_3$.

$$Co_2(CO)_6(PMePh_2)_2 \ + \ CO \ \underset{h\nu}{\overset{h\nu}{\rightleftharpoons}} \ Co_2(CO)_7(PMePh_2) \ + \ PMePh_2$$
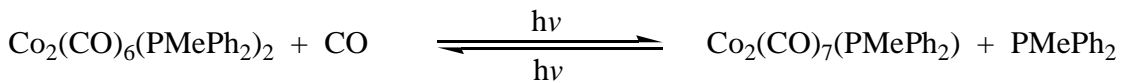
Rxn. 7

Interestingly, continued photolysis (λ_{exc} = 365 nm) of $Co_2(CO)_6(PMePh_2)_2$ in the chlorinated solvent 1,2-dichloroethane (DCE) produced markedly different results. Under an argon atmosphere the intensity of the σ-σ* transition at 386 nm rapidly decreased with no new bands generated. This is ascribed to photo-induced homolysis of the metal-metal bond to give the mononuclear "17-electron" metal based radicals, $\cdot Co(CO)_3(PMePh_2)$ (**A**, Scheme 3). These radicals can undergo two processes either bimolecular reaction with another such radical to reform the metal-metal bond (**B**, Scheme 3) or extraction of a chlorine atom from the solvent to form mononuclear chlorinated products (**C**, Scheme 3). Monitoring the reaction by IR spectroscopy provided further evidence for the formation of chlorinated mononuclear photoproducts. Bleaching of the ν(CO) bands characteristic of $Co_2(CO)_6L_2$ with concomitant growth of bands at 1981 and 1917 cm^{-1} were observed

which indicated the formation of $Co(CO)_3(PMePh_2)Cl$. Similar analogues, $Co(CO)_3(PEt_3)Cl$ and $Co(CO)_3(PEt_3)I$ were previously reported to display a strong $v(CO)$ band at 1977 and 1976 cm^{-1} respectively previously. Using various concentrations of DCE added to benzene the quantum yield for the disappearance of $Co_2(CO)_6(PMePh_2)_2$ followed by formation of $Co(CO)_3(PMePh_2)Cl$ upon irradiation was determined. The Φ values showed increased generation of the chlorinated photoproduct with increasing DCE concentration. This dependence of quantum yield on [DCE] is consistent with the photochemical homolytic cleavage of $Co_2(CO)_6(PMePh_2)_2$ to give the radical $\cdot Co(CO)_3(PMePh_2)$. This radical is expected to either react competitively by a second order recombination to give the parent carbonyl or with excess DCE by a pseudo first order pathway to give the mononuclear chlorinated species. The results obtained by Ford and co-workers are in agreement with previous studies that show dinuclear complexes can undergo both ligand labialisation and metal-metal bond homolysis when irradiated.[30]

$$Co_2(CO)_6(PMePh_2)_2 \xrightarrow{h\nu\,=\,365\,\text{nm}} [Co_2(CO)_6(PMePh_2)_2]^*$$

$$\mathbf{B}$$

$$2\ {}^{\bullet}Co(CO)_3(PMePh_2) \xrightarrow{DCE} Co(CO)_3(PMePh_2)Cl$$

$$\mathbf{A} \qquad\qquad \mathbf{C}$$
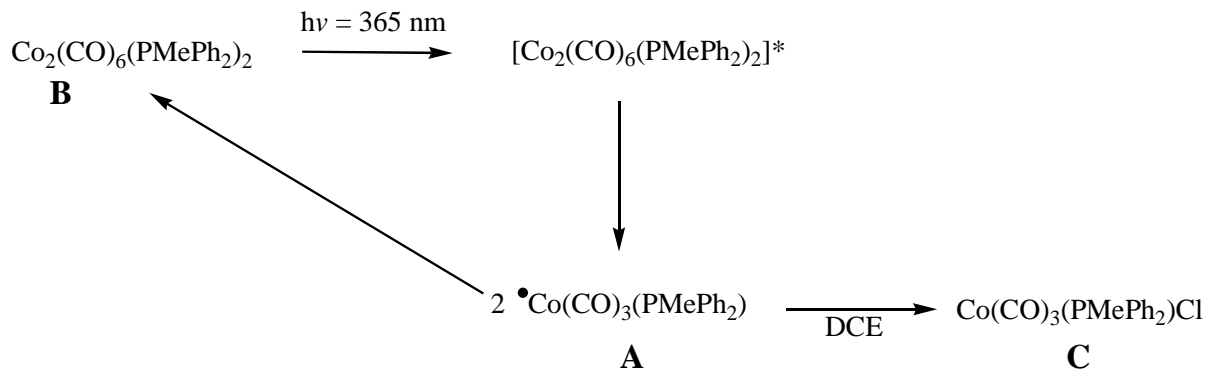
Scheme 3   Photochemical pathways following irradiation of Co₂(CO)₆(PMePh₂)₂ in DCE.

Flash photolysis studies were carried out (1) under argon, (2) under CO and (3) under argon with an excess of PMePh$_2$, to further investigate photochemical pathways and obtain kinetic data. (1) Flash photolysis of $Co_2(CO)_6(PMePh_2)_2$ in C_6D_6 under argon (λ_{exc} = 308 and 355 nm) resulted in bleaching of the parent carbonyl bands with simultaneous growth of a major product peak centred at 1940 cm^{-1}, 12 cm^{-1} lower than to the parent absorbance at 1952 cm^{-1}. The magnitude of the bleach of $Co_2(CO)_6(PMePh_2)_2$ was comparable for 308

and 355 nm photolysis however the absorbance at 1940 cm[1] was considerably larger in magnitude following 355 nm photolysis indicating that different photolysis wavelengths gave rise to different intermediates or else a different distribution of photoproducts. Kinetic traces of the changes in absorbance suggested that two photo processes occur. The faster process had a 2nd order rate constant of 2×10^7 M^{-1} s^{-1} following 308 nm excitation and 8×10^7 M^{-1} s^{-1} following 355 nm excitation, while the slower process had a higher rate constant (9.6×10^5 M^{-1} s^{-1}) following 308 nm irradiation compared to (2.4×10^5 M^{-1} s^{-1}) 355 nm irradiation. This indicated the slower process was preferentially preformed on 308 nm excitation. This was in keeping with other polynuclear metal carbonyl studies,[31] where CO photodissociation occurred preferentially following shorter wavelength irradiation. (2) Flash photolysis of $Co_2(CO)_6(PMePh_2)_2$ in C_6D_6 under a CO atmosphere (λ_{exc} = 308 and 355 nm) also resulted in bleaching of the parent absorbance at 1952 cm^{-1} with concomitant growth of a product band at 1939 cm^{-1}. Analysis of the transient decay of the absorbance at 1939 cm^{-1}, following 308 nm irradiation, *via* a double exponential fit, indicated that two photoprocesses occur which both absorb at 1940 cm^{-1} and both react with free CO. The faster component with a second order rate constant (2.6×10^6 M^{-1} s^{-1}) was ascribed to the CO loss product $Co_2(CO)_5(PMePh_2)_2$ reacting with CO to reform the parent species. The slower component with a second order rate constant (1.5×10^5 M^{-1} s^{-1}) was ascribed to the reaction of the photogenerated radical species $\cdot Co(CO)_3(PMePh_2)$ with CO *via* ligand dissociation to form $Co(CO)_4$. (3) Following photolysis of $Co_2(CO)_6(PMePh_2)_2$ in C_6D_6 (λ_{exc} = 308 nm) with added $PMePh_2$ three temporal processes were observed. An immediate bleach at 1950 cm^{-1} corresponded to the photolytic depletion of the parent carbonyl complex owing to primary photochemistry, a continued absorbance decrease at 1950 cm^{-1} due to the decay of transient species and a slow increase in absorbance attributed to formation of $Co_2(CO)_5(PMePh_2)_3$. The absorbance at 1940 cm^{-1} which corresponded to the intermediates $Co_2(CO)_5(PMePh_2)_2$ and $\cdot Co(CO)_3(PMePh_2)$ appeared then decayed below baseline as both transient species reacted with $PMePh_2$ according to (pseudo) first order kinetics. The reaction of $Co_2(CO)_5(PMePh_2)_2$ to produce $Co_2(CO)_5(PMePh_2)_3$ had a rate constant of 3.9×10^7 M^{-1} s^{-1}.

3.1.6 Pauson – Khand Reaction

The compounds produced from the reaction of alkynes with transition metals have found wide ranging uses but none more so than those of the type $(\mu_2\text{-alkyne})Co_2(CO)_6$ as they are important precursors in the formation of derivatised cyclopentanones. Metal-mediated co-cyclisation reactions have become more widely used in recent years especially since the discovery of the Pauson – Khand reaction (PKR).[32] The products of the PKR can be highly regio- and stereo-chemically pure and as such are invaluable synthetic intermediates in a number of natural products syntheses, the synthesis of biologically important compounds such as prostaglandins,[33] hirsutic acid[34] and *trans*-dihydrojasmonate[35] being just three examples.

The Pauson – Khand reaction represents the formal [2 + 2 + 1] cycloaddition involving an alkene, alkyne and carbon monoxide to produce derivatised cyclopentanones and represents one of the most convergent methods in the synthesis of such compounds. Although the exact mechanism of the PKR has yet to be elucidated, a chemically reasonable pathway was proposed by Magnus[36] and then by Schore,[37] in which the initially formed (μ-alkyne)dicobalt hexacarbonyl cluster (**d**, Scheme 4) loses a carbonyl ligand to form the pentacarbonyl cluster (**e**, Scheme 4) which provides an empty coordination site for alkene coordination (**f-1**, **f-2**, Scheme 4). It has been observed that the coordinating alkene positions itself closest to the least sterically bulky acetylenic substituent and that C-C bond formation occurs between this acetylenic carbon and the alkene. This results in the majority of cyclopentanones with the bulky acetylenic substituent in α position on the compound, next to the C=O bond. Subsequent coupling of the alkyne and alkene to form the metallocycle (**g**, Scheme 4), alkyl migration to incorporate the carbonyl moiety and reductive elimination of the cyclopentanone form the final product (**i**, Scheme 4).
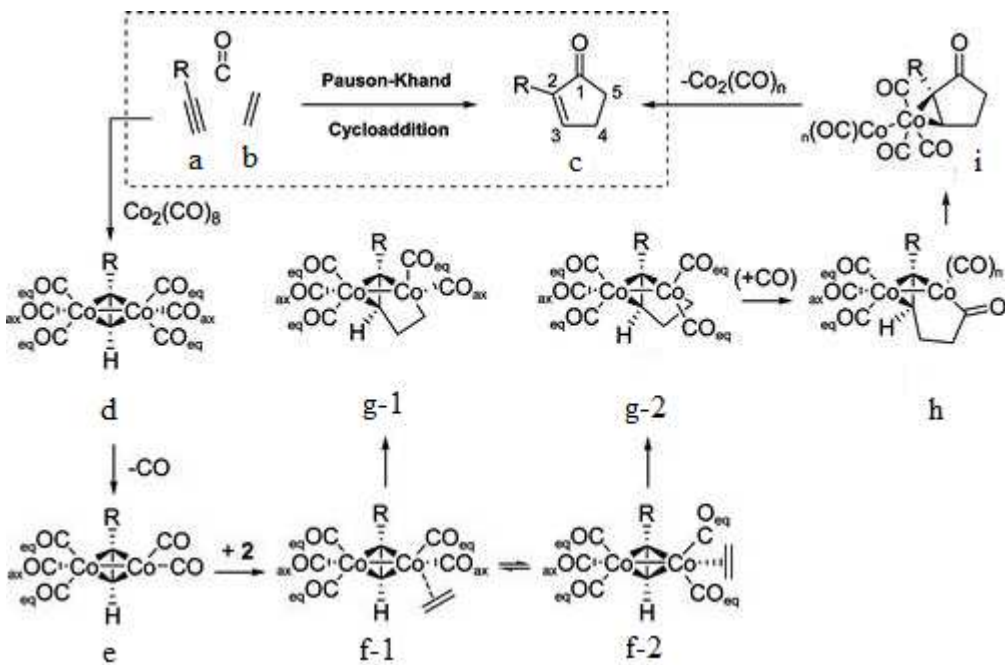
Scheme 4   *Proposed mechanism of the Pauson Khand reaction.* [38]

There are several disadvantages for the large scale commercial use of the classical PKR, namely the requirement for stoichiometric quantities of carbon monoxide (usually supplied by $Co_2(CO)_8$) and the high reaction temperature required. Several studies have been carried out in order to develop systems which use only catalytic quantities of the metal carbonyl compound and/or use light to prompt the chemical reaction. Metal carbonyl complexes undergo photoinduced CO dissociation and Livinghouse et al. used high-intensity visible light to facilitate catalytic Pauson- Khand reactions.[39] The purity of the dicobalt octacarbonyl catalyst and the choice of appropriate light source were found to be critical. Of those examined the Q-Beam light source proved most effective with a $Co_2(CO)_8$ concentration of 5 % providing the highest yields. Solvents including 1,2-dimethoxyethane (1,2-DME), ethyl acetate and diglyme also resulted in efficient conversion to the cyclopentanone. Thus under mild conditions (50 – 55 ºC) and 1 atm CO the photochemically driven PKR can proceed.

In order to aid elucidation of the mechanism of the photo-induced PKR, the photochemistry of phenylacetylene dicobalt hexacarbonyl, $(\mu_2\text{-PhC}\equiv\text{CH})\text{Co}_2(\text{CO})_6$, was

193

examined by matrix isolation techniques in conjunction with infra-red spectroscopy.[40] Irradiation of $(\mu_2\text{-PhC}\equiv\text{CH})\text{Co}_2(\text{CO})_6$ isolated in an argon matrix with $\lambda = 254$ nm resulted in depletion of the parent $v(\text{CO})$ stretches and formation of the coordinately unsaturated $(\mu_2\text{-PhC}\equiv\text{CH})\text{Co}_2(\text{CO})_5$ species ("e" type species, Scheme 4). A photostationary state was reached upon conversion of 25 % of the starting material. No evidence was observed for the formation of a tetracarbonyl species, even on extended irradiation. Broadband photolysis at > 400 nm regenerated the parent species although complete photoreversal could not be achieved. In an argon matrix doped with 10 % dinitrogen, irradiation at 254 nm resulted in the increased appearance of photoproducts with a greater amount of parent band depletion, indicative of a higher yielding photoreaction. The major photoproduct, the N_2 coordinated pentacarbonyl species $(\mu_2\text{-PhC}\equiv\text{CH})\text{Co}_2(\text{CO})_5\text{N}_2$, was observed as the appearance of new carbonyl stretches in the IR spectrum, along with a number of unknown species formed. Continued photolysis at 390 nm resulted in the coordinately unsaturated $(\mu_2\text{-PhC}\equiv\text{CH})\text{Co}_2(\text{CO})_5$ species but had little effect on the N_2 adduct. Broadband irradiation with $\lambda > 400$ nm, as observed in the argon matrix, resulted in bleaching of the product bands with simultaneous regeneration of the parent bands. Irradiation of $(\mu_2\text{-PhC}\equiv\text{CH})\text{Co}_2(\text{CO})_6$ in a 100 % nitrogen matrix using $\lambda = 254$ nm resulted in the rapid formation of the coordinated N_2 pentacarbonyl species. Generation of a second $v(\text{NN})$ band suggested the formation of a second N_2 coordinated photoproduct. Once again broadband irradiation at $\lambda > 400$ nm regenerated the parent species. Thus it was shown that the yield and rate of the pentacarbonyl formation increased as the N_2 matrix gas concentration increased. In pure argon matrices in-cage recombination of the photoejected CO with the pentacarbonyl species occurred readily. Also irradiation at 350 nm of the parent species $(\mu_2\text{-PhC}\equiv\text{CH})\text{Co}_2(\text{CO})_6$ had little effect; it appeared to be photochemically inert at this wavelength.

It is widely accepted that decarbonylation (d → e, Scheme 4) of an initially formed $(\mu_2\text{-alkyne})\text{Co}_2(\text{CO})_6$ species is the precondition to the overall Pauson – Khand reaction sequence. The photochemical properties of these important intermediates in the PKR were examined by Long and co-workers by both steady state and laser flash photolysis.[41] Generally these alkynyl dicobalt carbonyl compounds absorb across a broad range of wavelengths up to 630 nm providing a large choice of excitation wavelengths. Steady state photolysis of $(\mu_2\text{-PhC}\equiv\text{CH})\text{Co}_2(\text{CO})_6$ with $\lambda_{exc} > 340$ nm, in the presence of a trapping ligand (L = PPh_3 or C_5H_5N), produced the monosubstituted species, $(\mu_2\text{-}$

PhC≡CH)Co₂(CO)₅(L) with prolonged photolysis resulting in the disubstituted species **(μ₂-PhC≡CH)Co₂(CO)₄(L)₂**. Irradiation with $\lambda_{exc} > 400$ nm produced the same photoproducts although longer photolysis times were required. These results clearly showed that CO loss occurred *via* photochemical conditions, and the authors further investigated the process using monochromatic light sources. Laser flash photolysis of **(μ₂-RC₂H)Co₂(CO)₆** (R = C₆H₅ or H) in cyclohexane solution was carried out. Pulsed photolysis ($\lambda_{exc} > 355$ nm) resulted in depletion of the parent hexacarbonyl absorbances within the rise-time of the monitoring beam (~20 ns) followed by a rapid recovery to the pre-irradiation levels. No transient absorbance signals were detected as far out as 600 nm. The kinetics of the recovery to pre-irradiation absorbance levels was found to be first order with a rate constant of 4 x 10^7 s^{-1} at 298 K. The rate of recovery of the depleted absorbance was unaffected following the addition of CO to the solution which suggested that the depletion of the parent absorbance was not a result of CO loss. Experiments using pyridine as a trapping ligand in 20-fold excess with the parent hexacarbonyl compound produced spectral changes showing the depletion of the parent carbonyl that recovered with an identical rate constant to that measured in the presence of CO, indicating that the intermediate produced did not react with pyridine. No photochemistry occurred from irradiation with $\lambda_{exc} > 355$ nm, which was in keeping with the results of Gordon et al.[40] suggesting that **(μ₂-C₆H₅C₂H)Co₂(CO)₆** is not CO substitution labile at this wavelength. The spectral changes were attributed to homolytic cleavage of the cobalt – cobalt bond (Scheme 5), which rapidly underwent efficient recombination resulting in no permanent or long lived bleaching. However, pulsed photolysis with $\lambda_{exc} > 532$ nm produced a transient species that absorbed with a λ_{max} at 400 nm that was assigned to the pentacarbonyl species. Typical of the reaction of CO loss intermediates, addition of CO reduced the lifetime of the transient species although its yield remained unaffected. The observed rate constant, k_{obs}, was found to be linearly dependant on the concentration of CO, with a second order rate constant of 1.2 x 10^6 M^{-1} s^{-1} (298 K). In the presence of excess triphenylphosphine, irradiation produced a transient at 400 nm assigned to the pentacarbonyl species **(μ₂-RC₂H)Co₂(CO)₅(PPh₃)** (Scheme 5). The lifetime and yield of the transient species depended on the concentration of the PPh₃, as was the case in CO addition. The second order rate constant for the substitution was found to be 3 x 10^6 M^{-1} s^{-1} at 298 K.
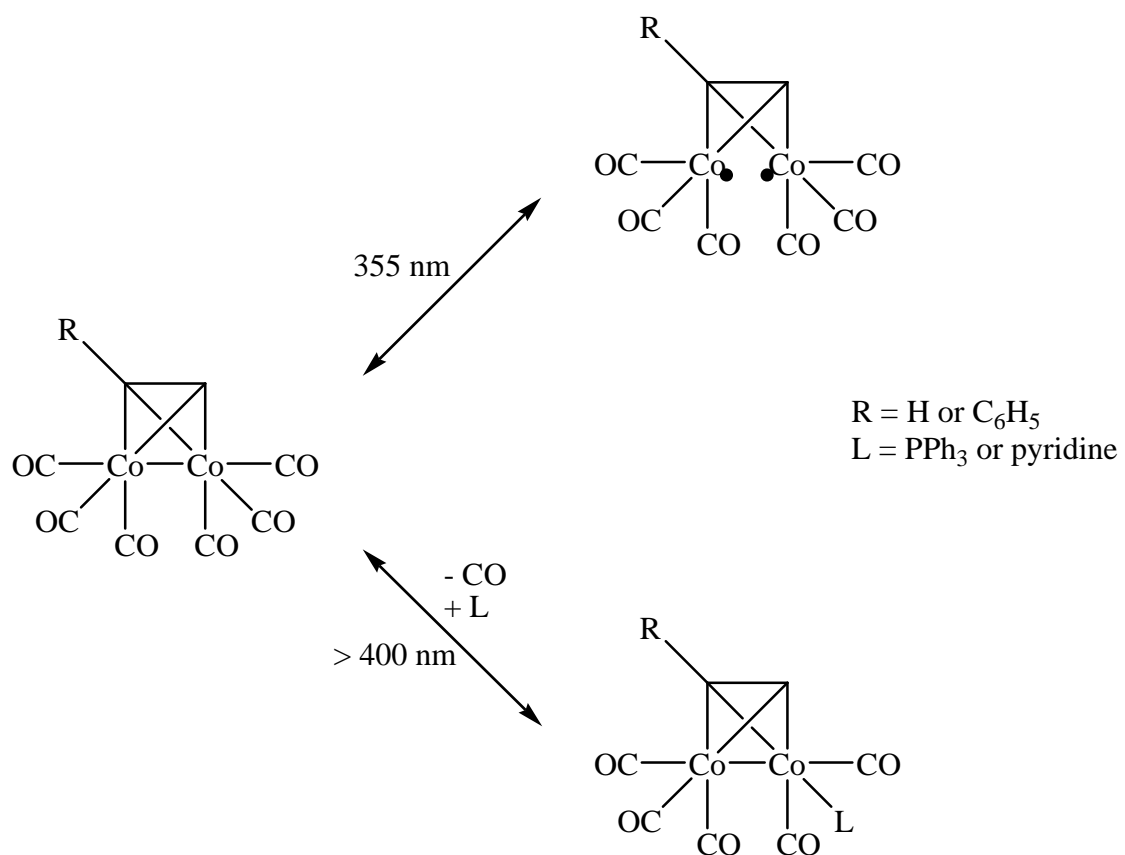
Scheme 5   *Observed wavelength dependent photochemistry of (**μ_2-RC$_2$H$_2$)Co$_2$(CO)$_6$** in cyclohexane solution, in the presence of either PPh$_3$ or pyridine.*

The factors influencing the regio-chemical outcome of the PKR were examined using theoretical methods.[42] In the vast majority of reactions, the larger acetylenic moiety was found at the α position in the resulting pentanone. The authors postulate that the regio-chemistry of the reaction is governed, through the discriminate loss of a CO, almost exclusively by the electronic nature of the acetylenic substituents. Numerous studies have indicated that the nature of these substituents can affect the electronic properties within the (μ_2-alkyne)Co$_2$(CO)$_6$ complex. [13]Carbon NMR analysis of the CO carbons in (μ_2-RC≡CR')Co$_2$(CO)$_6$ indicate that they are affected by the nature of the R/R' groups. An increase in the electron donating ability of the R groups causes downfield shifts of the CO resonances. Infra-red spectroscopy has also shown that the v(CO) stretches in the carbonyl region of the spectrum shift as a function of R/R' substituents. Increasing the electronegativity of R/R' causes an increase in the vibrational frequencies observed. The difference in electron density on the two acetylenic carbons in the complex may be

responsible for the discriminate loss of CO. DFT calculations indicated that different substituents on the acetylene give rise to different electronic densities on its carbon atoms which results in polarisation of the alkyne bond. The electronic effects caused by the different substituents influence the position from which carbon monoxide is lost and ultimately the regio-chemistry of the reaction. It is assumed that the initial step of CO loss from the (μ_2-alkyne)$Co_2(CO)_6$ provides a coordination site for the incoming alkene, the position of which fixes the regiochemistry of the resulting cyclopentanone adduct. In the case where the C_R of the acetylenic C_R-$C_{R'}$ bond possesses the larger electron density, a longer Co-CO bond length is calculated for the carbon monoxides that are *trans*-positioned with respect to R'. It is reasonable to expect that these CO ligands would dissociate more easily. A complex where the acetylenic C_R-$C_{R'}$ bond lacks significant polarisation, the Co-CO bond lengths were found to be almost identical. The CO ligands should dissociate with equal facility and therefore steric effects as opposed to electronic effects become the determining factor. Finally in the case where the acetylene substituents are sterically virtually identical but electronically different the result was found to be the same. The $C_{R'}$ of the C_R-$C_{R'}$ polarised bond had the higher electron density and resulted in the carbon monoxides that are *cis*-positioned with respect to the dissociating R group. This provides an alternative to the "steric rationale" for mechanistic interpretation of the PKR.

Recently, a series of (μ_2-alkyne)$Co_2(CO)_5$(η^2-alkene) complexes have been reported and as such are the first isolated examples in the next step of the PKR.[38] A range of 5-alkynyl-5*H*-dibenzo[*a,d*]cycloheptenes (**77 – 82A**, Fig. 15) were allowed to react with dicobalt octacarbonyl and two products were isolated: the major product (57 – 88 %) was the anticipated hexacarbonyl cluster (**77 – 82B**, Fig. 15) and the minor product (6.5 – 16 %) was the pentacarbonyl complex (**77 – 82C**, Fig. 15). In the pentacarbonyl species the third ligand site on one of the cobalt centres is occupied by the double bond of the seven membered ring. The thermal instability of the hexacarbonyl clusters and therefore the facile reaction to form the pentacarbonyl complex was surprising, decarbonylation of the hexacarbonyl and formation of the pentacarbonyl complex occurred in solution at room temperature. The authors suggested that CO loss was compensated for by formation of the cobalt-alkene complex as a chelate. Several theoretical studies calculated geometries for the incoming ethylene and found it favours a pseudoaxial site such that the distance between an alkene carbon and the nearer alkyne carbon is approximately 2.95 Å.

Crystallographic structures of (μ_2-alkyne)$Co_2(CO)_5$(η^2-alkene) complexes (**77 – 82C**, Fig. 15) revealed carbon-alkene-carbon distances of 2.133 to 2.184 Å, with cobalt-complexes alkene carbons within 2.817 – 2.880 Å from the nearer alkyne carbon, somewhat shorter than expected. Despite the proximity of these carbons, the pentacarbonyl complexes were reasonably stable and the PKR did not continue to the corresponding cyclopentanones (**77 – 82D**, Fig. 15). The authors postulated that alkene insertion in this type of complex occurred preferentially from the equatorial position and the continuation of the PKR was precluded by severe ring strain caused by the rigidity of this class of compound (**77 – 82C**). The activation energy for the decarbonylation process was found to be ~29 kcal mol^{-1} and the overall reaction was endothermic by ~14 kcal mol^{-1}. These values correlate very well with theoretically values calculated by Yamanaka and Nalamura[43] (E_{act} and $\Delta H =$ 26.4 and 14.6 kcal mol^{-1} respectively) and Pericàs et al.[44] (E_{act} and $\Delta H =$ 33.5 and 12 kcal mol^{-1} respectively) especially as their calculations are based on an *inter*molecular reaction to form (μ_2-C_2H_2)$Co_2(CO)_5$(η^2-C_2H_4), whereas the experimental data were obtained for a more heavily substituted *intra*molecular process.
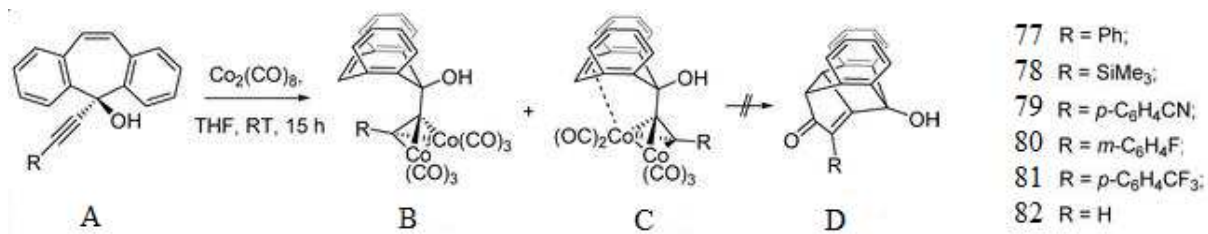
Figure 15   Isolated intermediates of the Pauson Khand reaction.[38]

3.2 Abstract

The aim of this chapter is to investigate the photochemistry of simple aromatic molecules and corresponding dicobalt hexacarbonyl complexes. Central to elucidating photochemical processes in more sophisticated assemblies is a fuller understanding of the spectroscopy and photochemistry of simple aromatic and organometallic molecules. Developing a better grasp of the photochemistry of simple molecules will aid the enhancement of our ability to create and improve practical applications in photochemical processes. In this chapter a concerted experimental investigation into the photochemistry dicobalt carbonyl complexes was undertaken, focusing on the effects of terminal group substitution on the aromatic core and the primary photoactivation processes in Co-Co complexes.

Thienylacetylene systems have been extensively studied yet the affect of terminal group substitution in such systems less so. Rodríguez et al. focused on chain length in these systems and the influence of double bonds versus triple bonds was examined.[13] Where the double bonds were replaced by a triple bond, an increase in fluorescence quantum yield was observed. Toyota et al. synthesised a series of compounds with a phenylene axis and a pair of thien-3-yl moieties at each end.[16] The effect of substitution of the thiophene with ethynylTMS, ethynylbenzene and ethynylpyridine units was examined. Results indicated that the additional aryl groups increase the conjugation within the molecule and as a result the electronic properties were altered. Coleman et al. examined a series of pyrene-thiophene dyads.[27] In all cases, luminescence from the pyrene chromophore was observed, which was reduced upon complexation with dicobalt hexacarbonyl. The luminescence of these compounds and complexes was affected by ligand substitution also. As discussed previously, experimental evidence for the accepted mechanism of the PKR has been limited. Long et al. carried out thorough investigations of dicobalt hexacarbonyl complexes.[41] Two possible photochemical pathways were proposed for (μ_2-alkyne)$Co_2(CO)_6$ complexes following excitation. Irradiation at $\lambda_{exc} = 355$ nm resulted in Co-Co bond homolysis with $\tau_{recomb} = 25$ ns, while irradiation at $\lambda_{exc} = 254$ nm in an argon matrix resulted in reversible CO loss. More recently Gibson et al. reported that Co-Co cleavage competes with CO loss and alkene binding in an (alkyne)(binap)tetracarbonyl dicobalt complex and that the Co-Co bond cleavage was a facile process.[45]

Thus, a series of simple organic thienylacetylene based molecules were synthesised, along with their corresponding dicobalt hexacarbonyl complexes (Fig. 16). Ligands, **NB-L1 – NB-L4**, were examined to delineate the effect of a thiophene moiety attached in the thien-2-yl or thien-3-yl position. While ligands, **NB-L1** and **NB-L5 – NB-L8**, can be used to investigate the effect of terminal group substitution on the organic moiety, with respect to their absorbance, emission and electrochemistry. A previously reported investigation into the photochemistry of diphenylacetylene revealed that it was a non fluorescent molecule which became weakly fluorescent when a terminal electron withdrawing group was attached. This too was investigated for the thienylacetylene systems by steady state fluorescence techniques.
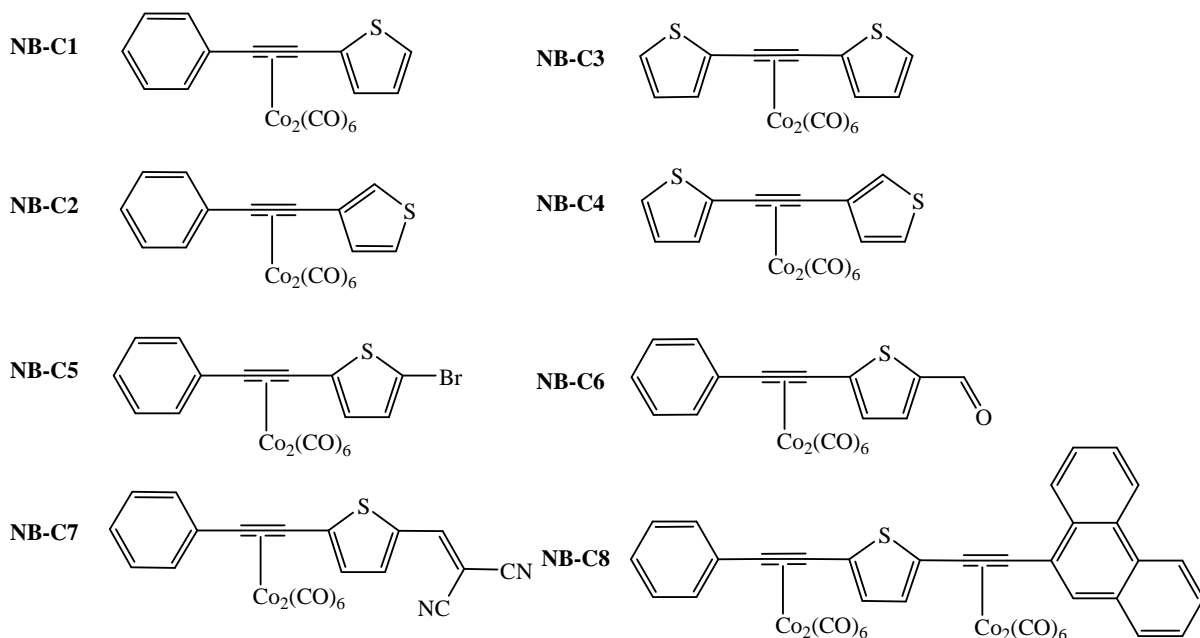
Figure 16   Complexes synthesised for the investigation in chapter 3

For the dicobalt hexacarbonyl complexes, the two competing routes of CO loss and Co-Co bond homolysis were investigated by various methods. Steady state photolysis and quantum yield measurements of CO loss was be carried out in order to examine whether CO loss occurred from these complexes and with what efficiency. TRIR spectroscopy with ps resolution will aid the identification of the primary photoprocesses that occur on a picosecond timescale following excitation.

A shift in the absorbance and emission maxima in the spectra of the thienylacetylene molecules is expected were appropriate substitution has occurred. It is expected that the more electronegative the terminal substituent the greater the spectral changes will be. The non fluorescent molecules may become weakly fluorescent upon appropriate terminal group substitution as was observed for diphenylacetylene.

For the dicobalt hexacarbonyl complexes, steady state photolysis in the presence of a trapping ligand is expected to result in CO loss as this has been observed for similar systems. The extent of CO loss may be substituent dependant, which will be revealed by the quantum yield measurements. To date, TRIR has not been used to investigate the photochemistry of $(\mu_2\text{-alkyne})Co_2(CO)_6$ type complexes. Thus, picosecond time resolved infrared spectroscopy was used to probe the photochemistry of three $(\mu_2\text{-alkyne})Co_2(CO)_6$ complexes. The results from TRIR spectroscopy will hopefully reveal what initial photoprocess occur following excitation (CO loss or Co-Co bond homolysis) and aid in the indentification of transient species formed. This is of particular interest as it relates to the initiation of the well known PKR.

3.3   Experimental

3.3.1   Materials

Any experiments that required an inert atmosphere were carried out under argon or nitrogen using standard Schlenk techniques. All solvents were supplied by the Aldrich Chemical Company. Dichloromethane, chloroform, diethyl ether, pentane and hexane were dried over $MgSO_4$ prior to use. Tetrahydrofuran (THF) was distilled from sodium / benzophenone solution and used immediately. Anhydrous triethylamine was used as received and diisopropylamine was distilled over potassium hydroxide prior to use. All organic reagents were purchased from the Aldrich Chemical Company. Diphenylacetylene and ethynylferrocene were used as received. 5-Bromothiophene-2-carboxaldehyde was purified by distillation using a Buchi Kügelrohr apparatus. All mobile phases for column chromatography were dried over $MgSO_4$ and silica gel (Merck) was used as received. All solvents used in absorbance, emission, lifetime and quantum yield experiments were of spectroscopic grade and used without further purification. All solvents were deoxygenated by purging with pure argon or nitrogen for ~10 minutes. The preface "**NB-**" is applied to compound codes indicating that these are novel compounds synthesised throughout this work.

3.3.2   Equipment

All syntheses involving air- and moisture-sensitive reagents were performed in oven or flame dried glassware. NMR spectra were recorded on a Bruker model AC 400 MHz spectrometer and Bruker model ANC 600 MHz spectrometer using $CDCl_3$ as solvent. All NMR spectra were calibrated according to the residual solvent peak, i.e. $CHCl_3$ at 7.26 ppm for all ^1H spectra and 77.16 ppm for all ^{13}C spectra. Chemical shifts (δ) are given in parts per million (ppm). Proton coupling constants (J) are given in Hertz (Hz). Melting points were measured on a Stuart Scientific SMP1 melting point apparatus. All UV-vis spectra were measured on an Agilent Technologies 8453 photodiode array spectrometer using a 1 cm^3 quartz cell. Emission spectra (accuracy $\pm$ 5 nm) were recorded at 298 K using a LS50B luminescence spectrophotometer, equipped with a red sensitive Hammatsu R928 PMT detector, interfaced with Elonex PC466 employing Perkin-Elmer FL WinLab custom built software. Luminescence lifetime measurements were made using an

Edinburgh Analytical Instruments (EAI) Time-Correlated Single Photon Counting apparatus (TCSPC) as described by Browne et al.[46] IR spectra were recorded on a Perkin-Elmer 2000 FT-IR spectrometer (2 cm^{-1} resolution) in a 0.1 mm sodium chloride liquid solution cell. Cyclic voltammetry experiments were carried out using a CH instruments model 600a electrochemical workstation at a scan rate of 0.1 VS^{-1}. Electrochemical studies were conducted using a three electrode system with 0.1 M solution of TBAPF$_6$ in anhydrous acetonitrile as supporting electrolyte. The working electrode was a 3 mm diameter Teflon shrouded platinum electrode, which was polished before each use. The counter electrode was a platinum wire and the reference electrode was a non-aqueous Ag/Ag$^+$ electrode. Deoxygenation of the solutions was achieved by bubbling through argon for approximately 10 minutes and a blanket of argon was maintained over the solution during all experiments. The filling solution for the Ag/Ag$^+$ reference electrode was 0.1 M TBAPF$_6$ and 10 mM AgNO$_3$ in anhydrous acetonitrile. All potentials are quoted with respect to the potentials of the ferrocene/ferricenium couple ($E^{0'} = 0.382$ V $vs.$ SCE).

3.3.3   Synthesis

Procedure for the preparation of compounds *via* the Sonogashira reaction.[1]

To a flame dried round bottom flask anhydrous triethylamine (~30 ml) was added and purged with nitrogen for 10 minutes. Following this, the appropriately substituted halogenated thiophene was added and the solution was purged for a further 5 minutes. A catalytic quantity of bis(triphenylphosphine)palladium(II)chloride, triphenylphosphine and cuprous iodide were added to the flask followed by an excess of aryl alkyne in quick succession. The reaction mixture was refluxed overnight under an inert atmosphere and then allowed to cool. Excess aryl and solvent was removed under reduced pressure. The crude product was extracted from the brown oil by first adding *ca.* 5 ml of dichloromethane followed by the addition of *ca.* 25 ml of petroleum ether (or hexane). The solvent layer was then decanted off. This process was repeated several times until the washings remained colourless. The washings were combined and dried over magnesium sulphate. The solvent was then removed *via* rotary evaporation affording a dark viscous oil. The crude product was then purified using a Kügelrohr or by column chromatography as described for each compound.

Procedure for the preparation of dicobalt hexacarbonyl complexes.

To a flame dried round bottom flask hexane was added and purged with nitrogen for 10 minutes. Molar equivalents of the relevant substituted ethynylthiophene ligand and $Co_2(CO)_8$ (in some cases an excess of the metal carbonyl was used) were added to the reaction vessel which was then covered in tin foil. This solution was stirred overnight at room temperature under inert conditions and to yield a dark brown solution. The crude product was subsequently purified by column chromatography on silica gel using a mobile phase of hexane (100 %) then increasing the polarity (as stated or individual compounds) to elute the desired product band.

3.3.3.1 2-(Phenylethynyl)thiophene (NB-L1)
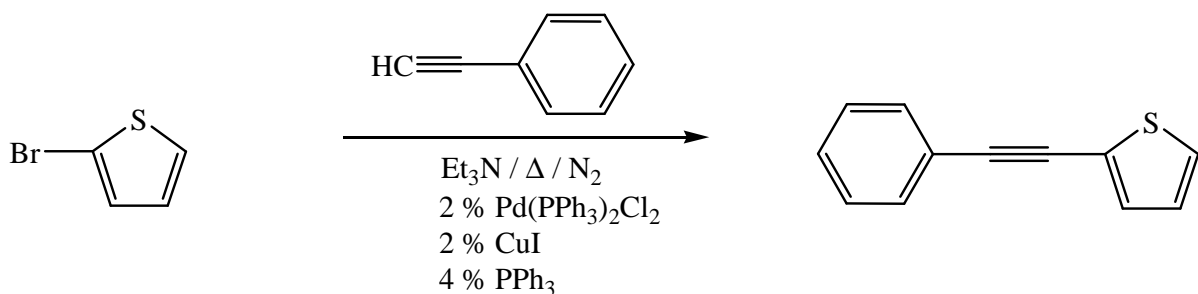
2-Bromothiophene (3.0 mmol, 0.29 ml), bis(triphenylphosphine) palladium(II)chloride (0.06 mmol, 42 mg, 2 %), triphenylphosphine (0.12 mmol, 31 mg, 4%), cuprous iodide (0.06 mmol, 11 mg, 2 %) and 1-phenylacetylene (5.7 mmol, 0.63 ml) were used. The crude product was purified using a Kügelrohr (240 ºC, 0.04 mm Hg) which afforded a white solid. Yield: 502 mg, 2.72 mmol, 91 %. Spectroscopic data were in good agreement with reported data.[47]

¹H NMR (600 MHz, CDCl$_3$): 7.53 – 7.51 (2H, m), 7.38 – 7.33 (3H, m), 7.30 – 7.29 (2H, m), 7.02 – 7.01 (1H, m) ppm. **¹³C NMR** (150 MHz, CDCl$_3$): 131.91, 131.44, 128.45, 128.39, 127.27, 127.12, 123.36, 122.96, 93.04, 82.63 ppm. **m.p.** = 51 – 52 ºC.

3.3.3.2 3-(Phenylethynyl)thiophene (NB-L2)
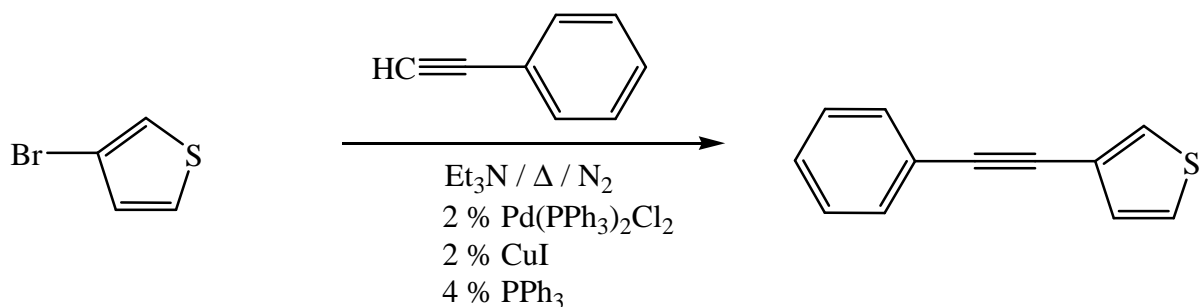
3-Bromothiophene (3.0 mmol, 0.28 ml), bis(triphenylphosphine) palladium(II)chloride (0.06 mmol, 42 mg, 2 %), triphenylphosphine (0.12 mmol, 31 mg, 4%), cuprous iodide (0.06 mmol, 11 mg, 2 %) and 1-phenylacetylene (5.7 mmol, 0.63 ml) were used. The crude product purified using a Kügelrohr (225 ºC, 0.04 mm Hg) which afforded an off white solid. Yield: 447 mg, 2.43 mmol, 81 %. Spectroscopic data were in good agreement with reported data.[48]

^{1}H NMR (600 MHz, CDCl$_3$): 7.52 – 7.51 (3H, m), 7.35 (1H, s), 7.34 – 7.32 (2H, m), 7.31 – 7.29 (1H, m), 7.21 – 7.19 (1H, m) ppm. **^{13}C NMR** (150 MHz, CDCl$_3$): 131.55, 129.90, 128.60, 128.35, 128.22, 125.37, 123.24, 122.35, 88.91, 84.52 ppm. **m.p.:** = 34-35 ºC.

3.3.3.3 2-(Thien-2-ylethynyl)thiophene (NB-L3)
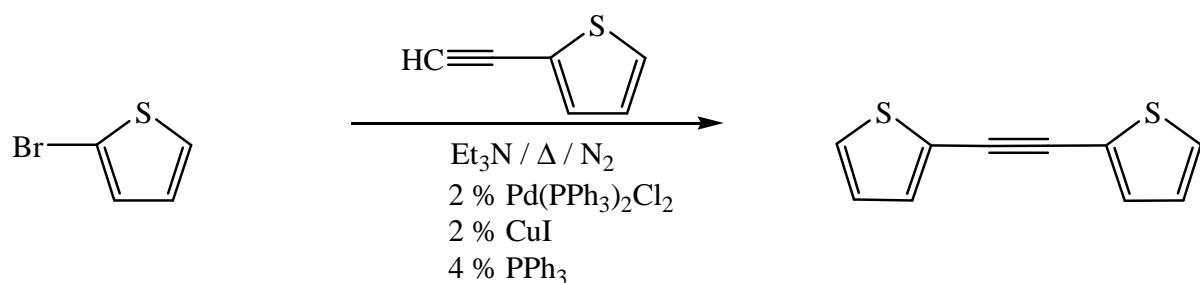
2-Bromothiophene (4.0 mmol, 0.38 ml), bis(triphenylphosphine)palladium(II)chloride (0.06 mmol, 42 mg, 2 %), triphenylphosphine (0.12 mmol, 31 mg, 4%), cuprous iodide (0.06 mmol, 11 mg, 2 %) and 2-ethynylthiophene (3.0 mmol, 0.30 ml) were used. The crude product was purified by careful by careful Kügelrohr distillation (115 ºC, 0.04 mm Hg) affording an off white solid. Yield: 427 mg, 2.24 mmol, 75 %. Spectroscopic data were in good agreement with reported data.[49]

^{1}H NMR (600 MHz, CDCl$_3$): 7.30 (2H, d, J = 6 Hz), 7.28 (2H, d, J = 6 Hz), 7.01 (2H, t, J = 6 Hz). **^{13}C NMR** (150 MHz, CDCl$_3$): 132.14, 127.66, 127.14, 122.95, 86.20 ppm. **m.p.:** 94-95 ºC.

3.3.3.4   2-(Thien-3-ylethynyl)thiophene (NB-L4)
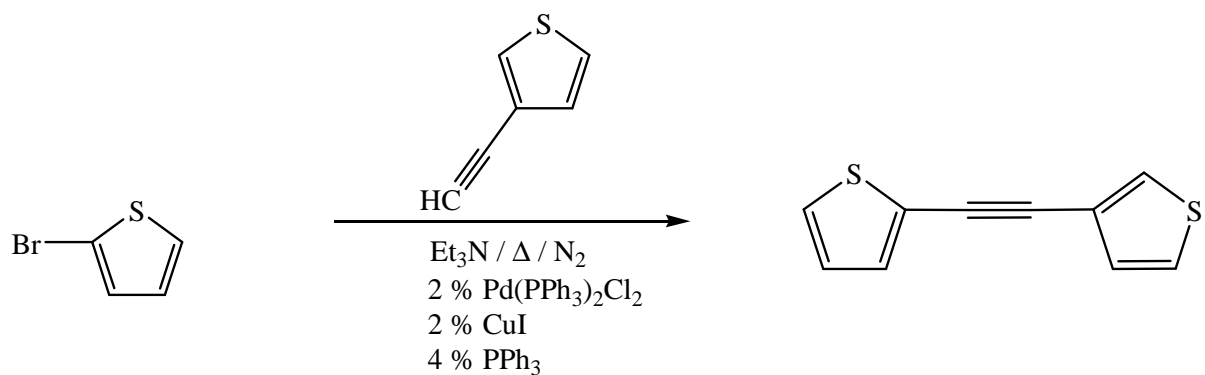
3-Bromothiophene (4.0 mmol, 0.38 ml), bis(triphenylphosphine)palladium(II)chloride (0.06 mmol, 42 mg, 2 %), triphenylphosphine (0.12 mmol, 31 mg, 4%), cuprous iodide (0.06 mmol, 11 mg, 2 %) and 2-ethynylthiophene (3.0 mmol, 0.30 ml) were used. The crude product purified using a Kügelrohr (125 °C, 0.04 mm Hg) which afforded a cream coloured solid. Yield: 352 mg, 1.85 mmol, 62 %. Spectroscopic data were in good agreement with reported data.

1H NMR (600 MHz, CDCl$_3$): 7.54-7.50 (1H, m), 7.31-7.30 (1H, m), 7.29-7.28 (1H, m), 7.27-7.26 (1H, m), 7.19-7.18 (1H, m), 7.01-7.69 (1H, m) ppm. **13C NMR** (150 MHz, CDCl$_3$): 132.17, 131.86, 129.73, 128.83, 127.21, 127.11, 125.49, 121.98, 88.21, 82.12 ppm. **IR** (CH$_2$Cl$_2$): (C≡C) 2203 cm^{-1}. **m.p.**: 88-89 °C.

3.3.3.5 2-Iodo-5-bromothiophene
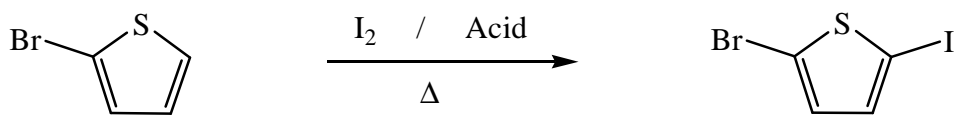
2-Iodo-5-bromothiophene was prepared in a similar manner to that described by Holmes et al.[50] Initially a flame dried round bottom flask was charged with CH_2Cl_2 (16 ml) and 2-bromothiophene (7.8 mmol, 0.76 ml) and purged with nitrogen for 10 minutes. Subsequently iodine (4.0 mmol, 1.0 g) was added followed by freshly prepared 8.5 M nitric acid (12 ml) (37.72 ml of conc. nitric acid in 100 ml H_2O). The reaction mixture was refluxed for six hours under an inert atmosphere. The reaction was quenched with water and the organic layer extracted with CH_2Cl_2. The crude product was then washed with 50 % w/v aqueous sodium thiosulphate and dried over $MgSO_4$. Excess solvent was removed under *via* rotary evaporation. The crude product was then purified by careful Kügelrohr distillation (95 ºC, 0.04 mm Hg) to give a colourless oil. Yield: 1.95 g, 6.75 mmol, 86 %. Spectroscopic data were in good agreement with reported data.[50]

^{1}H NMR (400 MHz, $CDCl_3$): 7.04 (1H, d, J = 3.6 Hz), 6.75 (1H, d, J = 3.6 Hz) ppm.
^{13}C NMR (100 MHz, $CDCl_3$): 137.28, 131.51, 115.10, 72.52 ppm

### 3.3.3.6 2-(Phenylethynyl)-5-bromothiophene (NB-L5)
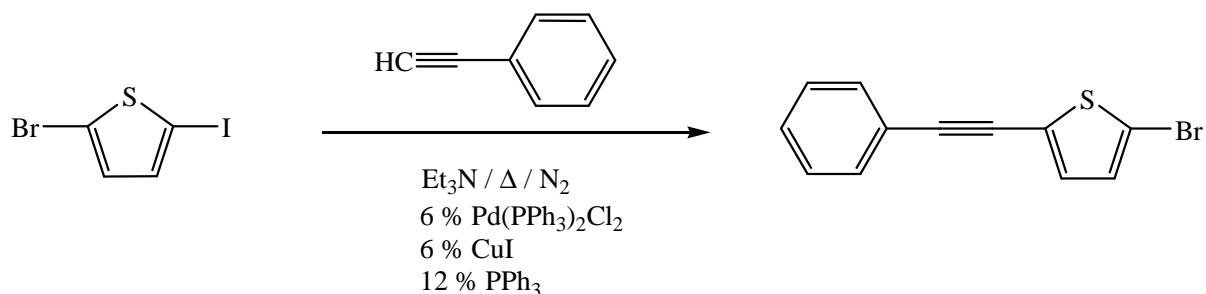
2-Bromo-5-iodothiophene (4.43 mmol, 1.28 g), bis(triphenylphosphine) palladium(II)chloride (0.27 mmol, 189 mg, 6 %), triphenylphosphine (0.54 mmol, 142 mg, 12 %), cuprous iodide (0.27 mmol, 51 mg, 6 %) and 1-phenylacetylene (5.7 mmol, 0.63 ml) were used. The crude product was purified using a Kügelrohr (150 ºC, 0.04 mm Hg) which afforded a white solid. Yield: 982 mg, 3.73 mmol, 83 %.

^{1}H NMR (600 MHz, CDCl$_3$): 7.53 – 7.48 (2H, m), 7.38 – 7.32 (3H, m) 7.02 (1H, d, $J = 4$ Hz), 6.96 (1H, d, $J = 4$ Hz) ppm. **^{13}C NMR** (150 MHz, CDCl$_3$): 131.46, 129.23, 128.72, 128.47, 128.44, 125.12, 122.54, 121.83, 94.06, 81.68 ppm. **IR** (CH$_2$Cl$_2$): (C≡C) 2207 cm^{-1}. **m.p.**: 54-55 ºC.

3.3.3.7 2-(Phenylethynyl)thiophene-5-methylenemalononitrile (NB-L7)
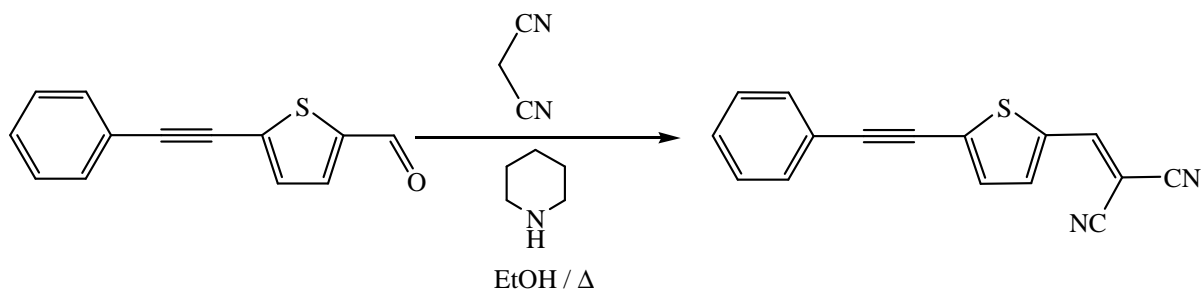
The dicyanovinyl derivative, **NB-L7**, was synthesised *via* a Knoevenagel condensation reaction of 2-(phenylethynyl)thiophene-5-carboxaldehyde (synthesis of the aldehyde, **NB-A1**, described in chapter 2, page 101). Argon purged ethanol (40 ml) was charged with 5-(phenylethynyl)thiophene-2-carboxaldehyde (4.0 mmol, 850 mg), malontirile (4.0 mmol, 0.25 ml) and 3-4 drops piperidine. This yellow solution was then heated to reflux for 1 hour under an inert atmosphere to yield a dark red solution. Solvent was removed under reduced pressure yielding a dark red-brown coloured solid. This residue was purified by column chromatography using silica gel and CH_2Cl_2 as mobile phase to yield a dark orange solid. Yield: 562 mg, 2.16 mmol, 54 %.

^{1}H NMR (400 MHz, CDCl$_3$): 7.77 (1H, s), 7.66 (1H, d, J = 4 Hz), 7.56 – 7.54 (2H, m), 7.43 – 7.37 (3H, m) 7.33 (1H, d, J = 4 Hz) ppm. **^{13}C NMR** (100 MHz, CDCl$_3$): 150.04, 138.55, 135.62, 134.98, 132.64, 131.80, 129.81, 128.67, 121.51, 113.84, 100.81, 81.70, 78.11 ppm. **IR** (CH$_2$Cl$_2$): (C=C) 1576, (C≡C) 2203, (C≡N) 2226 cm^{-1}. **m.p.:** 137-138 °C.

3.3.3.8   2-(Phenylethynyl)thiophene-5-ethynylphenanthrene (NB-L8)
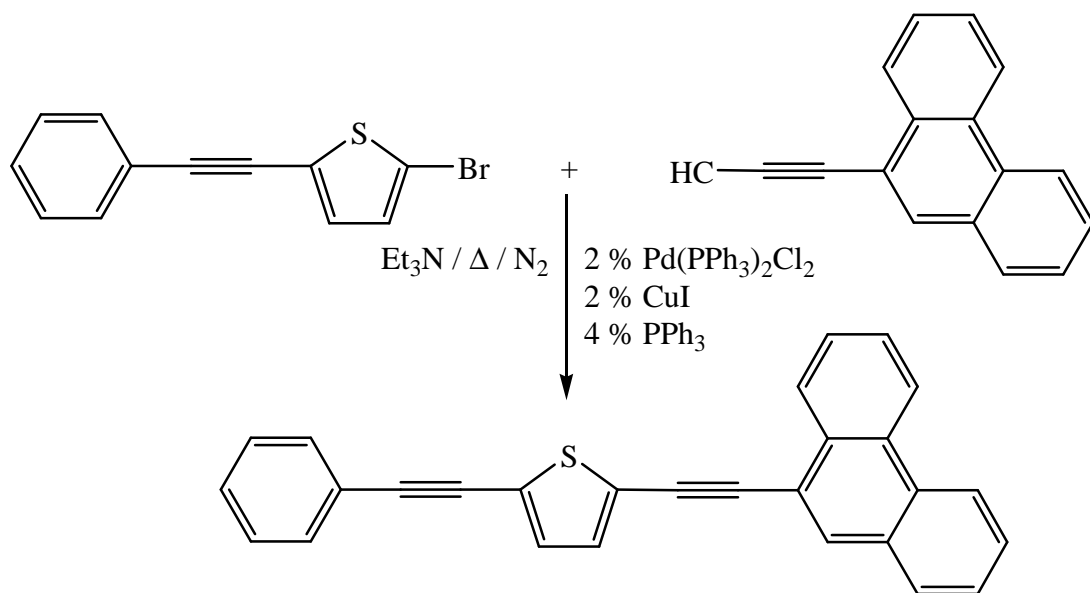
2-(Phenylethynyl)-5-bromothiophene (2.28 mmol, 600 mg), bis(triphenylphosphine) palladium(II)chloride (0.05 mmol, 32 mg, 2 %), triphenylphosphine (0.09 mmol, 24 mg, 4%), cuprous iodide (0.05 mmol, 9 mg, 2 %) and 9-ethynylphenanthrene (3.0 mmol, 607 mg) were used. The crude product purified by careful column chromatography using silica gel and CH_2Cl_2 / hexane (40:60) as mobile phase affording a bright yellow solid. Yield: 726 mg, 1.89 mmol, 83 %.

^{1}H NMR (400 MHz, CDCl$_3$): 8.72-8.70 (1H, m), 8.67 (1H, d, J = 8 Hz), 8.47-8.45 (1H, m), 8.09 (1H, s), 7.88 (1H, d, J = 8 Hz), 7.73-7.71 (2H, m), 7.70 – 7.67 (1H, m), 7.64-7.60 (1H, m), 7.56-7.52 (3H, m), 7.38-7.33 (4H, m), 7.29 (1H, d, J = 4 Hz), 7.22 (1H, d, J = 4 Hz) ppm. **^{13}C NMR** (100 MHz, CDCl$_3$): 131.47, 131.09, 131.02, 130.93, 130.48, 130.10, 129.73, 129.39, 129.06, 128.19, 127.69, 127.66, 127.42, 126.70, 126.21, 126.17, 126.04, 125.79, 123.88, 123.58, 121.83, 121.63, 121.54, 91.56, 85.67, 81.27 ppm. **IR** (CH$_2$Cl$_2$): (C≡C) 2201 cm^{-1}. **m.p.**: 150-151 ºC.

3.3.3.9 Diphenylacetylene dicobalt hexacarbonyl (PhCCPh-Co$_2$(CO)$_6$)
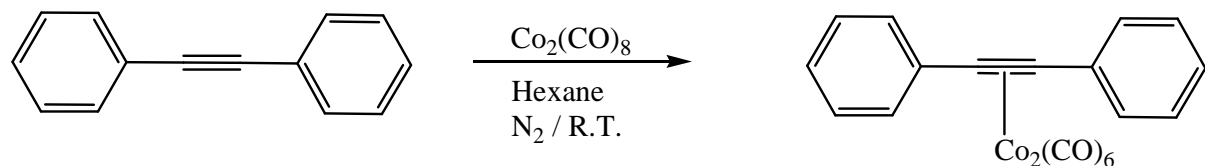
Diphenylacetylene (1.12 mmol, 200 mg) and Co$_2$(CO)$_8$ (1.12 mmol, 384 mg) were used. The crude product was purified by column chromatography using silica gel and hexane (100 %) as mobile phase which furnished the pure reddish-brown product. Yield: 483 mg, 1.04 mmol, 93 %. Spectroscopic data are in good agreement with reported data.[51]

^{1}H NMR (400 MHz, CDCl$_3$): 7.61-7.60 (m, 2H) 7.59-7.58 (m, 2H), 7.39-7.37 (m, 3H), 7.35-7.33 (m, 3H) ppm. **IR** (CH$_2$Cl$_2$): ν(CO) 2090, 2056, 2028 cm^{-1}.

3.3.3.10 2-(Phenylethynyl)thiophene dicobalt hexacarbonyl (NB-C1)
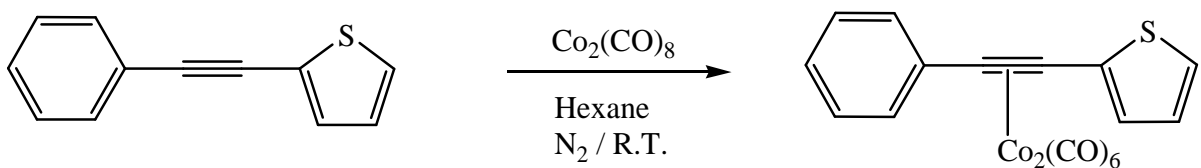
2-(Phenylethynyl)thiophene (1.08 mmol, 200 mg) and $Co_2(CO)_8$ (1.08 mmol, 370 mg) were used. The crude product was purified by column chromatography using silica gel and hexane : CH_2Cl_2 (70 : 30) as mobile phase which furnished the pure reddish-brown product. Yield: 457 mg, 0.97 mmol, 90 %

^{1}H NMR (600 MHz, CDCl$_3$): 7.70-7.68 (2H, m), 7.42-7.35 (5H, m), 7.06-7.04 (1H, m) ppm. **^{13}C NMR** (150 MHz, CDCl$_3$): 198.57, 141.57, 137.23, 137.64, 128.92, 128.73, 128.37, 127.88, 126.70, 91.58, 82.04 ppm. **IR** (CH$_2$Cl$_2$): ν(CO) 2091, 2058, 2030 cm^{-1}.

3.3.3.11 3-(Phenylethynyl)thiophene dicobalt hexacarbonyl (NB-C2)
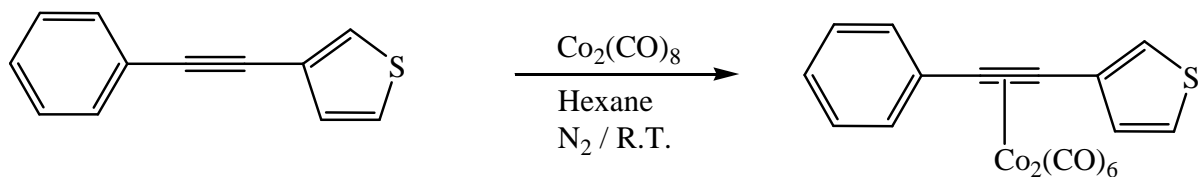
3-(Phenylethynyl)thiophene (1.63 mmol, 300 mg) and $Co_2(CO)_8$ (1.63 mmol, 557 mg) were used. The crude product was purified by column chromatography using silica gel and hexane : CH_2Cl_2 (70 : 30) as mobile phase, which furnished the pure reddish-brown product. Yield: 568 mg, 1.21 mmol, 74 %.

^{1}H NMR (400 MHz, CDCl$_3$): 7.62-7.60 (3H, m), 7.52-7.49 (3H, m), 7.34-7.32 (1H, m), 7.25-7.24 (1H, m) ppm. **^{13}C NMR** (100 MHz, CDCl$_3$): 198.3, 137.20, 130.50, 128.84, 128.16, 127.96, 127.36, 125.50, 122.71, 87.90, 83.40ppm. **IR** (CH$_2$Cl$_2$): ν(CO) 2090, 2055, 2028 cm^{-1}.

3.3.3.12   2-(Thien-2-ylethynyl)thiophene dicobalt hexacarbonyl (NB-C3)
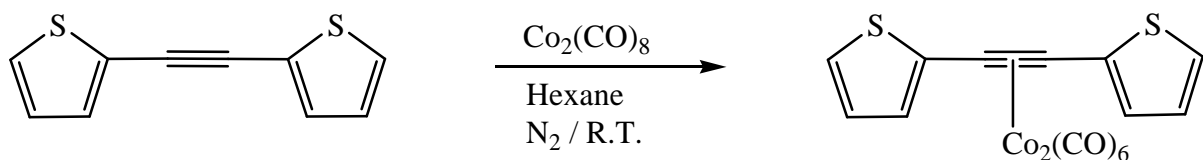
2-(Thien-2-ylethynyl)thiophene (0.82 mmol, 157 mg) and $Co_2(CO)_8$ (0.90 mmol, 308 mg) were used. The crude product was purified by column chromatography using silica gel and a mobile phase of hexane (100 %) followed by hexane : CH_2Cl_2 (70 : 30) which furnished the pure reddish-brown product. Yield: 333 mg, 0.70 mmol, 85 %

^{1}H NMR (400 MHz, CDCl$_3$): 7.42-7.41 (2H, m), 7.40-7.38 (2H, m), 7.06-7.03 (2H, m) ppm. **^{13}C NMR** (100 MHz, CDCl$_3$): 197.70, 140.40, 128.79, 127.01, 126.13, 81.12 ppm. **IR** (CH$_2$Cl$_2$): v(CO) 2091, 2058, 2031 cm^{-1}.

3.3.3.13 2-(Thien-3-ylethynyl)thiophene dicobalt hexacarbonyl (NB-C4)
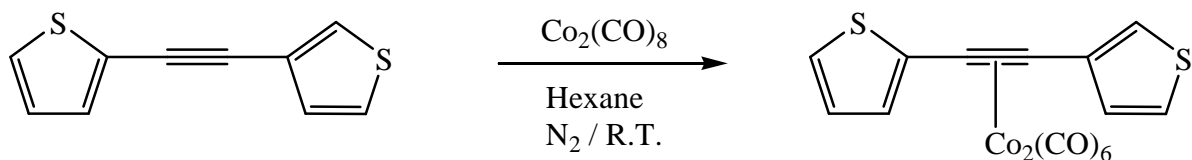
2-(Thien-3-ylethynyl)thiophene (0.66 mmol, 126 mg) and $Co_2(CO)_8$ (0.66 mmol, 226 mg) were used. The crude product was purified by column chromatography using silica gel and a mobile phase of hexane (100 %) followed by hexane : CH_2Cl_2 (70 : 30) which furnished the pure reddish-brown product. Yield: 247 mg, 0.52 mmol, 79 %.

^{1}H NMR (600 MHz, CDCl$_3$): 7.68-7.65 (1H, m), 7.45-7.33 (3H, m), 7.20-7.18 (1H, m), 7.05-7.01 (1H, m) ppm. **^{13}C NMR** (150 MHz, CDCl$_3$): 198.57, 132.12, 131.39, 131.03, 130.05, 129.07, 128.65, 128.37, 125.05, 93.99, 81.63 ppm. **IR** (CH$_2$Cl$_2$): ν(CO) 2091, 2059, 2032 cm^{-1}.

3.3.3.14   2-(Phenylethynyl)-5-bromothiophene dicobalt hexacarbonyl (NB-C5)
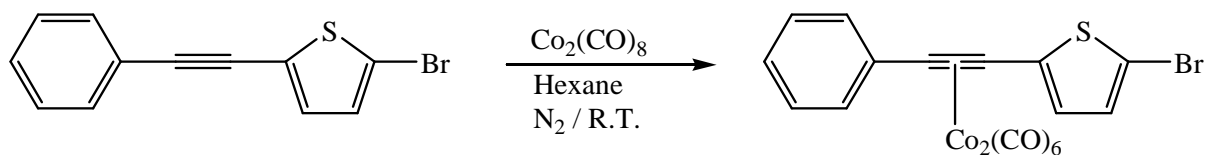
2-(Phenylethynyl)-5-bromothiophene (0.49 mmol, 128 mg) and $Co_2(CO)_8$ (0.54 mmol, 185 mg) were used. The crude product was purified by column chromatography using silica gel and a mobile phase of hexane (100 %) which furnished the pure reddish-brown product. Yield: 242 mg, 0.44 mmol, 90 %.

1H NMR (400 MHz, CDCl₃): 7.64-7.50 (3H, m), 7.40-7.30 (2H, m), 7.05-7.01 (2H, m) ppm. **¹³C NMR** (100 MHz, CDCl₃): 198.76, 137.89, 131.67, 129.50, 128.63, 128.06, 126.95, 126.67, 123.72, 88.08, 81.96 ppm. **IR** (CH₂Cl₂): ν(CO) 2092, 2057, 2030 cm⁻¹.

3.3.3.15 2-(Phenylethynyl)thiophene-5-carboxaldehyde dicobalt hexacarbonyl (NB-C6)
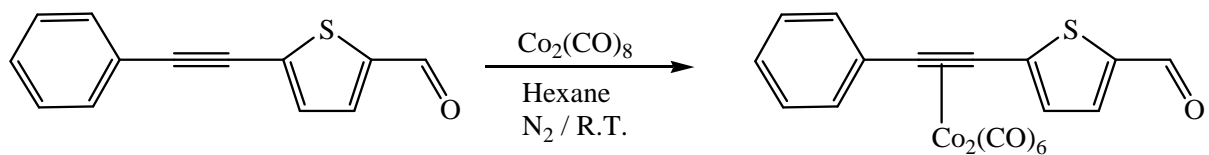
2-(Phenylethynyl)thiophene-5-carboxaldehyde (1.41 mmol, 300 mg) and $Co_2(CO)_8$ (1.55 mmol, 530 mg) were used. The crude product was purified by column chromatography using silica gel and a mobile phase of hexane (100 %) followed by hexane : diethyl ether (60 : 40) which furnished the pure reddish-brown product. Yield: 492 mg, 0.99 mmol, 70 %

1H NMR (400 MHz, CDCl$_3$): 9.88 (1H, s), 7.69-7.68 (1H, m), 7.63-7.62 (2H, m), 7.39-7.36 (4H, m) ppm. **13C NMR** (100 MHz, CDCl$_3$): 198.25, 182.50, 153.74, 143.23, 137.28, 137.15, 129.17, 128.89, 128.49, 92.64, 79.40 ppm. **IR** (CH$_2$Cl$_2$): ν(C=O) 1652, ν(M-CO) 2095, 2062, 2035 cm^{-1}.

3.3.3.16   2-(Phenylethynyl)thiophene-5-methylenemalononitrile dicobalt hexacarbonyl (NB-C7)
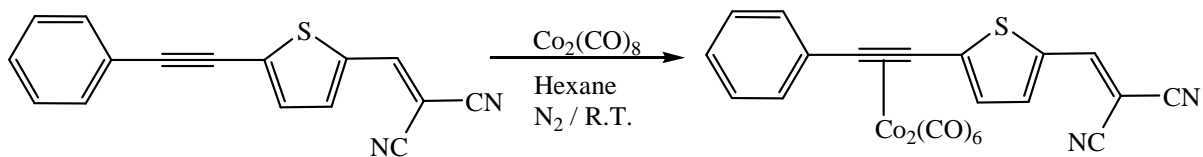
2-(Phenylethynyl)thiophene-5-methylenemalononitrile (0.48 mmol, 125 mg) and $Co_2(CO)_8$ (0.58 mmol, 198 mg) were used. To aid dissolution of the dicyanovinyl ligand THF (3 ml) was also used. The crude product was purified by column chromatography using silica gel and a mobile phase of hexane (100 %) followed by hexane : diethyl ether (3 : 2) which furnished the pure reddish-brown product. Yield: 109 mg, 0.20 mmol, 42 %

¹H NMR (600 MHz, CDCl$_3$): 7.75 (1H, s), 7.64-7.56 (3H, m), 7.49-7.35 (3H, m), 7.29-7.27 (1H, m) ppm. **¹³C NMR** (150 MHz, CDCl$_3$): 198.89, 152.47, 141.54, 137.23, 137.01, 132.86, 131.82, 128.93, 128.64, 126.33, 114.26, 105.56, 81.35, 79.75 ppm. **IR** (CH$_2$Cl$_2$): ν(CO) 2094, 2061, 2034 (C=C) 1576, (C≡N) 2226 cm^{-1}

3.3.3.17   2-(Phenylethynyl)thiophene-5-ethynylphenanthrene dicobalt hexacarbonyl (NB-C8)
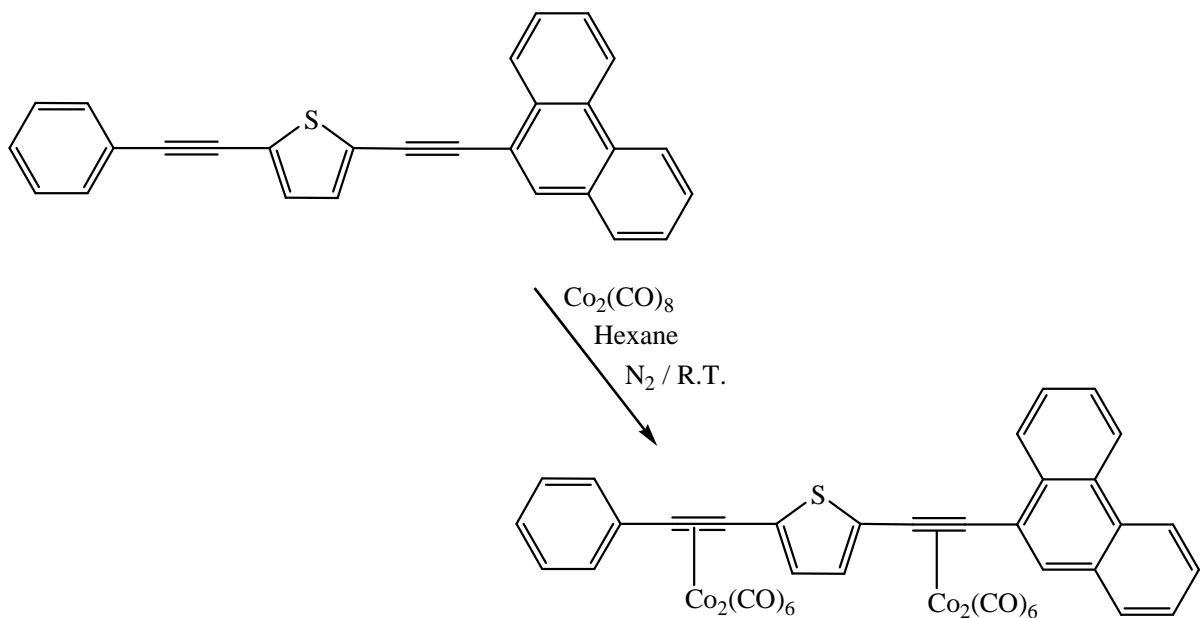
2-(Phenylethynyl)thiophene-5-ethynylphenanthrene (0.26 mmol, 100 mg) and an excess of $Co_2(CO)_8$ (0.60 mmol, 205 mg) were used. The crude product was purified by column chromatography using silica gel and hexane (100 %) followed by hexane : CH_2Cl_2 (75 : 25) as mobile phase which furnished a pure dark green solid. Yield: 143 mg, 0.15 mmol, 57 %

^{1}H NMR (600 MHz, CDCl$_3$): 8.78-8.77 (1H, m), 8.69-8.68 (1H, m), 8.23-8.15 (2H, m), 7.94-7.92 (1H, m), 7.71-7.68 (2H, m), 7.64-7.58 (3H, m), 7.35-7.29 (5H, m), 7.22-7.21 (1H, m) ppm. **^{13}C NMR** (150 MHz, CDCl$_3$): 197.91, 142.90, 142.66, 136.72, 132.21, 131.92, 129.56, 128.72, 128.20, 128.14, 127.95, 127.42, 127.08, 126.14, 125.96, 121.67, 94.95, 80.23 ppm. **IR** (CH$_2$Cl$_2$): ν(CO) 2094, 2088, 2060, 2031, 2014 cm^{-1}.

3.4 Results

3.4.1 UV-vis absorbance studies

Listed in table 1 are the absorbance maxima (λ_{max}) and extinction coefficient values (ε) for all compounds in this study. All UV-vis spectra were recorded in spectrophotometric grade CH_2Cl_2. The absorbance data of diphenylacetylene (**PhCCPh**) and diphenylacetylene dicobalt hexacarbonyl (**μ_2-PhCCPh-Co$_2$(CO)$_6$**) have previously been reported (Fig. 17).[52]
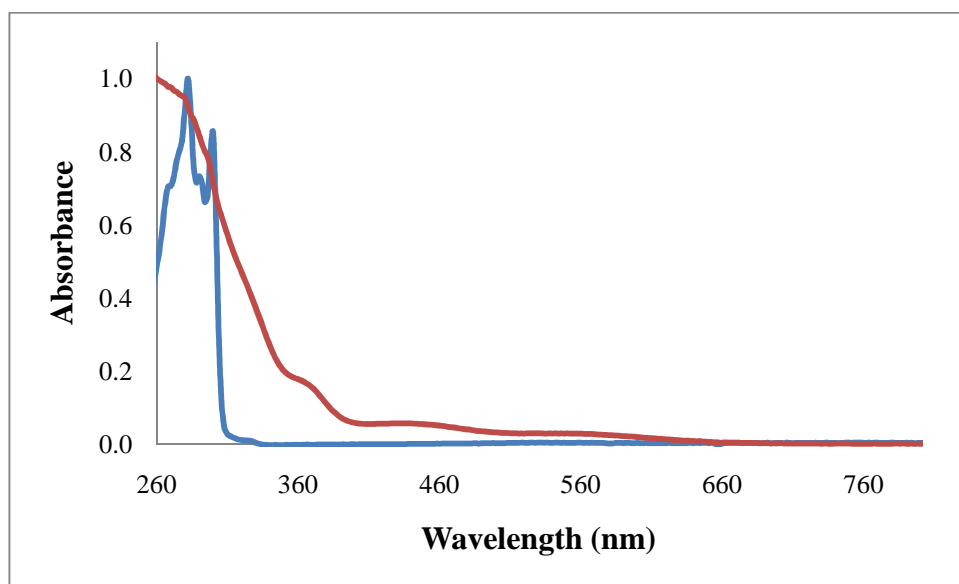
Figure 17 *UV-vis spectra of **PhCCPh** (blue line) and **PhCCPh-Co$_2$(CO)$_6$** (red line) recorded in CH$_2$Cl$_2$. Spectra have been normalised at their λ_{max}.*

All compounds (**NB-L1** – **NB-L8**) exhibit strong absorbance bands in the UV-vis region of the spectrum normally associated with ligand localised π-π* transitions. For the dicobalt hexacarbonyl complexes (**NB-C1** – **NB-C8**) weak low energy transitions are also observed between 580 and 600 nm, extending to 700 nm in some cases. These are assigned to weak CO (dπ) → ligand (π) charge transfer (MLCT) transitions.

Ligand	λ_{max} (nm), ε (x 10^4 M^{-1} cm^{-1})
PhCCPh	274, 282 (3.08), 290, 300 (2.62), 318
NB-L1	302 (2.08), 318 (1.61)
NB-L2	282 (2.11), 288 (1.77), 300 (1.79)
NB-L3	318 (2.38), 324 (2.02), 338 (1.61)
NB-L4	300 (1.64), 316 (1.30), 338 (0.18)
NB-L5	310 (2.81), 326 (2.27), 368 (0.12)
NB-L6	276 (0.79), 358 (2.19), 370 (2.14)
NB-L7	276 (1.17), 306 (0.50), 412 (3.72)
NB-L8	250 (3.32), 310 (1.80), 332 (2.20), 360 (3.12), 374 (2.98), 390 (2.14)

Complex	λ_{max} (nm), ε (x 10^4 M^{-1} cm^{-1})
PhCCPh-Co$_2$(CO)$_6$	280 (1.91), 364 (0.43), 440 (0.20), 560 (0.09)
NB-C1	282 (1.83), 322 (1.31), 450 (0.15), 568 (0.08)
NB-C2	282 (4.48), 300 (3.69), 330 (1.26), 444 (0.24), 578 (0.22)
NB-C3	280 (1.89), 322 (1.43), 464 (0.15), 584 (0.09)
NB-C4	274 (1.72), 328 (1.24), 458 (0.14), 576 (0.09)
NB-C5	274 (2.17), 318 (1.67), 458 (0.20), 578 (0.11)
NB-C6	272 (2.18), 350 (1.76), 464 (0.17), 554 (0.11)
NB-C7	274 (1.95), 404 (1.68), 440 (1.68), 546 (0.26)
NB-C8	272 (3.25), 330 (2.21), 366 (1.96), 480 (0.26), 590 (0.21)

Table 1   *UV-vis absorbance data of ligands and corresponding complexes are recorded in CH$_2$Cl$_2$.*

3.4.2 Steady state fluorescence studies

Room temperature emission studies of the compounds and complexes were carried out in CH_2Cl_2 as were luminescence lifetime measurements using the single photon counting (SPC) technique. Solutions were prepared such that they were isoabsorbtive at a selected wavelength having an optical density in solution of approximately 0.2 A.U. Ligands **NB-L1**, **NB-L2**, **NB-L3** and **NB-L4** did not fluoresce and in conjunction with this neither did their metal carbonyl complexes. Ligands **NB-L5**, **NB-L6** and **NB-L7** were found to be weakly emissive, and the corresponding cobalt carbonyl complexes (**NB-C5**, **NB-C6** and **NB-C7**) displayed very weak fluorescence, *albeit* with lower intensity than that of the ligands. Attachment of the fluorescent phenanthrenyl moiety, as in **NB-L8**, caused an increase in the fluorescence intensity of the molecule. Following coordination of the dicobalt carbonyl moiety, **NB-C8**, a reduction in emission intensity was observed, however there is no significant shift in the position of the emission band, thereby suggesting that the emission is ligand based without major MLCT contribution. The excitation spectra of the emissive compounds had the same profile as the corresponding absorbance spectra further suggesting that the emissive state was ligand based. The emission lifetimes were measured for all emissive compounds and complexes. The emission lifetimes are presented in table 2 below.

	λ_{em} (nm)	τ (ns)		λ_{em} (nm)	τ (ns)
NB-L5	386, 404	2.01	**NB-C5**	370	1.98
NB-L6	380, 396	2.18	**NB-C6**	404	1.32
NB-L7	467, 646	3.52	**NB-C7**	471	---
NB-L8	403, 425	2.62	**NB-C8**	405, 427	0.54

Table 2   *Luminescence lifetimes (298 K) of compounds **NB-L5** – **NB-L8** and the corresponding dicobalt hexacarbonyl complexes **NB-C5** – **NB-C8** recorded in CH_2Cl_2.*

3.4.3 Electrochemistry

Cyclic voltammetry studies were carried out on the compounds and complexes in a 0.1 M TBAPF$_6$/CH$_3$CN electrolyte solution. Table 3 presents the electrochemical data obtained at room temperature. In all cases one irreversible anodic peak corresponding to the oxidation of the thienyl unit was observed in the range +1.47 to 1.90 V *vs.* Fc/Fc$^+$ which is in good agreement with the values reported by Hao et al. where the oxidation of the thienyl moiety was observed in the range +1.53 to 1.74 V *vs.* Ag/Ag$^+$.[53] In some cases oxidation at potentials higher than +1.4 V lead to gradual loss of all characteristic oxidation and reduction potentials and sometimes resulted in deposition of a film onto the working and counter electrode surfaces which is attributed to "polymerisation" of the compound. Electropolymerisation processes are known for thiophene systems[54] and so these compounds require further investigation. Complextion with dicobalt hexacarbonyl caused only minor shifts in the thiophene oxidation potential, with an additional irreversible oxidation and irreversible reduction wave observed for each of the complexes. An irreversible oxidation process was observed in the range +0.88 to 0.99 V *vs.* Fc/Fc$^+$. This was ascribed to oxidation of the cobalt metal centre and is in agreement with previous studies for cobalt carbonyl systems where oxidation potentials were observed in the range +0.70 to 0.90 V.[55] The irreversible reduction of the cobalt metal centre was observed in the range -0.95 to -1.16 V *vs.* Fc/Fc$^+$ which corresponds to the reduction of the metal cluster and is in the range reported by Jung et al.[56] Again, in some cases oxidation at potentials higher than +1.4 V lead to loss of all characteristic oxidation and reduction potentials. This phenomenon has been previously observed for dicobalt carbonyl complexes and has been assigned to decomposition of the complex at the electrode surface and perturbs further electrochemical analysis.

Compound	E_{pa} (V) [Irr]	E_{pc} (V) [Irr]
PhCCPh[a]	1.92	
PhCCPh-Co$_2$(CO)$_6$	0.95, 1.91	-1.06
NB-L1[a]	1.65	
NB-C1	0.89, 1.60	-1.03
NB-L2[a]	1.78	
NB-C2	0.88, 1.72	-1.05
NB-L3[a]	1.47	
NB-C3	0.91, 1.41	-1.33
NB-L4[a]	1.55	
NB-C4	0.88, 1.58	-0.97
NB-L5[a]	1.72	
NB-C5	0.96, 1.76	-1.16
NB-L6[a]	---	
NB-C6	0.99, 1.95	-0.89
NB-L7	1.90	-0.98
NB-C7	---	
NB-L8[a]	1.39, 1.66, 1.99	
NB-C8	0.91, 1.39	-0.95

Table 3   *Electrochemical properties measured at room temperature with a scan rate of 0.1 V/s in 0.1 M TBAPF$_6$/CH$_3$CN solution. E_{pc} and E_{pa} correspond to the cathodic and anodic peak potentials respectively, all quoted in volts* vs. *Fc/Fc$^+$. [a] indicates no reduction processes were observed between 0 V and -2.1 V.*

Electrochemical analysis of **PhCCPh** and **PhCCPh-Co$_2$(CO)$_6$** was carried out as a standard to delineate the effect of the thienyl moiety. The cyclic voltammograms of ligands and complexes are included in appendices B1 – B7.

The cyclic voltammogramof **PhCCPh** is displayed in figure 18 (a). The CV of the reference compound shows a single irreversible oxidation process associated with the generation of the cation radical, with no second oxidation process out to the solvent limit. No reduction processes were observed. The E_{pa} value of the oxidation wave was +1.92 V *vs*. Fc/Fc$^+$ and was due to oxidation of the phenyl moiety. The cyclic voltammogram of **PhCCPh-Co$_2$(CO)$_6$** (Fig. 18, b) displays the oxidation due to the phenyl moiety at +1.91 V *vs*. Fc/Fc$^+$ and an additional irreversible oxidation was observed at +0.95 V *vs*. Fc/Fc$^+$ which was assigned to oxidation of the cobalt metal centre and is in agreement with previous literature observations.[55] An irreversible reduction wave was observed at E_{pc} = -1.06 V *vs*. Fc/Fc$^+$. The reduction peak was attributed to a monoelectronic reduction process at the metal centre. Upon scan reversal in CV, no coupled anodic peak was observed, however a new irreversible peak at +0.22 V appeared. This behaviour resembles other reported (μ_2-alkyne)Co$_2$(CO)$_6$ derivatives and indicates that a reduction process followed by fast decomposition of the radical anion into a variety of fragments occurred.[57] At higher potentials a coating formed on both the working and counter electrode. The reduction peak a -0.79 V *vs*. Fc/Fc$^+$ is assigned to the reduction of this chemically adsorbed cobalt containing product.[60]

227
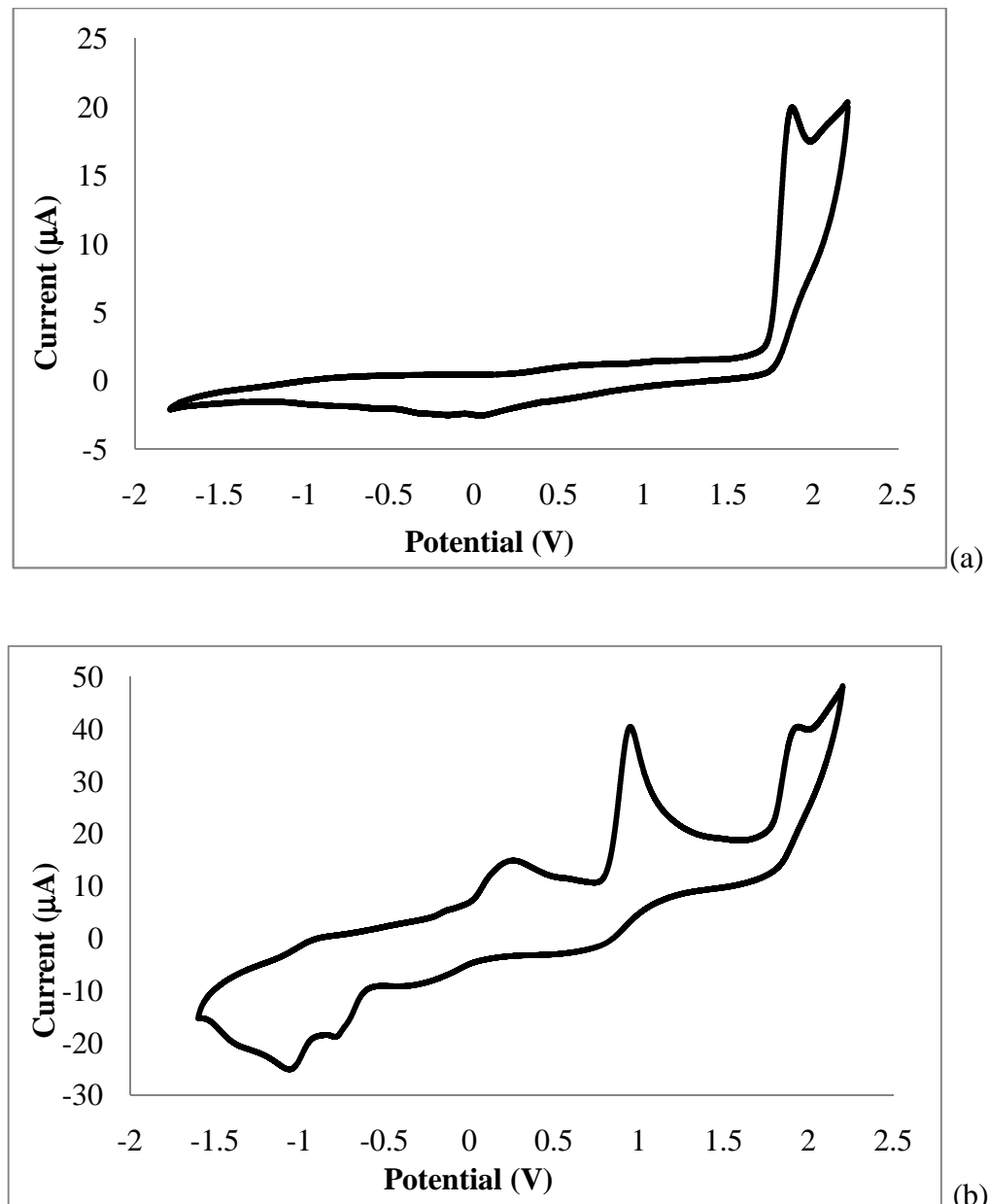
*Figure 18   Cyclic voltammogram of **PhCCPh** (a) and **PhCCPh-Co₂(CO)₆** (b) showing oxidation and reduction waves.*

The cyclic voltammogram of **NB-L1** is displayed in figure 19 (a). An irreversible anodic wave was observed at +1.65 V *vs*. Fc/Fc$^+$. By analogy to the previous system this process corresponds to the initial generation of the cation radical species. It was ascribed to the oxidation of the thienyl unit by comparison with the oxidation peak potential of thiophene (E_p = 1.73 V).[58] No second oxidation process was observed out to the solvent limit, by which stage deposition onto the electrodes occurred indicating that degradation (overoxidation) had occurred. No reduction processes were observed. The corresponding complex **NB-C1** displayed two irreversible oxidation peaks (Fig. 19, b). The oxidation of the cobalt metal centre occurred at +0.89 V *vs*. Fc/Fc$^+$ while oxidation of the thienyl moiety occurred at +1.60 V *vs*. Fc/Fc$^+$. The irreversible reduction of the metal centre was observed at -1.03 V *vs*. Fc/Fc$^+$. On following sweeps new oxidations at +0.14 V and +0.26 V were observed as well as a reduction at -0.74 V. These are attributed to the redox chemistry of a variety of cobalt degradation products discussed above.[57]
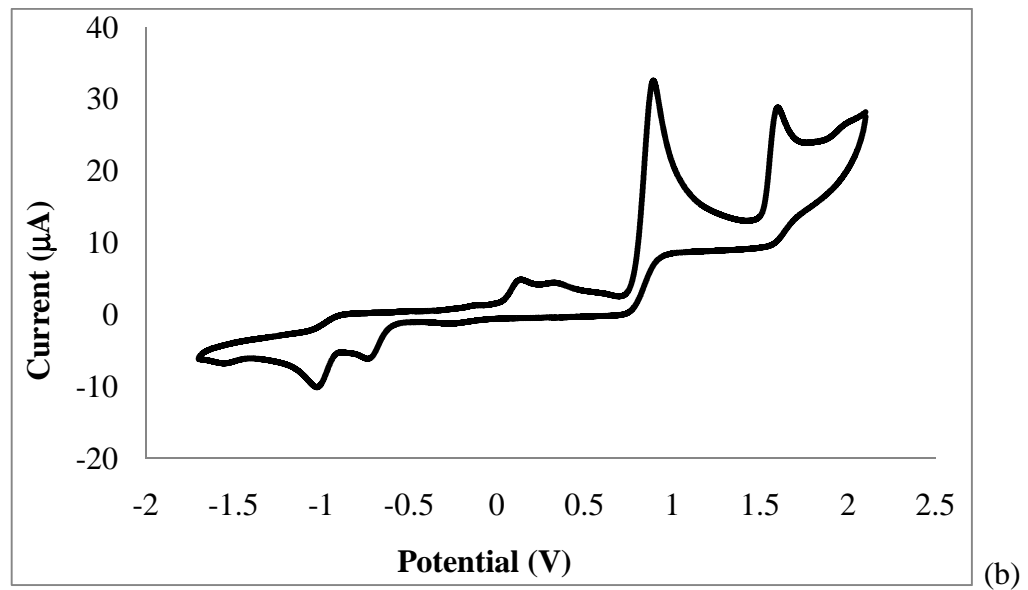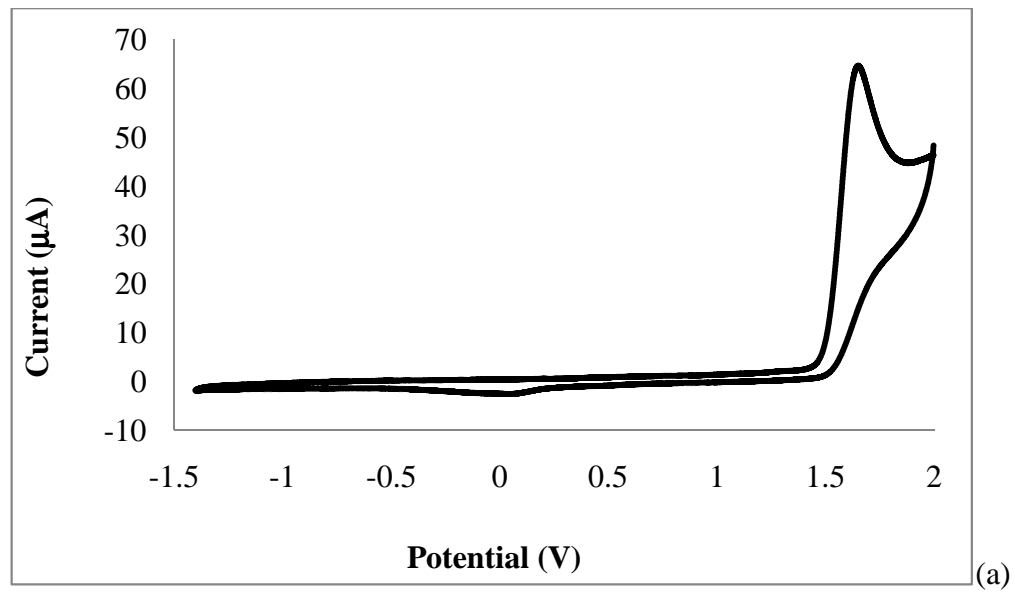
Figure 19   *Cyclic voltammogram of **NB-L1** (a) and **NB-C1** (b) showing oxidation and reduction waves.*

3.4.4 Steady state photolysis

Broadband photolysis ($\lambda_{exc} > 520$ nm, $\lambda_{exc} > 410$ nm and $\lambda_{exc} > 320$ nm) of the dicobalt hexacarbonyl complexes in the presence of the trapping ligand, PPh$_3$, resulted in the formation of a pentacarbonyl species. In each case, product bands were assigned by comparison with carbonyl bands of Co$_2$(CO)$_5$ type species in the literature.[27,40,41] In general, irradiation at $\lambda > 520$ nm resulted in the weak production of the triphenylphosphine trapped pentacarbonyl species. Following irradiation at $\lambda > 410$ nm an improved efficiency for production of the pentacarbonyl formation was observed, while irradiation at $\lambda > 320$ nm results in greatly improved efficiency for pentacarbonyl formation. Furthermore, formation of the tetracarbonyl photoproduct was observed under high energy irradiation ($\lambda > 320$ nm). The IR bands observed and assigned to formation of the trapped photoproducts (Co$_2$(CO)$_5$ species and Co$_2$(CO)$_4$ species) were in good agreement with those previously observed by Chia,[28] Gordon[40] and Long.[41] Table 4 gives the IR data for the parent dicobalt hexacarbonyl complexes and the photoproducts observed. Three steady state photolysis spectra are included and discussed in more detail. The remainder are included in appendices C1 – C5.

Complex	v(CO) (cm^{-1} ± 2 cm^{-1})
NB-C1-Co$_2$(CO)$_6$(*parent*)	2091, 2058, 2030
NB-C1-Co$_2$(CO)$_5$(PPh$_3$)	2064, 2018, 2005
NB-C1-Co$_2$(CO)$_4$(PPh$_3$)$_2$	1996, 1972, 1960
NB-C2-Co$_2$(CO)$_6$(*parent*)	2090, 2055, 2028
NB-C2-Co$_2$(CO)$_5$(PPh$_3$)	2064, 2018, 2005
NB-C2-Co$_2$(CO)$_4$(PPh$_3$)$_2$	1996, 1980, 1971
NB-C3-Co$_2$(CO)$_6$(*parent*)	2091, 2058, 2031
NB-C3-Co$_2$(CO)$_5$(PPh$_3$)	2065, 2020, 2007
NB-C3-Co$_2$(CO)$_4$(PPh$_3$)$_2$	1984, 1973, 1951, 1941
NB-C4-Co$_2$(CO)$_6$(*parent*)	2091, 2059, 2032
NB-C4-Co$_2$(CO)$_5$(PPh$_3$)	2065, 2019, 2007
NB-C4-Co$_2$(CO)$_4$(PPh$_3$)$_2$	1997, 1972, 1943
NB-C5-Co$_2$(CO)$_6$(*parent*)	2092, 2057, 2030
NB-C5-Co$_2$(CO)$_5$(PPh$_3$)	2065, 2019, 2007
NB-C5-Co$_2$(CO)$_4$(PPh$_3$)$_2$	1997, 1972, 1943
NB-C6-Co$_2$(CO)$_6$(*parent*)	2095, 2062, 2035
NB-C6-Co$_2$(CO)$_5$(PPh$_3$)	2068, 2024, 2011
NB-C6-Co$_2$(CO)$_4$(PPh$_3$)$_2$	1985, 1977, 1955, 1944
NB-C7-Co$_2$(CO)$_6$(*parent*)	2094, 2061, 2034
NB-C7-Co$_2$(CO)$_5$(PPh$_3$)	2067, 2021, 2009
NB-C7-Co$_2$(CO)$_4$(PPh$_3$)$_2$	1974, 1960
NB-C8-Co$_2$(CO)$_6$(*parent*)	2094, 2088, 2060, 2031
NB-C8-Co$_2$(CO)$_5$(PPh$_3$)	2065, 2053, 2021, 2005, 1975
NB-C8-Co$_2$(CO)$_4$(PPh$_3$)$_2$	2023, 2019, 2000, 1995, 1983, 1950

Table 4   *IR data for dicobalt hexacarbonyl complexes and the corresponding photoproducts produced following broadband irradiation in hexane solution in the presence of PPh$_3$.*

Extended broadband photolysis of the dicobalt hexacarbonyl complex, **NB-C1**, at $\lambda_{exc} >$ 520 nm for 30 minutes resulted in minor bleaching of the parent absorbance bands at 2091, 2058 and 2030 cm^{-1} and generation of weak product bands at 2064, 2018 and 2005 cm^{-1} (Fig. 20). Subsequent photolysis at $\lambda_{exc} >$ 410 nm for 12 minutes resulted in an increase in the intensity of these bands, assigned to formation of the pentacarbonyl species, **NB-C1-Co$_2$(CO)$_5$(PPh$_3$)**. Concomitant generation of weak bands at 1996, 1972 and 1960 cm^{-1} was observed which were tentatively assigned to generation of the tetracarbonyl species, **NB-C1-Co$_2$(CO)$_4$(PPh$_3$)$_2$**. Continued irradiation at $\lambda_{exc} >$ 320 nm for 5 minutes caused further depletion of parent bands and a notable intensification of the photoproduct bands. The assignment of bands to the pentacarbonyl species **NB-C1-Co$_2$(CO)$_5$(PPh$_3$)** and tetracarbonyl species **NB-C1-Co$_2$(CO)$_4$(PPh$_3$)$_2$**, were based on similarities with those observed by Coleman et al.[27] and Arnanz et al.[60] following formation of trapped pentacarbonyl and tetracarbonyl species respectively.
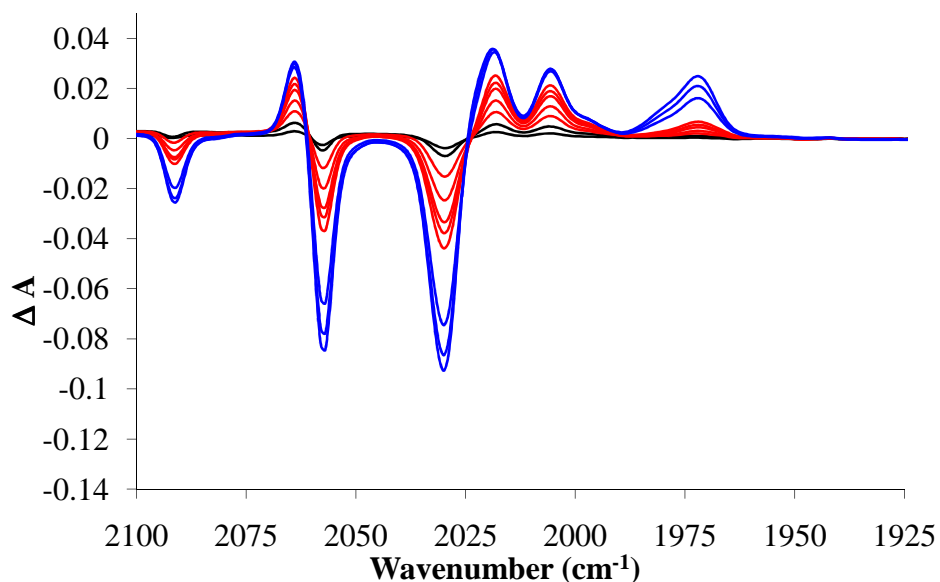
Figure 20   *Infrared difference spectra following irradiation of **NB-C1** in hexane with PPh$_3$ at $\lambda_{exc} >$ 520 nm (black lines, 30 minutes total irradiation), $\lambda_{exc} >$ 410 nm (red lines, 12 minutes total irradiation) and $\lambda_{exc} >$ 320 nm (blue lines, 5 minutes total irradiation). Negative bands indicate bleaching of the parent complex while positive bands indicate generation of the pentacarbonyl and tetracarbonyl species.*

The aldehyde complex, **NB-C6,** was subjected to broadband irradiation ($\lambda_{exc} > 520$ nm for 30 minutes, $\lambda_{exc} > 410$ nm for 10 minutes and $\lambda_{exc} > 320$ nm for 3 minutes) (Fig. 21). Minor depletion of the parent hexacarbonyl bands at 2095, 2062 and 2035 cm^{-1} was observed upon $\lambda_{exc} > 520$ nm irradiation with the growth of positive bands assigned to the pentacarbonyl complex **NB-C6-Co$_2$(CO)$_5$(PPh$_3$)** at 2068, 2024 and 2011 cm^{-1}. Irradiation with $\lambda_{exc} > 410$ nm resulted in intensification of the pentacarbonyl product bands (2068, 2024, 2011 cm^{-1}) and generation of bands at 1985, 1977, 1955 and 1944 cm^{-1} which were attributed to the tetracarbonyl product, **NB-C6-Co$_2$(CO)$_4$(PPh$_3$)$_2$.** Photolysis of the pentacarbonyl species, **NB-C6-Co$_2$(CO)$_5$(PPh$_3$),** also occurred, as the bands at 2068, 2024 and 2011 cm^{-1} decreased in intensity. The bands at 1985, 1977, 1955 and 1944 cm^{-1} increased in absorbance indicating increased production of the tetracarbonyl product **NB-C6-Co$_2$(CO)$_4$(PPh$_3$)$_2$.**[60]
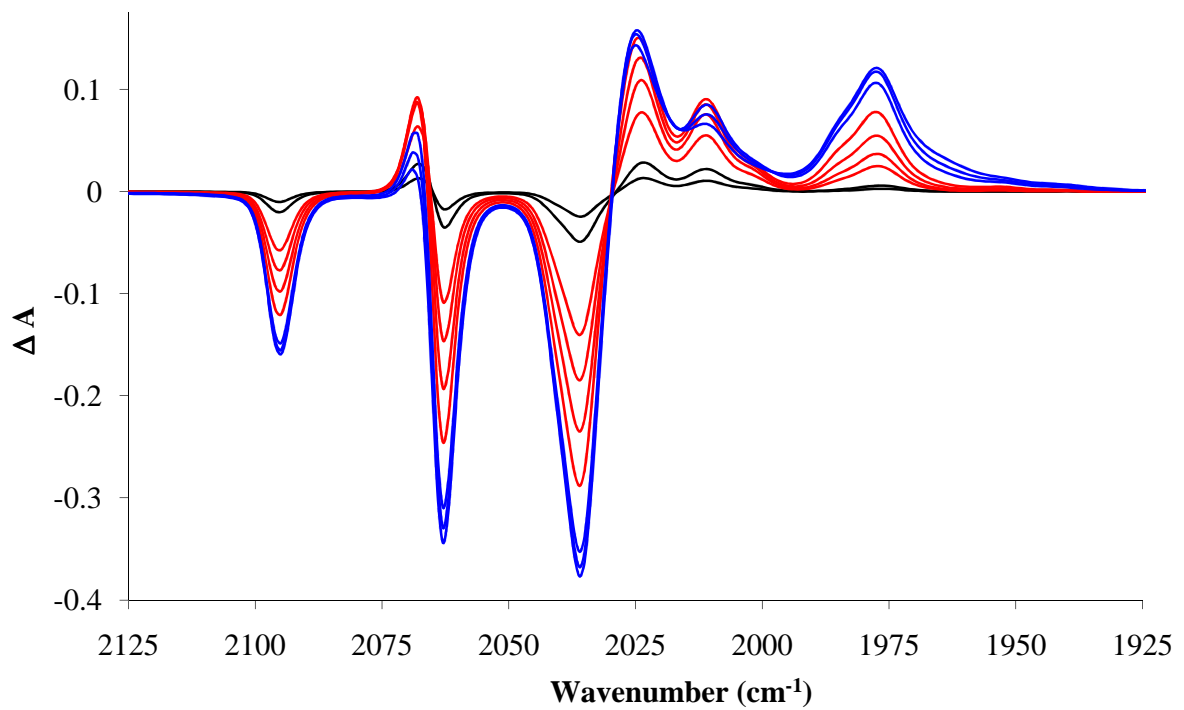
Figure 21   *Infrared difference spectra following irradiation of **NB-C6** in hexane with PPh$_3$ at $\lambda_{exc} > 520$ nm (black lines, 30 minutes total irradiation), $\lambda_{exc} > 410$ nm (red lines, 10 minutes total irradiation) and $\lambda_{exc} > 320$ nm (blue lines, 3 minutes total irradiation). Negative bands indicate bleaching of the parent complex while positive bands indicate generation of the pentacarbonyl and tetracarbonyl species.*

Extended broadband photolysis of **NB-C8** at $\lambda_{exc} > 520$ nm for 30 minutes resulted in bleaching of the parent bands at 2094, 2088, 2060 and 2031 cm^{-1} and the generation of weak product bands at 2065, 2053, 2021, 2009 and 1974 cm^{-1} due to pentacarbonyl formation (Fig. 22). These IR bands continued to grow following irradiation at $\lambda_{exc} > 410$ nm for a further 10 minutes. Photolysis $\lambda_{exc} > 320$ nm for 3 minutes resulted in the depletion of the photoproduct bands at 2065 and 2053 cm^{-1}. This indicated depletion of the pentacarbonyl photoproduct and the generation of the tetracarbonyl species. The bands at 2021 cm^{-1} splits into two bands, 2023 and 2019 cm^{-1} and continued to increase in intensity. The band at 2009 cm^{-1} shifted to lower wavenumber 2004 cm^{-1} and increased in intensity. Bands indicative of tetracarbonyl formation (2023, 1995, 1983, 1975 and 1948 cm^{-1}) also increased in intensity following irradiation at $\lambda_{exc} > 320$ nm (5 minutes). The larger number of bands, both for the parent hexacarbonyl complex **NB-C8** and photochemically generated pentacarbonyl and tetracarbonyl complexes was attributed to the two dicobalt hexacarbonyl centres in this molecule. The new absorbance bands are ascribed to the formation of the trapped species at both of the metal centres.
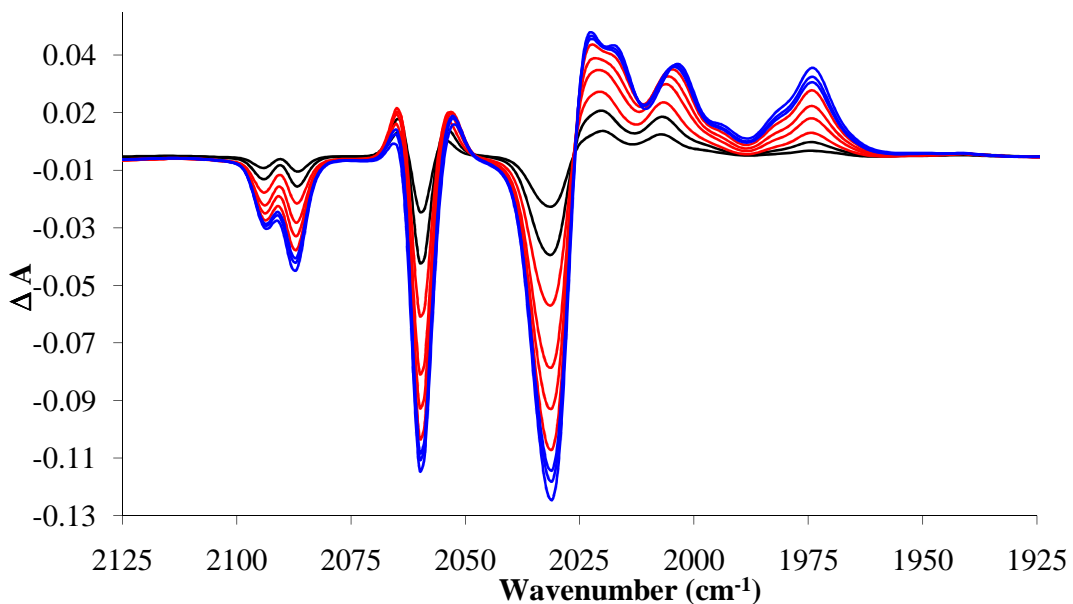
*Figure 22   Infrared difference spectra following irradiation of **NBC8** in hexane with PPh$_3$ at $\lambda_{exc} > 520$ nm (black, 30 minutes total irradiation), $\lambda_{exc} > 410$ nm (red, 10 minutes total irradiation) and $\lambda_{exc} > 320$ nm (blue, 3 minutes total irradiation). Negative bands indicate bleaching of the parent complex while positive bands indicate generation of the photoproduct.*

3.4.5 Quantum yield of CO loss

The quantum yield of the photoinduced expulsion of CO from three (μ_2-alkyne)$Co_2(CO)_6$ complexes was measured in a cyclohexane solution at 298 K. The experiments were undertaken for **PhCCPh-Co$_2$(CO)$_6$, ThCCPh-Co$_2$(CO)$_6$ (NB-C1)** and **FcCCH-Co$_2$(CO)$_6$** (Fig. 23). **FcCCH-Co$_2$(CO)$_6$** was synthesised according to literature methods and is detailed in appendix D. Potassium ferrioxalate actinometry was used to measure the incident light intensity. A 200 W Hg-Xe arc lamp was used and the required Hg spectral line selected using interface filters. Measurements were made using four excitation wavelengths of 313, 365, 405 and 546 nm. Triphenylphosphine was used as a trapping ligand for the photoproduced (μ_2-alkyne)$Co_2(CO)_5$ species. Prior to the photolysis experiments, the trapped (μ_2-alkyne)dicobalt pentacarbonyl species was isolated and characterised (appendices E1-E3). In all cases a new absorbance centred at approximately 400 nm was observed for the triphenylphosphine trapped pentacarbonyl species (Fig. 24), and it was at 400 nm that quantum yields were calculated.
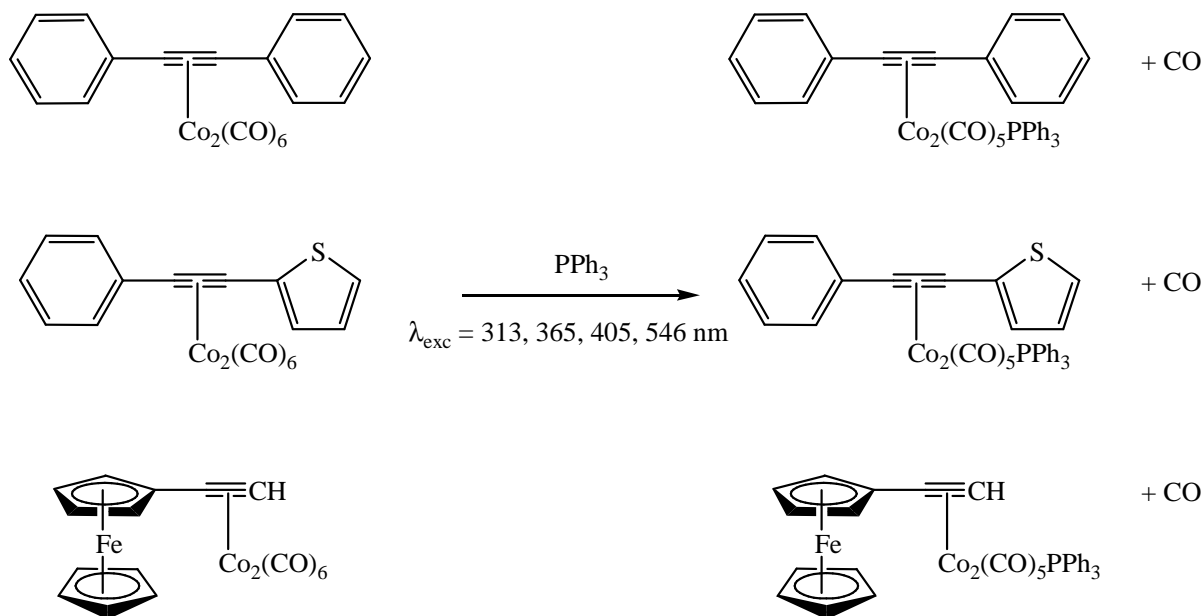
Figure 23   Reaction following photolysis of the dicobalt hexacarbonyl complexes and the trapped pentacarbonyl species produced.
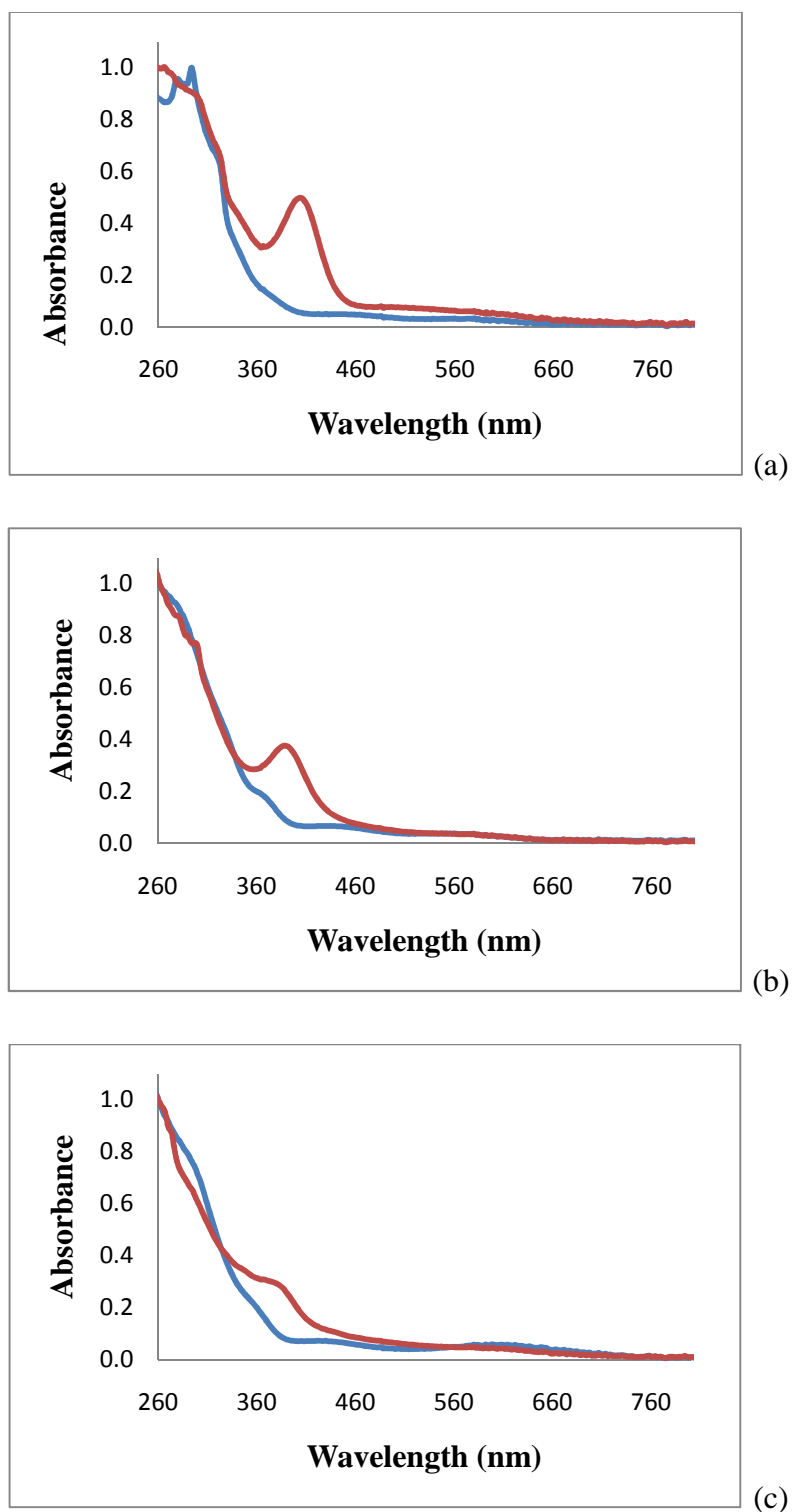
Figure 24 *Absorbance spectra of dicobalt hexacarbonyl complexes (blue lines), **PhCCPh-Co₂(CO)₆** (a), **ThCCPh-Co₂(CO)₆** (b), **FcCCH-Co₂(CO)₆** (c) and corresponding trapped pentacarbonyl complex (red lines) recorded in cyclohexane. Spectra have been normalised at their λ_max.*

Photosubstitution of the three complexes was monitored by UV-vis spectroscopy. In each experiment the number of photolysed molecules was determined by comparison of UV-vis spectra taken before and after photolysis. Further experimental details and all calculations are given in appendix F. Conversions were driven to a maximum of 10 % to minimise the effect of product absorbance at the excitation wavelength

The quantum yield for CO loss under steady state irradiation (Table 5) was determined by application of the Beer-Lambert law. The results show that the efficiency of CO loss is both wavelength and complex dependant.

	Irradiation	Wavelength		
Complex	313 nm	365 nm	405 nm	546 nm
$PhCCPh-Co_2(CO)_6$	0.078	0.035	0.027	0.045
$ThCCPh-Co_2(CO)_6$	0.145	0.080	0.045	0.106
$FcCCH-Co_2(CO)_6$	0.269	0.071	0.047	0.233

Table 5   Quantum yields for CO loss recorded in cyclohexane.

3.4.6   Picosecond time resolved infrared studies

A picosecond time resolved infrared study of the photochemical activation of (μ_2-alkyne)$Co_2(CO)_6$ complexes was carried out for **PhCCPh-Co$_2$(CO)$_6$, ThCCPh-Co$_2$(CO)$_6$** and **FcCCH-Co$_2$(CO)$_6$** in solution at room temperature (298 K). Photo-excitation ($\lambda_{exc} = 400$ nm, $\tau_{FWHM} = 150$ fs) of the three complexes (and in the case of **FcCCH-Co$_2$(CO)$_6$** also at 532 nm) resulted in depletion of the ground state $\nu(CO)$ bands of all three complexes with the appearance of new bands in the $\nu(CO)$ region. All complexes exhibited similar spectral changes and the kinetics were largely solvent independent. The photoproduct IR bands undergo vibrational cooling (over ~10 ps) with a shift in wavenumber to higher frequency. These new bands decay with complete product recovery of the initial spectrum on a picosecond timescale.

Lifetimes of the excited state transient species observed in the TRIR experiments were calculated and are presented in table 6 below. The kinetics of the recovery was largely solvent independent.

	Lifetime	τ (ps)	
Complex	THF	CH$_3$CN	Pentane
PhCCPh-Co$_2$(CO)$_6$	70	69	71
ThCCPh-Co$_2$(CO)$_6$	63	–	–
FcCCH-Co$_2$(CO)$_6$	38	50	–

Table 6   *Lifetimes for the excited state transient species produced following excitation at 400 nm. Lifetimes are +/- 5 ps.*

3.4.6.1 TRIR studies of PhCCPh-Co$_2$(CO)$_6$
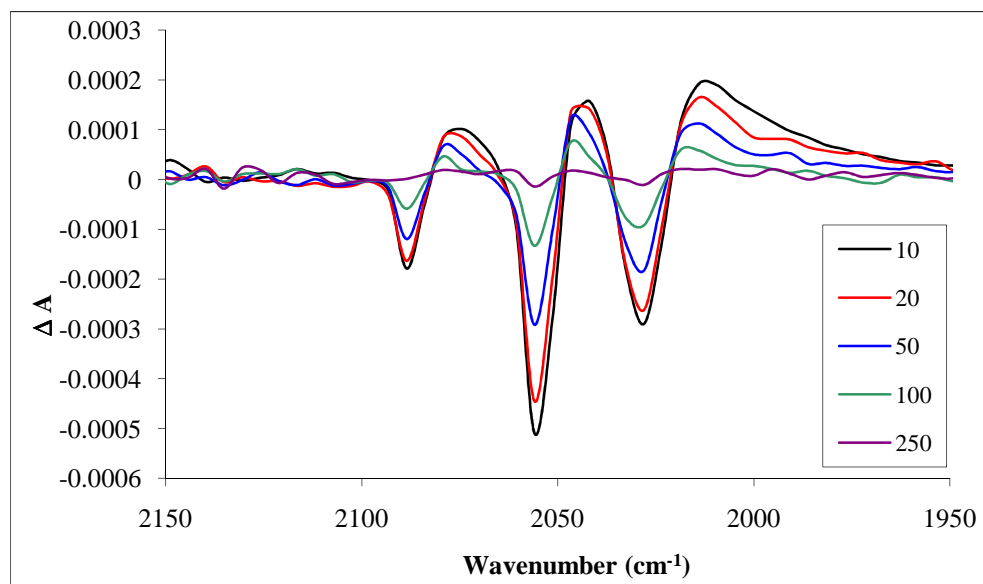
Figure 25   *Transient absorbance difference spectra at 10, 20, 50 100 and 250 ps, following excitation of **PhCCPh-Co$_2$(CO)$_6$** in THF at 400 nm.*

Photolysis of **PhCCPh-Co$_2$(CO)$_6$** (λ_{exc} = 400 nm, τ_{FWHM} = 150 fs) in THF solution at room temperature resulted in depletion of the ground state ν(CO) peaks at 2089, 2055 and 2028 cm^{-1} within 1 ps (first spectrum after 1 ps delay) (Fig. 25). Three new peaks were formed at 2070, 2040 and 2009 cm^{-1}. The IR bands underwent vibrational cooling (over ~10 ps), with a shift in wavenumber to higher frequency, to 2073, 2042 and 2012 cm^{-1}. The bands relax to the ground state with a lifetime of 70 ps with concomitant recovery of the parent bleaches.

In acetonitrile the three parent bands (2089, 2055 and 2031 cm^{-1}) are depleted within the laser pulse with concomitant formation of three new bands at 2074, 2041 and 2006 cm^{-1} following irradiation (λ_{exc} = 400 nm). These new bands undergo vibrational cooling and shift to 2082, 2048 and 2019 cm^{-1} where decay of the excited state is fully complete with a lifetime of 69 ps. No residual bleaches were observed in the final spectrum (appendix G1).

In pentane, irradiation at 400 nm depleted the parent peaks (2089, 2055 and 2031 cm^{-1}) and produced new peaks at 2069, 2041, 2016 and 2006 (sh) cm^{-1} within the instrument response time of 1 ps (appendix G2). The peaks then shift to 2079, 2045 and 2021 cm^{-1} over 10 ps due to vibrational cooling. Over the next 250 ps, the product peaks decay back to the ground state with a lifetime of 71 ps and simultaneous recovery of the parent bleaches was observed.

3.4.6.2 TRIR studies of ThCCPh-Co$_2$(CO)$_6$
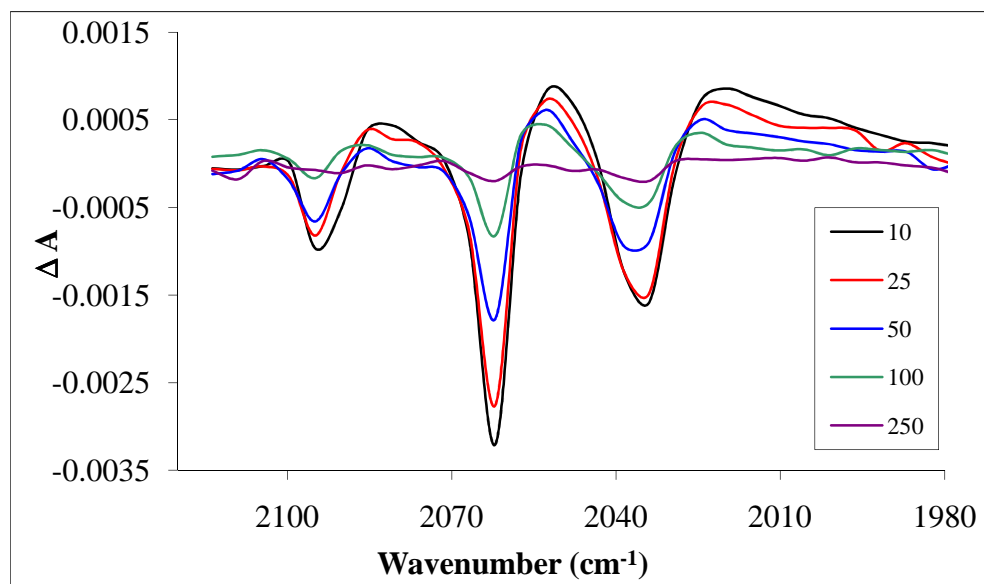
*Figure 26   Transient absorbance difference spectra at 10, 25, 50, 100 and 250 ps, following excitation of **ThCCPh-Co$_2$(CO)$_6$** in CH$_3$CN at 400 nm.*

Comparable spectroscopic changes in the ν(CO) region were observed for **ThCCPh-Co$_2$(CO)$_6$**. In CH$_3$CN solution, photolysis of the hexacarbonyl complex caused depletion of the infrared bands at 2091, 2058 and 2030 cm^{-1} (negative signals in Fig. 26) within the excitation pulse, with formation of bands initially at 2076, 2048 and 2006 cm^{-1}. The product (positive) peaks undergo vibrational cooling on the picosecond timescale and shift to 2081, 2048 and 2016 cm^{-1}. The transient bands relax to the ground state with a lifetime of 63 ps. Importantly compete recovery of the parent bands was also observed.

3.4.6.3 TRIR studies of FcCCH-Co$_2$(CO)$_6$
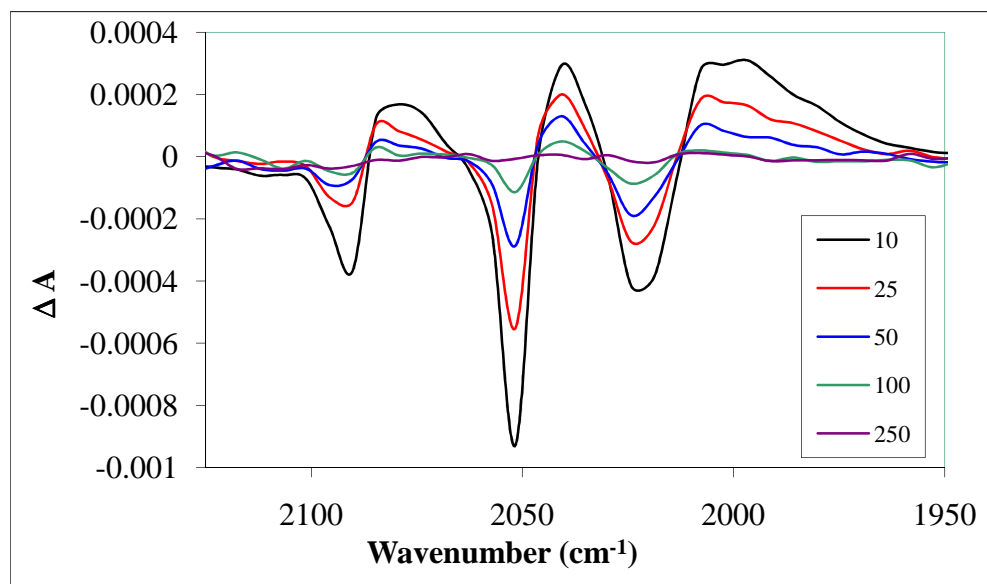
Figure 27   Transient absorbance difference spectra at 10, 20, 50, 75 and 250 ps,
*following excitation of **FcCCH-Co$_2$(CO)$_6$** in THF at 532 nm.*

Akin to the previous results, irradiation of **FcCCH-Co$_2$(CO)$_6$** in acetonitrile solution at λ_{exc} = 400 nm caused changes in the ν(CO) bands in the infrared spectrum (appendix G3). The parent bands of **FcCCH-Co$_2$(CO)$_6$** observed at 2090, 2052 and 2028 cm^{-1} depleted and three new bands at 2071, 2042 and 2005 cm^{-1} appeared within the laser pulse. The IR bands undergo vibrational cooling (over ~10 ps), with a shift in wavenumber to higher frequency, to 2080, 2046 and 2009 cm^{-1}. The bands decay a lifetime of 50 ps with concomitant recovery of the parent bleaches.

Photolysis was carried out at 532 nm to ascertain if there was a wavelength dependence on the photochemical processes observed in the complexes. Irradiation of a solution of **FcCCH-Co$_2$(CO)$_6$** in THF resulted in a bleaching of the parent IR bands with simultaneous formation of new bands at 2073, 2041, 2008 and 1997 (sh) cm^{-1} (Fig. 27). These bands undergo vibrational cooling and shift to 2079, 2041, 2007 and 1997 (sh) cm^{-1} where they fully decay and the parent bands recover to pre-irradiation levels as observed previously when using 400 nm excitation.

Photoexcitation of carbonyl complexes often results in photosubstitution of a carbonyl group by the solvent and formation of a solvent trapped pentacarbonyl species (μ_2-alkyne)$Co_2(CO)_5$(solvent). To rule out the possibility of a solvent pentacarbonyl species which absorbs in a similar region to either the parent complex, or underneath the new bands observed in this study, a trapping ligand was employed. A solution of **FcCCH-Co$_2$(CO)$_6$** in THF was doped with an excess of triphenylphosphine and irradiated at $\lambda_{exc.}$ = 532 nm. Spectroscopic changes in the ν(CO) region correspond well with those previously observed (appendix G4). The parent bands are depleted and new bands are observed at 2073, 2041, 2008 and 1997 cm^{-1} within 1 ps. The new bands undergo vibrational cooling and shift to 2084, 2046 and 2007 cm^{-1}. No new infrared bands were observed on the nanosecond timescale that could be assigned to (μ_2-alkyne)$Co_2(CO)_5(PPh_3)$ indicating that photosubstitution did not occur for this system within these experimental conditions. This is in contrast to steady state photolysis where, in the presence of PPh$_3$, the mono- and subsequently di-substituted complexes formed (appendix H).

3.5 **Discussion**

3.5.1 **Synthesis and spectroscopic characterisation**

Ligands **NB-L1** – **NB-L5** have been previously synthesised and spectroscopic data were in agreement with reported data. All other ligands and all complexes are novel compounds. The NMR spectroscopic data (^{1}H and ^{13}C) for ligands and complexes were consistent with their formulation. In the ^{1}H NMR spectra signals due to the thiophene ring(s) in addition to complex multiplets due to aromatic protons were observed in the range 7.0 – 8.5 ppm. In ^{13}C NMR spectra, the signals belonging to the thiophene ring (C_2, C_3, C_4 and C_5, Fig. 28) and the alkynyl units (C_6 and C_7, Fig. 28) were observed in the aromatic region of the spectrum. The signals of the free and coordinated acetylene units were easily observed in the region 74-100 ppm. The metal carbonyl resonances in all the complexes appeared as one signal at ~199 ppm.
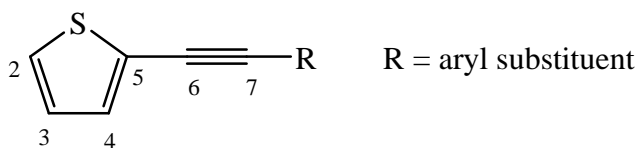
Figure 28   *Numbering of thienyl and ethynyl carbons.*

The IR spectra in the carbonyl region for the complexes show signals corresponding to terminal carbonyl ligands only. These spectral patterns are similar to those observed for previously reported alkyne dicobalt carbonyl complexes.[27, 41] The absence of the alkyne stretch, $\nu(C\equiv C)$, in the region of 2200 cm^{-1} indicated that the alkynyl bond has lost its triple bond character and was coordinated to $Co_2(CO)_6$.

3.5.2   UV-vis absorbance studies

All compounds in this chapter exhibit strong absorbance bands in the UV-vis region of the spectrum normally associated with ligand localised $\pi \rightarrow \pi^*$ transitions. The absorbance spectra of some of the ligands and complexes are shown and discussed below.

The $C_3 - C_4$ bond in the thiophene ring was reported to have less double bond character than the $C_2 - C_3$ bond[59] and as a consequence the overall conjugation of the 3-ethynylthiophene derivatives, **NB-L2** and **NB-L4,** is expected to be lower than in the 2-ethynylthiophene derivatives, **NB-L1** and **NB-L3**. This argument is supported by the electronic absorbance spectra for the compounds (Fig. 29). The λ_{max} for **NB-L1** and **NB-L3** are observed at 302 and 318 nm however the λ_{max} for **NB-L2** and **NB-L4** are significantly blue shifted to 282 and 300 nm respectively. This hypsochromic shift of 20 nm (for **NB-L1** $\rightarrow$ **NB-L2**) and 18 nm (for **NB-L3** $\rightarrow$ **NB-L4**) in the absorbance λ_{max} indicated less overall conjugation within the molecule. A similar shift was previously observed by Arnanz et al.[60] Sakar and Hanley also observed a hypsochromic shift in absorbance spectra when thiophenes were conjugated through the C_3 or C_4 position in [18]annulene ring systems.[61]
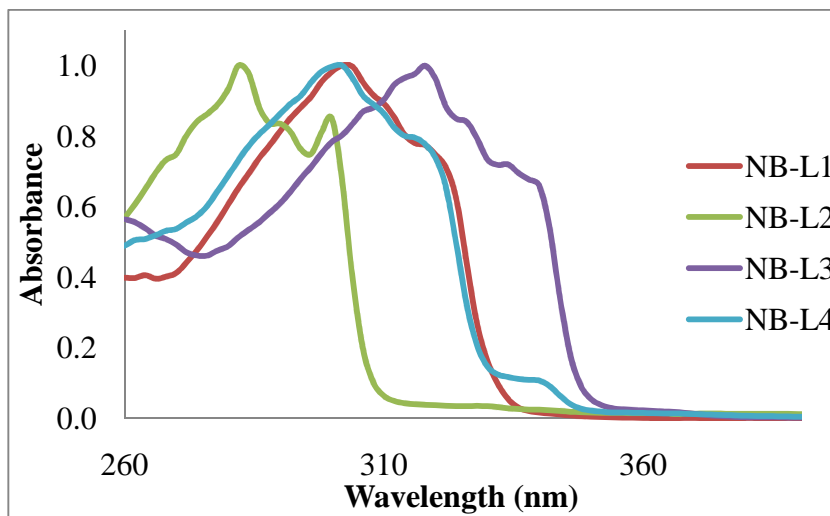
*Figure 29   Overlay of the electronic absorbance spectra of **NB-L1**, **NB-L2**, **NB-L3** and*
***NB-L4** in CH$_2$Cl$_2$. Spectra normalised at their λ_{max}.*

The absorbance spectra of ligands **NB-L1**, **NB-L5**, **NB-L6** and **NB-L7** are presented in figure 30. The absorbance λ_{max} are bathochromically shifted with appropriate substitution. On replacing the H at the thien-5-yl position in **NB-L1** with the more electronegative bromine (**NB-L5**), aldehyde (**NB-L6**) and dicyanovinyl unit (**NB-L7**) the absorbance maxima shifts from 318 nm to 326 nm to 358 nm to 412 nm respectively. This is possibly due to an increase in electron delocalisation within the molecule on adding more electron accepting terminal groups. This is in agreement with the results published by Coleman et al. where terminal group substitution affected the absorbance of organic molecules.[27]
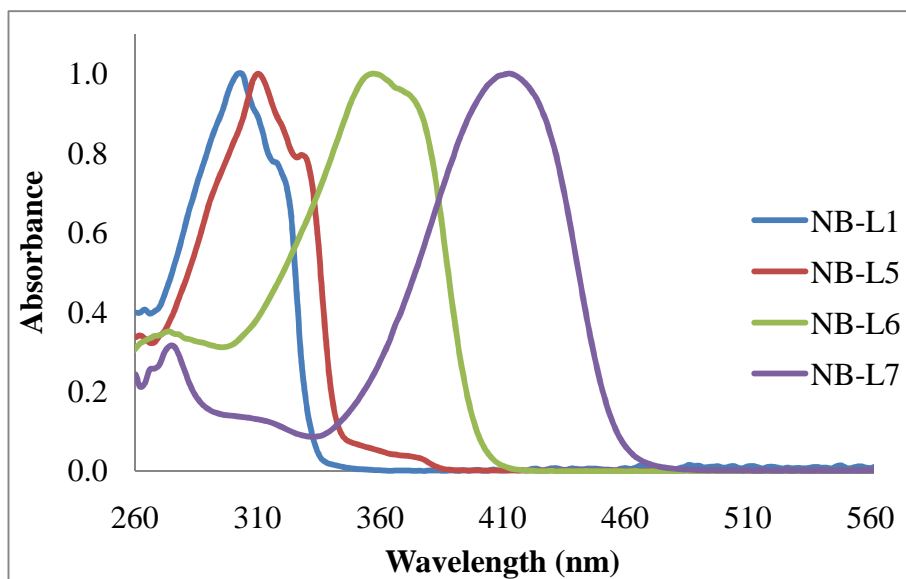
*Figure 30   Overlay of the UV-vis absorbance spectra of **NB-L1**, **NB-L5**, **NB-L6** and*
*   **NB-L7** in CH₂Cl₂. Spectra normalised at their λ$_{max.}$*

Coordination of the dicobalt carbonyl moiety (**NB-C1 – NB-C8**) resulted in broader absorbance bands with less definition in the electronic spectrum. Figure 31 depicts the change in absorbance upon coordination of the metal carbonyl to the ethynyl moiety for ligand and complex pairs, **NB-L3**/**NB-C3** and **NB-L5**/**NB-C5**. The high energy transitions are now π-π* with metal - π* (M = Co) transitions. Ligand field transitions maybe present but the contribution will be small in relation to π-π* transitions. For all the $Co_2(CO)_6$ complexes, weak low energy bands are observed between 430 and 600 nm which extend to approximately 680 nm. These may be assigned to weak Co ($d\pi$) $\rightarrow$ ligand (π) charge transfer (MLCT) transitions and weak d-d transitions between the two metal centres. The

metal upsets the symmetry in the system and that changes how the high energy π-π^* transition absorbs. The fine structure of the transitions still exists but they are not resolved as in the free ligand.

(a)

(b)
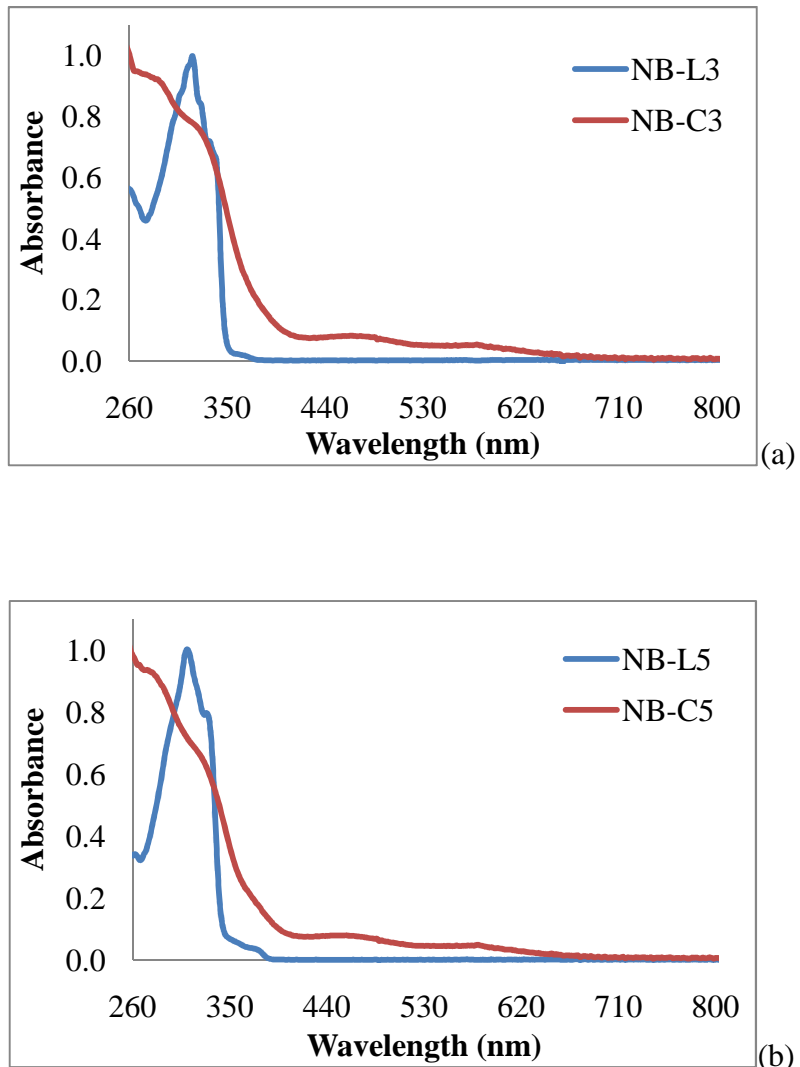
Figure 31   *Absorbance spectra of ligand and complex pairs **NB-L3/NB-C3** (a) and **NB-L5/NB-C5** (b) recorded in CH₂Cl₂. Spectra normalised at their λ_max.*

3.5.3 Steady state fluorescence studies

Diphenylacetylene has previously been reported to have a weak emission at room temperature in CH_2Cl_2 however at low temperature (77 K) an intense well resolved emission was recorded.[52b] This temperature dependence of emission is attributed to the close vicinity of the S_2 and S_1 excited states. The latter is a non-emissive "dark" state with a distorted geometry. The activation energy barrier renders the $S_2 \rightarrow S_1$ decay thermally activated and operative at room temperature the result of which is the fast depopulation of S_2 causing a very weak and short lived emission. The ground state of diphenylacetylene belongs to the D_{2h} point group. Hirata et al. carried out picosecond time resolved absorbance measurements and reported a "bright" state with a fluorescent lifetime of about 8 ps which is a precursor to the dark state.[62] The fluorescing state was assigned to the higher singlet state.

The excited-state dynamics of most organic molecules is concerned with low-lying excited states of π-π* character. More recently computational and experimental studies on aromatic ethynes show that the bound excited state of a π-σ* configuration which rises from the promotion of an electron from the aromatic π orbital to the σ* orbital, localised on the –C≡CH, can be low-lying and has pronounced effects on the fluorescence of these molecules.[63] TD-DFT was used to probe these low-lying excited states. The results indicated that the lowest-energy singlet state is the π-π* state in linear compounds of D_{2h} symmetry, the non-emissive π-σ* state is the lowest energy in bent C_{2h} symmetry compounds. The quantum chemical calculations indicate that due to the differing geometry of the π-σ* state relative to that of the fluorescent π-π* state, the π-σ* state crosses the fluorescent π-π* state along the nuclear coordinate involving bending of the –C≡CH triple bonds. The crossing between the bright π-π* state and the dark (or very weakly fluorescent) π-σ* state can account for loss of fluorescence at higher temperatures in solution. A threshold temperature for the thermal quenching of fluorescence was found to be ~120 K for diphenylacetylene. However the attachment of an electron withdrawing group (such as –CN) to diphenylacetylene increases the energy of the π-σ* state and moves the π-π*/π-σ* intersection far away from the Franck-Condon region of the initially prepared π-π* state. The π-π* → π-σ* state switch is therefore not expected to occur in diphenylacetylene with an electron-withdrawing substituent. Extension of the

computational study to di-2-thienylacetylene indicated that the dark π-σ^* state is very slightly above the lowest energy $^1\pi$-π^* state at the linear geometry. The state crossing from the $^1\pi$-π^* to the $^1\pi$-σ^* state is predicted to involve little (if any) energy barriers. Consistent with this prediction, di-2-thienylacetylene does not exhibit fluorescence in solution at room temperature.

Diphenylacetylene was measured as a model compound. It displayed a weak emission with λ_{max} = 325 nm. The linear organic conjugated molecules (**NB-L1** – **NB-L7**) display very low emission or no emission at all. This is not surprising. **NB-L1**, **NB-L2**, **NB-L3** and **NB-L4** did not fluoresce. **NB-L1** was previously reported to be non-fluorescent.[63] The other ligands, **NB-L2**, **NB-L3** and **NB-L4**, also possess C_{2h} symmetry and as such were not expected to fluoresce. According to Zgierski, crossing the state from the $^1\pi$-π^* to the $^1\pi$-σ^* is facile and results in a quenching of fluorescence.[63]

The authors also noted that attachment of an electron withdrawing group to diphenylacetlyene caused the compound to become weakly fluorescent.[63] For compounds **NB-L5**, **NB-L6** and **NB-L7** with electron withdrawing groups at the thien-5-yl position weak fluorescence was observed. A substantial red shift was noted in the emission maxima of **NB-L7** (Table 2). This was attributed to improved electron accepting ability of the dicyanovinyl unit. Following coordination with $Co_2(CO)_6$ a reduction in emission intensity was observed, although no change in the position of the emission band was observed. This suggested that in complexes **NB-C5** - **NB-C7**, the observed emission bands were ligand based without much contribution from the metal centre.

By incorporating a luminescent organic chromophore into linear organic molecules the emission of such species can be greatly increased. This was the case for the ligand and complex pair **NB-L8**/**NB-C8**. They were more luminescent at room temperature (298 K) and showed the highest emission intensity within the study (Fig. 32). Upon complexation the emission bands were significantly reduced in intensity. However no shift in band position or generation of new emission bands was observed. This suggested that for both **NB-L8** and **NB-C8** the emission is solely ligand based.
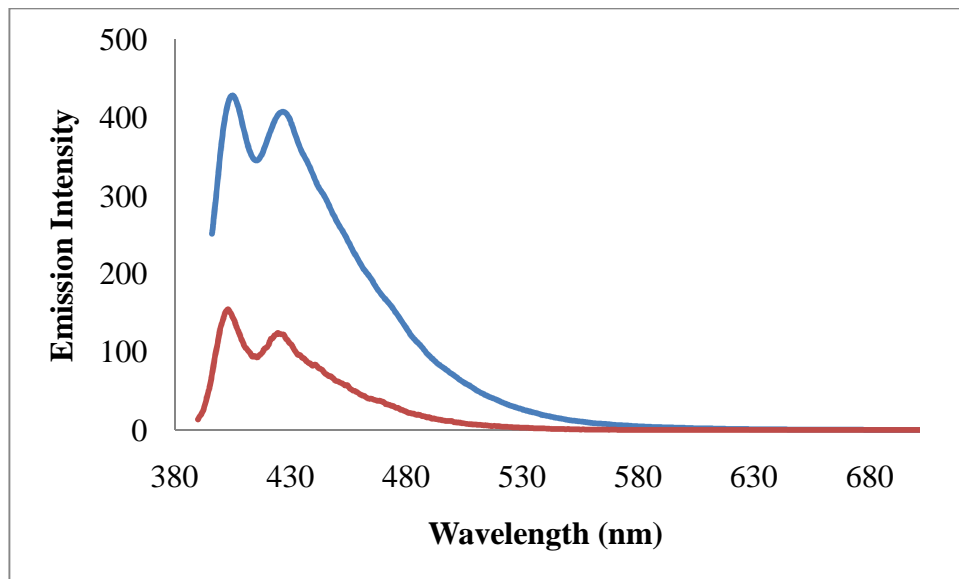
Figure 32　　*Room temperature emission spectra of compounds **NB-L8** (blue line) and **NB-C8** (red line) recorded in CH$_2$Cl$_2$ solution following excitation at 332 nm. Solutions were isoabsorbtive 0.2 AU at λ$_{exc}$ = 332 nm.*

An increase in fluorescence lifetime was observed with increasing the electronegativity of the terminal substituent on the organic ligand (1.94, 2.18 and 3.52 ns for **NB-L5**, **NB-L6** and **NB-L7** respectively). One possibility for the increase in lifetimes along this series is the increase in electron delocalisation within the molecule on replacing the terminal moiety at the thien-5-yl position. The emission intensity and lifetimes of the dicobalt complexes were less than those of the uncomplexed ligands. This was to be expected and has been observed previously.[27] It is attributed to the heavy atom effect. The lifetime of **NB-L8** was measured as 2.62 ns while that of the carbonyl complex **NB-C8** was found to decrease to 0.56 ns at room temperature. Low temperature (77 K) emission studies showed no change in the emission band of **NB-C8** however a lifetime of 2.19 ns was obtained.

3.5.4 Electrochemistry

Again comparing ligands **NB-L1** with **NB-L2** and **NB-L3** with **NB-L4** showed how the effective conjugation in the ligands affected the electrochemical properties. Ligands **NB-L2** and **NB-L4** which possess lesser overall conjugation were oxidised at higher potentials than **NB-L1** and **NB-L3**. It is noteworthy that **NB-L2** and **NB-L4** show greater overall chemical stability than the closely related species **NB-L1** and **NB-L3** derived from 2-thiophene. Arnanz et al. observed similar redox properties which the authors attributed to steric arguments.[60]

Compounds **NB-L1**, **NB-L5** and **NB-L7** are sequentially oxidised at higher potentials. This is due to the inductive effects of the bromine and dicyanovinyl units attached to the thien-5-yl position. The bromine atom in **NB-L5** caused a 70 mV shift to higher potential while the dicyanovinyl moiety caused a shift of 250 mV. This effect of electron withdrawing substituents on the oxidation potentials was previously observed by Zhao and co workers.[64] Thus the addition of an electron withdrawing terminal groups, increased electron delocalisation within the molecule and as a result stabilised the molecules. A similar effect was observed for the corresponding dicobalt hexacarbonyl complexes. Replacement of the H with an electron withdrawing group as in complex **NB-C5** had a similar influence on the oxidation potentials of the complex compared to **NB-C1**. A positive shift of 160 mV in the cathodic direction was observed for the thienyl oxidation when comparing the two complexes.

In all complexes the observed redox behaviour was typical of dicobalt hexacarbonyl complexes. The $Co_2(CO)_6$ entity bound to the alkyne undergoes an irreversible oxidation and an irreversible reduction followed by the fast decomposition of the radical anion into a variety of fragments (EC mechanism).[65]

The electrogenerated monoanion is very unstable and undergoes fast cleavage of the Co-Co bond which produced $Co(CO)_4^-$. This species was observed in the subsequent oxidation sweep where the $Co(CO)_4^-$ fragment was oxidised to the radical $Co(CO)_4^{\cdot}$. A subsequent reduction is ascribed to the reduction of degradation products that were chemically adsorbed onto the electrode. This behaviour was reported previously in related hexacarbonyl complexes of the form $(\mu_2\text{-alkyne})Co_2(CO)_6$.[66] The reduction corresponds to

the formation of the radical anion in which the extra electron occupies a predominantly metal-metal antibonding orbital.[67] Subsequently, rapid metal-metal bond cleavage takes place and disintegration of the anion radical, into variety of fragments, occurs.

The stabilising effect observed for the ligands did not bestow stability onto the complexes. IR spectroelectrochemistry carried out by Osella et al. showed that the radical $Co(CO)_4^{\cdot}$ could recombine with the $[Co(CO)_2(ethynylestradiol)]^{\cdot}$ radical to regenerate almost quantatively the parent complex. No such process was observed for these systems. Rapid poisoning of the electrodes due to adsorption of the electroactive species prevented further analysis.

3.5.5   Steady state photolysis and quantum yield of CO loss

For all complexes under investigation, steady state photolysis of the dicobalt complexes in the presence of a trapping ligand, PPh_3, resulted in CO loss and formation of the triphenylphosphine trapped pentacarbonyl and tetracarbonyl species ([(μ_2-alkyne)$Co_2(CO)_5(PPh_3)$] and ([(μ_2-alkyne)$Co_2(CO)_4(PPh_3)_2$]).

Photosubstitution occurred following photolysis at $\lambda > 520$ nm *albeit* in minor amounts. Irradiation at $\lambda > 410$ nm caused increased formation of the pentacarbonyl photoproduct. However irradiation at $\lambda > 320$ nm resulted in a significant amounts of both the pentacarbonyl and tetracarbonyl photoproduct.

Subsequently, the quantum yield of CO loss was calculated at various wavelengths to investigate the wavelength dependence of the photochemical process. The quantum yields of CO loss were determined at 313, 365, 405 and 546 nm for **PhCCPh-Co$_2$(CO)$_6$**, **ThCCPh-Co$_2$(CO)$_6$** and **FcCCH-Co$_2$(CO)$_6$**.

The UV-vis absorbance spectra for all three hexacarbonyl complexes show an intense absorbance in the UV region up to 370 nm with two broad low intensity absorbances in the visible region extending to 600 nm (to 750 nm for **FcCCH-Co$_2$(CO)$_6$**). Photolysis of all three complexes resulted in minor growth of a new absorbance in the range 380 – 420 nm which indicated photosubstitution of a carbonyl ligand with a triphenylphosphine moiety was occurring.

The mean values of all quantum yield experiments are given in table 5 and summarised in figure 32. The results show that the photochemical quantum yield of CO dissociation was dependent on the excitation energy. The quantum yield of CO loss was highest when the sample was irradiated at high energy ($\lambda_{exc} = 313$ nm and $\lambda_{exc} = 365$ nm) where the complexes possess strong π-π* absorbance bands. At 405 nm, the UV-vis spectra of all three complexes display only small absorbance bands and all quantum yields were found to be less than 5 % at this wavelength. However the quantum yield increased with $\lambda_{exc} = 546$ nm. The CO loss process ranged from 5 – 23 %. This was unexpected given that the absorbance bands at 546 nm are weaker transitions than those at 405 nm. Importantly the

quantum yield decreased on going from 546 nm to 405 nm, but increased on going from 405 nm to 365 nm to 313 nm.

At all wavelengths **PhCCPh-Co$_2$(CO)$_6$** possessed the lowest quantum yield for CO loss (3 – 8 %) which may indicate that this complex is more stable towards photosubstitution reactions. CO loss quantum yields for **ThCCPh-Co$_2$(CO)$_6$** were in the range 4 – 15 % while **FcCCH-Co$_2$(CO)$_6$** showed the highest quantum yields (5 – 23 %), except at 365 nm where **ThCCPh-Co$_2$(CO)$_6$** produced slightly more of the trapped pentacarbonyl photoproduct. The high quantum yield and hence facile nature of CO loss in the ferrocenyl complex may be due to less steric hindrance within the complex as there is only one substituent on the ethynyl bridge.
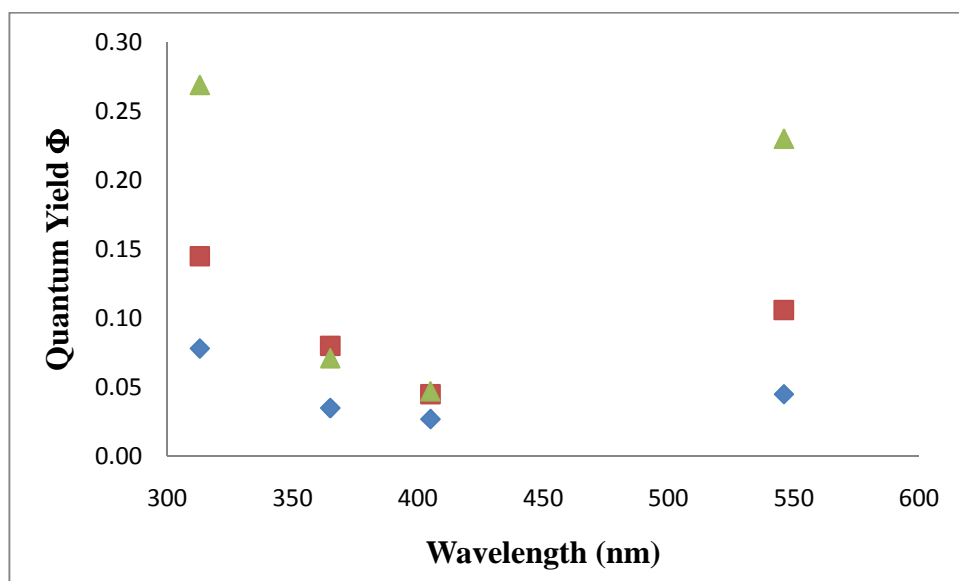
Figure 32   *Results of quantum yield experiments for CO loss in **PhCCPh-Co$_2$(CO)$_6$** (blue diamond), **ThCCPh-Co$_2$(CO)$_6$** (red square) and **FcCCH-Co$_2$(CO)$_6$** (green triangle).*

3.5.6 Picosecond time resolved infrared studies

Experimental evidence for the accepted mechanism of the PKR has been limited. Laser flash photolysis with UV-vis detection and matrix isolation studies with IR detection suggested two possible photochemical pathways for (μ_2-alkyne)$Co_2(CO)_6$ complexes following excitation. Irradiation at λ_{exc} = 355 nm resulted in Co-Co bond homolysis with $\tau_{recomb.}$ = 25 ns,[41] while irradiation at λ_{exc} = 254 nm in an argon matrix resulted in reversible CO loss. More recently Gibson et al. reported that Co-Co cleavage competes with CO loss and alkene binding in an (alkyne)(binap)tetracarbonyl dicobalt complex (binap = 2,2'-bis(diphenylphoshino)-1,1'-binaphthyl) and that cobalt-cobalt bond cleavage was a facile process.[45] TRIR spectroscopy has not been used to investigate the photochemistry of (μ_2-alkyne)$Co_2(CO)_6$ type complexes. Thus, picosecond time resolved infrared spectroscopy was used to probe the photochemistry of three (μ_2-alkyne)$Co_2(CO)_6$ complexes.

As discussed previously the UV-vis absorbance spectra of the complexes investigated, **PhCCPh-Co$_2$(CO)$_6$**, **ThCCPh-Co$_2$(CO)$_6$**, and **FcCCH-Co$_2$(CO)$_6$**, display a π-π* transition with ligand field character at < 280 nm, in addition to a band at approximately 350 nm and two weak bands in the range 380 – 730 nm which were attributed to metal to ligand charge transfer transitions (Fig. 33). Molecular orbital calculations were carried out by Hoffmann et al.[68] on (μ_2-alkyne)$Co_2(CO)_6$ complexes at the Hückel level and demonstrated that in the perpendicular isomer, the HOMO a_2 level corresponded to alkyne-to-metal back-bonding, while the HOMO-1 a_1 level corresponded to a Co-Co bond. The LUMO b_2, and LUMO+1 b_1 levels are antibonding with respect to the alkyne-to-metal bonds. These results are in agreement with *ab initio* molecular orbital calculations reported by Van Dam et al.[69] Photoelectron spectroscopy subsequently confirmed the relative order of the bonding orbitals proposed using molecular orbital calculations.
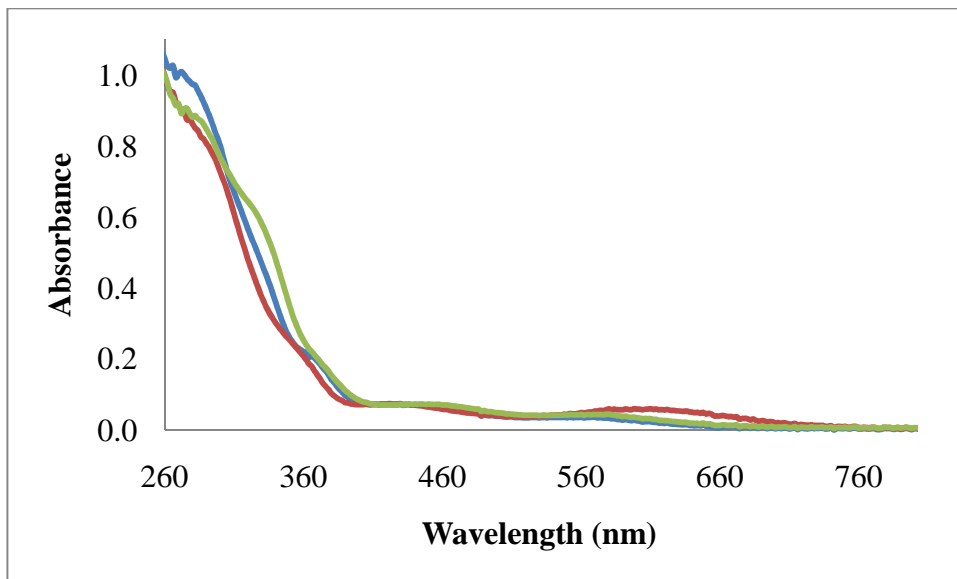
Figure 33   *Overlay of the absorbance spectra of **PhCCPh-Co$_2$(CO)$_6$** (blue line), **ThCCPh-Co$_2$(CO)$_6$** (green line), and **FcCCH-Co$_2$(CO)$_6$** (red line) recorded in pentane. Spectra have been normalised at their λ$_{max.}$*

Photoexcitation (λ$_{exc}$ = 400 nm, τ$_{FWHM}$ = 150 fs) of all three complexes resulted in depletion of the ground state ν(CO) bands of the complex, together with the generation of three new bands in the carbonyl region within the laser pulse (Table 7). The initial IR bands corresponded to a vibrationally hot species and the bands shifted to higher wavenumber over 10 ps. Vibrational cooling was observed for all three complexes and has been observed previously on a ps timescale as reported by Vlček et al. for a number of metal carbonyl systems.[70] These virbationally cooled bands then decay with complete recovery of the initial bleaches. The lifetimes of the transient species was calculated to be in the range 38 - 71 ps. All three complexes in this study displayed similar spectral changes (Table 7, Fig. 25-27) and the kinetics were largely solvent independent (Table 8).

Complex	v(CO) bands (cm^{-1})		
	CH$_3$CN	THF	Pentane
PhCCPh-Co$_2$(CO)$_6$			
Parent bands	2092, 2056, 2028	2084, 2050, 2022	2089, 2055, 2031
"Hot" species	2072, 2044, 2009	2064, 2036, 2008	2074, 2040, 2016
Triplet diradical	2082, 2048, 2019	2073, 2040, 2012	2079, 2045, 2021
ThCCPh-Co$_2$(CO)$_6$			
Parent bands	2093, 2058, 2029	---	---
"Hot" species	2078, 2049, 2008	---	---
Triplet diradical	2083, 2052, 2018	---	---
FcCCH-Co$_2$(CO)$_6$			
Parent bands	2090, 2052, 2024	2089, 2050, 2022	---
"Hot" species	2071, 2042, 2005	2079, 2041, 2002	---
Triplet diradical	2080, 2046, 2009	2084, 2046, 2007	---

Table 7   Observed IR stretching frequencies following excitation at 400 nm in CH$_3$CN, THF and pentane.

Complex	CH$_3$CN	THF	Pentane
PhCCPh-Co$_2$(CO)$_6$	69	70	71
ThCCPh-Co$_2$(CO)$_6$	63	---	---
FcCCH-Co$_2$(CO)$_6$	50	38	---

*Table 8   Lifetimes, following vibrational cooling, of transient species produced following 400 nm excitation of complexes **PhCCPh-Co$_2$(CO)$_6$**, **ThCCPh-Co$_2$(CO)$_6$** and **FcCCH-Co$_2$(CO)$_6$**.*

To discount the possibility of the observed bands belonging to a solvent pentacarbonyl species, (μ_2-alkyne)Co$_2$(CO)$_5$(solvent), triphenylphosphine was added to a solution of **FcCCH-Co$_2$(CO)$_6$**. However excitation at 400 nm and also at 532 nm showed no new bands on the nanosecond time scale in the TRIR experiments that could be assigned to **FcCCH-Co$_2$(CO)$_5$(PPh$_3$)**. This is in contrast to steady state photolysis, where in the presence of PPh$_3$, the monosubstituted complex, **FcCCH-Co$_2$(CO)$_5$(PPh$_3$)**, and subsequently the disubstituted complex **FcCCH-Co$_2$(CO)$_4$(PPh$_3$)$_2$** formed with bands observed at 2062, 2011 and 2004 cm^{-1} and 1989, 1971 and 1966 cm^{-1} respectively (appendix H).

Conventional electron counting in organometallic chemistry implies that the cobalt compounds discussed throughout this chapter should have a Co-Co single bond, however, a recent charge density study on the bonding interactions in (HC≡CC$_6$H$_{10}$OH)Co$_2$(CO)$_6$, indicates that the Co-Co bonding is weak and a singlet diradical character is proposed for this compound.[71] An earlier theoretical study by Platts et al. also proposed that the more appropriate designation for (μ_2-C$_2$H$_2$)-Co$_2$(CO)$_6$ is that of a singlet diradical, where the ground state electronic structure has a partial occupation of both Co-Co bonding and antibonding orbitals.[23]

Quantum chemical calculations (B3LYP/LANL2DZ+p) were carried out[72] and provided a model for transient species following photoexcitation of (μ_2-alkyne)Co$_2$(CO)$_6$ complexes and predicted IR spectra of possible intermediate species (Table 9 and Appendix I). The IR properties of (μ_2-alkyne)Co$_2$(CO)$_6$ on both the singlet and triplet ground state surfaces were calculated. It was apparent that on moving from the singlet to the triplet surface the ν(CO) bands of the model complex, (μ_2-C$_2$H$_2$)Co$_2$(CO)$_6$, move to lower energy. In fact, the transient ν(CO) bands observed in the TRIR experiments were all at lower energy compared to the parent bands (Fig. 25-27, Table 7). In addition, the calculated Co-Co bond length increases from 2.47 Å on the singlet surface (equal to twice cobalt's covalent radius of 1.25 Å) to 3.10 Å for the triplet species. This suggests that the Co-Co interaction is considerably weaker in the triplet state.

ν(CO)	(cm⁻¹)				
Observed	2097.8	2058.5	2033.7	2028.1	2016.6
Singlet	2097.9	2051.3	2037.6	2035.1	2012.7
Triplet	2087.5	2057.9	2024.1	2021.7	2015.2

Table 9 *Observed and calculated singlet and triplet state spectra for (μ₂-C₂H₂)Co₂(CO)₆. A correlation factor of 1.0222 was used to correct the calculated ν (CO) bands of the ground state triplet species.*[73]

Thus, combined picosecond TRIR studies and theoretical calculations allowed for the identification of the radical species generated following excitation of (μ₂-alkyne)Co₂(CO)₆ complexes. The data indicate the formation of a triplet diradical species. Therefore, the transient species observed in the TRIR experiments was assigned to the ³(μ₂-alkyne)Co₂(CO)₆ diradical species, generated by rapid Co-Co bond homolysis with subsequent recombination to form the parent complex.

The observation of a triplet species in the picosecond TRIR experiments requires fast intersystem crossing from the singlet excited state on the order of 1×10^{12} s⁻¹. While this is fast, it is not without precedence in the literature.[74, 75]

Other possibilities for the species observed that were considered include: the isomer in which the alkyne lies parallel to the Co-Co bond, a species where one Co-alkyne bond is cleaved, and a Co→CO charge transfer excited state. Hoffmann found that the parallel isomer lies 2.5 eV higher in energy than that of the perpendicular isomer. As the TRIR experiments carried out at λ_{exc} = 532 nm produced transient species identical to those observed following 400 nm excitation, the possibility of the parallel isomer can be ruled out based on energetic arguments. However, as these studies were carried out over 25 years ago, further theoretical studies were preformed to rule out the possibility of involvement of the parallel isomer in the complexes under investigation.[72] DFT methods were used in an attempt to calculate the energy difference between the two isomeric forms, though, repeated attempts to locate the parallel isomer at the minimum on the singlet potential energy surface failed. It was concluded that the parallel isomer did not play a

significant role in the photochemistry of the **PhCCPh-Co$_2$(CO)$_6$**, **ThCCPh-Co$_2$(CO)$_6$** and **FcCCH-Co$_2$(CO)$_6$** complexes. An intermediate arising from cleavage of the Co-C alkyne bonds was also excluded based on the number of IR bands observed. Although a Co-to-CO charge transfer excited state should be considered, the most likely explanation for the short lived species is that of the triplet diradical based on the results proposed here.

There was no evidence of the CO loss photoproduct in the TRIR experiments following excitation at 400 nm and 532 nm. Addition of a molar excess of trapping ligand to a sample of **FcCCH-Co$_2$(CO)$_6$** produced TRIR spectra practically identical to that without the trapping ligand. The quantum yield experiments revealed, CO loss for the three complexes **PhCCPh-Co$_2$(CO)$_6$**, **ThCCPh-Co$_2$(CO)$_6$** and **FcCCH-Co$_2$(CO)$_6$** was low at 405 nm. The quantum yield for CO loss was less than 5 % at this wavelength, which was close to the excitation wavelength used for TRIR experiments (400 nm). It is unlikely that a photoprocess with such a low quantum yield would be observed in the TRIR experiments.

The quantum yield for CO loss varied with excitation wavelength. At 546 nm the quantum yield for CO loss was 5 – 23 %. It is unlikely that the low quantum yield photoprocesses (< 10 %) would be observed, thus the TRIR experiments are in good agreement with the quantum yields obtained for **PhCCPh-Co$_2$(CO)$_6$** and **ThCCPh-Co$_2$(CO)$_6$**. However, the quantum yield for CO loss in **FcCCH-Co$_2$(CO)$_6$** was 23 %. No evidence for the CO loss photoproduct was observed. This is a genuinely puzzling aspect of the results and the experiments will need to be repeated if an opportunity arises.

The diagrammatical representation below (Fig. 34) shows the photophysical processes that occur following excitation. Following 400 nm pulsed excitation the (μ_2-alkyne)Co$_2$(CO)$_6$ complex absorbs light and is excited to its singlet excited state, rapid intersystem crossing to the triplet state occurs. Following this Co-Co bond homolysis and recombination occurs followed by full recovery of the ground state. However, continuous wave irradiation (λ_{exc} = 546 nm) resulted in CO loss as shown below.
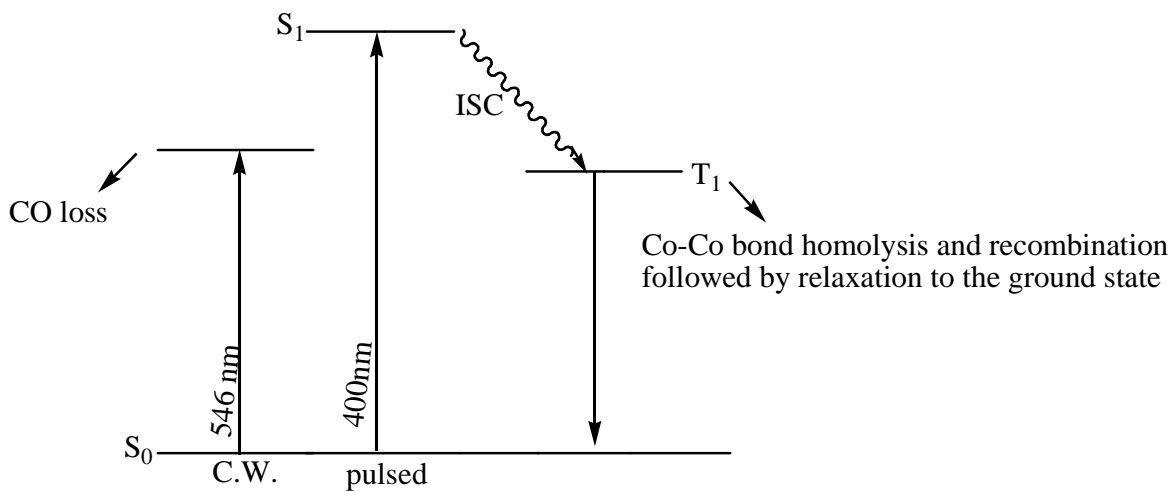
Figure 34   Diagrammatical representation of the photophysical processes that occur following 400 nm pulsed irradiation and 546 nm continuous wave (C.W.) irradiation.

Thus, combined picosecond TRIR studies and theoretical calculations allowed for the identification of the radical species generated following excitation of (μ_2-alkyne)$Co_2(CO)_6$ complexes. The data indicate the formation of a triplet diradical species that rapidly recombined to regenerate the parent complex in all cases (Scheme 6). Lifetimes for the triplet diradical species were in the range 38 – 71 ps.[51]
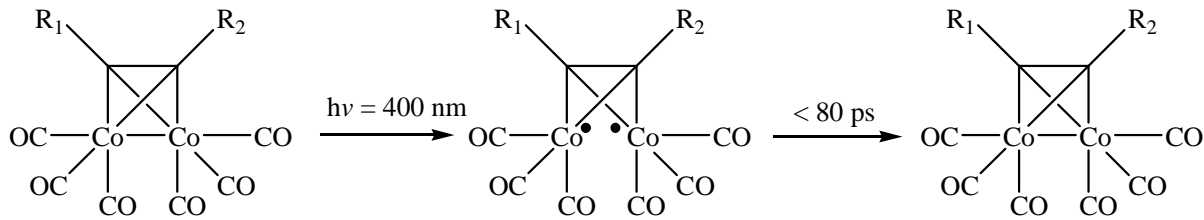
R_1 = Phenyl or ferrocene, R_2 = H, phenyl or thiophene

Scheme 6   Co-Co bond homolysis and recombination following 400 nm excitation.

3.6   Conclusions

In this chapter experimental work concerning the excited state dynamics of linear organic molecules and their organometallic counterparts has been presented. Ligands, **NB-L1** and **NB-L5 – NB-L7** were used to investigate the effect of terminal group substitution on the organic moiety, with respect to their absorbance, emission and electrochemistry. The results showed that the attachment of an electron withdrawing moiety to the organic ligand resulted in bathochromic shifts in the absorbance spectra. The non-fluorescent **NB-L1** became weakly fluorescent upon terminal substitution, the intensity of the emission increased with increasing electronegativity of the terminal substituent and in conjunction with this the fluorescent lifetimes of the molecules were increased also. Electrochemistry showed that thienyl molecules become more stable when an electron withdrawing group was attached due to increased electron delocalisation within the molecules.

Steady state photolysis carried out in the dicobalt hexacarbonyl complexes resulted in CO loss and quantum yields for the CO loss process indicated that the photochemical process was wavelength dependant. The photochemical activation of (μ_2-alkyne)$Co_2(CO)_6$ complexes was studied by ps-TRIR and combined theoretical calculations allowed for the identification of the formation of a triplet diradical species that rapidly recombined to regenerate the parent complex. Lifetimes for the triplet diradical species were in the range 38 – 71 ps.

3.7   Bibliography

1   (a) K. Sonogashira, Y. Tohda, N. Hagihara, *Tet. Lett.*, **1975**, 50, 4470.

2   (a) E. Negishi, S. Baba, *J. Org. Chem. Soc., Chem. Comm.*, **1976**, 596. (b) S. Baba, E. Negishi, *J. Am. Chem. Soc.*, **1976**, 98, 6729.

3   N. Miyaura, K. Yamada, A. Suzuki, *Tet. Lett.*, **1979**, 20, 3437. (b) N. Miyaura, A. Suzuki, *J. Chem. Soc., Chem. Comm.*, **1979**, 866.

4   R.F. Heck, J.P. Nolley, *J. Org. Chem.*, **1972**, 37, 2320.

5   (a) D. Milstein, J.K. Stille, *J. Am. Chem. Soc.*, **1978**, 100, 3636. (b) D. Milstein, J.K. Stille, *J. Am. Chem. Soc.*, **1978**, 101, 4992.

6   E. Negishi, L. Anastasia, *Chem. Rev.*, **2003**, 103, 1979.

7   N. Miyaura, A. Suzuki, *Chem. Rev.*, **1995**, 95, 2457.

8   Y.-Q. Fang, M.I.J. Polson, G.S. Hanan, *Inorg. Chem.*, **2003**, 42, 5.

9   S. Schroter, C. Stock, T. Bach, *Tetrahedron*, **2005**, 61, 2245.

10   M.G. Hutchings, I. Ferguson, D.J. McGeein, J.O. Morley, J. Zyss, I. Ledoux, *J. Chem. Soc., Perkin Trans. 2*, **1995**, 171.

11   M. Manuele, M. Raposo, A.M.R.C. Sousa, G. Kirsh, P. Cardoso, M. Belsey, E. De Matos Gomes, A.M.C. Fonseca, *Org. Lett.*, **2006**, 8, 2681.

12   B. Muhling, S. Theisinger, H. Meier, *Synthesis*, **2006**, 6, 1009.

13   (a) J.G. Rodriguez, A. Lafuente. L. Rubio, *Tet. Lett.*, **2004**, 45, 5685. (b) J.G. Rodriguez, A. Lafuente, L. Rubio, J. Esquivias, *Tet. Lett.*, **2004**, 45, 7061. (c) J.G. Rodriguez, J. Esquivias, A. Lafuente, L. Rubio, *Tetrahedron*, **2006**, 62, 3112.

14   J. Li, Y. Pang, *Marcomolecules*, **1998**, 31, 5740.

15   P. Bauerle, J. Cremer, *Chem. Mater.*, **2008**, 20, 2696.

16   K. Toyota, K. Okada, H. Katsuta, N. Morita, *Tetrahedron*, **2009**, 65, 145.

17   T.M. Pappenfus, K.R. Mann, *Org. Lett.*, **2002**, 4, 3043.

18   W. Reppe, M. Schlichting, K. Klager, T. Toepel, *Justus Leibigs Ann. Chem..*, **1948**, 560, 1.

19   W. Hübel, *Organic Syntheses via Metal Carbonyls*; I. Wender, P. Pino Eds.; Wiley: New York, 1968, Vol. 1, p 273.

20   H. Greenfield, H.W. Sternberg, R.A. Friedel, J.H. Wotiz, R. Markby, I. Wender, *J. Am. Chem. Soc.*, **1956**, 78, 120.

21   R.S. Dickson, D.B.W. Yawney, *Anal. J. Chem.*, **1968**, 21, 1077.

22   W.G. Sly, *J. Am. Chem. Soc.*, **1959**, 81, 18.

23   J.A. Platts, G.J.S. Evans, M.P. Coogan, J. Overgaard, *Inorg. Chem.*, **2007**, 46, 6291.

24   G. Li, Q.-S. Li, Y. Xie, R.B. King, H.F. Schaefer III, *Organometallics*, **2009**, 28, 3390.

25   T.S. Jung, J.H. Kim, E.K. Jang, D.H. Kim, Y.-B. Shim, B. Park, S.C. Shin, *J. Organomet. Chem.*, **2000**, 599, 232.

26   E. Champeil, S.M. Draper, *J. Chem. Soc., Dalton Trans.*, **2001**, 1440.

27   A. Coleman, M.T. Pryce, *Inorg. Chem.*, **2008**, 47, 10980.

28   L.S. Chia, W.R. Cullen, M. Franklin, A.R. Manning, *Inorg. Chem.*, **1975**, 14, 2521.

29   J. Marhenke, S.M. Massick, P.C. Ford, *Inorg. Chim. Acta*, **2007**, 360, 825.

30   (a) H.B. Abrahamson, C.C. Frazier, D.S. Ginley, H.B. Gray, J. Librenthal, D.R. Tyler, M.S. Wrighton, *Inorg. Chem.*, **1977**, 16, 1554. (b) T.J. Meyer, J.V. Caspar, *Chem. Rev.*, **1985**, 85, 187. (c) D.R. Tyler, M.A. Schmidt, H.B. Gray, *J. Am. Chem. Soc.*, **1983**, 105, 6018. (d) H.B. Abrahamson, M.C. Palazzotto, C.L. Reichel, M.S. Wrighton, *J. Am. Chem. Soc.*, **1979**, 101, 4123.

31   (a) M.F. Desrosiers, D.A. Wink, R. Trautman, A.E. Friedman, P.C. Ford, *J. Am. Chem. Soc.*, **1986**, 108, 1917. (b) J. DiBenedetto, D.W. Ryba, P.C. Ford, *Inorg. Chem.*, **1989**, 28, 3503. (c) T.J. Meyer, J.V. Caspar, *Chem. Rev.*, **1985**, 85, 187.

32   (a) I.U. Khand, G.R. Knox, P.L. Pauson, W.E. Watts, M.I. Foreman, *J. Chem. Soc., Perkin Trans. 1*, **1973**, 977. (b) P.L. Pauson *Tetrahedron*, **1985**, 41, 5855. (c) N.E. Shore, *Chem. Rev.*, **1988**, 88, 1081.

33   (a) L. Daalman, R.F. Newton, P.L. Pauson, R.G. Taylor, A. Wadsworth, *J. Chem. Res (S)*, **1984**, 344. (b) H.J. Jeffer, P.L. Pauson, *J. Chem. Res. (M)*, **1983**, 2201.

34   (a) P. Magnus, C. Exon, P. Albrough-Robertson, *Tetrahedron,* **1985**, 41, 5861. (b) P. Magnus, L. Principle, *Tet. Lett.*, **1985**, 26, 4851. (c) C. Exon, P. Magnus, *J. Am. Chem. Soc.*, **1983**, 105, 2477.

35   V. Rautenshrauch, P. Megard, J. Conesa, W. Kuster, *Angew. Chem. Int. Ed. Engl.*, **1990**, 29, 1413.

36   (a) P. Magnus, L.-M. Principe, *Tet. Lett.,* **1985**, 26, 4851. (b) P. Magnus, C. Exon, P. Albaugh-Robertson, *Tetrahedron*, **1985**, 41, 5861. (c) P. Magnus, L.-M. Principe, M.J. Slater, *J. Org. Chem.,* **1987**, 52, 1483.

37   B.E. La Belle, M.J. Knudsen, M.M. Olmstead, H. Hope, M.D. Yanuck, N.E. Schore, *J. Org. Chem.*, **1985**, 50, 5215.

38   S.A. Brusey, E.V. Banide, S. Dorrich, P. O'Donohue, Y. Ortin, H. Muller-Bunz, C. Long, P. Evans, M.J. McGlinchey, *Organometallics*, **2009**, 28, 6308.

39   B.L. Pagenkopf, T. Livinghouse, *J. Am. Chem. Soc.*, **1996**, 118, 2285.

40   C.M. Gordon, M. Kiszka, I.R. Dunkin, W.J. Kerr, J.S. Scott, J. Gebicki, *J. Organomet. Chem.*, **1998**, 554, 147.

41   S.M. Draper, C. Long, B.M. Myers, *J. Organomet. Chem.*, **1999**, 588, 195.

42   F. Robert, A. Milet, Y. Gimbert, D. Konya, A.E. Greene, *J. Am. Chem. Soc.*, **2001**, 123, 5396.

43   M. Yamanaka, E. Nakamura, *J. Am. Chem.. Soc.*, **2001**, 123, 1703.

44   M.A. Pericàs, J. Balsells, J. Castro, I. Marchueta, A. Moyano, V. Riera, J. Vázquez, X. Verdaguer, *Pure Appl. Chem.*, **2002**, 74, 167.

45   S.E. Gibson, K.A.C. Kaufmann, P.R. Haycock, A.J.P. White, D.J. Hardick, M.J. Tozer, *Organometallics,* **2007**, 26, 1578

46   W.R. Browne, C.M. O'Connor, C. Villani, J.G. Vos, *Inorg. Chem.*, **2001**, 40, 5461.

47   (a) S.B. Park, H. Apler, *Chem. Commun.*, **2004**, 1306. (b) A.R. Katritzky, A.A.A. Abdel-Fattah, M. Wang, *J. Org. Chem.*, **2002**, 67, 7526.

48   (a) C. Torborg, A. Zapf, M. Beller, *Chem. Sus. Chem.*, **2008**, 1, 91. (b) M. Feuerstein, H. Doucet, M. Santelli, *J. Molecular Catalysis A: Chem.*, **2006**, 256, 75.

49   A. Carpita, A. Lessi, R. Rossi, *Synthesis*, **1984**, 571.

50   B.T. Holmes, W.T. Pennington, T.W. Hanks, *Molecules*, **2002**, 7, 447-455.

51   N.M. Boyle, A.C. Coleman, C. Long, K.L. Ronayne, W.R. Browne, B.L. Feringa, M.T. Pryce, *Inorg. Chem.*, **2010**, 49, 10214

52   (a) M. Wahadoszamen, T. Hamada, T. Iimori, T. Nakabayashi, N. Ohta, *J. Phys. Chem.*, **2007**, 111, 9544. (b) C. Aurisicchio, B. Ventura, D. Bonifazi, A. Barbieri, *J. Phys. Chem. C*, **2009**, 113, 17927.

53   E. Hao, B. Fabre, F.R. Fronczek, M.G.H. Vicente, *Chem. Mater.*, **2007**, 19, 6195.

54   J. Areephong, T. Kudernac, J.J.D. de Jong, G.T. Carroll, D. Pantorotta, J. Hjelm, W.R. Browne, B.L. Feringa, *J. Am. Chem. Soc.*, **2008**, 130, 12850.

55   (a) M. Shiotsuka, Y. Inui, Y. Sekioka, Y. Yamamoto, S. Onaka, *J. Organomet. Chem.*, **2007**, 692, 2441. (b) N. Esho, B. Davies, J. Lee, R. Dembinski, *Chem. Comm.*, **2002**, 332.

56   T.S. Jung, J.H. Kim, E.K. Jang, D.H. Kim, Y.-B. Shim, B. Park, S.C. Shin, *J. Organomet. Chem.*, **2000**, 599, 232.

57   A. Arnanz, M.-L. Marcos, C. Moreno, D.H. Farrar, A.J. Lough, J.O. Yu, S. Delgado, J. Gonzalez-Velasco, *J. Organomet. Chem.,* **2004**, 689, 3218.

58   A.F. Diaz, J. Crowley, J. Bargon, G.P. Gardini, J.B. Torrance, *J. Electroanal. Chem.*, **1981**, 121, 355.

59   F. Fringuelli, G. Marino, A. Taticchi, G. Grandolini, *J. Chem. Soc., Perkin Trans. 2: Phys. Org. Chem.*, **1974**, 4, 332.

60   A. Arnanz, M.-L. Marcos, S. Delgado, J. Gonzalez-Velasco, C. Moreno, *J. Organomet. Chem.*, **2008**, 693, 3457.

61   A. Sakar, M.M. Haley, *Chem. Comm.,* **2000**, 1733.

62   Y. Hirata, T. Okada, N. Mataga, T. Nomoto, *J. Phys. Chem.*, **1992**, 96, 6559.

63   M. Z. Zgierski, T. Fujiwara, E.C. Lim, *Accounts of Chemical Research*, **2010**, 43, 506.

64   X. Zhao, H.K. Sharma, F. Cervantes-Lee, K.H. Pannell, G.J. Long, A.M. Shahin, *J. Organomet. Chem.*, **2003**, 686, 235.

65   M.L. Marcos, M.J. Macazaga, R.M. Medina, C. Moreno, J.A. Castro, J.L. Gomez, S. Delgado, J. Gonzalez-Velasco, *Inorg. Chim. Acta*, **2001**, 312, 249.

66   D. Osella, J. Fiedler, *Organometallics*, **1992**, 11, 3875.

67   (a) D.L. Thom, R. Hoffmann, *Inorg. Chem.*, **1978**, 17, 126. (b) B.M. Peake, P.H. Reiger, B.H. Robinson, J. Simpson, *J. Am. Chem. Soc.*, **1980**, 102, 156.

68   D.M. Hoffmann, R. Hoffmann, C.R. Fisel, *J. Am. Chem. Soc.*, **1982**, 104, 3858.

69   H. Van Dam, D.J. Stufkens, A. Oskam, M. Doran, I.H. Miller, *J. Electron Spetrosc. Relat. Phenom.*, **1980**, 21, 47.

70   (a) M. Busby, P. Matousek, M. Towrie, A. Vlček, *J. Phys. Chem. A*, **2005**, 109, 3000. (b) M. Busby, P. Matousek, M. Towrie, A. Vlček, *Inorg. Chim. Acta.,* **2007**, 360, 885.

71   J. Overgaard, H.F. Clausen, J.A. Platts, B.B. Inversen, *J. Am. Chem. Soc.,* **2008**, 130, 3834.

72   Theoretical calculations were carried out by Prof. C. Long at Dublin City University.

73   Y. Iwashita, F. Tamura, A. Nakmura, *Inorg. Chem..,* **1969**, 8, 1179.

74   A.L. Smeigh, M. Creelman, R.A. Mathies, J.K. McCusker, *J. Am. Chem. Soc.*, **2008**, 130, 14105.

75   W. Gawelda, A. Cannizzo, V.-T. Pham, F. Van Mourik, C. Bressler, M. Chergui, *J. Am. Chem. Soc.*, **2007**, 129, 8199.

Chapter 4

**The synthesis and photochemistry
of freebase and zinc monopyridyl
porphyrins and the corresponding
metal carbonyl porphyrin
complexes.**

*Chapter four commences with
literature survey focusing on the
photophysics of pyridyl porphyrins
and related organometallic systems.
The aims and objectives of the
chapter are discussed. The synthesis
of the monopyridyl porphyrin and
metal carbonyl derivatives produced
for this study is then described. The
photochemistry of the complexes was
examined by pump and probe TRIR
spectroscopy on a picosecond
timescale.*

4.1　　Literature Survey

4.1.1　　Introduction to pyridyl porphyrins

Porphyrin metal complexes have found great use in photosynthetic research. From the first man made porphyrins to the supramolecular arrays of today, porphyrins and related macrocycles have been studied for their electron transfer and energy transfer potential.[1] Systems that undergo electron transfer processes from porphyrins to externally but covalently linked transition metal complexes have been extensively studied since the mid nineties. Among supramolecular systems, those that contain a porphyrin coordinated to a peripheral transition metal are of particular interest as these arrays can mimic the electron or energy transfer processes observed in photosynthesis. Pyridyl porphyrins are particularly attractive building blocks for the construction of photoactive supramolecular systems. The structures shown in figure 1 display a variable number of 4-pyridyl (*n*) and phenyl (4 - *n*) groups at the *meso* position(s) of the porphyrin macrocycle. As with all porphyrins, these mixed pyridyl/phenyl porphyrins have attractive spectroscopic, photophysical and redox properties. In addition, the *meso* pyridyl groups provide great synthetic flexibility as the peripheral nitrogen atom(s) can be coordinated to metal complexes of various coordination numbers and geometries. Complexation at the peripheral pyridyl nitrogen provided a simple route to a new class of porphyrins. The *meso* pyridyl group can act as a ligand for metal sites that are held at a fixed distance and angle to the porphyrin macrocycle.

MPyTPP   *c*-**DPyDPP**   *t*-**DPyDPP**

TrPyMPP   **TPyP**
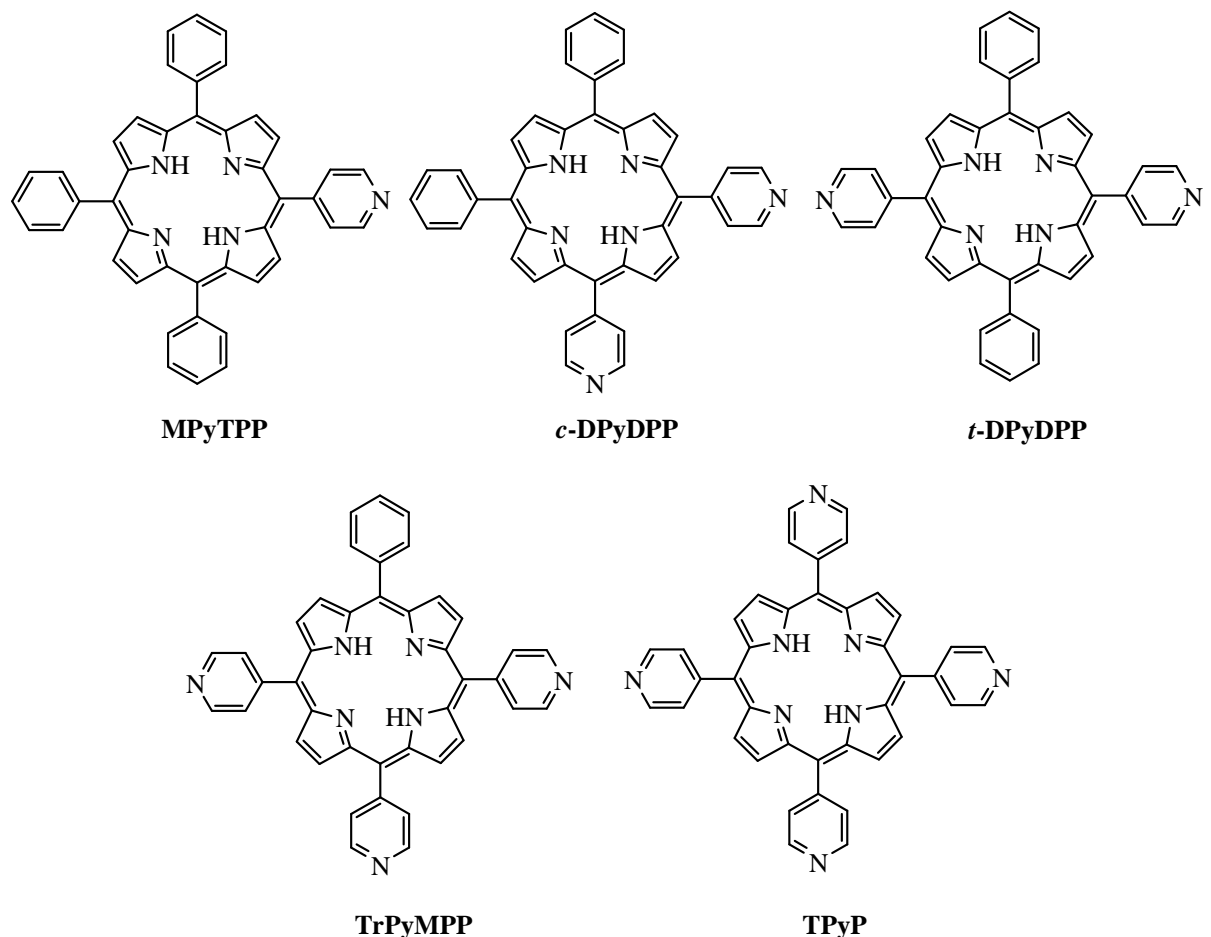
Figure 1   Five 4-pyridyl (n) and phenyl (4 - n) meso *substituted porphyrins.*

4.1.2   Porphyrins coordinated to metal carbonyls.

Coordination of a metal carbonyl to a porphyrin allows the study of the extent of electron or energy transfer between the two units using the extensive data for the excited states of the individual porphyrin and metal carbonyl fragments. Various porphyrins have been coordinated to transition metal carbonyls including (μ-H)-Os(CO)$_{10}$, Re(CO)$_3$Cl, RuCl$_2$(DMSO)$_2$CO, Cr(CO)$_3$ and W(CO)$_5$ some of which are discussed below. However only a few of these system have had their photochemistry examined.

Mono and disubstituted pyridyl porphyrins (**1 - 3**, Fig. 2) were treated with an excess of Os$_3$(CO)$_{10}$(NCMe)$_2$ to give triosmium cluster complexes (**4 - 6**, Fig. 2).[2] In complex **4**, the pyridyl ring of the porphyrin was orthometallated and bridged one edge of the Os$_3$ triangle. This afforded a four membered ring containing Os, Os, C and N with a hydride ligand bridging one Os-Os edge. Complex **5** was isostructural with complex **4**. The coordinated clusters of complex **6** can be *cis* or *trans* to one another (relative to the porphyrin plane). The absorbance spectra of **4 - 6** were similar to the uncomplexed pyridyl porphyrins **1 – 3**, except for a blue shift of the Soret band by 4, 3 and 7 nm respectively and an increase in absorbance between 220 and 420 nm where the cluster absorbance bands were evident. The fluorescence spectra intensities and excited state lifetimes of **4 - 6** were somewhat quenched compared to **1-3**. The fluorescence lifetimes were 0.76, 0.70, 0.76, 0.30, 0.37 and 0.21 ns for **1 - 6** respectively. Fluorescence quenching was attributed to the heavy atom effect arising from the metal cluster rather than energy- or electron-transfer processes between the cluster and the porphyrin.
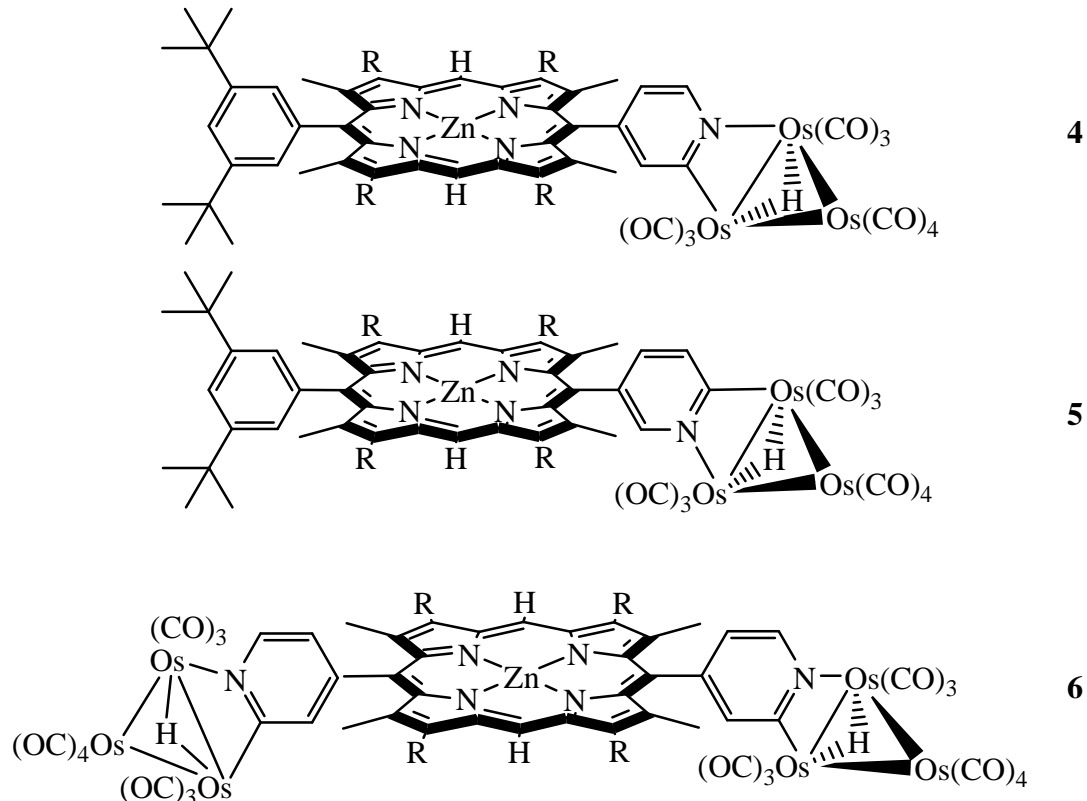
1 - 3 = uncomplexed pyridyl porphyrins, R = n-hexyl

Figure 2   *Pyridyl porphyrins coordinated to triosmium clusters*

Sullivan and co-workers synthesised **7** (Fig. 3) in which a labile triflate group was replaced by a pyridine ligand.[3] Subsequently osmium exclusively bound to the exterior of a porphyrin through direct coordination of the pyridyl linkage was reported by Hyslop et al.[4] **H$_2$8** (Fig. 3) was prepared *via* a modified version of this method and metallated with zinc (**Zn8**, Fig. 3). **MPyTPP**, **ZnTPP** and **7** were used as model compounds to delineate the effect of coordination of the Os unit onto the pyridyl porphyrin. Comparisons of the electrochemical redox properties of **H$_2$8** to **MPyTPP** and **Zn8** to **ZnTPP** showed only minor shifts in both the osmium and porphyrin potentials indicating that the ground states were unperturbed in the dyads. With regard to the model **7**, incorporation of the CO unit onto the osmium metal centre caused a blue shift of the MLCT absorbance band so that it occurred at the same energy as the Soret band of **MPyTPP** (λ_{max} = 417 nm). The

bipyridine π-π* bands of **H₂8** and **Zn8** (~290 nm) were separated from the porphyrin Soret and Q bands thus permitting preferential excitation of the Os portion of the molecule. The emission maximum of **7** (λ_{em} = 590 nm) overlapped with the Q band absorbance of **MPyTPP** (590 nm) and **ZnTPP** (586 nm) thus creating an ideal system for energy transfer. UV-vis spectra of the complexes **H₂8** and **Zn8** were not simple superpositions of the parent **7** and **MPyTPP** or **ZnTPP** respectively. Complexation of the porphyrin to osmium resulted in the addition of a bipyridine π-π* transition in the UV region while the Soret and Q bands in both the freebase and zinc porphyrins were broadened, decreased in intensity and red-shifted with respect to the model porphyrins (Table 1), which indicated electronic coupling. Excitation of the porphyrin dyads, **H₂8** and **Zn8**, was carried out at 260 nm (osmium based bipyridine π-π* transition) and at 420 nm (porphyrin Soret band). Excitation of **H₂8** at 420 nm resulted in emission at 659 nm, a red shift of 8 nm compared to **MPyTPP** with a decrease in intensity by a factor of 5. Excitation at 260 nm gave similar results with the emission bathochromically shifted and a similarly decreased in intensity. The decrease in emission intensity was typical of the heavy atom effect. The red shifted absorbance and emission maxima for **H₂8** and lack of change in electrochemical potentials suggested that the ground state energies of the porphyrin unit remained the same while the excited state energies were lowered by the attachment of the Os group. Emission occurred only from the porphyrin moiety of **H₂8** regardless of excitation wavelength, indicating that energy transfer from the osmium group to the porphyrin occurred. The metallated derivative, **Zn8**, produced different results. Model compounds, **ZnTPP** and **ZnMPyTPP**, possess almost identical emission spectra with two bands at 598 and 648 nm, the latter more intense than the former. Excitation of **Zn8** at 460 nm yielded a bathochromically shifted (17 nm) and significantly quenched (by a factor of 11) fluorescence spectrum in which the higher energy band was the most intense. Some quenching of the emission was attributed to the heavy atom effect however additional quenching processes were considered as the total quenching was nearly three times higher than that of the freebase derivative. The authors suggested that the almost complete quenching and change in profile of the emission when the Os bipyridine moiety of **Zn8** is excited supports the occurrence of electron transfer.
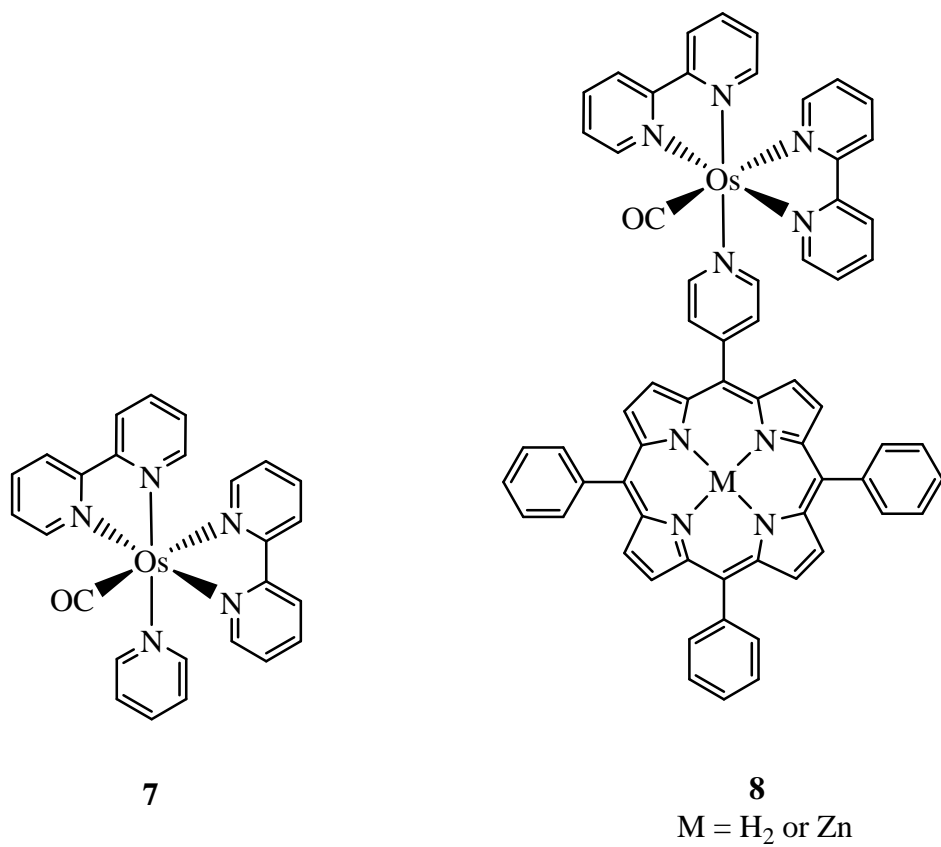
Figure 3   *Pyridyl porphyrin / osmium bpy dyad, 8 and model compound 7.*

Compound	λ_{max} (nm)	Soret FWHM (cm^{-1})	λ_{em} (nm)
7	262, 302, 422		589
H$_2$8	260, 302, 423, 518, 57, 592, 649	1340	659
Zn8	251, 261, 302, 425, 552, 596,	1320	614
MPyTPP	417, 514, 548, 590, 645, 690	690	651
ZnTPP	419, 548, 586	570	597

Table 1   *Photophysical data for osmium porphyrin assemblies and model compounds.*

Pyridyl porphyrins functionalised with Re(CO)$_5$Cl resulted in the formation of porphyrin dimers (**9** and **10**, Fig. 4).[5] The dimers featured a rigid co-planar geometry for the donor and acceptor chromophores *via* coordinative assembly. Thus the rigidity of the compounds provided an efficient geometry for singlet energy transfer and made them candidates for both through-bond and through-space energy transfer. The porphyrin dimers consist of homodimers (**9\10a** and **9\10b**, Fig. 4) and mixed dimers (**9\10c**, Fig. 4). The porphyrin Soret band was broadened and reduced in intensity upon incorporation into dimers indicating slight electronic coupling in this region while the Q band region was the sum of the individual zinc and freebase monomers indicating little or no electronic coupling. Consistent with coordination to Re(I), the absorbance and fluorescence maxima were red shifted by 8 – 10 nm with respect to the monomer porphyrins. Singlet lifetimes and quantum yields were typical of singlet porphyrin emission with the freebase porphyrin complexes more emissive than their zinc analogues. Despite complexation with rhenium the assemblies remained fluorescent. However, a 75 % decrease in emission quantum yield upon dimer formation was observed and ascribed to heavy atom effect. Similar to other studies on Zn-Fb porphyrin pairs, dimers **9c** and **10c** displayed efficient singlet energy transfer from the zinc porphyrin to the freebase porphyrin. Excitation of the Soret region resulted in significantly reduced emission from the zinc component of **9c** and enhanced emission from the freebase component. Steady state fluorescence studies of **9c** and **10c**, using the respective symmetric dimers as reference compounds gave energy transfer rate constants of 1.3×10^{10} and 9.7×10^{9} s^{-1}. This was similar to rate constants observed for organic Zn-Fb porphyrin dimers in which aromatic spacers were implicated for EnT mediation[6] and faster than closely related assemblies in which through-space EnT dominated.[7] In these systems the structured rigidity and enforcement of donor-acceptor coplanarity for both **9c** and **10c** could enhance either pathway.

9a: R = OCH$_3$, M$_1$ = M$_2$ = H$_2$
9b: R = OCH$_3$, M$_1$ = M$_2$ = Zn
9c: R = OCH$_3$, M$_1$ = H$_2$, M$_2$ = Zn

10a: R = CO$_2$CH$_3$, M$_1$ = M$_2$ = H$_2$
10b: R = CO$_2$CH$_3$, M$_1$ = M$_2$ = Zn
10c: R = CO$_2$CH$_3$, M$_1$ = H$_2$, M$_2$ = Zn
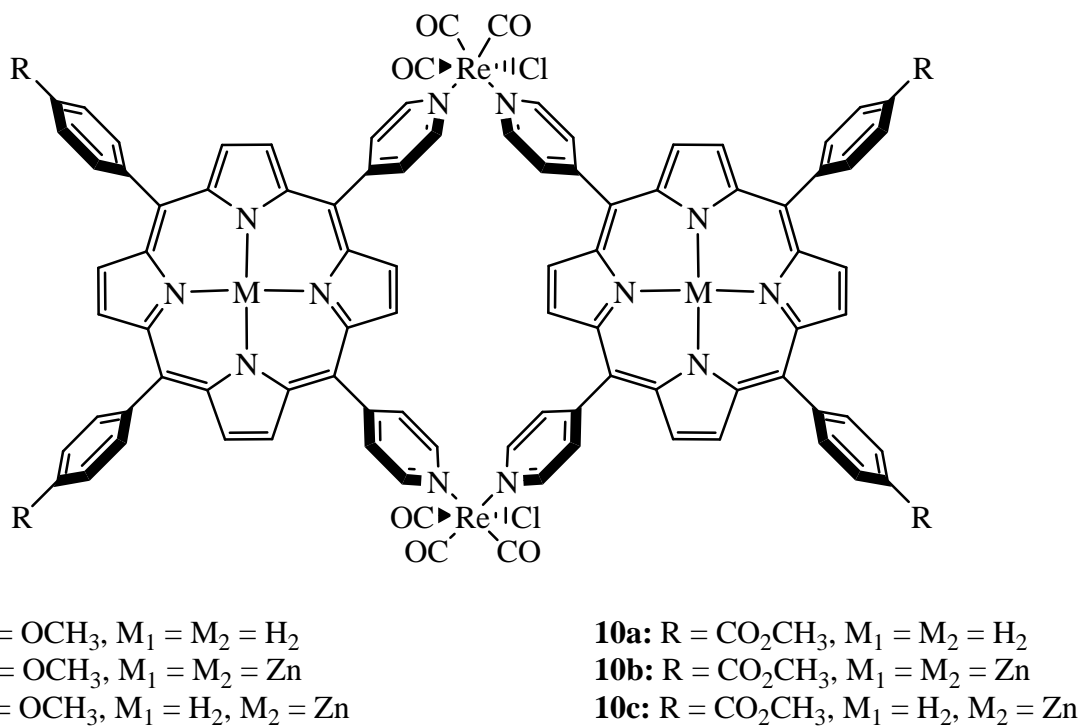
Figure 4   *Pyridyl porphyrin dimers functionalised with Re(CO)$_3$Cl.*

Metal carbonyls have also been used to create porphyrin squares such as **11** (Fig. 5).[8] 5,15-*meso*-pyridylporphyrins were used as bridging ligands and Re(CO)$_3$Cl moieties were used as a corners to form molecular squares, while porphyrin metallation provided a basis for single or multipoint guest binding *via* axial ligation. Square formation induced a ~6 nm red shift in the porphyrin Soret band which is consistent with net removal of electron density from the porphyrin π system upon complextion. Near-UV fluorescence (MLCT region) indicated that the metal corners have a structural role rather than a photophysical role within the framework. Complexes remained luminescent but with fluorescence generated from porphyrin localised excited states, lifetimes of 3.0 and 2.4 ns were observed for **H$_2$11** and **Zn11**. Addition of pyridine to **Zn11** led to a significant bathochromic shift in the fluorescence, a response not observed for **H$_2$11**, clearly demonstrating axial ligation of the porphyrin bound zinc by pyridine. Thus the molecular square can be used in host-guest complex construction.
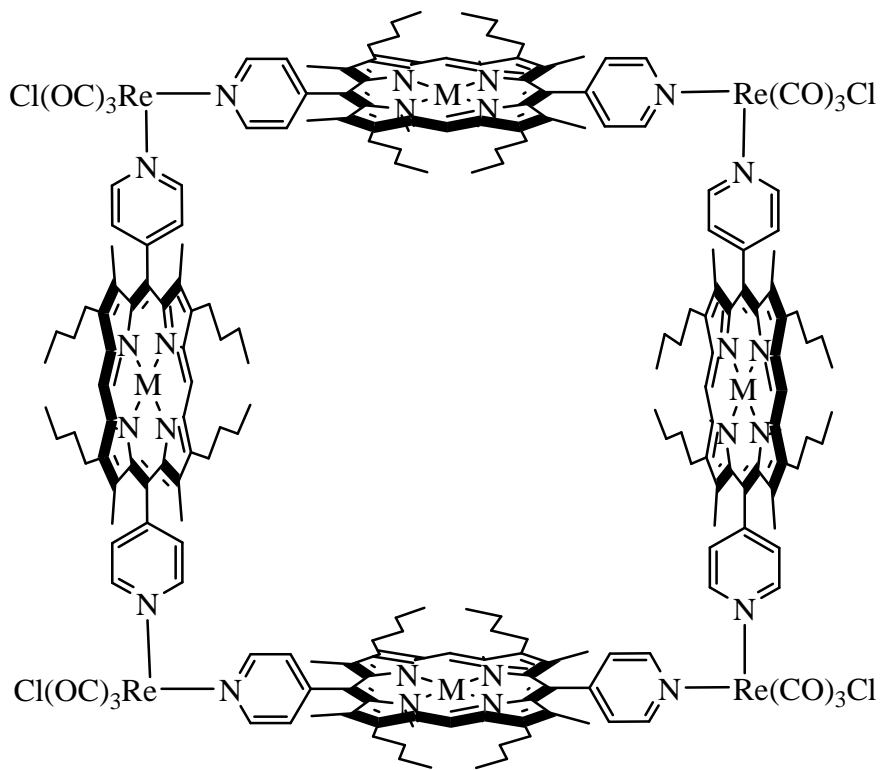
Figure 5   *Porphyrin square with Re(CO)₃Cl corners, 11.*

Compounds containing a [*fac*-Re(CO)$_3$(diimine)]$^+$ unit are electron acceptors and in solution display intense luminescence in the visible region due to a long lived Re-π*(diimine) MLCT excited state. There are two ways that [*fac*-Re(CO)$_3$(diimine)]$^+$ can be connected to a porphyrin: the porphyrin can act as a ligand through a peripheral *meso* pyridyl group and is bound directly to the Re(I) centre adjacent to the coordinated diimine or the diimine is functionalised and then conjugated to a peripheral group on the porphyrin (in this case the coordination sphere of Re(I) must be completed by a sixth ligand, either neutral or anionic).

Casanova et al. synthesised porphyrin-Re(I) conjugates of the first type, where the pyridyl porphyrin was directly coordinated to the Re(I) electron-acceptor fragment, [*fac*-Re(CO)$_3$(diimine)]$^+$.[9] Assemblies contained either 4-pyridyl *meso* porphyrins which were mono or tetra substituted (**12** and **13**, Fig. 6) or 3-pyridyl systems (**14** and **15**, Fig. 6) and the porphyrins were also metallated with zinc(II). Apart from minor red shifts in the absorbance spectra with respect to the corresponding uncomplexed porphyrin, the spectra

278

of **12 - 15** were the summation of the molecular components, indicating that interaction between the porphyrin and rhenium was weak. All were dominated by the porphyrin Soret band with Q bands ranging from 500-700 nm. The Re(bpy) unit did not absorb appreciably above 350 nm and the Re→bpy MLCT transition (λ = 350 nm) was obscured by the porphyrin Soret band. The porphyrin-Re(I) conjugates possessed typical porphyrin-based fluorescence with a small shift in relation to **ZnTPP**. A moderate but significant decrease of the emission intensity and lifetime is observed for **Zn12** and the effect was more pronounced for the pentad **Zn13**. In general the porphyrin fluorescence was affected but not strongly quenched by the presence of the peripherally bound rhenium unit(s). Possible mechanisms for the quenching observed were (a) electron transfer quenching and (b) the heavy atom effect. The emission for **Zn12** and **Zn15** were further investigated in the presence of pyridine. A marked shortening in the lifetime of **Zn12** (from 900 ps to ~250 ps) with a proportional decrease in the emission intensity was observed. Excitation in the UV region where the rhenium(I)bpy absorbed did not produce MLCT emission clearly indicating that its triplet state was efficiently quenched in all compounds. The authors concluded that the heavy atom effect was the cause of fluorescence quenching as it was more efficient for pentameric than dimeric species. Nanosecond time resolved absorbance spectroscopy of the Zn(II)porphyrin-Re dyads showed decay of a transient for **Zn12** with a lifetime of > 20 μs that corresponded to the triplet state. Ultrafast spectroscopy, with 560 nm excitation, was also carried out. The initial spectrum for **Zn12** taken after the laser pulse (1 ps) displayed typical zinc porphyrins S_1 features and evolved to a final spectrum practically identical to that of the nanosecond laser experiment which corresponded to the triplet state. The singlet excited state spectrum evolved to that of the triplet over ~1 ns. The ultrafast experiments were then repeated in the presence of pyridine. The temporal spectral changes observed were substantially different than that observed in the absence of pyridine, with a biphasic behaviour taking place for t $\leq$ 80 ps and t $\geq$ 80 ps. A time constant of 20 ps was obtained for the first process at 618 nm and 300 ps for the second process at 585 nm. The final spectrum recorded at 1000 ps was almost identical to the triplet spectrum observed in the nanosecond experiments. This biphasic behaviour was consistent with a charge separated state (ZnPorph$^+$ - Re(bpy)$^-$) which was sufficiently close in energy to the singlet state (S_1) to allow fast equilibrium between them. In the presence of pyridine the processes that occurred were (a) an electron transfer process from the singlet of the zinc-porphyrin to the Re(bpy) fragment, with a time

constant of 20 ps, which led to a charge separated state and (b) the equilibrium mixture of singlet and charge separated states that decayed to the triplet state in 300 ps.

12: M = H$_2$ or Zn
14 = 3-pyridyl, M = H$_2$ or Zn

13: M = H$_2$ or Zn
15 = 3-pyridyl, M = H$_2$ or Zn
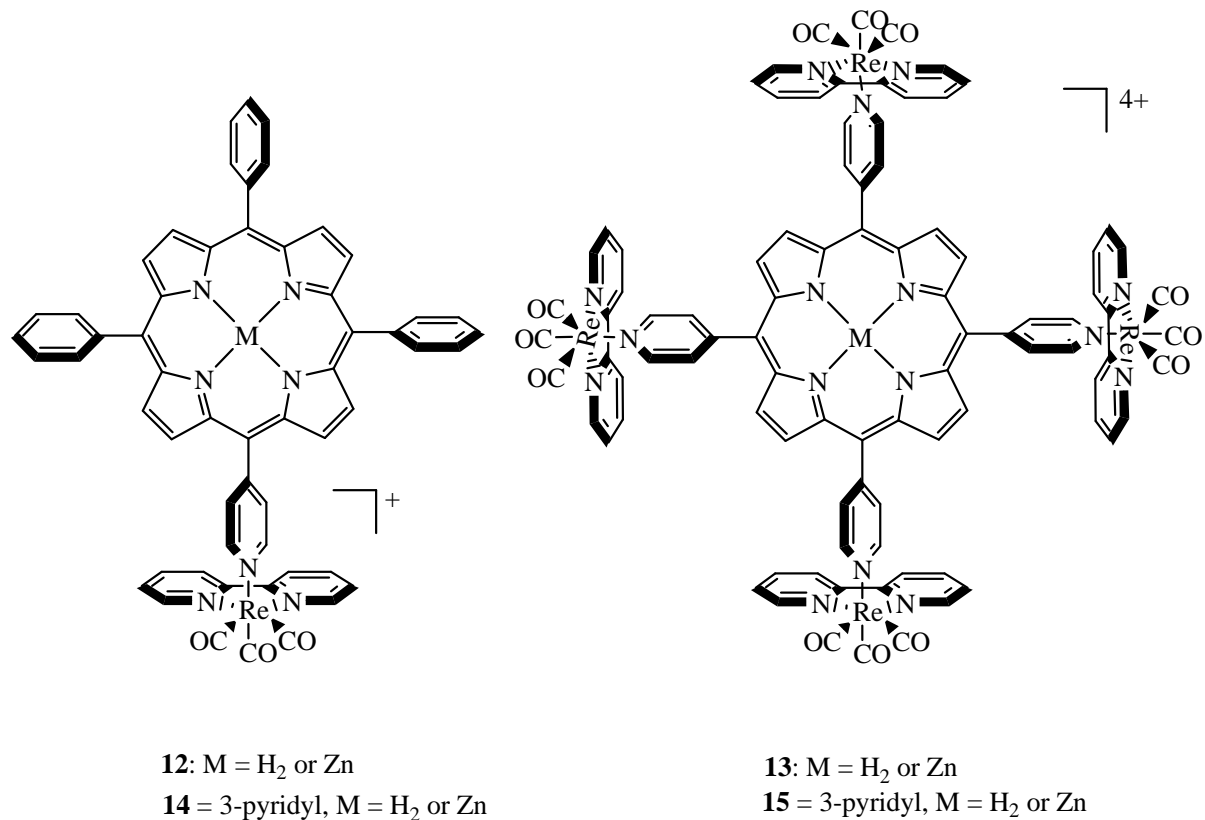
Figure 6   Porphyrin-Re(I) conjugates

Complexes of the type [Re(CO)$_3$(bpy)L]^n (n = 0, +1) with a metalloporphyrin covalently linked to the rhenium unit, have also been synthesised (**16 – 20**, Fig. 7) and their photochemistry and electrochemistry were examined.[10] UV-vis spectra were dominated by the porphyrin absorbance bands. The Re-(bpy) MLCT band anticipated in the range 350 – 420 nm was masked by the porphyrin Soret band. Time resolved absorbance studies (10 ns laser pulse, 355 nm excitation) were carried out. The absorbance spectra of the parent porphyrin, **20**, and porphyrin complex, **17**, were characteristic of the porphyrin $^3(\pi-\pi^*)$ excited state. There was no evidence of excited state absorbance due to Re → bipyridylporphyrin MLCT transitions, most likely because these bands were weak in

comparison to the porphyrin transient bands observed. Transient species of **20** and **17** decayed with lifetimes of $\tau = 2 \times 10^{-5}$ s and $\tau = 3 \times 10^{-6}$ and respectively. The emission spectrum observed for the porphyrin complex **17** was typical of metalloporphyrins with peaks at 606 and 656 nm. Emission intensity was 50 % lower than that of **20**. Emission from the ^{3}MLCT excited state of Re(CO)$_3$-(bpy)Br is observed at 620 nm and time resolved emission from the ^{3}MLCT excited state of Re(CO)$_3$Br(bpy) was observed (in the range 580-670 nm) with a lifetime of 63 ns. No emission was detected in this region for **17** which indicated that emission was quenched by the metalloporphyrin chromophore. Quenching of the steady state fluorescence of **20** also indicated an excited state interaction.

16$^+$: [M] = [*fac*-Re(CO)$_3$(3-Me-Py)]$^+$
17 : [M] = [*fac*-Re(CO)$_3$Br]
18$^+$: [M] = [*fac*-Re(CO)$_3$(THF)]$^+$
19$^+$: [M] = [*fac*-Re(CO)$_3$(PrCN)]$^+$
20 : [M] = no rhenium moiety

21
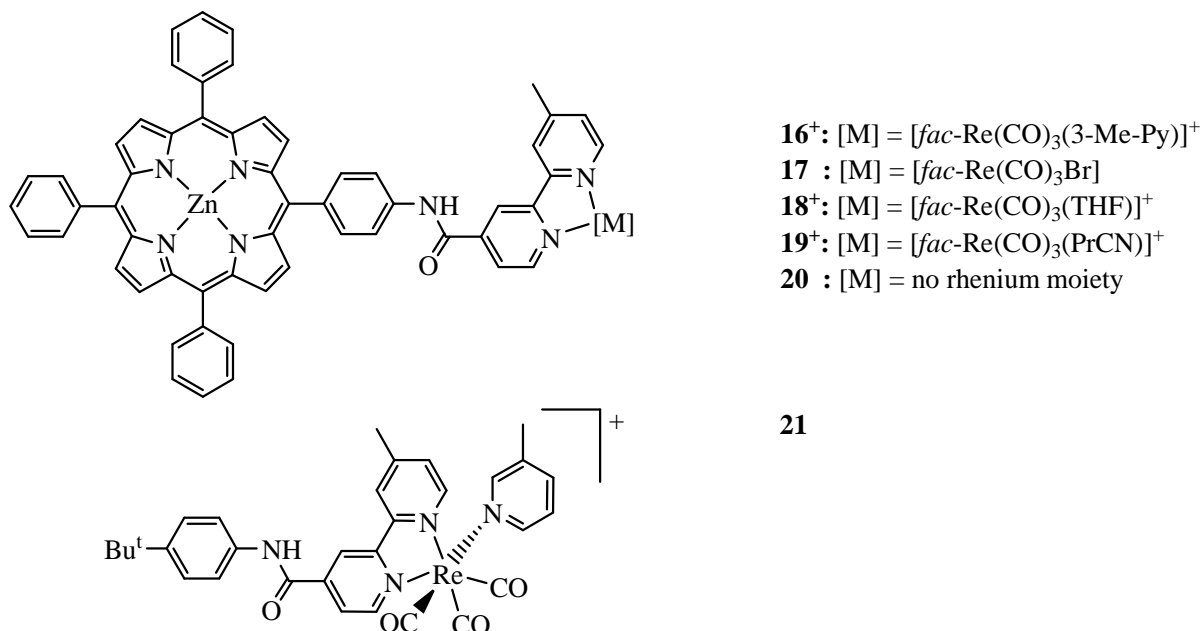
Figure 7   Rheniumtricarbonyl units covalently linked to metalloporphyrins

In a subsequent study, photolysis of **16$^+$** with $\lambda > 495$ nm in the presence of triethylamine revealed that a new metal carbonyl complex was formed. Comparison of the IR spectrum with [Re(CO)$_3$(bpy)(THF)]$^+$ indicated that the axial ligand was displaced by the solvent to yield the THF complex **18$^+$**. Repeating the photoreaction with excess bromide and triethylamine resulted in the formation of complex **17**. Both these reactions produced 18-

electron products; however photolysis in the presence of a trace quantity of free 3-Me-pyridine produced IR features indicative of the radical **16·** (Table 2). Evidence for a rhenium bipyridine based radical, either **16·** or **19·**, was obtained by EPR and IR spectroscopy following photolysis of **16$^+$** with triethylamine and excess 3-Me-pyridine in PrCN as well as the cationic solvent complex **19$^+$**. The authors suggested that the porphyrin acted as a sensitiser upon visible light excitation and product formation depended on electron transfer from triethylamine. As a control, complex **21** without the porphyrin unit was synthesised. Photolysis (λ > 495 nm) of **21$^+$** in THF in the presence of Et$_3$N yielded no product. Spectroelectrochemistry with UV-vis detection showed the reversible oxidation of **16$^+$** and **17** was based on the porphyrin moiety and occurred at the same potential as that of **20** and **ZnTPP** (380 mV *vs.* Fc/Fc$^+$ in THF). IR detection indicated that the reduction observed in CV occurred on the rhenium bipyridine site for both **16$^+$** and **17**. The reduction waves were different from the simple models, **21$^+$**, [Re(CO)$_3$(bpy)Br] and from **20**. Reduction of **16$^+$** resulted in three new IR bands at 2016, 1914, 1892 cm^{-1} and was assigned to **18$^+$**, whereas reduction at low temperature (223 K) in butyronitrile gave bands at 2010, 1903 and 1893 cm^{-1} consistent with the radical species **16·**. Thus reduction of **16$^+$** occurred at the Re-(bpy) site whereas reduction of **20** occurred at the porphyrin. As no ligand substitution occurred without reduction, the radical **16·** was the species that underwent substitution. On reduction of **16$^+$** in the presence of bromide ions, the 3-Me-pyridine was displaced by bromide and the radical anion **17·−** formed, was then reoxidised to compound **17** quantitatively. Analogue **20**, without Re was effectively photoreduced by triethylamine to the porphyrin radical anion **20·−**, reiterating that triethylamine can transfer an electron to the excited state of the porphyrin. Intramolecular electron transfer occurred with a driving force of -0.25 eV and *ca.* 0.06 eV for **16$^+$** and **17** respectively. Despite this similarity, **17** did not undergo photochemical reduction under the same conditions as **16$^+$**. It was reduced at more negative potential than **16$^+$** and an irreversible reduction wave was observed in THF. It was possible to displace an axial ligand in **17** by THF during reduction and subsequent reoxidation gave the cationic THF complex **18$^+$**. Thus the introduction of the pyridyl porphyrin into the design of **16$^+$** induced substitution at a remote site as a result of photo-induced electron transfer.[10]

Complex	Solvent	$\nu(CO)$ (cm^{-1})
16$^+$	THF	2031, 1927 (br)
16·	PrCN	2010, 1903, 1893
16·	THF	2011, 1907, 1893
17	THF	2020, 1920, 1897
17·$^-$	THF	1998, 1888, 1868
18$^+$	THF	2016, 1914, 1892
19$^+$	PrCN	2038, ~1835
19	PrCN	2010, 1903(br), 1893(br)
21$^+$	THF	2031, 1927(br)
21·	THF	2010, 1905, 1892

Table 2   *CO stretching frequencies of complexes in photolysis study.*

Two types of freebase and zinc tetraaryl porphyrins were synthesised (**22** and **23**, Fig. 8), then mono substituted with tungsten pentacarbonyl *via* a pyridine linker (**22-W(CO)$_5$** and **23-W(CO)$_5$**, Fig. 8).[11] This series of porphyrins, coordinated to a single metal carbonyl unit *via* a pyridyl linker, was used to further investigate interactions between the two chromophores. Complexes **24** and **25** were used as model systems for comparative purposes. The UV-vis spectra were dominated by porphyrin transitions with no shift in band position observed upon peripheral metallation with W(CO)$_5$, although a reduction in extinction coefficients of the Soret bands occurred. No tungsten based absorbances were detected for the porphyrin-W(CO)$_5$ complexes. The MLCT bands of both **22-W(CO)$_5$** and **23-W(CO)$_5$** occurred in the range 390 – 400 nm (by comparison with **24** and **25**) and so were overlapped by the porphyrin Soret. Luminescence studies of **H$_2$22-W(CO)$_5$** and **H$_2$23-W(CO)$_5$** revealed fluorescence spectra typical of freebase porphyrins, but the metalloporphyrins **Zn22-W(CO)$_5$** and **Zn23-W(CO)$_5$** demonstrated unusual luminescence behaviour. The emission profiles recorded immediately after preparation were typical of zinc porphyrins with two bands at 605 and 655 nm. Following longer exposure to the excitation lamp a new band was observed between the two Q band emissions at 628 nm. In the case of **Zn23-W(CO)$_5$** in THF, the third band was observed rapidly with excitation at 435 nm but not observed immediately with 556 nm excitation. Due the intensity and width of the third band the authors postulated that the extra band originated from a porphyrin based transition and tentatively suggested that it resulted from photoinduced electron transfer. Time-resolved emission ($\lambda_{ex} > 355$ nm) were carried out on **H$_2$22** and

283

Zn22, **H$_2$22-W(CO)$_5$** and **Zn22-W(CO)$_5$**. All four porphyrins displayed $^1(\pi\text{-}\pi^*)$ excited state emission and no difference was observed between either **H$_2$22** and **H$_2$22-W(CO)$_5$** or **Zn22** and **Zn22-W(CO)$_5$**. The lifetime of the fluorescence was 22 ns for the freebase porphyrins and less than 10 ns for the zinc derivatives (width of the excitation pulse). Time resolved spectra were in agreement with steady state emission spectra in which the freebase porphyrin exhibited two fluorescence bands at 650 and 720 nm. The zinc analogues emitted at higher energy each displayed two bands at *ca*. 610 and 650 nm. The time resolved emission spectra of **Zn22-W(CO)$_5$** differed from **Zn22** in that it had a third emission band at 630 nm, similar to that obtained after slightly prolonged exposure to the excitation source in the steady state fluorimetry. Time resolved absorbance spectroscopy was used to probe the $^3(\pi\text{-}\pi^*)$ excited states of **H$_2$22**, **Zn22**, **H$_2$22-W(CO)$_5$** and **Zn22-W(CO)$_5$**. Both the freebase and metalloporphyrins showed strong transient signals from 440 to *ca*. 480 nm with maxima at 440 nm for freebase porphyrins and at 460 nm for metalloporphyrins. The transient spectra were typical of porphyrin $^3(\pi\text{-}\pi^*)$ excited states and the presence of a W(CO)$_5$ moiety had no effect on the spectra. Reports in literature indicate transient absorbance features are observed at *ca*. 440-460 nm and *ca*. 600 nm for [(4'-X-Py)-W(CO)$_5$] (where X = electron withdrawing group). No transient feature at *ca*. 600 nm was observed for the porphyrin systems possibly due to the fact that at 355 nm excitation, the porphyrin sub-unit will preferentially excited. Steady state photolysis of the models, **24** and **25**, and porphyrin complexes led to the formation of the same product that was readily assigned to [W(CO)$_5$(THF)] as observed by IR spectroscopy. Photolysis of **H$_2$22-W(CO)$_5$** and **Zn22-W(CO)$_5$** with $\lambda_{ex} > 395$ nm showed evidence for formation of the THF adduct. Excitation using $\lambda_{ex} > 495$ nm prevented photosubstitution as light was absorbed only by the porphyrin Q bands. As almost all the light in this excitation range ($\lambda_{ex} > 395$ - $\lambda_{ex} > 495$ nm) was absorbed by the porphyrin the authors postulated that tungsten based excited states were populated by energy transfer from the porphyrin moiety. The fluorescence spectra of **Zn22-W(CO)$_5$** and **Zn23-W(CO)$_5$** which exhibited an extra emission band also suggested a photochemical process occurred, most likely electron transfer.[11]
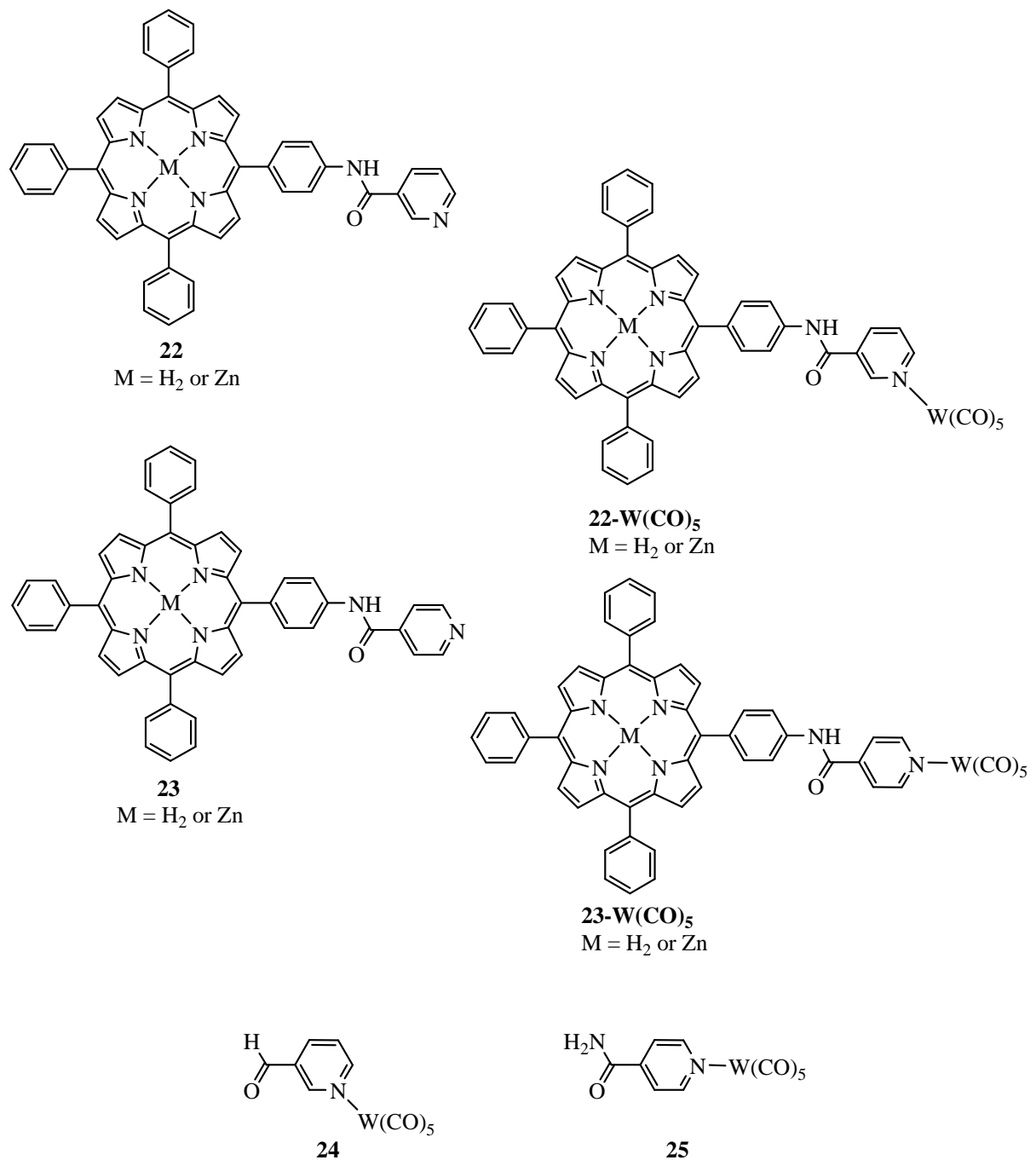
Figure 8   Tetraaryl porphyrin monosubstituted with tungsten pentacarbonyl

Rhenium(bipyridine)(tricarbonyl)(picoline) units were then linked covalently to tetraphenylmetalloporphyrins *via* an amide bond between the pyridine and one phenyl substituent of the porphyrin to produce [Re(CO)₃(Pic)Bpy-MTPP][OTf] (**26**, M = Zn or Mg, Fig. 9).[12] In the ground state UV-vis spectrum, the rhenium appended complex **26**

showed only small changes the when compared to the uncomplexed porphyrin (**20**, M = Zn or Mg, Fig. 7). The MLCT and IL transitions expected around 370 and 300 nm were masked by the porphyrins transitions. **Mg26** showed a bathochromic shift of all bands in comparison to the **Zn26**. The IR spectra of both porphyrin complexes displayed two bands at 2031 and 1927 cm^{-1} in THF. Steady state emission spectroscopy indicated that the zinc and magnesium porphyrins emitted strongly from the first singlet excited state. **Zn26** exhibited two sharp bands at 604 and 655 nm like that of the Re free model, **Zn20**. Emission quantum yield was strongly affected by solvent polarity, as the solvent polarity increased the emission intensity of **Zn26** was reduced compared to **Zn20**, to 15 % in toluene, further decreasing to 6.6 % in THF and 4.5 % in PrCN. The model **Mg20** displayed two fluorescence bands at 612 and 665 nm in MeCN, the same position as **Mg26** although the latter showed emission intensity only 2.5 % that of **Mg20**. Such dependence of quenching behaviour on solvent media is characteristic of electron-transfer processes. Energetic calculations support electron transfer from metalloporphyrin to Re(bpy) as the most likely quenching mechanism. At low temperature a reduction in quenching was observed, which supported an electron transfer mechanism.

IR spectroelectrochemistry of **Zn26$^+$** (**[Re(CO)$_3$(Pic)-Bpy-ZnTPP]$^+$**) in PrCN and THF was carried out. In PrCN, reduction of **Zn26$^+$** resulted in a loss of intensity of the precursor ν(CO) bands at 2035 and 1933 cm^{-1} and new bands generated at 2012 and 1928 cm^{-1}; the latter a very broad stretch like the corresponding band of the precursor. New bands were assigned to the radical species **[Re$^+$(CO)$_3$(Pic)-Bpy$^{·-}$-ZnTPP]** and showed the characteristic shift to lower frequency. No significant substitution of picoline with PrCN was observed. Subsequent irreversible reduction of **[Re$^+$(CO)$_3$(Pic)-Bpy$^{·-}$-ZnTPP]** produced a mixture of two anionic species **[Re(CO)$_3$(PrCN)-Bpy-ZnTPP]$^-$** (major) and **[Re(CO)$_3$Bpy-ZnTPP]$^-$** (minor) characterised by high frequency bands at 1983 and 1948 cm^{-1}, respectively, with overlapping broad low frequency bands between 1900 and 1840 cm^{-1}. In THF, the reduction of **[Re(CO)$_3$(Pic)-Bpy-ZnTPP]$^+$** was irreversible with the parent ν(CO) bands at 2033 and 1928 cm^{-1} shifting to 2011, 1906 and 1982 cm^{-1} for the corresponding radical which gradually underwent solvent exchange with a picoline moiety and produced the cation **[Re(CO)$_3$(THF)-Bpy-ZnTPP]$^+$** with bands at 2019, 1914 and 1897 cm^{-1}. Time-resolved visible absorbance (TRVIS) spectroscopy determined the transient lifetimes of the rhenium-appended porphyrins which were reduced dramatically

compared to their rhenium-free counterparts, but possessed identical spectral profiles. The picosecond TRVIS spectrum of **26** (M = Zn or Mg) in PrCN strongly resembled those of **20** (M = Zn or Mg) in PrCN which in turn were very similar to those of **ZnTPP** and **MgTPP** with typical porphyrin S_1 features of strong broad absorbance at 460 nm and stimulated emission at 610 and 660 nm. However, in harsh contrast to **Zn\Mg 20**, lifetimes of transient species derived from **Zn\Mg 26** were much shorter, in PrCN decays with τ = 23.7 $\pm$ 0.2 ps (**Zn26**) and 16.7 $\pm$ 0.7 ps (**Mg26**) were observed. The signals decayed with first order kinetics, which were strongly solvent dependent, decaying faster in PrCN than THF. The rate of decay of the transient from **Mg26** is over two orders of magnitude greater than that of **Mg20**. Nanosecond time resolved absorbance spectroscopy probed the first triplet state of the zinc porphyrins. Excitation of **Zn20** and **Zn26** in THF at 470 nm produced a transient due to the T_1 excited state although the transient of **Zn26** had only 6% of the intensity observed for **Zn20** and a much longer lifetime. Picosecond TRIR was used to probe charge or energy transfer in the rhenium porphyrin dyads. The TRIR spectrum of **Mg26** in MeCN, following excitation at 600 nm (Q band region) resulted in two bleaches, one sharp at 2033 cm^{-1} and one broad at *ca.* 1931 cm^{-1}, due to depletion of the ground state on a sub picosecond timescale, bands were at a maximum in the first spectrum, delay 1.5 ps (Fig. 10). The bleach recovered completely with a lifetime of 34 $\pm$ 4 ps. Also in the initial spectrum after 1.5 ps were product bands, assigned to a charge separated state (CS), at their maximum intensity at 2008 and 1900 cm^{-1} with a positive shoulder overlapping the bleach at *ca.* 2028 cm^{-1}. The CS bands closely resembled the one electron reduced species detected by IR spectroelectrochemistry. These TRIR product bands decayed with a lifetime of 20 $\pm$ 2 ps, revealing, after 6 ps, a pair of bands at 2023 and 1908 cm^{-1}, assigned to a hot ground state (HS), which in turn decayed with a lifetime of 35 $\pm$ 8 ps, similar to that of the recovery of the bleach. The CS state showed considerable shifts to lower frequency compared to the starting material, consistent with charge transfer from porphyrin to Re(bpy). The TRIR spectrum of **Mg26** in PrCN and following excitation at 560 and 600 nm produced decay kinetics and spectral shapes identical to those discussed above. Picosecond TRIR spectra of **Zn26** in PrCN showed bleaches at 2031 and 1932 cm^{-1} formed within 1 ps of excitation (first spectrum after laser pulse, delay 1 ps) which continued to grow to a maximum after *ca.* 10 ps and then decayed with a lifetime of 55 $\pm$ 8 ps (Fig. 11). A sharp product band (labelled π-π*) was observed at 2006 cm^{-1} on the low energy side of the parent bleach after 2 ps with an associated band contributing to the broad maximum at 1906 cm^{-1}. These bands decayed over 10 ps when a

new band appeared at 2007 cm^{-1} and the low energy broad maximum shifted to *ca.* 1896 cm^{-1}. These CS bands reached their maximum at 10 ps and then decayed with a rate constant of 40 $\pm$ 4 ps. Product CS bands gave way to a hot species after 40 ps with maxima shifted to 2021 and 1905 cm^{-1}. The decay of this third species was almost complete within 100 ps. Thus when the assemblies were excited at long wavelengths in the region where the porphyrin unit absorbed electron transfer from the porphyrin to rhenium bipyridine occurred on an ultrafast timescale. The magnesium derivative, **Mg26**, displayed charge separated IR bands within 1.5 ps which decayed in 20 ps while for the zinc analogue, **Zn26**, the charge separated IR bands rise over 5 ps and then decayed over 40 ps. The charge separated state was described as **[Re$^+$ (CO)$_3$(Pic)-Bpy$^-$ -MTPP$^{\cdot+}$]** (M = Zn or Mg). When the transient state decayed a further state was identified, characterised by a reduced low frequency shift of the ν(CO) bands and assigned to a vibrationally excited ground state. The assemblies return to the initial ground state with a time constant of 35 – 55 ps. Rapid charge separation and back electron transfer provided a mechanism for quenching of the porphyrin emission that was solvent dependant.
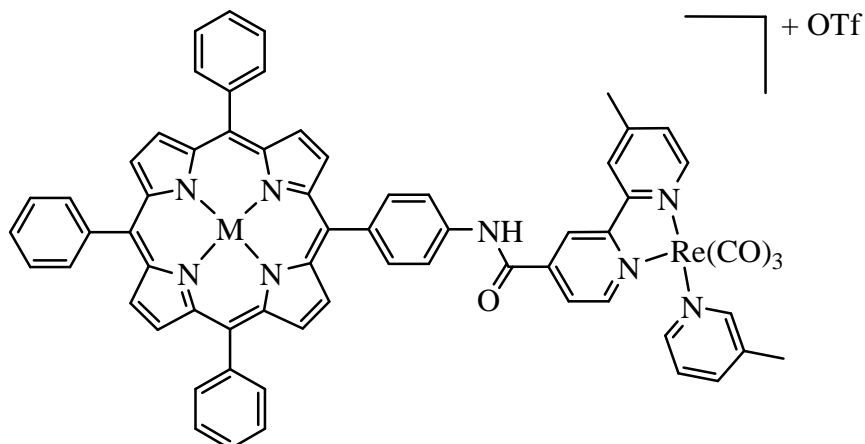
Figure 9   [Re(CO)$_3$(Pic)Bpy-MTPP][OTf], **26**, M = Zn or Mg.
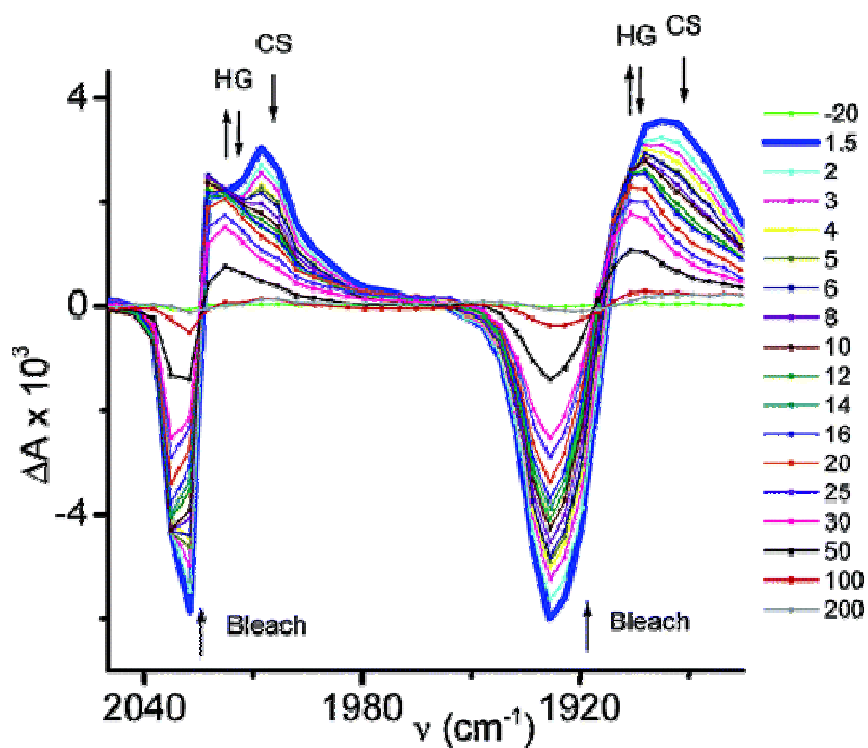
Figure 10   *TRIR spectra of **Mg26** in MeCN observed following 600 nm excitation. Time delays are in ps and arrows indicate rise and decay of transients.[12]*
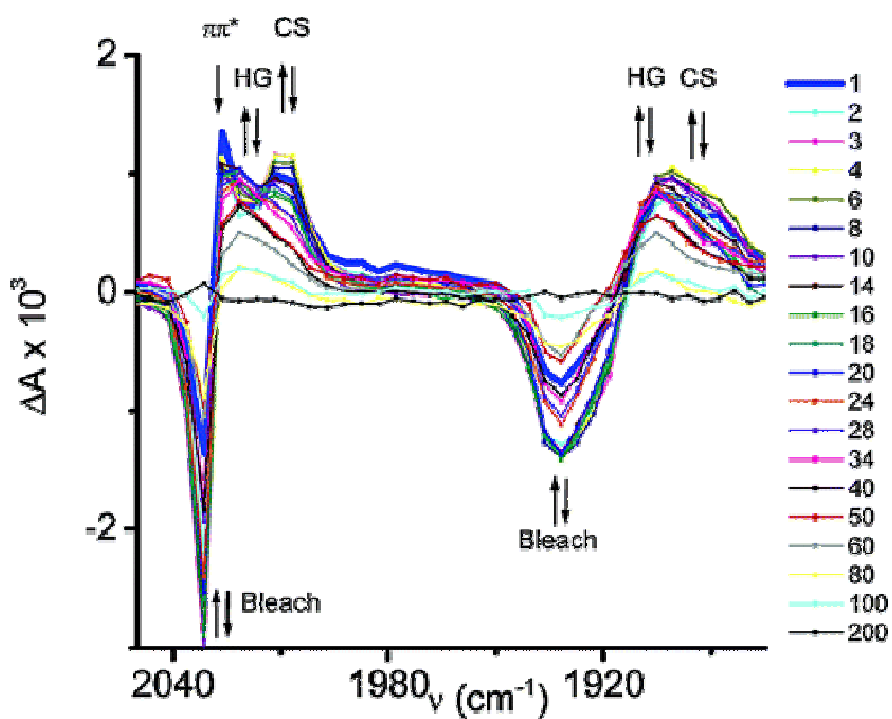
Figure 11   *TRIR spectra of **Zn26** in PrCN observed following 560 nm excitation. Time delays are in ps and arrows indicate rise and decay of transients.[12]*

289

4.2   Abstract

The aim of this chapter is to investigate the efficiency of communication between a porphyrin and a metal carbonyl moiety across π substituents arranged in an orthogonal manner at the *meso* position of a porphyrin macrocycle. Photophysical measurements have been carried out on these systems and are discussed below.[14] With respect to this study, an increased understanding of the initial photoprocesses that occur immediately after excitation of the monopyridyltriphenyl porphyrin metal pentacarbonyl complexes (M = W or Cr) was sought. TRIR spectroscopy with picosecond resolution should provide such information. **Pyridine-W(CO)₅** was used as a model compound.

M = H,   **MPyTPP-Cr(CO)₅**
M = Zn, **ZnMPyTPP-Cr(CO)₅**

M = H,   **MPyTPP-W(CO)₅**
M = Zn, **ZnMPyTPP-W(CO)₅**
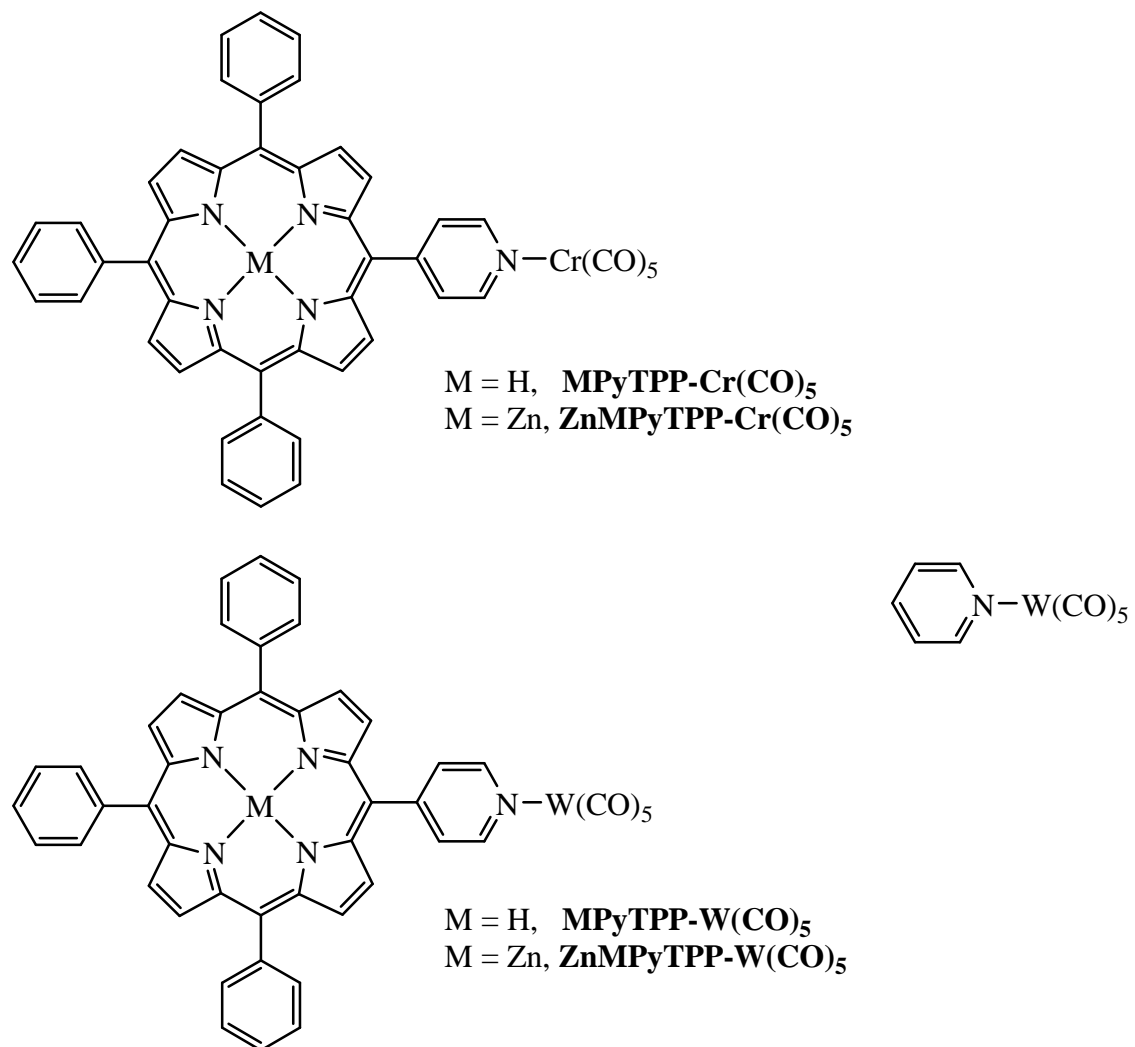
Figure 12   *Porphyrin metal pentacarbonyl systems under investigation.*

The porphyrin metal pentacarbonyl complexes were synthesised previously and examined by steady state fluorescence techniques and transient absorbance spectroscopy on a μs timebase. Only minor perturbations in the absorbance and luminescence properties of the porphyrins resulted from the presence of the metal carbonyl adducts when compared to the non-coordinated porphyrin.

Steady state photolysis of the complexes showed that sensitisation of the porphyrin (λ_{exc} = 550 nm) resulted in efficient cleavage of the metal pentacarbonyl moiety. In CO saturated solution, cleavage of the pyridine N – M bond (M = W or Cr) resulted in the formation of $M(CO)_6$ as was evidenced by a new absorbance band at ~ 290 nm. Even in Ar saturated solutions, cleavage of the N-M bond was observed. For the zinc porphyrins, spectral changes indicated cleavage of the pyridine N – M bond (M = W or Cr) was followed by coordination of zinc from one porphyrin with a pyridine of another and formation of a zinc porphyrin polymer. Since the pyridine-$M(CO)_5$ moiety (M = W or Cr) does not itself absorb above 480 nm, this would suggest that although the porphyrins retain their spectroscopic identity upon complexation, there is significant communication between the two molecular components.

Transient absorbance spectroscopy (λ_{exc} = 532 nm) on a μs timebase of **ZnMPyTPP-M(CO)₅** showed population of the excited states associated with the metalloporphyrin unit and not the pyridine-$M(CO)_5$ moiety. The transient absorbance difference spectrum possessed spectral features similar to that of the triplet state of the uncomplexed metalloporphyrin, **ZnTPP**. The lifetimes of the triplet excited state were somewhat shorter for the metal carbonyl metalloporphyrin (~15 μs) compared to the uncoordinated metalloporphyrin (20 μs). Also measurements carried out using various concentrations of CO confirmed that the lifetime of the triplet state was unaffected. The sample underwent loss of $M(CO)_5$ during the experiments as formation of $M(CO)_6$ was confirmed by IR spectroscopy. Changes observed in the Q band region of the porphyrin complex were attributed to cleavage of the N – M bond (M = W or Cr) and subsequent formation of the zinc porphyrin polymer.

A comprehensive investigation into the primary photoprocesses that occur following excitation will be carried out using TRIR spectroscopy. The metal pentacarbonyl moieties act as excellent reporter groups for infrared vibrational spectroscopy. A wealth of publications on various substituted pyridine-$M(CO)_5$ complexes exists which should aid in the identification of transient species and subsequent product formation. With the ability of picosecond techniques, time resolved studies of reaction dynamics on the time scale of solvent motion can be probed.

Time resolved infrared studies allowed the direct observation of photoactive states, formed following excitation, through shifts in metal carbonyl absorbance bands. The TRIR data enabled identification of key excited states which are populated following photolysis.

4.3 Experimental

4.3.1 Materials

All syntheses were carried out under an atmosphere of argon or nitrogen using standard Schlenk techniques unless otherwise stated. All solvents were supplied by the Aldrich Chemical Company. Dichloromethane, chloroform, diethyl ether, pentane and hexane were dried over $MgSO_4$ prior to use. Tetrahydrofuran (THF) was distilled from sodium metal using benzophenone and used immediately. All organic reagents were purchased from the Aldrich Chemical Company and used without further purification unless stated otherwise. Pyrrole was distilled over KOH under reduced pressure prior to use. The hexacarbonyls, $W(CO)_6$ and $Cr(CO)_6$ were used without further purification. All mobile phases for column chromatography were dried over $MgSO_4$ and silica gel (Merck) was used as received. All solvents used in TRIR experiments were of spectroscopic grade and used without further purification. All solvents were deoxygenated by purging with pure argon or nitrogen for ~10 minutes.

4.3.2 Equipment

NMR spectra were recorded on a Bruker model AC 400 MHz spectrometer and Bruker model ANC 600MHz spectrometer using $CDCl_3$ as solvent. All NMR spectra were calibrated according to the residual solvent peak, i.e. $CHCl_3$ at 7.26 ppm for all ^1H spectra and 77.16 ppm for all ^{13}C spectra . Chemical shifts (δ) are given in parts per million (ppm). Proton coupling constants (J) are given in Hertz (Hz). All UV-vis spectra were measured on an Agilent Technologies 8453 photodiode array spectrometer using a 1 cm^3 quartz cell. IR spectra were recorded on a Perkin-Elmer 2000 FT-IR spectrophotometer (2 cm^{-1} resolution) in a 0.1 mm sodium chloride liquid solution cell. Picosecond time resolved infra-red spectroscopy was carried out as described previously.[13]

4.3.3 Synthesis

All porphyrins were synthesised as described[14] using an adapted method by Adler et al.[15] The pentacarbonyl complexes were synthesised using a method described by Stromeier.[16]

4.3.3.1 5-(4-Pyridyl)-10,15,20-triphenyl porphyrin (MPyTPP)
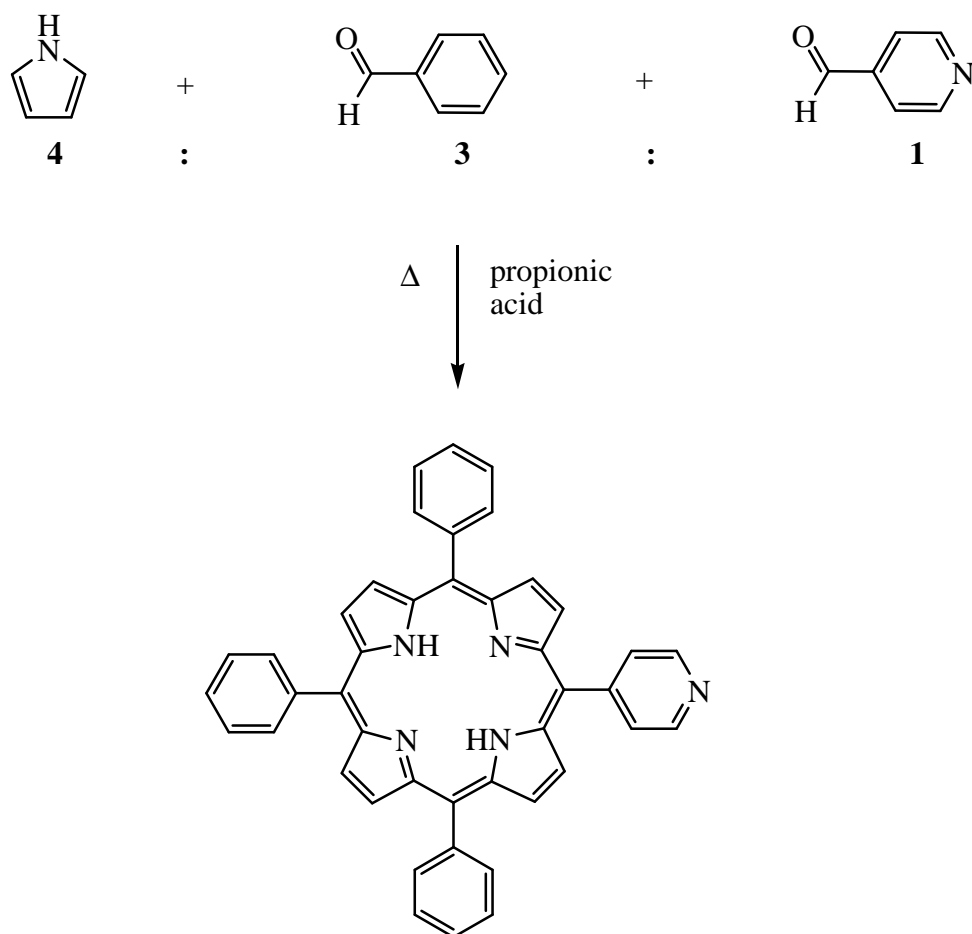
+ H$_2$TPP and four other pyridyl porphyrins depicted in figure 1

The monopyridyltriphenyl porphyrin was prepared *via* a mixed aldehyde condensation reaction. Freshly distilled pyrrole (100 mmol, 7.0 ml), benzaldehyde (75 mmol, 8.0 ml) and 4-pyridine carboxaldehyde (25 mmol, 2.35 ml) were added to 99 % propionic acid (250 ml) and brought to reflux temperature. The acidic solution was allowed to reflux for 2 hrs and gradually turned black. The mixture was allowed to cool and placed in the fridge overnight. The black solution was filtered and the purple crystals formed were collected and washed several times with methanol to give a bright purple crystalline solid. This method typically gave a yield of 2 g of crude product.

Thin layer chromatography using chloroform : ethanol (98 : 2) as mobile phase indicated the presence of a mixture of six porphyrins formed during the reaction. The compounds formed were 5,10,15,20-tetraphenylporphyrin (**H₂TPP**), 5-(4-pyridyl)-10,15,20-triphenylporphyrin (**MPyTPP**), *cis*-5,10-(4-dipyridyl)-15,20-diphenylporphyrin (***cis*-DPyDPP**), *trans*-5,15-(4-dipyridyl)-10,20-diphenylporphyrin (***trans*-DPyDPP**), 5,10,15-(4-pyridyl)-20-phenylporphyrin (**TPyMPP**) and 5,10,15,20-tetra(4-pyridyl)porphyrin (**TPyP**).

The crude porphyrin mixture was purified on a silica gel column. The initial eluent was chloroform : ethanol (98 : 2) and this eluted the first fraction containing **H₂TPP**. Subsequent purifications by column chromatography used a mobile phase with increasing polarity (chloroform : ethanol (97 : 3) and chloroform : ethanol (96 : 4)) to separate the remaining porphyrins. Only **MPyTPP** was required for this study.

¹H NMR (400 MHz, CDCl₃): 9.04 (2H, d, *J* = 8 Hz), 8.89 (2H, d, *J* = 4 Hz), 8.86 (4H, s), 8.80 (2H, d, *J* = 4 Hz) 8.23 – 8.20 (6H, m), 8.18 (2H, d, *J* = 8 Hz) 7.81 – 7.73 (9H, m), -2.83 (2H, s) ppm. **UV-vis** (CH₂Cl₂): 418, 514, 548, 588, 644 nm.

4.3.3.2   Zinc(II) 5-(4-pyridyl)-10,15,20-triphenyl porphyrin (ZnMPyTPP)

ZnMPyTPP was synthesised *via* Lindsey's method for the metallation of porphyrins. The freebase porphyrin, **MPyTPP**, (0.32 mmol, 200 mg) was dissolved in *ca.* 50 ml chloroform and the solution was purged with argon for 10 minutes. An excess of $Zn(OAc)_2$ (0.40 mmol, 73 mg) was first dissolved in *ca.* 5 ml MeOH and then added to the porphyrin solution. The reaction mixture was allowed to stir overnight at room temperature under a nitrogen atmosphere. All solvents were removed under reduced pressure leaving a purple solid. This solid was dissolved in CH_2Cl_2 and washed successively with 5 % aqueous $NaHCO_3$, followed by water. The organic layer was dried over $MgSO_4$ and the solvent removed under reduced pressure. The metalloporphyrin were purified by column chromatography using silica and neat chloroform as mobile phase. Yield: 130 mg, 0.19 mmol, 60 %.
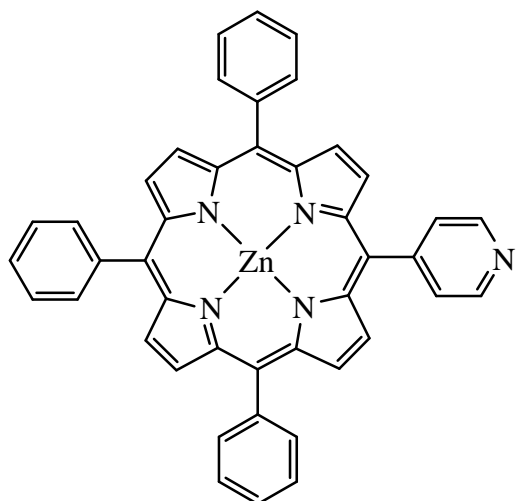
Zinc pyridyl porphyrins aggregate in non-coordinating solvents and are a darker blue colour compared to the purple colour of **ZnTPP**.[17]   The ^{1}H NMR showed evidence of aggregation.

^{1}H NMR (400 MHz, $CDCl_3$): 8.87 – 8.82 (m, pyrrole), 8.23 – 8.15 (m, pyrrole), 8.15 – 8.09 (m, phenyl) 7.77 – 7.64 (m, phenyl), 4.61 – 4.59 (m, 3,5-pyridyl), 23.58 – 3.56 (m, 2,6-pyridyl) ppm. **UV-vis** (CH_2Cl_2): 418, 562, 604 nm.

4.3.3.3 Preparation of 5-(4-pyridyl)-10,15,20-triphenyl porphyrin metal pentacarbonyl complexes (M = Cr or W)

4.3.3.3.1 5-(4-Pyridyl)-10,15,20-triphenyl porphyrin chromium pentacarbonyl (MPyTPP-Cr(CO)₅)
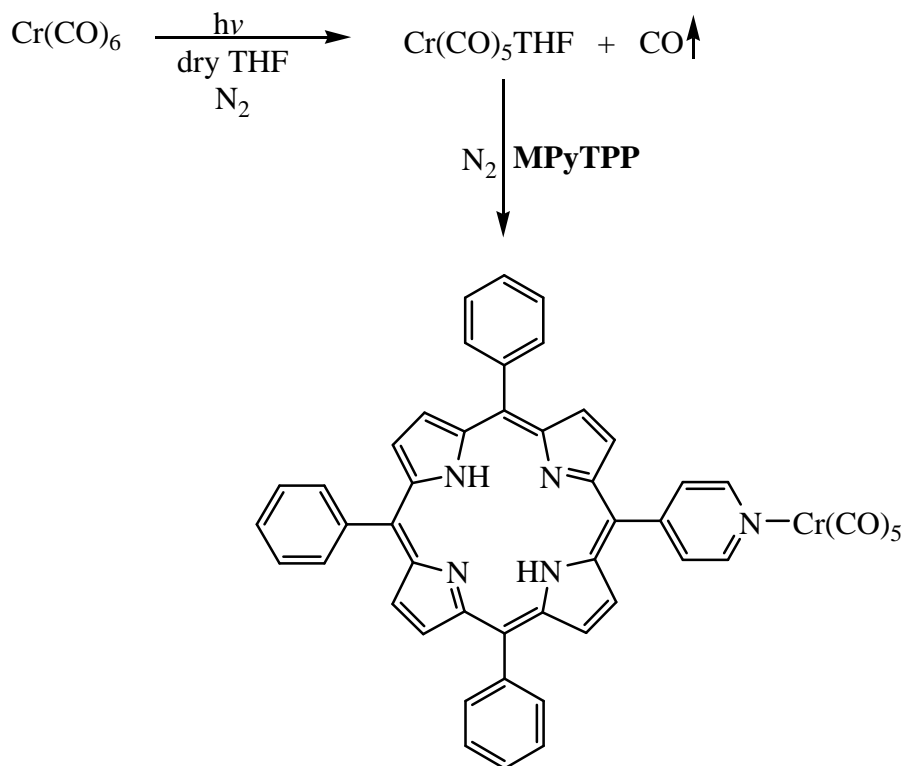
Initially chromium hexacarbonyl (0.68 mmol, 150 mg) was photolysed in freshly distilled THF (150 ml) that had been degassed for 15 minutes with nitrogen. The solution was photolysed with a Hg lamp. The solution was continually purged with nitrogen and after about 40 minutes the solution had turned a strong orange colour. Completion of photolysis and the formation of $Cr(CO)_5THF$ was determined by IR spectroscopy. Depletion of the hexacarbonyl peak at 1979 cm^{-1} and formation of the new pentacarbonyl peaks (2072, 1936 and 1893 cm^{-1}) indicated completion of the reaction. Following this, 5-(4-pyridyl)-10,15,20-triphenylporphyrin (0.32 mmol, 200 mg) was added to $Cr(CO)_5THF$ under an atmosphere of nitrogen and allowed to stir overnight in darkness under an inert

atmosphere. Removal of the THF was carried out under reduced pressure on the rotary evaporator. The complex was then dissolved in chloroform and purified on a silica gel column using chloroform : pentane (90 : 10) as mobile phase. Unreacted hexacarbonyl was eluted initially from the column with any further hexacarbonyl impurities removed by sublimation under reduced pressure. The complex was recrystallised from cold pentane affording purple crystals. Yield: 163 mg, 0.20 mmol, 63 %. Spectroscopic data were in good agreement with reported data.[14]

^{1}H NMR (400 MHz, CDCl$_3$): 9.01 – 8.99 (2H, m), 8.94 – 8.92 (2H, m), 8.86 (4H, s), 8.81 – 8.77 (2H, m), 8.21 (6H, d, J = 8 Hz), 8.10 (2H, d, J = 4Hz), 7.87-7.74 (9H, m), -2.83 (2H, s) ppm. **IR** (CH$_2$Cl$_2$): ν(CO) 2068, 1935, 1898 cm^{-1}. **UV-vis** (CH$_2$Cl$_2$): 420, 516, 552, 590, 646 nm.

4.3.3.3.2 Zinc(II)5-(4-pyridyl)-10,15,20-triphenyl porphyrin chromium pentacarbonyl (ZnMPyTPP-Cr(CO)₅)

$$Cr(CO)_6 \xrightarrow[\substack{dry\ THF \\ N_2}]{h\nu} Cr(CO)_5THF \ + \ CO\uparrow$$
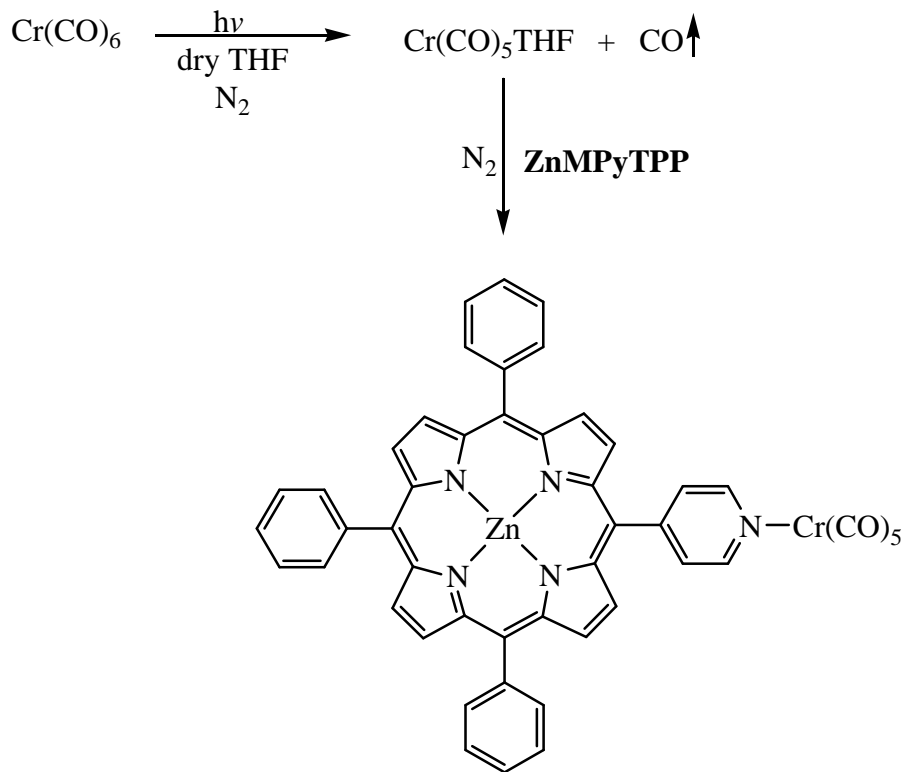
$$N_2 \downarrow \ \textbf{ZnMPyTPP}$$

Synthesis of **ZnMPyTPP-Cr(CO)₅** was carried out in the same manner. Chromium hexacarbonyl (0.45 mmol, 100 mg) and **ZnMPyTPP** (0.074 mmol, 50 mg) were used. The complex was purified on a silica gel column using chloroform : pentane (90 : 10) as mobile phase. Unreacted hexacarbonyl impurities were removed by sublimation under reduced pressure. The complex was recrystallised from cold pentane affording purple crystals. Yield: 34 mg, 0.039 mmol, 53 %. Spectroscopic data were in good agreement with reported data.[14]

^{1}H NMR (400 MHz, CDCl₃): 9.03-9.01 (1H, m), 8.98 – 8.95 (4H, m), 8.89 – 8.86 (3H, m), 8.85 – 8.83 (2H, m), 8.24 – 8.21 (4H, m), 8.12 – 8.07 (4H, m), 7.81 – 7.48 (9H, m) ppm. **IR** (CH₂Cl₂): ν(CO) 2069, 1934, 1895 cm⁻¹. **UV-vis** (CH₂Cl₂): 422, 548, 588 nm.

4.3.3.3.3   **5-(4-Pyridyl)-10,15,20-triphenyl porphyrin tungsten pentacarbonyl (MPyTPP-W(CO)₅)**
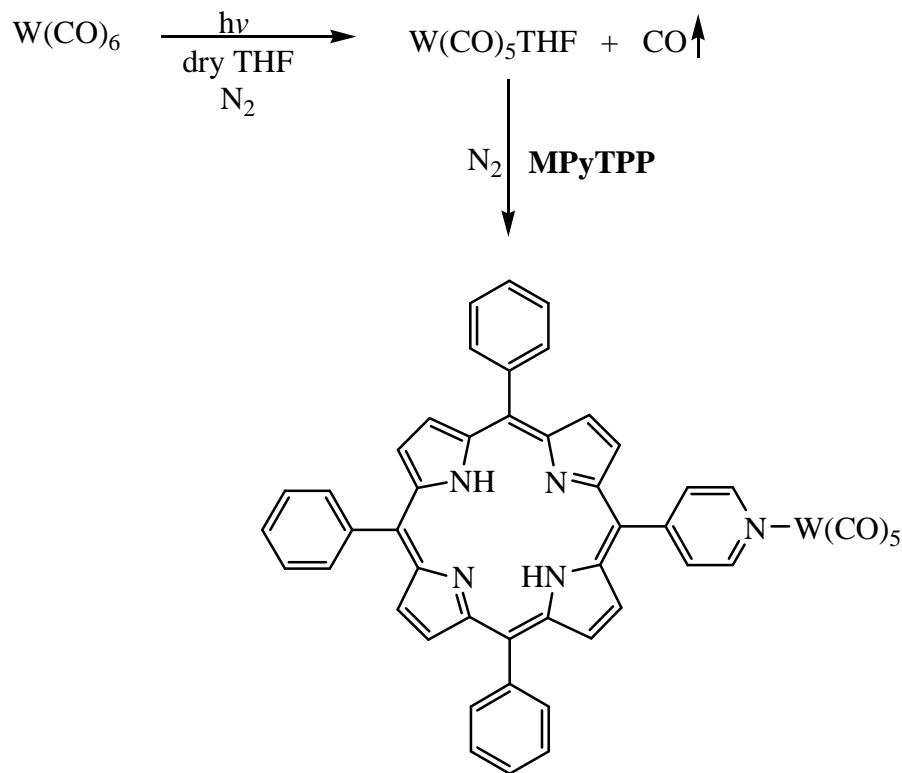
Synthesis of **MPyTPP-W(CO)₅** was carried out in the same manner. Tungsten hexacarbonyl (0.43 mmol, 150 mg) and freebase porphyrin, **MPyTPP**, (0.32 mmol, 200 mg) were used. Purification on a silica gel column using chloroform : pentane (90 : 10) followed by sublimation under reduced pressure yielded the porphyrin complex. The product was recrystallised from cold pentane affording brownish-purple crystals. Yield: 204 mg, 0.22 mmol, 68 %. Spectroscopic data were in good agreement with reported data.[14]

¹H NMR (400 MHz, CDCl₃): 8.91 (2H, d, $J = 8$ Hz), 8.86 (2H, d, $J = 4$ Hz), 8.79 (4H, s), 8.71 (2H, d, $J = 4$ Hz), 8.14 – 8.12 (6H, m), 8.02 (2H, m), 7.76 – 7.66 (9H, m), -2.83 (2H, s) ppm. **IR** (CH₂Cl₂): ν(CO) 2070, 1928, 1896 cm⁻¹. **UV-vis** (CH₂Cl₂): 422, 516, 552, 590, 646 nm.

4.3.3.3.4   Zinc(II)   5-(4-pyridyl)-10,15,20-triphenyl   porphyrin   tungsten pentacarbonyl (ZnMPyTPP-W(CO)₅)
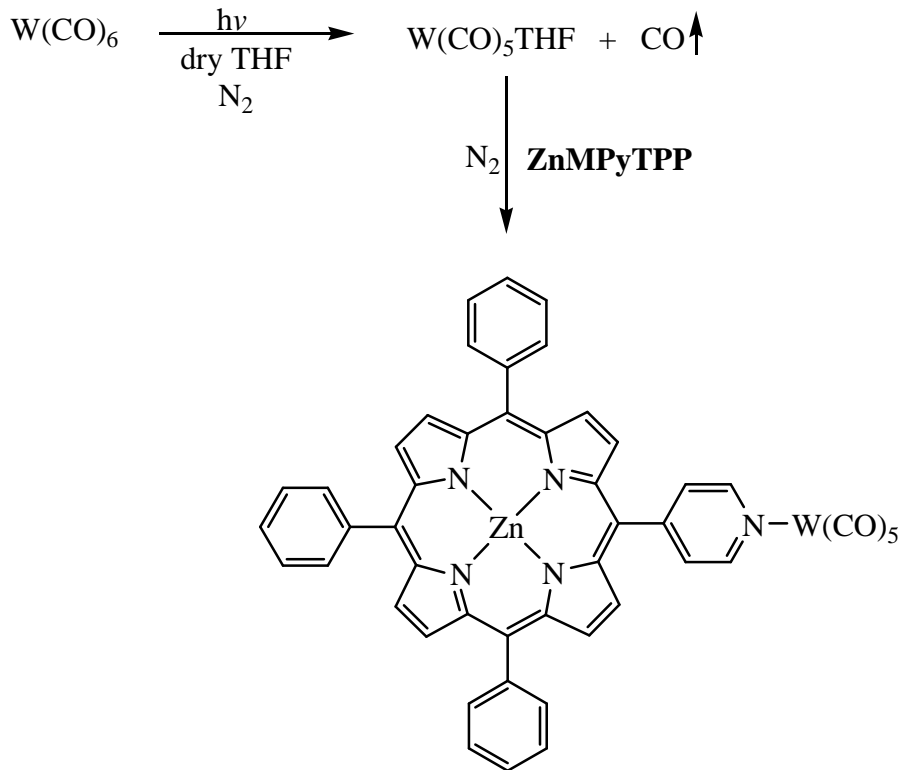
Synthesis of **ZnMPyTPP-W(CO)₅** was carried out in the same manner. Tungsten hexacarbonyl (0.28 mmol, 100 mg) and the zinc porphyrin, **ZnMPyTPP**, (0.074 mmol, 50 mg) were used. Purification on a silica gel column using a mobile phase of chloroform : pentane (90 : 10) followed by sublimation at reduced pressure gave the porphyrin complex. Recrystallised from cold pentane afforded the product as pinkish-purple crystals. Yield: 33 mg, 0.033 mmol, 45 %. Spectroscopic data were in good agreement with reported data.[14]

¹H NMR (400 MHz, CDCl₃): 9.02 – 8.97 (5H, m), 8.89 – 8.84 (3H, m), 8.85 – 8.83 (2H, m), 8.20 – 8.17 (4H, m) 8.10 – 8.05 (4H, m), 7.80 – 7.55 (9H, m) ppm. **IR** (CH₂Cl₂): ν(CO) 2071, 1929, 1894 cm⁻¹. **UV-vis** (CH₂Cl₂): 420, 550, 590 nm.

4.4 Results

4.4.1 UV-vis absorbance studies

The UV-vis spectrum of **pyridine-W(CO)₅** is displayed in figure 13. Similar to other pyridine-W(CO)$_5$ complexes it possesses a LF transition at 382 nm and a MLCT band at *ca.* 430 nm.[18]
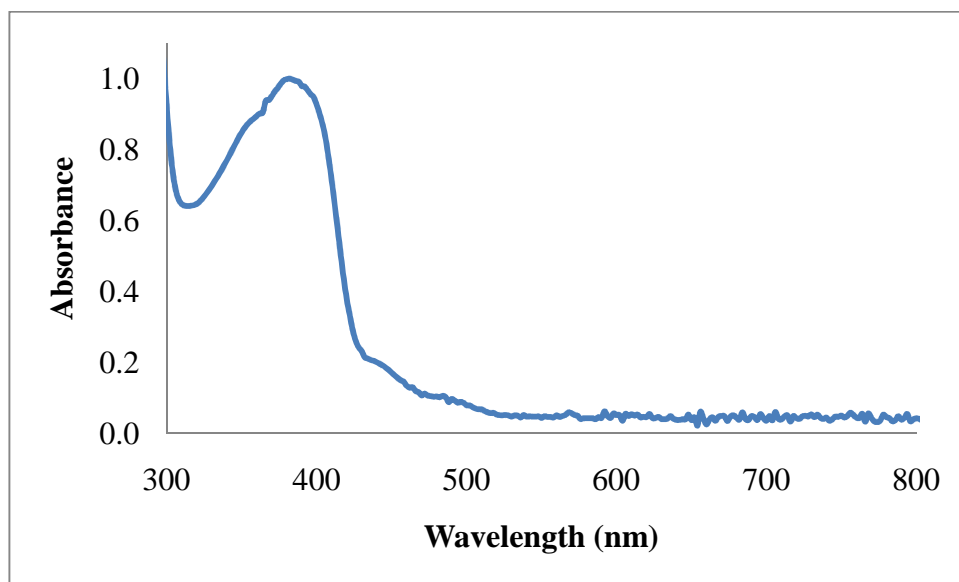
Figure 13   *UV-vis spectra of **pyridine-W(CO)₅** recorded in CH₂Cl₂.*

Figure 14 displays the UV-vis spectra of **MPyTPP** and **ZnMPyTPP**. The absorbance spectra have been reported previously.[19] The UV-vis spectrum of the uncomplexed freebase porphyrin, **MPyTPP**, is similar to that of **H₂TPP**. It displayed a Soret λ_{max} at 418 with four Q bands in the range 514 – 644 nm (Table 3). The UV-vis spectrum of **ZnMPyTPP** is akin to that of **ZnTPP** with a Soret λ_{max} observed at 418 nm and two Q bands at 562 and 604 nm (Table 3). Pyridine is known to coordinate to the metal centre of a metalloporphyrin. In this case the N atom of the pyridine unit coordinates to the Zn atom of another porphyrin, leading to formation of a polymer.[19]
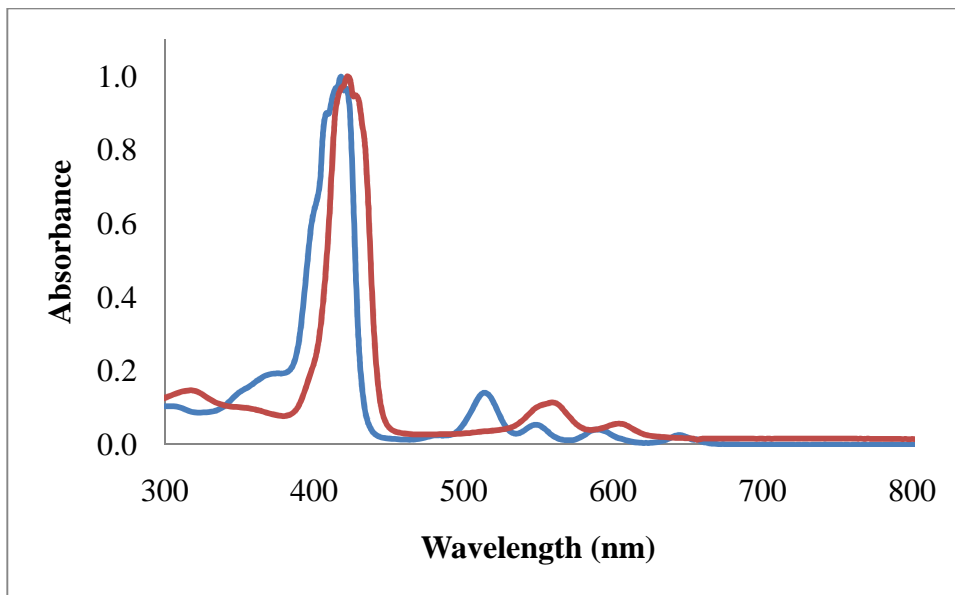
Figure 14   *UV-vis spectra of **MPyTPP** (blue line) and **ZnMPyTPP** polymer (red line) recorded in CH_2Cl_2. Spectra have been normalised at their $\lambda_{max.}$*

Following complexation of the monopyridyltriphenyl porphyrins with $W(CO)_5$ and $Cr(CO)_5$, the UV-vis spectra were still dominated by porphyrin transitions with only a slight shift in band position observed (Fig. 15). No tungsten or chromium based absorbances were detected for the porphyrin-$W(CO)_5$ and porphyrin-$Cr(CO)_5$ complexes. The electronic absorbance spectral features of the porphyrins synthesised in this study are listed in table 3.

The freebase pyridyl porphyrins complexed with metal pentacarbonyls, **MPyTPP-W(CO)₅** and **MPyTPP-Cr(CO)₅**, possessed an intense Soret band and four Q bands, the Soret band red shifted by 2 and 4 nm respectively with a 2 nm red shift observed in all Q bands. No pyridine-$M(CO)_5$ transitions are observed in the porphyrin metal pentacarbonyl complexes. However these transitions may be masked by the intensity of the porphyrin Soret band ($\varepsilon = 40,000 - 80,000$ M^{-1} cm^{-1}) compared to that of pyridine-$M(CO)_5$ ($\varepsilon = \sim 7,000$ M^{-1} cm^{-1}). The small but consistent bathochromic shift of the Soret and Q bands indicates a weak electronic interaction between the metal centre and the porphyrin macrocycle.[20]

Complexation of the zinc porphyrin with the metal pentacarbonyl moiety produced electronic absorbance spectra that were similar to that of the uncomplexed zinc porphyrins. However substantial blue shifts were observed in the Q band region of 14 – 16 nm (Table 3). The reason for this large shift in the Q bands (compared to the 2 nm red shift observed with freebase analogues) is that the environment of the *meso* pyridyl group was changed more dramatically. The N-Zn bond is intrinsically weak and a complexing ligand such as M(CO)$_5$ breaks the bond. The pyridine ligand of the metalloporphyrin was no longer coordinated to the zinc atom of an adjacent macrocycle but coordinated to the metal pentacarbonyl fragment. Again, the UV-vis spectra are dominated by porphyrin transitions and no pyridyl tungsten or pyridyl chromium based absorbances were detected in the porphyrin complexes. As the extinction coefficients of the porphyrin are higher than that of the free pyridine metal pentacarbonyl, it was expected that the tungsten (or chromium) based absorbance would be masked.
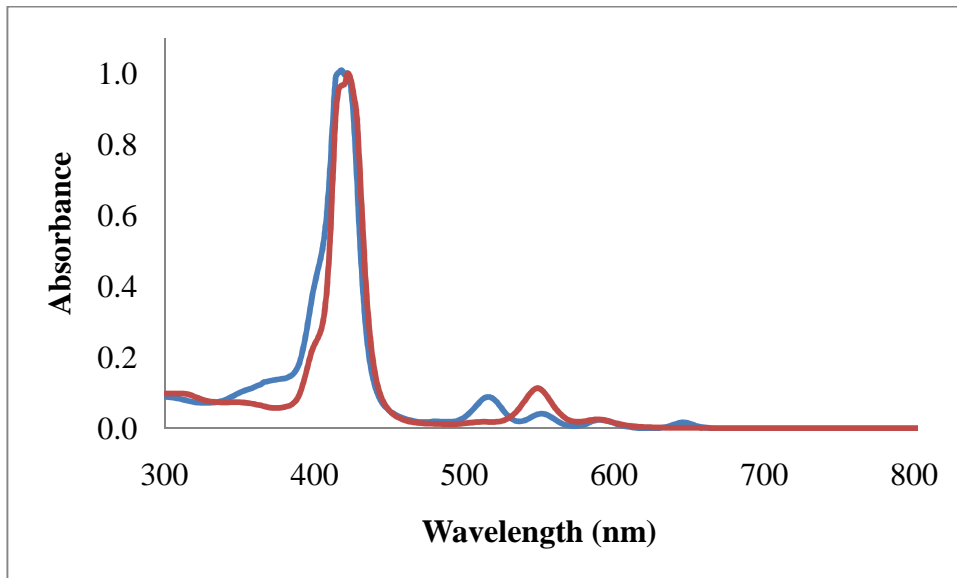
Figure 15   *UV-vis spectra of **MPyTPP-Cr(CO)$_5$** (blue line) and **ZnMPyTPP-Cr(CO)$_5$** (red line) recorded in CH$_2$Cl$_2$. Spectra have been normalised at their λ$_{max}$*

Porphyrin	Soret λ_{max} (nm)	Q bands (nm)
MPyTPP	418	514, 548, 588, 644
ZnMPyTPP polymer	418	562, 604
MPyTPP-W(CO)$_5$	422	516, 552, 590, 646
ZnMPyTPP-W(CO)$_5$	420	548, 588
MPyTPP-Cr(CO)$_5$	420	516, 552, 590, 646
ZnMPyTPP-Cr(CO)5	422	548, 588

Table 3   *Absorbance maxima of freebase and zinc(II) porphyrins and metal pentacarbonyl complexes.*

4.4.2 IR studies

The ground state IR spectrum of **pyridine-W(CO)₅** was reported previously[18] and displays three IR active ν(CO) vibrations at 2073, 1935 and 1921 cm⁻¹ (Fig. 16). **Pyridine-W(CO)₅** possesses a C_{4v} local symmetry and as such displays three IR-active ν(CO) vibrations which correspond to $2A_1$ and E stretching vibrations.[18] The infrared spectrum was dominated by the strong E band. The weak A_1^2 band, attributed to in-phase stretching vibrations of the four *cis* CO ligands, occurred at higher frequency. The A_1^1 ν(CO) vibration, involving mainly the *trans* CO ligand, was displayed on the lower energy side of the E band.
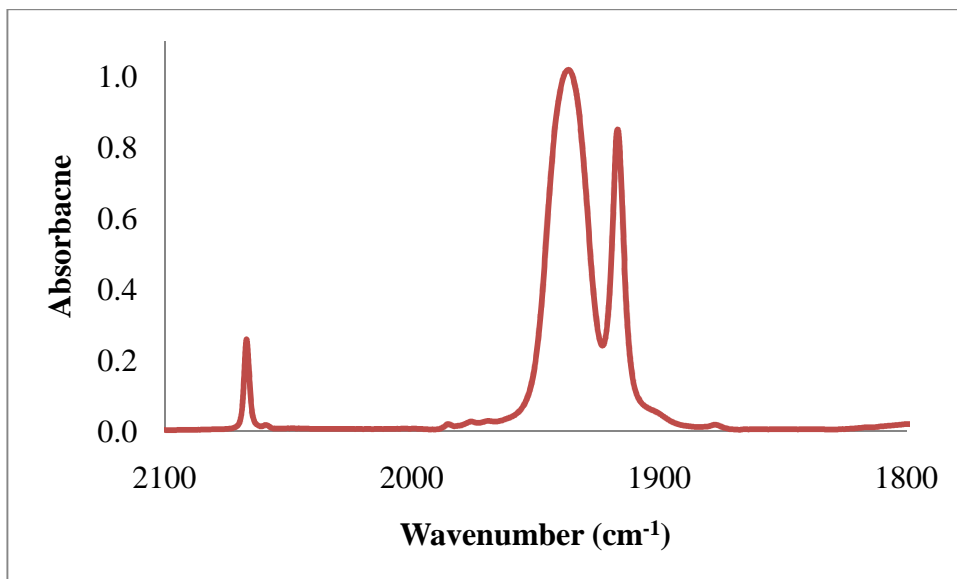
Figure 16   *IR spectrum of **pyridine-W(CO)₅** recorded in CH₂Cl₂.*

Complexation of tungsten pentacarbonyl and chromium pentacarbonyl with the pyridyl porphyrins resulted in IR spectra with three similar IR vibrations. The IR spectra of the freebase and zinc(II) pyridyl porphyrin chromium pentacarbonyl complexes is shown in figure 17.
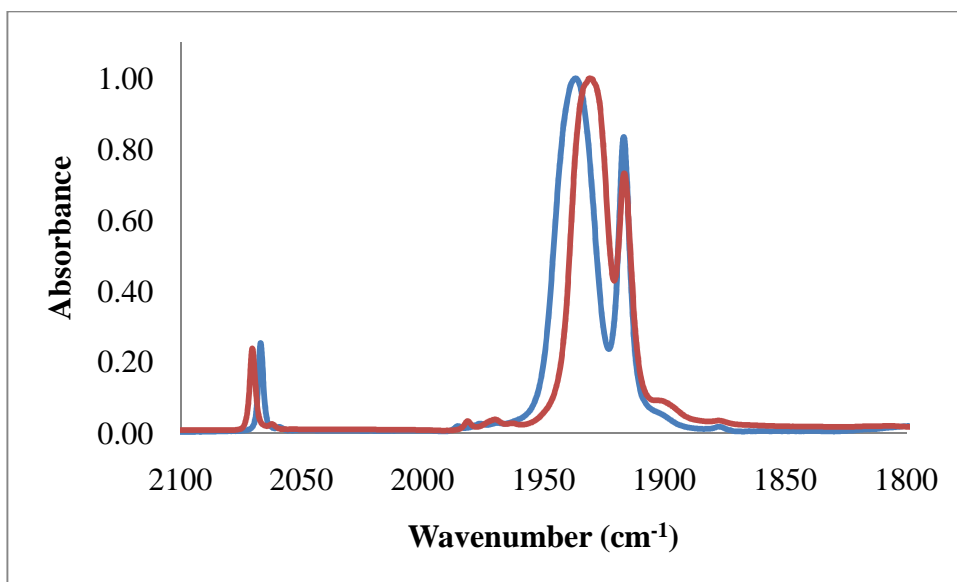
Figure 17   IR spectra of **ZnMPyTPP-Cr(CO)₅** *(blue line) and* **ZnMPyTPP-W(CO)₅** *(red line) recorded in CH₂Cl₂. IR bands have been normalised at their maxima.*

The IR spectroscopic data (metal carbonyl region) for the freebase and zinc monopyridyltriphenyl porphyrin $M(CO)_5$ complexes are presented in Table 4. The ground state infrared spectra displayed three bands in the range 2072 - 1895 cm^{-1}. This was consistent with the local C_{4v} symmetry of the pentacarbonyl moiety.[21] As observed for **pyridine-W(CO)₅**, the largest stretching vibration was the E band, a weak A_1^2 band attributed to predominantly in-phase stretching vibrations of the four *cis* carbonyl ligands was at higher frequencies. The A_1^1 ν(CO) vibration, involving mainly the *trans* CO ligand, was manifested on the low-energy side of the E band.[22] According to Kolodziej et al.[23] the spectral data in figure 17 confirms that the metal atom is bound to the nitrogen atom in the porphyrin complex. No evidence of the disubstituted tetracarbonyl complex due to co-ordination of two porphyrin moieties to the metal was observed. Variation of the solvent from THF to dichloromethane to acetonitrile had little effect on the carbonyl stretching frequencies (less than 2 cm^{-1}).

Complex	$\nu(CO)$ (cm^{-1})
Pyridine-W(CO)₅	2073, 1935, 1921
MPyTPP-W(CO)₅	2070, 1928, 1896
ZnMPyTPP-W(CO)₅	2071, 1930, 1894
MPyTPP-Cr(CO)₅	2068, 1935, 1898
ZnMPyTPP-Cr(CO)₅	2069, 1936, 1895

Table 4   *Carbonyl stretching frequencies of pyridine and porphyrin metal pentacarbonyl complexes.*

4.4.3 Picosecond time resolved infrared studies

A ps-TRIR investigation of **pyridine-W(CO)$_5$**, and monopyridyltriphenyl porphyrin metal pentacarbonyls (M = W or Cr) was performed. All of the TRIR studies reported herein were conducted in THF solution. Excitation was achieved using ~ 150 fs pulses of 400 and 532 nm radiation, and the resulting spectral changes were measured with picosecond time resolution in the 1800 – 2100 cm^{-1} region.

The TRIR spectrum of **pyridine-W(CO)$_5$** in THF was obtained following 400 nm excitation (Fig. 18). Within 1 ps of the excitation pulse the ν(CO) bands of the parent complex at 2069, 1937 and 1924 cm^{-1} were depleted (negative bands in the difference spectra) and new features were formed at 2074, 1960, 1928 and 1887 cm^{-1}. Over the subsequent 100 ps these IR stretching vibrations decayed with the appearance of new bands at 2074, 1937 and 1887 cm^{-1}, which remained on the nanosecond timescale. Reliable decay kinetics could not be obtained as the bleaches and transients overlapped each other.
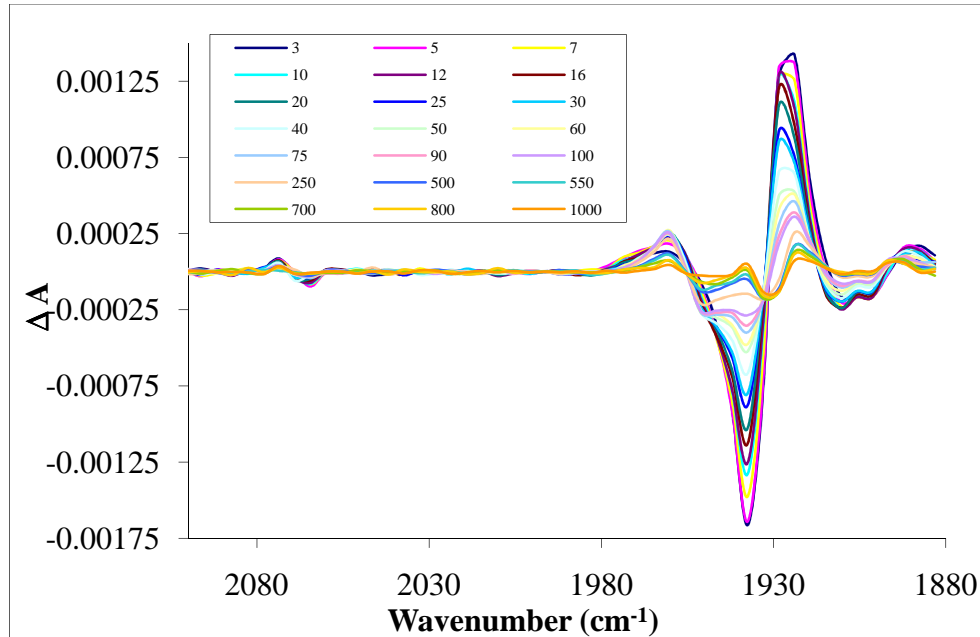
*Figure 18   TRIR difference spectra in the delay range 3 – 1000 ps following excitation of **pyridine-W(CO)$_5$** in THF following 400 nm excitation.*

309

The TRIR spectra of **MPyTPP-W(CO)₅** in THF was obtained following 400 nm excitation (Fig. 19). The spectral features were quite different to those previously observed for **pyridine-W(CO)₅**. Depletion of the parent bands at 2070, 1931 and 1989 cm^{-1} occurred within the laser pulse. Simultaneously, three new bands were produced at 1912 and 1944 with a third band in the region 2075 - 2065 cm^{-1}. As the latter band overlapped with the bleach of the parent material (2070 cm^{-1}) the position of the band could not be accurately determined. Over the subsequent 100 ps these bands decayed with almost complete regeneration of the parent species. Very weak bands were present at 2070, 1935 and 1894 cm^{-1} in the spectrum recorded at 1 ns.
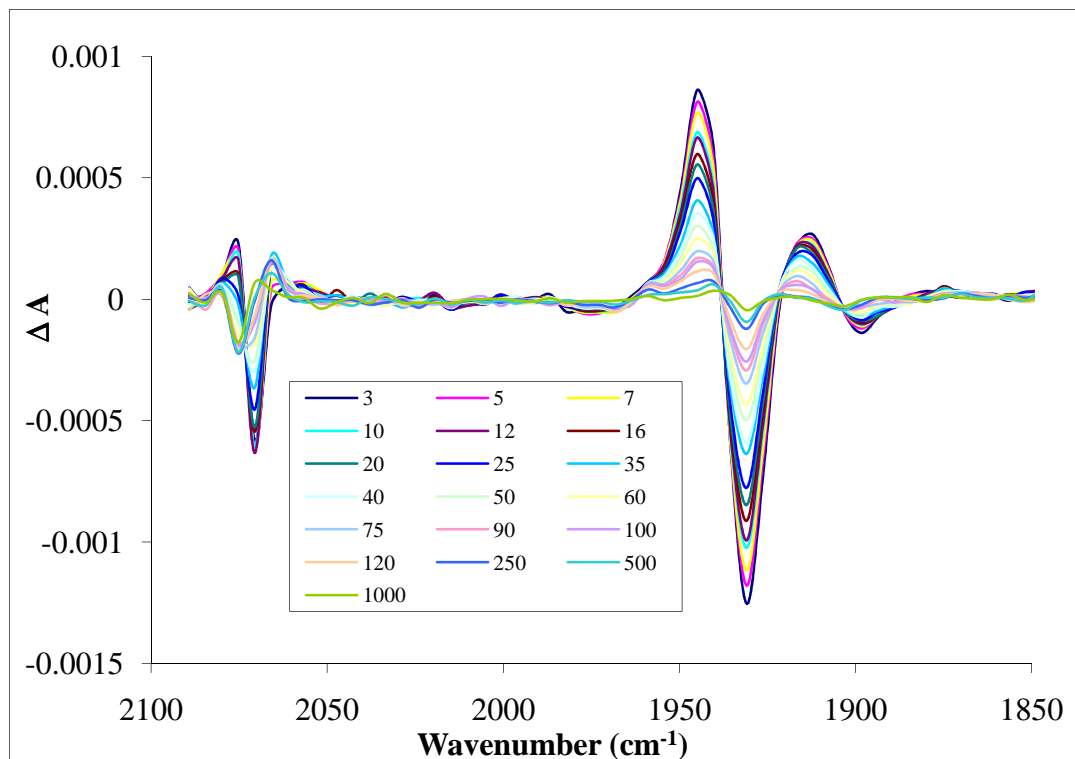
Figure 19   *TRIR difference spectra in the delay range 3 – 1000 ps following excitation of **MPyTPP-W(CO)₅** in THF following 400 nm excitation.*

The TRIR spectra of **ZnMPyTPP-W(CO)$_5$** in THF were obtained following excitation at 400 nm (Fig. 20). Metallation of the porphyrin macrocycle with zinc appeared to have little effect on the processes observed in the ν(CO) spectral range. Depletion of the parent carbonyl bands at 2071, 1930 and 1898 cm^{-1} occurred within the laser pulse (1 ps) with concomitant generation of positive metal carbonyl bands at 1912 and 1944 cm^{-1} with a third band in the range 2065 – 2075 cm^{-1}. The third band overlapped with the parent bleach and was at the edge of the observation window thus a reliable position for the band could not be obtained. These bands decayed over approximately 100 ps. Weak bands were observed in the 1 ns spectrum at 2071, 1940 and 1984 cm^{-1} which indicated that a minor photoproduct was formed, *albeit* in very small quantities.
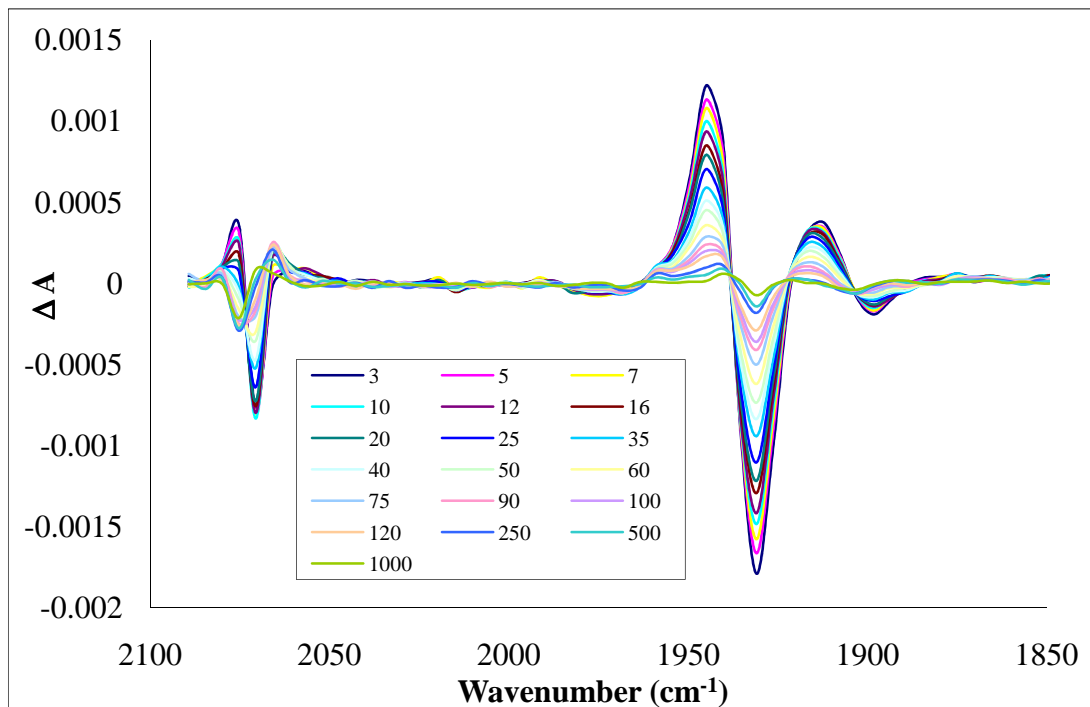
Figure 20   *TRIR difference spectra in the delay range 3 – 1000 ps following excitation of **ZnMPyTPP-W(CO)$_5$** in THF following 400 nm excitation.*

The TRIR spectrum of **MPyTPP-Cr(CO)$_5$** in THF was obtained following excitation at 400 nm (Fig. 21). The excited state spectral profile acquired was similar to that of the tungsten system. Bleaching of the parent bands at 2069, 1934 and 1901 cm^{-1} was observed within the laser pulse with product bands simultaneously generated at 1915, 1952 cm^{-1} and a third in the region of the parent bleach 2064 – 2073 cm^{-1}. Decay of the transient species occurred over approximately 100 ps. However, the chromium system was not as reversible as the tungsten analogues and product bands were evident at 1968 and 1838 cm^{-1} in the final spectrum (1 ns) with a further IR band possibly where the parent bleach occurs at 2069 cm^{-1}. (Note: the negative band at 2012 cm^{-1} and corresponding positive band at 2017 cm^{-1} were artefacts in the system as they were present in negative time delays.)
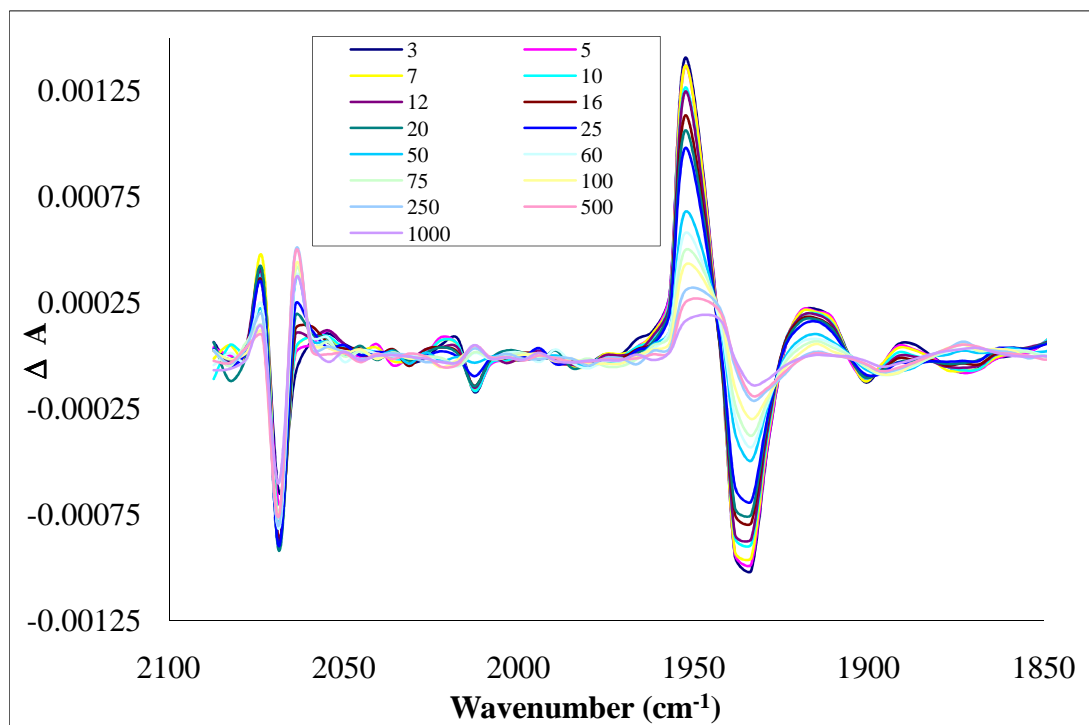

*Figure 21   TRIR difference spectra in the delay range 3 – 1000 ps following excitation of **MPyTPP-Cr(CO)$_5$** in THF following 400 nm excitation.*

The TRIR spectrum of **ZnMPyTPP-Cr(CO)$_5$** in THF was obtained by excitation at 400 nm (Fig. 22). As observed previously for the tungsten analogues, metallation of the porphyrin macrocycle with zinc caused little change in the ν(CO) spectroscopic region of the chromium pentacarbonyl complex. The TRIR spectra was characterised by negative bleaching of the ground state carbonyl stretches at 2066, 1935 and 1901 cm^{-1}, observed in the first delay taken after the laser pulse (1 ps). Positive bands were generated concomitantly at 1954 and 1916 cm^{-1} and again the higher frequency band overlapped with the parent bleach in the region 2066 – 2076 cm^{-1}. The transient species decayed over approximately 100 ps with apparent recovery of the parent bleaches. However the system was not fully reversible and permanent product bands remained in the final spectrum (1 ns) at 1952, 1915 and 1873 cm^{-1}. (Note: the negative band at 2012 cm^{-1} and corresponding positive band at 2017 cm^{-1} were artefacts in the system as they were present in negative time delays.)
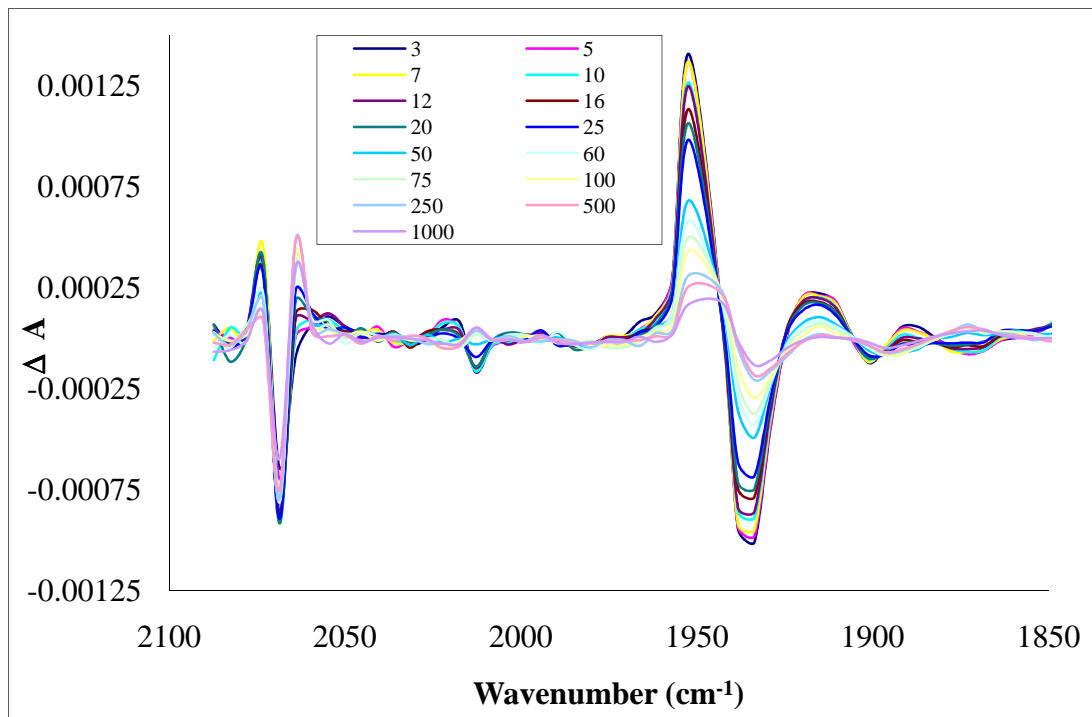
*Figure 22   TRIR difference spectra in the delay range 3 – 1000 ps following excitation of **ZnMPyTPP-Cr(CO)$_5$** in THF following 400 nm excitation.*

The TRIR spectrum of **MPyTPP-Cr(CO)$_5$** in THF was obtained following excitation at 532 nm (Fig. 23). The spectral features were quite different to those previously observed following excitation at 400 nm. Depletion of the parent bands at 2064, 1935 and 1890 cm^{-1} was observed within the laser pulse (1 ps) with product bands simultaneously generated at 1952, 1917 and 1895 cm^{-1}. Over the subsequent 30 ps these IR bands decayed with the appearance of new IR bands at 1943, 1903 and 1890 cm^{-1} which remained on the nanosecond timescale. (Note: The high frequency band at 2064 cm^{-1} was excluded from the spectrum as it was at the very edge of the observation window and reliable information could not be obtained.)
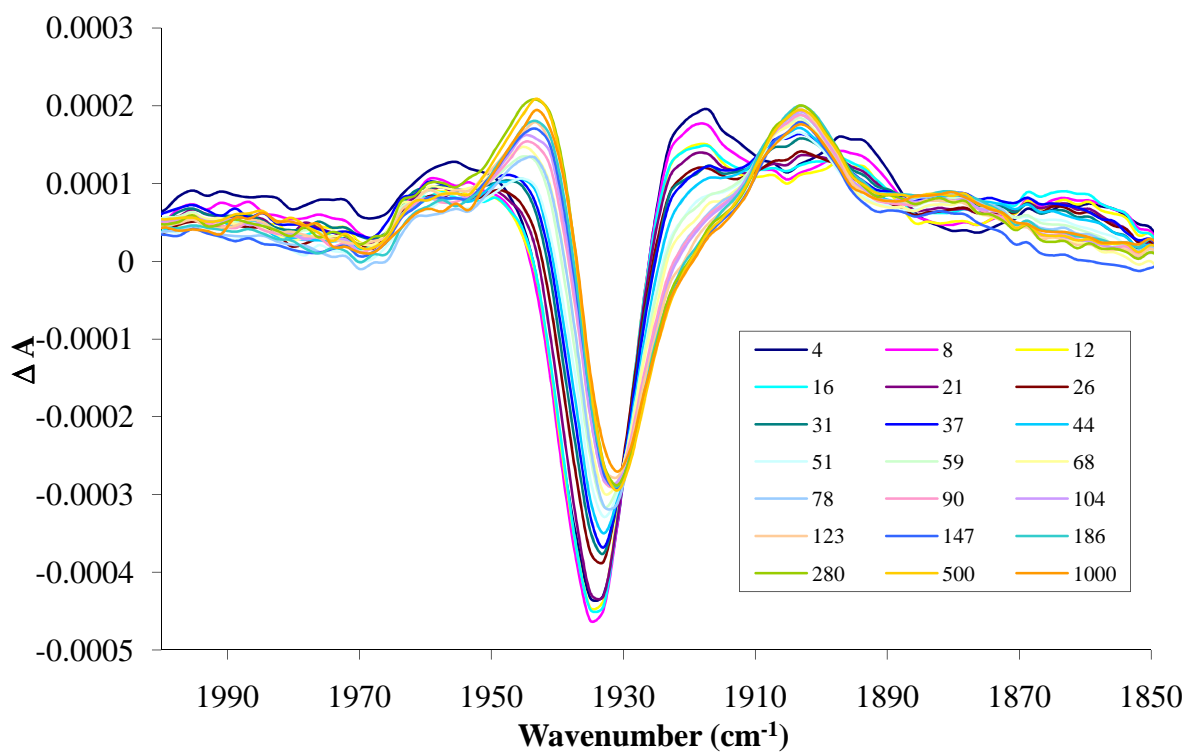
Figure 23   *TRIR difference spectra in the delay range 3 – 1000 ps following excitation of **MPyTPP-Cr(CO)$_5$** in THF following 532 nm excitation.*

4.5   Discussion

4.5.1   Picosecond time resolved infrared studies

Transient visible absorbance spectroscopy is very well suited to study the porphyrin moiety of the complexes due to the strong excited state absorbance. However the complexes in this study benefit from the inclusion of metal carbonyls which provide a spectroscopic handle in the infrared through CO-stretching frequencies. Accordingly, picosecond time resolved infrared spectroscopy is an ideal tool for probing excited states.

The photochemistry of $M(CO)_6$ (M = Cr, W or Mo) has been extensively studied and their photochemistry is well documented. Transient visible absorbance studies have shown that CO loss occurs in less than 300 fs and that a solvent molecule occupies the vacant CO position in less than 2 ps.[24] Transient IR experiments probing the CO-stretching region of $W(CO)_6$ showed a bleach at 1983 cm^{-1} following irradiation which corresponded to the depletion of the ground state species and generation of new bands at 1956 and 1928 cm^{-1} assigned to the photoproduct, $W(CO)_5$(*n*-hexane).[25] Previous experiments have shown that after CO loss from $M(CO)_6$ (M = Cr, W or Mo) the stable photoproduct is not the bare $M(CO)_5$ molecule but a hexa-coordinate species of the form $M(CO)_5$(solvent), where a solvent molecule is weakly bound at the sixth ligand and forms rapidly even in relatively inert solvents.[26]

4.5.1.1 Pyridine-W(CO)$_5$

Time resolved infrared studies on picosecond timescale for **pyridine-W(CO)$_5$** in THF revealed very interesting excited state dynamics. Depletion of the ground state metal carbonyl stretches together with the generation of new IR bands occurred within the laser pulse (initial spectrum taken after 1 ps time delay). The negative IR bands in figure 18 were attributed to cleavage of the pyridyl nitrogen – tungsten bond. Cleavage of the N – W bond has been observed previously and reported to occur on a femtosecond timescale.[25] To provide assignments for the new IR features observed it is necessary to consider all possible outcomes of the initial solvation. THF has two effective binding arrangements: a σ bond to one of the H atoms or a η^1 coordination to oxygen. Previous studies have shown that a coordinated alkyl group can be best described as a "token ligand" that interacts weakly with the metal centre.[27] If a stronger interaction is possible, then rearrangement to the thermodynamically favoured product will occur. In these studies the bands observed at 2074, 1960, 1928 and 1887 cm^{-1} correspond to an intermediate formed by a H bond between the tungsten and the THF as shown in scheme 1. This species then rearranges in less than 100 ps to form the more stable (CO)$_5$W-η^1(O)-THF photoproduct, with IR stretching vibrations at 2074, 1937 and 1887 cm^{-1}.

Migration of solvated metal pentacarbonyl species (Cr(CO)$_5$) on solvent molecules is detailed in the literature for solvents other than THF.[28] For instance, in pentanol, where both hydroxyl and alkyl groups were available for coordination to the site vacated by the photoeliminated carbonyl ligand, migration was observed from the alkyl to hydroxyl end of the solvent. The most thermodynamically stable complex involved coordination of the hydroxyl end of the solvent molecule to the metal carbonyl. If the initial solvation produced intermediates where the alkyl group was coordinated to the metal, rearrangement or exchange with solvent molecules occurred to form the most stable complex.

The rearrangement observed here is analogous to that previously reported for group 6 metal carbonyls in 1-hexanol and 1-hexyne.[27] In the case of 1-hexanol, rearrangement occurred until the metal fragment coordinated to the hydroxyl group of the alcohol (from initially the alkyne end). For Cr(CO)$_6$ in 1-hexanol the rearrangement from alkyl to

hydroxyl was 1.2 ns. In the case of 1-hexyne, rearrangement from the alkyl end to a η^2 interaction with the alkyne occurred in less than 70 ps. The differences observed for $Cr(CO)_5$ in moving from 1-hexanol to 1-hexyne was attributed to viscosity differences in these two solvents. 1-Hexanol exhibits a viscosity of 6.00 cP, while 1-hexyne has a much lower viscosity of 0.34 cP.[29] A more viscous solvent will result in a large rearrangement time since the local solvent motions are smaller.

In the case of the ps-TRIR studies presented here, the rearrangement from the alkyl to oxygen bonded metal centre occurred over a slightly longer timescale of 100 ps. This is not surprising since the viscosity of THF is 0.46 cP.[29] The applicability of bulk solvent viscosity in such type of rearrangements is not without precedence. Thus the changes observed in the TRIR spectra of **pyridine-W(CO)$_5$** are assigned to cleavage of the nitrogen tungsten bond, followed by formation of a weak σ bond from the metal to a H of THF. This species then rearranges in less than 100 ps to form $(CO)_5W-\eta^1(O)$-THF. Evidence for the latter species was observed on the nanosecond timescale, and the bands observed at 2074, 1937 and 1887 cm^{-1} compare well to those reported for $(CO)_5W-\eta^1(O)$-THF.
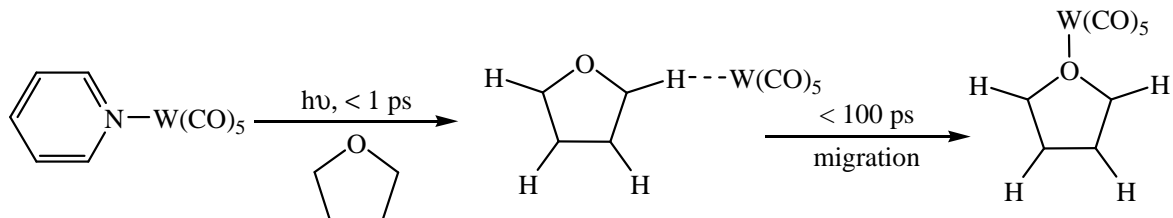
*Scheme 1   Photoreaction following excitation at 400 nm of **pyridine-W(CO)$_5$** in THF.*

4.5.1.2 Monopyridyltriphenylporphyrin-W(CO)$_5$ complexes

The photochemistry of **MPyTPP-W(CO)$_5$** was quite different from that of **pyridine-W(CO)$_5$**. Depletion of the parent bands occurred within the laser pulse together with the generation of positive bands (Table 5). The negative bands in the TRIR spectra are due to a depletion of the ground state while the positive bands are assigned to an excited state species. This excited state species decays in less than 100 ps, with almost complete regeneration of the parent complex. Weak bands were evident at ~2071, 1935 and 1984 cm^{-1} in the spectrum recorded after 1 ns. These bands compare well with those for W(CO)$_5$(THF), and are therefore attributed to minor quantities of this photoproduct.

Photolysis of the zinc porphyrin, **ZnMPyTPP-W(CO)$_5$**, resulted in excited state dynamics that were similar to that described for the freebase analogue. Depletion of the parent IR bands together with the generation of new bands occurred within the laser pulse (1 ps) (Table 5). The new bands are assigned to an excited state transient species that decays in less than 100 ps. Minor bands were observed at 1940 and 1984 cm^{-1} are attributed to W(CO)$_5$(THF), *albeit*, in small quantities.

Complex	v(CO) (cm^{-1})
MPyTPP-W(CO)$_5$	~2070, 1931, 1898
MPyTPP-W(CO)$_5$* initial	~ 2075, 1944, 1912
MPyTPP-W(CO)$_5$ final	~2070, 1935, 1894
ZnMPyTPP-W(CO)$_5$	~2071, 1930, 1898
ZnMPyTPP-W(CO)$_5$* initial	~2075, 1944, 1912
ZnMPyTPP-W(CO)$_5$ final	~2073, 1940, 1984
W(CO)$_5$(THF)	2075, 1930, 1890

Table 5   Frequencies (cm^{-1}) in the v(CO) region of species involved in photochemistry of porphyrin pyridyl tungsten pentacarbonyl.

The transient species generated for both the freebase and zinc pyridyl porphyrin tungsten pentacarbonyl were attributed to a porphyrin excited state which was formed on a picosecond timescale. Relaxation of the porphyrin excited state results in regeneration of most of the parent complex, as observed by recovery of the parent bleaches and decay of the transient species, indicating that the pyridyl porphyrin tungsten pentacarbonyl system underwent a process that was almost fully reversible. However, minor amounts of cleavage of the nitrogen – tungsten bond occurred as was evidenced by the small residual peaks at $\sim$ 2070, 1935 and 1894 cm^{-1} due to the formation of $W(CO)_5(THF)$.

Cleavage of the N-W bond is not very efficient following excitation at 400 nm, for the monopyridyltriphenyl porphyrin $W(CO)_5$ complexes studied which contrasts with quantum yields reported for pyridine-$W(CO)_5$. Wrighton et al. studied the photosubstitution reactivity of a series of substituted pyridine tungsten pentacarbonyl complexes.[18a] Photosubstitution of both the pyridine and CO were observed, but the dominant reaction is efficient dissociation of the pyridine moiety following irradiation is into its lowest LF absorbance band Quantum yields in the range 0.62 – 0.82 have been reported for various pyridine-$W(CO)_5$ complexes following 436 nm excitation.[18]

4.5.1.3   Monopyridyltriphenylporphyrin-Cr(CO)$_5$ complexes

The CO-stretch frequencies of the pyridyl porphyrin chromium pentacarbonyl complexes and transient species generated following photolysis (Table 6) were slightly shifted to higher energy when compared to those observed for the tungsten species which is consistent with previously observed systems.[25]   Both the freebase and zinc analogues, **MPyTPP-Cr(CO)$_5$** and **ZnMPyTPP-Cr(CO)$_5$,** underwent a similar process to the tungsten porphyrins following 400 nm excitation.   Excitation of the freebase derivative **MPyTPP-Cr(CO)$_5$** resulted in bleaching of the parent bands with generation of an excited state transient species within the laser pulse.   These IR bands decayed over approximately 100 ps, to regenerate the parent complex.   The chromium system does not appear to be as photoreversible as the tungsten systems, as it is obvious from the final spectrum (1 ns) that the parent bands do not recover.   Also the intensity of the bands assigned to Cr(CO)$_5$THF at ~2071, 1938 and 1968 cm^{-1}, present in the final spectrum recorded after 1 ns are greater than those observed for the tungsten analogues.   A higher quantum yield for photoprocesses involving chromium carbonyl systems is not without precedence in the literature.[30]   A comparable sequence of events was observed for **ZnMPyTPP-Cr(CO)$_5$** following 400 nm excitation.

Complex	v(CO) (cm^{-1})
MPyTPP-Cr(CO)$_5$	2069, 1934, 1901
MPyTPP-Cr(CO)$_5$* initial	~2072, 1952, 1915
MPyTPP-Cr(CO)$_5$ final	~2072, 1938, 1968
ZnMPyTPP-Cr(CO)$_5$	~2066, 1935, 1901
ZnMPyTPP-Cr(CO)$_5$* initial	~2074, 1954, 1916
ZnMPyTPP-Cr(CO)$_5$ final	~2072, 1949, 1873
Cr(CO)$_5$(THF)	2071, 1938, 1895

Table 6   Frequencies (cm^{-1}) in the v(CO) region of species involved in photochemistry of porphyrin pyridyl tungsten pentacarbonyl.

In addition to studies at 400 nm, the freebase pyridyl porphyrin chromium pentacarbonyl was also studied at 532 nm. The spectral characteristics following 532 nm excitation were significantly different to those observed following 400 nm excitation. They were in fact similar to the spectral characteristics observed for **pyridine-W(CO)$_5$** as opposed to the porphyrin metal pentacarbonyl systems. Following excitation of **MPyTPP-Cr(CO)$_5$** at 532 nm, depletion of the ground state metal carbonyl stretch occurred within the laser pulse (1 ps) together with the generation of positive transient bands. These bands decay in 30 ps with the generation of positive bands that remained on a nanosecond timescale. In this study, the parent band does not recover indicating efficient photocleavage of the pyridyl nitrogen – chromium bond occurred. The initial bands observed correspond to the intermediate formed by a H bond between the chromium pentacarbonyl and the solvent, THF. This species rearranges to form the more stable $(CO)_5Cr-\eta^1(O)THF$ photoproduct, with new IR stretching bands growing in after 30 ps. However due to overlap of the parent bleach and stretching vibrations of the photoproduct accurate band positions for the $(CO)_5Cr-\eta^1(O)THF$ photoproduct is difficult to determine. Excitation at 532 nm, where absorbance by the porphyrin moiety occurs preferentially, caused efficient photocleavage of the nitrogen – chromium bond and thus photoejection of the chromium pentacarbonyl species within 1 ps. Therefore communication between the porphyrin moiety and the metal centre must be very efficient at 532 nm.

However it is unexpected that photophysical process would be different following 400 nm excitation compared to 532 nm excitation. This is because excitation at $\lambda_{exc} = 400$ nm populates the S$_2$ state of the porphyrin, which would be expected to lead to efficient population of the S$_1$ state *via* rapid internal conversion. Since the S$_1$ state is populated directly by 532 nm excitation similar behaviour would be expected at both excitation wavelengths.

For the uncomplexed freebase porphyrin, **MPyTPP**, excitation at λ_{exc} = 532 nm resulted in formation of the S_1 singlet excited state with a lifetime of 10 ns followed by population of the triplet excited state *via* intersystem crossing. The triplet lifetime was measured to be 30 μs. A representation of the processes is shown below (Fig. 24).
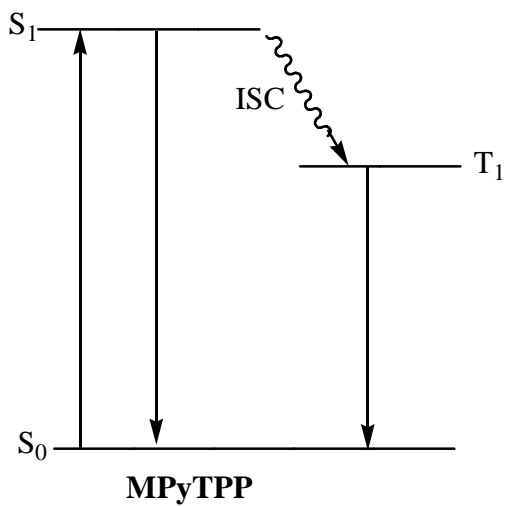
MPyTPP

Figure 24   *Energy level diagram depicting the photoprocesses in **MPyTPP** following 532 nm excitation.*

Excitation of **MPyTPP-M(CO)$_5$** (M = W or Cr) at λ_{exc} = 400 nm (Soret band) results in population of the S$_2$ state of the porphyrin (Fig. 25). Rapid internal conversion leads to population of the S$_1$ excited state. Intersystem crossing then occurs leading to the triplet excited state followed by relaxation to the ground state. Cleavage of the pyridyl N – M bond (M = W or Cr) does not occur.
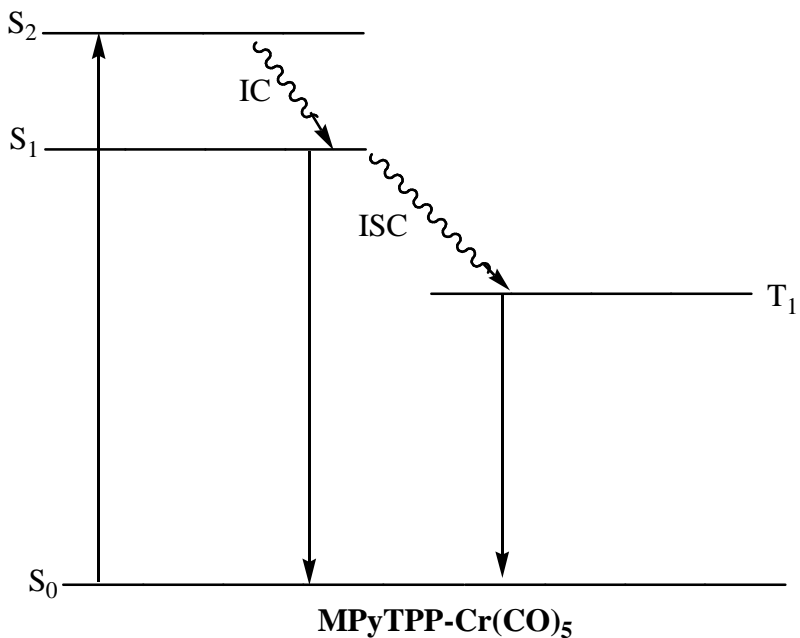
Figure 25 *Energy level diagram depicting the photoprocesses in **MPyTPP-M(CO)$_5$** M = (W or Cr) following 400 nm excitation.*

Excitation of **MPyTPP-Cr(CO)$_5$** at λ_{exc} = 532 nm (Q band region) results in formation of the first singlet excited state, the lifetime of which was reported as 6 ns, shorter than that of the uncomplexed porphyrin, **MPyTPP**. Efficient cleavage of the pyridyl nitrogen - chromium bond takes place on a picosecond timescale leading to formation of $Cr(CO)_5(THF)$ which rearranges in the solvent to the most thermodynamically stable form over 30 ps. The uncomplexed porphyrin in its triplet state, was previously observed following cleavage and possessed a lifetime of 27 μs (Fig. 26).
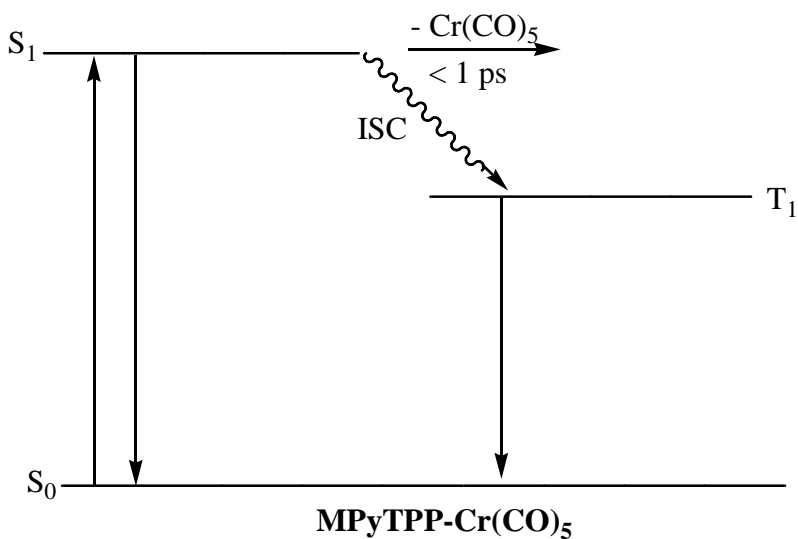
Figure 26   *Energy level diagram depicting the photoprocesses in* **MPyTPP-Cr(CO)$_5$** *following 532 nm excitation.*

Clearly another process occurs following 400 nm excitation that can explain the discrepancy observed in the TRIR data and discussed above. Further investigative work on these systems is therefore required.

A plausible schematic representation of the observed photochemistry is depicted below. Excitation at λ_{exc} = 532 nm, causes population of the singlet state of **MPyTPP-Cr(CO)$_5$**. Loss of the M(CO)$_5$ moiety occurs from this excited state in less than 1 ps. Subsequent intersystem crossing leads to population of the excited triplet state of the uncomplexed porphyrin where relaxation to the ground state occurs. The M(CO)$_5$ moiety is efficiently scavenged by the solvent and forms the Cr(CO)$_5$(THF) adduct.
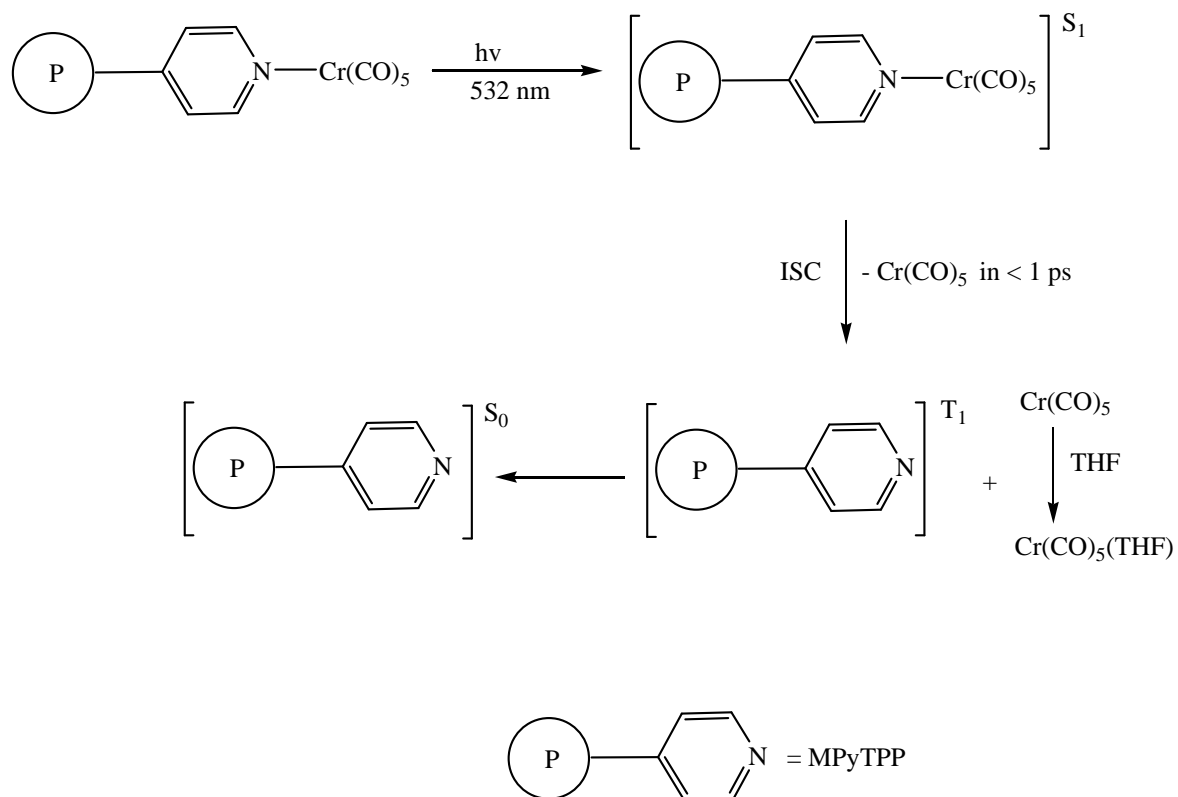
Scheme 2   Plausible schematic diagram of photoprocesses occurring following 532 nm excitation.

4.6 Conclusion

Picosecond TRIR studies were carried out on **pyridine-W(CO)$_5$** and a range of pyridyl porphyrin metal pentacarbonyl complexes in THF, which allowed for the identification of intermediate species following photolysis. Excitation of **pyridine-W(CO)$_5$** at 400 nm resulted in photodissociation of the metal pentacarbonyl moiety with subsequent coordination to a solvent molecule within 1 ps. Over 100 ps, rearrangement of the initially formed σ H bond between the tungsten pentacarbonyl and THF to the more stable (CO)$_5$Cr-η^1(O)THF photoproduct occurred. This is the first report detailing the rearrangement of metal pentacarbonyl species in THF solution.

Excitation of all porphyrin complexes at 400 nm resulted in formation of a porphyrin based excited state that decayed in less than 100 ps to regenerate the parent porphyrin complexes. As TRIR only provides information about the carbonyl moiety, little information can be garnered from this. There is a radial redistribution of electron density in the porphyrin macrocycle which results in less electron density on the metal (M = W or Cr). This results in less backbonding on the carbonyl ligands thus the observed IR bands of the transient species were at higher energy. For both tungsten and chromium analogues evidence for both (THF)Cr(CO)$_5$ and (THF)W(CO)$_5$, were present in the final spectra (1 ns), although the IR bands were weak.

However excitation of **MPyTPP-Cr(CO)$_5$** at 532 nm resulted in photodissociation of the metal pentacarbonyl moiety, with subsequent coordination to a solvent molecule within 1 ps, and rearrangement of the initially formed σ H bond between the chromium pentacarbonyl and the THF to the more stable (CO)$_5$Cr-η^1(O)THF photoproduct. This is the first report detailing the rearrangement of metal pentacarbonyl species in THF solution.

4.7 Bibliography

1   (a) V. Balzani, F. Scandola, *Supramolecular Photochemistry*, **1991**, Ellis Horwood, Chichester. (b) I.I. Dilung, E.I. Kapinus, *Russian Chemical Review*, **1978**, 47, 43.

2   S.L. Darling, P.K.Y. Goh, N. Bampos, N. Feeder, M. Montalti, L. Prodi, B.F.G. Johnson, J.K.M. Sanders, *Chem. Comm.,* **1998**, 2031.

3   B.P. Sullivan, J.V. Caspar, T.J. Meyer, *Organometallics*, **1984**, 3, 1241

4   A.G. Hyslop, M. Orphanide, U. Javed, E.G. Megehee, *Inorg. Chim. Acta.*, **2003**, 355, 272.

5   K.E. Splan, M.H. Keefe, A.M. Massari, K.A. Waters, J.T. Hupp, *Inorg. Chem.* **2002**, 41, 619.

6   J.-S. Hsiao, B.P. Kreuger, R.W. Wagner, T.E. Johnson, J.K. Delaney, D.C. Mauzerall, G.R. Fleming, J.S. Lindsey, *J. Am. Chem. Soc.*, **1996**, 118, 11181

7   V.S.-Y. Lin, S.G. Dimagno, M.J. Therin, *Science*, **1994**, 264, 1105.

8   R.V. Slone, J.T. Hupp, *Inorg. Chem.*, **1997**, 36, 5422.

9   (a) M. Ghirotti, C. Chiorboli, M.T. Indelli, F. Scandola, M. Casanova, E. Iengo, E. Alessio, *Inorg. Chim. Acta.* **2007**, 60, 1121. (b) M. Casanova, E. Zangrando, E. Iengo, M.T. Indelli, F. Scandola, M. Orlandi, *Inorg. Chem.*, **2008**, 47, 10407.

10   (a) C.J. Aspley, J.R. Lindsay Smith, R.N. Perutz, *J. Chem. Soc., Dalton Trans.*, **1999**, 2269. (b) A. Gabrielsson, F. Hartl, J.R. Lindsay Smith, R.N. Perutz, *Chem. Comm.*, **2002**, 950.

11   C.J. Aspley, J.R. Lindsay Smith, R.N. Perutz, D. Pursche, *J. Chem. Soc., Dalton Trans.*, **2002**, 170.

12   A. Gabrielesson, F. Hartl, H. Zhang, J.R. Lindsay Smith, M. Towrie, A. Vlcek Jr., R.N. Perutz, *J. Am. Chem. Soc.,* **2006**, 128, 4253

13   M. Towrie, D.C. Grills, J. Dyer, J.A. Weinstein, P. Matousek, R. Barton, P.D. Bailey, N. Subramaniam, W.M. Kwok, C. Ma, D. Phillips, A.W. Parker, M.W. George, *Applied Spectroscopy*, **2003**, 57, 367.

14   K. Mc Donnell, PhD thesis, **2004**, Dublin City University, Dublin 9.

15   A.D. Adler, F.R. Longo, J.D. Finarelli, J. Goldmacher, J. Assour, L. Korsalioff, *J. Org. Chem.*, **1967**, 32, 476.

16   W. Strohmeier, *Agnew. Chem. Int. Ed.*, **1964**, 3, 730.

17   (a) A.K. Burrell, D.L.Officer, D.C.W. Reid, K.Y. Wild, *Agnew. Chem. Int. Ed.*, **1998**, 37, 114. (b) C.A. Hunter, R.K. Hyde, *Agnew. Chem. Int. Ed.*, **1996**, 35, 1936.

18   (a) M.S. Wrighton, H.B. Abrahamson, D.L. Morse, *J. Am. Chem. Soc.*, **1976**, 98, 4105. (b) C. Maralejo, C.H. Langford, D.K. Sharma, *Inorg. Chem.*, **1989**, 28, 2205.

19   K. Kalyanasundaram, *Photochemistry of Polypyridyl and Porphyrin Complexes,* Academic Press, London, **1992**, chapter 12.

20   N.M. Rowley, S.S. Kurek, J.-D. Foulon, T.A. Hamor, C.J. Jones, J.A. McCleverty, S.M. Hubig, E.J.L. McInnes, N.N. Paynes, L.J. Yellowlees, *Inorg. Chem.*, **1995**, 34, 4414.

21   P. Glyn, F.P.A. Johnson, M.W. George, A.J. Lees, J.J. Turner, *Inorg. Chem.*, **1991**, 30, 3543.

22   S. Zalis, M. Busby, T. Kotrba, P. Matousek, M. Towrie, A. Vlcek, *Inorg. Chem.*, **2004**, 43, 1723.

23   R.M. Kolodziej, A.J. Lees, *Organometallics*, **1986**, 5, 450.

24   (a) A.G. Joly, K.A. Nolan, *J. Phys. Chem.*, **1989**, 93, 2876. (b) A.G. Joly, K.A. Nolan, *Chem. Phys.*, **1991**, 152, 69.

25   T.P. Dougherty, E.J. Heilweil, *Chem. Phys. Lett.*, **1994**, 227, 19.

26   R.N. Perutz, J.J. Turner, *J. Am. Chem. Soc.*, **1975**, 97, 4791.

27   J.E. Shanoski, C.K. Payne, M.F. Kling, E.A. Glascoe, C.B. Harris, *Organometallics*, **2005**, 24, 1852.

28   (a) J.D. Simon, X. Xie, *J. Phys. Chem.*, **1986**, 90, 6751. (b) J.D. Simon, X. Xie, *J. Phys. Chem.*, **1987**, 91, 5538.

29   (a) J.A. Dean, *Lange's Handbook of Chemistry*; McGraw-Hill Inc., New York, **1999**. (b) D.S Viswanath, G, Natarajan, *Data Book of Viscosity of Liquids*; Hemisphere Pub. Corp., New York, **1989**.

30   (a) J. Nasielski, A. Colas, *Inorg. Chem.*, **1978**, 17, 237. (b) J. Nasielski, A. Colas, *J. Organomet. Chem.*, **1975**, 101, 215.

Chapter 5

**The synthesis and photophysical
properties of a series of
dipyrromethanes, a related
borondifluoride dipyrrin and
bis(dipyrrinato)zinc(II) complex.**

*Chapter five commences with a short
literature review on the synthesis and
photophysics of dipyrromethanes and
dipyrrin compounds. The synthesis of a
series of substituted thienyl
dipyrromethanes, related dipyrrin
complexes and corresponding dicobalt
complexes is presented. Preliminary
photophysical measurements are also
discussed.*

5.1   Literature Survey

5.1.1   Dipyrromethanes

Polypyrrolic compounds are of wide interest in various fields of research from porphyrin chemistry[1] to medicine.[2] Dipyrromethanes occupy a central place in these areas as they are building blocks for many of the architectures involved. Similar to porphyrins, the bi-pyrrolic molecules can bear substituents at the β or *meso* positions. In the past a great number of step wise procedures have been published detailing the synthesis of both β substituted and *meso* substituted dipyrromethanes. The first synthetic dipyrromethanes were β substituted which were produced during the late 1960's under very harsh conditions.[3] Subsequent procedures focused on *meso* substituted derivatives and involved the self-condensation of an appropriate pyrrole carbinol cation precursor under acidic conditions using Montmorillonite clay[4] or *p*-toluenesulphonic acid.[5] One-flask condensations of pyrrole and the desired aldehyde in various acidified organic solvents were also reported.[6] Workup generally involved several steps including column chromatography. Hammel et al. reported purification by flash chromatography followed by Kügelrohr distillation.[7]

Since then, Lindsey et al. developed the synthesis of *meso* aryl substituted dipyrromethanes *via* a more accessible route.[8] Their one flask synthetic method involved the room temperature reaction of an aldehyde with excess pyrrole. The appropriate aldehyde was dissolved in a 40 fold excess of pyrrole in the absence of solvent and the reaction was catalysed by an acid, e.g. trifluoroacetic acid or $BF_3.OEt_2$. This method afforded nine *meso* substituted dipyrromethanes bearing different functional groups (Fig. 1).
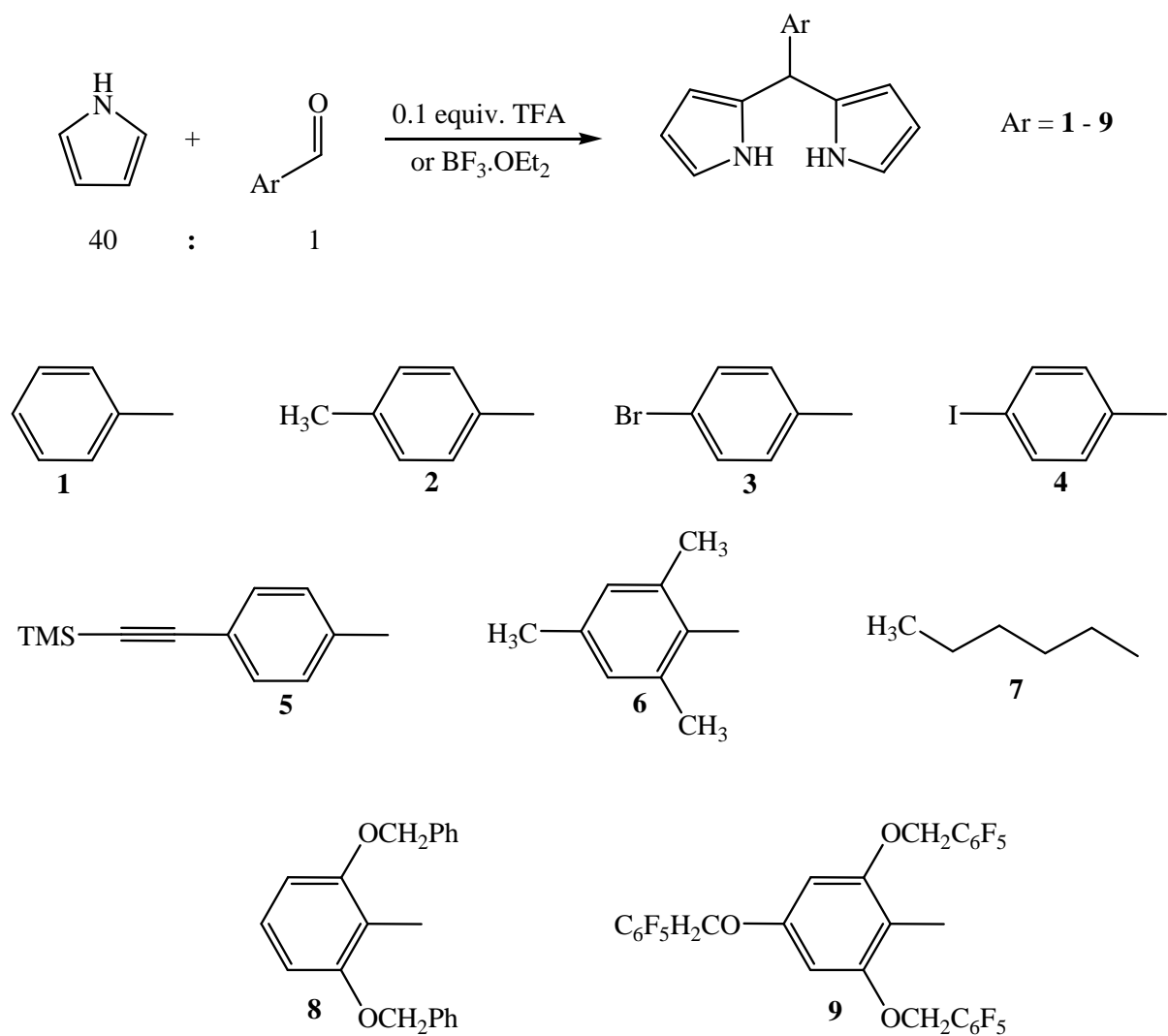
Figure 1   *Synthesis of* meso-*substituted dipyrromethanes* via *Lindsey's procedure.*

However purification of the product by column chromatography restricted application of the synthetic method to small scale production (< 1 g batches). Examination of the crude reaction mixture revealed three principal reaction products: (**1a**) dipyrromethane, (**1b**) α,β-linked "N-confused" dipyrromethane and (**1c**) tripyrrane (Fig. 2).[9] An extensive GC-MS investigation into the reaction parameters was undertaken using *meso* phenyl dipyrromethane (**1a**) to establish what factors affected product composition. Initially it was noted that the rate of the reaction was rapid. Total consumption of the aldehyde was observed 5 minutes after addition of the acid catalyst. The concentration of acid catalyst was examined: increased concentration (0.316 equiv.) resulted in decreased production of

331

1c, reduced concentration (0.031 equiv.) caused a small increase in **1b** and **1c** production. Thus a 0.1 equivalent was selected as an optimal acid concentration. Also, TFA catalysis gave significantly lower amounts of **1b** and **1c** compared to $BF_3.OEt_2$. The pyrrole : aldehyde ratio was examined from 5 : 1 to 80 : 1 and indicated that changing the ratio resulted in a change in product distribution: the higher the ratio the higher the yield of dipyrromethane, consistent with the hypothesis that a high pyrrole : aldehyde ratio prevents polymerisation. Purification by bulb-to-bulb distillation followed by recrystallisation resulted in analytically pure dipyrromethanes.

| **1a** | **1b** | **1c** |
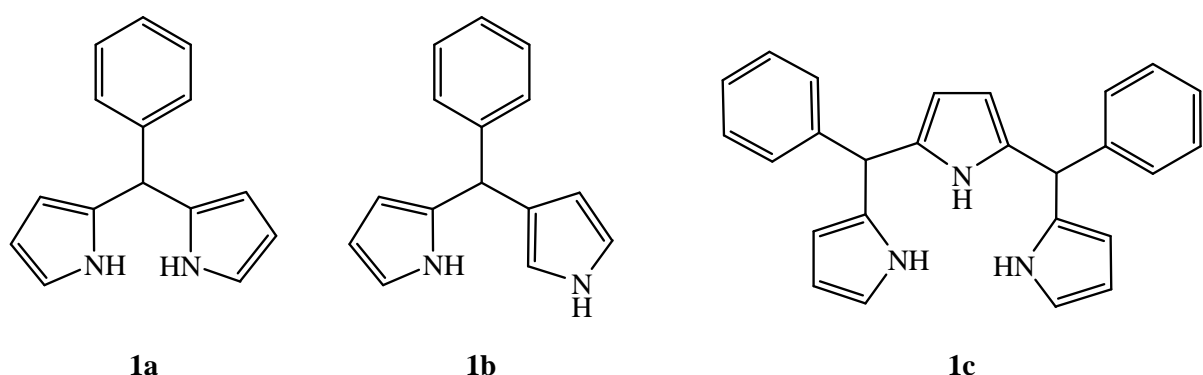
Figure 2   Products following acid catalysed condensation of benzaldehyde in excess pyrrole.

However, dipyrromethanes derived from aldehydes bearing sensitive or large substituents could not be distilled and in such cases column chromatography was again employed for purification. Thus further refinement of the solventless synthesis of **1** (Fig. 1) was reported.[10] Altering the pyrrole : aldehyde ratio (25 : 1 to 400 : 1) changed the product composition and reaction rate. Increasing excess pyrrole decreased reaction rate as the acid concentration was reduced. Although increasing the concentration of acid caused no significant change in product distribution. Darkening of the reaction mixture had been observed previously and the darkening was attributed to formation of oligomeric by-products that could not be identified. A series of Brønsted and Lewis acid catalysts were investigated. The ideal acid should give negligible unreacted aldehyde, a high yield of dipyrromethane and no darkening of reaction medium. Brønsted acids produced a substantial amount of tripyrrane and darkened reaction mixtures. Lewis acids gave good yield of the desired product with little darkening. $InCl_3$ and $MgBr_2$ produced the best

results of both product distribution and relative absence of darkening of the reaction mixture. Comparison of $InCl_3$ with TFA, revealed TFA catalysed condensations were faster and gave complete consumption of the aldehyde within 30 minutes. Although another distinction was observed, TFA catalysis gave a dark brown crude product which required further treatment with charcoal in hot ethanol in addition to the designed workup. The four step workup devised included: (1) quenching – using excess powdered NaOH, (2) filtering – recovered acid catalyst and base, (3) removal of excess pyrrole – repeated distillation enabled recovery of excess pyrrole, and (4) recrystallisation – afforded dipyrromethane **1** (Fig. 1) as white crystals with yields greater than 50 %.

An efficient one – step synthesis of dipyrromethanes in water was later reported.[11] The dropwise addition of pyrrole to an aqueous solution (90 ℃) of aldehyde in the presence of HCl, followed by 30-45 minutes stirring under an inert atmosphere, gave the corresponding dipyrromethane in high yields. The dipyrromethane was released from the aqueous layer as the reaction proceeded thus forcing the reaction to completion and protecting the product from further reactions. GC-MS indicated that exclusive formation of the dipyrromethane in the first 30 minutes at 90 ℃ for all reactions. Only after 3 hours refluxing were the N-confused dipyrromethane and tripyrrane detected. This low production of secondary products along with high yields and the non-toxic environmentally friendly solvent make this method quite advantageous.

Cation exchange resins have been used to produce *meso* substituted dipyrromethanes.[12] The resins acted as heterogeneous solid acid catalysts that consist of a styrene divinylbenzene co-polymer matrix with sulphonic acid groups and each resin particle can be viewed as a mini reactor. Cation exchange resin was added to a solution of the substituted aromatic aldehyde and neat excess pyrrole which subsequently afforded the corresponding dipyrromethanes that were readily crystallised in high yields (70 – 80 %). The mechanism of ion exchanger catalysed reactions in a non aqueous media is similar to that operating for usual heterogeneous catalysts – adsorption, surface reaction, desorption. The use of the macroporous cation exchange resin resulted in high selectivity and purity of product due to trace side reactions.

A photochemical synthesis of dipyrromethanes was reported by D'Auria et al.[13]   In this procedure, a mixture of pyrrole and aldehyde (694 : 1) was photolysed with a 125 W high pressure Hg arc lamp surrounded by a Pyrex water jacket for 3 hours. Reported yields for phenyldipyrromethane (**1**, Fig. 1) and thien-2-yldipyrromethane (**10**, Scheme 1) were 50 and 59 % respectively.   However Lindsey et al. questioned the validity of the photochemical reaction on a number of conditions.[9]   Illumination by a high pressure mercury lamp produces a significant amount of heat and the experimental information give by D'Auria et al. was deemed insufficient to assess the radiation absorbed by the reaction mixture as well as the reaction temperature. Lindsey and co-workers carried out thermal condensations of pyrrole and benzaldehyde. Stirring the mixture in the dark at 22 ℃ for 24 hours in the absence of acid catalyst produced phenyldipyrromethane in 3 % yield. At 40 ℃, yields akin to the deliberately acid catalysed reaction were obtained (56 % after distillation). Reaction at 90 ℃ was complete within 90 minutes with 42% isolated yield. Since the formation of dipyrromethane has been shown to occur thermally, formation of the dipyrromethanes by purely photochemical processes has yet to be proven.

Meso thien-2-yl and thien-3-yl dipyrromethane were produced *via* a modification of Lindsey's TFA catalysed condensation from the respective thiophenecarboxaldehyde and excess pyrrole (Scheme 1).[14]   Incorporation of a heterocycle (thiophene) in place of the usual arene group at the *meso* position retains the *Cs* symmetry of the molecule and imparts a third donor atom for metal binding. The geometry of the thiophene group in thien-2-yl dipyrromethane was suitable to participate in tripodal [NNS] type metal chelation, whereas the geometry of the thien-3-yl analogue does not allow such binding. Crystal structures of both dipyrromethanes were obtained. The X-ray structures confirm methane angles of *ca*. 111 – 112 ° defining pyramidalisation of the *meso* carbon.
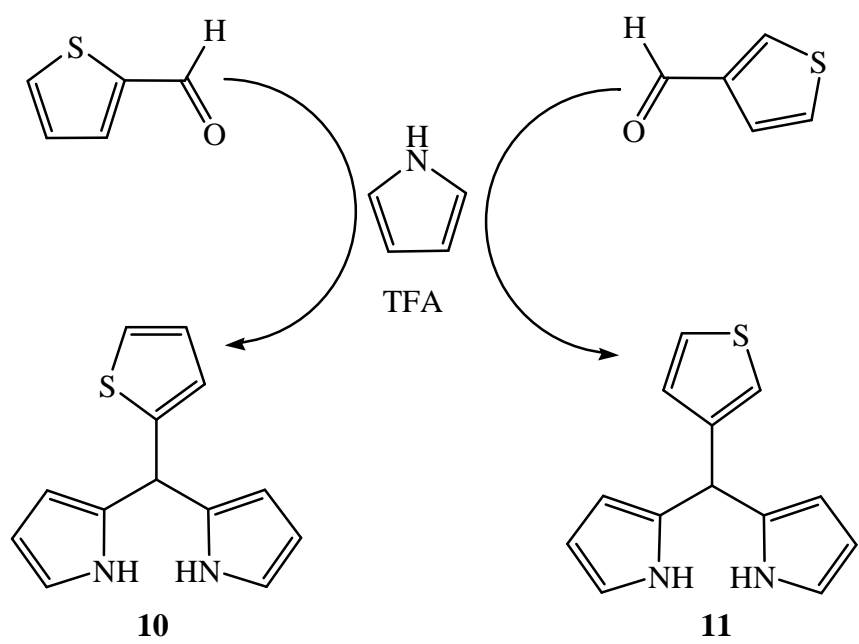
Scheme 1   Synthesis of thienyl dipyrromethanes.

5.1.2 Dipyrrins

Dipyrrins are formally composed of a pyrrole ring and an azafulvene attached to each other through the α position. [15]   The acid catalysed condensation of 2-formyl pyrrole with a pyrrole unsubstituted at the 2' position produces *meso* unsubstituted dipyrrin (Rxn. 1).

R = alkyl substituent
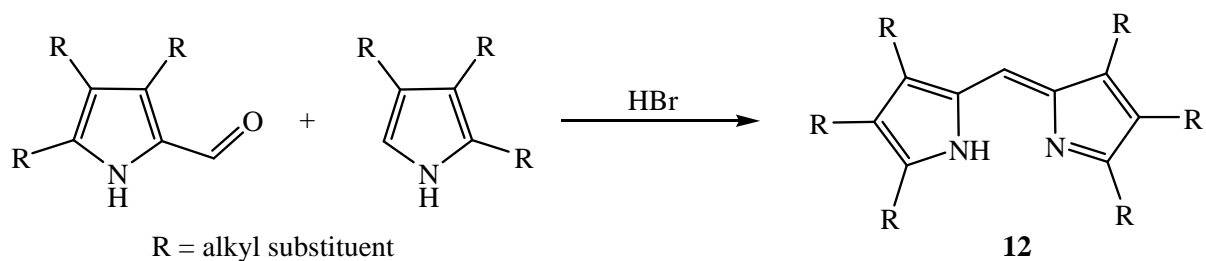
Rxn. 1   *Synthesis of* meso *unsubstituted dipyrrin,* **12**, *by acid catalysed condensation.*

Meso substituted dipyrromethanes can be oxidised to yield dipyrrins that are often stable in their freebase form. Oxidation of dipyrromethanes can be accomplished with a number of reagents, the most popular of which are 2,3-dichloro-5,6-dicyano-1,4-benzoquinone (DDQ) and *p*-chloranil. Limitations occur when the *meso* substituent is an alkyl group or the dipyrromethane is *meso* unsubstituted. In these cases consumption of the starting material without yielding the appropriate product is observed. The NMR spectra of freebase *meso* substituted dipyrrins demonstrate rapid tautomerisation. The signal arising from the proton bonded to the nitrogen is not always apparent and is generally attributed to hydrogen bonding with the solvent.

Although freebase *meso* aryl dipyrrins can be isolated, by column chromatography and/or recrystallisation, in most cases they are reacted *in situ* with a metal salt to form homoleptic *meso* aryl(dipyrrinato)metal complexes or with boron trifluoride diethyletherate to form borondifluoride dipyrrins.

5.1.3 Dipyrrinato metal(II) complexes

In general, following deprotonation, the monoanionic dipyrrinato ligands form neutral homoleptic complexes. Dipyrrins have the propensity to form stable complexes with variety of metal ions resulting in bis (dipyrrinato) metal (II) or tris (dipyrrinato) metal (III) complexes, which are ideal for utilisation in supramolecular coordination chemistry. There have been numerous reports on dipyrrinato complexes with a wide variety of metals including, but not limited to Ni(II),[16] Cu(II),[17] and Zn(II).[16a] Historically, dipyrrins typically contained a full complement of α and β substituents around the chromophores. Though in recent years there has been an increase in publications on α,β-unsubstituted dipyrrinato complexes.[18]

Dehydrogenation of m*eso* phenyl dipyrromethane (**1**, Fig. 1) with DDQ and subsequent reaction with copper(II), nickel(II) and zinc(II) yielded the corresponding highly coloured metal chelates (Scheme 2).[19] The UV-vis properties of the metal chelates were strongly dependent on the central metal. Nickel chelates (**Ni-13** and **Ni-14**, Scheme 2) possessed very similar absorbance spectra. The phenyl moiety was approximately perpendicular to the plane of the dipyrrin, consequently it was not in full conjugation with the pyrrolic system and substituents on the phenyl group had minimal influence on the π system. The UV-vis spectrum of the zinc chelate (**Zn-14**, Scheme 2) was similar to that of the protonated ligand, with a λ_{max} at 486 nm and less intense transitions in the region 320 – 350 nm, which indicated the absence of any metal-metal interactions. The λ_{max} band was assigned to intraligand π-π* transitions and the bands at higher energy were attributed to charge transfer transitions. The nickel and copper chelates, (**Ni-13** and **Cu-14**, Scheme 2), possessed the same spectral pattern with λ_{max} at 474 nm and 484 nm respectively. These absorbance properties were similar to related α alkyl substituted metal chelates but hypsochromically shifted. The stereochemistry of the ligands around the central metal was strongly dependant on the metal type. Crystal structure analysis of **Ni-13** revealed the molecule had D_2 symmetry, with two equivalent dipyrrin ligands. This endowed a C_2-axis passing through the *p*-hydrogens of the *meso* substituent, the methine carbons and the central metal. The N-Ni-N bond angle was 152.5 ° and all four Ni-N distances were equal (1.879 Å). Both the nickel and copper bis(dipyrrinato)complexes (**Ni-13**, **Ni-14**, **Cu-14**) were assigned distorted square planar geometry while the zinc complex (**Zn-14**) was assigned a tetrahedral geometry.
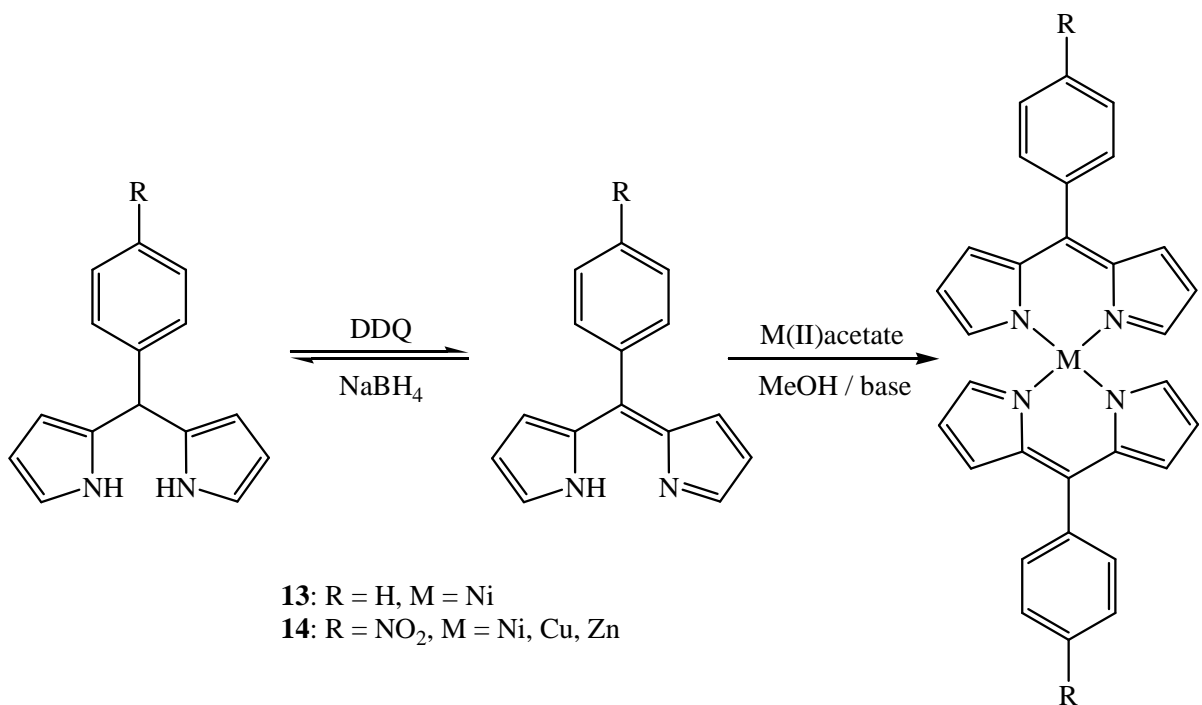
Scheme 2   Synthesis of dipyrrins and bis(dipyrrinato)complexes from dipyrromethanes.

Several methods were examined for the preparation of the dipyrromethane precursors fused with a variety of phenylacetylene building blocks.[20] Subsequent metallation of the freebase dipyrromethanes resulted in formation of the target (dipyrrinato)copper(II) complexes (**Cu15** - **Cu18**, Fig. 3).   The complex, **Cu15**, was examined by X-ray crystallography.   It displayed a four coordinate distorted square planar coordination geometry.   The four Cu-N bond lengths were in the range 1.942 – 1.951 Å.   The phenylacetylene arms lay out of the plane of the dipyrrin chelating groups and were essentially linear for both ligands attached to the copper centre.   The combination of dipyrrin chelators with phenylacetylene groups provided rich absorbance chemistry. Precursor dipyrromethanes of **15** and **16** displayed a λ_{max} at 298 and 302 nm respectively, attributed to π-π* transitions of the phenylacetylene. A new absorbance band centred at 435 nm was observed for all dipyrrins following oxidation with DDQ, which was attributed to the π-π* transition of the dipyrrin aromatic system. Additional absorbances at higher energy (330 – 345 nm) were observed for the uncoordinated *para* substituted phenylacetylene dipyrrins (R = **15** and **17**) that were not seen for uncoordinated *meta* substituted systems (R = **16** and **18**), indicating that *meta* substitution on the central benzene ring disrupted the extended conjugation of the π system. In complexes **Cu15** –

Cu18 the high energy transition became more defined and shifted bathochromically (350 – 355 nm), and the authors tentatively assigned the absorbance band to π-π* charge transfer processes between the π system of the dipyrrin groups and the π system of the phenylacetylene moiety. In the absorbance spectra of **Cu15 – Cu18**, the feature associated solely with the dipyrrin π-π* transitions (λ_{max} = 435 nm) was lost in favour of two new transitions centred at 468 and 500 nm, the intensities of which differed significantly (ε = 61,700 *vs*. 32,600 M^{-1} cm^{-1}), that were consistent with similar compounds reported previously.[19,21] The fluorescence spectra were obtained and notably only the *para* substituted dipyrromethanes (**15** and **17**) exhibited significant fluorescence with emission maxima at 352, 368 and ~460 nm. The two higher energy emission bands were ascribed to fluorescence from the extended phenylacetylene moiety. All oxidation products, dipyrrins and bis(dipyrrinato)copper(II) complexes were found to be virtually non-fluorescent.
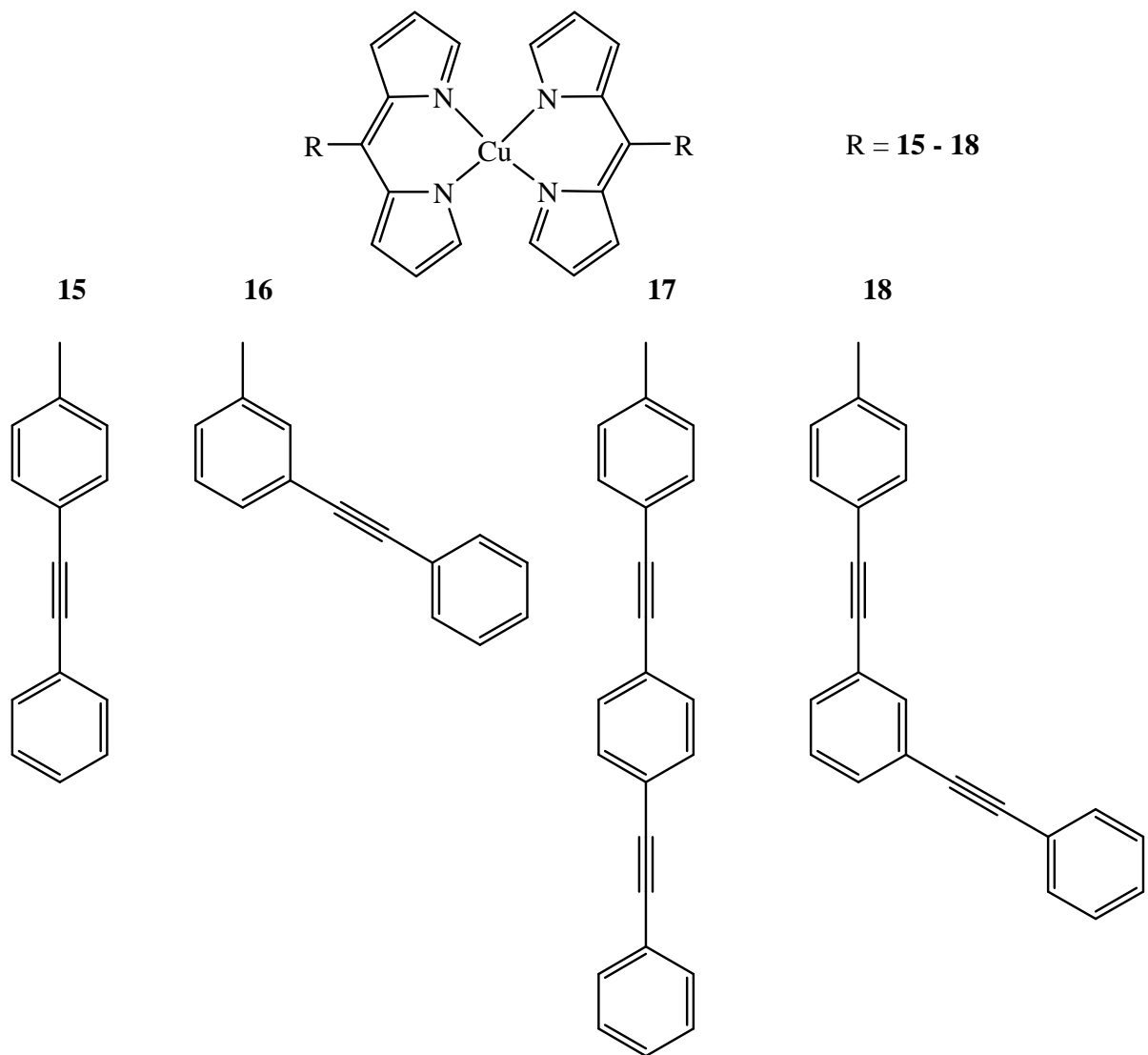
Figure 3   *Bis(dipyrrinato)copper(II)complexes **15 - 18**.*

En route to producing self assembling triads composed of two porphyrins and an intervening bis(dipyrrinato)metal complex, the synthesis and spectroscopic properties of bis(dipyrrinato)metal(II) complexes was described (**19**, Fig. 5).[22] The facile formation of the complexes *via* a one flask synthesis involved oxidation of freebase dipyrromethane with DDQ in the presence of metal acetates, resulted in bis(*meso*-phenyl-dipyrrinato)metal(II) complexes (**19**, M = Cu, Pd, and Zn). There was a striking difference in the absorbance spectra of freebase dipyrrins and their bis(dipyrrinato) metal(II) complexes, a change in the broad-band absorbance of the former to the more intense sharp features of the metallo complexes was observed. The absorbance and emission spectra of bis(*meso*phenyldipyrrinato)zinc(II), **Zn19** are shown in figure 4. The absorbance band

340

centred at 485 nm arose from an $S_0 \rightarrow S_1$ excited state transition.[16] The fluorescence spectrum possessed approximate mirror symmetry to the absorbance spectrum, with a Stokes shift of ~660 cm^{-1}, although the vibronic overtone feature was less prominent in the emission. The fluorescence quantum yield was 0.007 in toluene and 0.002 in benzonitrile. Time resolved absorbance spectroscopy was carried out. In toluene **Zn19** displayed multicomponent excited-state profiles. A fast phase (*ca.* 9 ps) was attributed to vibrational cooling in the excited state manifold while a slower component (*ca.* 93 ps) reflected population decay from **Zn19***. The latter phase was accompanied by substantial ground state recovery, indicative of little formation of longer lived transients such as a triplet excited state. In benzonitrile, the dynamics were different although the authors did state some uncertainty in the assignments. A fast phase (*ca.* 6.5 ps) associated with **Zn19*** was followed by a slower decay phase (~1 ns) that may have developed from another excited state (e.g. charge transfer), followed by a substantial contribution (*ca.* 30 %) to a longer lived state (> 5 ns).
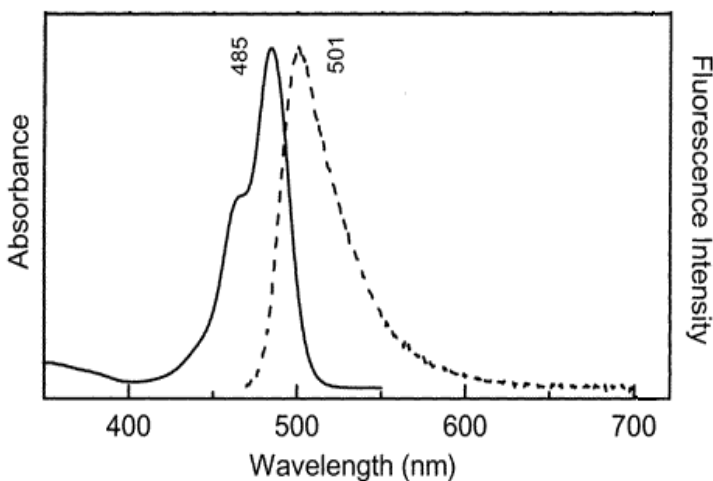
*Figure 4   Absorbance spectrum (——) and fluorescence spectrum (-----) of **Zn19** recorded in toluene at room temperature.[22]*

An ensuing study revealed that minor modifications of the *meso* substituents in bis(dipyrrinato)zinc(II) complexes transformed the molecules from very weak emitters that deactivated within 100 ps of photoexcitation to highly fluorescent chromophores with multi-nanosecond singlet excited state lifetimes.[23] Replacement of phenyl with *p-tert-*

butylphenyl or mesityl groups (**Zn19**, **Zn20**, **Zn21** respectively, Fig. 5), constrained aryl ring rotation. Only minor changes were observed in the absorbance characteristics of **Zn19**, **Zn20** and **Zn21**, with intense absorbance bands (ε = 115,000 M^{-1} cm^{-1}) in the range 482 – 487 nm. Fluorescence spectra of **Zn19**, **Zn20** and **Zn21** were approximately mirror images of the absorbance spectra with a Stokes shift of 660, 580 and 940 cm^{-1} respectively. Notably the Stokes shift of **Zn20** was reduced compared to **Zn19** (and **Zn21**), which reflected less conformational freedom in the ground and/or excited states, due to steric hindrance. Complexes **Zn19** and **Zn21** displayed similar low fluorescence quantum yields (Φ_{fl} = 0.006 and 0.007 respectively), but complex **Zn20** emitted strongly with a ~50 fold increase (Φ_{fl} = 0.36). Analogous differences were found for the excited state lifetime as determined by transient absorbance spectroscopy. A lifetime of 90 ± 10 ps was obtained for **Zn19** whereas a lifetime of 3 ± 1 ns was observed for **Zn20**. The transient absorbance data revealed significant differences between **Zn19** and **Zn20**. At very short times (0.5 ps) following the laser pulse, **Zn19** and **Zn20** displayed similar transient absorbance difference spectra that contained bleaching of the ground state bands and excited state stimulated emission. The initial spectrum of each complex was assigned to that of the Franck-Condon form of the S_1 excited state that underwent vibrational cooling over 9 ± 3 ps and 25 ± 5 ps respectively and formed a relaxed excited state. The relaxed S_1 excited state of **Zn19** subsequently decayed with a 90 ps time constant and the lifetime was dominated by internal conversion to the ground state. In contrast, the relaxed S_1 excited state of **Zn20** decayed in *ca*. 3 ns. The decay included repopulation of the ground state but also formation (~ 30 % yield) of a longer-lived transient state. The authors ascribed the long-lived transient to the lowest triplet excited state. Thus, hindered rotation of the *meso* aryl rings with respect to the dipyrrin framework (by the mesityl moiety in **Zn20** compared to the phenyl group in **Zn19** substantially slowed non-radiative relaxation to the ground state. Consequently the bis(dipyrrinato)zinc(II) complex was transformed from a weakly emissive and rapidly deactivating system to a strongly emitting complex with a multi-nanosecond excited state lifetime.
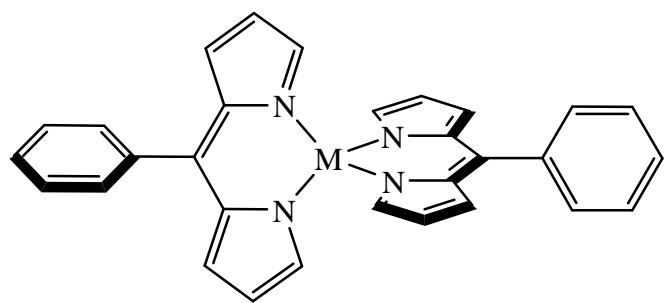
19
M = Zn, Cu, Pd
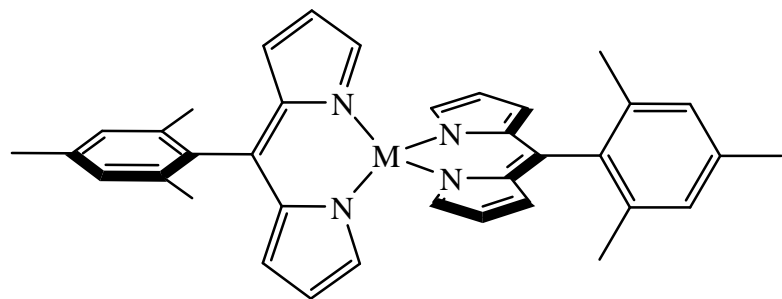
20
M = Zn
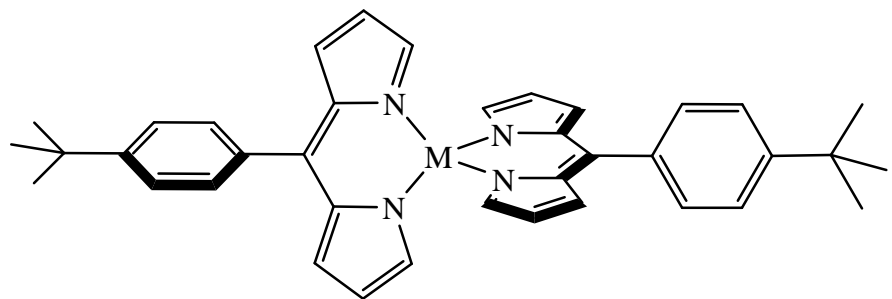
21
M = Zn

Figure 5　　　　　*Bis(dipyrrinato)metal(II) complexes, **19**, **20**, **21**.*

343

5.1.4 Borondifluoride dipyrrins

Borondifluoride dipyrrin complexes, boradiazaindacene dyes, *N,N'*-difluoroboryl dipyrrins or 4,4-difluoro-4-bora-3a,4a-diaza-s-indacenes are comprised of only one dipyrrin ligand complexed to a borondifluoride moiety and shall be abbreviated hereafter as BODIPY. This type of dipyrrin complex is the most popular of the dipyrrin complexes owing to their applications as biological fluorescent labels, probes and in lasing applications.[24] The basic spectroscopic characteristics of BODIPY complexes were overviewed in chapter 1 and substantial reviews of these dyes also exist.[25] Briefly, their characteristics include moderately strong (ε = 40,000 – 100,000 M^{-1} cm^{-1}) and sharp (FWHM *ca.* 25 nm) blue-green absorbance centred around 500 nm, Stokes shifts in the range 500 – 900 cm^{-1} and fluorescence lifetimes of *ca.* 5 ns.[26] The fluorescent properties of BODIPYs can be tuned preparatively by introduction of functional substituents on the dipyrrin framework, replacing the *meso*-CH position with a nitrogen bridge to create azadipyrromethenes, or by substitution of the fluorine atoms.[25b, 27]

A series of *meso* substituted BODIPY dyes were synthesised for inclusion in light harvesting arrays, however they were found to be only weakly fluorescent when compared to a commercially available BODIPY complex.[26] Commercially available BODIPY dyes are generally substituted at the β position of the pyrrole ring (**22**, Fig. 6). Complex **23** displayed an absorbance λ_{max} at 516 nm and emission maximum at 535 nm. The quantum yield for fluorescence was 0.058 in toluene and the singlet excited state lifetime consisted of a fast component (15 $\pm$ 4 ps) attributed to excited state relaxation dynamics followed by a short lifetime of 520 $\pm$ 50 ps. This was in contrast to the intense fluorescence of the commercial β-substituted BODIPY dye **22** (Φ_{fl} = 0.51, τ = 5000 $\pm$ 30 ps).
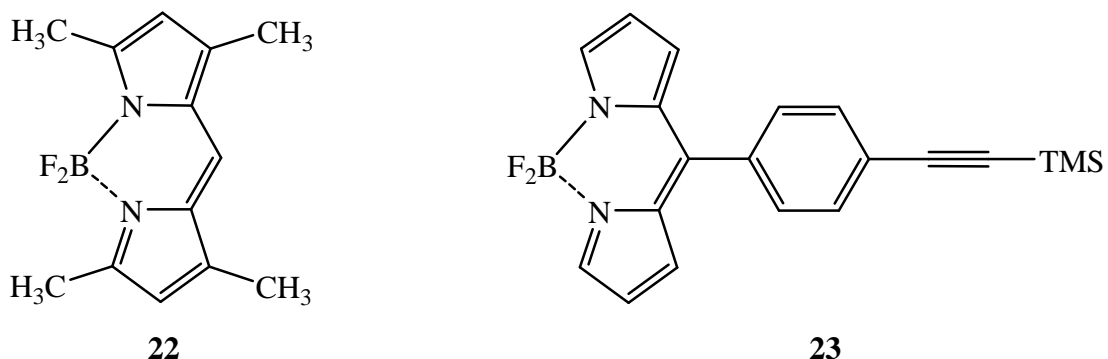
Consequently the BODIPYs **24** – **27** (Fig. 7) were prepared to investigate if modification of the *meso* substituent would increase fluorescence yields as was observed for the bis(dipyrrinato)zinc(II) complexes.[28]   In all compounds the boron-dipyrrin framework, which includes both pyrrole rings and the central six membered ring containing the boron atom were essentially planar. One of the most pronounced effects of the *meso* aryl moiety was observed in the dihedral angle between the *meso* aryl ring and the planes defining various dipyrrin elements. The angle increased from ~60 ° and ~50 ° for **24** and **25** where no steric hindrance for aryl rotation was present, to ~85 ° and ~75 ° for **26** and **27** when motion was restricted. Regardless of the presence or nature of the *meso* substituent all of the UV-vis ground state absorbance spectra contained a $S_0{\rightarrow}S_1$ transition with a λ_{max} between 490 – 500 nm and vibronic components spanning *ca*. 25 nm to higher energy. A parallel transition ($S_1{\rightarrow}S_0$) existed in the fluorescence spectra with standard Stokes shift observed (500 – 900 cm^{-1}). Although the substituents on the aryl ring of the BODIPYs had only modest impact on the absorbance and fluorescence profiles, the nature of the aryl moiety had a profound effect on the fluorescence quantum yield and lifetime of the S_1 excited state. The fluorescence quantum yield and lifetime increased in order **24** (Φ_{fl} = 0.062, τ = 0.45 ns), **25** (Φ_{fl} = 0.069, τ = 0.55 ns), **26** (Φ_{fl} = 0.93, τ = 5.8 ns) and **27** (Φ_{fl} = 0.93, τ = 6.6 ns). Low emission yield and short excited state lifetimes obtained for aryl substituted complexes without steric hindrance (**24** and **25**) indicated a facile S_1 excited state non radiative decay that was restricted when steric constraints were imposed (**26** and **27**). Transient absorbance data and theoretical calculations showed the short excited state lifetimes resulted from excited state conformational changes that drove fast internal conversion to the ground state.
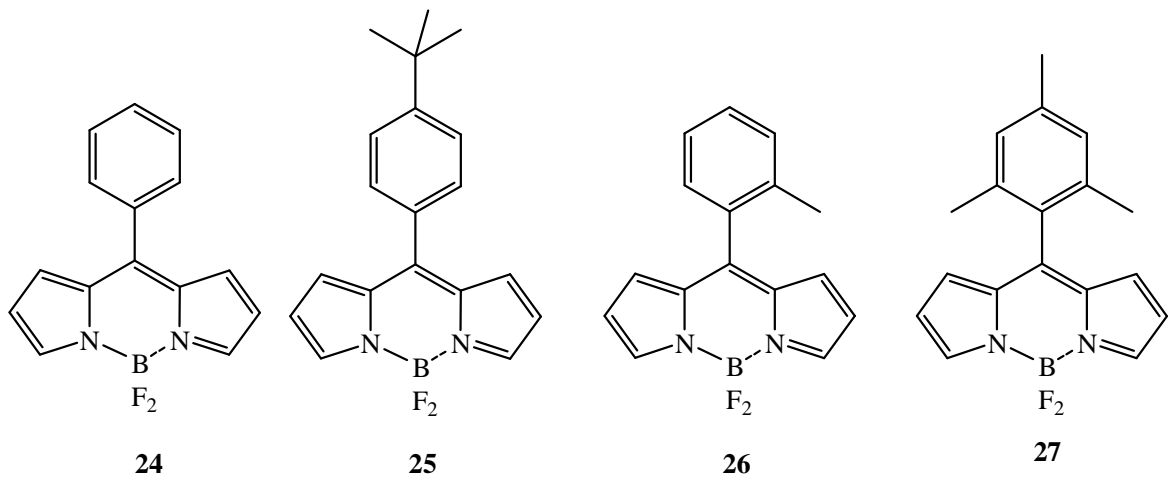
Figure 7   *Borondifluoride dipyrrin complexes* **24 - 27**.

Compounds containing both a chromophore and a redox group incorporated in to a single molecule have been extensively studied.[29] Four different types of covalently linked BODIPY-ferrocene conjugates (**28 – 31**, Fig. 8) were synthesised following several different routes.[30] The compounds **28 – 31** exhibit characteristic UV-vis absorbance spectra with a characteristic strong band in the region 520 – 560 nm, which corresponded to the $S_0 \rightarrow S_1$ transition, with a vibronic overtone at higher energy. An ill-defined band a *ca*. 400 nm was attributed to the $S_0 \rightarrow S_2$ transition. For conjugates **28 – 30** an additional broad band was observed in the region 660 – 680 nm. The low energy band was assigned to the intramolecular charge transfer transition, which was very intense for compound **29** that possessed two ferrocenyl moieties. The charge transfer band was not observed for compound **31** where the conjugation between the BODIPY and ferrocene group was less effective. All compounds showed negligible fluorescence supporting rapid photoinduced electron transfer from the donor ferrocenyl group(s) to the acceptor boron-dipyrrin unit. However fluorescence was restored through preclusion of electron transfer from the ferrocene to the BODIPY moiety. Oxidation of the ferrocene unit to the ferricenium ion in conjugates **28** and **29** was achieved by chemical oxidation and changes in both the absorbance and emission spectra were monitored. When **29** was oxidised, the charge transfer band at 682 nm in the UV-vis spectrum decreased in intensity until it disappeared while the $S_0 \rightarrow S_1$ band increased in intensity, broadened and shifted to higher wavelength with an isobestic point at 640 nm. Concomitantly emission was restored and a strong fluorescence band at 612 nm with a shoulder at longer wavelength was observed. A singlet state lifetime of 5.2 ns with a quantum yield of 0.31 was observed for **29**. Thus by

346

oxidation of the ferrocenyl moiety and elimination of the electron transfer pathway, the fluorescence of the BODIPY dyes can be "switched on" and by analogy reduction will "switch off" fluorescence.
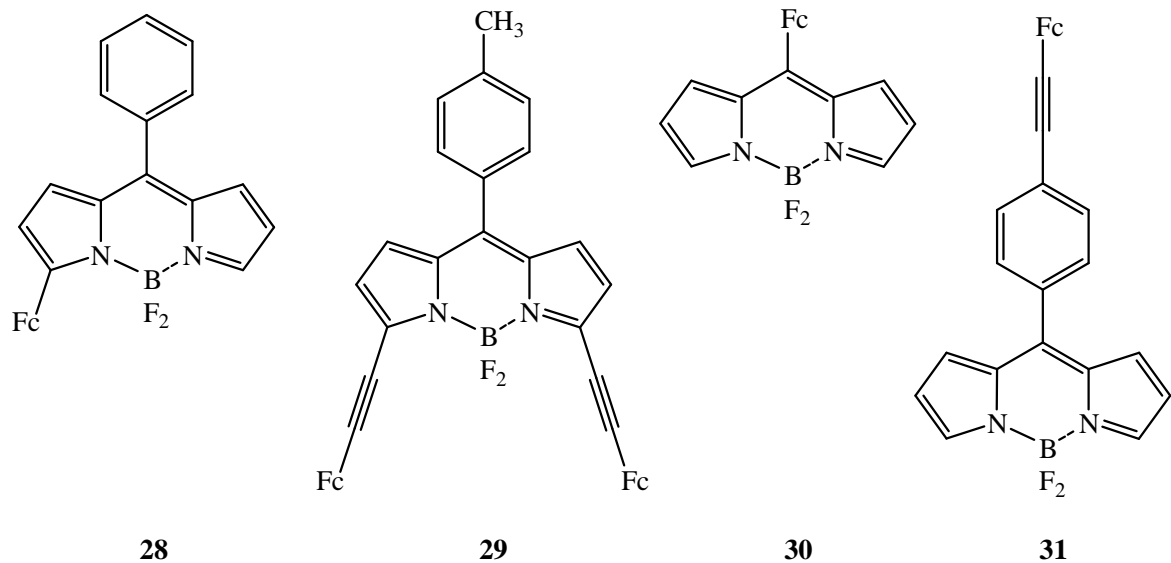

Figure 8   *BODIPY-ferrocene conjugates, where Fc = ferrocene.*

BODIPYs bearing ethynylpyrene units were constructed in a step by step procedure based on Pd(0) catalysed coupling reactions resulting in dual dye systems (**32 – 34**, Fig. 9).[31] Molecular modelling studies and X-ray crystallography indicated that the pyrene unit was orthogonal to the borondifluoride dipyrrin unit in compounds **32**, **33** and **34**. The lowest energy conformation of **33** showed the phenylene and pyrene units were coplanar to each other but orthogonal to the BODIPY moiety. All compounds exhibited similar absorbance spectral characteristics. The absorbance spectrum of model compound **35**, without a pyrene moiety, showed a strong $S_0 \rightarrow S_1$ (π-π*) transition with a λ_{max} at 527 nm ($\varepsilon = 60,000$ M^{-1} cm^{-1}) attributed to the BODIPY chromophore. The less intense and relatively broad absorbance band located at $\lambda = 357$ nm was ascribed to the $S_0 \rightarrow S_2$ (π-π*) transition also located on the BODIPY unit. The higher energy transition, $\lambda = 283$ nm, was assigned to the (π-π*) transition localised on the phenyl-ethynyl subunit. The inclusion of a pyrene unit onto the BODIPY framework produced an absorbance spectral profile that was essentially the superposition of the spectra of the individual components. For compound **32**, three bands are clearly observed at 230, 270 and *ca*. 340 nm, in addition to the BF_2-dipyrrin $S_0 \rightarrow S_1$ (π-π*) and $S_0 \rightarrow S_2$ (π-π*) transitions at $\lambda = 528$ and *ca*. 370 nm. The

former bands are assigned to (π-π*) transitions localised on the pyrene unit. The profile of **33** was similar to that of **32** except for a broadening of the (π-π*) transitions associated with the pyrene chromophores, while the profile of **34**, with two pyrene units, possessed a set of intense transitions in the range $\lambda = 340 - 480$ nm. No charge transfer absorbance bands were evident at long wavelengths. Fluorescence from the BODIPY fragment was apparent in all compounds and the emission profile showed good mirror symmetry with the corresponding absorbance band, with small Stokes shifts of *ca.* 600 cm^{-1} observed. Fluorescence lifetimes of the BODIPY are generally in the range $4 - 7$ ns. However both the quantum yield and fluorescence lifetime of **33** and **34** were reduced compared to **32**. For the directly linked dual dye, **32**, the fluorescence excitation spectrum matched the absorbance spectrum exactly. In particular, photons absorbed by the pyrene-like moiety subunit were channelled to the BF$_2$-dipyrrin unit with high efficiency. No fluorescence was detected from the pyrene unit in the range $350 - 500$ nm. The singlet lifetime and quantum yield were calculated to be 140 ns and 0.76 respectively, thus the pyrene based excited state in **32** was quenched by at least 100 fold and suggested a rate constant for energy transfer of **32** of $> 10^{10}$ s^{-1}. Both **33** and **34**, following direct excitation into the pyrene based absorbance bands, resulted in very weak fluorescence at *ca.* $400 - 500$ nm where characteristic emission from ethynylated pyrene derivatives is observed. Excitation spectra recorded for emission from the BODIPY unit were consistent with fast energy transfer from the pyrene fragment. This showed that intramolecular energy transfer occurred with an efficiency of ~95 and 90 % for **33** and **34** and energy transfer rates of 3.0 x 10^{10} s^{-1} and 7 x 10^9 s^{-1} for the respective compounds were calculated. The authors also found that the two pyrene subunits in **34** acted as a single giant chromophores rather than two separate species.
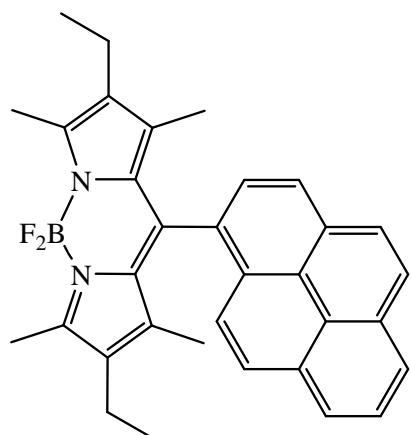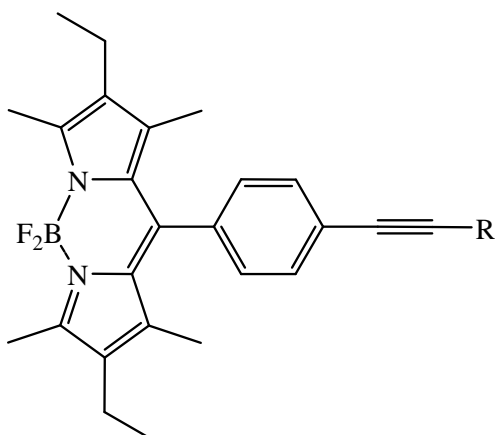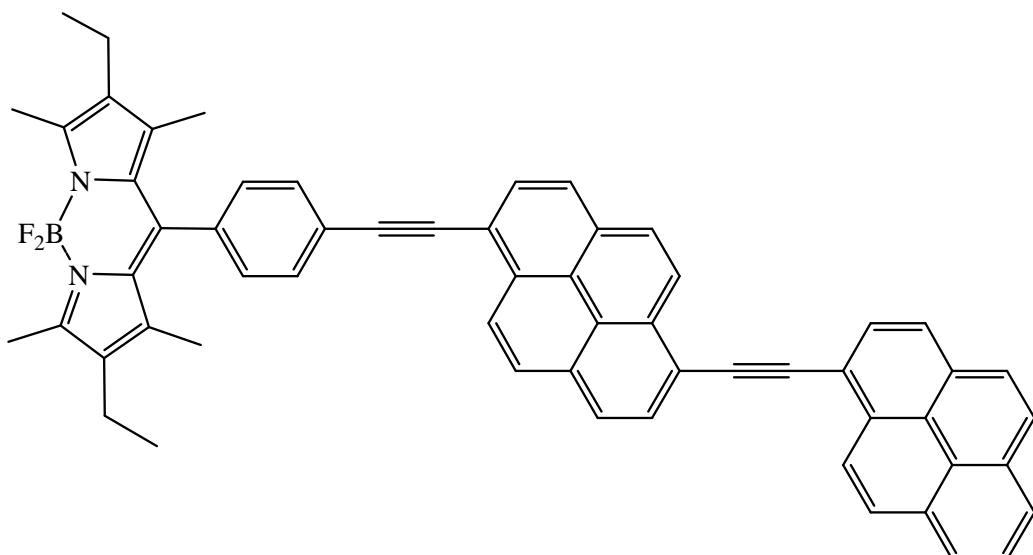
Figure 9   *BODIPY-pyrene molecular dyads.*

Intense absorbance and emission from singlet states in the visible region are often desirable features for components in larger arrays. The ability to fine tune excited state characteristics *via* minor structural modifications of bis(dipyrrinato)metal(II) complexes and BODIPYs increases the number of applications for this class of compounds.

5.2 Abstract

This chapter serves as a preliminary investigation into the synthesis and photophysics of thienyl dipyrromethanes and dipyrrin complexes. By examination of the basic photophysical processes that occur in dipyrromethanes and dipyrrins with a *meso* thienyl moiety a greater understanding can be gained as to how these compounds may be included in larger supramolecular arrays.

The studies available in the literature clearly show that the electronic properties of a porphyrin macrocycle are greatly altered when six membered *meso* aryl groups are replaced with five membered aromatic heterocycles.[32] Dipyrromethanes / dipyrrins are porphyrinogenic molecules – precursors and side products. A perusal of the literature revealed that dipyrrin chemistry with five membered *meso* substituents has remained largely unexplored.[14] There is however a wealth of information about dipyrrin complexes *meso* substituted with six membered phenyl ring.

Halper and Cohen investigated the effect of phenylacetylene rods attached to dipyrromethanes/dipyrrins at the *meso* position.[20] The combination of the phenylacetylene groups with the dipyrrin moieties resulted in rich absorbance spectroscopy for the compounds. Lindsey et al. reported that restricted rotation of the *meso* aryl groups in BODIPYs and bis(dipyrrinato)metal complexes transformed very weakly emitting molecules into highly fluorescent chromophores.[23,28] BODIPY-ferrocene conjugates which contain a redox group incorporated into the molecular framework of the chromophore have been synthesised.[30] These complexes showed that when the ferrocene was attached to the molecular framework *via* a *meso* phenylethynyl moiety there was little or no communication between the two components. BODIPYs bearing pyrene units were also investigated.[31] The compounds contained pyrene groups attached to different positions of the dipyrrin framework. Crystal structures of the molecule that possessed a *meso* phenylethynylpyrene group showed that the *meso* phenylethynylpyrene substituents were coplanar to each other but orthogonal to the dipyrrin framework. In all these cases the *meso* phenyl ring is expected to lie in a low energy conformation, an idealised orthogonal arrangement.

Studies on porphyrins have showed that *meso* thienyl substituents lie in a co-planar arrangement with respect to the porphyrin macrocycle. The co-planar arrangement allows for overlapping of the two π systems. The changes observed in the spectra of porphyrins (bathochromically shifted absorbance and emission spectra) are attributed to both the conformation which the thienyl groups adopt and the effect of the thiophene itself.

Thus a series of dipyrromethanes were produced. The dipyrromethanes are *meso* substituted with a thien-2-yl moiety which is substituted at the thien-5-yl position with other aryl moieties. A preliminary study of the photophysics of the dipyrromethanes and dipyrrins will be carried out.

5.3   Experimental

5.3.1   Materials

All manipulations were carried out under an atmosphere of argon or nitrogen using standard Schlenk techniques. All solvents were supplied by the Aldrich Chemical Company. Dichloromethane, chloroform, petroleum ether 40:60, pentane and hexane were dried over $MgSO_4$ prior to use. Diisopropylamine was distilled over potassium hydroxide before use. Methanol was distilled over magnesium turnings and iodine before use. 5-Bromo-2-thiophenecarboxaldehyde was purified by distillation using a Büchi Kügelrohr apparatus. Pyrrole was distilled over sodium hydroxide using a short path distillation apparatus prior to use. All other chemicals were obtained commercially and were used without further purification. Silica gel (Merck) was used as received. All mobile phases for column chromatography were dried over $MgSO_4$ before use. The preface "**NB-**" is applied to compound codes indicating that these are novel compounds synthesised throughout this work.

5.3.2   Equipment

^{1}H NMR and ^{13}C NMR were recorded on a Bruker AC 400 spectrometer and Bruker ANC 600 spectrometer in $CDCl_3$ and were calibrated according to the residual solvent peak i.e. $CHCl_3$ at 7.26 ppm for all ^{1}H spectra and 77.16 ppm for all ^{13}C spectra. Chemical shifts (δ) are given in parts per million (ppm). Proton coupling constants (J) are given in Hertz (Hz). Melting points were measured on a Stuart Scientific SMP1 melting point apparatus. IR spectra were recorded on a Perkin-Elmer 2000 FT-IR spectrophotometer (2 cm^{-1} resolution) in a 0.1 mm sodium chloride liquid solution cell. All UV-vis spectra were measured on an Agilent Technologies 8453 photodiode array spectrometer using a 1 cm^3 quartz cell. Emission spectra (accuracy $\pm$ 5 nm) were recorded at 298 K using a LS50B luminescence spectrophotometer, equipped with a red sensitive Hammatsu R928 PMT detector, interfaced with Elonex PC466 employing Perkin-Elmer FL WinLab custom built software.

5.3.3 Synthesis

General procedure for synthesis of compounds *via* the Sonogashira reaction.[33]

To a flame dried round bottom flask anhydrous triethylamine (~30 ml) was added and purged with nitrogen for 10 minutes. The halogenated aryl reactant was added and the solution was further purged for 5 minutes. A catalytic quantity of bis(triphenylphosphine) palladium(II)chloride, triphenylphosphine and cuprous iodide were added to the flask followed by an excess of aryl alkyne in quick succession. The reaction mixture was refluxed overnight under an inert atmosphere then allowed to cool. Solvent and excess aryl alkyne was removed under reduced pressure. The crude product was extracted from the oil by adding CH_2Cl_2 (*ca*. 5 ml) followed by the addition of petroleum ether (or hexane) (*ca*. 25 ml). The solvent was then decanted off. This extraction process was repeated several times until the organic layer remained colourless. The organic layers were combined and dried over magnesium sulphate. The solvent was then removed *via* rotary evaporation affording a dark residue. The crude product was purified by column chromatography as described for each individual compound.

General procedure for the preparation of *meso* substituted dipyrromethanes.

Meso substituted dipyrromethanes were prepared *via* a one-step synthetic route similar to that described by Lindsey et al.[9] Pyrrole (25 equivalents) and the appropriate aldehyde (1 equivalent) were added to a dry round bottom flask and degassed with nitrogen for 10 minutes. Trifluoroacetic acid (0.1 equivalents) was then added and the solution stirred for 5 minutes under an inert atmosphere at room temperature and then quenched with 0.1 M NaOH. Ethyl acetate was added and the organic phase was washed with water and dried over magnesium sulphate. The solvent was removed under reduced pressure to afford an oil. The crude product was purified using a Kügelrohr or by column chromatography to give the pure dipyrromethane as a solid.

5.3.3.1 5-(Naphthalenylethynyl)thiophene-2-carboxaldehyde (NB-A8)
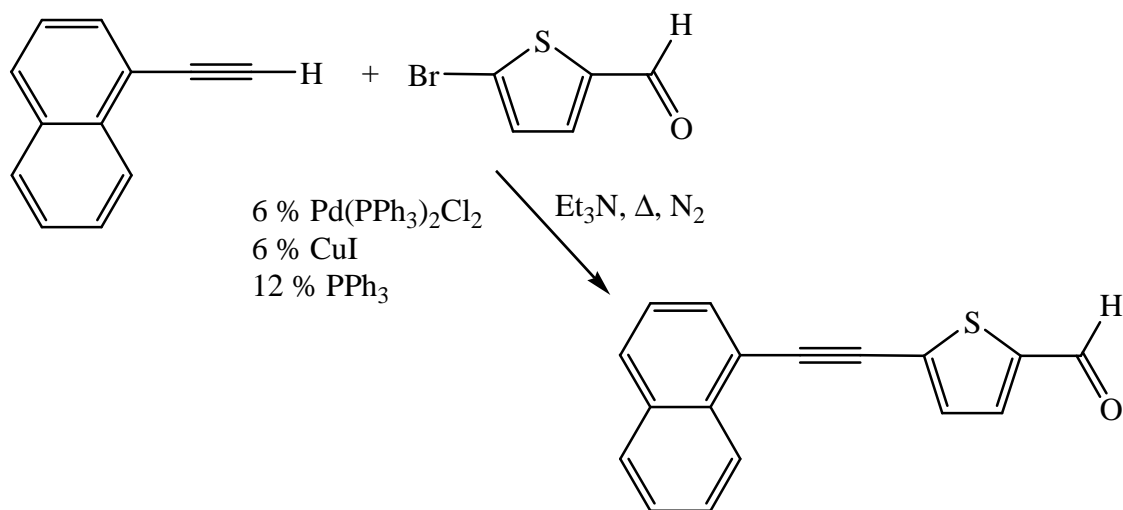
5-(Naphthalenylethynyl)thiophene-2-carboxaldehyde was prepared *via* the Sonogashira reaction. 5-Bromo-2-thiophenecarboxaldehyde (1.0 mmol, 0.12 ml), bis(triphenylphosphine)palladium(II)chloride (0.06 mmol, 42 mg, 6 %), triphenylphosphine (0.12 mmol, 31 mg, 12 %), cuprous iodide (0.06 mmol, 11 mg, 6 %) and 1-ethynylnaphthalene (1.25 mmol, 0.18 ml) were used. The crude product was purified by column chromatography using silica gel and a mobile phase of CH_2Cl_2 : petroleum ether 40:60 (50 : 50) which afforded a yellow solid. Yield: 192 mg, 0.73 mmol, 73 %.

^{1}H NMR (400 MHz, $CDCl_3$): 9.91 (1H, s), 8.33 (1H, d, *J* = 8.4 Hz), 7.90 (2H, t, *J* = 7.6 Hz), 7.80-7.78 (1H, m), 7.73 (1H, d, *J* = 4 Hz), 7.66-7.61 (1H, m), 7.59-7.54 (1H, m), 7.51-7.47 (1H, m), 7.43 (1H, d, *J* = 4 Hz) ppm. **^{13}C NMR** (100 MHz, $CDCl_3$): 182.45, 143.99, 136.17, 133.16, 132.97, 132.93, 132.56, 131.05, 130.01, 128.51, 127.27, 126.76, 125.86, 125.29, 119.48, 96.28, 86.67 ppm. **IR** (CH_2Cl_2): (C≡C) 2204 cm^{-1}. **m.p.**: 85-86 ºC

5.3.3.2 5-(Phenanthren-9-ylethynyl)thiophene-2-carboxaldehyde (NB-A9)
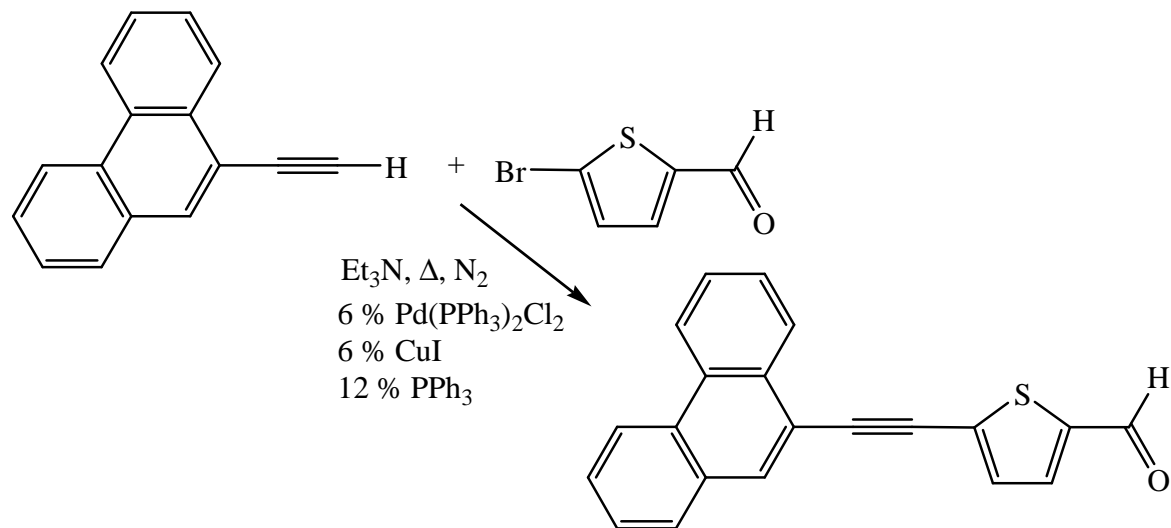
5-(Phenanthren-9-ylethynyl)thiophene-2-carboxaldehyde was prepared *via* the Sonogashira method.   5-Bromo-2-thiophenecarboxaldehyde   (1.0   mmol,   0.12   ml), bis(triphenylphosphine)palladium(II)chloride   (0.06   mmol,   42   mg,   6   %), triphenylphosphine (0.12 mmol, 31 mg, 12 %), cuprous iodide (0.06 mmol, 11 mg, 6 %) and 9-ethynylphenanthrene (1.25 mmol, 253 mg) were used.   The crude product was purified by column chromatography using silica gel and CH_2Cl_2 : hexane (45 : 55) which afforded a yellow solid. Yield: 256 mg, 0.82 mmol, 82 %.

^{1}H NMR (400 MHz, CDCl$_3$): 9.90 (1H, s), 8.72-8.69 (1H, m), 8.67 (1H, d, *J* = 8 Hz), 8.43-8.40 (1H, m), 8.12 (1H, s), 7.89 (1H, d, *J* = 8 Hz), 7.74-7.68 (4H, m), 7.62 (1H, t, *J* = 7.4 Hz), 7.44 (1H, d, *J* = 3.6 Hz) ppm. **^{13}C NMR** (100 MHz, CDCl$_3$): 182.46, 144.04, 136.17, 132.92, 132.66, 130.97, 128.88, 128.15, 127.42, 127.36, 127.21, 126.65, 122.96, 122.73, 118.32, 96.49, 86.30 ppm. **IR** (CH$_2$Cl$_2$): 2198 (C≡C) cm^{-1}. **m.p.**: 173-174 ºC

5.3.3.3 1-Trimethylsilylethynylpyrene
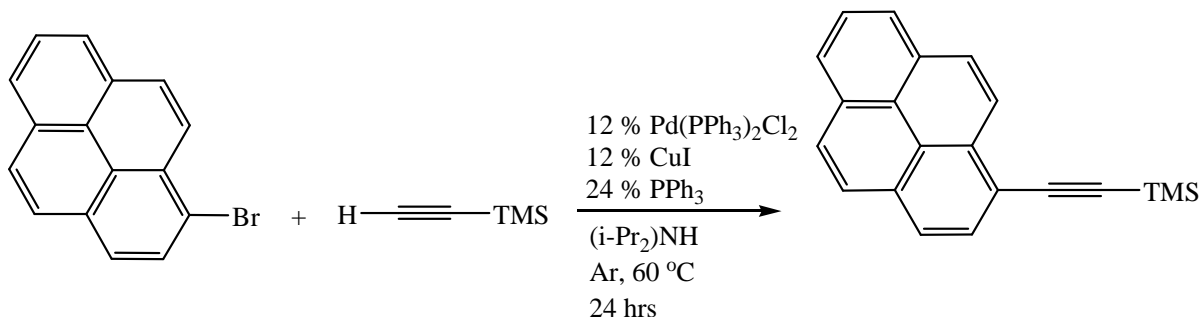
1-Trimethylsilylethynylpyrene was prepared *via* the Sonogashira reaction. 1-Bromopyrene (1.06 mmol, 300 mg), bis(triphenylphosphine) palladium(II)chloride (0.13 mmol, 91 mg, 12 %), triphenylphosphine (0.25 mmol, 65 mg, 24 %), cuprous iodide (0.13 mmol, 24 mg, 12 %) and trimethylsilylacetylene (2.10 mmol, 0.29 ml) were used. The solution was heated to 60 ºC and stirred overnight under an inert atmosphere. [Note: Due to the volatile nature of the TMSacetylene the flow of nitrogen should be sufficiently lowered for the course of the reaction.] The crude product was purified by column chromatography using silica gel and petroleum ether 40:60 (100 %) as mobile phase which afforded a pale yellow solid. Yield: 177 mg, 0.59 mmol, 56 %. Spectroscopic data were in good agreement with reported data.**Error! Bookmark not defined.**

^{1}H NMR (400 MHz, CDCl$_3$): 8.56 (d, 1H, *J* = 8.8 Hz), 8.23-7.99 (m, 8H), 0.39 (s, 9H) ppm. **m.p.:**102 - 103 ºC

5.3.3.4 1-Ethynylpyrene
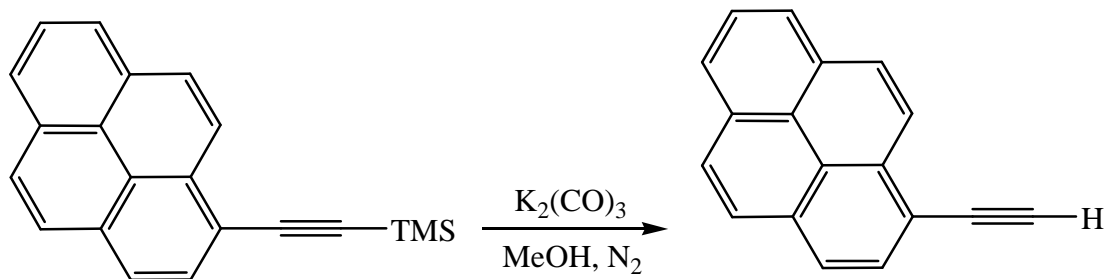
1-Ethynylpyrene was prepared by deprotection reaction as described by Austin et al.[34] Trimethylsilylethynylpyrene (2.01 mmol, 600 mg) was dissolved in dry methanol (~15 ml) and a small amount of dry CH_2Cl_2 (~3 ml) to aid dissolution. $K_2(CO)_3$ (0.20 mmol, 28 mg) was added and the solution was stirred for 3 hours during which time a cream coloured precipitate formed. The solvent was removed under reduced pressure and the resulting cream solid was dissolved in CH_2Cl_2 (~60 ml) and washed with aliquots of 5 % $NaHCO_3$ (4 x 25 ml). The organic phase was extracted, dried over $MgSO_4$ and solvent removed *via* rotary evaporation affording a beige solid.   Yield: 403 mg, 1.78 mmol, 88 %. Spectroscopic data were in good agreement with reported data.**Error! Bookmark not defined.**

^{1}H NMR (400 MHz, $CDCl_3$): 8.72 (d, 1H, J = 8.8 Hz), 8.29-8.23 (m, 4H), 8.17-8.14 (m, 2H), 8.10-8.05 (m, 2H), 3.65 (s, 1H) ppm. **m.p.:** 100 - 101 ºC

5.3.3.5 5-(Pyrenylethynyl)thiophene-2-carboxaldehyde (NB-A10)
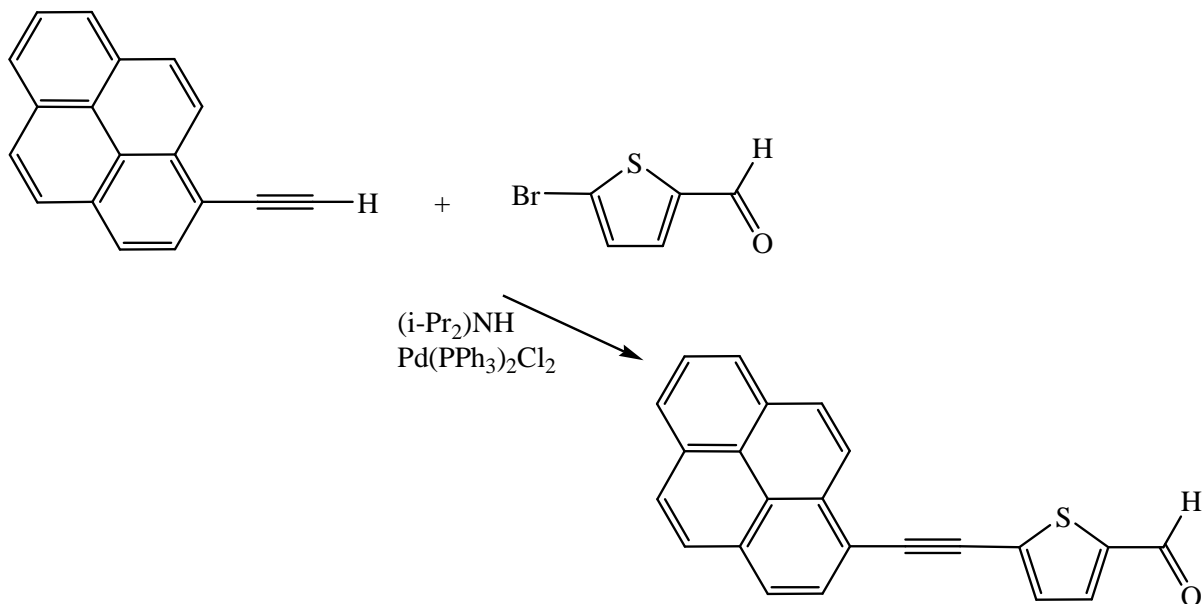
5-(Pyrenylethynyl)thiophene-2-carboxaldehyde was prepared *via* the Sonogashira reaction. Diisopropyamine (20 ml), 1-ethynylpyrene (1.0 mmol, 226 mg), bis(triphenylphosphine) palladium(II)chloride (0.06 mmol, 42 mg, 6 %), triphenylphosphine (0.12 mmol, 31 mg, 12 %), cuprous iodide (0.06 mmol, 11 mg, 6 %) and 5-bromo-2-thiophenecarboxaldehyde (1.0 mmol, 0.12 ml) were used. The reaction mixture was stirred overnight under an inert atmosphere. The crude product was purified by column chromatography on silica gel using CH_2Cl_2 : pentane (70 : 30) as mobile phase which afforded a yellow-orange solid. Yield: 282 mg, 0.84 mmol, 84 %.

^{1}H NMR (400 MHz, CDCl$_3$): 9.92 (1H, s), 8.54 (1H, d, *J* = 8.8 Hz), 8.26-8.03 (8H, m), 7.74 (1H, d, *J* = 4 Hz), 7.47 (1H, d, *J* = 4 Hz) ppm. **^{13}C NMR** (100 MHz, CDCl$_3$): 183.04, 133.13, 132.51, 132.10, 132.06, 131.18, 130.96, 129.67, 128.93, 128.85, 127.22, 126.48, 126.09, 126.04, 125.09, 124.61, 124.41 96.45, 81.77 ppm. **IR** (CH$_2$Cl$_2$): (C≡C) 2197 cm^{-1}. **m.p.**: 122-123 ℃.

5.3.3.6 5-(Ferrocenylethynyl)thiophene-2-carboxaldehyde (NB-A11)
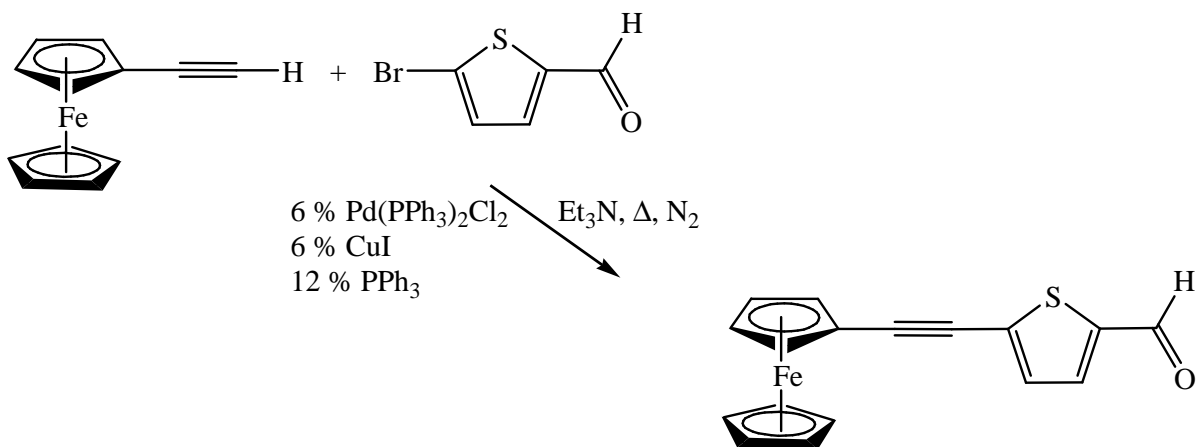
5-(Ferrocenylethynyl)-2-thiophenecarboxaldehyde was prepared *via* the Sonogashira reaction. 5-Bromo-2-thiophenecarboxaldehyde (1 mmol, 0.12 ml), bis(triphenylphosphine)palladium(II)chloride (0.06 mmol, 42 mg, 6 %), triphenylphosphine (0.12 mmol, 31 mg, 12 %), cuprous iodide (0.06 mmol, 11 mg, 6 %) and ethynylferrocene (1.25 mmol, 263 mg) were used. The crude product was purified by column chromatography using silica gel and CH_2Cl_2 : petroleum ether 40:60 (50 : 50) which afforded a red solid. Yield: 273 mg, 0.73 mmol, 73 %.

^{1}H NMR (400 MHz, CDCl$_3$): 9.85 (1H, s), 7.64 (1H, d, *J* = 4 Hz), 7.22 (1H, d, *J* = 4 Hz), 4.62-4.58 (2H, m), 4.38-4.34 (2H, m), 4.31 (5H, s) ppm. **^{13}C NMR** (100 MHz, CDCl$_3$): 182.38, 142.92, 136.35, 134.02, 131.64, 98.67, 78.54, 71.73, 70.22, 69.69 ppm. **IR** (CH$_2$Cl$_2$): (C≡C) 2209 cm^{-1}. **m.p.:** 157-158 ℃.

### 5.3.3.7 *Meso* (phenyl)dipyrromethane (Ph-DPM)
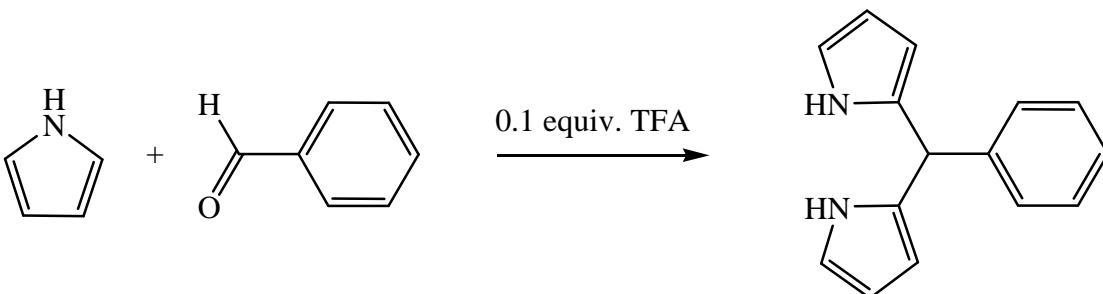
Meso (phenyl)dipyrromethane was prepared *via* a procedure described by Lindsey et al. Pyrrole (125 mmol, 8.67 mmol), benzaldehyde (5 mmol, 0.51 ml) and trifluoroacetic acid (0.5 mmol, 0.04 ml) were used. The crude product was purified by column chromatography using silica gel and neat CH_2Cl_2 as mobile phase which afforded an off-white solid. Yield: 0.37 g, 1.66 mmol, 33 %. Spectroscopic data were in good agreement with reported data.[9]

¹H NMR (400 MHz, CDCl₃): 7.90 (2H, br s), 7.35-7.18 (5H, m), 6.71-6.67 (2H, m), 6.19-6.16 (2H, m), 5.93-5.91 (2H, m), 5.47 (1H, s) ppm. **m.p.**: 98 – 99 ℃.

5.3.3.8 *Meso* (mesityl)dipyrromethane (Ms-DPM)
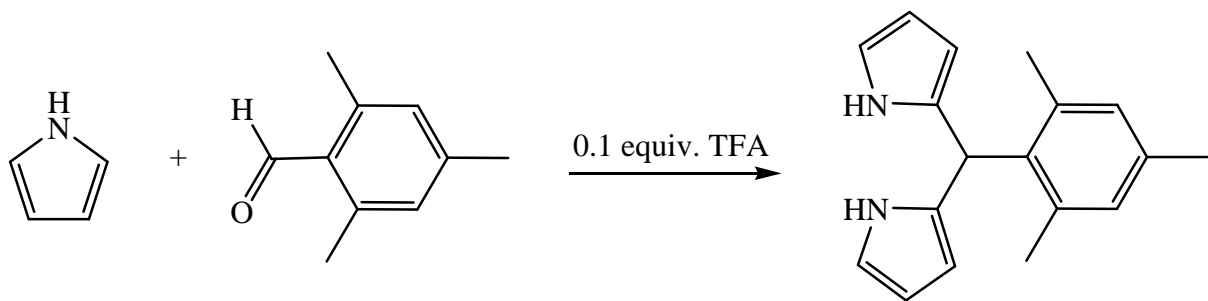
Meso (mesityl)dipyrromethane was prepared *via* a procedure described by Lindsey et al. Pyrrole (125 mmol, 8.67 ml), mesitylaldehyde (5 mmol, 0.74 ml) and trifluoroacetic acid (0.5 mmol, 38 μl) were used. The crude product was purified by using a Kügelrohr (170 ºC, 0.04 mm Hg) which afforded a yellow solid. Yield: 0.35 g, 1.32 mmol, 26 %. Spectroscopic data were in good agreement with reported data.[9]

^{1}H NMR (400 MHz, CDCl$_3$): 7.94 (2H, br s), 6.86 (2H, s), 6.67-6.65 (2H, m), 6.18-6.16 (2H, m), 6.01-5.99 (2H, m), 5.92 (1H, s), 2.27 (3H, s), 2.05 (6H, s) ppm. **m.p.**: 174 - 175 ºC

5.3.3.9 *Meso* (thien-2-yl)dipyrromethane (NB-DPM-1)
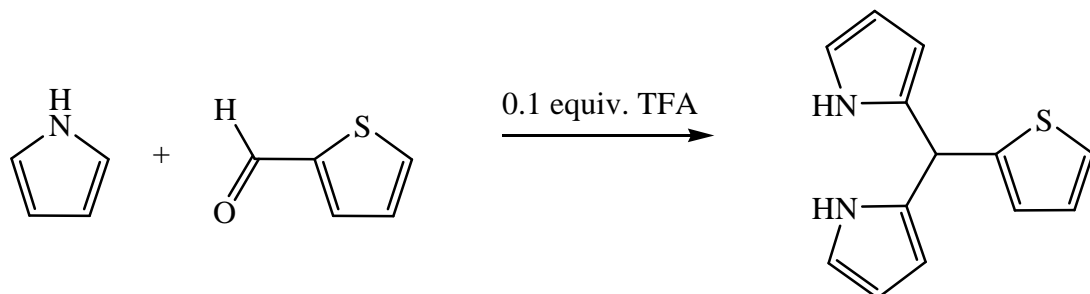
Meso (thien-2-yl)dipyrromethane was prepared according to the method reported by Maiti et al.[14] Pyrrole (64.9 mmol, 4.5 ml) and 2-thiophenecarboxaldehyde (10.7 mmol, 1 ml) were added to a round bottom flask and purged with argon for 10 minutes. Trifluoroacetic acid (1.1 mmol, 84 μl) was added and the solution was stirred for 30 minutes. The reaction was quenched with a molar excess of triethylamine (~1 ml), extracted into ethyl acetate, washed with water and dried over MgSO$_4$. Excess pyrrole and solvent was removed under reduced pressure resulting in red oil. The crude product was purified by column chromatography on silica gel using CH$_2$Cl$_2$: Pet. Ether 40:60 (40 : 60) as mobile phase affording a pale yellow solid. Yield: 0.94 g, 4.11 mmol, 38 %. Spectroscopic data were in good agreement with reported data.[13, 14]

1H NMR (400 MHz, CDCl$_3$): 7.99 (1H, br s), 7.23-7.22 (1H, m), 6.97-6.95 (1H, m), 6.90-6.89 (1H, m), 6.70-6.68 (2H, m), 6.19-6.17 (2H, m), 6.06-6.04 (2H, m), 5.57 (1H, s) ppm.

5.3.3.10 *Meso* (5-bromothien-2-yl)dipyrromethane (NB-DPM-2)
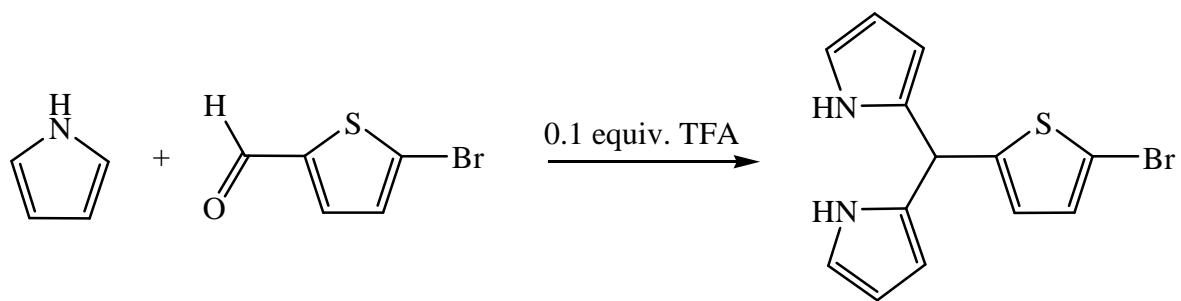
Meso (5-bromothien-2-yl)dipyrromethane was prepared according to the method reported by Maiti et al.[14] Pyrrole (6 mmol, 0.41 ml), 5-bromothiophene-2-carboxaldehyde (1 mmol, 12 ml) and trifluoroacetic acid (0.2 mmol, 15 μl) were used. The crude product was purified by column chromatography on silica gel using CH_2Cl_2 : Pet. Ether 40:60 (50 : 50) as mobile phase which afforded a pale yellow solid. Yield: 104 mg, 0.34 mmol, 34 %

^{1}H NMR (400 MHz, CDCl$_3$): 7.98 (2H, br s), 6.89 (1H, d, J = 3.6 Hz), 6.72-6.69 (2H, m), 6.63 (1H, d, J = 3.6 Hz), 6.18-6.16 (2H, m), 6.06-6.05 (2H, m), 5.65 (1H, s) ppm.

5.3.3.11   *Meso* (5-(trimethylsilylethynyl)thien-2-yl)dipyrromethane (NB-DPM-3)
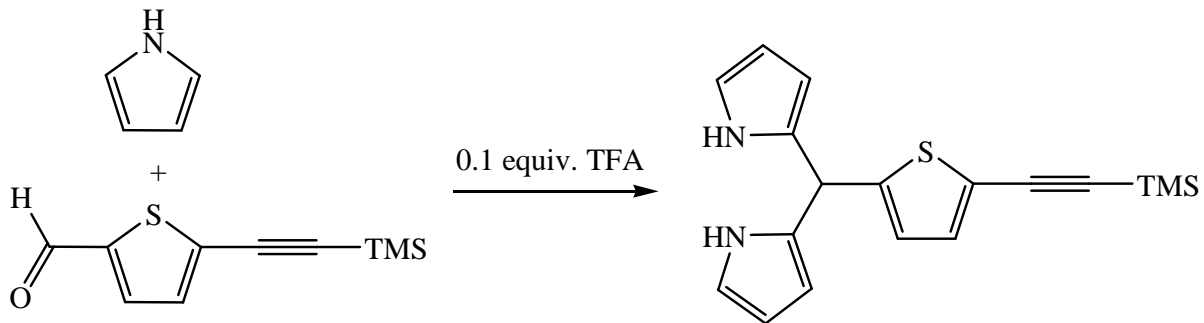
Meso (5-(trimethylsilylethynyl)thien-2-yl)dipyrromethane was prepared *via* Lindsey's synthetic method.   Pyrrole (12 mmol, 0.83 ml), 5-trimethylsilylethynyl-2-thiophenecarboxaldehyde (0.48 mmol, 100 mg) and trifluoroacetic acid (0.05 mmol, 4 μl) were used. The crude product was purified by column chromatography using silica gel and CH$_2$Cl$_2$: Et$_3$N (99 : 1) as mobile phase which afforded a brownish yellow solid. Yield: 42 mg, 0.13 mmol, 27 %.

^{1}H NMR (400 MHz, CDCl$_3$): 7.89 (2H, br s), 7.11 (1H, d, *J* = 3.6 Hz), 6.74 (1H, dd, *J* = 2.8, 1.2 Hz), 6.69-6.67 (2H, m), 6.30-6.28 (2H, m), 6.08-6.05 (2H, m), 5.64 (1H, s) 0.26 (9H, s) ppm.

5.3.3.12 *Meso* (5-ethynylthien-2-yl)dipyrromethane (NB-DPM-4)
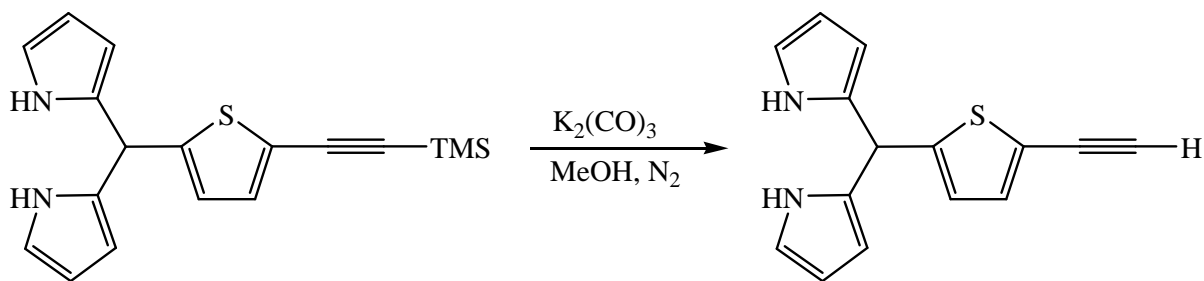
Meso (5-ethynylthien-2-yl)dipyrromethane was prepared by a deprotection reaction as described in literature.[34] *Meso* (5-(trimethylsilylethynyl)thien-2-yl)dipyrromethane (0.23 mmol, 75 mg) was added to dry methanol (~15 ml) along with anhydrous $K_2(CO)_3$ (0.05 mmol, 6 mg) and the reaction mixture allowed to stir overnight under an inert atmosphere. The solvent was removed under reduced pressure. The crude product was dissolved in CH_2Cl_2 and washed with aliquots of 5 % $NaHCO_3$ (3 x 50 ml). The organic phase was extracted and dried over $MgSO_4$. Removal of solvent under reduced pressure which afforded a light brown solid. Yield: 41 mg, 0.16 mmol, 71 %

¹H NMR (400 MHz, CDCl₃): 8.02 (2H, br s), 7.11 (1H, d, *J* = 3.6 Hz), 6.74-6.73 (1H, m), 6.71-6.69 (2H, m), 6.16 (2H, m), 6.06-6.03 (2H, m), 5.68 (1H, s) 3.32 (1H, s) ppm.

### 5.3.3.13   *Meso* (5-(phenylethynyl)-thien-2-yl)dipyrromethane (NB-DPM-5)
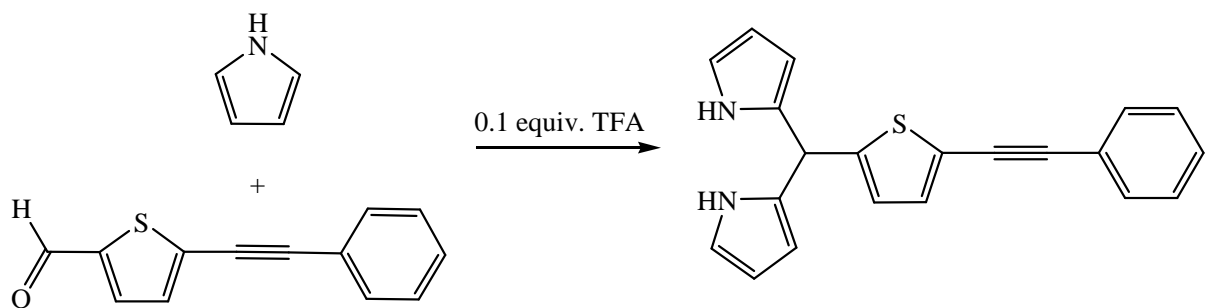
Meso (5-(phenylethynyl)thien-2-yl)dipyrromethane was prepared *via* Lindsey's method. Pyrrole (26.5 mmol, 1.9 ml), 5-(phenylethynyl)-2-thiophenecarboxaldehyde (1.06 mmol, 225 mg) and trifluoroacetic acid (0.11 mmol, 8µl) were used. The crude product was purified by column chromatography on silica gel using CH_2Cl_2 : Et_3N (99 : 1) as mobile phase which afforded a yellowish brown solid. Yield: 149 mg, 0.45 mmol, 43 %.

^{1}H NMR (400 MHz, CDCl$_3$): 8.03 (2H, br s), 7.50-7.47 (2H, m), 7.35-7.33 (3H, m), 7.13 (1H, d, *J* = 3.6 Hz), 6.78 (1H, d, *J* = 3.6 Hz), 6.71-6.70 (2H, m), 6.19-6.15 (2H, m), 6.08 (2H, m), 5.69 (1H, s) ppm. **^{13}C NMR** (100 MHz, CDCl$_3$): 146.85, 130.71, 130.58, 130.33, 130.30, 127.34, 124.58, 121.82, 121.35, 116.67, 107.48, 107.03, 106.24, 92.10, 81.67 ppm.

5.3.3.14 *Meso* 5-(naphthalenylethynyl)thien-2yl)dipyrromethane (NB-DPM-6)
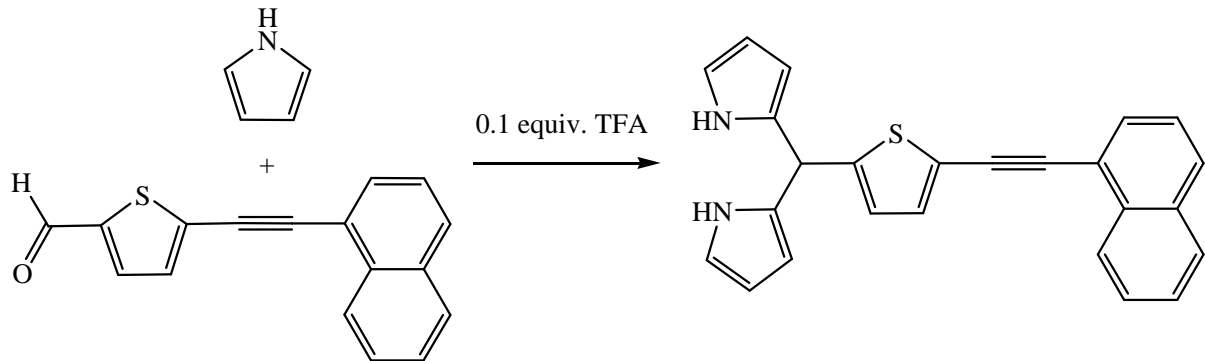
Meso 5-(naphthalenylethynyl)thien-2-yl)dipyrromethane was prepared *via* Lindsey's method.   Pyrrole   (19   mmol,   1.32   ml),   5-(naphthaleneylethynyl)-2-thiophenecarboxaldehyde (0.76 mmol, 200 mg) and trifluoroacetic acid (0.076 mmol, 6 μl) were used. The crude product was purified by column chromatography using silica gel and CH_2Cl_2 : Et_3N (99 : 1) as mobile phase which afforded a dark solid. Yield: 89 mg, 0.24 mmol, 31 %.

^{1}H NMR (400 MHz, $CDCl_3$): 8.32 (1H, d, *J* = 8.4 Hz), 8.11 (2H, br s), 7.83 (2H, t, *J* = 8.6 Hz), 7.69 (1H, m), 7.59-7.51 (2H, m), 7.43 (1H, t, *J* = 8.4 Hz), 7.22 (1H, d, *J* = 4 Hz), 6.85-6.83 (1H, m), 6.74-6.72 (2H, m), 6.19-6.17 (2H, m), 6.10-6.09 (2H, m), 5.73 (1H, s) ppm.

5.3.3.15 *Meso* **(5-(phenanthren-9-ylethynyl)-thien-2-yl)dipyrromethane (NB-DPM-7)**
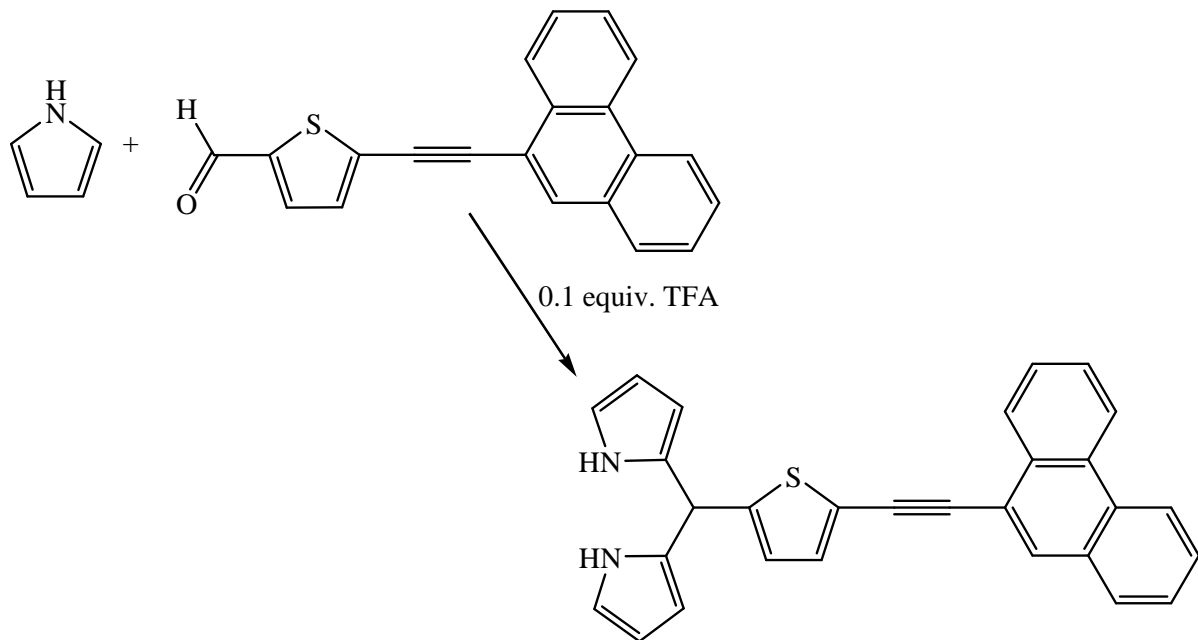
Meso (5-(phenanthren-9-ylethynyl)thien-2-yl)dipyrromethane was prepared *via* Lindsey's method.   Pyrrole (8.80 mmol, 0.61 ml), 5-(phenanthren-9-ylethynyl)thiophene-2-carboxaldehyde (0.35 mmol, 110 mg) and trifluoroacetic acid (0.035 mmol, 2.7 μl) were used. The crude product was purified by column chromatography using silica gel and CH_2Cl_2 : Et_3N (99 : 1) as mobile phase which afforded a dark yellowish solid. Yield: 36 mg, 0.08 mmol, 24 %.

^{1}H NMR (400 MHz, $CDCl_3$): 8.73-8.66 (2H, m), 8.43-8.40 (1H, m), 8.12 (1H, s), 7.90-7.88 (1H, m), 7.73-7.67 (5H, m), 7.44 (1H, d, *J* = 4 Hz), 6.75-6.73 (2H, m), 6.21-6.18 (2H, m), 6.12-6.09 (2H, m), 5.76 (1H, s) ppm.

**5.3.3.16** *Meso* **(5-(pyrenylethynyl)thien-2-yl)dipyrromethane (NB-DPM-8)**
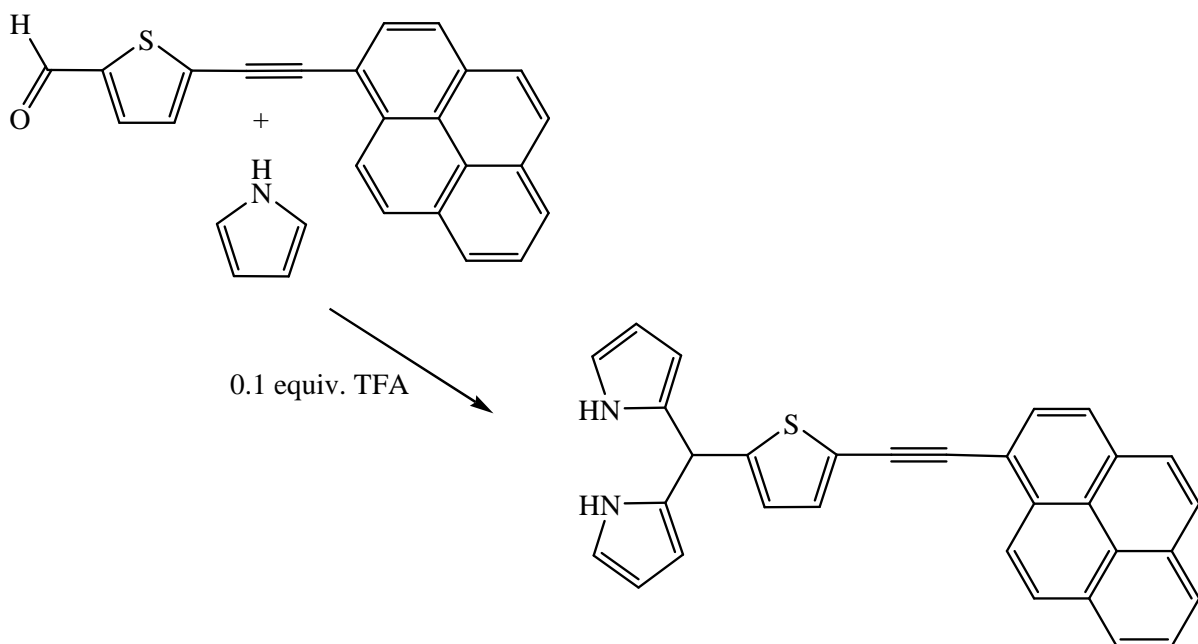
Meso (5-(pyrenylethynyl)-thien-2-yl)dipyrromethane was prepared according *via* Lindsey's method. Pyrrole (37 mmol, 2.58 ml), 5-(pyrenylethynyl)thiophene-2-carboxaldehyde (1.5 mmol, 500 mg) and trifluoroacetic acid (0.15 mmol, 12 μl) were used. The crude product was purified by column chromatography on silica gel using CH_2Cl_2 : Et_3N (99 : 1) as mobile phase which afforded a brownish yellow solid. Yield: 142 mg, 0.31 mmol, 21 %

^{1}H NMR (400 MHz, $CDCl_3$): 8.55 (1H, d, *J* = 8.8 Hz), 8.24-8.01 (10H, m), 7.29 (1H, d, *J* = 3.6 Hz), 6.87 (1H, m), 6.76-6.74 (2H, m), 6.22-6.19 (2H, m), 6.13-6.11 (2H, m), 5.78 (1H, m) ppm.

5.3.3.17　　*Meso* (5-(ferrocenylethynyl)thien-2-yl)dipyrromethane (NB-DPM-9)
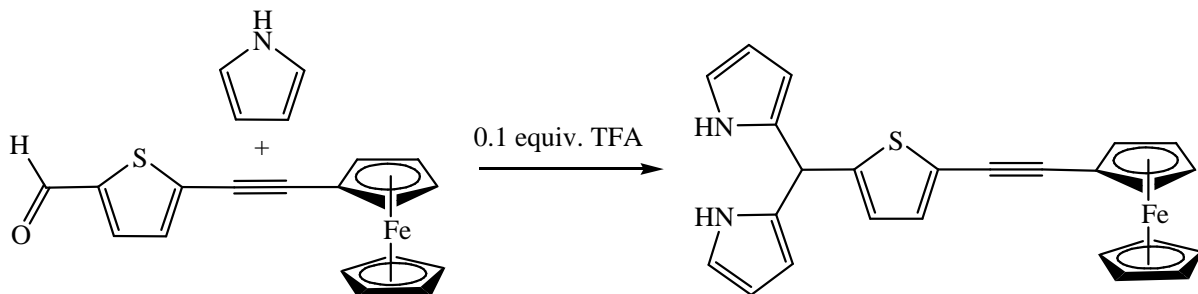
Meso (5-(ferrocenylethynyl)thien-2-yl)dipyrromethane was prepared *via* Lindsey's method. Pyrrole (30 mmol, 2.08 ml), 5-(ferrocenylethynyl)thiophene-2-carboxaldehyde (1.2 mmol, 387 mg) and trifluoroacetic acid (0.12 mmol, 9 µl) were used. The crude product was purified by column chromatography on silica gel using CH_2Cl_2 : Et_3N (99 : 1) as mobile phase which afforded a reddish solid. Yield: 148 mg, 0.41 mmol, 34 %.

^{1}H NMR (400 MHz, $CDCl_3$): 8.00 (1H, br s), 7.05 (1H, d, J = 3.6 Hz), 6.76-6.74 (1H, m), 6.72-6.70 (2H, m), 6.19-6.17 (2H, m), 6.08-6.06 (2H, m), 5.69 (1H, s), 4.47-4.46 (2H, m), 4.25-4.24 (2H, m), 4.23 (5H, s) ppm.

5.3.3.18 *Meso (5-(phenylethynyl)thien-2-yl)dipyrromethane dicobalt hexacarbonyl (NB-DPM-5-Co2(CO)₆)*
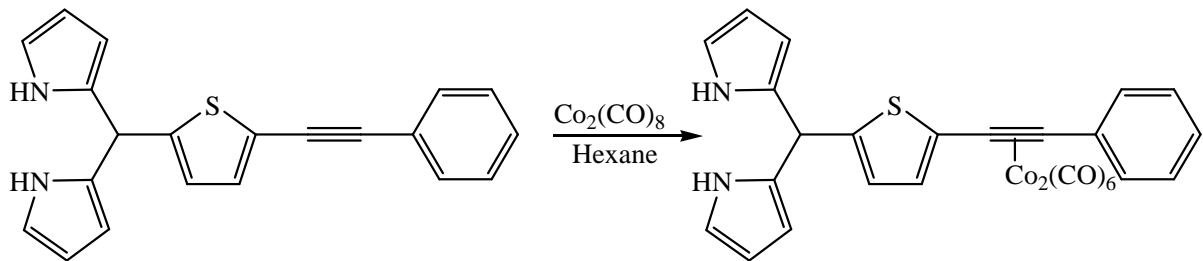
Molar equivalents of *meso* (5-(phenylethynyl)thien-2-yl)dipyrromethane (0.21 mmol, 68 mg) and dicobalt octacarbonyl (0.21 mmol, 70 mg) were added to nitrogen purged hexane (25 ml) with CH_2Cl_2 (~1 ml) added subsequently to aid dissolution of the dipyrromethane. The reaction mixture was allowed to stir overnight under a nitrogen atmosphere, covered in tinfoil. The solvent was removed under reduced pressure resulting in a brown residue. The crude product was purified by column chromatography on silica gel using neat hexane followed by CH_2Cl_2 : hexane (75 : 25) affording a brown solid. Yield 138 mg, 0.23 mmol, 75 %.

^{1}H NMR (400 MHz, CDCl$_3$): 8.08 (2H, br s), 7.66-7.64 (2H, m), 7.39-7.34 (3H, m), 7.19 (1H, d, J = 4 Hz), 6.78 (1H, d, J = 4 Hz), 6.74-6.73 (2H, m), 6.19-6.17 (2H, m), 6.09-6.08 (2H, m), 5.69 (1H, s) ppm. **IR** (CH$_2$Cl$_2$): ν(CO) 2091, 2057, 2030 cm^{-1}.

5.3.3.19 *Meso* (5-(naphthalenylethynyl)thien-2-yl)dipyrromethane dicobalt hexacarbonyl (NB-DPM-6-Co₂(CO)₆)
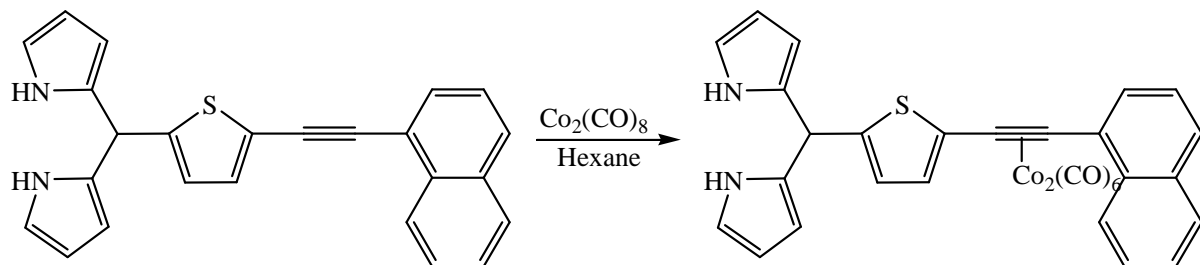
Meso (5-(naphthalenylethynyl)thien-2-yl)dipyrromethane (0.13 mmol, 50 mg) and dicobalt octacarbonyl (0.18 mmol, 62 mg) were added to nitrogen purged hexane (25 ml) with CH_2Cl_2 (~1 ml). The reaction mixture was allowed to stir overnight under an inert atmosphere in the dark. The solvent was removed by rotary evaporation resulting in a dark brown residue. The crude product was purified by column chromatography on silica gel using CH_2Cl_2 : petroleum ether 40:60 (30 : 70) as mobile phase which afforded a brown solid. Yield: 75 mg, 0.11 mmol, 86 %.

¹H NMR (400 MHz, CDCl₃): 8.02-7.99 (5H, m), 7.54-7.48 (2H, m), 7.44-7.39 (1H, m), 7.08 (1H, d, *J* = 4 Hz), 6.76 (1H, d, *J* = 4 Hz), 6.73-6.70 (2H, m), 6.18-6.16 (2H, m), 6.09-6.07 (2H, m), 5.68 (1H, s) ppm. **IR** (CH_2Cl_2): ν(CO) 2090, 2058, 2028 cm⁻¹.

5.3.3.20 *Meso* (5-(pyrenylethynyl)thien-2-yl)dipyrromethane dicobalt hexacarbonyl (NB-DPM-8-Co₂(CO)₆)
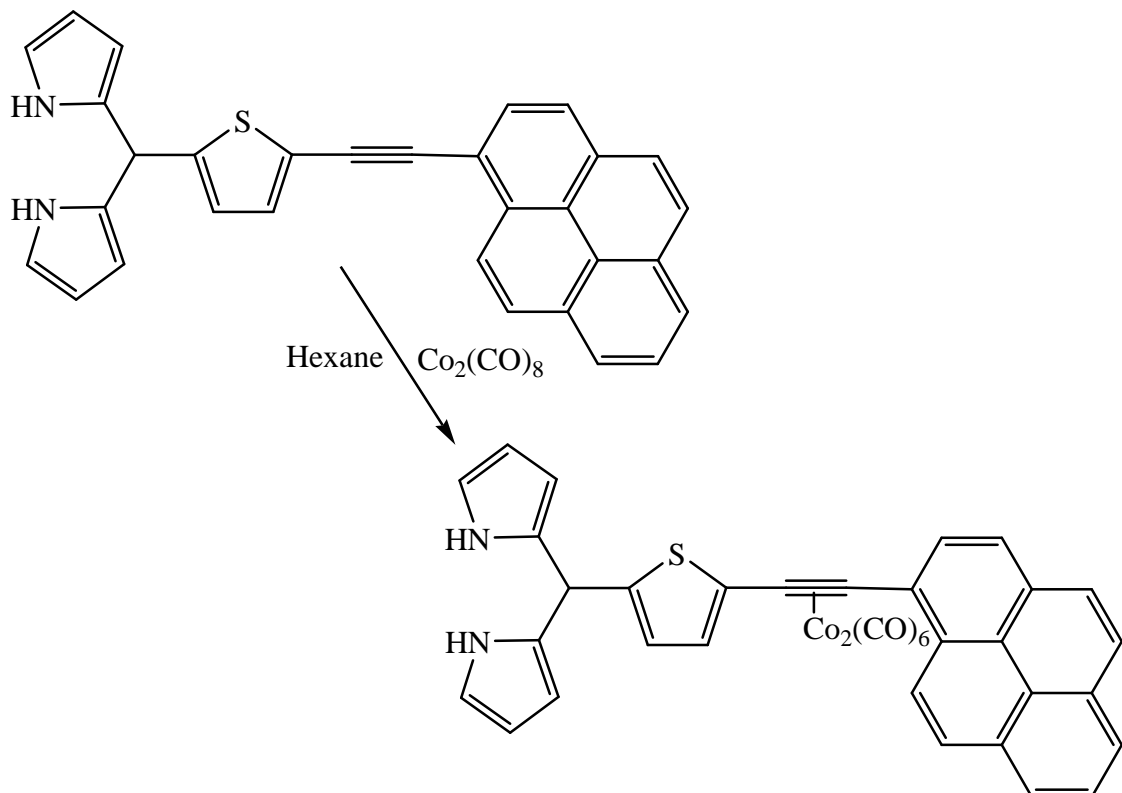
Meso (5-(pyrenylethynyl)thien-2-yl)dipyrromethane (0.89 mmol, 300 mg) and dicobalt octacarbonyl (0.89 mmol, 304 mg) were added to nitrogen purged hexane (25 ml) containing CH_2Cl_2 (~1 ml). The reaction mixture was allowed to stir overnight under an inert atmosphere in the dark. The solvent was removed under reduced pressure resulting in a brown residue. The crude product was purified by column chromatography using silica gel and neat hexane followed by neat CH_2Cl_2 as mobile phase. The solvent was removed immediately affording a light brown solid. Yield: 452 mg, 0.61 mmol, 92 %.

¹H NMR (400 MHz, CDCl₃): 8.36-8.01 (11H, m), 7.15 (1H, d, *J* = 3.6 Hz), 6.81 (1H, d, *J* = 3.6 Hz), 6.75-6.70 (2H, m), 6.17-6.15 (2H, m), 6.11-6.09 (1H, m), 5.71 (1H, s) ppm. **IR** (CH₂Cl₂): ν(CO) 2091, 2058, 2031 cm⁻¹.

5.3.3.21   Borondifluoride-(thien-2-yl)-dipyrrin (NB-BODIPY-1)
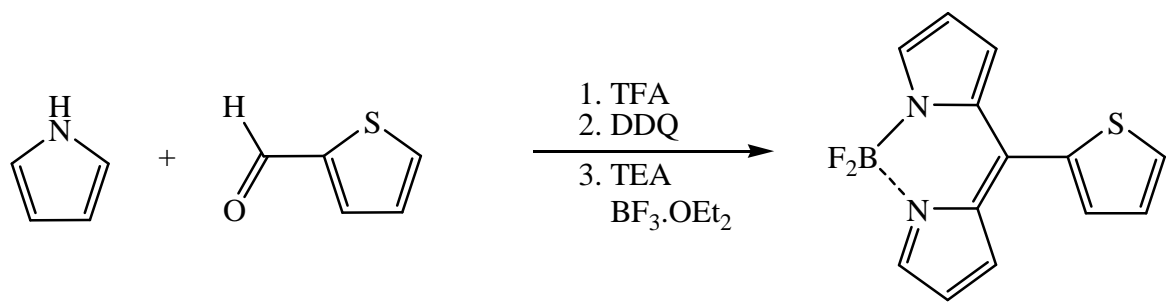
Borondifluoride-(thien-2-yl)-dipyrrin was synthesised *via* an adapted literature method.[35] A solution of CH_2Cl_2 (50 ml) was purged with argon for 10 minutes charged with 2-thiophenecarboxaldehyde (1.0 mmol, 0.09 ml) and pyrrole (2.3 mmol, 0.16 ml) and further purged for 5 minutes. Trifluoroacetic acid (0.2 mmol, 15 μl) was added and the reaction mixture was allowed stir overnight under nitrogen. Subsequently a solution of DDQ (1.0 mmol, 227 mg) in CH_2Cl_2 (10 ml) was added. The mixture was stirred at room temperature for an additional 30 minutes. Triethylamine (17.0 mmol, 2.37 ml) and $BF_3.OEt_2$ (18.6 mmol, 2.36 ml) were added, followed by stirring for 6 hours. The reaction mixture was washed with water and dried over $MgSO_4$. The solvent was removed under reduced pressure resulting in a dark brownish orange residue. The crude product was purified by column chromatography on silica with CH_2Cl_2 : hexane (50 : 50) as mobile phase which afforded an orange solid. Yield: 24 mg, 0.09 mmol, 9 %.

^{1}H NMR (400 MHz, CDCl$_3$): 7.-7.67 (2H, m), 7.58-7.56 (1H, m), 7.40-7.38 (1H, m), 7.18-7.16 (1H, m), 6.97-6.96 (2H, m), 6.45-6.44 (2H, m) ppm.

5.3.3.22   Bis(thien-2-yl-dipyrrinato)zinc(II) complex.

(NB-bis(dipyrrinato-1-)zinc(II))
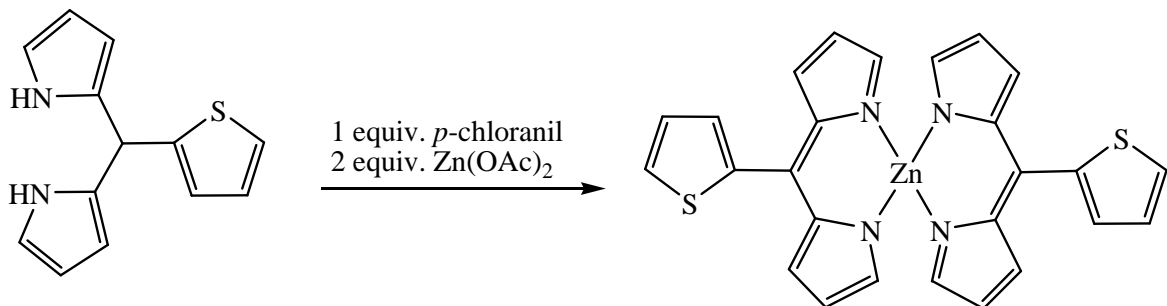
Bis(thien-2-yl-dipyrrinato)zinc(II) complex was prepared according to Lindsey's method.[22] Freshly distilled THF (15 ml) was charged with *meso* (thien-2-yl)dipyrromethane (0.87 mmol, 200 mg), an equimolar amount of *p*-chloranil (0.87 mmol, 215 mg) and an excess of $Zn(OAc)_2$ (2.19 mmol, 402 mg). The reaction mixture was stirred overnight at room temperature. TLC analysis indicated that no dipyrromethane remained at that time. The solvent was removed under reduced pressure and the residue was dissolved in $CHCl_3$. The organic phase was washed with aqueous $NaHCO_3$ and water and dried ($MgSO_4$). The crude product was purified by column chromatography on silica gel using $CHCl_3$: MeOH (98 : 2) affording an orange solid with a greenish surface lustre. Yield: 85 mg, 0.16 mmol, 38 %.

^{1}H NMR (400 MHz, $CDCl_3$): 7.54-7.53 (2H, m), 7.52-7.51 (4H, m), 7.42-7.40 (2H, m), 7.17-7.15 (2H, m), 7.04-7.03 (4H, m), 6.44-6.42 (4H, m) ppm.

5.4   Results

5.4.1   UV-vis absorbance studies

A UV-vis spectrum typical of a dipyrromethane and bis(dipyrrinato)zinc(II) complex is displayed in figure 10.   The electronic absorbance spectral features (λ_{max}) of the dipyrromethanes synthesised in this study are listed in table 1.   The absorbance spectrum of **Ph-DPM** has been previously reported in the literature.[22]
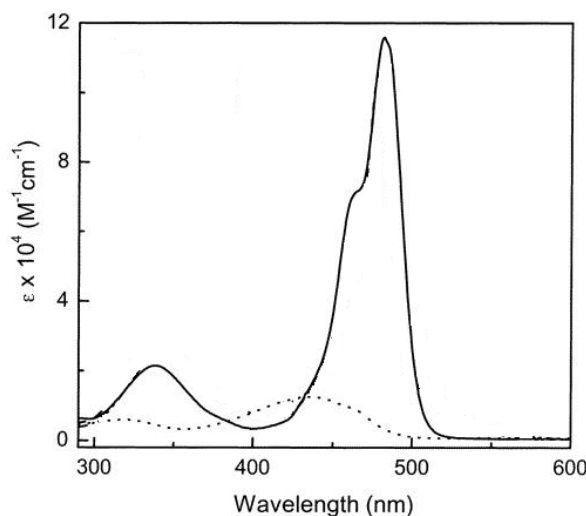
*Figure 10   Electronic absorbance spectra of **tert-butylphenyl-DPM** (------) and* **bis(tert-butylphenyl-dipyrrinato)zinc(II)** *(——) recorded in CH$_2$Cl$_2$.[22]*

Compound	λ_{max} (nm)
Ph-DPM	304, 422
Ms-DPM	316, 400
NB-DPM-1	314, 384, 428
NB-DPM-5	314, 330, 368, 466
NB-DPM-8	288, 310, 380, 402
NB-DPM-9	312, 364, 444
NB-BODIPY-1	286, 386, 484, 510
Bis(dipyrrinato-1)zinc(II)	344, 470, 492

Table 1   UV-vis absorbance data of dipyrromethanes and dipyrrins recorded in CH$_2$Cl$_2$

A relatively small change was observed in the absorbance spectra of the dipyrromethanes when the *meso* substituent was a thiophene (Fig. 11). **NB-DPM-1** showed absorbance features that stretched further in to the red region of the spectrum compared to the phenyl derivatives. However when the conjugation of the *meso* substituent was extended as in **NB-DPM-5**, **NB-DPM-8** and **NB-DPM-9** a significant increase in the high energy transitions was observed. Both **NB-DPM-5** and **NB-DPM-9** displayed increased intensity in the transition centred at 314 and 312 nm respectively, attributed to π-π* transitions localised on the thienylethynyl unit. **NB-DPM-8** showed a dramatic increase in absorbance with transitions observed at 288, 310, 380 and 402 nm. By analogy with transitions observed by Ziessel et al.[31] these transitions were assigned to π-π* transitions localised on the *meso* thienylethynylpyrene component.
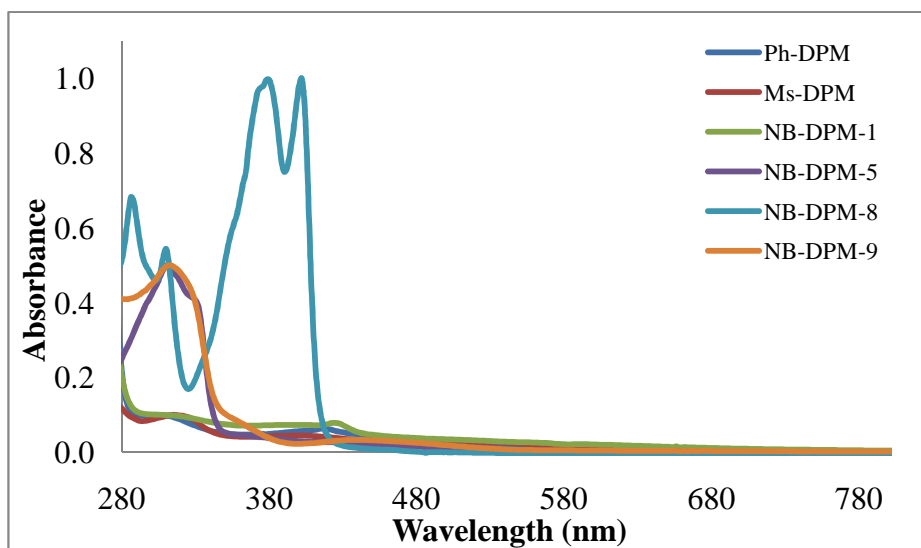
Figure 11   Electronic absorbance spectra of dipyrromethanes recorded in CH$_2$Cl$_2$.

Following coordination to $Co_2(CO)_6$, the UV-vis spectrum of **NB-DPM-8-Co$_2$(CO)$_6$,** displayed broader less well-defined bands that stretched out as far as 700 nm (Fig. 12). The low intensity absorbance bands in the range 490 – 620 nm were tentatively assigned to d-d transitions.
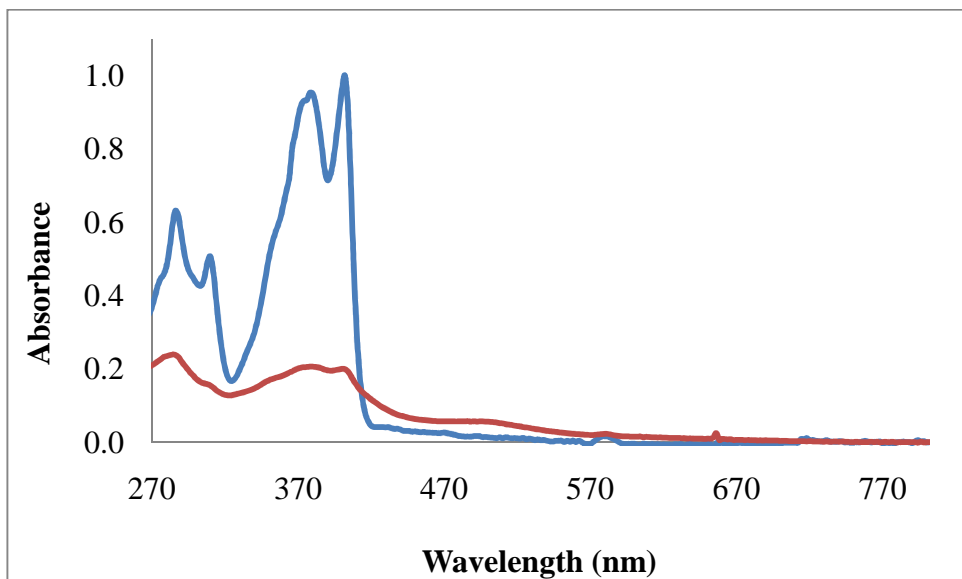
Figure 12   *Electronic absorbance spectra of **NB-DPM-8** (red line) and **NB-DPM-8-Co$_2$(CO)$_6$** (blue line) recorded in CH_2Cl_2.*

There is a dramatic change in the absorbance spectrum upon formation of the borondifluoride analogue, **NB-BODIPY-1** (Fig. 13). An intense absorbance band was observed at $\lambda = 510$ nm attributed to the $S_0{\rightarrow}S_1$ (π-π^*) transition on the dipyrrin with a virbonic overtone at *ca*. 484 nm. The $S_0{\rightarrow}S_2$ (π-π^*) transition appeared at $\lambda = 386$ nm. A third band at higher energy ($\lambda = 286$ nm) was previously ascribed to a π-π^* transition on the *meso* subunit.[30, 31] These transitions observed in the UV-vis spectrum agree well with those observed in other borondifluoride dipyrrin compounds.[31]
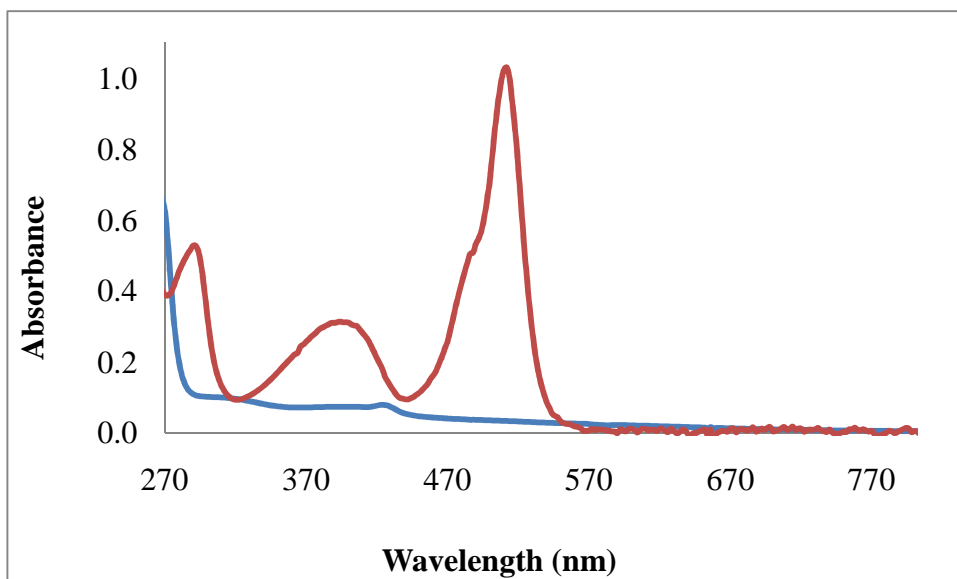
Figure 13   *Electronic absorbance spectra of* **NB-DPM-1** *(blue line) and* **NB-BODIPY-1** *(red line) recorded in* CH_2Cl_2.

The **bis(dipyrrinato-1)zinc(II)** complex displayed a $S_0 \rightarrow S_1$ transition with a λ_{max} at 494 nm with a vibronic overtone at 470 nm (Fig. 14). This was attributed to a π-π^* transition on the dipyrrin framework. The $S_0 \rightarrow S_2$ π-π^* transition was observed at $\lambda = 354$ nm.
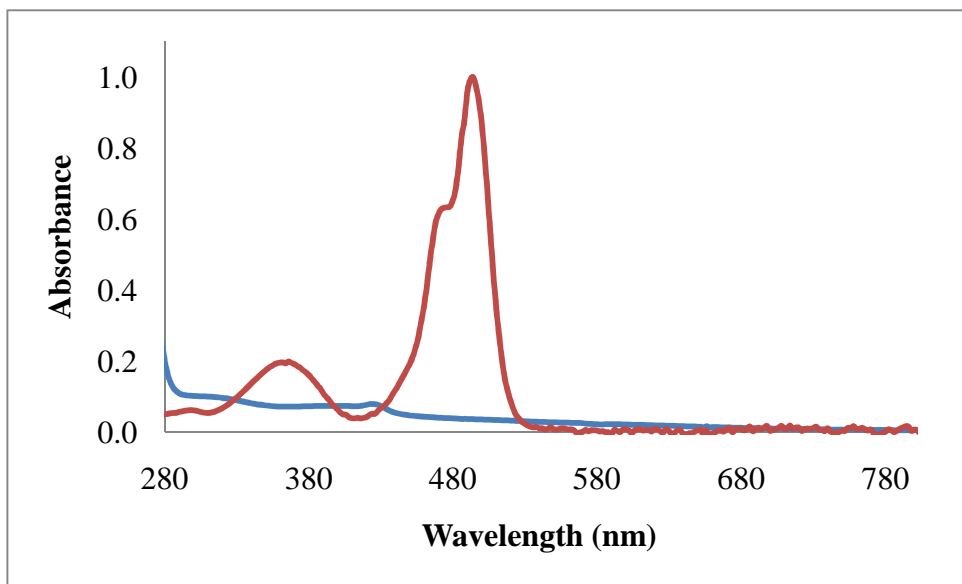
Figure 14   *Electronic absorbance spectra of* **NB-DPM-1** *(blue line) and* **bis(NB-dipyrrinato-1)zinc(II)** *(red line) in* CH_2Cl_2.

5.4.2 Steady state fluorescence studies

Room temperature emission studies of some of the compounds were carried out in CH_2Cl_2 (Fig. 15). Solutions were prepared such that they were isoabsorbtive at a selected wavelength having an optical density in solution of approximately 0.2 A.U. **Ph-DPM**, **Ms-DPM**, **NB-DPM-1** and **NB-DPM-9** were found to be only weakly emissive. The bromothiophene analogue, **NB-DPM-2**, showed increased fluorescence intensity as did **NB-DPM-5**. Table 2 below lists the emission maxima for the compounds studied.

Compound	λ_{em}	λ_{exc}
Ph-DPM	356, 418	300
Ms-DPM	360, 516	315
NB-DPM-1	359	315
NB-DPM-5	380	315
NB-DPM-8	410, 430	400
NB-DPM-9	357	315
NB-DPM-8-Co$_2$(CO)$_6$	410, 430	400

Table 2   *Fluorescence maxima of dipyrromethanes and dicobalt hexacarbonyl complex recorded in CH_2Cl_2 at room temperature. Absorbance = 0.2 at excitation wavelength.*
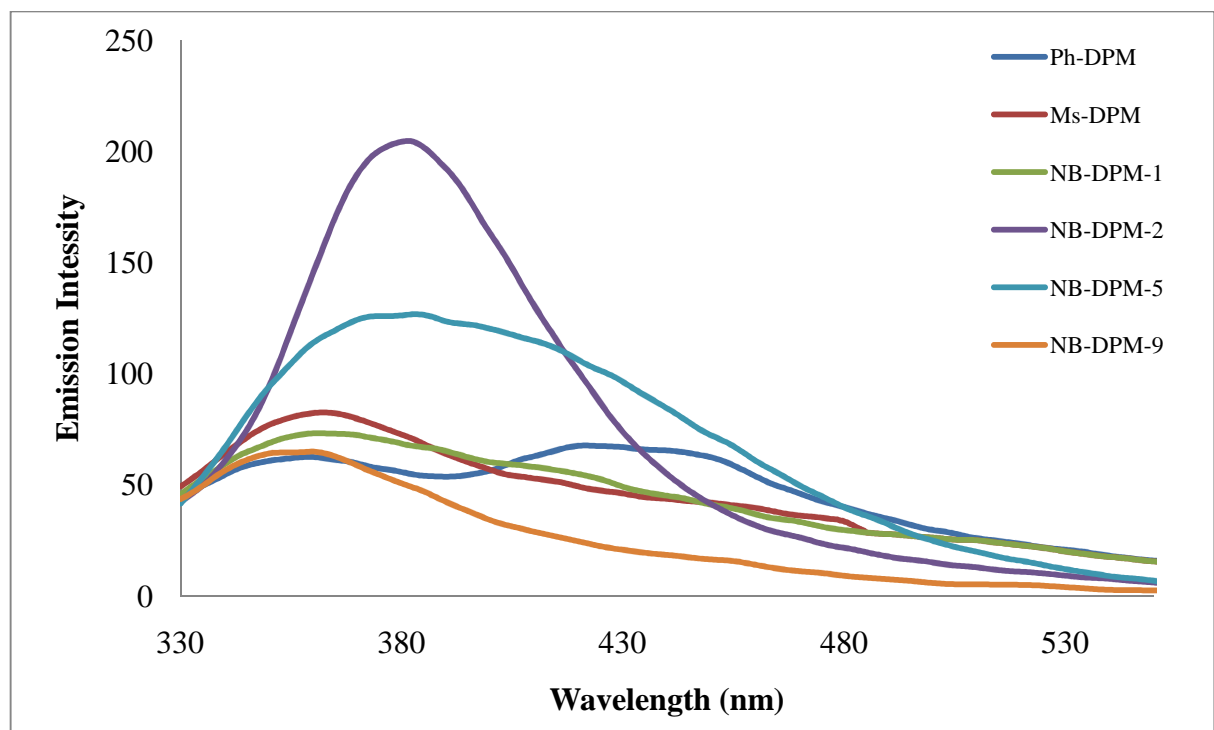
Figure 15 *Steady-state emission spectrum of dipyrromethanes recorded in CH_2Cl_2 at room temperature (λ_{exc} = 315 nm, abs. = 0.2 at 315 nm).*

Attachment of the fluorescent pyrenyl chromophore as in **NB-DPM-8** had a profound effect on the fluorescence of the dipyrromethane (Fig. 16). A substantial increase in the fluorescence intensity of the molecule was observed such that the emission silts were reduced by 75 % compared to all other dipyrromethanes. Two emission bands were observed at 408 and 430 nm typical of pyrene fluorescence.
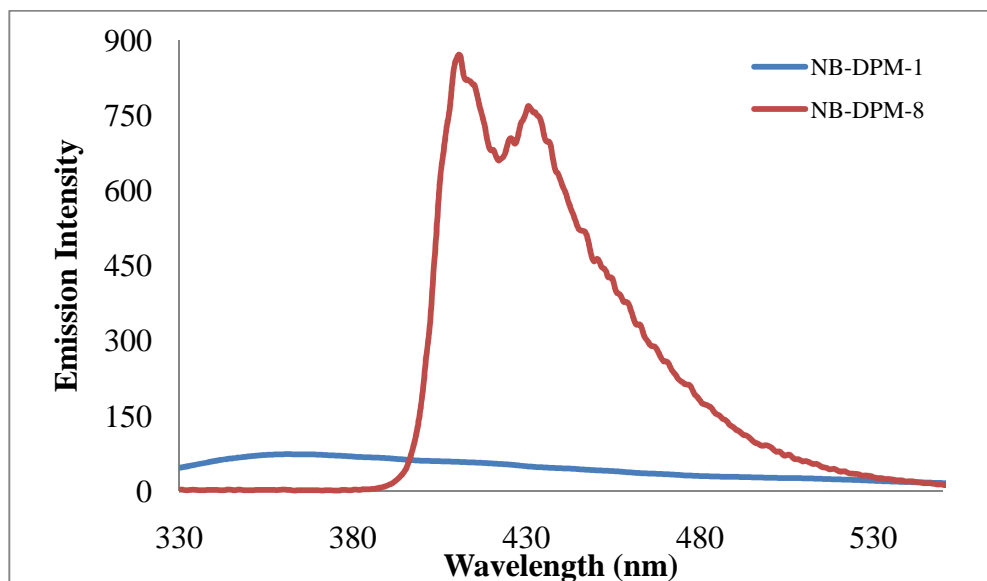
*Figure 16   Steady-state emission spectrum of **NB-DPM-1** and **NB-DPM-8** recorded in CH$_2$Cl$_2$ at room temperature (λ_{exc} = 315 nm, abs. = 0.2 at 315 nm). Slits reduced by 75 % for **NB-DPM-8** in comparison to **NB-DPM-1**.*

Following coordination of the dicobalt carbonyl moiety a reduction in emission intensity was observed (Fig. 17), however, there is no significant shift in the position of the band suggesting that the emission is ligand based without major MLCT contribution. The excitation spectra of the emissive compounds have the same profile as the corresponding absorbance spectra further suggesting that the emissive state is ligand based.
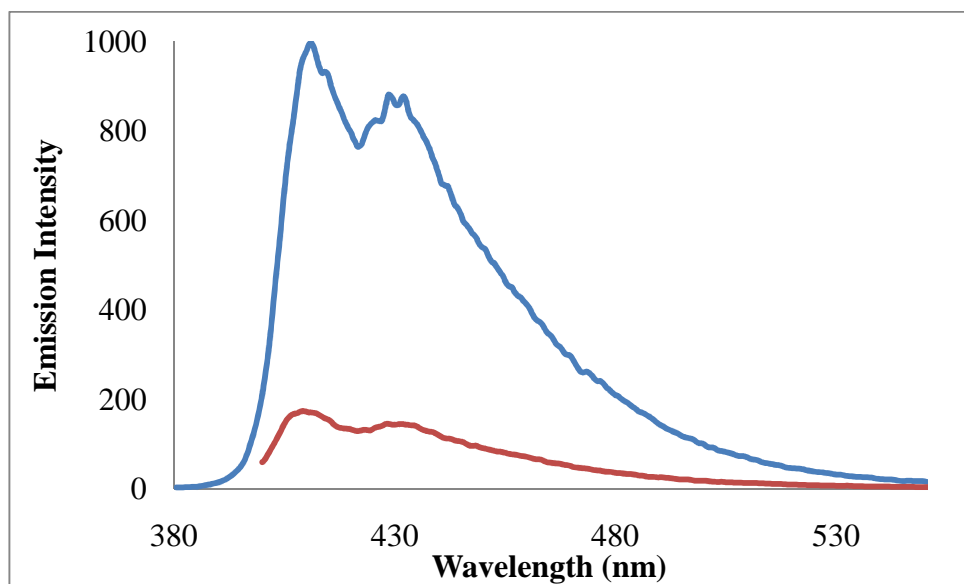
Figure 17   *Steady-state emission spectra of **NB-DPM-8** (blue line) and **NB-DPM-8-Co₂(CO)₆** (red line) recorded in CH₂Cl₂ at room temperature (λₑₓc = 400 nm, abs. = 0.2 at 400 nm).*

5.4.3   Steady state photolysis

Broadband photolysis of the dicobalt hexacarbonyl complex, **NB-DPM-1-Co$_2$(CO)$_6$**, at $\lambda_{exc} > 520$ nm for 10 minutes resulted in bleaching of the parent bands at 2091, 2057 and 2030 cm^{-1} and generation of weak product bands at 2062, 2023, 2006 and 1971 cm^{-1} (Fig. 18). Subsequent photolysis at $\lambda_{exc} > 410$ nm for 10 minutes resulted in an obvious increase in the intensity of these bands indicative of increased formation of the pentacarbonyl species **NB-DPM-1-Co$_2$(CO)$_5$(PPh$_3$)**. Irradiation at $\lambda_{exc} > 320$ nm for 5 minutes caused further depletion of the parent bands. The product band at 2062 cm^{1} also underwent depletion which indicated that the pentacarbonyl photoproduct was also undergoing a photoreaction to produce the tetracarbonyl species, **NB-DPM-1-Co$_2$(CO)$_4$(PPh$_3$)$_2$**. Product bands in the final IR difference spectrum were observed at 1974, 1962 and 1937 (br) cm^{-1}, which are indicative of (μ_2-alkyne)Co$_2$(CO)$_4$(L)$_2$ type species.[36]
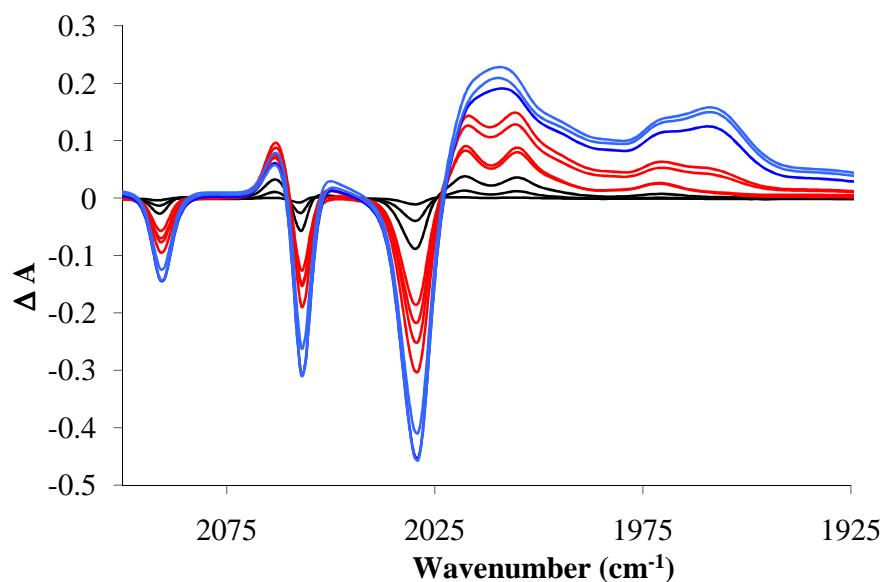
*Figure 18   Infrared difference spectra following broadband irradiation of **NB-DPM-1-Co$_2$(CO)$_6$** in hexane at $\lambda_{exc} > 520$ nm for 10 minutes (black lines, 10 minutes total irradiation), $\lambda_{exc} > 410$ nm for 10 minutes (red lines, 10 minutes total irradiation) and $\lambda_{exc} > 320$ nm for 5 minutes (blue lines, 5 minutes total irradiation). Negative bands indicate beaching of the parent complex while positive bands indicate formation of the pentacarbonyl and tetracarbonyl species.*

Extended broadband photolysis of the dicobalt hexacarbonyl complex, **NB-DPM-8-Co$_2$(CO)$_6$,** at $\lambda_{exc} > 520$ nm for 30 minutes, $\lambda_{exc} > 410$ nm for 60 minutes and $\lambda_{exc} > 320$ nm for 60 minutes showed only minor depletion of the parent hexacarbonyl bands (Fig. 19). New bands were generated at 1970 and 1926 cm^{-1}, however these bands were not indicative of pentacarbonyl or tetracarbonyl photoproducts. As this is such a highly fluorescent complex it is possible that it does not undergo photosubstitution reactions. One possible cause for the generation of these bands is photodecomposition of the pyrenyl dipyrromethane complex.
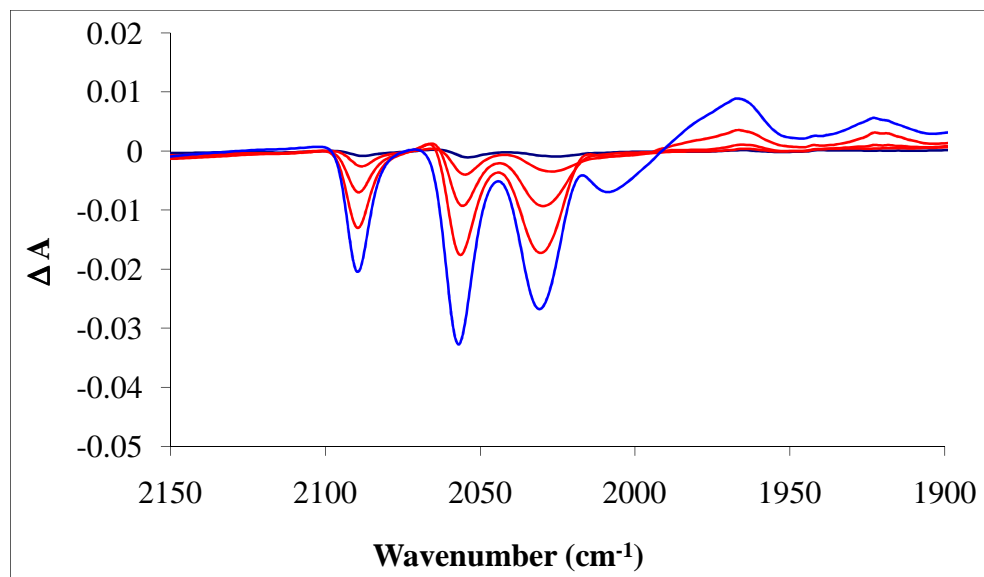
Figure 19   *IR difference spectra following broadband irradiation of* **NB-DPM-8-Co$_2$(CO)$_6$** *in hexane at $\lambda_{exc} > 520$ nm (black line, 30 minutes irradiation), $\lambda_{exc} > 410$ nm (red lines, 60 minutes total irradiation) and $\lambda_{exc} > 320$ nm (blue line, 60 minutes total irradiation).*

5.5　　Discussion

The reaction at room temperature of an aldehyde in an excess of pyrrole, catalysed with TFA, afforded the *meso* substituted dipyrromethanes. The dipyrromethanes were purified by column chromatography. The dipyrromethanes were prepared in yields of 18 – 43 %. The freebase dipyrromethanes were assessed for purity by TLC and characterised by ^{1}H NMR. The ^{1}H NMR spectra of all dipyrromethanes display complex coupling patterns derived from the protons on the dipyrromethane unit in addition to those on the *meso* aryl substituent. For the freebase dipyrromethanes a broad singlet was observed in the region 7.90 – 8.66 ppm that corresponds to the N-H pyrrolic protons. This signal shifted slightly further downfield for *meso* thien-2-yl substituted dipyrromethanes as the conjugation of the *meso* substituent increased following the order: **NB-DPM-1** (7.99 ppm), **NB-DPM-5** (8.03 ppm), **NB-DPM-6** (8.32 ppm). The peak related to CH on the methine bridge appeared at *ca.* 5.55 ppm It is worthy of note that dipyrromethanes are highly unstable and should be subsequently reacted with due haste to form the more stable BODIPY or bis(dipyrrinato)metal complexes.

Dipyrromethanes are known to have a low intensity broad band in the high energy region of the UV-vis spectrum.[22] The UV-vis spectra of the dipyrromethanes in this study showed similar absorbance bands. Absorbance bands with increased intensity were observed when the *meso* substituents was highly conjugated. These transitions were attributed to π-π* transitions on the *meso* moiety rather than the dipyrromethane itself.

However the UV-vis spectra of the dipyrrin compounds, **NB-BODIPY-1** and **NB-bis(dipyrrinato-1)Zn(II)**, revealed new transitions that were characteristic of π-π* transitions on the dipyrrin framework. The λ_{max} in each spectra (484 nm and 494 nm respectively) is bathochromically shifted with respect to borondifluoride phenyldipyrrin and bis(phenyldiyprrinato)Zn(II). Comparison of the homoleptic complexes showed a bathochromic shifted by 7 nm. This is comparable to the shift observed between *meso* tetra phenyl and thienyl porphyrins, **ZnTPP** (λ_{max} = 419 nm) and **ZnTThP** (λ_{max} = 429 nm). The conformation of the thienyl ring relative to the dipyrrin framework should be considered.

5.6   Conclusion

In this chapter experimental work was based on the synthesis of *meso* thien-2-yl dipyrromethane compounds and some related dipyrrin and metal carbonyl complexes. Some initial photophysical measurements were taken. This work was a preliminary investigation into thienyl based dipyrrin systems.

The phenyl group lies approximately perpendicular to the plane of the dipyrrin. Consequently, the phenyl group in not in full conjugation with the pyrrolic system and substituents on the phenyl ring will have minimal influence on the π system of the dipyrrin.

The red shifted spectrum of tetra thienyl porphyrins has been attributed to the co-planar arrangement of the thienyl groups and porphyrins macrocycle. It is therefore likely this is the cause of the bathochromically shifted spectra of the dipyrrin complexes.

As observed in chapter 2 thienyl substitution of porphyrin systems altered the photophysical and electrochemical properties of the macrocycle, thus great promise lies in the potential of thienyl based dipyrrin complexes. Further work related to these systems is discussed in chapter six.

5.6   Bibliography

1   (a) K.C. Braaten, D.G. Gordon, M.M. Aphibal, G.R. Geier III, *Tetrahedron*, **2008**, 64, 9828. (b) J.S. Lindsey, *Accounts of Chemical Research,* **2010**, 43, 300.

2   R. Ziessel, G. Ulrich, A. Harriman, *New J. Chem.,* **2007**, 31, 496.

3   (a) A. Treibs, N. Haberle, *Leibigs. Ann. Chem.*, **1968**, 718, 183, (b) P.S. Clezy, G.A. Smythe, *Aust. J. Chem.*, **1969**, 22, 239.

4   A.H. Jackson, R.K. Pandey, K.R.N. Rao, E. Roberts, *Tet. Lett.*, **1985**, 26, 793.

5   S.E. Bari, J. Iturraspe, B. Frydman, *Tetrahedron*, **1995**, 51, 2255.

6   (a) S.J. Vigamond, M.C. Chang, K.M.R. Kallury, M. Thompson, *Tet. Lett.*, **1994**, 35, 2455. (b) G. Shipps Jr., J. Rebek Jr., *Tet. Lett.,* **1994**, 35, 6823.

7   D. Hammel, P. Erk, B. Schuler, J. Heinze, K. Müllen, *Adv. Mater.*, **1992**, 4, 737.

8   C.H. Lee, J.S. Lindsey, *Tetrahedron*, **1994**, 50, 11427.

9   B.J. Littler, M.A. Miller, C.-H. Hung, R.W. Wagner, D. O'Shea, P.D. Boyle, J.S. Lindsey, *J. Org. Chem.*, **1999**, 64, 1391

10   J.K. Laha, S. Dhanalekshmi, M. Taniguchi, A. Ambroise, J.S. Lindsey, *Organic Process Research and Development*, **2003**, 7, 799.

11   A.J.F.N. Sobral, N.G.C.L. Rebanda, M da Silva, S.H. Lampreia, M. Ramos, Silva, A. Matos, Beja, J.A. Paixão, A.M. d'A. Rocha Gonsalves, *Tet. Lett.*, **2003**, 44, 3971.

12   R. Naik, P. Joshi, S.P. Kaiwar, R.K. Deshpande, *Tetrahedron*, **2003**, 59, 2207.

13   M. D'Auria, E. De Luca, V. Esposito, G. Mauriello, R. Racioppi, *Tetrahedron*, **1997**, 53, 1157.

14   N. Maiti, J. Lee, Y. Do, H. Soo Shin, D.G. Churchill, *J. Chemical Crystallography*, **2005**, 35, 949.

15   T.E. Wood, A. Thompson, *Chem. Rev.*, **2007**, 107, 1831.

16   (a) C.R. Porter, *J. Chem. Soc.*, **1938**, 368. (b) R.J. Motekaitis, A.E. Martell, *Inorg. Chem.*, **1970**, 9, 1832.

17   (a) M.A.T. Rogers, *J. Chem. Soc.*, **1943**, 596. (b) A.H. Corwin, M.H. Melville, *J. Am. Chem. Soc.*, **1955**, 77, 2755.

18   Y. Murakami, Y. Matsuda, K. Sakata, *Inorg. Chem.*, **1971**, 10, 1728. (b) Y. Zhang, Z. Wang, C. Yan, G. Li, J. Ma, *Tet. Lett.*, **2000**, 41, 7717.

19   C. Brückner, V. Karunaratne, S.J. Rettig, D. Dolphin, *Can. J. Chem.*, **1996**, 74, 2182.

20   S.R. Halper, S.M. Cohen, *Chem. Eur. J.*, **2003**, 9, 4661.

21   (a) C. Brückner, Y. Zhang, S.J. Rettig, D. Dolphin, *Inorg. Chim. Acta.*, **1997**, 263, 279.

22   L. Yu, K. Muthukumaran, I.V. Sazanovich, C. Kirmaier, E. Hindin, J.R. Diers, P.D. Boyle, D.F. Bocian, D. Holten, J.S. Lindsey, *Inorg. Chem.*, **2003**, 42, 6629.

23   I.V. Sazanovich, C. Kirmaier, E. Hindin, L. Yu, D.F. Bocian, J.S. Lindsey, D. Holten, *J. Am. Chem. Soc.*, **2004**, 126, 2664.

24   (a) R.P Haugland, *Handbook of Fluorescent Probes and Research Chemicals*, 9th Ed.; Molecular Probes Inc.: O.R. Eugene, 2002. (b) In *Molecular Probes*; Invitrogen Corporation: Carlsbad, CA, USA, **2006.**

25   (a) F. Lopez Arbeloa, J. Banuelos, V. Martinez, T. Arbeloa, I. Lopez Arbeloa, *Int. Rev. Phys. Chem.*, **2005**, 24, 339. (b) A. Loudet, K. Burgess, *Chem. Rev.*, **2007**, 107, 4891.

26   F. Li, S.I. Yang, Y. Ciringh, J. Seth, C.H. Martin III, D.L. Singh, D. Kim, R.R. Birge, D.F. Bocian, D. Holten, J.S. Lindsey, *J. Am. Chem. Soc.*, **1998**, 120, 10001.

27   (a) G. Ulrich, R. Ziessel, A. Harriman, *Agnew. Chem. Int. Ed.*, **2008**, 47, 1184.

28   H.L. Kee, C. Kirmaier, L. Yu, P. Thamyongkit, W.J. Youngblood, M.E. Calder, L. Ramos, B.C. Noll, D.F. Bocian, W.R. Schiedt, R.R. Birge, J.S. Lindsey, D. Holten, *J. Phys. Chem.*, **2005**, 109, 20433.

29   (a) J. Rochford, A.D.Rooney, M.T. Pryce, *Inorg. Chem.*, **2007**, 46, 7247. (b) A.K. Burell, W.M. Campbell, D.L. Officer, S.M. Scott, *J. Chem. Soc., Dalton Trans.*, **1999**, 3349.

30   M. Rajeswara Rao, K.V. Pavan Kumar, M. Avikanth, *J. Organomet. Chem.*, **2010**, 695, 863.

31   R. Ziessel, C. Goze, G. Ulrich, M. Cesario, P. Retailleau, A. Harriman, J.P. Rostron, *Chem. Eur. J.*, **2005**, 11, 7366.

32   N.M. Boyle, J. Rochford, M.T. Pryce, *Coord. Chem.. Rev.*, **2010**, 254, 77.

33   (a) K. Sonogashira, Y. Todha, N. Hagihara, *Tet. Lett.*, **1975**, 4467. (b) E.I. Negishi, L. Anastacia, *Chem. Rev.*, **2003**, 103, 1979.

34   (a) W.B. Austin, N. Bilow, W.J. Kellaghan, K.S.Y. Lau, *J. Org. Chem.*, **1981**, 46, 2280. (b) J. Rochford, Ph.D. Thesis, Dublin City University, **2004**.

35   Z. Li, R. Bittman, *J. Org. Chem.*, **2007**, 72, 8376.

36   (a) A.C Coleman, M.T. Pryce, *Inorg. Chem.,* **2008**, 47, 10980. (b) A. Arnanz, M.L. Marcos, C. Moreno, D.H. Farrar, A.J. Lough, J.O. Yu, S. Delgado, J. Gonzalez-Velasco, *J. Organomet. Chem.,* **2004**, 689, 3218.

Chapter 6

Conclusions and future work

Chapter six provides a condensed review of the experimental findings from this study. A number of experiments that could be completed in order to advance our understanding of some of the photochemical processes that occurred in various chapters throughout this thesis are suggested.

6.1.1 Future work for chapter 2

Porphyrins **NB-ZnP1 – NB-ZnP3** were synthesised with substituents at the thien-5-yl position. This induced bathochromic shifts in the UV-vis and fluorescence spectra. The absorbance spectra and FWHM values of the Soret band indicated that there was increased coupling of the thienyl and porphyrin π systems. A reduction in singlet and triplet lifetimes was observed which was in agreement with lifetime data published previously.

The thien-2-yl porphyrins substituted at the thien-4-yl position, **NB-ZnP4** and **NB-ZnP5** were very interesting. There was little of no change in their absorbance spectra with respect to **ZnTThP**. This indicated that the conjugation between the substituents on the thienyl moiety and the porphyrin macrocycle was not as effective as that observed in **NB-ZnP1 – NB-ZnP3**. However, there was a significant increased in the triplet lifetimes of both these porphyrins when compared to **ZnTThP**. This would suggest that the conformation of the thien-2-yl substituents with respect to the porphyrin macrocycle is changed when the *meso* thienyl rings are substituted at the thien-4-yl position and that caused the increase in lifetime as opposed to conjugation within the *meso* substituents. Future work should include obtaining a crystal structure of the porphyrins to check the conformation.

The phenyl porphyrins, **NB-ZnP6** and **NB-ZnP7**, should adopt an idealised orthogonal arrangement with respect to the porphyrin plane and in doing so the π systems of the porphyrin and *meso* substituents will no longer overlap. The absorbance spectra of the phenyl porphyrins was bathochromically shifted with respect to **ZnTPP** and there was a significant change in the fluorescence profile although the lifetimes were only slightly altered. The most perceptible change was the triplet lifetime of **NB-ZnP7** which was double that of **ZnTPP**. Clearly there is a contribution from the *meso* substituents even though the conformation prevents coupling of the π systems. A crystal structure of **NB-ZnP7** would allow further analysis of the conformation of the *meso* substituents and therefore the degree of π overlap.

These results show that varying the structure in thienyl porphyrins does induce changes in the general types of spectra as well as the lifetimes associated with the excited states. The changes observed in the spectra of **NB-ZnP4** – **NB-ZnP7** are not a result of the increased coupling of the π systems. The crystal structures of these porphyrins will provide information about the conformation of the *meso* thienyl and phenyl rings with respect to the porphyrin macrocycle. This may prove that the increased lifetimes observed were due to the conformation of the porphyrin systems.

In this porphyrin study, the effect of conjugation *vs.* conformation was investigated for the porphyrins in series **2** (Fig. 1). The majority of the porphyrins depicted in figure 1 have been synthesised and their photophysical properties reported in chapter 2. The remaining porphyrins from series **1** and **3** (Fig. 1) should be synthesised and have their ground and excited states examined. The results obtained could then be compared to those reported for series **2**. This would provide further experimental evidence to support the arguments discussed in this chapter.
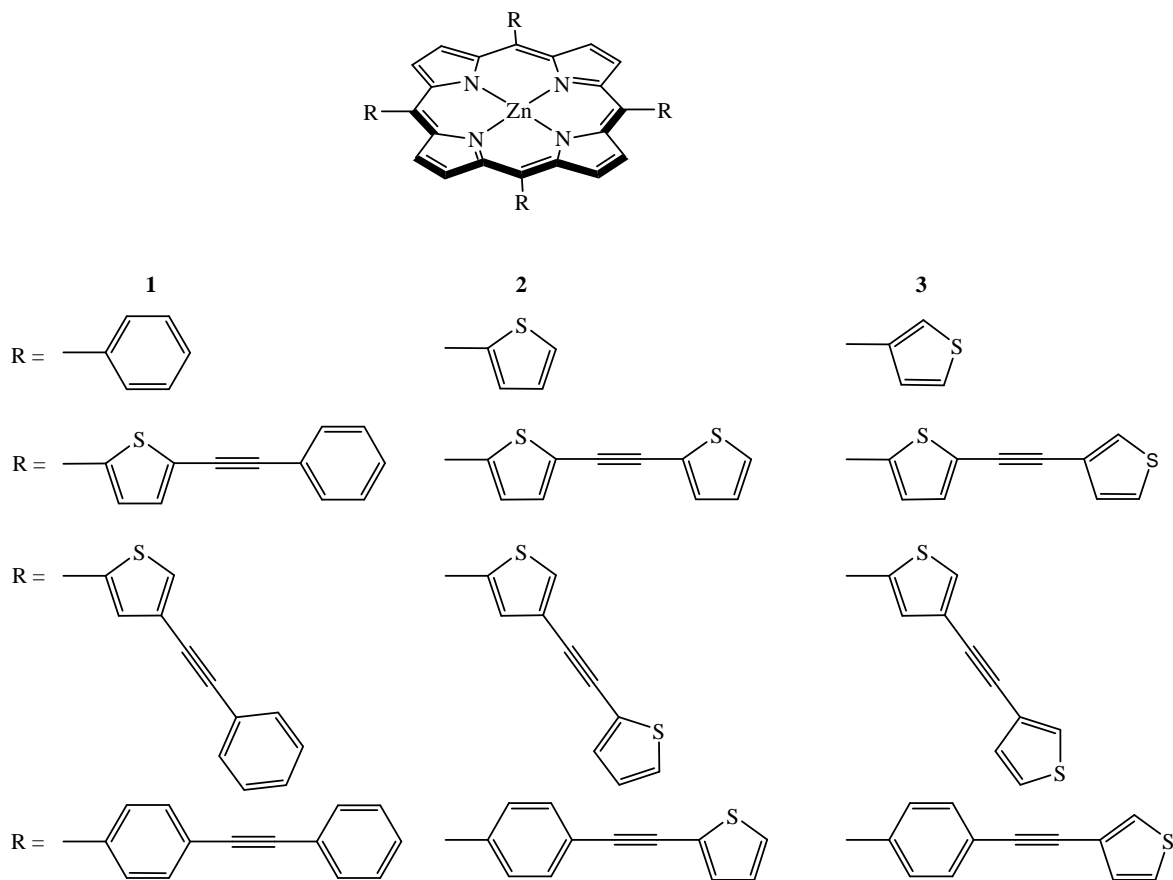
Figure 1   Three series of porphyrins with various (aryl)ethynyl) spacers.

In PDT of cancer, a photosensitiser, visible light and oxygen are combined to produce lethal agents which destroy or inactivate tumour cells. In is widely agreed that singlet oxygen is the primary cytotoxic agent responsible for the photobiological activity. Photosensitisers should exhibit the following properties: high extinction coefficients in the spectral region of excitation, a triplet state with appropriate energy to allow efficient energy transfer to ground state oxygen and long lived triplet state lifetimes ($\tau_T > 1$ µs) with high quantum yields ($\Phi_T > 0.4$). The quantum yield of singlet oxygen formation, Φ_Δ, is dependent on the quantum yield of the triplet state of the sensitiser, Φ_T. Porphyrins **NB-ZnP7**, **NB-ZnP6** and to a lesser extent **NB-ZnP4** all possess triplet lifetimes that are sufficiently long to interact with ground state oxygen and generate singlet excited state oxygen. Future work on these porphyrins should include a quantum yield investigation of singlet oxygen generation.

395

6.1.2 Future work for chapter 3

Steady state photolysis, carried out in the dicobalt hexacarbonyl complexes, resulted in CO loss and quantum yields for the CO loss process indicated that the photochemical process is wavelength dependant. The quantum yield of CO loss was highest when the sample was irradiated at high energy (λ_{exc} = 313 and 365 nm). At 405 nm all quantum yields were found to be less than 5 %. However the quantum yield increased with λ_{exc} = 546 nm. The CO loss process ranged from 5 – 23 %. This was unexpected given that the absorbance bands at 546 nm are weaker transitions than those at 405 nm. This is a puzzling aspect to the quantum yields of CO loss and repeat experiments will need to be carried out to verify the validity of this result.

The photochemical activation of (μ_2-alkyne)$Co_2(CO)_6$ complexes was studied by ps-TRIR and combined theoretical calculations allowed for the identification of the formation of a triplet diradical species, following excitation at 400 nm and 532 nm. The radical species rapidly recombined to regenerate the parent complex, with no evidence for CO loss arising from this species. Lifetimes for the triplet diradical species were in the range 38 – 71 ps. The quantum yield of CO loss was low with 400 nm irradiation. Future work to improve the competitiveness of the CO loss pathway may consist of the inclusion of a luminescent chromophore in the (μ_2-alkyne)$Co_2(CO)_6$ complex. Coleman et al. reported that complexation of luminescent pyrene-thiophene dyads with $Co_2(CO)_6$ significantly quenched ligand based emission, possibly as a result of energy transfer from the luminescent pyrene moiety to the cobalt metal centre.[1] A ps-TRIR investigation into such complexes would reveal whether this resulted in increased CO loss on the ps timescale.

The observation of competing pathways to CO loss allows for a better understanding of the photochemical properties of (μ_2-alkyne)$Co_2(CO)_6$ complexes in developing a photochemically driven catalytic approach in the Pauson Khand reaction.

6.1.3 Future work for chapter 4

Picosecond TRIR studies were carried out on **pyridine-W(CO)$_5$** in THF. Excitation of **pyridine-W(CO)$_5$** at 400 nm resulted in photodissociation of the metal pentacarbonyl moiety with subsequent coordination to a solvent molecule within 1 ps. Over 100 ps, rearrangement of the initially formed σ H bond between the tungsten pentacarbonyl and THF to the more stable (CO)$_5$Cr-η^1(O)THF photoproduct occurred. This is the first report detailing the rearrangement of metal pentacarbonyl species in THF solution. Further studies could include temperature dependant kinetics at 400 nm excitation and investigation of the reaction dynamics in other coordinating solvents. **Pyridine-Cr(CO)$_5$** should also be investigated to delineate the effect of the Cr atom on the reaction kinetics.

Excitation of **MPyTPP-Cr(CO)$_5$** at 532 nm resulted in photodissociation of the metal pentacarbonyl moiety, with subsequent coordination to a solvent molecule within 1 ps, and rearrangement of the initially formed σ H bond between the chromium pentacarbonyl and the THF to the more stable (CO)$_5$Cr-η^1(O)THF photoproduct. This is surprising since at 532 nm it is the porphyrin S$_1$ excited state that is populated. The result would indicate that there is good communication between the porphyrin macrocycle and the metal pentacarbonyl even though they are connected through the pyridyl moiety which lies orthogonal to the porphyrin plane, thus preventing overlap of the π systems. Further ps-TRIR studies should be carried out on the remaining porphyrin complexes at 532 nm in various solvents.

Irradiation of all porphyrin complexes at 400 nm resulted in formation of a porphyrin based excited state that decayed in less than 100 ps to regenerate the parent porphyrin complexes. Excitation at 400 nm of the porphyrin complexes would populate the S$_2$ state, rapid internal conversion to the S$_1$ excited state should occur. Thus the photochemistry was expected to be similar to that observed following 532 nm excitation. As TRIR only provides information about the carbonyl moiety, little information about the porphyrin excited state can be garnered from these results. There is a radial redistribution of electron density in the porphyrin macrocycle which results in less electron density on the metal (M = W or Cr).

This resulted in less backbonding on the carbonyl ligands thus the observed IR bands of the transient species were at higher energy. For both tungsten and chromium analogues evidence for both $(THF)Cr(CO)_5$ and $(THF)W(CO)_5$, were present in the final spectra (1 ns), *albeit* the IR bands were weak. Spectroelectrochemistry with IR detection should be carried out in order to aid the identification of the porphyrin excited state formed and the relaxation pathway it follows.

6.1.4 Future work for chapter 5

In view of the preliminary synthesis undertaken for *meso* thien-2-yl dipyrromethanes, the synthesis of the borondifluoride dipyrrin complexes and bis(dipyrrinato)zinc(II) complexes is an attractive prospect. It is anticipated that the former complexes may possess unique photophysical properties typical of BODIPYs that is intense absorbance and fluorescence spectroscopy. The dipyrromethane analogue, *meso* (5-pyrenylethynylthien-2-yl)dipyrromethane, should form a BODIPY complex similar to that reported by Ziessel et al., with the *meso* phenyl moiety replaced by a thienyl group. Inefficient energy transfer from pyrene fragment to the BODIPY framework was observed by Ziessel attributed to the arrangement of the dipyrrin framework and the *meso* phenyl substituents.[2] Similarly, the *meso* (5-ferrocenylethynylthien-2-yl)dipyrromethane, should form a BODIPY complex similar to that reported by Rao and co-workers [3] where the ferrocenyl moiety quenched the fluorescence of the complex but oxidation of the complex "switched on" the fluorescence. Of the dipyrrins produced by Rao et al. no fluorescence switching was observed for the complex that linked the ferrocene and dipyrrin through a *meso* phenylethynyl moiety. The authors ascribed this to lack of communication between the two components due to conformation. The combined studies of Rochford et al.[4] and Brückner et al.[5] of thienyl porphyrins showed considerable electronic communication between the thienyl and porphyrin π systems in both the ground and excited states. The relatively strong coupling of the two π systems was attributed in part to co-planar arrangement of the thienyl ring with respect to the porphyrin macrocycle. Assuming that the thienyl moiety would adopt a comparable co-planar arrangement with respect to the BODIPY framework, similar enhancements of both the ground and excited states should occur.

6.2 Bibliography

1   A. Coleman, M.T. Pryce, *Inorg. Chem.,* **2008**, 47, 10980.

2   R. Ziessel, C. Goze, G. Ulrich, M. Cesario, P. Retailleau, A. Harriman, J.P. Rostron, *Chem.. Eur. J.*, **2005**, 11, 7366

3   M. Rajeswara Rao, K.V. Pavan Kumar, M. Avikanth, *J. Organomet. Chem.*, **2010**, 695, 863.

4   J. Rochford, S. Botchway, J.J. McGarvey, A.D. Rooney, M.T. Pryce, *J. Phys. Chem.*, **2008**, 112, 11611.

5   C. Brückner, P.C.D. Foss, J.O. Sullivan, R. Pelto, M. Zeller, R.R. Birge, G. Crundwell, *Phys. Chem. Chem. Phys.*, **2006**, 8, 2402

Appendix

A   **Sample preparation for laser flash photolysis.**

All samples were prepared for laser flash photolysis in a quartz fluorescence cell which was attached to a glass degassing bulb. The appropriate porphyrin was dissolved in the appropriate spectrophotometric grade solvent and the solution was filtered to avoid the presence of light scattering particles. The concentration of porphyrin in each sample was adjusted so that the absorbance at the excitation wavelength (λ_{exc} = 532 or 355 nm) was 0.08 ± 0.02 absorbance units. The sample was then degassed by three cycles of a freeze-pump-thaw procedure to 10^{-3} Torr, followed by a substantial liquid pump phase in order to remove trace quantities of water and carbon dioxide not removed in the degassing procedure. One atmosphere of argon was then placed over the sample under the guidance of a pressure gauge.

Laser flash photolysis was carried out and monitored in the range of 800 – 300 nm, with the aid of filters for λ > 500, 400 and 320 nm to reduce excessive photodegradation of the sample. The UV-vis absorbance spectrum was recorded before and after each flash photolysis experiment and also after every 5 – 15 strikes of the laser (depending on sample sensitivity) to observed any possible spectral changes and to ensure sample stability.[1]

B1 Electrochemistry of NB-L2 and NB-C2

For **NB-L2**, the irreversible oxidation of the thienyl group was observed at +1.78 V *vs.* Fc/Fc$^+$ (Fig. B1, a).[2] No further oxidations were observed at higher potentials. Potential cycling over the peak potential produced deposition on the electrodes and the redox response became progressively distorted. The cyclic voltammogram of **NB-C2** (Fig. B1, b) contains the previously mentioned irreversible oxidation of the thienyl unit at approximately +1.72 V *vs.* Fc/Fc$^+$. A second irreversible oxidation wave is also observed at +0.88 V *vs.* Fc/Fc$^+$, and is assigned to the oxidation of the cobalt centre. The irreversible reduction of the metal centre is observed at -1.05 V *vs.* Fc/Fc$^+$. The radical anion then undergoes fast decomposition into several fragments including Co(CO)$_4^-$ as is evidenced by the oxidation at -0.13 V. This is in good agreement with the results published by Arnanz et al.[3] Another new oxidation peak at -0.12 V and reduction peak at -0.77 V *vs.* Fc/Fc$^+$ were also observed and these are ascribed to decomposition products followed by reduction of the chemically adsorbed cobalt containing product on the electrodes.[4]
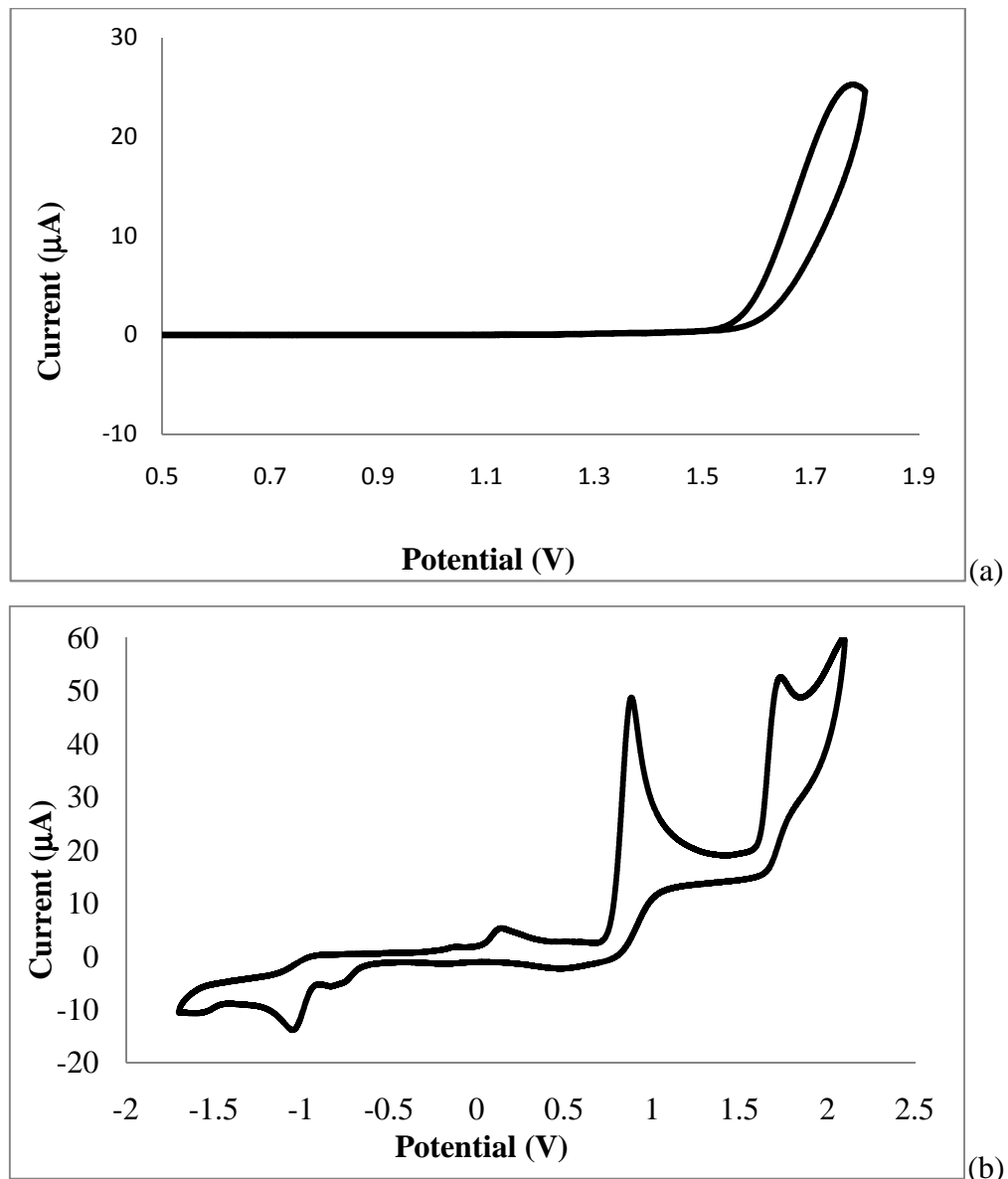
*Figure B1   Cyclic voltammogram of **NB-L2** (a) and **NB-C2** (b) showing oxidation and reduction waves.*

B2   **Electrochemistry of NB-L3 and NB-C3**

The dithien-2-ylacetylene ligand, **NB-L3**, proved easier to oxidise than **NB-L1** and **NB-L2**. The single irreversible oxidation wave was observed at E_{pa} = +1.47 V *vs*. Fc/Fc$^+$ (Fig. B2, a). Zotti et al. reported the oxidation of dithien-2-ylacetylene at E_{pa} = +1.07 V.[5] However the authors used a different supporting electrolyte (0.1 M Et$_4$NClO$_4$) which may account for the difference in oxidation potential. Potential cycling over the peak potential caused rapid deposition onto the electrode indicating that material degradation (overoxidation) or electropolymerisation occurred. Cyclic voltammetry of the related complex **NB-C3** produced two irreversible oxidation waves due to the metal centre and thienyl moiety at +0.91 and +1.41 V *vs*. Fc/Fc$^+$ respectively (Fig. B2, b). The irreversible reduction of the cobalt occurred at -1.33 V *vs*. Fc/Fc$^+$. Continued sweeps indicated that the reduction process was followed by decomposition as the oxidation at +0.15 V is indicative of the oxidation of the Co(CO)$_4^-$ fragment. Further sweeps lead to loss of all characteristic oxidation and reduction potentials.
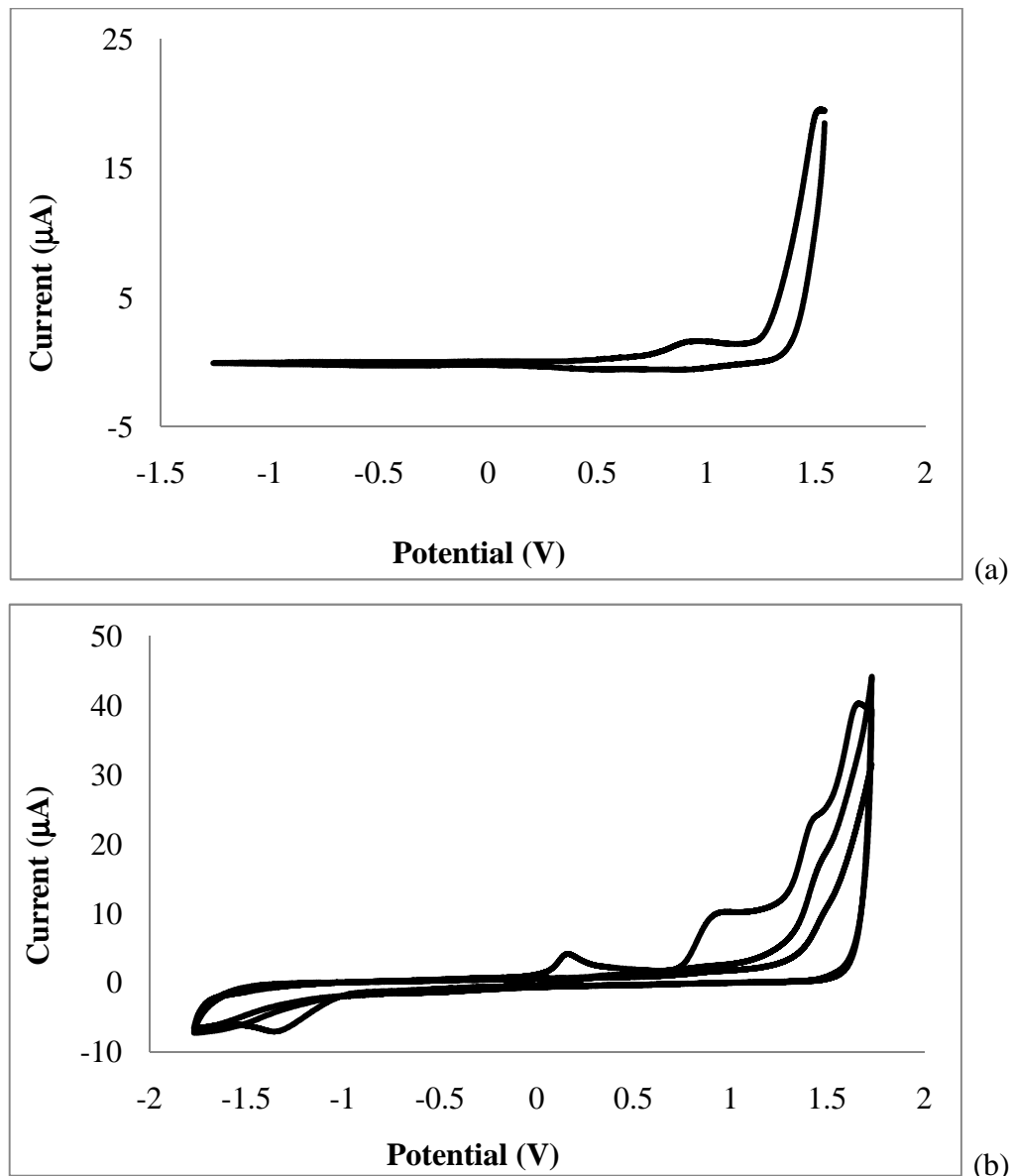
Figure B2   *Cyclic voltammogram of **NB-L3** (a) and **NB-C3** (b) showing oxidation and*
         *reduction waves. The CV of **NB-C3** shows loss of all wave definition due to*
         electropolymerisation and/or overoxidation.

B3 **Electrochemistry of NB-L4 and NB-C4**

Cyclic voltammetry on **NB-L4** provided a comparable oxidation wave at +1.55 V *vs.* Fc/Fc$^+$ (Fig. B3, a). Successive redox cycles resulted in deposition on the working and counter electrode and caused loss of all wave definition. The CV of **NB-C4** (Fig. B3, b) shows an irreversible oxidation due to the thienyl group at +1.58 V *vs.* Fc/Fc$^+$ and the irreversible oxidation of the cobalt unit at +0.88 V *vs.* Fc/Fc$^+$. The reduction of the metal centre was observed at -0.97 V *vs.* Fc/Fc$^+$. In subsequent sweeps an oxidation at +0.17 V was observed along with a new small anodic peak at +0.59 V *vs.* Fc/Fc$^+$ and two new cathodic waves at -0.22 V and -0.75 V. These smaller peaks, produced after the initial oxidation and reduction cycles, are a result of decomposition and deposition onto the working and counter electrodes.


(a)

(b)
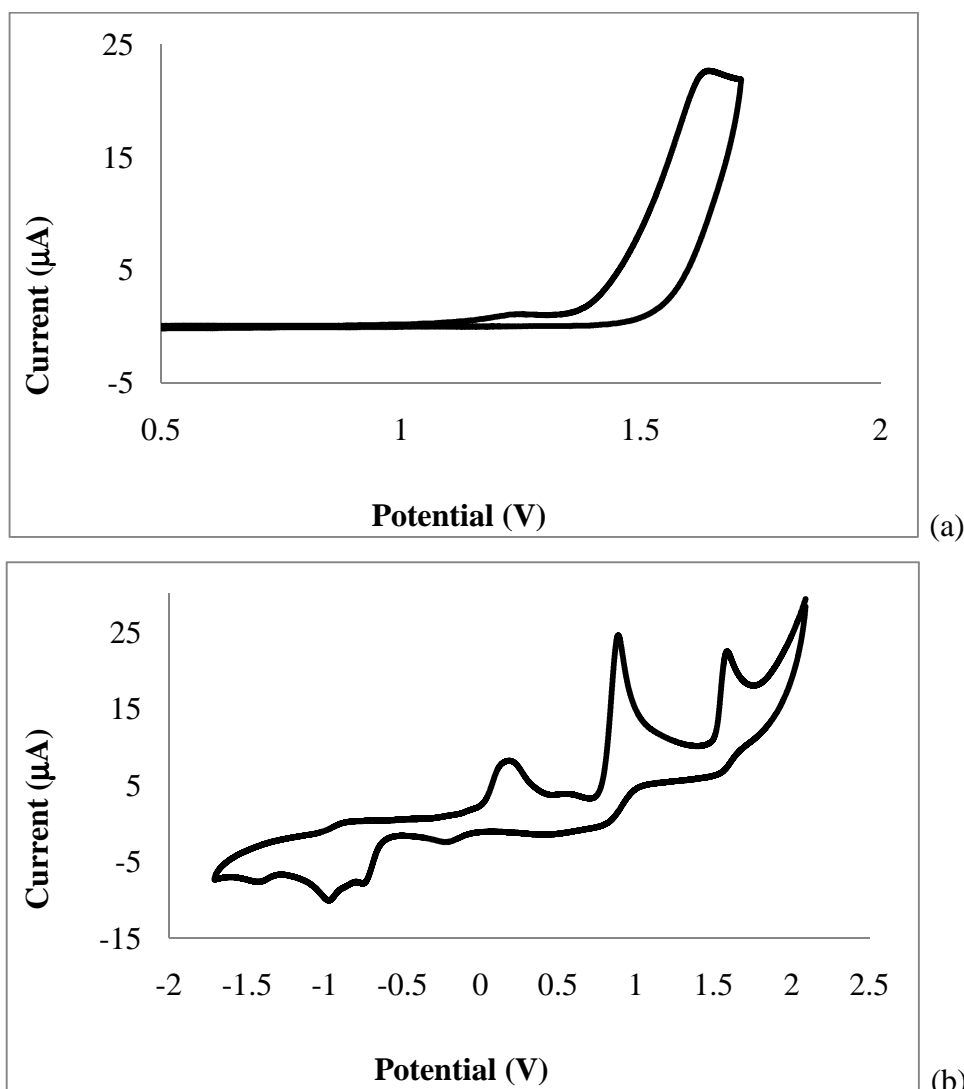
Figure B3   *Cyclic voltammogram of **NB-L4** (a) and **NB-C4** (b) showing oxidation and reduction waves.*

B4   Electrochemistry of NB-L5 and NB-C5

The cyclic voltammogram of the bromothiophene analogue, **NB-L5**, also exhibits an irreversible oxidation process at +1.72V *vs.* Fc/Fc$^+$ attributed to the oxidation of the thienyl moiety (Fig. B4, a). This is higher than the oxidation potential of the thiophene observed in **NB-L1** (+1.65 V *vs.* Fc/Fc$^+$) where the 5' position is occupied by a H atom rather than a Br. Displayed in figure B4 (b) is the cyclic voltammogram of **NB-C5**. As expected an irreversible oxidation is observed at +0.96 V *vs.* Fc/Fc$^+$ of the coordinated Co carbonyl unit. This assignment is based on comparison with the peak position of $Co_2(CO)_6$ coordinated complexes observed by Esho et al.[6] Irreversible oxidation of the thienyl moiety was observed at +1.76 V *vs.* Fc/Fc$^+$. The irreversible reduction of the cobalt centre is displayed at -1.16 V *vs.* Fc/Fc$^+$. In the subsequent sweep an oxidation wave attributed to $Co(CO)_4^-$ at +0.15 V was observed along with the reduction at -0.74 V *vs.* Fc/Fc$^+$ attributed to reduction of cobalt decomposition products on the electrode.

(a)

(b)
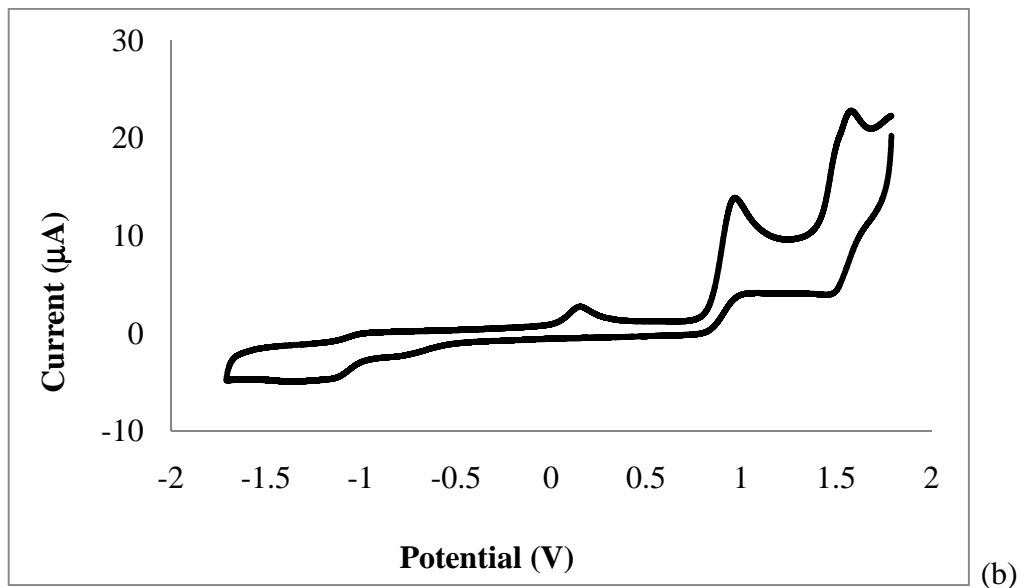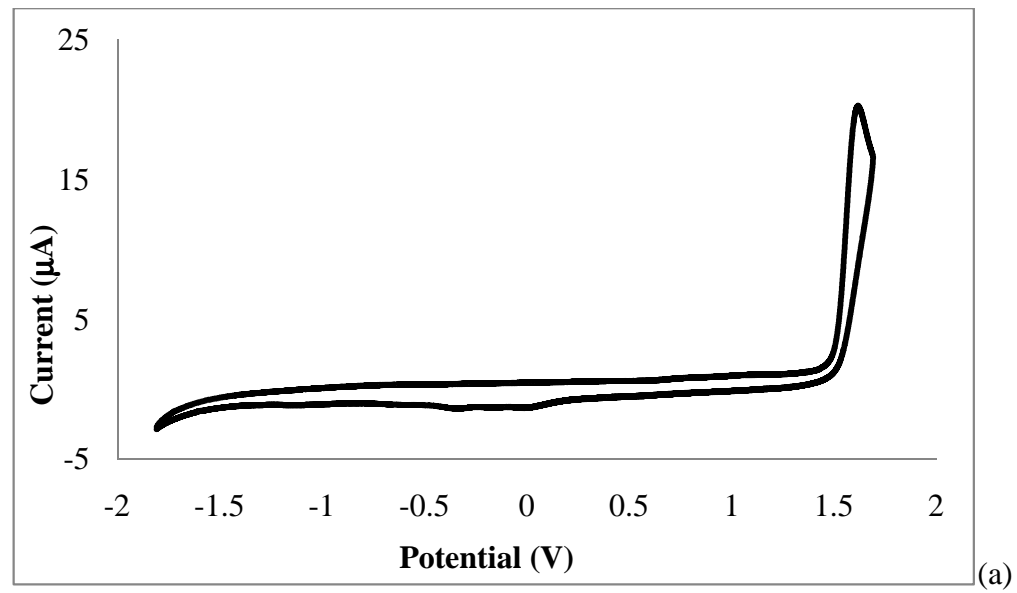
Figure B4   *Cyclic voltammogram of **NB-L5** (a) and **NB-C5** (b) showing oxidation and*
reduction waves.

B5 **Electrochemistry of NB-C6**

The cyclic voltammogram of the aldehydic complex, **NB-C6** (Fig. B5), possesses a positive potential at +0.99 V *vs.* Fc/Fc$^+$ due to the irreversible oxidation of the cobalt moiety, along with a second positive potential wave at +1.95 V *vs.* Fc/Fc$^+$ due to the oxidation of the thienyl group. The irreversible reduction of the metal centre is observed at -0.89 V *vs.* Fc/Fc$^+$. Subsequent cycles indicate that decomposition of the complex occurs, with new peaks at +0.13 V in the anodic direction and +0.55 V, -0.12 V and -0.74 V *vs.* Fc/Fc$^+$ in the cathodic direction being produced. A reduction in the intensity of the reductive peak at -0.74 V relative to the reduction of the cobalt unit (-0.89 V) was observed compared for this system. This would suggest that while decomposition of the complex is occurring, deposition onto the electrodes is not.
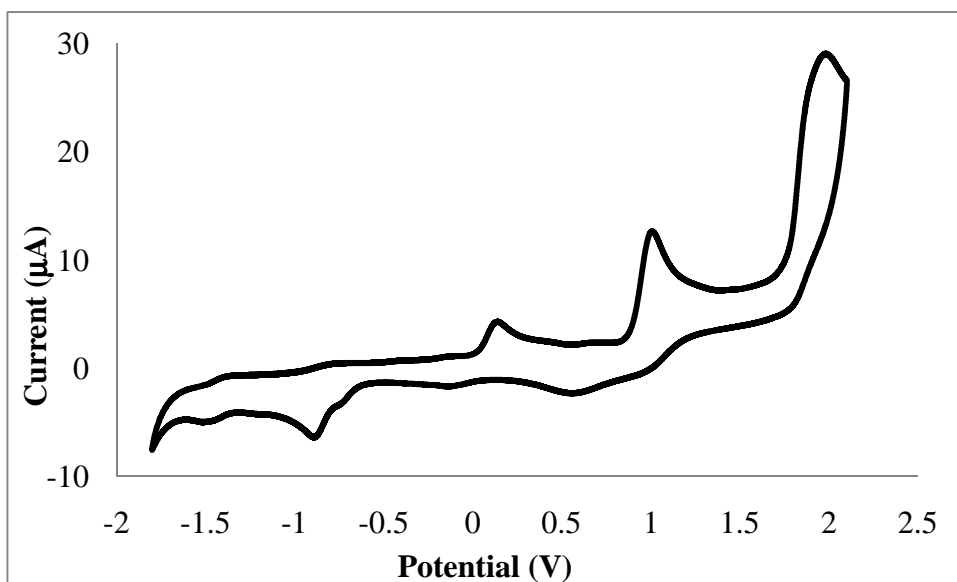
*Figure B5   Cyclic voltammogram of **NB-C6** showing oxidation and reduction waves.*

B6   Electrochemistry of NB-L7

In **NB-L7**, the CV displays one irreversible oxidation and one irreversible reduction (Fig. B6). The oxidation due to the thienyl group occurs at E_{pa} = +1.90 V *vs.* Fc/Fc$^+$. This is higher than that of the previous thiophene based oxidations and is due to the electron withdrawing nature of the dicyanovinyl moiety attached at the 5' position of the thiophene group. The dicyanovinyl unit itself is reduced irreversibly at E_{pc} = -0.98 V *vs.* Fc/Fc$^+$. This value corresponds well with published results where the irreversible reduction of a dicyanovinyl moiety attached to an aryl group is reduced at approximately 1 V.[7]
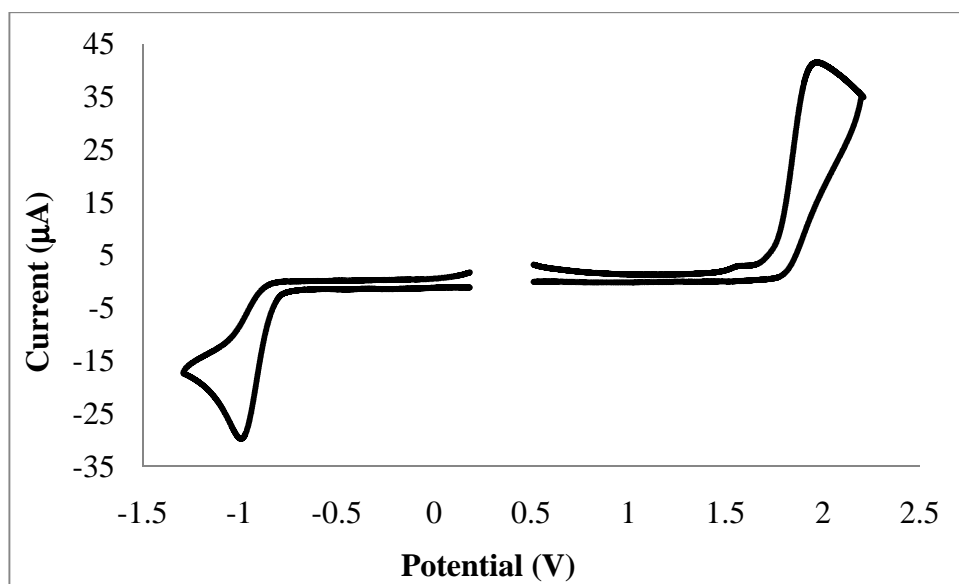

*Figure B6   Cyclic voltammogram of **NB-L7** showing oxidation and reduction waves.*

B7   **Electrochemistry of NB-L8 and NB-C8**

For **NB-L8**, the irreversible oxidation of the thienyl group was observed at +1.39 V *vs.* Fc/Fc$^+$ (Fig. B7, a). Two further oxidations were observed at higher potentials, +1.66 and +1.99 V *vs.* Fc/Fc$^+$. These are tentatively assigned to the oxidation of the phenanthrene moiety. Potential cycling over the peak potential produced a deposition on the electrodes and the redox response became progressively distorted. Also a new reductive peak at -0.12 V *vs.* Fc/Fc$^+$ was observed which may indicate that decomposition was occurring. The disubstituted dicobalt complex **NB-C8** gave results analogous to the other dicobalt carbonyl complexes discussed above. Two anodic waves were observed at potentials of +0.91 V and +1.39 V *vs.* Fc/Fc$^+$ which are attributed to irreversible oxidations on the metal centre and thiophene unit (Fig. B7, b). No other oxidation processes were observed out to the solvent limit. Reductive cycling produced an irreversible cathodic wave at -0.95 V *vs.* Fc/Fc$^+$ which is due to the formation of the radical anion. Successive redox cycles produced a new anodic wave at +0.16 followed by a cathodic wave at -0.66V *vs.* Fc/Fc$^+$. The former oxidation is ascribed to the degradation of the radical anion produced by the initial reductive process while the latter reductive wave corresponds well to the reduction of chemically adsorbed cobalt containing products on the electrode.

(a)

(b)
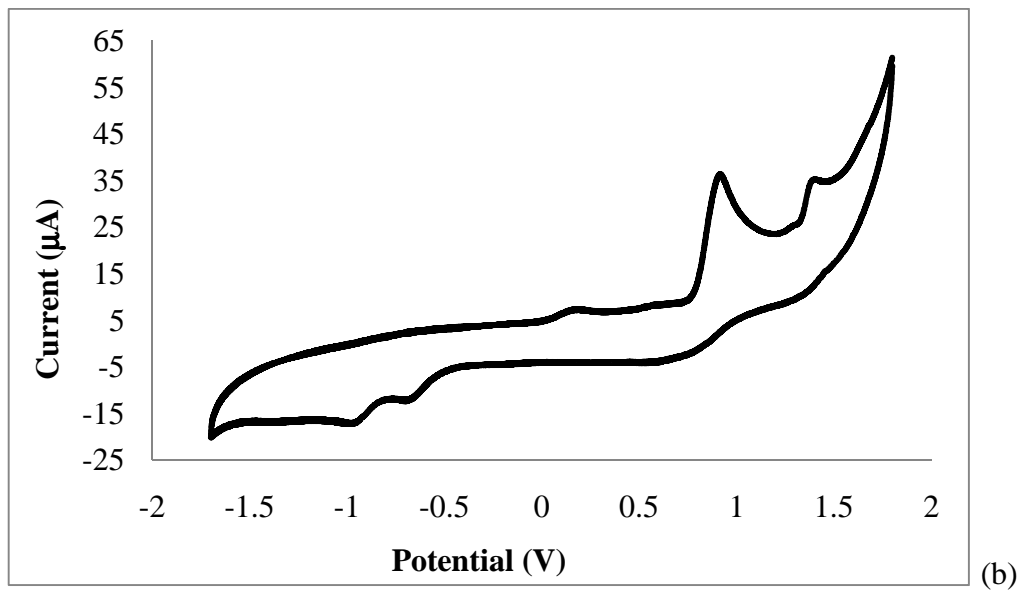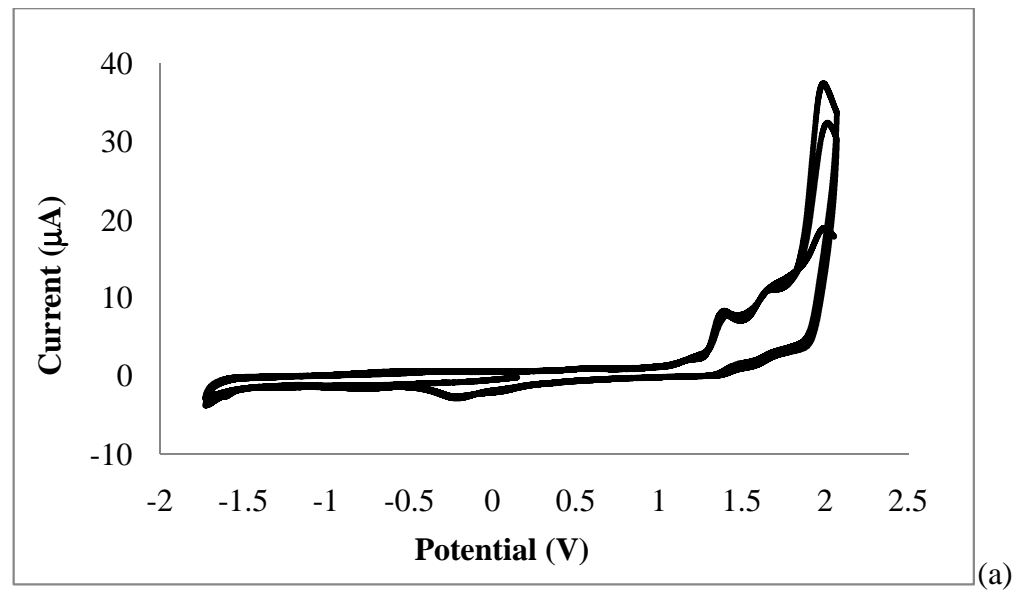
Figure B7   *Cyclic voltammogram of **NB-L8** (a) and **NB-C8** (b) showing oxidation and reduction waves.*

C1 Steady state photolysis of NB-C2

Photolysis of **NB-C2** at $\lambda_{exc} > 520$ nm for 30 minutes resulted in bleaching of the parent absorbance bands at 2090, 2055 and 2028 cm^{-1} and generation of weak product bands at 2064, 2018 and 2005 cm^{-1} assigned to formation of the pentacarbonyl species **NB-C2-Co$_2$(CO)$_5$(PPh$_3$)** (Fig. C1). Subsequent photolysis at $\lambda_{exc} > 410$ nm for 12 minutes resulted in a substantial increase in the intensity of these bands along with the appearance of new bands at 1996, 1980 and 1971 cm^{-1} which were tentatively assigned to the disubstituted species, **NB-C2-Co$_2$(CO)$_4$(PPh$_3$)$_2$**. Continued irradiation of the sample at $\lambda_{exc} > 320$ nm (5 minutes) resulted in minimal growth of the pentacarbonyl product bands and substantial growth of the tetracarbonyl species. The product bands compared favourably with those observed by Coleman et al.[9] and Arnanz et al.[3,4]
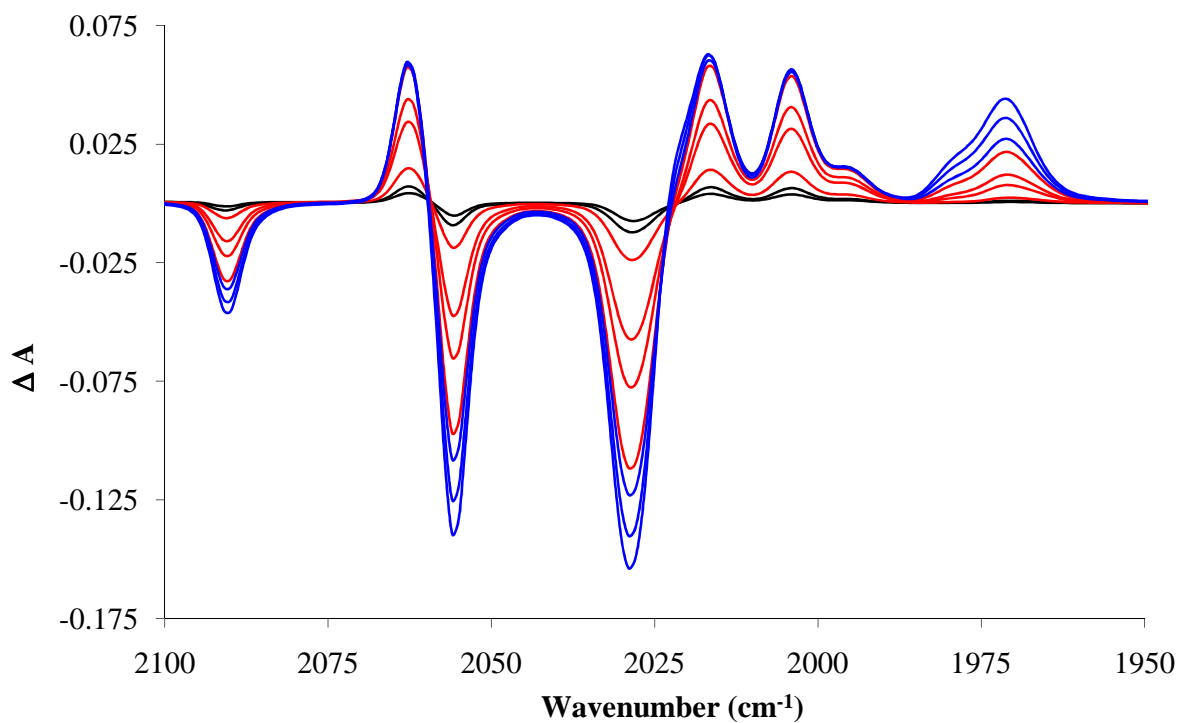
Figure C1   *Infrared difference spectra following irradiation of **NB-C2** in hexane with PPh$_3$ at $\lambda_{exc} > 520$ nm (black lines, 30 minutes total irradiation), $\lambda_{exc} > 410$ nm (red lines, 12 minutes total irradiation) and $\lambda_{exc} > 320$ nm (blue lines, 5 minutes total irradiation). Negative bands indicate bleaching of the parent complex while positive bands indicate generation of the PPh$_3$ trapped photoproducts.*

413

C2   **Steady state photolysis of NB-C3**

Irradiation of **NB-C3** in hexane solution in the presence of triphenylphosphine at $\lambda_{exc} > 520$ nm for 30 minutes resulted in the depletion of the parent bands at 2091, 2058 and 2031 cm^{-1} with concomitant generation of positive bands at 2065, 2020 and 2007 cm^{-1} (Fig. C2) that correspond to the trapped monosubstituted triphenylphosphine species, **NB-C3-Co$_2$(CO)$_5$(PPh$_3$)**. Irradiation at $\lambda_{exc} > 410$ nm for 10 minutes resulted in intensification of the product bands and the appearance bands due to the tetracarbonyl photoproduct at 1984 and 1973 cm^{-1}. Irradiation at $\lambda_{exc} > 320$ nm (5 minutes) resulted predominantly in the growth of the tetracarbonyl bands. Two additional weak bands were observed at 1951 and 1941 cm^{-1} which were also attributed to the tetracarbonyl species, **NB-C3-Co$_2$(CO)$_4$(PPh$_3$)$_2$**. Product assignment was based on matching of IR bands with those in literature.[4,9]
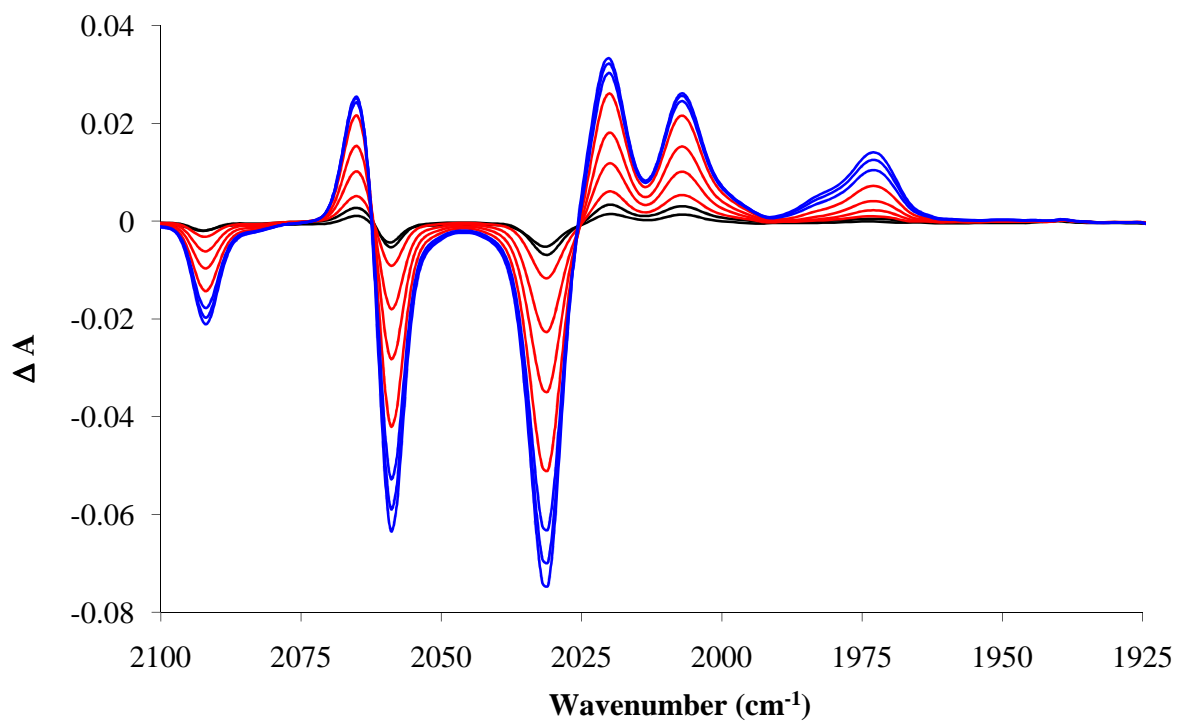
Figure C2   *Infrared difference spectra following irradiation of **NB-C3** in hexane with PPh$_3$ at $\lambda_{exc} > 520$ nm (black lines, 30 minutes total irradiation), $\lambda_{exc} > 410$ nm (red lines, 10 minutes total irradiation) and $\lambda_{exc} > 320$ nm (blue lines, 5 minutes total irradiation). Negative bands indicate bleaching of the parent complex while positive bands indicate generation of the pentacarbonyl and tetracarbonyl species.*

C3   Steady state photolysis of NB-C4

Under similar conditions ($\lambda_{exc} > 520$ nm for 30 minutes, $\lambda_{exc} > 410$ nm for 22 minutes and $\lambda_{exc} > 320$ nm for 5 minutes) **NB-C4** resulted in bleaching of the parent absorbance bands at 2091, 2082, 2059 and 2032 cm^{-1} and generation of bands at 2065, 2019 and 2007 cm^{-1} which were assigned to the pentacarbonyl species, **NB-C4-Co$_2$(CO)$_5$(PPh$_3$)** and bands at 1997, 1972 and 1943 cm^{-1} that were assigned to **NB-C4-Co$_2$(CO)$_4$(PPh$_3$)$_2$** (Fig. C3). These product bands are similar to those observed by Long et al.[8] and Arnanz et al.[4]
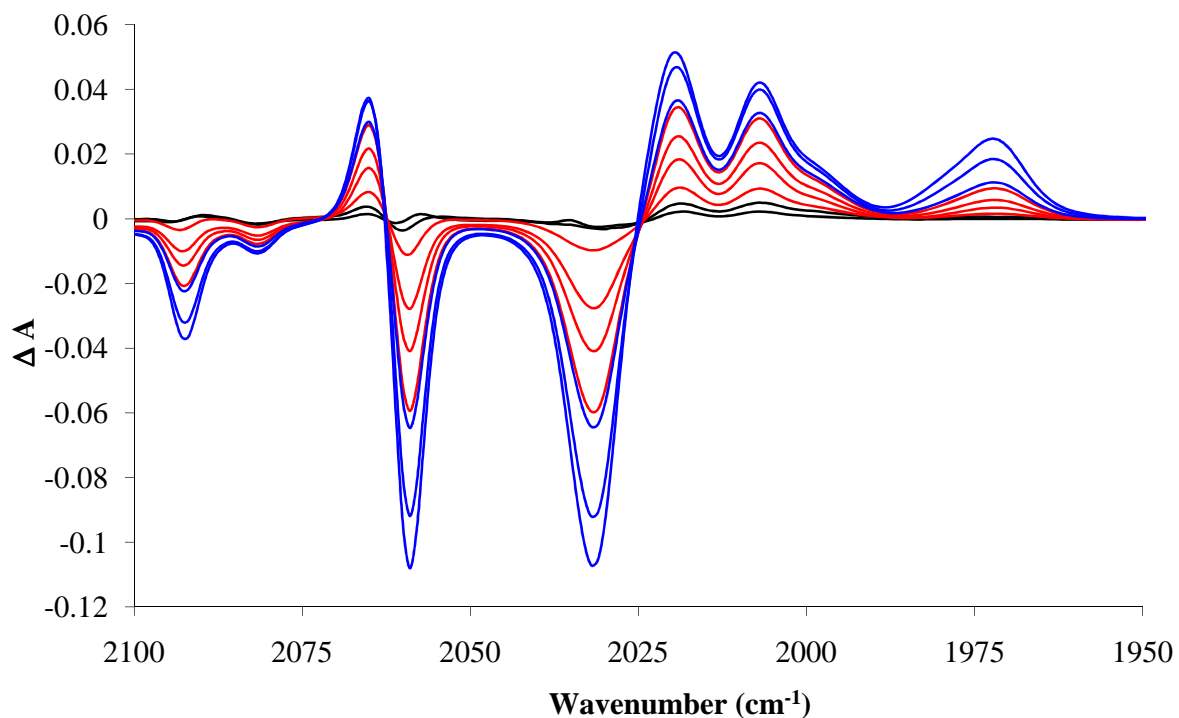
*Figure C3   Infrared difference spectra following irradiation of **NB-C4** in hexane with PPh$_3$ at $\lambda_{exc} > 520$ nm (black lines, 30 minutes total irradiation), $\lambda_{exc} > 410$ nm (red lines, 22 minutes total irradiation) and $\lambda_{exc} > 320$ nm (blue lines, 5 minutes total irradiation). Negative bands indicate bleaching of the parent complex while positive bands indicate generation of the pentacarbonyl and tetracarbonyl species.*

C4   Steady state photolysis of NB-C5

Irradiation of the dicobalt hexacarbonyl complex, **NB-C5,** in hexane solution with trapping ligand (PPh₃) at $\lambda_{exc} > 520$ nm for 30 minutes resulted in the depletion of parent bands at 2092, 2057, 2030 cm^{-1} and the generation of weak product bands at 2065, 2019 and 2007 cm^{-1} that were assigned to the pentacarbonyl photoproduct **NB-C5-Co₂(CO)₅(PPh₃)** (Fig. C4). Further photolysis at $\lambda_{exc} > 410$ nm for 20 minutes caused intensification of the pentacarbonyl bands and generated bands at 1997 and 1972 cm^{-1} while 5 minutes photolysis at $\lambda_{exc} > 320$ nm produced a weak band at 1943 cm^{-1}. By comparison with the results obtained by Long et al.[8] these new absorbance bands are indicative of formation of the triphenylphosphine trapped pentacarbonyl species, and by comparison with results obtained by Arnanz et al subsequent formation of the tetracarbonyl species.[4]
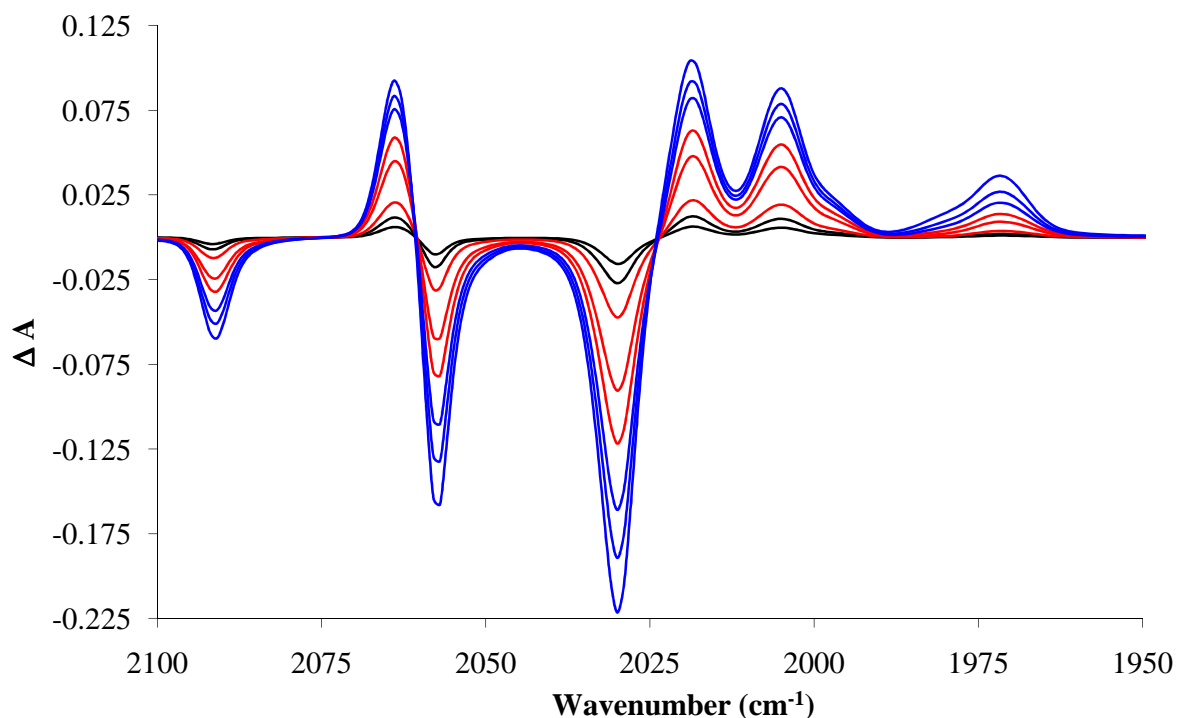

*Figure 41   Infrared difference spectra following irradiation of **NB-C5** in hexane with PPh₃ at $\lambda_{exc} > 520$ nm (black lines, 30 minutes total irradiation), $\lambda_{exc} > 410$ nm (red lines, 20 minutes total irradiation) and $\lambda_{exc} > 320$ nm (blue lines, 5 minutes total irradiation). Negative bands indicate bleaching of the parent complex while positive bands indicate generation of the pentacarbonyl and tetracarbonyl species.*

C5   Steady state photolysis of NB-C7

When the dicobalt hexacarbonyl complex, **NB-C7,** was photolysed under the analogous conditions ($\lambda_{exc} > 520$ nm, $\lambda_{exc} > 410$ nm and $\lambda_{exc} > 320$ nm) similar processes were observed. Depletion of parent bands at 2094, 2061 and 2034 cm^{-1} occurred together with the generation of weak new pentacarbonyl product bands at 2067, 2021 and 2009 cm^{-1} assigned to **NB-C7-Co$_2$(CO)$_5$(PPh$_3$)** following irradiation at $\lambda_{exc} > 520$ nm for 30 minutes (Fig. C5). Higher energy broadband irradiation ($\lambda_{exc} > 410$ nm for 10 minutes) increased the rate of pentacarbonyl product formation signified by growth of the bands at 2067, 2021 and 2009 cm^{-1} with the concomitant generation of a new band at 1974 cm^{-1}. The new band increased in intensity following irradiation at $\lambda_{exc} > 320$ nm (5 minutes) with growth of a further weak band at 1960 cm^{-1} confirming the formation of the tetracarbonyl species, **NB-C7-Co$_2$(CO)$_4$(PPh$_3$)$_2$**. All bands observed agree well with those reported for other dicobalt pentacarbonyl and tetracarbonyl complexes.[4,8,9]
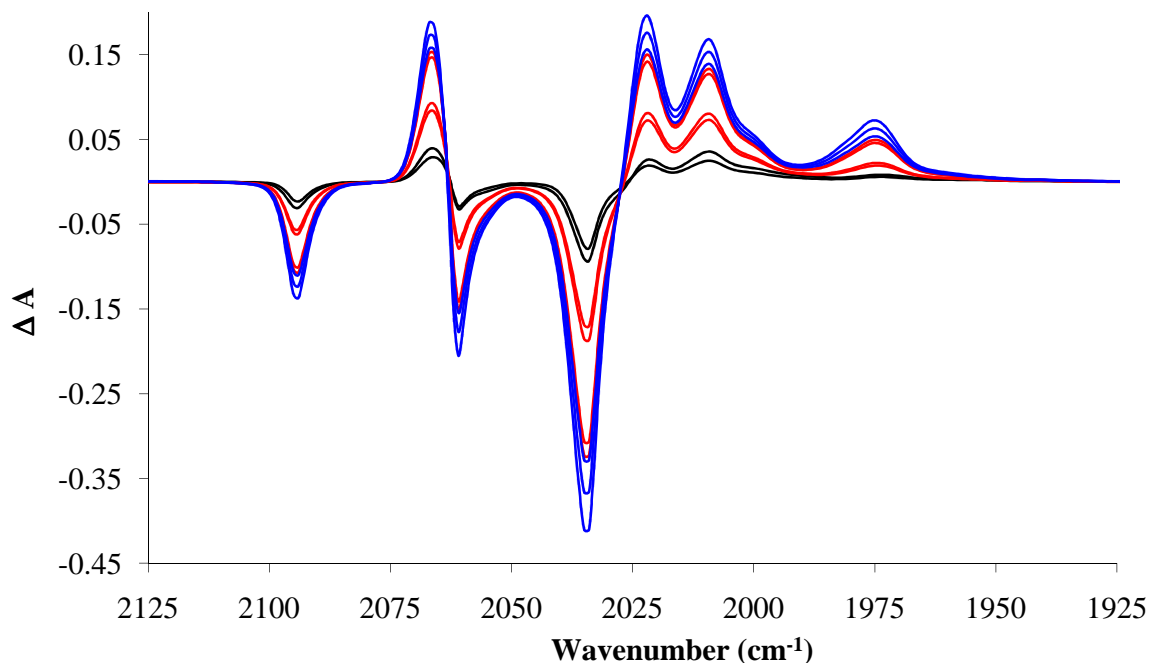

Figure C5   *Infrared difference spectra following irradiation of **NB-C7** in hexane with PPh$_3$ at $\lambda_{exc} > 520$ nm (black lines, 30 minutes total irradiation), $\lambda_{exc} > 410$ nm (red lines, 10 minutes total irradiation) and $\lambda_{exc} > 320$ nm (blue lines, 5 minutes total irradiation). Negative bands indicate bleaching of the parent complex while positive bands indicate generation of the pentacarbonyl and tetracarbonyl species.*

D   Synthesis   of   Ethynylferrocene   dicobalt   hexacarbonyl
(μ$_2$-FcCCH-Co$_2$(CO)$_6$)
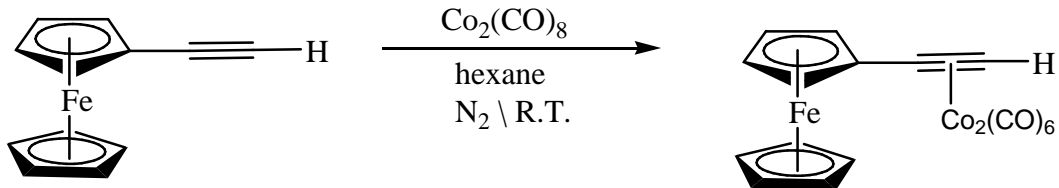
Ethynylferrocene was synthesised according to the method outlined by Coleman et al.[9]

HLPC grade, nitrogen purged hexane was charged with ethynylferrocene (0.95 mmol / 200 mg) and Co$_2$(CO)$_8$ (0.95 mmol / 320 mg). The solution was allowed to stir for 18 hours under an inert atmosphere in the dark. The solvent was removed *via* rotary evaporation resulting in a dark residue. The crude product was purified by column chromatography on silica gel using hexane : CH$_2$Cl$_2$ 70 : 30 as mobile phase affording a dark green solid. Yield: 210 mg, 0.42 mmol, 44 %.

^{1}H NMR (400 MHz, CDCl$_3$): 6.28 (1H, s), 4.35 (2H, s), 4.33 (2H, s), 4.16 (5H, s) ppm.
IR (CH$_2$Cl$_2$): ν(CO) 2093, 2054, 2032, 2022, 2210 cm^{-1}.

E1 Synthesis of diphenylacetylene dicobalt pentacarbonyl triphenylphosphine, PhCCPh-Co$_2$(CO)$_5$(PPh$_3$)
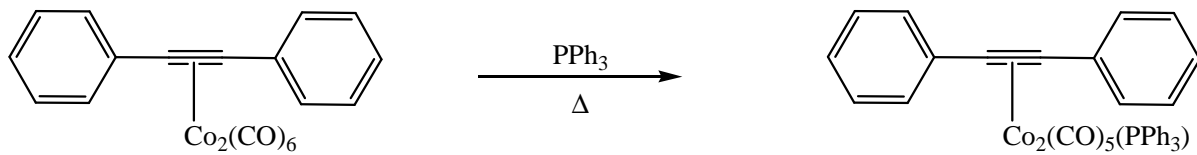
Diphenylacetylene dicobalt pentacarbonyl triphenylphosphine was prepared by a thermal substitution reaction. Diphenylacetylene dicobalt hexacarbonyl was dissolved in hexane (25 ml) and purged with nitrogen for 5 minutes. A molar excess of triphenylphosphine was added and the solution was heated to 50 °C. The progress of the reaction was monitored by TLC. The diphenylacetylene dicobalt hexacarbonyl, pentacarbonyl and tetracarbonyl complexes possess R$_f$ values on silca [petroleum ether : CH$_2$Cl$_2$ (3 : 1)] of 0.73, 0.50 and 0.17 respectively. The reaction mixture was cooled and the solvent removed when the tetracarbonyl species was first observed by TLC. The crude reaction mixture was purified by column chromatography on silica gel using petroleum ether : CH$_2$Cl$_2$ (3 : 1) as mobile phase which afforded the pure pentacarbonyl product as a brown solid.

^{1}H NMR (400 MHz, CDCl$_3$): 7.60-7.56 (10H, m), 7.47-7.43 (15H, m) ppm. **IR** (hexane): ν(CO) 2062, 2016, 2005 cm^{-1}

E2   **Synthesis of 2-(phenylethynyl)thiophene dicobalt pentacarbonyl triphenylphosphine, ThCCPh-Co$_2$(CO)$_5$(PPh$_3$)**
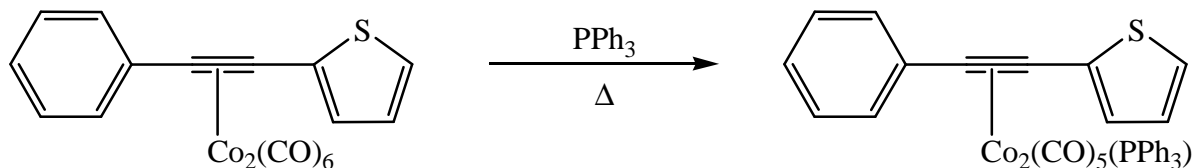
2-(Phenylethynyl)thiophene dicobalt pentacarbonyl triphenylphosphine was prepared by a thermal substitution reaction. 2-(Phenylethynyl)thiophene dicobalt hexacarbonyl was dissolved in hexane (25 ml) and purged with nitrogen for 5 minutes. A molar excess of triphenylphosphine was added and the solution was heated to 75 ℃. The progress of the reaction was monitored by TLC. The R$_f$ values of the hexacarbonyl, pentacarbonyl and tetracarbonyl complexes possess R$_f$ values on silca [petroleum ether : CH$_2$Cl$_2$ (3 : 1)] of 0.77, 0.42 and 0.13 respectively. The reaction mixture was cooled and the solvent removed when the tetracarbonyl species was first observed by TLC. The crude reaction mixture was purified by column chromatography on silica gel using petroleum ether : CH$_2$Cl$_2$ (3 : 1) as mobile phase which afforded the pure pentacaebonyl product as a brown solid.

^{1}H NMR (400 MHz, CDCl$_3$): 7.57-7.52 (8H, m), 7.50-7.34 (10H, m) 7.32-7.25 (5H, m) ppm. **IR** (hexane): ν(CO) 2063, 2021, 2005 cm^{-1}

E3   **Synthesis   of   Ethynylferrocene   dicobalt   pentacarbonyl triphenylphosphine FcCCH-Co$_2$(CO)$_5$(PPh$_3$)**
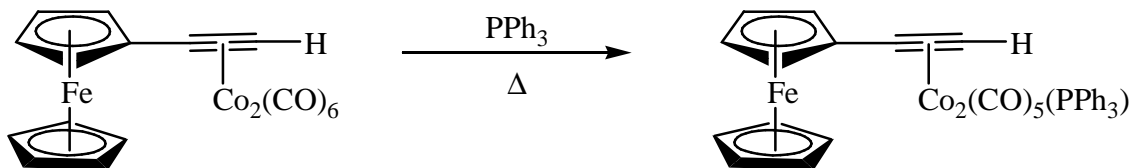
Ethynylferrocene dicobalt pentacarbonyl triphenylphosphine was prepared by a thermal substitution reaction. Ethynylferrocene dicobalt hexacarbonyl was dissolved in hexane (25 ml) and purged with nitrogen for 5 minutes. A molar excess of triphenylphosphine was added and the solution was heated to 50 ºC. The progress of the reaction was monitored by TLC. The R$_f$ values of the respective ethynyl dicobalt hexacarbonyl, pentacarbonyl and tetracarbonyl complexes possess R$_f$ values on silca [petroleum ether : CH$_2$Cl$_2$ (3 : 1)] of 0.75, 0.43 and 0.18 respectively.. The reaction mixture was cooled and the solvent removed when the tetracarbonyl species was first observed by TLC. The crude reaction mixture was purified by column chromatography on silica gel using petroleum ether : CH$_2$Cl$_2$ (3 : 1) as mobile phase which afforded the pure pentacarbonyl product as a dark green solid.

^{1}H NMR (400 MHz, CDCl$_3$): 7.52-7.40 (9H, m), 7.11-7.04 (6H, m), 6.06 -6.04 (1H, m), 4.38 (2H, s), 4.22 (2H, s), 4.03 (5H, s) ppm. **IR** (hexane): ν(CO) 2063, 2012, 2004 cm^{-1}

F1   Quantum yield method

All quantum yields were carried out using a liquid-phase potassium ferrioxalate actinometer. The actinometer was prepared by mixing three volumes of 1.5 M $K_2C_2O_4$ solution with one volume of 1.5 M $FeCl_3$ solution with agitation. The precipitated $K_3Fe(C_2O_4)_3.3H_2O$ was then recrystallised three times from warm water and dried in a current of warm air. To prepare 1 L of 0.006 M $K_3Fe(C_2O_4)_3.3H_2O$ solution, 2.947 g of the precipitate was dissolved in 800 ml water, 100 ml 1.0 N sulphuric acid was added and filled to the mark with water. While the 0.15 M actinometric solution required 73.68 g of precipitate to be added to the same volumes of liquid. For all quantitative work the preparation and manipulation of the ferrioxalate solutions must be carried out in a darkroom, using a red photographic safelight. The light intensity in a photochemical reaction is determined by irradiating ferrioxalate solution and monitoring the subsequent change in absorbance at 510 nm. A carousel was used to house both the actinometer and sample cells so that they were equally exposed to a uniform amount of irradiation during each experiment. The carousel operated inside a black box to prevent any stray light reaching the sample or actinometer solutions. An autopipette was to ensure all volumes were accurately measured.

For each actinometeric measurement a quartz cuvette was charged with 3 ml (V_1) of ferrioxalate solution. The cell was placed in the carsoul and irratiated. After the determined irratidation time (t), the solution was well mixed and an aliquot volume (2 ml, V_2) was pipette into a volumetric flask (10 ml, V_3). Buffer solution of volume equal to half the volume of photolyte placed in the flask was added (1 ml), so too was 2 ml phenanthroline solution (0.1 g per cent by weight solution). The solution was diluted with distilled water to the V_3 volume mark and mixed well. The flask was wrapped in tinfoil and the solution allowed to develop. After one hour, the absorbance of the solution was measured in a 1cm cell at 510 nm in spectrophotometer using a blank iron free solution as a reference.

The number of Fe^{2+} ions ($n_{Fe^{2+}}$) formed during photolysis can be calculated from:

$$n_{Fe^{2+}} = \frac{6.023 \times 10^{20} \, V_1 \, V_3 \, \log_{10} (I_0/I)}{V_2 \, l \, \varepsilon}$$

where

V_1 = Volume of actinometer solution irradiated (ml)

V_2 = Volume of aliquot taken for analysis (ml)

V_3 = Final volume to which the aliquot V_2 is diluted (ml)

$\text{Log}_{10} (I_0/I)$ = measured optical density of the solution

l = path length of the spectrophotometer cell used (cm)

ε = experimental value of the molar extinction coefficient of Fe^{2+} complex, determined from the slope of the calibration plot (approx. equal to $1.11 \times 10^4 \, l \, mol^{-1} \, cm^{-1}$).

The number of quanta absorbed by the actinometer (n_a) per second is obtained from

$$n_a = n_{Fe^{2+}} / \Phi_\lambda \, t$$

where t is the time in seconds.

For each sample under investigation, a solution of known concentration was prepared so that the optical density of each was 0.8 ± 0.1 AU at 400 nm. A 10 % excess of triphenyl phosphine was used as a trapping ligand throughout the measurements and added to each solution immediately prior to irradiation. Each sample cuvette was accurately charged with 3 ml of the alkynyl dicobalthexacarbonyl / triphenylphosphine solution. The sample cell was placed in the carousel with the actinometric solutions and were irradiated in parallel. The change in absorbance of the sample solution was measured at 400 nm to calculate the yield of CO loss that occurred.

Hexacarbonyl Complex	ε (M^{-1} cm^{-1}) at 400 nm
PhCCPh-Co$_2$(CO)$_6$	1440
ThCCPh-Co$_2$(CO)$_6$	2211
FcCCH-Co$_2$(CO)$_6$	1500

Photolytic/thermal substitution products	ε (M^{-1} cm^{-1}) at 400 nm
PhCCPh-Co$_2$(CO)$_5$PPh$_3$	8179
ThCCPh-Co$_2$(CO)$_5$PPh$_3$	4680
FcCCH-Co$_2$(CO)$_5$PPh$_3$	2717

Extincition coefficients of dicobalt hexacarbonyl complexes and corresponding pentacarbonyl complexes recorded in cyclohexane.

F2   **Quantum yield calculations**

(a)   **Quantum yield determinations of CO loss for [(μ2- PhCCPh)-Co$_2$(CO)$_6$] (1)**

Molar excitation coefficients at 400 nm

(μ_2- PhCCPh)-Co$_2$(CO)$_6$ **(1)**   1,140 M^{-1} cm^{-1}

(μ_2- PhCCPh)-Co$_2$(CO)$_5$(PPh$_3$)   8,179 M^{-1} cm^{-1}

Irradiation of 1 at 313 nm **(21 mins)**

Increase in intensity of band at 400 nm = 0.16

Molar increase = 2.34 x 10^{-5} molar

Moles converted per second = 1.9 x 10^{-8} moles/s

For a 3 cm^3 sample, number of molecules photolysed per second = 3.35 x 10^{13} molecules/s

Change in absorbance of actinometer solution at 510 nm

Absorbance at 510 nm = 0.823

Number of Fe^{2+} ions = 6.70 x 10^{17} ions

Using a quantum yield for Fe^{2+} production of 1.24 at 313 nm

Number of photons emitted by the source at 313 nm = 5.40 x 10^{17}

Number of photons emitted per second by the source at 313 nm = 4.29 x 10^{14} photons/s

Number of photons absorbed by the sample = 4.29 x 10^{14} photons/s

Quantum yield of photochemical reaction is (3.35 x 10^{13}) / (4.29 x 10^{14}) = 0.078

Irradiation of 1 at 365 nm **(20 mins)**

Increase in intensity of band at 400 nm = 0.15

Molar increase = 2.19 x 10^{-5} molar

Moles converted per second = 1.8 x 10^{-8} moles/s

For a 3 cm^3 sample, number of molecules photolysed per second = 3.30 x 10^{13} molecules/s

Change in absorbance of actinometer solution at 510 nm

Absorbance at 510 nm = 1.70

Number of Fe^{2+} ions = 1.39 x 10^{18} ions

Using a quantum yield for Fe^{2+} production of 1.21 at 365 nm

Number of photons emitted by the source at 365 nm = 5.40×10^{17}

Number of photons emitted per second by the source at 313 nm = 9.56×10^{14} photons/s

Number of photons absorbed by the sample = 9.56×10^{14} photons/s

Quantum yield of photochemical reaction is $(3.30 \times 10^{13}) / (9.56 \times 10^{14}) = 0.035$

*Irradiation of 1 at **405 nm** (15 mins)*

Increase in intensity of band at 400 nm = 0.074

Molar increase = 1.09×10^{-5} molar

Moles converted per second = 1.2×10^{-8} moles/s

For a 3 cm^3 sample, number of molecules photolysed per second = 2.19×10^{13} molecules/s

Change in absorbance of actinometer solution at 510 nm

Absorbance at 510 nm = 1.02

Number of Fe^{2+} ions = 8.31×10^{17} ions

Using a quantum yield for Fe^{2+} production of 1.14 at 405 nm

Number of photons emitted by the source at 405 nm = 7.29×10^{17}

Number of photons emitted per second by the source at 405 nm = 8.10×10^{14} photons/s

Number of photons absorbed by the sample = 8.10×10^{14} photons/s

Quantum yield of photochemical reaction is $(2.19 \times 10^{13}) / (8.10 \times 10^{14}) = 0.027$

*Irradiation of 1 at **546 nm** (60 mins)*

Increase in intensity of band at 400 nm = 0.114

Molar increase = 1.69×10^{-5} molar

Moles converted per second = 5.0×10^{-9} moles/s

For a 3 cm3 sample, number of molecules photolysed per second = 8.47×10^{12} molecules/s

Change in absorbance of actinometer solution at 510 nm

Absorbance at 510 nm = 0.123

Number of Fe^{2+} ions = 1.00×10^{17} ions

Using a quantum yield for Fe^{2+} production of 0.15 at 546 nm

Number of photons emitted by the source at 546 nm = 6.68×10^{17}

Number of photons emitted per second by the source at 5 46nm = 1.87 x 10^{14} photons/s

Number of photons absorbed by the sample = 1.87 x 10^{14} photons/s

Quantum yield of photochemical reaction is (8.47 x 10^{12}) / (1.87 x 10^{14}) = 0.045

(b) Quantum yield determinations of [(μ2- ThCCPh)-Co$_2$(CO)$_6$] (2)

Molar excitation coefficients at 400 nm

[(μ$_2$- PhCCPh)-Co$_2$(CO)$_6$] **(2)**	2,314 M^{-1} cm^{-1}
[(μ$_2$- PhCCPh)-Co$_2$(CO)$_5$(PPh$_3$)	4,829 M^{-1} cm^{-1}

Irradiation of 2 at 313 nm (**10 mins**)

Increase in intensity of band at 400 nm = 0.077

Molar increase = 3.07 x 10^{-5} molar

Moles converted per second = 5.1 x 10^{-8} moles/s

For a 3 cm^3 sample, number of molecules photolysed per second = 9.21 x 10^{13} molecules/s

Change in absorbance of actinometer solution at 510 nm

Absorbance at 510 nm = 0.5862

Number of Fe^{2+} ions = 4.77 x 10^{17} ions

Using a quantum yield for Fe^{2+} production of 1.24 at 313 nm

Number of photons emitted by the source at 313 nm = 3.85 x 10^{17}

Number of photons emitted per second by the source at 313 nm = 6.41 x 10^{14} photons/s

Number of photons absorbed by the sample = 6.41 x 10^{14} photons/s

Quantum yield of photochemical reaction is (9.21 x 10^{13}) / (6.41 x 10^{14}) = 0.145

Irradiation of 2 at 365 nm (**15 min**)

Increase in intensity of band at 400 nm = 0.099

Molar increase = 3.94 x 10^{-5} molar

Moles converted per second = 4.4 x 10^{-8} moles/s

For a 3 cm^3 sample, number of molecules photolysed per second = 7.91 x 10^{13} molecules/s

Change in absorbance of actinometer solution at 510 nm

Absorbance at 510 nm = 1.3191

Number of Fe^{2+} ions = 1.07 x 10^{18} ions

Using a quantum yield for Fe^{2+} production of 1.21 at 365 nm

Number of photons emitted by the source at 365 nm = 8.87 x 10^{17}

Number of photons emitted per second by the source at 313 nm = 9.85 x 10^{14} photons/s

Number of photons absorbed by the sample = 9.85 x 10^{14} photons/s

Quantum yield of photochemical reaction is (7.91 x 10^{13}) / (9.85 x 10^{14}) = 0.0803

*Irradiation of 2 at **405 nm** (15 mins)*

Increase in intensity of band at 400 nm = 0.046

Molar increase = 1.83 x 10^{-5} molar

Moles converted per second = 2.0 x 10^{-8} moles/s

For a 3 cm^3 sample, number of molecules photolysed per second = 3.67 x 10^{13} molecules/s

Change in absorbance of actinometer solution at 510 nm

Absorbance at 510 nm = 1.02

Number of Fe^{2+} ions = 8.31 x 10^{17} ions

Using a quantum yield for Fe^{2+} production of 1.14 at 405 nm

Number of photons emitted by the source at 405 nm = 7.29 x 10^{17}

Number of photons emitted per second by the source at 405 nm = 8.10 x 10^{14} photons/s

Number of photons absorbed by the sample = 8.10 x 10^{14} photons/s

Quantum yield of photochemical reaction is (3.67 x 10^{13}) / (8.10 x 10^{14}) = 0.045

*Irradiation of 2 at **546 nm** (40 mins)*

Increase in intensity of band at 400 nm = 0.073

Molar increase = 2.91 x 10^{-5} molar

Moles converted per second = 1.2 x 10^{-9} moles/s

For a 3 cm^3 sample, number of molecules photolysed per second = 2.19 x 10^{13} molecules/s

Change in absorbance of actinometer solution at 510 nm

Absorbance at 510 nm = 0.0907

Number of Fe2+ ions = 7.38 x 10^{16} ions

Using a quantum yield for Fe^{2+} production of 0.15 at 546 nm

Number of photons emitted by the source at 546 nm = 4.92 x 10^{17}

Number of photons emitted per second by the source at 546nm = 2.05 x 10^{14} photons/s

Number of photons absorbed by the sample = 2.05 x 10^{14} photons/s

Quantum yield of photochemical reaction is (2.19 x 10^{13}) / (2.05 x 10^{14}) = 0.106

(c) Quantum yield determinations of [(μ_2-FcCCH)-Co$_2$(CO)$_6$] (3)

Molar excitation coefficients at 400 nm

(μ_2-FcCCH)-Co$_2$(CO)$_6$ (3)   1,497 M^{-1} cm^{-1}

(μ_2-FcCCH)-Co$_2$(CO)$_5$ (PPh$_3$)   2,717 L mol-1 cm-1

Irradiation of 3 at 313 nm (20mins)

Increase in intensity of band at 400 nm = 0.072

Molar increase = 1.21 x 10^{-4} molar

Moles converted per second = 1.0 x 10^{-7} moles/s

For a 3 cm^3 sample, number of molecules photolysed per second = 1.81 x 10^{14} molecules/s

Change in absorbance of actinometer solution at 510 nm

Absorbance at 510 nm = 1.2258

Number of Fe^{2+} ions = 9.98 x 10^{17} ions

Using a quantum yield for Fe^{2+} production of 1.24 at 313 nm

Number of photons emitted by the source at 313 nm = 8.04 x 10^{17}

Number of photons emitted per second by the source at 313 nm = 6.71 x 10^{14} photons/s

Number of photons absorbed by the sample = 6.71 x 10^{14} photons/s

Quantum yield of photochemical reaction is (1.81 x 10^{14}) / (6.71 x 10^{14}) = 0.269

Irradiation of 3 at 365 nm (25 mins)

Increase in intensity of band at 400 nm = 0.084

Molar increase = 6.68 x 10^{-5} molar

Moles converted per second = 4.6 x 10^{-8} moles/s

For a 3 cm^3 sample, number of molecules photolysed per second = 8.26 x 10^{13} molecules/s

Change in absorbance of actinometer solution at 510 nm

Absorbance at 510 nm = 1.993

Number of Fe^{2+} ions = 1.62 x 10^{18} ions

Using a quantum yield for Fe^{2+} production of 1.21 at 365 nm

Number of photons emitted by the source at 365 nm = 1.34 x 10^{18}

Number of photons emitted per second by the source at 365 nm = 1.16 x 10^{15} photons/s

Number of photons absorbed by the sample = 1.16 x 10^{15} photons/s

Quantum yield of photochemical reaction is (8.26 x 10^{13}) / (1.16 x 10^{15}) = 0.071

*Irradiation of 3 at **405 nm** (25 mins)*

Increase in intensity of band at 400 nm = 0.044

Molar increase = 3.61 x 10^{-5} molar

Moles converted per second = 2.4 x 10^{-8} moles/s

For a 3 cm^3 sample, number of molecules photolysed per second = 4.35 x 10^{13} molecules/s

Change in absorbance of actinometer solution at 510 nm

Absorbance at 510 nm = 1.952

Number of Fe^{2+} ions = 1.59 x 10^{18} ions

Using a quantum yield for Fe^{2+} production of 1.14 at 405 nm

Number of photons emitted by the source at 405 nm = 1.39 x 10^{18}

Number of photons emitted per second by the source at 405 nm = 9.30 x 10^{14} photons/s

Number of photons absorbed by the sample = 9.30 x 10^{14} photons/s

Quantum yield of photochemical reaction is (4.35 x 10^{13}) / (9.30 x 10^{14}) = 0.047

*Irradiation of 3 at **546 nm** (35 mins)*

Increase in intensity of band at 400 nm = 0.133

Molar increase = 5.27 x 10^{-5} molar

Moles converted per second = 2.5 x 10^{-8} moles/s

For a 3 cm^3 sample, number of molecules photolysed per second = 4.54 x 10^{13} molecules/s

Change in absorbance of actinometer solution at 510 nm

Absorbance at 510 nm = 0.075

Number of Fe^{2+} ions = 6.14 x 10^{16} ions

Using a quantum yield for Fe^{2+} production of 0.15 at 546 nm

Number of photons emitted by the source at 546 nm = 4.09 x 10^{17}

Number of photons emitted per second by the source at 546nm = 1.95 x 10^{14} photons/s

Number of photons absorbed by the sample = 4.09 x 10^{14} photons/s

Quantum yield of photochemical reaction is (4.54 x 10^{13}) / (1.95 x 10^{14}) = 0.233
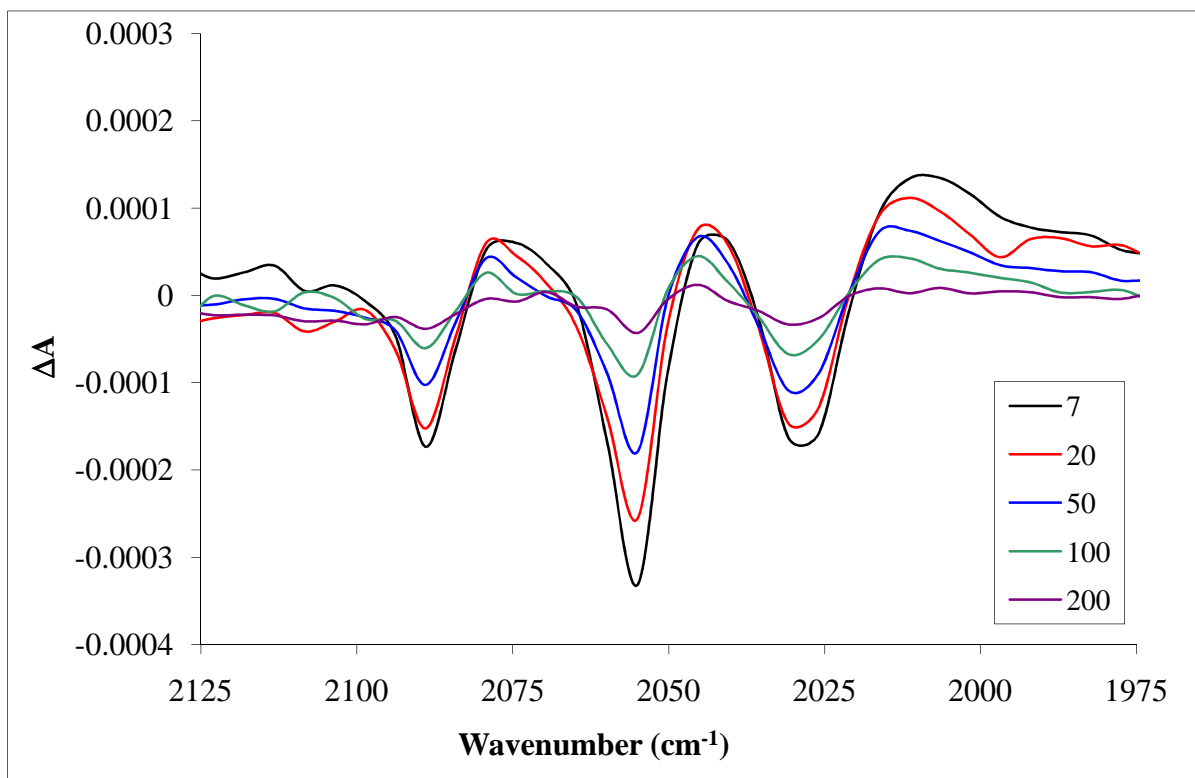
*TRIR difference spectra at 7, 20, 50, 100 and 200 ps following excitation of **PhCCPh-Co$_2$(CO)$_6$** in CH$_3$CN at 400 nm.*

G2   **TRIR of PhCCPh-Co₂(CO)₆ in pentane**
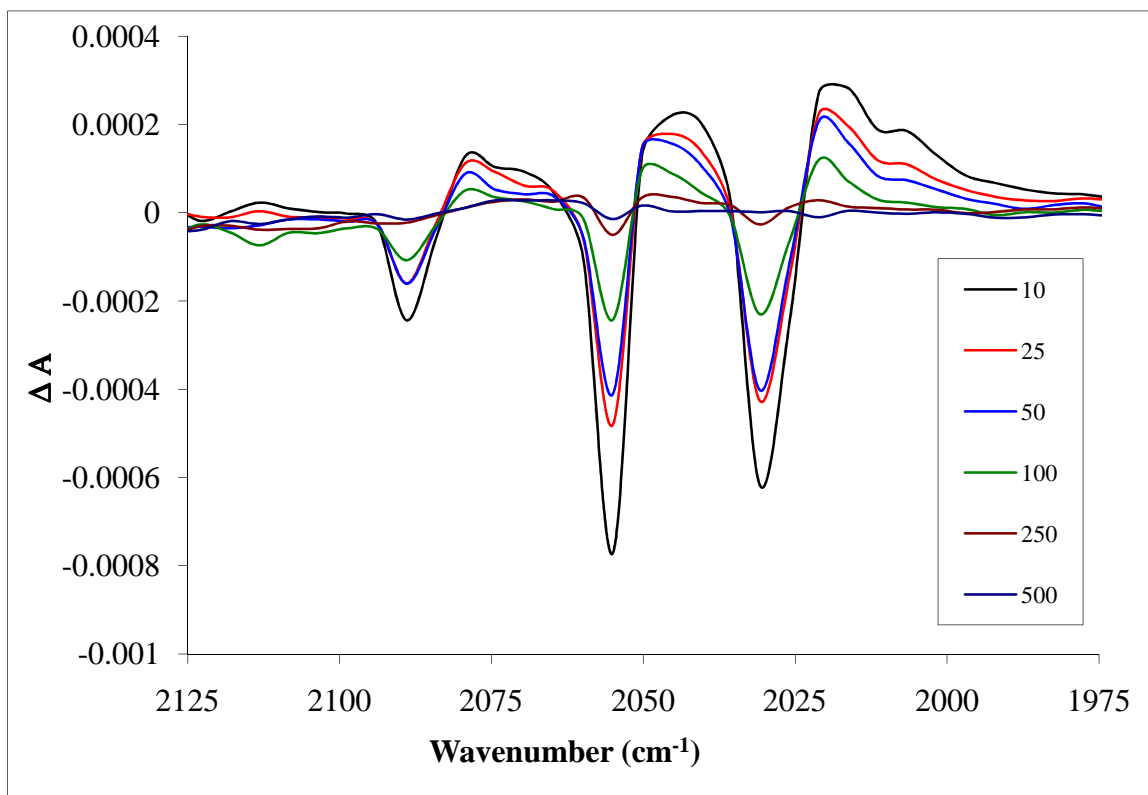
TRIR difference spectra at 10, 25, 50, 100 250 and 500 ps following excitation of PhCCPh-Co₂(CO)₆ in pentane at 400 nm.
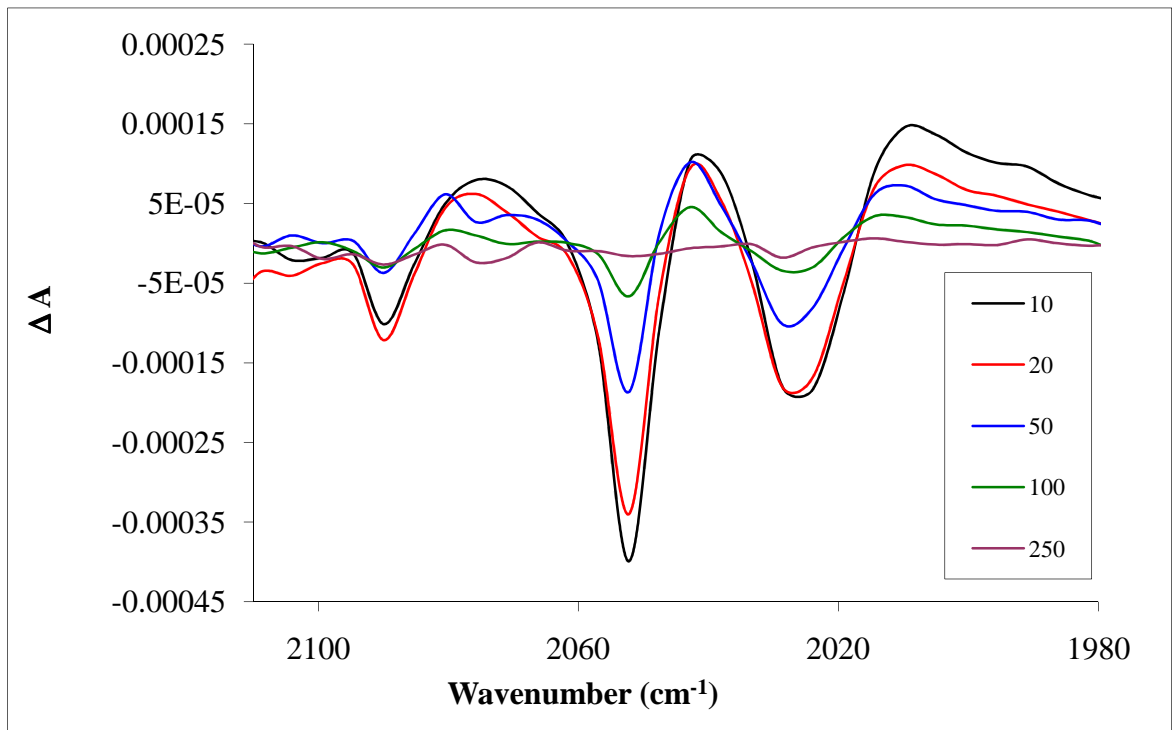
G3   **TRIR of FcCCH-Co$_2$(CO)$_6$ in CH$_3$CN**

*TRIR difference spectra at 10, 25, 50, 100 and 250 ps following excitation of **FcCCH-Co$_2$(CO)$_6$** in CH$_3$CN at 400 nm.*
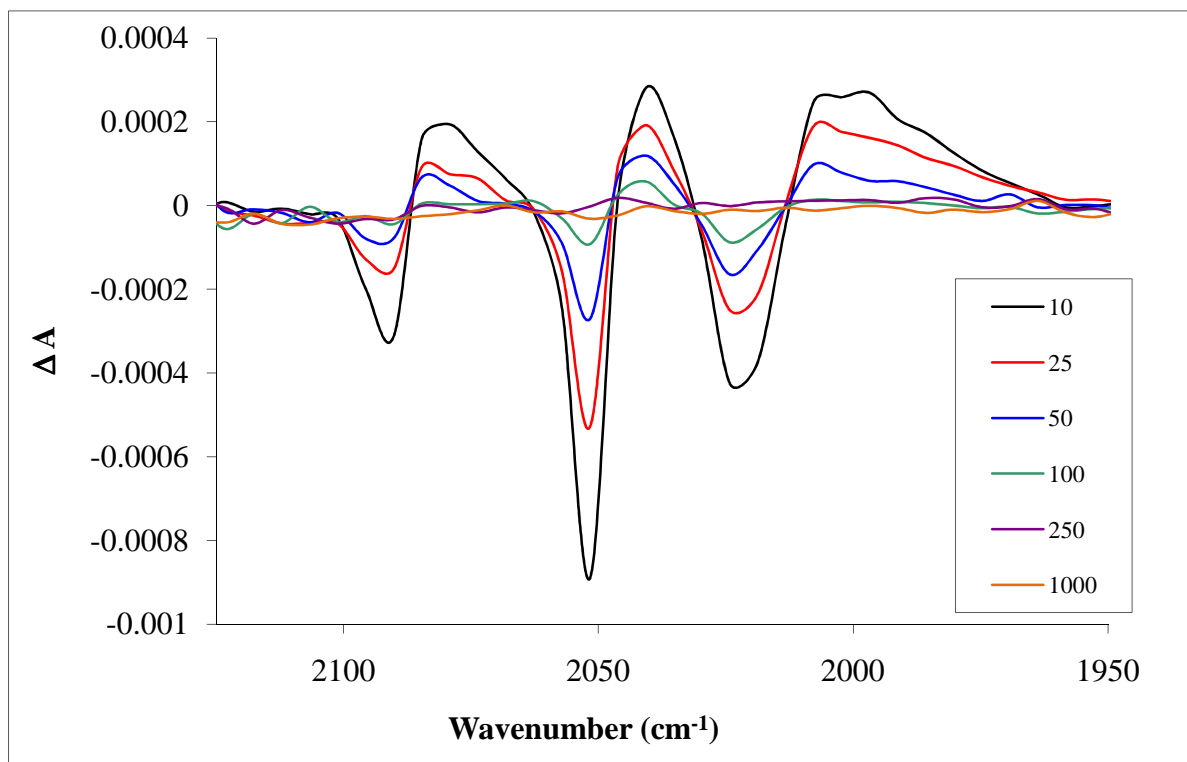
TRIR difference spectra at 10, 25, 50, 100, 250 and 1000 ps following excitation of **FcCCH-Co$_2$(CO)$_6$** *in THF at 532 nm with PPh$_3$ as trapping ligand .*

H   **Steady state photolysis of FcCCH-Co$_2$(CO)$_6$**

Extended monochromatic photolysis of the dicobalt hexacarbonyl complex, **FcCCH-Co$_2$(CO)$_6$,** in hexane solution in the presence of triphenylphosphine at λ_{exc} = 546 nm for 30 minutes caused minor changes in the IR spectrum. Bleaching of the parent IR bands at 2093, 2054, 2032 and 2022 cm^{-1} with concomitant generation of weak product bands at 2063, 2012, and 2004 cm^{-1} was observed and assigned to the generation of the pentacarbonyl photoproduct, **FcCCH-Co$_2$(CO)$_5$(PPh$_3$)**. These IR bands continued to grow following irradiation at λ_{exc} = 436 nm for 20 minutes with the generation of a further bands at 1992, 1974 and 1941 cm^{-1} which were attributed to the tetracarbonyl species, **FcCCH-Co$_2$(CO)$_4$(PPh$_3$)$_2$**. Subsequent photolysis at λ_{exc} = 313 nm for 20 minutes resulted in a notable increase in the intensity of the pentacarbonyl and tetracarbonyl photoproducts. The assignment of bands to the pentacarbonyl species, **FcCCH-Co$_2$(CO)$_5$(PPh$_3$)**, was based on IR bands of isolated **FcCCH-Co$_2$(CO)$_5$(PPh$_3$)** complex while the assignment of the tetracarbonyl species were based on similarities with isolated tetracarbonyl complexes.[10]
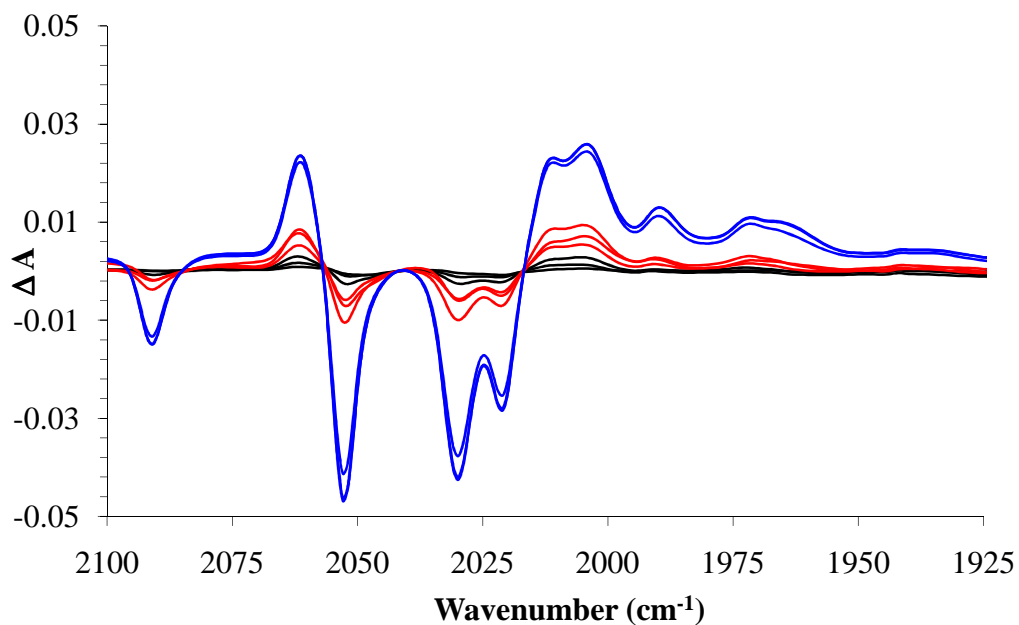
*Infrared difference spectra following monochromatic irradiation of **FcCCH-Co$_2$(CO)$_6$** in hexane with PPh$_3$ at λ_{exc} = 546 nm (black lines, 20 minutes total irradiation), λ_{exc} = 436 nm (red lines, 30 minutes total irradiation time) and λ_{exc} = 313 nm (blue lines, 30 minutes total irradiation time). Negative bands indicate bleaching of the parent complex while positive bands indicate generation of the pentacarbonyl species.*

I   Theoretical calculations

All theoretical calculations were carried out by Prof. C. Long, at Dublin City University.

Initial coordinates for the structural optimization of $(\mu_2\text{-}C_2H_2)Co_2(CO)_6$ were obtained from

Platts et al.[11]   The B3LYP/LANL2DZp model chemistry was used for all the calculations as

implemented in Gaussian03.[12]

The Hessian matrix was calculated to predict the infrared spectrum of $(\mu_2\text{-}C_2H_2)Co_2(CO)_6$. The predicted $\nu(CO)$ bands of this complex were corrected by comparison with the published IR spectrum.[13]   This yielded a correction factor of 1.0222 which was then used to correct the calculated $\nu(CO)$ bands of the equivalent ground state triplet species.

	$\nu(CO)$	(cm^{-1})			
Observed	2097.8	2058.5	2033.7	2028.1	2016.6
Singlet	2097.9	2051.3	2037.6	2035.1	2012.7
Triplet	2087.5	2057.9	2024.1	2021.7	2015.2
$\Delta \upsilon$	10.3	0.6	9.6	6.3	1.4

Table 1   *Observed spectrum and calculated singlet and triplet state spectra for (μ_2-C₂H₂)Co₂(CO)₆*

Mulliken atomic spin densities:

1 Co   1.092758

2 Co   1.092758

3 C   -0.052279

4 C   -0.052279

5 H   -0.009581

6 H   -0.009581

7 C   -0.007863

8 O   -0.017921

9 C   -0.007863

10 O   -0.017921

11 C   -0.007863

12 O   -0.017921

13 C   -0.007863

14 O   -0.017921

15 C   0.044255

16 O   -0.023586

17 C   0.044255

18 O   -0.023586

Sum of Mulliken spin densities= 2.00000

Table 2   Mulliken atomic spin densities: for $^{3}(\mu_2\text{-}C_2H_2)Co_2(CO)_6$ at B3LYP/LANL2DZp

TD DFT Results for Singlet to Singlet transitions in $(\mu_2-C_2H_2)Co_2(CO)_6$

Excitation energies and oscillator strengths:

Excited State 1:   Singlet-B1   2.1748 eV   570.09 nm f=0.0013
    59 -> 67   -0.12921
    66 -> 67   0.64946

This state for optimization and/or second-order correction.

Copying the excited state density for this state as the 1-particle RhoCI density.

Excited State 2:   Singlet-B2   2.9485 eV   420.50 nm f=0.0006
    57 -> 67   -0.10783
    64 -> 67   0.66633
    65 -> 67   0.10100

Excited State 3:   Singlet-A2   3.0145 eV   411.29 nm f=0.0000
    58 -> 67   0.10349
    62 -> 67   0.66856

Excited State 4:   Singlet-A1   3.0321 eV   408.90 nm f=0.0002
    60 -> 67   0.52324
    63 -> 67   0.41758

Excited State 5:   Singlet-A1   3.0944 eV   400.67 nm f=0.0012
    60 -> 67   -0.44065
    63 -> 67   0.50257

Excited State 6:   Singlet-B2   3.2176 eV   385.33 nm f=0.1090
    59 -> 68   -0.10106
    61 -> 67   -0.22033
    64 -> 67   -0.10484
    65 -> 67   0.53699
    66 -> 72   0.11054
    66 -> 76   -0.23921
    66 -> 78   0.16302

Energy calculations on parallel and perpendicular structures as per Hoffmann et al.[14]

Repeated attempts to locate a parallel isomer on the singlet potential energy surface using both B3LYP/Lanl2dzp and B3LYP/Tzvp model chemistries failed. However the semiempirical approach used by Hoffmann was used to estimate the energy of this species and this was compared to the energy of the optimized perpendicular structure at the B3LYP/Tzvp level. The results are outlined in the following table.

Based on semi empirical Calculations as per Hoffmann

	a.u.	Joules	kJ mol^{-1}	ΔE (kJ mol^{-1})	eV	nm
Parallel	-3523.19	-1.54E-14	-9251468.5	490.12	5.07975	244.106
Perpindic	-3523.37	-1.54E-14	-9251958.6			

Coordinates used in calculation of energy

Perpendicular

Center	Atomic	Atomic	Coordinates (Angstroms)		
Number	Number	Type	X	Y	Z

1	27	0	0.000000	1.245131	0.135724
2	27	0	0.000000	-1.245131	0.135724
3	6	0	0.664790	0.000000	1.509350
4	6	0	-0.664790	0.000000	1.509350
5	1	0	1.519242	0.000000	2.164530
6	1	0	-1.519242	0.000000	2.164530
7	6	0	-1.466459	1.550542	-0.909410
8	8	0	-2.392424	1.753069	-1.541215
9	6	0	1.466459	-1.550542	-0.909410
10	8	0	2.392424	-1.753069	-1.541215
11	6	0	-1.466459	-1.550542	-0.909410
12	8	0	-2.392424	-1.753069	-1.541215
13	6	0	1.466459	1.550542	-0.909410
14	8	0	2.392424	1.753069	-1.541215
15	6	0	0.000000	-2.749518	1.110337
16	8	0	0.000000	-3.690341	1.753145
17	6	0	0.000000	2.749518	1.110337
18	8	0	0.000000	3.690341	1.753145

Parallel (using semi empirical approach of Hoffmann[14])

Center	Atomic	Atomic	Coordinates (Angstroms)		
Number	Number	Type	X	Y	Z

1	27	0	-1.487486	-0.000006	-0.492449
2	27	0	1.264463	0.000003	0.177477
3	6	0	-0.097841	-0.000007	-1.908892
4	6	0	1.225453	0.000014	-1.778237
5	1	0	-0.667274	-0.000023	-2.852391
6	1	0	2.002389	0.000025	-2.538454
7	6	0	-2.913345	-0.000002	0.600978
8	8	0	-3.852387	0.000001	1.300668
9	6	0	2.068659	-1.590428	0.087772
10	8	0	2.740401	-2.552648	0.003461
11	6	0	0.803169	-0.000010	1.914838
12	8	0	0.483037	-0.000017	3.044055
13	6	0	-1.218637	-1.775736	-0.511149
14	8	0	-1.031831	-2.929402	-0.550616
15	6	0	2.068627	1.590449	0.087789
16	8	0	2.740351	2.552683	0.003490
17	6	0	-1.218640	1.775725	-0.511155
18	8	0	-1.031841	2.929392	-0.550628

-

Bibliography

1   J. Makranczy, K. Megyery-Balog, L. Rosz, D. Patyt, *Hung. J. Ind. Chem.*, **1974**, 4, 269

2   A.F. Diaz, J. Crowley, J. Bargon, G.P. Gardini, J.B. Torrance, *J. Electroanal. Chem.*, **1981**, 121, 355.

3   A. Arnaz, M.-L. Marcos, C. Moreno, D.H. Farrar, A.J. Lough, J.O. Yu, S. Delgado, J. Gonzalez-Velasco, *J. Organomet. Chem.,* **2004**, 689, 3218.

4   A. Arnanz, M.-L. Marcos, S. Delgado, J. Gonzalez-Velasco, C. Moreno, *J. Organomet. Chem.*, **2008**, 693, 3457.

5   G. Zotti, G. Schiavon, S. Zecchin, A. Berlin, *Synth. Met.*, **1998**, 97, 245.

6   (a) M. Shiotsuka, Y. Inui, Y. Sekioka, Y. Yamamoto, S. Onaka, *J. Organomet. Chem.*, **2007**, 692, 2441. (b) N. Esho, B. Dvies, J. Lee, R. Dembinski, *Chem. Comm.*, **2002**, 332.

7   (a) C. Herbivo, A. Comel, G. Kirsh, A.M.C. Fonesca, M. Belsley, M.M.M. Raposo, *Dyes and Pigments*, **2010**, 86, 217. (b) Y. Liu, J. Zhou, X. Wan, Y. Chen, *Tetrahedron*, **2009**, 65, 5209.

8   S.M. Draper, C. Long, B.M. Myers, *J. Organomet. Chem.*, **1999**, 588, 195.

9   A.C. Coleman, C. Long, A. Meetsma, B.L. Feringa, W.R. Browne, M.T. Pryce, *Dalton Trans.,* **2009**, 7885.

10   A. Arnanz, M.-L. Marcos, S. Delgado, J. Gonzalez-Velasco, C. Moreno, *J. Organo. Chem.*, **2008**, 693, 3457.

11   Platts, J. A.; Evans, G. J. S.; Coogan, M. P.; Overgaard, J. *Inorg. Chem.* **2007**, *46*, 6291-6298

12   Frisch, M. J. ; Trucks, G. W.; Schlegel, H. B.; Scuseria, G. E.; Robb, M. A.; Cheeseman, J. R.; Montgomery, J. J. A.; Vreven, T.; Kudin, K. N.; Burant, J. C.; Millam, J. M.; Iyengar, S. S.; Tomasi, J.; Barone, V.; Mennucci, B.; Cossi, M.; Scalmani, G.; Rega, N.; Petersson, G. A.; Nakatsuji, H.; Hada, M.; Ehara, M.; Toyota, K.; Fukuda, R.; Hasegawa, J.; Ishida, M.; Nakajima, T.; Honda, Y.; Kitao, O.; Nakai, H.; Klene, M.; Li, X.; Knox, J. E.; Hratchian, H. P.; Cross, J. B. ; Adamo, C.; Jaramillo, J.; Gomperts, R.; Stratmann, R. E.; Yazyev, O.; Austin, A. J.; Cammi, R.; Pomelli, C. J.; Ochterski, W.; Ayala, P. Y.; Morokuma, K.; Voth, G. A.; Salvador, P.; Dannenberg, J. J.; Zakrzewski, V. G.; Dapprich, S.; Daniels,

A. D.; Strain, M. C.; Farkas, O.; Malick, D. K.; Rabuck, A. D.; Raghavachari, K.; Foresman, J. B.; Ortiz, J. V.; Cui, Q.; Baboul, A. G.; Clifford, S.; Cioslowski, J.; Stefanov, B. B.; Liu, G.; Liashenko, A.; Piskorz, P.; Komaromi, I.; Martin, R. L.; Fox, D. J.; Keith, T.; Al-Laham, M. A. Peng, C. Y.; Nanayakkara, A.; Challacombe, M.; Gill, P. M. W.; Johnson, B.; Chen, W.; Wong, M. W.; Gonzalez C.; Pople, J. A. Gaussian, Inc., Wallingford CT, **2004**.

13   Iwashita, Y.; Tamura, F.; Nakmura, A., *Inorg. Chem.* **1969**, *8*, 1179-1183

14   D.M. Hoffmann, R. Hoffmann, C.R. Fisel, *J. Am. Chem. Soc.*, **1982**, 104, 3858.